RUSSIAN ACADEMY OF SCIENCES
B. P. Konstantinov Petersburg Nuclear Physics Institute

PNPI

High Energy Physics Division

MAIN SCIENTIFIC ACTIVITIES
2002–2006

GATCHINA
2007

PREFACE

This volume presents summary of activities of the High Energy Physics Division (HEPD) in the five years period 2002–2006. It can be considered as a continuation of the previous editions describing the HEPD activities prior to 1997 (PNPI-XXV, High Energy Physics Division. Main Scientific Activities 1971–1996) and for the period 1997–2001 (PNPI-XXX, High Energy Physics Division. Main Scientific Activities 1997–2001).

The HEPD of today is a laboratory with the total staff of 360 persons, including 155 physicists and 110 engineers, 112 of them being candidates and doctors of sciences. As in the previous years, the HEPD strategy was, on one hand, to exploit in a maximum possible way the accelerator facilities available at PNPI and, on the other hand, to maintain active international cooperation in fundamental research in the world's most advanced accelerator centers.

The PNPI 1-GeV proton synchrocyclotron remains a valuable and reliable instrument for nuclear studies, for medical applications, as well as for radiation studies of various materials and equipment. The beam time provided by the synchrocyclotron in the last years was around 2000 hours per year. Together with PNPI users, scientists from other scientific centers, including research groups from Japan, France, Italy and USA, participated in the experiments at the synchrocyclotron. The medical 1-GeV proton beam was successfully used for neurosurgery. The total number of patients treated at the PNPI Proton Therapy Center reached 1300. Besides the synchrocyclotron, the PNPI electrostatic accelerator was also active, being used for sensitive control of the surface material contamination. At the same time, the PNPI engineers continued construction of the 80 MeV high-intensity isochronous proton cyclotron which should be specialized on radioactive isotopes production and on various medical applications.

During this period, the HEP Division participated in many experiments at leading accelerator centers. Among them: the L3 experiment at CERN, D0 experiment at FNAL (USA), PHENIX and Crystal Ball experiments at BNL (USA), HERMES experiment at DESY (Germany), MuCap experiment at PSI (Switzerland), several experiments at GSI (Germany), COSY experiment at Juelich (Germany), ISOLDE experiment at CERN, and some other experiments at the accelerators at IHEP (Protvino), at ITEP (Moscow), at JINP (Dubna), as well as at the accelerators in the Universities in Darmstadt (Germany), in Jyvaskyla (Finland), in Bonn (Germany), in Mainz (Germany).

One of the major activities of the HEP Division in the last ten years was preparations for the LHC experiments CMS, ATLAS, ALICE and LHCb. A great amount of various experimental equipment was produced for each of these experiments at specially organized production sites at PNPI. More than 100 PNPI specialists were involved in this work. This production was completed by the end of 2006. The produced equipment was tested and delivered to CERN for installation into the LHC detectors. The commissioning of the LHC detectors should be completed by mid of 2008.

The future plans of the HEP Division include participation in the experiments at the new accelerator complex FAIR at GSI (Germany). PNPI will participate in design and construction of the large-scale detectors CBM and PANDA, and also will take part in the NuStar program.

After the start up of the LHC collider, participation in the LHC experiments will be an important part of the physics program at PNPI. Also, we shall continue participation in the fixed target experiments, whenever we could offer some new ideas and expect high quality physics.

Alexey Vorobyov,
Director of High Energy Physics Division

STATUS OF ACCELERATOR FACILITIES AT PNPI

PNPI SYNCHROCYCLOTRON IN 2002–2006

N.K. Abrossimov, G.F. Mikheev, G.A. Riabov, and the accelerator staff

1. The PNPI synchrocyclotron and its facilities

The PNPI synchrocyclotron (SC) was designed for research in the field of elementary particle and nuclear physics, solid state physics, and for applied physics. SC is intensively used also for proton therapy and nuclear medicine [1].

Figure 1 shows a view of the PNPI synchrocyclotron complex.

Fig. 1. A view of the PNPI synchrocyclotron complex

A scheme of the synchrocyclotron experimental area is shown in Fig. 2. The main SC parameters are as follows: proton energy – 1000 MeV, internal beam intensity – 3 μA, intensity of the extracted proton beam – 1 μA, macro bunch duration – 10 ms, micro bunch duration – 10 ns, repetition rate – 50 Hz, accelerating voltage amplitude – 8 kV, accelerating frequency range of a dee – 30.2–13.0 MHz, macro duty cycle – 0.52, magnet weight – 8000 tons, consumed electrical power – 2.3 MW. The experimental area is about 20000 m^2. The SC staff is about 70 persons.

After 35 years of successful operation, PNPI SC remains an actively operating proton accelerator, executing a competitive research program in the field of nuclear and applied physics. In spite of the fact that modern "meson factories" exceed considerably PNPI SC in the beam intensity, nevertheless, due to some accelerator features, there is a significant area of researches which is not overlapped by other facilities.

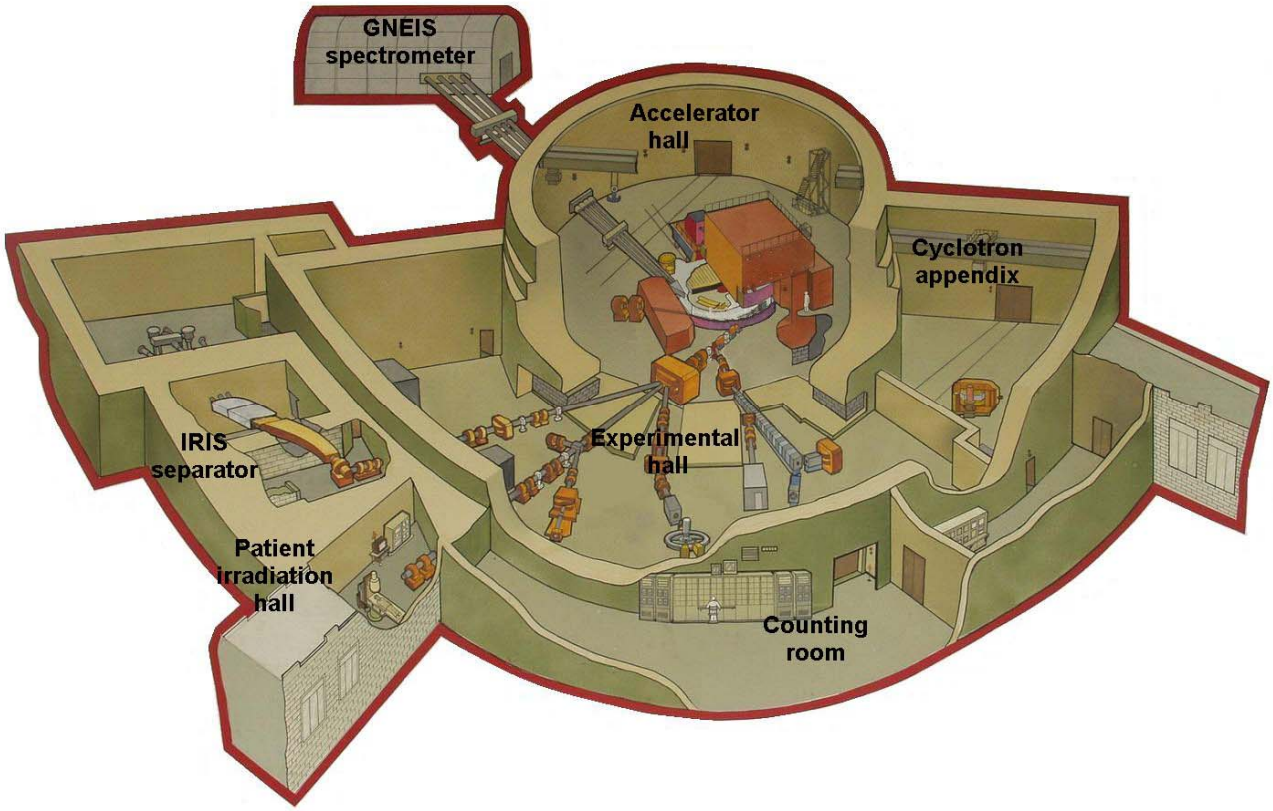

Fig. 2. Scheme of the synchrocyclotron experimental area

PNPI SC accelerates protons up to the energy of 1000 MeV, that is to the energy higher than that at the meson factories. The energy of 1000 MeV is optimal for nuclear physics of intermediate energies, in particular, for an investigation of nuclear density distributions by measurement of proton-nucleus scattering. It appeared possible to study the production of K^+-mesons and η-mesons at proton and at pion beams, respectively. The proton energy of 1000 MeV is also considered to be optimal for transmutation researches. Due to a higher energy of the primary beam, the energy of secondary π-meson beams of SC is higher than that of the meson factories, which is essential for partial wave analyses of pion-nucleon scattering and for baryon spectroscopy investigations. Beam lines of PNPI SC are shown in Fig. 3, and the beam parameters are presented in Tables 1–3.

Table 1

Proton beams

Particle	Energy, MeV	Energy resolution, %	Intensity, s^{-1}	Beam line	Comments
p	1000	1	6×10^{12}	P1, P2, P3	Primary beam
p	1000	1	10^8	P2	Medical beam 3–5 mm
p	1000	3×10^{-3}	10^{10}	P2	Monochromatic beam
p	1000	1	10^{10}		Second medical beam

Table 2

Secondary particle beams

Particle	Momentum, MeV/c	$\Delta p/p$, %	Intensity, s^{-1}	Beam line	Comments
π^+ π^-	450 450	6 6	10^6 3×10^5	π1-channel	Achromatic mode
π^+ π^- μ^+	250 250 29	2.5–12 2.5–12 12	3×10^5–10^7 10^5–5×10^6 3×10^4	π2-channel	Achromatic mode “Surface” mesons
μ^+ μ^-	170 160	10 10	3×10^5 9×10^4	μ-channel	Separated beams

Table 3

Neutron beams

Energy, MeV	Intensity*, s^{-1}	Pulse duration	Frequency, Hz
10^{-2} eV–10^2 MeV	3×10^{14}	10 ns	50

* Total intensity at the neutron production target

Some specialized experimental facilities are developed at PNPI SC.

The IRIS facility is aimed at investigations of short lived isotopes far from β-stability line. New types of targets for a high production rate of rare isotopes have been developed at PNPI in collaboration with scientists from Italy, France and Canada. The IRIS Laboratory is a well known world research center. This laboratory is working in cooperation with other centers, such as ISOLDE at CERN.

The neutron time-of-flight facility. The time-of-flight neutron spectrometer GNEIS has a 10 ns spark pulse and a 48.5 m flight base. The neutron beam is used for investigations of neutron interaction cross sections. The cross sections for inelastic neutron-nucleus interaction in the case of heavy nuclei have been measured in collaboration with Japan scientists in the frame of ISTS-19-72 program.

The proton therapy facility. The proton therapy facility has been developed at PNPI SC in collaboration with the Central Research Institute of Roentgenology and Radiology (CRIRR) of the Russian Ministry of Public Health. The main peculiarity of the Gatchina facility is application of the 1000 MeV proton beam for irradiation of intracranial targets in human brain. Up to now, more than 1300 patients have been treated.

Cooperation with the scientific community. 9 grants of RFBR and 4 grants of ISTS have been obtained last five years for support of researches at PNPI SC.

36 scientists from 20 foreign centers of the USA, Switzerland, Japan, France, Italy and others took part in 2002–2006 in the SC scientific program.

Also, the Russian research centers – Khlopin Radium Institute, St.-Petersburg; JINR, Dubna; RNC SIIEP, Saratov; GSC PEI, Obninsk; ITEP, Moscow; RSC KI (the Russian Scientific Center “Kurchatov Institute”), Moscow; SEA SPELS, MEPhI, Moscow; Ioffe PhTI, St.-Petersburg and others – took part in the experimental program at SC.

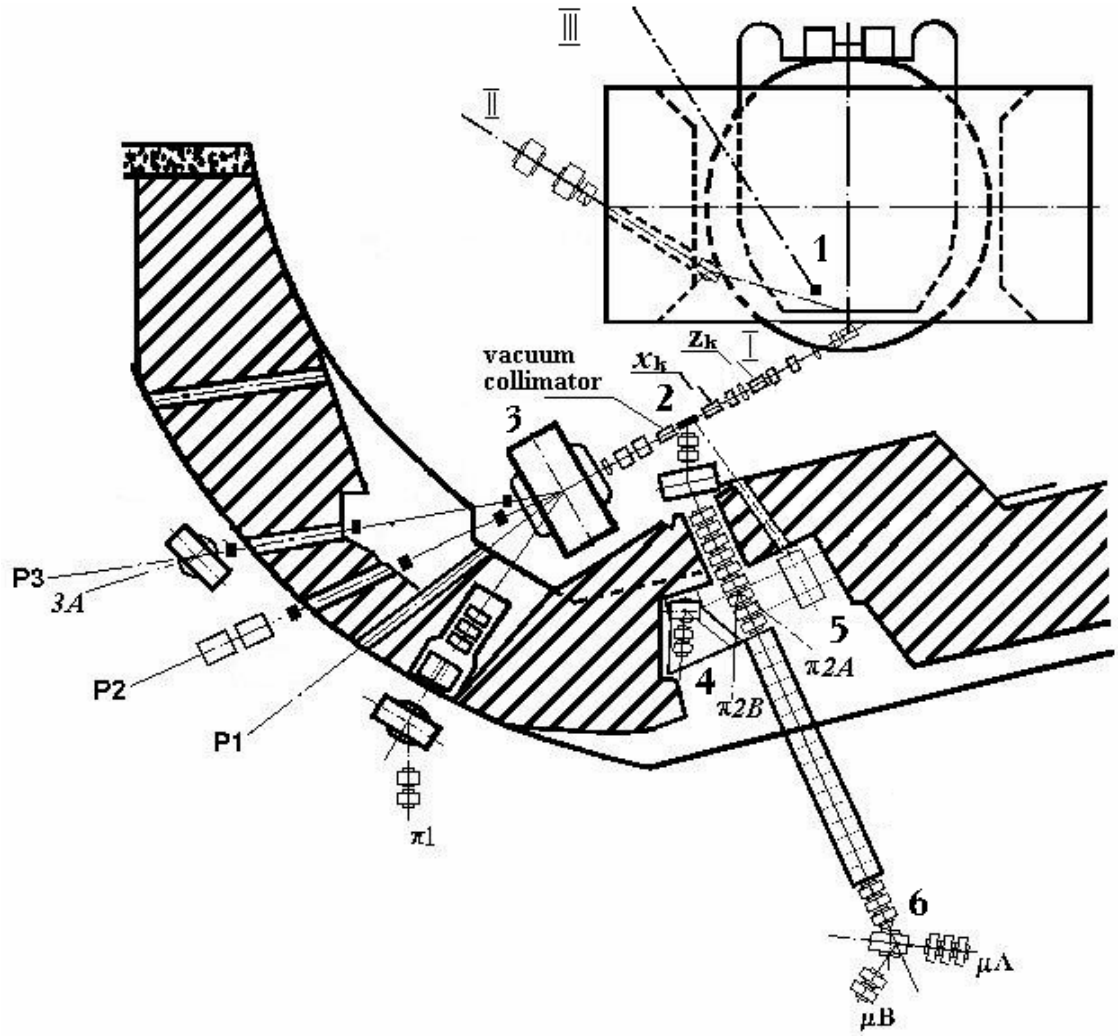

Fig. 3. Beam lines of PNPI SC. **I –** the primary proton beam 6×10^{12} s^{-1}; **II** – an additional small intensity proton beam 10^{10} s^{-1}; **III** – a neutron beam; **P1, P2, P3** – directions of proton beams; **1** – neutron production target; **2** – meson production target; **3** – distributing magnet of the proton beam; **π1** – high energy meson channel; **4**, **5** – removable platform with the second magnet for **π2A**, **π2B** – low energy meson beams; **6** – separated μ-meson beams **μA**, **μB**; $\mathbf{z_k}$ – vertical magnet-corrector; $\mathbf{x_k}$ – horizontal magnet-corrector; black squares – intermediate proton beam dampers

2. SC operation in 2002–2006

During this period, PNPI SC was in operation for physical experiment ~2500 hours per year only.

The accelerator time distribution between physical experiments and applied researches is presented in Table 4 and in Fig. 4.

PNPI SC has a support from the Russian Academy of Sciences and from the Ministry of Science and Education.

In 2002–2006, SC users published 140 articles and reports including 20 articles on accelerator technology. 9 candidate and 2 doctor dissertations have been defended.

Table 4

№	Subject		2002	2003	2004	2005	2006	Σ hours
1	IRIS		408	384	720	864	648	3024
2	μSR-experiment		355	336	372	432	850	2345
3	Pion-nucleon interactions		384	336	288	288	264	1560
4	Baryon spectroscopy		216	–	254	408	360	1238
5	Proton therapy		240	252	276	228	264	1260
6	Nuclear fission		149	120	120	–	–	389
7	GNEIS		–	384	–	–	–	384
8	Radiation test	RPL	48	24	60	84	72	288
9		AD	24	36	24	68	48	200
10	FAMILON		120	–	–	12	–	132
11	Beam channeling and reflection by bent crystals		0	0	0	120	168	288
	Summary time		1944	1872	2114	2504	2674	11108

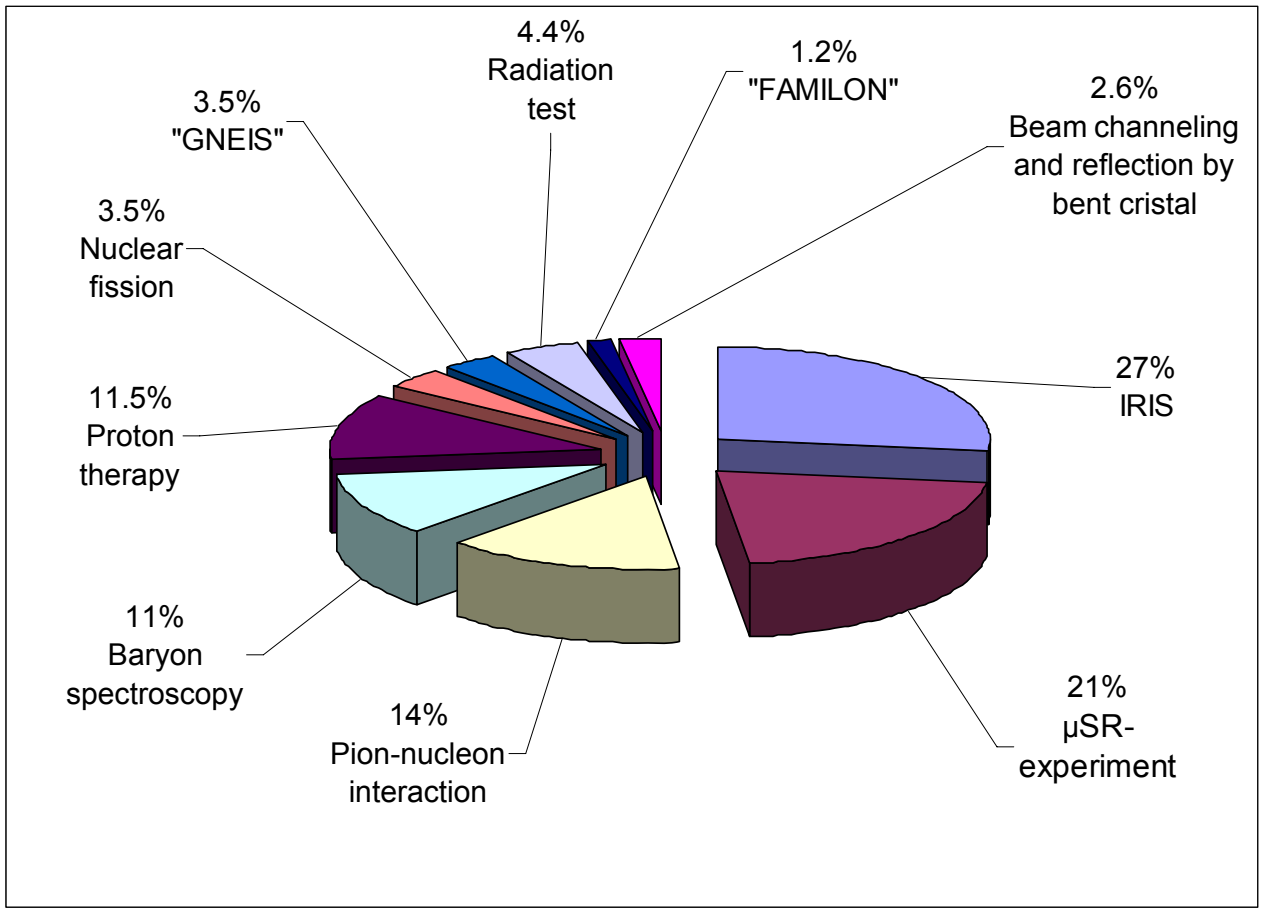

Fig. 4. Distribution of SC operation time among the experimental programs in 2002–2006

3. New experimental facilities at PNPI SC

In parallel with a routine SC operation, an upgrade of the SC facilities has been performed in 2002–2006.

3.1. A new proton beam of variable energy (ISTC № 1405)

The purpose of the project is to obtain a proton beam with an energy from 200 up to 1000 MeV by using the beam moderation in a degrader. PNPI SC accelerates protons up to the fixed energy of 1000 MeV with an intensity of 1 μA. However, for a solution of some problems of fundamental physics, as well as for some application tasks there is a necessity for a proton beam with variable energy. It is a common practice to decrease energy of the primary proton beam using a degrader. An advantage of the degrader method is absence of π-meson background at the exit channel. A shortcoming of this method is connected with a decrease of the beam intensity and with an increase of the beam size, as well as of the divergence and the energy spread due to interaction of the beam with the degrader substance. A Monte Carlo simulation was used to optimize the proton beam of variable energy. An application of the Monte Carlo method to this problem makes it possible to find all parameters of the beam in detail. The calculation algorithm consists of two major stages. At the first stage, the parameters of the beam after the degrader are simulated with the well-known "GEANT-3" code. At the second stage, the coordinates and momentum vectors of each proton after the degrader are used as input data for "MESON" and "OPTIMUM" codes [2, 3]. Experimental studies showed good agreement with the results of calculations of the intensity, beam size and momentum spread, as well as of the magnetic fields in dipole magnets and the gradients in quadrupole lenses of the beam line. The intensity of the variable energy proton beam is presented in Table 5 for two beam-line regimes (with one or two focusing doublets of quadrupole lenses) when the intensity of the primary beam at 1000 MeV is equal to 3×10^{12} s^{-1}.

Table 5

Intensity of the variable energy proton beam when the intensity of the primary proton beam is equal to $3\cdot10^{12}$ s^{-1}

E, MeV	P, MeV/c	Intensity of variable energy proton beams, s^{-1}		
		one doublet experiment	two doublets experiment	two doublets calculations
207	657	1.84×10^{7}	4.02×10^{7}	6.36×10^{7}
301	810	4.62×10^{7}		2.49×10^{8}
404	960	9.69×10^{7}	2.07×10^{8}	7.50×10^{8}
505	1097	2.07×10^{8}		2.11×10^{9}
612	1234	2.58×10^{8}		5.46×10^{9}
702	1345	6.72×10^{8}	2.37×10^{9}	1.41×10^{10}
802	1466	1.00×10^{9}	9.03×10^{9}	4.26×10^{10}
899	1580	2.13×10^{9}	3.09×10^{10}	1.77×10^{11}

The variable energy beam developed in the frame of ISTS program can be used also for nuclear physics, for investigation of radiation effects in electronic components, for proton therapy, *etc*.

The method of calculation tested in our experiment can be recommended for the implementation at other accelerators to design beam lines with absorbers.

3.2. Upgrade of the proton therapy facility

The proton stereotaxic therapy facility [4, 5] at PNPI has been in operation since 1975. The upgrade program includes designing of two new computer-controlled proton beam collimators, a system of proton beam profilometers for the beam position and size diagnostics, a computer regulation of currents in dipole magnets and quadrupole lenses of the beam line and a computer control of dosimetry and beam diagnostics at the irradiation point [6, 7]. A necessity of modernization is prescribed by the fact that the beam collimators components have come close to the radiation damage limit, and computer control and regulation systems have become out of date. The first collimator, located at the accelerator hall, consists of two pairs of horizontal and vertical copper plates cooled by water, with a length of 250 mm along the beam, which can be moved transversely to the beam. Four remotely regulated electric drives are used to move the plates and to adjust the collimator hole. A regulation range of the size of this hole for a beam is from zero (that is when the beam is completely blocked) up to 180 mm × 180 mm.

The second halo collimator, located in the accelerator experimental hall, has a fixed hole with the diameter of 20 mm. The external diameter of this collimator is 150 mm, the length along the beam is 700 mm, 5 electric motors for an alignment of the collimator components along the beam being used. A new mechanical construction with new electric drives has been developed and manufactured. Step-by-step motors are used for an electric drive, and an automatic control system with a new hardware and software has been designed and manufactured. The beam position and size along the beam line are measured using new profilometers. Each profilometer consists of two pairs of semi-conducting plate-probes which can be moved transversely to the beam axis to measure the X- and Y-profiles of the beam. A semiconductor probe measures the beam current distribution along the X- and Y-coordinates with a 1 mm step. A beam scanner at the irradiation point with a measurement range of 25 mm × 25 mm was reconstructed also. A computer system regulates the probe movement, performs on-line processing of the results of the beam profile measurements, and makes it possible a visualization on a computer display of the horizontal and vertical profiles and 2D isocount contour distributions. A new absorbed dose monitor is used to control the expose dose and beam current stability, and to switch off the accelerator in case when a planned dose is reached over. Four PCs with Windows XP operation system, integrated in a local area network, are used for the current control of the proton therapy facility.

In the frame of the proton therapy facility upgrade, new collimators with a long guaranteed lifetime and a new computer control system have been developed. This increases reliability of the irradiation, reduces time for a beam tuning and enlarges the facility capacity. The upgrade program has been executed with a financial support of the Leningrad district Government.

3.3. Modernization of the SC equipment

The PNPI synchrocyclotron has been in operation since 1970, and some SC equipment is out of the guaranteed lifetime, and is morally outdated. A program of the equipment repair, replacement and modernization was carried out during 2002–2006.

1. The water-cooling system goes out of operation before other systems due to corrosion effects. A new compact water-cooling tower with forced air ventilating such as GRD-350, fabricated at the St.-Petersburg plant "TEPLOMASH", has been put into operation in connection with a productivity decrease and degradation of the old aerobic water-cooling tower. The main parameters of the new tower are as follows: water expenditure – 350 m^3/hours, thermal flux – 2×10^3 kW, air expenditure – 165×10^3 m^3/hour, ventilator power – 7.5 kW, weight – 3.2 tons. Two new heat exchangers have been installed between the first and second loops of the water-cooling system. It is a high-performance, turbulent, plate-type heat exchanger T40 MHL/CDS16/86 with a total power heat transfer of 2.3 MW.

2. A number of high-power and high-voltage underground cables between the transformer substations and the SC building have been replaced to save efficiency of the 10 MW SC power supply system.

3. A modernization of the SC radiation control (RC) system has been carried out. A new system provides the data acquisition of radiation fields in technological zones and on workplaces of SC. The RC system provides the personal radiation monitoring for all SC users (about 400 persons). The thermo-luminescent

dosimeters on the basis of detectors DTG-4 are used for the individual radiation control. The RC system passes an annual Government trial and metrology certification.

4. Plans for future

At present, the program of improvements of the PNPI accelerator facilities is in the stage of discussion. The SC maintenance is the top task of the accelerator staff. The next task is an upgrade program for SC and the experimental area. By now, this program includes the next stage upgrade of the proton therapy facility, the development and modernization of the facility for radiation tests of electronics components, and putting into operation of the new isochronous cyclotron.

4.1. Development and modernization of the radiation test facility

The radiation test facility for the investigation of electronics components is in operation at a PNPI SC proton beam. Usually test experiments are fulfilled in cooperation with specialized organizations, such as Research Institute "Electronstandart" in St.-Petersburg, the Scientific Research Institute of Apparatus in Lytkarino, Moscow district, Scientific association "Specialized Electronic Systems SPELS", MEPhI, Moscow, *etc.* We are going to improve the service quality by using new computer-controlled equipment. In addition to the existing proton beam, we intend to develop a specialized neutron beam to perform radiation tests also at a neutron beam. According to the international regulation JEDEC STANDARD, all integrated schemes used in aircraft should pass through a radiation control on neutron beams with a neutron spectrum similar to that in the near-earth space. A neutron facility simulating a neutrons flux spectrum in atmosphere with an intensity of 10^8 times higher than that in the atmosphere has been developed at the Los Alamos accelerator with 800 MeV protons. One hour of irradiation at such a beam is equivalent to 100 years of flight. Due to high proton energy of PNPI SC, a similar neutron beam can be developed at PNPI. Such a neutron beam would be the second in the world, and unique in Europe, for electronics components tests. A commercial use of such a beam will be possible as far as the European corporations show interest to this beam in Europe. The cost of an exposition on such a beam is approximately 600–800 € per hour.

4.2. A 80 MeV H^--ion isochronous cyclotron with the beam intensity of 100 μA

The status of this project in more detail is presented in Ref. [8].

Putting into operation of a new cyclotron will provide:

– further development of the existing at PNPI fundamental and applied researches (investigation of short-lived isotopes, nuclear fission, study of nucleus structure, biophysics, *etc.*);

– production of high quality radioactive isotopes for medicine, which are inaccessible in reactors (fluorine-18, potassium-43, iron-52, gallium-67, bromine-77, indium-111, iodine-123, thallium-201, *etc.*);

– proton therapy of eyes melanoma, surface cancer, *etc*.

4.3. A project of multiple-discipline proton therapy facility at PNPI SC for treatment of oncological internal organs diseases and brain diseases

The proton stereotaxic therapy facility on a 1000 MeV proton beam has been in operation since 1975. The irradiation is performed in a specialized medicine appendix. A special proton beam with the diameter of 3–5 mm with a small background of secondary particles was formed. By now about 1300 patients have been treated in the Gatchina center. The proton therapy at 1000 MeV yields very good results, but its application is expedient for a limited set of diseases only. In this connection, it was decided to investigate an opportunity of developing at the PNPI synchrocyclotron a proton beam with an energy of 100–200 MeV for traditional treatment of oncological diseases of internal organs using the Bragg peak. Preliminary investigations show a possibility to produce such a beam. The use of a beam with an energy of 200 MeV for irradiations of cancer diseases will raise a treatment potential of the Gatchina proton therapy facility.

Thus, on the basis of the existing in Gatchina proton therapy facility it is possible to develop – without a

new civil work and at rather modest expenditures – a new multiple-discipline proton therapy facility with the following capabilities:

- Existing patients treatment by the 1000 MeV proton beam using "Gatchina method";
- Patients treatment of oncological internal organ diseases by the 200 MeV proton beam using the Bragg peak irradiation method;
- Treatment of eyes melanoma and skin oncological diseases by the 80 MeV proton beam;
- Development of **PET** – tomography using cyclotron isotopes;
- Production of high quality medical isotopes for all Northwest region.

5. Conclusion

The PNPI synchrocyclotron has been actively operating since 1970 for a purpose of physical experiments in the range of intermediate energies up to 1000 MeV. A rich arsenal of research installations and equipment and the availability of world-rate experts and scientists allow us to carry out at the PNPI synchrocyclotron a wide spectrum of fundamental and applied research programs and to fulfil a competitive scientific programs in close cooperation with foreign and Russian research centers working in the given scientific direction.

References

1. N.K. Abrossimov, A.A. Vorobyov and G.A. Riabov, in *PNPI-XXV, High Energy Physics Division. Main Scientific Activities 1997–*2001, Gatchina, 2002, p. 6.
2. N.K. Abrossimov *et al.,* Preprint PNPI-2525, Gatchina, 2003. 31 p.
3. G.A. Riabov, V.G. Riabov and M.G. Tverskoy, Nucl. Instr. Meth. A **558**, 44 (2006).
4. N.K. Abrossimov, A.A. Vorobjev *et al.*, Medical Radiology, **№ 8**, 10 (1987).
5. N.K. Abrossimov *et al.*, in *PNPI-XXV, High Energy Physics Division. Main Scientific Activities 1997–2001*, Gatchina, 2002, p. 312.
6. N.K. Abrossimov *et al.*, in *Proceedings of the 11th International Conference on Charged Particles Accelerators Applied in Medicine and Industry* (St.-Petersburg, 10 – 14 October 2005), SPbSU, 2006, p. 172.
7. N.K. Abrossimov *et al.*, in *Book of Abstracts of the Conference on New Trends in Nuclear Physics Applications and Technology* (Pavia, Italy, 5 – 9 September 2005), p. 93; Journal of Physics: Conference Series **41**, 424 (2006).
8. N.K. Abrossimov *et al.*, this issue, page 15.

DESIGN AND CONSTRUCTION OF A 80 MeV H^--ION ISOCHRONOUS CYCLOTRON WITH BEAM CURRENT OF 100 μA

N.K. Abrossimov, S.A. Artamonov, V.P. Gres, V.A. Eliseev, E.M. Ivanov, Yu.T. Mironov, G.F. Mikheev, A.S. Pokrovsky, G.A. Riabov, V.A. Smolin, I.A. Petrov, B.B. Tokarev

1. Introduction

Design and construction of a 75–80 MeV H^--ion cyclotron with the beam current of 100 μA are in progress at PNPI. When making the decision to build such a cyclotron, the following considerations were taken into account: increasing production of radioisotopes for medicine, organizing at PNPI an ocular melanoma irradiation facility, as well as extending traditional studies of short-lived isotopes. The accelerator itself is installed in the building of the existing PNPI synchrocyclotron in the available area of the experimental hall. To minimize the expenditures while designing the cyclotron, an attempt was made to use at most the existing synchrocyclotron infrastructure, *i.e.* the building, the bridge crane for 30 tons, the electrical power, water cooling, ventilation systems, *etc.* The iron yoke of the existing synchrocyclotron magnet model is used for the magnet system. For protection against synchrocyclotron secondary beam radiation, a wall from concrete blocks with a thickness of 1.2 m and a height of 4.6 m has been constructed. Figure 1 shows a view of the cyclotron magnet.

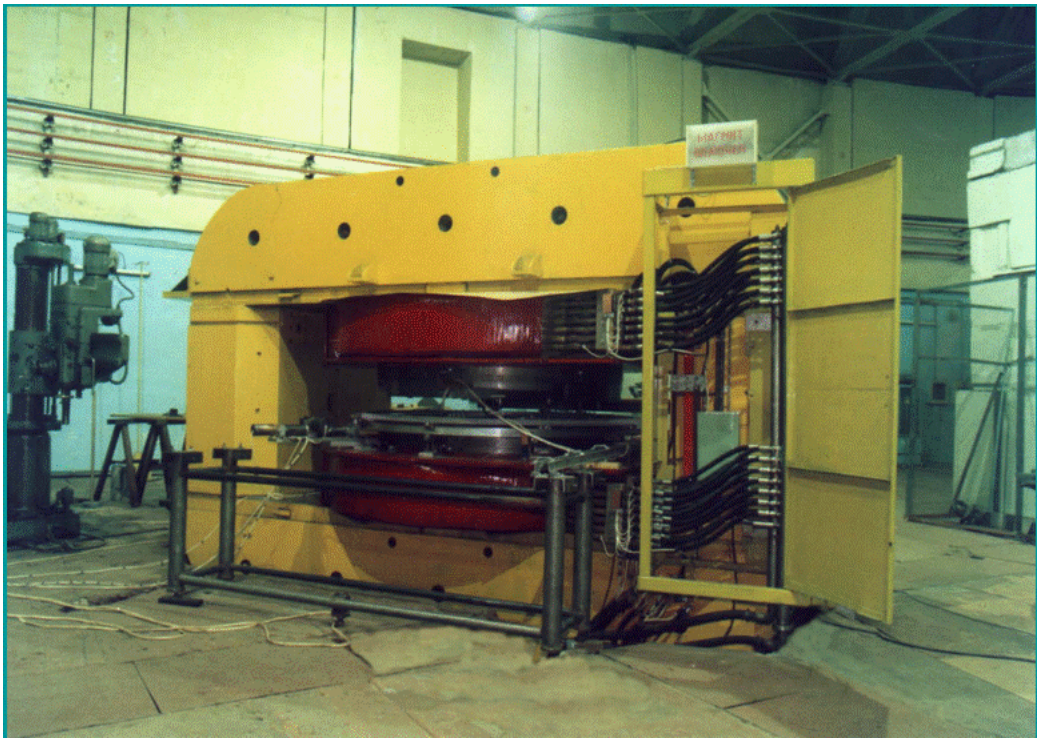

Fig. 1. The cyclotron magnet

To have an access inside the chamber, the upper magnet bar with a pole and the chamber lid can be lifted on 450 mm using four hydraulic jacks.

The cyclotron parameters are given in Table 1.

The project has been published in the Proceedings of the International and National cyclotron conferences [1, 2]. The status of the project development before 2000 is described in Ref. [3]. The progress report for the period of 2001–2006 is presented below.

Table 1

The cyclotron parameters

MAGNET	
Pole diameter	2.05 m
Valley gap	386 mm
Hill gap (min.)	156 mm
Number of sectors	4
Spiral angle (max.)	65 degree
Isochronous field in the center	1.352 T
Flutter (max.)	0.025
Extraction radii	0.40–0.90 m
Ampere – turns	3.4×10^5
Power	120 kW
Weight	250 t
RF SYSTEM	
Frequency	41.2 MHz
Voltage	60 kV
Harmonic	2
RF power	2×40 kW
VACUUM	
Pressure	10^{-7} torr
2 cryogenic pumps	2×6500 l/s (H_2)
Turbo molecular pump	
H^- SOURCE	
Surface-plasma, d. c.	2.5 mA
Multipole source d. c.	1.5 mA
Injection energy	26 kV
AXIAL INJECTION SYSTEM	
Transport beam line from source:	
Solenoid lens,	
The solenoid,	
Inflector	
EXTRACTION	
Energy	45–80 MeV
Method	Stripping

2. Progress in development of the cyclotron subsystems and the project upgrade in 2002–2006

The magnet and the magnetic field. The cyclotron magnet has been installed by 2002 simultaneously with the radiation protecting wall, power supplies and a system of water-cooling. After that, magnetic measurements have been started.

The cyclotron magnetic field must meet some requirements: isochronism of particle orbits in the whole energy range is needed, the magnetic rigidity on the final radius of acceleration must correspond to 80 MeV energy, an azimuthal variation of the magnetic field must provide axial focusing. In addition, for accelerating H^- -ions, there is a supplementary and very essential requirement related to H^- losses due to electro-dissociation in the magnetic field. In our case, to limit beam losses by 5%, the maximum field (in the field hills) on final radii should not exceed 17 kGs. To accelerate H^--ions up to the energy of 80 MeV in the 2 m diameter magnet, a special structure of the magnetic field has been developed. This structure is characterized by a low level of the magnetic field in the hills, a small flutter and the greatest spiral angle about 65–70 degrees. A view of the cyclotron magnet tips with the spiral sectors is shown in Fig. 2.

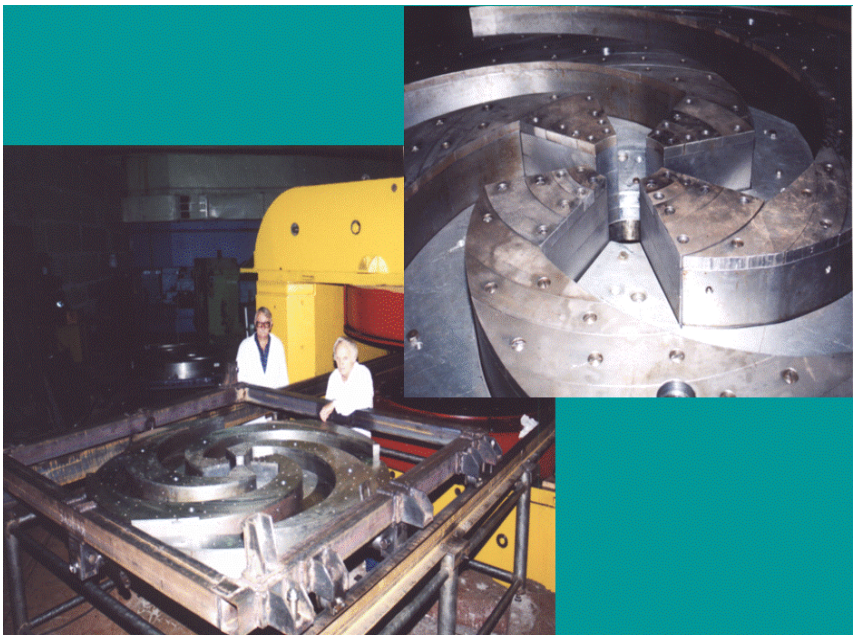

Fig. 2. A view of the cyclotron magnet tips with the spiral sectors before installation in the magnet

The iron sector pieces, usually named as shims, were used to correct the cyclotron magnetic field and to bring it to the required conditions. The initial set of shims has been chosen on a small model magnet with the scale 1:8 and has been manufactured at a plant together with other magnet components. The first measurements showed that the magnetic rigidity and vertical focusing can be provided in the magnet with the initial shim set, but the isochronism cannot. An azimuthally average magnetic field on radii near r = 70 cm was lower by 500 Gs than necessary. A correction of the shim configuration is to be done on a full-scale magnet as a result of consecutive approximations and tedious measurements. For this purpose, special equipment was developed: a computer-controlled measuring system with an accuracy of 10^{-4} based on 20 Hall probes, a computer-controlled magnet current regulator with an accuracy up to 10^{-5}, a NMR-probe for an exact field level fixation, an additional power supply for demagnetization of the magnet iron after the magnet is switched off. A new set of shims was found by using the method of trial-and-error. Four additional shims were installed on the magnet poles at the positions corresponding to the magnetic field hills and valleys as it is shown in Fig. 3.

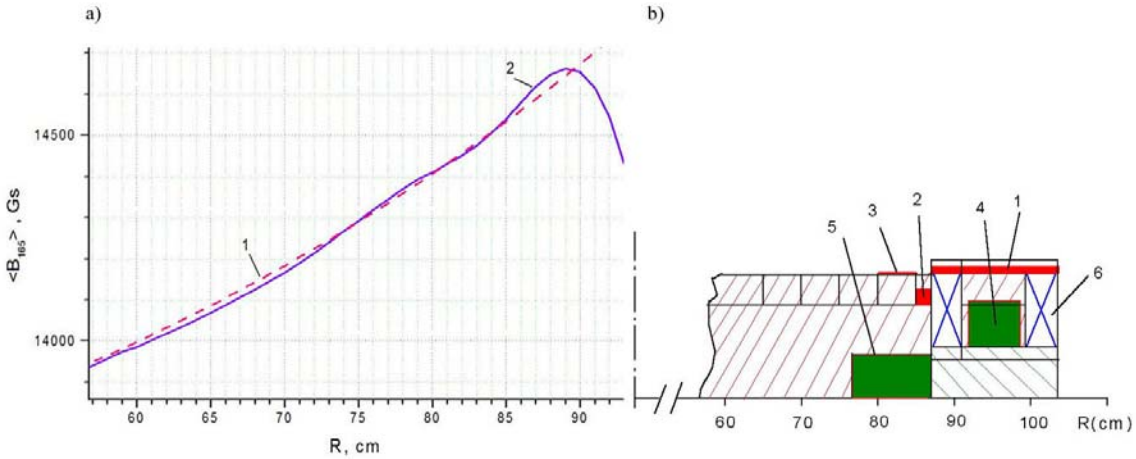

Fig. 3. Four additional shims installed on the magnet hills and valleys in 2006.
a) Azimuthally averaged magnetic field versus radius: 1– isochronous field; 2 – experimental situation at the end of 2006.
b) Modification of the shim set in 2006. Additional shims on hills are shown by red color, on valleys by green: 1 – 10 mm shim is replaced by 5 mm one, 2 – 18 mm shim is replaced by 9 mm one, 3 – 2 mm thickness shim is added on hills, 4 –5 – two 45 mm shims are added on valleys, 6 – harmonical coils

The installation of additional shims in the field valleys gives rise of the averaged magnetic field without increasing the field in the hills to restrict H^--ions electro-dissociation below 2%. The new set of shims has allowed to approach the necessary isochronous field to within 70 Gs. This process is in the correct direction, and it should be continued to achieve the isochronous magnetic field with an accuracy of several Gs.

The process of experimental selection and shims manufacturing appears to be very time-consuming and expensive. As a consequence, in parallel with measurements, attempts of shim selection by using three-dimensional magnetic field calculations has been undertaken. The Novosibirsk code MERMAID was used to calculate our complicated geometry magnet. In a test calculation, 20 million nodes have been used, and the results of the calculations agree with the experimentally measured ones within 10–20 Gs. Thus, with the help of calculations, we hope to find a combination of the magnet current and the shim configuration providing isochronism with an accuracy of 10–20 Gs. We expect that the final isochronism tuning with an accuracy of several Gs will be performed by experimental shimming.

H^--ion sources. Two types of H^--ion sources have been considered as prototypes of the cyclotron source. Each of the sources is installed on its own test facility. The first one is a surface-plasma Novosibirsk H^--ion source developed for the a. c. operation regime with the repetition rate of 100 Hz and 300–500 μs pulse duration. For the d. c. mode of operation the discharge power was increased up to 1 kW, and extensive anode and cathode cooling by water at 10 atmospheres was introduced. By now, the surface-plasma source generates 3.5 mA of d. c. H^--ion current at the energy of 4 keV and the cathode current of 3 A during a short time period. The lifetime of the cathodes is about one hour only due to the cathode material sputtering.

Our volume-plasma or multi-cusp source has been developed at the Efremov Institute for Gatchina cyclotron. Recent years, the source parameters have been considerably improved, and the source yields of 2 mA H^--ion current in the d. c. regime have been achieved. The lifetime of a 1 mm diameter cathode at 10 A cathode current is about 60 hours. The axial injection system tuning is to be started using this source.

Project upgrade. The project upgrade motivation can be formulated as follows:

– Recently, an essential progress in external sources and axial injection technology has been achieved. A rejection of the inner source and connected with it hydrogen leakage in the chamber has to offer essential relaxation for requirements to a productivity of the cyclotron pumping and vacuum equipment cost. In addition, a cyclotron with the external source is a clean machine – having in mind the radiation considerations – due to elimination of H^--ion losses on gas molecules emitted from the source.

– A copper cladding manufacturing with the explosion technology was replaced by a traditional one to reduce the project cost and production time.

– Furthermore, a new round vacuum chamber, a new arrangement of the chamber mechanism and extraction windows allow to increase adaptability to manufacturing and to reduce the project cost.

The chamber. The external diameter of the chamber is 3.3 m, the height of the chamber is 0.5 m in the region between the magnet coils and 162 mm in the magnet gap region, the thickness of the top and bottom lids being equal to 16 mm. The weight of the chamber made of stainless steel is 980 kg. To produce the vacuum of 10^{-7} torr inside the chamber, two cryopumps of the НВК-400-6.5 type with the total pumping capacity of 13000 l/s, a turbo molecular pump 01АБ-1500-004 and a for-vacuum pump НВР-90 were used. For pumping the external injection channel, two pumps 01АБ-1500-004 and two pumps НВР-25 were applied.

Accelerating system (AS). The cyclotron accelerating system is composed of two identical ¼-wave dee subsystems excited at a fixed frequency of 41.2 MHz (the second harmonic of ion revolution). Two 60° dees are conductivity coupled in the center, and together with the resonance tanks form a uniform ½-wave system with a maximum voltage in the center and a 17% voltage drop at the final radius. At 60 kV, AS provides 200 keV energy gain per turn to limit the number of revolutions to ~ 400 and the total H^--ion losses to 5% due to electro-dissociation and dissipation on residual gas. The design of AS is presented in Fig. 4 where only one right half of AS is shown.

The resonant tank of the rectangular form has a bolted connection in a median plane. The top and bottom half of the resonant tank are jointed with the top and bottom claddings in a uniform one-piece construction. Usual claddings are fastened to the vacuum chamber lids. In our case, the claddings are attached to the central plug. An inflector is placed within the plug which represents a grounded box electrode. In the central region, the top and bottom dee plates are connected with each other by the vertical short-circuit with

diaphragms for a beam passage. The grounded box electrodes and the windows in the dee vertical partition form the central beam optics system intended for effective beam acceleration and focusing on the first several revolutions. This is a rather sophisticated system, which to a great extent defines the cyclotron beam intensity and quality. Each half of AS consists of the resonance tank, dee and top and bottom claddings which are integrated in the unified construction fastened to the vacuum chamber wall, and can be removed from the vacuum chamber as an unitized construction for the repair and setting work outside the accelerator. By contrast with the initial AS variant when the modeling was used, the three-dimensional program ISFEL 3D[1] was applied to calculate both the resonant frequency and the current distribution for the new design.

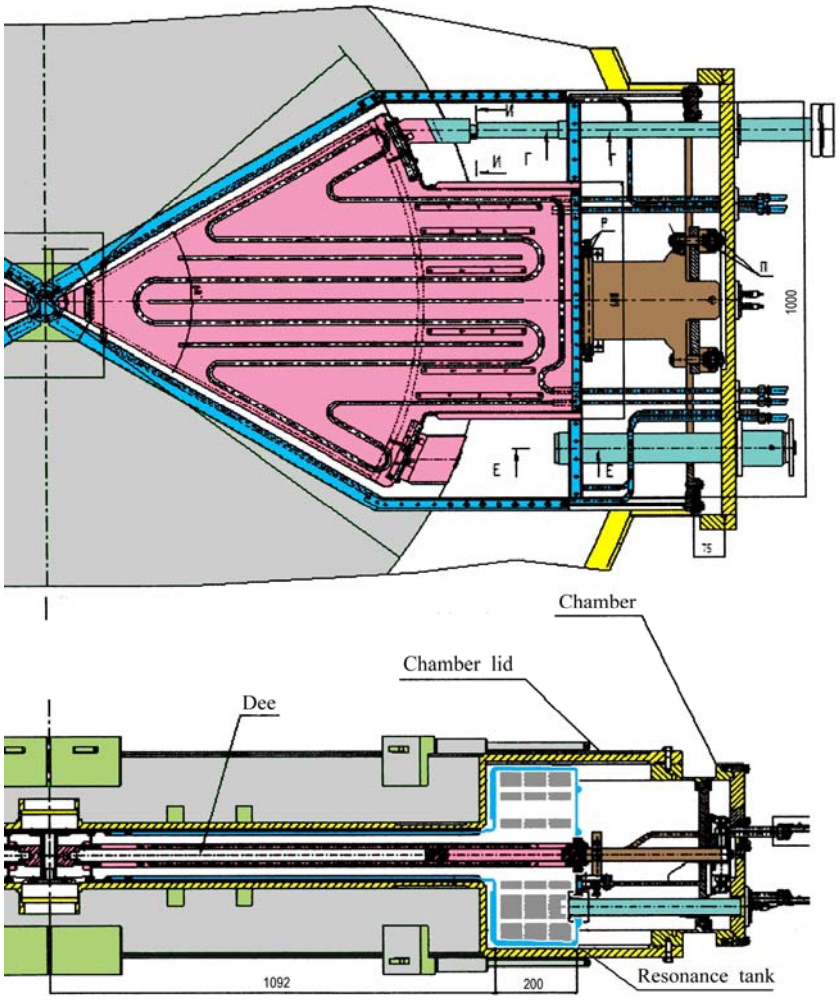

Fig. 4. Design of the accelerating system (AS) in the vacuum chamber

The high-frequency generator. Within 2002–2006, the excitation generator on frequency $f = 41.2$ MHz and the pre-amplifier of power up to 15 kW with a voltage stability of 10^{-6} have been constructed. The output of this pre-amplifier is switched *via* two feeder lines with two final cascades of 40 kW, which are now constructed and tested. The power supply rectifier of 10 kV and 160 kW with a fast response protection against breakdown has been constructed also. A thyristor rectifier on 160 kW power to feed the generator anode is under construction. An external view of the pre-amplifier and power amplifier is shown in Fig. 5.

[1] S.A. Silaev, in *Proceedings of the International University Conference on Electronics and Radiophysiccs of Ultra-High Frequencies* (St.-Petersburg, 24 – 28 May 1999), St.-Petersburg, 1999, p. 356.

A full scale model of the accelerating system with the feeder line was used as a load of the generator to investigate the system Q-factor, power dissipation, and to tune the generator at a low level voltage. Additional investigations on full power will be performed when the dee system is manufactured.

Fig. 5. The external view of the power amplifier, on the back plane is shown the pre-amplifier with the feeder

External injection system (EIS). EIS is the mostly-used technology for a modern cyclotron design. It allows to use a complicated and unhandy construction of an ion source, such as multi-cusp in our case, to produce a beam with necessary parameters and gives opportunity to improve vacuum in the chamber. The beam from the source is transported through a hole drilled in the magnet pole, and then it is turned by 90 degree in the median plane by a spiral inflector. By now, the conceptual design of the external injection has been accomplished. The technical project and working drawings have been developed. A conceptual scheme of the external injection is shown in Fig. 6.

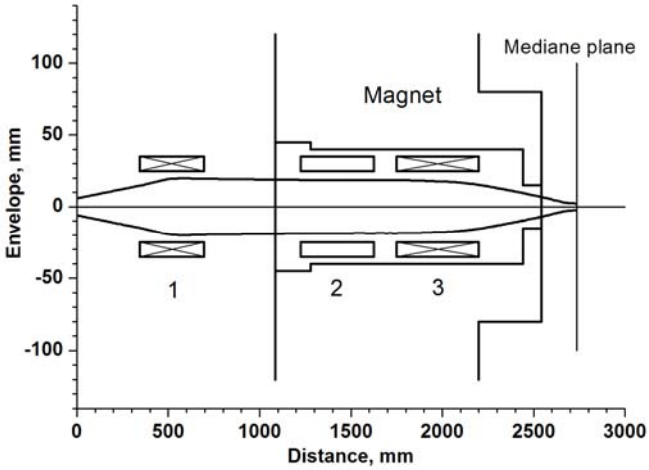

Fig. 6. The optical scheme of the axial injection: zero distance corresponds to the ion source exit, 1 – solenoidal lens, 2 – correction magnets, 3 – solenoid, the distance between the ion source exit and the accelerator median plane is about 273.5 cm

For this design, the following input data have been used: injection energy – 26 keV, continuous current from the source – 1.5 mA, beam diameter – 15 mm, beam divergence – 25 mrad, normalized emittance – 0.5π mm × mrad.

The beam transportation line from the source into the median plane consists of the solenoidal lens, the solenoid and the inflector. Optical element parameters have been selected on the assumption of a successful beam transportation along the injection line and matching with the cyclotron accelerating system. Main parameters of the optical elements can be presented as follows:

Solenoidal lens: maximum magnetic field – 0.35 T, beam aperture – 70 mm, effective length – 350 mm, lens center position – 520 mm from the output flange of the source.

Solenoid: maximum magnetic field – 0.14 T, beam aperture – 70 mm, effective length of the magnetic circuit – 450 mm; solenoid center position – at the distance of 760 mm from the cyclotron median plane.

Buncher: A buncher is used to increase a part of the d. c. beam from the source captured in the acceleration. The buncher transforms the continuous beam from the source to a short packet bunch with the repetition rate of the acceleration frequency at the first acceleration gap. The bunched beam is delivered to the acceleration gap only in the moment when the accelerating RF phase is suitable for acceleration.

Inflector: An inflector is to turn the H^--ion beam with 1.5 mA current and 26.07 keV energy from the vertical injection beam line into the median plane. Beam dynamics in the inflector was investigated by integration of the equations of movement in pre-set electric and magnetic fields. The inflector electric field was calculated using a 3D code with the mesh size of 0.25 mm. The influence of diaphragms on the inflector entrance and exit was taken into account. The inflector with a twist parameter $k' = 0.04$ was selected *via* axial trajectory calculations in a 3D electric field with account of an edge effect in the electric field distribution. Axial trajectory parameters at the first acceleration gap were calculated. Calculations of trajectories along the inflector showed an average current of 320–380 μA to be obtained at the inflector entrance, the beam loss within the inflector being less than 6%. A great number of trajectories were traced from the inflector exit through the cyclotron central region resulting in an average current of 250–300 μA achievable in our cyclotron.

Present status and the coming years prospects. The design of the main cyclotron systems of the 80 MeV H^--ion isochronous cyclotron with the beam current of 100 μA has been completed, and the working drawings have been developed. The cyclotron magnet has been installed in the unused part of the existing experimental hall of the synchrocyclotron. The cyclotron magnet is now in operation, and extensive magnetic measurements are in progress in order to obtain the magnetic field distribution within the necessary tolerance. The 41.2 MHz high frequency generator on 80 kW is in operation also. Two types of the H^--ion sources are investigated. To put into operation the isochronous cyclotron and to obtain the first beam, the following tasks should be accomplished:

- manufacturing of the vacuum chamber, the acceleration system and the axial injection system;
- purchase of vacuum pumps and vacuum equipment for all cyclotron systems;
- design and construction of automatic and computer-controlled cyclotron sub-systems.

Additional equipment is to be designed to use the cyclotron for isotope production and for proton therapy:

- isotope production target station;
- beam transport lines;
- radiochemical equipment for the isotope separation;
- a special cabin and chair for patients irradiation.

References

1. N.K. Abrossimov *et al*., in *Proceedings of the 13th International Conference on Cyclotrons and Their Application* (Vancouver, Canada, 6 – 10 July 1992), World Scientific Publishing Co., 1993, p. 58.
2. N.K. Abrossimov *et al*., in *Proceeding of the 13th Workshop on Charged Particle Accelerators* (Dubna, 13 – 15 October 1992), Dubna, 1993, vol. 2, p. 205.
3. N.K. Abrossimov and G.A. Riabov, in *PNPI-XXV, High Energy Physics Division. Main Scientific Activities 1997–2001,* Gatchina, 2002, p. 15.

STATUS OF LHC EXPERIMENTS

PNPI PARTICIPATION IN LHC EXPERIMENTS

The outstanding discoveries in the experimental and theoretical physics of elementary particles resulted in formulation of the Standard Model that provides now a self-consistent picture of the elementary particles world and describes with remarkable precision practically all observed experimental facts. These achievements were closely related with the progress in the accelerator technology. In particular, very important contributions to development and validation of the Standard Model were made by recent experiments at the e^+e^--collider LEP (90 GeV + 90 GeV) at CERN and at the $p\bar{p}$-collider Tevatron (1 TeV + 1 TeV) at FNAL. Note that PNPI took an active part in the L3 experiment at LEP, and it participates now in the D0 experiment at Tevatron.

In the tremendously successful Standard Model one important link is still missing. The spontaneously broken SU(2) × SU(1) gauge symmetry introduced by this model leads to existence of a scalar Higgs field. The observation of the predicted Higgs Boson is at present the most fundamental task in the high energy physics. Recent fits within the Standard Model to all available electroweak data combined with the measured top quark mass predict the Higgs Boson mass to be in the range 100–500 GeV with the most probable value around 130 GeV. The on-going Tevatron experiments D0 and CDF with the upgraded luminosity of 5×10^{32} cm^{-2} s^{-1} have some chance to discover the Higgs Boson if its mass is below 120 GeV. More extensive search (studies) of the Higgs Boson will be the primary goal for the Large Hadron Collider (LHC) at CERN. The energy of the colliding proton beams will be 7 TeV + 7 TeV, and the luminosity will reach 10^{34} cm^{-2} s^{-1}. With these parameters, LHC will have high discovery potential for the Higgs Boson in the whole predicted mass region.

It is generally accepted that the Standard Model is not yet a complete theory, and some "new physics" should appear at the energy scale of several TeV. A possible extension of the Standard Model is Supersymmetry that allows unification of the three coupling of the gauge interactions at the very high energy scale. Superpartners for all the presently observed particles are expected at the TeV mass scale. At the LHC, the search for the Superparticles could be carried out over the entire theoretically plausible mass range.

The other research areas covered by LHC, where the "new physics" could appear, are searches for new heavy gauge bosons (Z',…), the compositeness of the leptons and quarks, the extra-dimensions. Also, LHC offers rich possibilities to extend studies of the "classical" subjects, such as physics of the top-quark, gluon density at very low x-values, diffraction processes, total cross sections behavior at the highest energies.

Study of the *CP* violation in decays of *B* mesons is also one of the major goals at LHC. The LHC colliding beams will be an incomparable in intensity source of B_d and B_s mesons as well as *B*-baryons. This could allow to study *CP* violation in many decay channels, thus providing a stringent test of the Standard Model. Also, study of rare *B*-decays, forbidden in the Standard Model, offers a way to search for the "new physics" beyond the Standard Model.

In addition to running as a proton-proton collider, LHC will be used to collide heavy ions at the center-of-mass energy of 5.5 TeV per nucleon. The collision energy densities will be well above the predicted threshold for formation of the quark-gluon plasma. The search for the new state of matter will be among the important physics goals at LHC.

LHC will be constructed in the existing 27 km tunnel (former LEP tunnel). There will be four intersection points where four detectors (ATLAS, CMS, ALICE, and LHCb) will be located, designed to explore the full discovery potential of LHC. Among these detectors, ATLAC and CMS are general purpose detectors aimed at search for the Higgs Bosons and the "new physics" using the colliding beams at the highest achievable luminosity. The LHCb detector will be specialized on studies of the *B*-physics emphasizing powerful particle identification, while ALICE is designed for investigation of the heavy nuclei collisions with the goal to detect signatures of the quark-gluon plasma. These experiments will play the leading role in the world's fundamental research program in the forthcoming decades, and they may have a decisive impact on the future of the particle physics. The LHC experiments should be ready for running by mid of 2008.

Since 1997, PNPI participates in construction of the ATLAS, CMS, ALICE, and LHCb detectors with important contributions to each of these projects. In particular, PNPI shared responsibilities for design and construction of some major parts of the detectors, such as the Endcap Muon system for CMS, the Muon systems for LHCb and ALICE, the Transition Radiation Tracker for ATLAS. This work was conducted under general Agreement between CERN and the Government of Russian Federation on participation in construction of the LHC. The Government of RF provided the financial support for these activities. The unprecedented for our institute large amount of experimental equipment to be produced at PNPI for the LHC projects required organization at PNPI of several production sites equipped with unique tooling and measuring devices. The work was carried out in close cooperation with Western groups following the strategy: most of the materials are provided by the collaborations, while the assembling and testing of the created equipment is performed at PNPI. More than 100 PNPI specialists were involved in this tremendous work during nearly 10 years. Finally, by the end of 2006, this work was successfully completed. Strictly according to the production schedule, all the equipment was produced, tested and delivered to CERN for installation in the experimental setups. All collaborations pointed out the high quality of the equipment produced at PNPI. The next step is installation and commissioning of the LHC detectors. The PNPI specialists play important roles in this work. The presented below reports describe in some details the work done at PNPI for preparations of the LHC experiments.

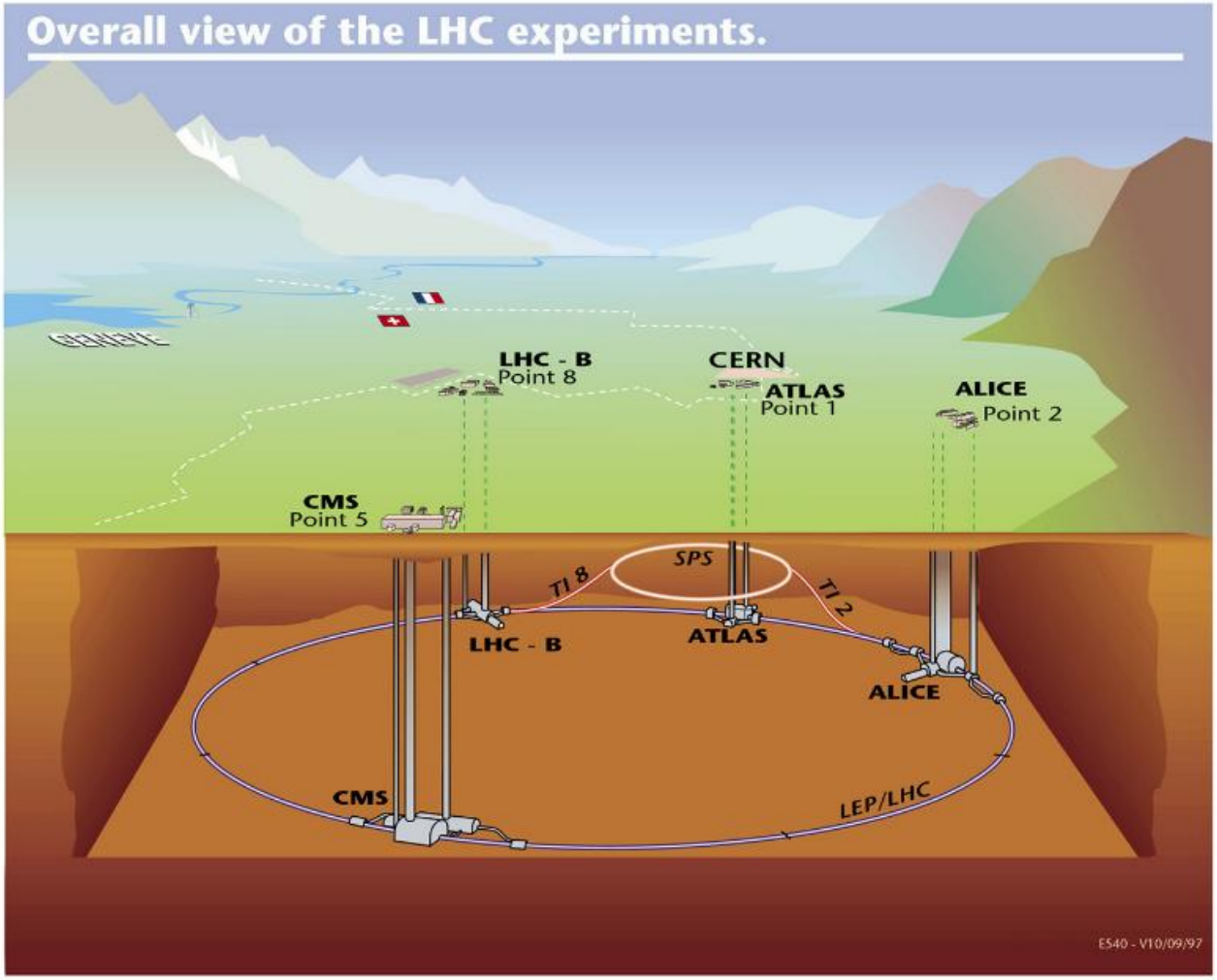

CMS EXPERIMENT

A.A. Vorobyov, D.M. Seliverstov, Yu.M. Ivanov, V.L. Golovtsov, V.S. Kozlov, N.F. Bondar, A.S. Denisov, A.G. Golyash, Yu.I. Gusev, V.I. Lazarev, V.D. Lebedev, P.M. Levchenko, G.V. Makarenkov, E.M. Orischin, A.A. Petrunin, A.I. Shchetkovsky, L.A. Schipunov, V.A. Sknar, V.V. Sulimov, V.I.Tarakanov, I.I. Tkatch, L.N. Uvarov, S.A. Vavilov, G.N. Velichko, S.S. Volkov, An.A. Vorobyov, V.I. Yatsura, G.F. Zhmakin

1. Introduction

The Compact Muon Solenoid (CMS) is a general-purpose detector designed to study physics of proton-proton collisions at center-of-mass energy of 14 TeV at full LHC luminosity up to $L = 10^{34}$ cm^{-2} s^{-1}. The primary goals of the CMS experiment will be the Top-quark physics, search for the Standard Model Higgs bosons, as well as search for physics beyond the Standard Model (super-symmetric particles, new heavy gauge bosons, extra-dimensions …). The design of the CMS detector emphasizes the importance of precise momentum measurements of muons, electrons, and photons, resulting in excellent mass resolution needed for discovery of the new particles. Figure 1 shows general view of the CMS detector. The basic elements of this detector are:

- Superconducting solenoid
- Return iron yoke
- Inner tracker
- Crystal electromagnetic calorimeter
- Hadron calorimeter
- Muon system
- Very forward calorimeter

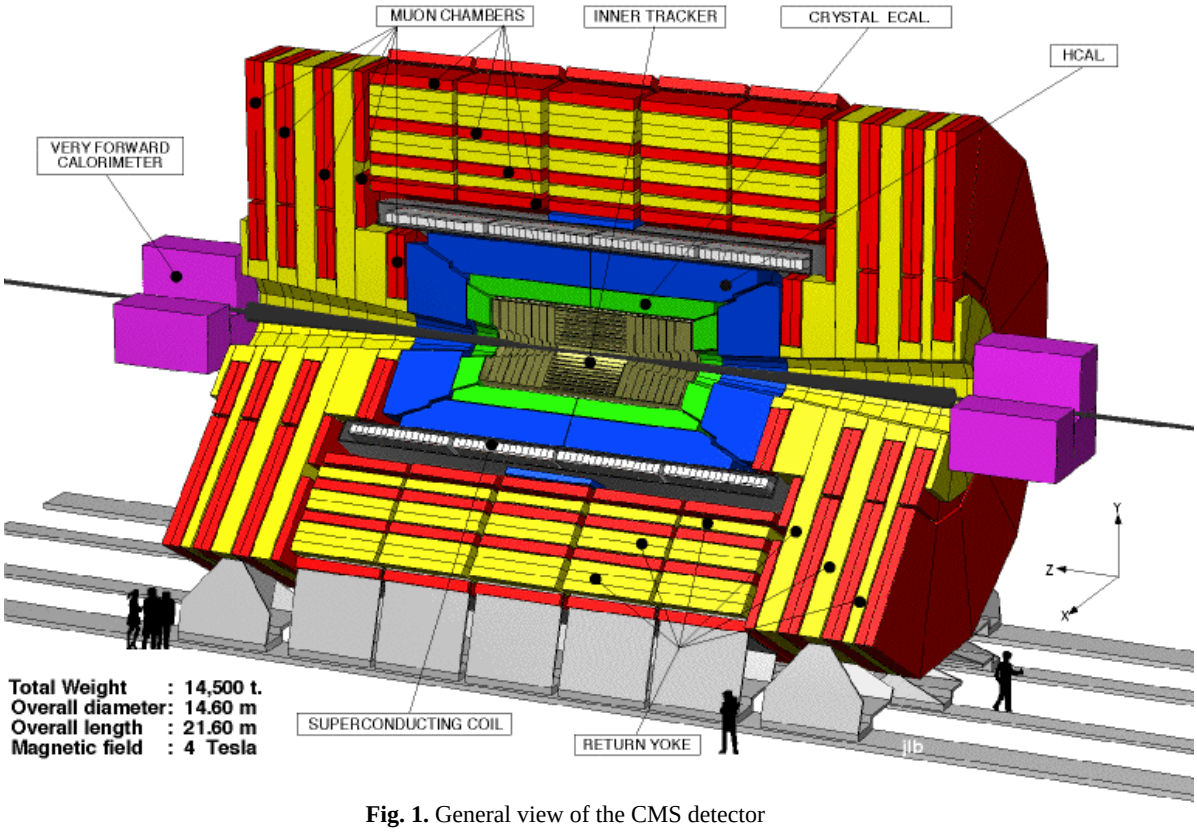

Fig. 1. General view of the CMS detector

2. Muon System of the CMS detector

The Muon System has three functions: muon identification, muon momentum measurements, and muon trigger with well defined p_t threshold from a few GeV/c to 100 GeV/c in the rapidity range up to $\eta = 2.1$. The momentum resolution $\delta p_t/p_t$ in the stand-alone mode is around 10% at $p_t = 10$ GeV/c and around 30% at $p_t = 1$ TeV/c. The global momentum resolution after matching with the Central Tracker is about 1.5% at $p_t = 10$ GeV/c and about 15% at $p_t = 1$ TeV/c. The Muon System is embedded inside the magnet return yoke. It consists of two parts – Barrel and Endcaps.

The main PNPI responsibility in the CMS project is participation in design, construction and operation of the Endcap Muon System. This work was carried out since 1994 in close cooperation with the teams from Fermilab, from University of Florida, and from some other US Universities.

In fact, development of a muon system for collider detectors began at PNPI already in 1991, when construction of the proton-proton Super Collider SSC for the energy of 20 TeV + 20 TeV was started in the USA. At that time, PNPI together with Brookhaven National Laboratory proposed the Muon System for the GEM detector, which was one of the two collider detectors to be constructed at SSC. This system was based on application of multiwire Cathode Strip Chambers (CSCs). During preparation of this project, several CSC prototypes have been constructed and tested. Also, various gas mixtures were investigated, and one of them ($Ar/CO_2/CF_4$) was recommended. It was demonstrated that such system can provide the required spatial and time resolution, and it can generate the stand-alone muon trigger. At the beginning of 1993, this project was considered by the GEM collaboration together with two other competitive projects. As the result, our CSC based project was selected for the whole GEM Muon System. Unfortunately, construction of the SSC was stopped by the USA Congress in October 1993. After that decision, several US teams organized new collaboration which proposed in February 1994 to build the Endcap Muon System for the CMS detector, similar to that designed for the GEM detector. PNPI became a member of this collaboration.

The CMS Endcap Muon System (EMU) consists of two symmetric parts (forward and backward). Each of these parts contains four Muon Stations (ME1 to ME4). The Muon Stations are composed of muon chambers placed between the iron discs of the magnet return yoke. Each of these discs has 14 meters in diameter. The station ME1 has three rings of muon chambers (ME1/1, ME1/2, ME1/3). The stations ME2 and ME3 are composed of two rings of the chambers (ME2,3/1 and ME2,3/2), while the station ME4 has only one ring of the chambers (ME4/1), the construction of the ring ME4/2 being staged due to financial limitations. The total area covered by the muon chambers is about 1000 m^2.

The muon chambers [1–4] are specially designed six-plane CSCs of trapezoidal shape as shown in Fig. 2. Cathode planes are formed by honeycomb panels with copper clad FR4 skins. Strips run radially in the endcap geometry and provide the φ-coordinate of muon hits with an accuracy of ~100 μm. Wires are stretched across the strips and, for readout purposes, are grouped in bunches from 5 to 16. They provide the radial coordinate of the muon hits with a few cm precision. In total, the EMU system comprises 540 muon chambers which contain about 2.5 million wires grouped into 210,816 anode channels. Also, there are 273,024 cathode channels.

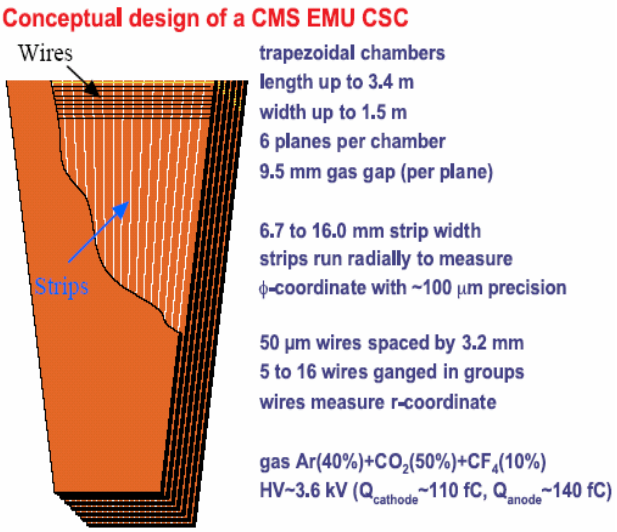

Fig. 2. Sketch view and some parameters of a CSC

3. Assembling of EMU muon chambers at PNPI

The design of the muon chambers and development of technology for the chamber production were performed with active participation of the PNPI team. The assembling and testing of the chambers was distributed between several laboratories. PNPI was responsible for assembling and tests of all muon chambers for the regions ME2/1, ME3/1, and ME4/1. In total, 120 muon chambers (40 chambers of each type) were to be produced at PNPI. Each chamber contains six sensitive planes. So, in fact, we had to build 720 one-plane chambers with total area of more than 1400 m^2 and with total number of the anode wires about half a million.

To accomplish this task, a special facility (muon chamber factory) was prepared at PNPI. This facility occupied about 500 m^2 area, including some clean rooms. It was equipped with special tooling developed jointly by PNPI and US_CMS specialists. In particular, this equipment included a wire-winding machine, a wire pitch and tension measuring machine, special gluing tables, assembling tables, a setup for cleaning the anode wires with ionized nitrogen gas, a gas leak test stand, a γ-rays test stand, a cosmic rays test stand, and some other tooling. This equipment allowed to organize the chamber assembling under well controlled conditions with the necessary production rate of one six-plane chamber per week. The developed chamber assembling technology was approved by the EMU collaboration after the Production Readiness Review which was held at PNPI in June 2001.

The mass production of the muon chambers at PNPI was started in October 2001. The US_CMS collaboration provided prefabricated parts of the muon chambers (honeycomb panels, anode and cathode bars, *etc*.) and most of the materials needed for assembling the chambers. The metallic chamber frames were produced at PNPI. The assembling procedure was controlled at each step: flatness of the honeycomb panels, height of the gas gaps, wire tension, wire pitch, gas tightness. The assembled chambers were trained under high voltage with simultaneous measurement of the dark current. It was required that the dark current should not exceed 100 nA in each plane at the nominal high voltage HV = 3.6 kV. In case of problems, the chambers could be disassembled for additional cleaning. The gas gain uniformity was controlled on the γ-rays test stand by measuring current induced by a collimated γ-source movable over the chamber surface (Fig. 3). The variations of the gas gain should not exceed ± 50%. All details of the assembling procedure for each chamber together with the results of the control measurements were collected in special folders (Fig. 4) which will accompany the chamber in its further life. Also, this information was placed in a special data base reachable for the EMU collaboration *via* Internet.

Fig. 3. Muon chamber on the γ-rays test stand

Fig. 4. Muon chamber ready for installation of the on-chamber electronics

The on-chamber electronics was installed on the chambers which passed the above mentioned tests (Fig. 5). After that, the chambers were tested on the cosmic rays tests stand (Fig. 6).

Fig 5. Installation of the on-chamber electronics

Fig. 6. Final tests of the muon chambers on the cosmic ray test stand

The on-chamber electronics included anode and cathode FE boards and also logical boards ALCT and CLCT which allowed on-line reconstruction of the tracks using hits from the six layers of the chamber. The final test program included 36 various tests with pulse generator and with cosmic muons. Figure 7 shows one of the cosmic rays events detected by the muon chamber. The measured amplitudes of the signals in the cathode strips in all six layers are shown by red bars, while the blue bars represent the hits in the anode wire groups. After final tests, the chambers were stored in a special room for one month training under nominal high voltage. Then the chambers were prepared for transportation to CERN – see Figs. 8–9. By the end of 2006, all 120 muon chambers produced at PNPI were safely delivered to CERN.

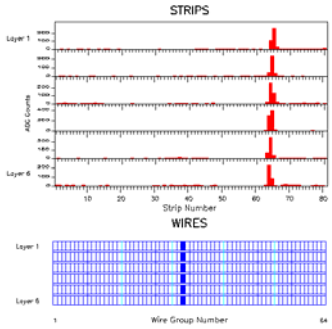

Fig. 7. Display of a cosmic ray event

Fig. 8. The PNPI team in front of the last muon chambers ready for transportation to CERN

Fig. 9. The track with twenty muon chambers prepared to move for CERN

4. Testing of EMU muon chambers at CERN and installation in the CMS detector

Fig. 10. High-level visitors at the EMU test stand. CERN General Director R. Aymar, Minister of Science and Education of the Russian Federation A. Fursenko and others

All muon chambers produced at PNPI, FNAL (USA), and IHEP (China) were transported to CERN where they have been tested again on a special test stand, following the same test program as in the production centers. The PNPI team played the leading role in these tests. In total, about 500 chambers have been tested. All chambers showed very good performance: high detection efficiency with a large HV plateau, low noise. During these tests, some minor problems in the electronics have been detected and fixed.

Some of the muon chambers were tested on the γ-radiation facility GIF at CERN to study their aging properties. It was demonstrated that the chamber performance is not deteriorated noticeably up to the integrated radiation dose corresponding about 30 years operation of the EMU system.

Figure 10 illustrates attendance of the EMU test stand by high-level visitors.

The assembling of the CMS detector was performed in two stages. First, all the subsystems were installed in the on-surface hall. Figure 11 shows how one of the muon chambers is lifted by a special transporting system for installation on the iron disc of the magnet return yoke. One can see also the chambers already fixed at the disc. All the infrastructure and electronics are installed at the same time. This allowed to perform some tests of the EMU system already in this phase of installation. In particular, important tests were carried out in 2006 with cosmic rays using a part of the assembled EMU system comprising muon chambers in all muon stations. In the second phase of installation, the separate pieces of the CMS detector are lowered down in the underground hall for the final assembling. Figure 12 demonstrates the process of lowering of one of the iron discs with the muon chambers and all related infrastructure. Note that the weight of the disc exceeds 1000 tons.

The PNPI team takes an active part in installation of the EMU system. The full installation of the CMS detector should be finished at the beginning of 2008.

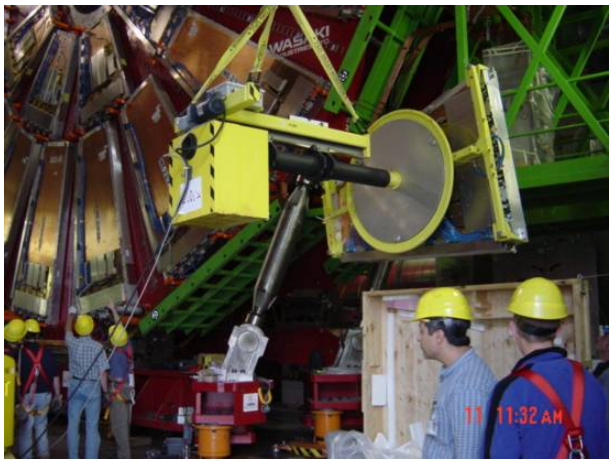

Fig. 11. Installation of a muon chamber on the iron disc of the magnet return yoke

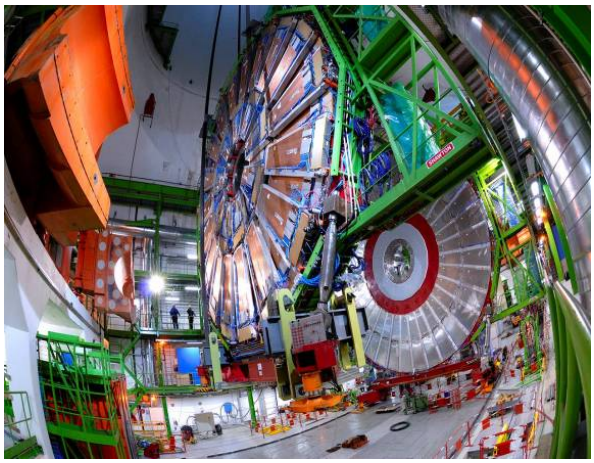

Fig. 12. The lowering down of one iron disc with muon chambers in the underground hall

5. Multi-channel high voltage supplier for the EMU system

The EMU system comprises 468 six-plane muon chambers. In addition, the HV line in each layer is divided in several sections (5 sections in chambers ME2,3/2 and 3 sections in all other chambers). So in total there are more than 9000 sections with independent HV lines. This increases essentially the redundancy of the system as, in case of problems, only one section will be switched off that should not deteriorate noticeably performance of the whole EMU system. Such design dictated development of a special multi-channel HV system which could satisfy the requirements of the CMS experiment. This problem was solved by joint efforts of specialists from PNPI and University of Florida. The block diagram of a quarter of the designed HV system is presented in Fig. 13, the stand for tests of EMU high voltage system at PNPI is shown in Fig. 14. The high voltage from the Primary HV power supplier is distributed for about 2400 HV lines with independent regulation of the voltage in each line. Also, the current in each line is under control with a possibility to switch off any line by burning off a fuse, if necessary. The HV distribution is done in two stages. First, it is distributed by nine Master Boards into 72 HV lines with HV regulation from 0 to 4 kV. These lines go *via* ~100 meter long cables to 72 Remote Distribution Boards. Each such board has 30 or 36 outputs going directly to the muon chambers. The Board 30 feeds one big chamber ME2,3/2, the Board 36 feeds two smaller chambers. The Remote Distribution boards can regulate the voltage in each output channel by 1 kV down from HV_{max} .The maximal current in each channel of the HV system is 100 μA.

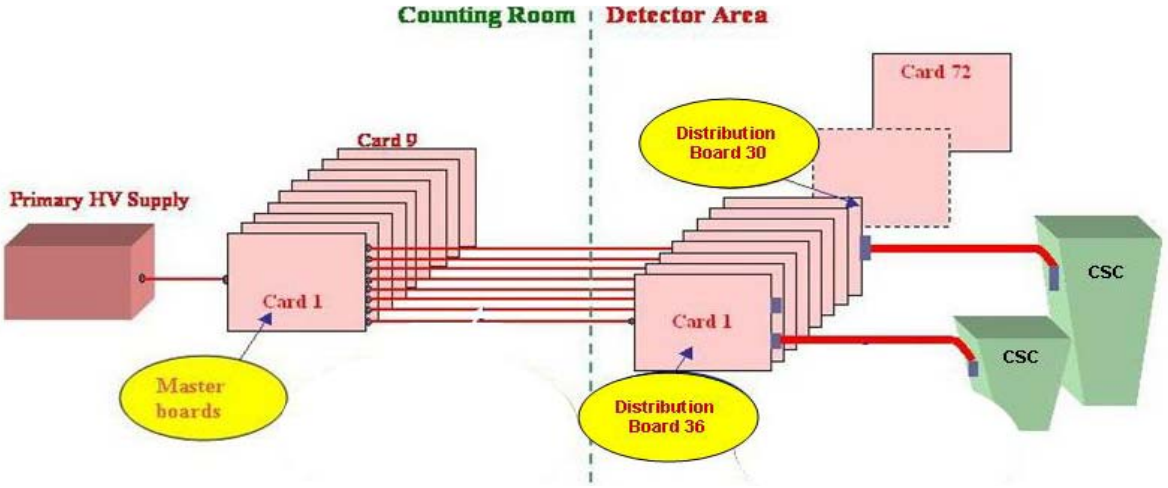

Fig. 13. Block diagram of a quarter of EMU HV system

The HV system is controlled by computors *via* the Host Cards (not shown in Fig. 13). Each Host Card controles up to 16 Distribution or Master boards. An important requirement is radiation hardness of the Remote Distribution boards as they are placed close to the muon chambers. The tests of the designed boards with gamma and neutron radiation showed that they can operate without problems in the expected radiation environment. The production of the designed HV system was accomplished by the PNPI-UF collaboration. By mid of 2006, all modules for the 9000-channel HV system (plus spare modules for 2500 HV channels) were produced, tested, and delivered to CERN for installation.

Fig. 14. Tests of EMU high voltage system at PNPI

6. Track-finding processor for the EMU system

The Track Finding Processor (TFP) is a basic element of the EMU trigger system [5–6]. The purpose of the TFP is to link track segments from the individual muon stations into complete tracks, to measure the transfer momentum from the sagitta induced by the magnetic bending, and to report the number and quality of the tracks to the Level-1 global trigger. The TFP was designed by PNPI engineers in cooperation with the University of Florida. It is implemented as 12 processors working in parallel. Each of them should identify up to three best muons in the corresponding 60° azimuthal sectors. The block diagram of the TFP is shown in Fig. 15, the demonstration of Track-Finding Processor is presented in Fig. 16. The design of the TFP is based on the most advanced Field Programmable Gate Array (FPGA) chips, each of them containing more than one million logical elements.

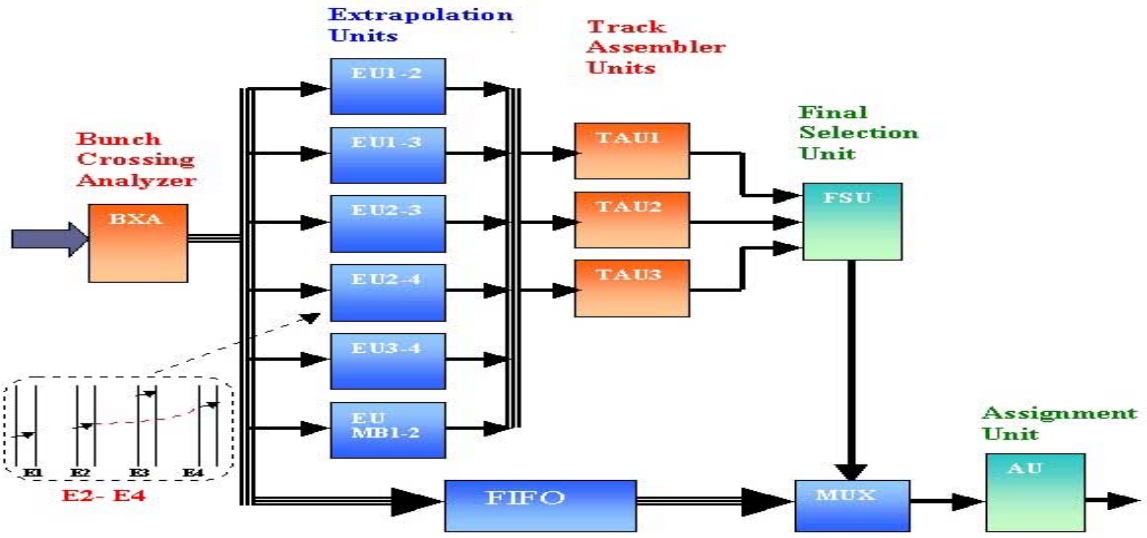

Fig. 15. Block diagram of Track-Finding Processor

The first TFP prototype was fabricated in 2000 and successfully tested in 2000–2001. This was quite a big system containing forty eight 9U VME modules . The processing time of this TFP was 375 ns. The experience obtained from testing of this prototype and also appearance on market of more powerful FPGA chips allowed to design a new, more advanced TFP. The total volume of this TFP was decreased by a factor of 4 (twelve 9U VME modules), and the processing time was reduced down to 175 ns. The TFP was fabricated in the US industry, while testing and commissioning of this system was done by PNPI engineers in cooperation with specialists from University of Florida. The combined tests of the EMU trigger system performed in the proton beam (2004) and with cosmic rays (2006) showed very good performance of the constructed Track-Finding Processor.

Fig. 16. Demonstration of Track-Finding Processor

7. Anode front-end electronics

The PNPI engineers in cooperation with Carnegie-Mellon University designed the anode front-end electronics for the EMU muon chambers [7]. For this purpose two integrated circuit chips were designed. One of them (CMP16 – see Fig. 17) included 16-channel amplifier-shaper-discriminator. The other one (DEL16) provided a programmable delay line for each channel which allows time alignment of the signals with a delay step of 2 ns. On the basis of the CMP16 chip, a 16-channel Anode FE (AD16) board was designed. The designed board passed through various reliability and radiation tests. The fabrication of the CMP16 and DEL16 chips, as well as the AD16 boards was carried out in the US industry. The tests of the produced chips (22,000 chips) and boards (12,000 boards) were performed by the PNPI specialists. These tests showed that the major part of the produced electronics was of good quality. By the end of 2002 all the boards were tested and provided for installation onto the muon chambers.

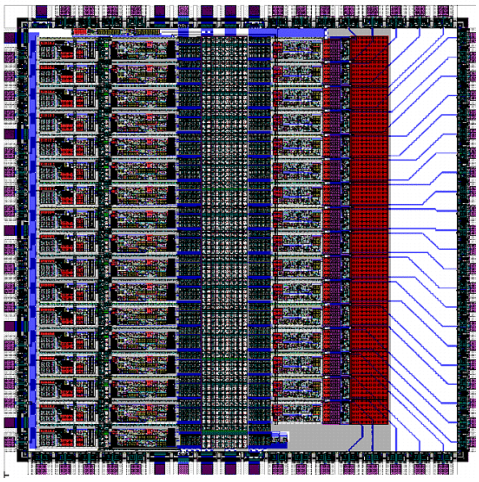

Fig, 17. CMP16 (Bondar's chip) layout

8. Alignment of the muon chambers in the EMU system

The 468 EMU muon chambers are fixed on the magnet return discs covering the area of 1000 m^2. Their geometry position in the CMS absolute coordinate system should be known with 100 micron precision in the azimuthal plane and with 1mm precision in the Z-direction. This task becomes even more complicated because of significant deformation of the iron discs in the magnetic field. Therefore, permanent control for positions of the muon chambers is needed. For these purposes, a complicated system was developed comprising several hundreds of position-sensitive detectors irradiated by the laser beams. This work was done by engineers from the Wisonsin University with active participation of PNPI specialists [8]. The global tests of this alignment system were carried out in 2006 with the half of the EMU system assembled in the on-surface hall. These tests showed very satisfactory results. The second half of the EMU system will be equipped with alignment devices in 2007.

9. Photodetectors for CMS Endcap Electromagnetic Calorimeter

The CMS Electromagnetic Calorimeter (ECAL) is based on lead tungsten crystals ($PbWO_4$). These crystals offer excellent energy resolution due to high density (8.28 g/cm^3), a small Moliere radius (2.0 cm), and a short radiation length (0.89 cm). Also, they provide a quite fast (~10 ns) output signal, and they can operate in high radiation environment. ECAL consists of the Barrel part ($|\eta| < 1.48$) and two Endcaps ($1.48 < |\eta| < 3.0$) with 61200 and 21528 crystals, respectively. The total volume of the crystals amounts to 8.14 m^3 (67.4 tons) in the Barrel and 3.04 m^3 (25.2 tons) in the Endcaps.

The light from the crystals should be detected with radiation hard photodetectors, especially in the Endcaps where the radiation level is much higher than in the Barrel. After extensive studies, the preference was given to the Silicon Avalanche Photodetectors (APD) in the Barrel and to the more radiation hard Vacuum Phototriods (VPT) in the Endcaps. PNPI in cooperation with the Research Institute Electron (RIE, St.-Petersburg) carried out studies of various kinds of VPTs produced at RIE [9–10]. These studies resulted in construction of a VPT (FEU-188) which could satisfy the requirements of the CMS experiment. This VPT has a flat geometry with a photocathode (25.5 mm in diameter) followed by a mesh and by a solid dynode. The VPT provides the required gain of 10–12, and (what is most important) this gain does not decrease in the presence of magnetic field up to B = 4 T. Another advantage of the developed VPT is low sensitivity to variations of the anode voltage.

As a first step, a sample of 500 VPTs was produced at RIE. The gamma radiation tests of these VPTs showed that the gain degrades only by ~7% after the radiation doze of 20 kGy (the doze expected for 10 LHC years). Also, VPTs were tested with a real ECAL prototype showing very good performance. Based on these results, the CMS collaboration decided to equip the ECAL Endcaps with the FEU-188 and has signed a contract with RIE for production of 16000 VPTs. The production of the VPTs was completed by mid of 2006, and they were delivered to CERN. The new tests demonstrated high quality of the produced VPTs. As the result, the CMS collaboration has taken decision to reward the Research Institute Electron by a special CMS Gold Medal 2007 for outstanding contribution of the industry to construction of the CMS detector – see Fig. 18.

Fig. 18. The CMS Gold Medal-2007 to Research Institute "Electron" for outstanding contribution to construction of the CMS detector

References

1. D. Acosta, …, N. Bondar, …, O. Kiselev, …, O. Prokofiev, V. Razmyslovich, …, V. Sedov, …, S. Sobolev, V. Soulimov, …, N. Terentiev, A. Vorobyov *et al*., Nucl. Instr. Meth. A **453**, 182 (2000).
2. D. Acosta, …, N. Bondar, …, G. Gavrilov, …, Yu. Ivanov, …, P. Levchenko, …, O. Prokofiev, V. Razmyslovich, …, L. Shchipunov, V. Sedov, I. Smirnov, …, S. Sobolev, V. Soulimov, V. Suvorov, N. Terentiev, …, S. Vavilov, …, A. Vorobyov *et al*., Nucl. Instr. Meth. A **494**, 504 (2002).
3. O. Prokofiev, …, N. Bondar, …, Yu. Ivanov, ..., G. Gavrilov, ..., A. Krivshich, E. Kuznetsova, ..., P. Levchenko, ..., V. Razmyslovich, ..., L. Shchipunov, I. Smirnov, V. Suvorov, ..., N. Terentiev, ..., S. Vavilov, ..., A. Vorobyov *et al*., Nucl. Instr. Meth. A **515**, 226 (2003).
4. D.V. Balin and G.N. Velichko, "Performance simulation of the cathode strip chambers for CMS endcap muon system", CERN-CMS-NOTE-2005-014, April 2005. 30p.
5. D. Acosta, …, A. Atamanchuk, V. Golovtsov, V. Sedov, B. Razmyslovich *et al.*, Nucl. Instr. Meth. A **496**, 64 (2003).
6. D. Acosta, …, V. Golovtsov, M. Kan, L. Uvarov *et al.*, talk presented at *the Conference on Computing in High Energy and Nuclear Physics CHEP2003* (La Jolla, USA, 24 – 28 March 2003).
7. F. Ferguson, N. Bondar, A. Golyash, V. Sedov, N. Terentiev and I. Vorobiov, Nucl. Instr. Meth. A **539**, 386 (2005).
8. M. Hohlmann, …, O. Prokofiev, V. Sknar *et al.*, in *Proceedings of the Nuclear Medical Imaging Conference* (San Diego, USA, 29 October – 4 November 2006), p. 489.
9. Yu. Blinnikov, Yu. Gusev, …, F. Moroz,, …, D. Seliverstov *et al*., Nucl. Instr. Meth. A **504**, 228 (2003).
10. Yu.I. Gusev, A.I. Kovalev, L.A. Levchenko, F.V. Moroz, D.M. Seliverstov, V.Yu. Trautman, D.O. Yakorev *et al*., Nucl. Instr. Meth. A **535**, 511 (2004).

TRANSITION RADIATION TRACKER FOR ATLAS PROJECT

O.L. Fedin, E.G. Danilevich, A.E. Khristachev, L.G. Kudin, S.N. Kovalenko, V.P. Maleev, A.V. Nadtochy, S.K. Patrichev, Yu.F. Ryabov, D.M. Seliverstov, V.A. Schegelsky, E.M. Spiridenkov, A.Yu. Zalite

1. Introduction

PNPI is participating in the ATLAS project in creation of the Transition Radiation Tracker (TRT). TRT is one of the three sub-systems of the Inner Detector of the ATLAS experiment [1]. Besides TRT, the ATLAS Inner Detector includes the Pixel Detector and the Semi-Conductor Tracker (Fig. 1). TRT is designed to operate in a 2T solenoidal magnetic field at the design LHC luminosity (10^{34} cm^{-2}s^{-1}). TRT provides a combination of continues tracking, based on individual drift-tubes (straws), and of electron identification based on registration of the transition radiation (TR) photons which are produced in the radiators foils interleaved between the straw layers. The TRT geometry provides registration of the charged particles with p_t>0.5 GeV/c and with pseudo-rapidity $|\eta|$<2.1. TRT contributes to the accuracy of the momentum measurement in the Inner Detector by providing at all luminosities precise measurements in the R-φ plane. The accuracy of this R-φ measurement, expressed as an average over all drift-time measurements in the straws, is required to be close to 30 μm statistically and not worse than 50 μm if one includes systematic uncertainties. It means that the accuracy of one straw measurement should be about 180 μm. TRT contributes to the electron identification together with the ATLAS liquid argon electromagnetic calorimeter. Electron identification at LHC is much more difficult than at existing hadron colliders, and it has been demonstrated that the TR-signature is needed to identify a clean sample of inclusive electrons in the p_t-range between 20 and 40 GeV/c. The TR-signature is crucial for extraction of the signals from decay processes with huge combinatorial background of charged-particles pairs and also for identification of soft electrons in b-quark jets.

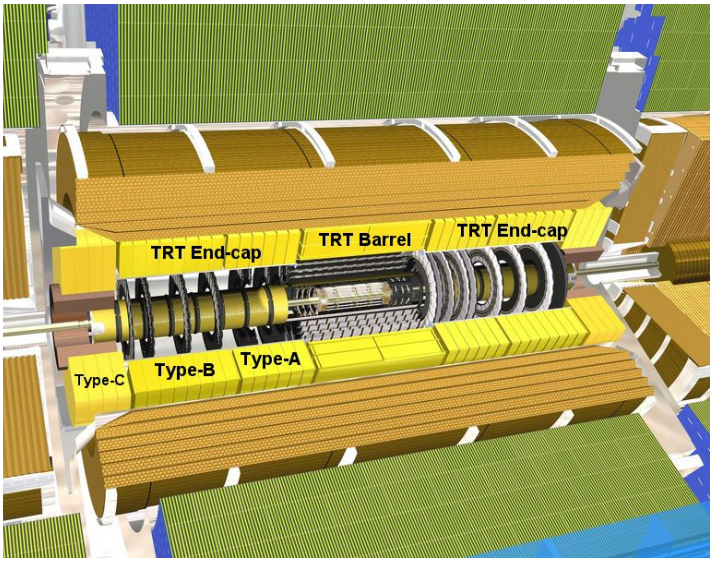

Fig. 1. ATLAS Transition Radiation Tracker

2. Straw design and basic properties

The operating conditions in the ATLAS experiment at LHC demand stringent requirements on the straw properties [2]. All choices of materials, the straw design, the active gas and the operating point were made to ensure safe and efficient operation in the high radiation environment. A large tube diameter would assure a high hit efficiency but it would not be able to collect all electrons in the short bunch crossing time of 25 ns. The straw diameter was chosen to be 4 mm as a reasonable compromise between speed of response, number of ionization clusters, and mechanical and operational stability. The straw tube wall is made of 35 μm thick multilayer film which is produced on the base of 25 μm Kapton film. On one side of the Kapton film an aluminium layer of 0.2 μm thickness is deposited. The Al-layer provides good electrical conductivity. The aluminium layer is then protected against damage from cathode etching effects and from occasional discharges by a 5–6 μm thick graphite-polyimide layer containing 55% of carbon. The other side of the film

is coated with a 4–5 μm polyurethane layer acting as a heat-seal compound. The straw is manufactured by winding two 10 mm wide tapes on a precisely tooled rod at temperature of ~260°C. The Kapton film alone has poor mechanical properties. The straw would be affected by thermal and humidity variations. In order to improve the straw mechanical properties, they were reinforced along its length with four sets of thin carbon fibre bundles. The C-fibres were bounded to the tube outer surface at 90° with respect to each other, using a special machine (Straw Reinforcement Machine – SRM), which was designed at CERN. The SRM is a semi-automatic device. After a group of naked straws is loaded into the drum, the carbon fibre pass over a series of rollers, and an impregnation pot wets the fibres with epoxy resin ensuring uniform resin distribution and tension. A specialized workshop has been organized at PNPI for the straw reinforcement (Fig. 2). The PNPI SRM workshop has produced ~110,000 long reinforced straws (1650 mm length). Stringent quality control steps were implemented in the straw reinforcement process. They include fibre delamination tests and straw geometry measurements (straightness, inner and outer diameters and local deformations or defects). The production yield was 98% at the production rate of ~6000 straws per month.

Fig. 2. View of Straw Reinforcement Machine at PNPI

The anode wire for the TRT straws was chosen to be of golden-plate tungsten 30 μm in diameter. To achieve high registration efficiency of the TR photons, a xenon-based gas mixture is used. The xenon fraction of 70% marks the balance between transition radiation performance, operational stability and electron collection time. The optimal gas composition was found to be 70%Xe+27%CO_2+3%O_2. The TRT is typically operated at 1530 V, corresponding to a gas gain of 2.5×10^4 for the chosen gas mixture [3]. The energy deposition in the straw is the sum of ionization losses of charged particles (~2 keV in average) and of the larger deposition due to TR photon absorption (>5 keV).

At the LHC design luminosity, the straw counting rate is very high, about 12 MHz [4]. This counting rate comes from the ionizing particles, slow neutrons and low-energy photons. The heat dissipation is directly proportional to the straw counting rate and estimated to be 10–20 mW per straw at the LHC design luminosity. The temperature gradient along each straw should not exceed 10°C to keep straw operation stability and gas gain uniformity. To evacuate the dissipated heat, a flow of CO_2 gas along the straw is used. The flow of CO_2 also evacuates any xenon gas which could leak out of the straws and thereby reduce the transition radiation registration efficiency.

3. Straw preparation

To use the straws for the TRT modules assembly, it should pass through several steps of the preparation procedure (a general view of the straw preparation workshop is shown in Fig. 3). Each of the reinforced straws is 1650 mm long, and at the first step they need to be cut into few short straws (four ~400 mm long straws for the A/B type modules, or three ~500 mm long straws for the C type modules). The straw pre-cutting is not precise and is chosen only for convenient work. The pre-cut straws pass through the test for the inner surface conductivity because high voltage distribution and signal propagation along the straw depend

on it. Then a conductive past is put on one edge of the straw to provide conductivity between the inner and outer surfaces. After that an end-piece (which provides gas distribution into the straw, wire fixation, and fixation of the straw in the wheel) is glued on the straw. At the final step, the straw is cut precisely with an accuracy of ~100 μm.

Fully equipped straws passed several quality tests. First of all they were checked for gas-tightness under overpressure of 1 atm. If the pressure drop was more than 0.1 mbar/bar/min, the straws were rejected. Then the straws were checked for straightness, and simultaneously their length was measured. The straws with the sagitta less than 200 μm and the length deviated from the specification by not more than 100 μm are used for the TRT modules assembly. At the last step, a visual inspection of the straws was done to check for any damages, bubbles in glued parts, runs of glue *etc*.

Fig. 3. Straw preparation workshop at PNPI

The described procedures require unique devices which were designed and produced in collaboration of PNPI with CERN. A special workshop was organized at PNPI to accomplish this task. The straw preparation team has produced and tested more than 170,000 straws for the A/B wheels, and more than 47,000 straws for the C-type wheels. The production yield was 96% at production rate of 320 straws/day.

4. Design and construction of the TRT endcaps

The TRT design [5] follows the tight requirements in terms of rigidity, stability, minimum amount of material, as well as other requirements typical for any tracking system in a collider experiment. TRT consists of one barrel and two endcap parts. The full length of the detector is 6.8 meters. The diameter is about 2 meters.

Each of the two endcap TRT parts consists of two sets of identical and independent modules (wheels). They are called the 8-plane wheels, because they contain eight planes of radially oriented straws. Each TRT endcap contains two different types of wheels called A and B.

Twelve 8-plane wheels of type A per side are located closest to the interaction point between 827 < Z < 1715 mm. Each wheel contains 6144 straws positioned in eight successive layers spaced by 8 mm along Z. Each layer contains 768 straws in the azimuthal plane. The free space of 4 mm between successive layers is filled with 15 μm thick polypropylene radiator foils. The distance between straws in the azimuthal plane varies from 5.2 mm at the inner radius of 640 mm to 8.4 mm at the outer radius of 1010 mm. The A-type wheels were assembled at PNPI.

Eight 8-plane wheels of B-type per side are located between 1719 < Z < 2725 mm. The B-type wheels are identical to the A-type wheels except for the spacing between the successive straw layers which is increased to 15 mm. This free space is filled with larger number of radiators foils. The B-type wheels were assembled at JINR in Dubna.

Originally the TRT endcap was designed with extension the rapidity region up to $|\eta| = 2.5$ (Z < 3363 mm) by using the third ring of wheels (C-type wheels). They should contain 4608 straws positioned in eight successive layers spaced by 8 mm along Z (as for the A-type wheels). Each layer, however, should contain only 576 straws in the azimuth plane, a smaller number than for the A/B-type wheels. The C-type straws should be longer by 14 cm than the straws of A/B-type to extend the η-coverage of the TRT. The construction of the C-type wheels has been staged, and they will not be assembled at present.

The endcap TRT therefore comprises a total of 245,760 straws with a quite uniform occupancy. A typical track will cross between 32 and 45 straws.

5. Wheel design and assembly

The 8-plane wheel is assembled from two back-to-back 4-plane wheels, which are the basic assembly unit for the detector. A 4-plane TRT module is assembled in the first stage.

The straws are inserted and glued (Fig. 4) into precisely drilled holes in the inner and the outer C-fibre rings, which serve as support structures for the straws. To ensure optimal uniformity in the number of straws crossed by particles as a function of azimuth, each straw in a given layer is angularly displaced with respect to its neighbor in the previous layer by 3/8 of azimuthal spacing between straws in the same layer. The straws themselves are reinforced and are part of the mechanical structure of the module. The straw straightness is required to be remained better than 300 μm, because their operational stability strongly depends on the displacement of the anode wire from the tube axis. Each straw is therefore visually inspected after insertion and after gluing. The problematic straws were replaced. The assembled 4-plane mechanical structure (C-fibre rings and straws) passed through inspection and quality-control measurements (dimensions and gas tightness of the mechanical structure).

Fig. 4. Assembly of TRT wheels at PNPI. Straw insertion and gluing into the carbon support rings

Flex-rigid printed circuit boards (Wheel Electronic Board – WEB) are used to distribute high-voltage to the straw cathode and to readout signals from the anode wires. There are 32 separate WEBs per one wheel. The flex-rigid printed circuit board contains two flexible layers of the circuit made from polyamide film. Each flex circuit contains holes with inward-printing petals. The first layer of the flex circuit is used to provide a reliable high-voltage connection to the straw cathode. The high-voltage plastic plugs are inserted through the petals into the straw making contact with the inner straw walls. The signal connection is done in an analogous way using the second flexible layer and the custom-designed copper crimp-tubes inserted through the petals in the second layer. These copper crimp-tubes are used to fix the anode wires on the outer radius (Fig. 5). The other custom-designed copper crimp-tubes with isolation are used to fix the anode wires on the inner radius. The WEB transmits the signals to the front-end electronics boards through three connectors each corresponding to 32 channels.

Fig. 5. Assembly of TRT wheels at PNPI. 4-plane wheel prepared for the wire stringing

A third C-fibre ring at the outer radius is glued to the rigid part of the WEB. On the opposite side of the rings fixed to the WEB, the glass-fibre boards are glued. They provide a sturdy box-like support. This box-like structure serves as an outer gas manifold for the 4-plane wheel. The inner gas manifold is made of reinforced polyamide material and glued to the inner C-fibre ring. The gas flows into one of the two 4-plane wheels, assembled together as an 8-plane wheel, through this outer gas manifold along the straws into the inner gas manifold and through eight plastic connecting elements into the second 4-plane wheel, where it traverses the straws in the opposite direction and is collected in its outer gas manifold.

The whole 8-plane wheel is covered with a thin metal-clad polyamide membrane on each side at the inner radius, which provides a signal-return path from the inner radius of the straws to the outer radius where the electronics ground is defined. The wheels are held together as a stack through a set of axial metallic tie-rods.

A specialized workshop has been organized at PNPI for the wheels assembly. The wheels assembly process includes not only mechanical assembly but also components preparation and final and intermediate tests, resulting in establishment of a passport for each wheel.

Each component used for wheels assembly, when received from a manufacturer or produced in-house, has to be checked for conformance and cleaned before use. Some of the components go through several stages of assembly before going into wheels (straws, flex-rigid printed-circuit boards, inner gas manifolds). The quality control is performed after each essential stage of assembly.

The tight tolerance for the TRT, which is placed in-between the SCT and Liquid Argon calorimeter, is required to comply with the given dimensional envelopes. The critical dimensions of the endcap wheels (such as the inner and the outer radii, the thickness of the endcap wheels) are checked and compared to the specifications.

In the gas leak test, the assembled 4-plane or 8-plane wheels are filled with 20 mbar over-pressured argon. The leak rate is evaluated by measuring the pressure drop in the closed detector gas volume over a sufficiently long period of 4–8 hours. After applying temperature and volume corrections, only a leak rate of smaller than 1 mbar/min/bar is accepted.

The tension of the wires is measured during the stringing process itself and after completion of the module. This test is repeated also after reception of the modules at CERN. Control of the wire tension is necessary to avoid instabilities from the wires gravitational suffering and electrostatic sag. This required special attention since all wires in the TRT modules are crimped. All straws with less than 55 g wire tension, that is with tension loss greater than 5 g, were disconnected. A device based on the acoustic feed-back loop is used to accurately determine the wire tension. The wire is excited acoustically, and the characteristic frequency is measured by capacitance-oscillation sensing. The device was developed and produced at PNPI. Typically, one wire out of 3072 (one per 4-plane module) was neutralized because of the wire tension lower than the specification.

High-voltage tests are carried out at three different steps during assembly to identify and repair problematic elements. A final high-voltage conditioning is performed, when two 4-plane wheels are assembled together in a 8-plane wheel. For the binary gas mixture 70%Ar and 30%CO_2 used in this test, the high voltage is 1480 V. The voltage was applied to the wheel during several weeks. The current drawn should remain below 150 nA for groups of about 200 straws.

The problematic wires out of specification were removed and restrung when ever possible during assembly of the modules. Part of them were neutralized (disconnected from the high-voltage group by unsoldering the protection resistor), since the design of the endcap does not permit restringing of the wires after assembly of the module. Basically, all tests were repeated after transportation of the modules to CERN, before the modules enter the stage of final assembly to the super-modules equipped with front-end electronics.

6. The wheels tests and acceptance criteria

The most stringent requirement for accepting the assembled wheels [6] is the need for a stable and robust operation of the TRT detector over many years of running at the LHC. The aspired goal was to achieve a full detector with less than 1% of dead channels, although up to 3% are acceptable with respect to physics performance. Therefore all assembled TRT wheels are passed through various tests and the quality control procedures. The careful testing and analysis helped to detect non-obvious problems in the production cycle.

All the module characteristics are recorded in the production data base. In the large scale project like the TRT, the modern database is needed not only for trivial follow up of the component stores, but also to document more complicated test results, and to provide possibilities to trace the reasons of the detector failure. Even after many years of running, information on the batch of components used, on the person names

Fig. 6. View of the 8-plane wheel prepared for the tests on the WTS with radioactive source ^{55}Fe

involved into production and tests, environment conditions during the tests can be extracted from the TRT Data base.

The verification of the straw straightness, or wire offset (eccentricity) with respect to its nominal position within the straw, is the most critical test of the full set of acceptance criteria. For a wire offset of more than 400 μm, the local increase of electric field substantially modifies the gas gain. Under such conditions, the rate of discharges and large-amplitude signals increases significantly, making the straw very unstable under standard LHC running conditions. Therefore such wires are disconnected from the high-voltage supply. The actual overall wire offset can arise from several sources, *e.g.* the mechanical positioning of the crimp tube in the straw plastic end-pieces, bent or non-cylindrical straws, *etc.*

The technical difficulty in direct determination of wire positions in 370,000 straws demands an indirect way to access eccentricity and other geometric deformations of the straws. The method is based on the measurements of the gas gain uniformity along the straw tube. The verification is performed by installing the 8-plane wheel under test in a vertical position in the automated setup (called Wheel Test Station) equipped with an array of ^{55}Fe radioactive sources – see Fig. 6.

The WTS is rather complicated setup, it includes all complexities starting from precise mechanics, sophisticated electronics, computing and data acquisition system, on-line and off-line programming up to a dedicated data base. PNPI provided main contributions to this project from design to construction of the WTS key elements.

The ^{55}Fe sources are mounted on arms placed at six different radii on a star-shaped support. Through an automatic rotation of the arms, the signal amplitude, obtained from the straws filled with a 70%Ar and 30%CO_2 gas mixture, is read out at six points along the full length of each individual straw. For a perfectly straight straw with an anode wire exactly centered at the straw ends, the amplitude of the signal should be uniform along the full length of the straw. With the help of calibration curves, the wire eccentricity can be extracted from the change in the gas gain and from deterioration of the peak width. The calibration curves have been determined in experiments with controlled deformation of the straw tubes. The gas gain variation is defined by the difference of the largest and the smallest gain points. In addition, the shape of the measured peak provides an indication of the nature of the anomaly. After applying safety factors accounting for uncertainties, it was decided that straws with amplitude variations greater than 9% are subject to critical review and possibly to face disconnection. The results of all acceptance tests are stored in production database and summarized in so-called electronic endcap wheel passports.

The wheels were assembled on time according to the plans of the TRT collaboration. Less than 1% of the channels were dead. After delivery to CERN, the wheels were tested again with the results reproducing well the measurements at PNPI.

7. Integration and commissioning

During 2004–2006, stacking of all endcap wheels with their electronics into the TRT endcaps has been performed. The endcap services were connected to the detector after rotating the endcap stacks from their original horizontal position to the vertical position within a service support structure and the Faraday cage.

Before final installation in the ATLAS cavern in the beginning of 2007, the TRT has been fully characterized and qualified as an operational system separately and together with the silicon-strip detector (SCT). Common survey, mechanical and geometrical test, services test and system test have been done. The dedicated cosmic runs, stand-alone and combined with the SCT, have been performed. The major goal of the cosmic rays studies was to test combined operation of the SCT and the TRT (Fig. 7) and to check the inter-detector effects. To represent and analyse the readout data from the TRT detector, a program called Event Display was written by the PNPI team.

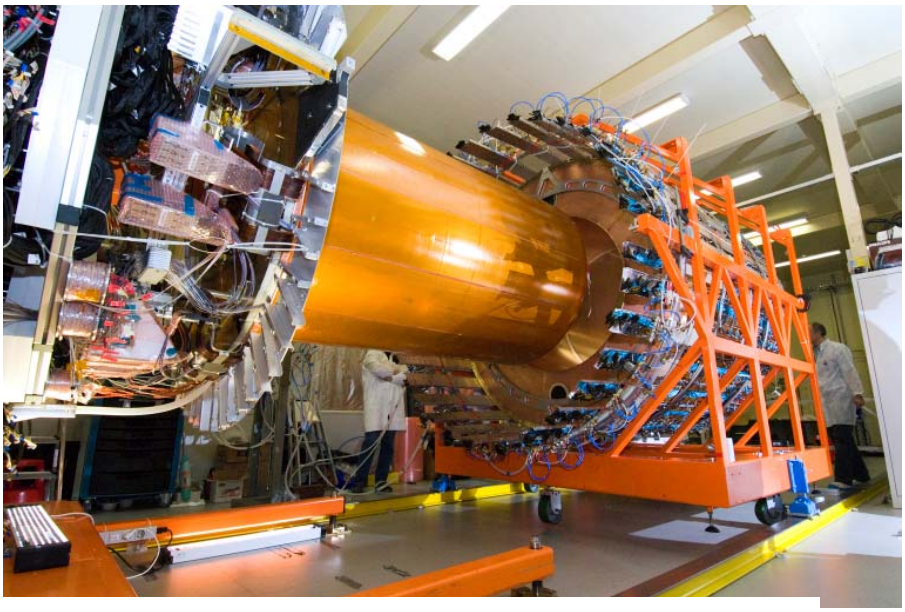

Fig. 7. View of the TRT endcap during integration with the SCT endcap at CERN

PNPI physicists made principal contribution to the TRT detector description for the GEANT4 detector simulation. Currently, studies of the TRT performance for electron identification are in progress within the Physics e/gamma group. PNPI physicists participate also in the work of the Top-physics group and the Jet/EtMiss working group.

References

1. T. Akesson , O. Fedin, A. Khristachev, L. Kudin, S. Kovalenko, V. Maleev, A. Nadtochy, S. Patrichev, Y. Ryabov, V. Schegelsky, D. Seliverstov, E. Spiridenkov, A. Zalite *et al*., IEEE Transactions, Nuclear Science **51**, 994 (2004).
2. M. Cappeans, O. Fedin, A. Khristachev, L. Kudin, S. Kovalenko, V. Maleev, A. Nadtochy, S. Patrichev, Y. Ryabov, V. Schegelsky, D. Seliverstov, E. Spiridenkov, A. Zalite *et al*., IEEE Transactions, Nuclear Science **51**, 960 (2004).
3. T. Akesson, O. Fedin, A. Khristachev, L. Kudin, S. Kovalenko, V. Maleev, A. Nadtochy, S. Patrichev, Y. Ryabov, V. Schegelsky, D. Seliverstov, E. Spiridenkov, A. Zalite *et al*., Nucl. Instr. Meth. A **522**, 50 (2004).
4. T. Akesson, O. Fedin, A. Khristachev, L. Kudin, S. Kovalenko, V. Maleev, A. Nadtochy, S. Patrichev, Y. Ryabov, V. Schegelsky, D. Seliverstov, E. Spiridenkov, A. Zalite *et al*., Nucl. Instr. Meth. A **522**, 25 (2004).
5. T. Akesson, O. Fedin, A. Khristachev, L. Kudin, S. Kovalenko, V. Maleev, A. Nadtochy, S. Patrichev, Y. Ryabov, V. Schegelsky, D. Seliverstov, E. Spiridenkov, A. Zalite *et al*., Nucl. Instr. Meth. A **522**, 131 (2004).
6. P. Cwetanski, O. Fedin, A.Khristachev, L. Kudin, S. Kovalenko, V. Maleev, A. Nadtochy, S. Patrichev, Y. Ryabov, V. Schegelsky, D. Seliverstov, E.Spiridenkov, A. Zalite *et al*., IEEE Transactions, Nuclear Science **52**, 2911 (2005).

LHCb EXPERIMENT

A.A. Vorobyov, B.V. Bochin, N.F. Bondar, O.E. Fedorov, V.L. Golovtsov G.A. Gorodnitsky, S.A. Guets, A.P. Kaschuk, V.S. Kozlov, Z.G. Kudryashova, V.I. Lazarev, V.D. Lebedev, O.E. Maev, G.V. Makarenkov, P.V. Neustroev, N.R. Sagidova, E.M. Spiridenkov, N.M. Stepanova, V.I. Tarakanov, A.Yu. Tsaregorodtsev, S.S. Volkov, An.A. Vorobyov, A.A. Zhdanov

1. Introduction

The LHCb experiment is aimed at detailed studies of *CP*-violation effects in various decays of *B* mesons and also at search for rare *B* decays suppressed in the Standard Model. These studies should check the predictions of the Standard Model on a high precision level and, in this way, may reveal some presence of the "new physics" beyond the Standard Model. At present, the main information in this research area is coming from the e^+e^--colliders (BABAR experiment at SLAC (USA) and BELLE experiment at KEK (Japan)). Also, some important results were obtained recently in the CDF and D0 experiments at Tevatron (1 TeV + 1 TeV $p\overline{p}$ -collider at FNAL (USA)). Compared to the e^+e^--colliders, LHCb will be much more abundant source of *B* mesons. Moreover, a larger variety of *b*-mesons and *b*-baryons will be produced. As concerns the CDF and D0 experiments, they are general purpose experiments, not optimized for *B*-decay studies. The LHCb experiment, being a dedicated *B*-physics experiment, will have serious advantages (forward geometry, particle identification) over the Tevatron experiments.

In the initial stage of formulation the physics program for LHC, there were three different proposals for dedicated studies of *B* physics. One of them (COBEX) proposed to use the *pp*-colliding beams, the other proposals considered two options of fixed target experiments. None of these proposals was accepted by the LHC Committee. Instead, it was recommended to the three collaborations to merge in one collaboration and to present a new proposal oriented on utilization of the *pp*-colliding beam. Following this recommendation, such collaboration (LHCb collaboration) was soon organized and started to work out the new project. The COBEX layout was considered as a starting point. The PNPI group, being a member of the COBEX collaboration, took an active part in development of the new project. In particular, the PNPI group suggested the most radical change in the COBEX layout: it was proposed to replace the COBEX magnetic system (a large quadrupole magnet followed by a small dipole magnet) by one large aperture dipole magnet. This proposal was based on simulation studies of the detector performance, including the background conditions. After hot discussions, this proposal was accepted by the collaboration. The Letter of Intent was presented in August 1995, and it was approved by the LHCC. Since then, the PNPI group focused the efforts on development of the LHCb Muon System.

2. LHCb detector

The Technical Proposal (TP) of the LHCb experiment was approved in September 1998. The LHCb detector was designed as a single-arm spectrometer with a forward angular coverage from 10 mrad to 300 (250) mrad in the bending (unbending) plane. The choice of the detector geometry was motivated by the fact that at high energies both $b(\overline{b})$-hadrons are predominantly produced in the same forward cone. The production rate of the $b\overline{b}$ -pairs being very high, the LHCb experiment plans to operate at reduced luminosity of 2×10^{32} cm^{-2}s^{-1}, still producing unprecedented amounts of the $b\overline{b}$ -pairs (10^{12} per year). This allows to study rare *B*-decay channels, under condition that these channels could be well separated from the background reactions. The strategy of the LHCb experiment was formulated as follows:

- powerful particle identification;
- high precision vertex detector;
- high momentum resolution for charged particles;
- efficient trigger for selected *B*-decay channels with *b*-tag;
- selection of the bunches with only one interaction per bunch.

These features should make the LHCb detector a unique facility for future *B*-physics.

The LHCb detector comprises a large aperture magnet, a vertex locator, a tracking system, two RICH counters, an electromagnetic calorimeter with a preshower detector, a hadronic calorimeter, and a muon system. It occupies space of 20 meters along the beam direction. One important parameter of the detector is the amount of material traversed by the particles before they enter the calorimeter. This material deteriorates the detection capability of electrons and photons, increases the multiple scattering of the charged particles, and increases occupancies of the tracking stations. Unfortunately, after completion of the Technical Design Reports (TDRs) by the end of 2001, it was realized that the material budget of the LHCb detector is a factor of 1.5 higher than expected in the TP. On the other hand, it was understood that the amount of material can be reduced to the TP values by reoptimizing some of the detector systems without deterioration of its performance.

Figure 1 shows the layout of the reoptimized LHCb detector. The basic layout remains unchanged from that of the TP. The main changes are in the number of tracking stations (4 stations instead of 11), in the number of stations in the vertex detector (21 instead of 25), in the thickness of the silicon sensors (220 μm instead of 300 μm), and in the number of detecting planes in the first muon station M1 (two planes instead of four). Also, there is some reduction of material in RICH1 (due to changing the mirror material) and in the beam pipe (due to replacing the Be-Al alloy by Be in the sections up to the calorimeters. The resulting material budget in front of RICH2 is now 20–30% of the radiation length X_0 and 12% of the nuclear interaction length λ_I, compared to the TP values: 40% of X_0 and 10% of λ_I.

The design of the reoptimized LHCb detector was approved in 2003 [1].

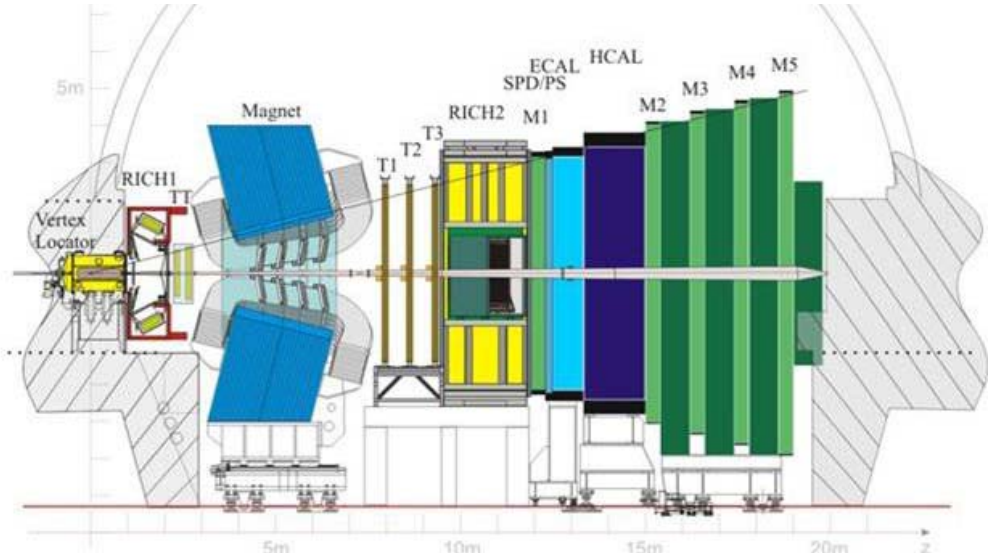

Fig. 1. Reoptimized LHCb detector layout showing the Vertex Locator (VELO), the dipole magnet, the two RICH detectors, the four tracking stations TT and T1–T3, the Scintillating Pad Detector (SPD), Preshower (PS), Electromagnetic (ECAL) and Hadronic (HCAL) calorimeters, and the five muon stations M1–M5

3. PNPI participation in design and construction of the LHCb Muon System

3.1. LHCb Muon System. General layout and principle of operation

The Muon System performs two functions: the muon identification and the Level-0 muon trigger. Also, it should provide matching of the selected muon trajectory to the Tracking System for precision measurement of the muon momentum. The principle of operation of the Muon System was formulated by the PNPI group in 1997 [2]. It was demonstrated that the Muon System can provide the muon trigger in a stand-alone mode using information only from the muon chambers. As it is described in the Muon TDR [3], the Muon System contains a longitudinally segmented shield to attenuate hadrons, photons, and electrons. The shield components comprise ECAL, HCAL, and four iron walls. The total weight of the iron shield is 1800 tons. Five muon stations, M1–M5, are located as shown in Fig. 1. Muon station M1 is positioned in front of ECAL Stations M2–M4 are embedded in the 40 cm space available between the iron walls, being mounted on movable platforms as illustrated in Fig. 2. The inner and outer acceptance (horizontal-vertical) of the Muon

System is 25 mrad × 15 mrad and 294 mrad × 250 mrad, respectively. The sensitive area of the muon stations varies from 42 m^2 (M1) to 106 m^2 (M5).

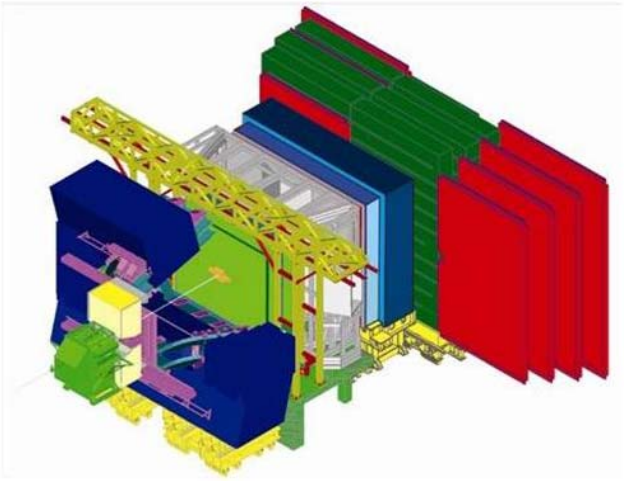

Fig. 2. Artist's view of LHCb.
The muon detectors in stations M2-M3 (red color) can slide sidewise the beam line to allow access. The figure shows the right-hand side detectors in maintenance position

As it was proposed in Ref. [2], the muon track finding procedure starts with detecting a hit in station M3. Then hits in the other stations are searched in the "fields of interest" close to the line connecting the hit in M3 with the interaction point. Finally, the muon trajectory is reconstructed using the hits in M2 and M1, while the hits in the other stations serve to reduce the background. Thus found muon trajectory is traced back to the interaction point. The deviation of the projected trajectory from the interaction point (impact parameter) is a measure of the muon transfer momentum p_t. The muon trigger selects events with p_t higher than a preset value (~ 1.5 GeV/c). The simulation shows that such trigger can provide ~ 40% registration efficiency for the $B \to \mu$ events with suppression factor of ~100 for the minimum bias events. The described above M1/M2 p_t cut exploits information from M1 station which is located in front of ECAL in most severe background conditions. However, in case of problems with M1, the muon trajectory could be determined using hits in M2 and M3. The performance of such M2/M3 p_t cut is still satisfactory: ~30% $B \to \mu$ efficiency with the same suppression factor for the minimum bias events. The described algorithm was implemented in Muon Trigger System which provides the Level-0 trigger signal in less than 3 μs time after the interaction.

3.2. Choice of the muon detector technology

A serious problem in the Muon System is the high background. Our studies with GCALOR simulation program [4] showed that fluxes of charged particles in station M1 vary from 200 kHz/cm^2 in the region close to the beam pipe to 10 kHz/cm^2 in the outer region. The background in stations M2–M5 is lower by nearly two orders of magnitude, but still it is very high. To a great extent, the high background level determines the choice of the detector technology. The detector should be fast and radiation hard. The trigger algorithm requires the very high detection efficiency in each muon station. It should be 99% in a 20 ns window to determine reliably the correct bunch crossing. On the other hand, the space resolution of the muon detectors might be rather modest, coherent with the muon track diffusion due to Coulomb scattering in the iron shield. To satisfy these requirements, a 2D-pad structure has been chosen with the pad dimensions in each station scaled so that the pad configuration in M1–M5 is projective to the interaction point. Each station is divided into four regions, R1–R4, with different pad sizes. Several technologies have been considered for the muon station detectors. The PNPI group suggested to use specially designed fast operating wire chambers with anode and/or cathode readout. The other technologies were so-called Thin Gap Chambers (TGC) and Resistive Plate Chambers (RPC). After extensive R&D studies, the LHCb collaboration has chosen the wire chambers proposed by PNPI for the whole Muon System except a small but the most "hot" region R1 in station M1 where GEM detectors will be used.

The proposed wire chambers have a rectangular geometry with the sensitive area $S = H \times L$, where the chamber height H varies from 20 cm (M1, R1–R4) to 31 cm (M5, R1–R4) and the chamber length L from 24–37 cm (R1, M1–M5) to 96–150 cm (R4, M1–M5). An important feature of this design is identical chamber height for all regions within one station. This allows to use the "ladder structure" and to avoid complications in boundary areas between different regions. This structure is illustrated by Figs. 3, 4.

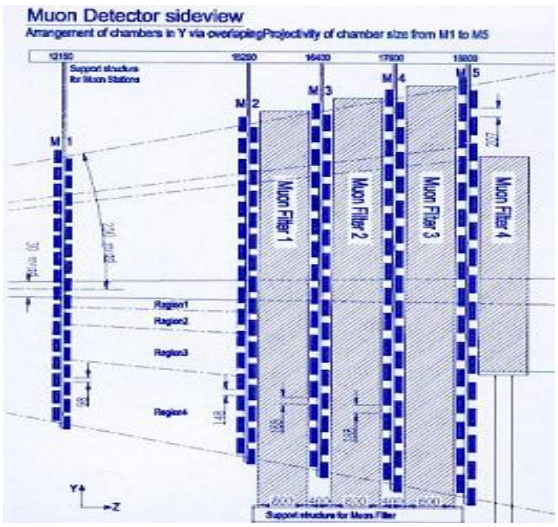

Fig. 3. Side view of the muon system in the YZ-plane

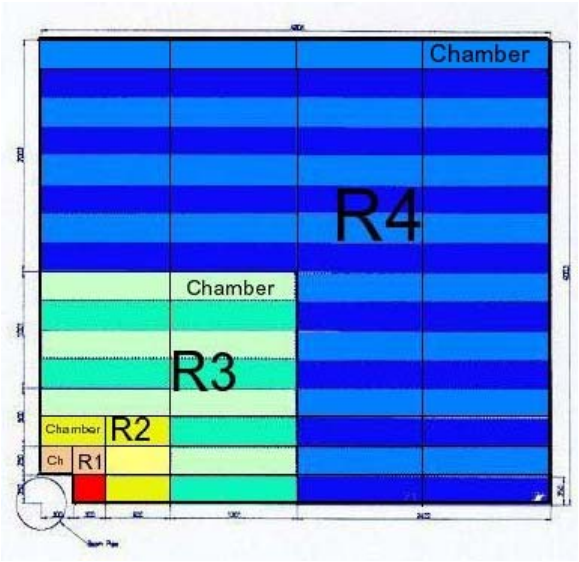

Fig. 4. XY-view of a quarter of station M2. Regions R4, R3, R2, and R1 are marked in blue, green, yellow and red, respectively

The wire chambers have symmetrical cells with the following geometry parameters:

- the anode-to-cathode distance – 2.50 mm ,
- the anode wire diameter – 30 μm,
- the anode wire spacing – 2.0 mm.

The wire is wound along the short side of the chamber in the vertical (Y) direction. In the region R4, the wire length coincides with the required pad size in the Y-direction. Therefore, wire pads are used in these regions by grouping several wires in one readout circuit. For example, the wire pad size in the region M3R4 is 54×270 mm^2. The other regions have cathode pads with the pad sizes reduced in both directions by the factors 2 (R3 region), 4 (R2 region), and 8 (R1 region). The pad size remains constant within each region.

Each chamber in stations M2–M5 contains four sensitive gaps which are connected as two double-gap layers. Such multi-gap structure helps to satisfy the requirements of fast operation and high detection efficiency. Also, it should provide a sufficient redundancy of the Muon System designed for many-years operation of the LHCb experiment. Note, however, that the station M1 contains only one double-gap, due to space and material budget constraints for this region.

3.3. Study of muon chamber prototypes

During the period 1998–2002, a series of muon chamber prototypes (10 prototypes in total) were constructed at PNPI and tested in a pion beam at CERN [5] – see Fig. 5. These R&D studies allowed to optimize the chamber geometry parameters, the gas mixture, and the front-end electronics parameters. Also, simulation studies of the muon chamber performance were carried out.

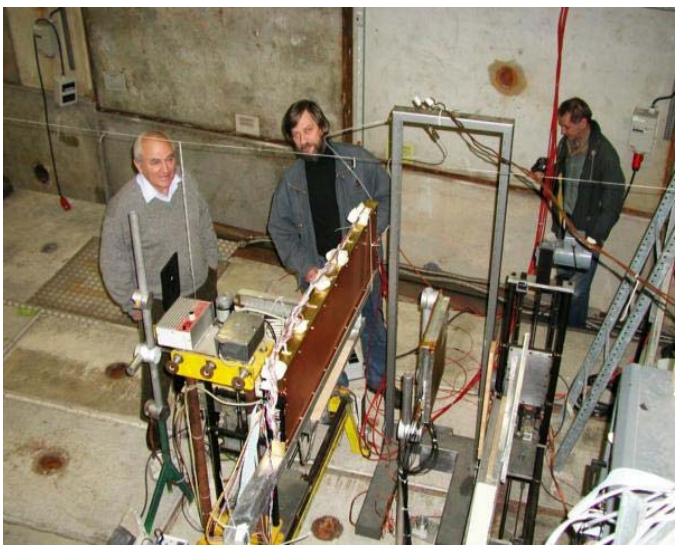

Fig. 5. One of the muon chambers constructed at PNPI in the T11 test beam area at CERN. In total, 10 muon chamber prototypes have been constructed at PNPI and tested in the 3 GeV/c pion beam at CERN. The results of these tests were decisive for selection of the proposed detector technology for the LHCb Muon System

Various gas mixtures have been tested, and the mixture of $Ar/CO_2/CF_4$ (40:50:10) was recommended. This gas mixture provides high electron drift velocity (~100 μm/ns), increased stability again discharges, and good aging properties. Note that these studies were performed with 1.5 mm wire spacing in the chambers. The conclusions from these studies were as follows.

- One double-gap layer of the muon chamber can provide the required 99% detection efficiency in a 20 ns time window in the high voltage (HV) range from 3.15 kV to 3.35 kV, the efficiency being not so sensitive to staggering of the wire planes and to the incident angle of the muons.
  With two double-gap layers, the 99% efficiency can be obtained starting from HV = 2.95 kV.
- The gas gain was around 10^5 at HV = 3.15 kV. Its variation over the whole chamber area was measured to be within ±20% (equivalent to ±30 V variation in HV).
- The chambers could operate at high beam intensity. The tests with a 150 kHz beam did not show deterioration of the detection efficiency.
- The total cross talk probability in a double-gap layer was measured to be less than 10% at HV ≤ 3.2 kV, and it was dominated by the cross-talk to the neighbor pads.

These results demonstrated that the designed muon chambers can satisfy the requirements of the LHCb experiment with the redundancy which was considered even as excessive. That is why the collaboration decided to increase the wire spacing from 1.5 mm to 2.0 mm, thus reducing the cost and simplifying the assembling procedure. Further tests showed that the chamber performance was not deteriorated significantly. After that, the chamber technology was fixed, and the construction of the Muon System has been started.

3.4. Assembling of muon chambers at PNPI

The LHCb Muon System contains 1380 muon chambers in total, 600 of them were to be assembled at PNPI. These are the four-gaps chambers with the wire pad readout for the region R4 in the stations M2, M3, and M4. They cover 75% of the total area of these stations (Fig. 4). The sensitive area of each chamber is 120 × 25 cm^2 (M2R4), 130 × 27 cm^2 (M3R4), 140 × 29 cm^2 (M4R4). In total, they contain about 1500000 anode wires.

According to the specifications, the gas gain should be uniform over the chamber area within ±30%. This is translated to the following constraints: the gap size of 5.0 ± 0.1 mm, the anode wire spacing of 2.0 ± 0.1 mm, the anode wire tension of 65 ± 5 g.

The chambers have no frames. The chamber planes are glued together, so the chambers could not be opened after assembling. This requires a reliable assembling technology with control at at each step. Such technology has been developed at PNPI, and it was approved by the collaboration after the Production Readiness Review on January 30, 2004. Then chamber assembling was started in a specially prepared assembling facility (PNPI-1) – see Figs. 6, 7. From mid of 2005, the second facility (PNPI-2) – see Figs. 8, 9 – joined this activity. More than 40 PNPI specialists were involved in this project. A clean area (800 m^2) was prepared for this work. Both facilities were equipped with special tooling: six bar-gluing tables, two automated wiring machines, an automated wire-soldering machine, two wire-spacing and wire-tension control machines, two γ-rays test stands, various test equipment. This tooling was designed and fabricated jointly by the PNPI and CERN teams.

Fig. 6. Bar gluing tables at PNPI-1 facility

Fig. 7. Automated wire soldering and wire pitch and tension measuring machines at PNPI-1

Unprecedented production rate has been reached: up to one chamber per working day in each facility. By the end of 2006, all 600 chambers have been assembled and tested. According to the tests, all chambers were well within the specification requirements.

Fig. 8. Automated wiring machine at PNPI-2 facility

Fig. 9. The PNPI-2 team in front of containers with the last muon chambers assembled at PNPI and prepared for the transportation to CERN on November 20, 2006.

All results from the tests are stored in the CERN Oracle Database Server accessible *via* Internet by any member of the LHCb collaboration – see Fig. 10.

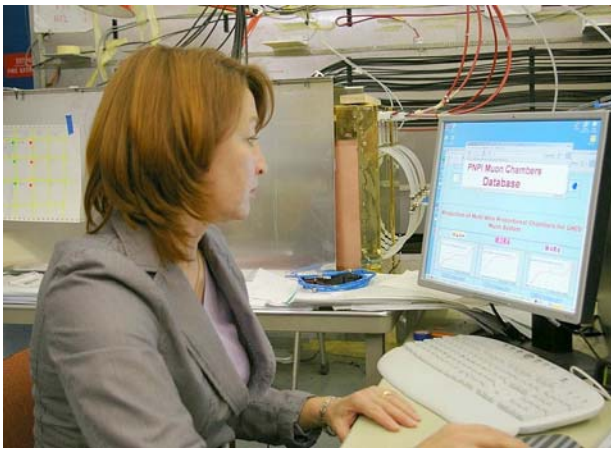

Fig. 10. Special Web-Application was developed in order to implement all test results into the CERN Oracle Database Server. The database contains full information on chamber tests at all stages from the beginning of construction till the installation into the LHCb Muon System

3.5. Testing of muon chambers at CERN and installation into LHCb Muon System

By the end of 2006, all 600 muon chambers assembled and tested at PNPI were transported to CERN. At CERN, the tests were repeated (gas leak tests and HV tests). After that, the chambers were installed in a storage area and permanently flushed with dry nitrogen. Then the chambers were dressed with Faraday cages and with low voltage and high voltage lines, and were passed the final "pre-installation" tests on a special cosmic-rays test stand. Some chambers were also tested in the CERN high-flux gamma-rays facility GIF. All this work was done by the PNPI team.

After the pre-installation tests, the chambers were sent to the LHCb pit for installation into the Muon System. The installation process required tremendous efforts from the PNPI team. This procedure included preparation of the gas lines, tracing the HV, LV, and readout cables, fixation of the chambers in their positions in the muon stations, alignment of the chambers, gas leak tests, and tests of the readout electronics. A team of 10 people from PNPI participated in this work from mid of 2006. The installation and commissioning of the muon chambers should by finished by the end of 2007, when the Muon System should be prepared for the pilot run of LHC.

All the above mentioned stages of testing of muon chambers at CERN and their installation into LHCb Muon System are illustrated by Figs. 11–16.

Fig. 11. Muon chambers in containers after arrival at CERN

Fig. 12. Muon chambers in storage area at CERN

Fig. 13. Preparing of muon chambers for final tests

Fig. 14. Testing of muon chambers at cosmic-rays test stand

Fig. 15. Installation of muon chambers into the LHCb Muon System.

Fig. 16. PNPI team participating in installation of the LHCb Muon System

3.6. Design and construction of multi-channel high voltage system for LHCb Muon detector

The LHCb Muon System contains 1380 muon chambers with about 5000 detecting layers. For better redundancy of the system, it would be important to have independent high voltage supply (up to 3 kV) for each layer. However, the cost of such multi-channel HV system available on market proved to be unacceptable for the LHCb collaboration. A much less expensive HV system for 11000 channels has been constructed recently by joined efforts of PNPI and Florida University for the CMS detector. The LHCb collaboration offered PNPI to build a similar HV system for most part of the LHCb Muon detector (for 4000 channels). Taking into account the critical situation in construction of the HV system for the LHCb Muon detector, PNPI agreed with this proposal, though this work was not in the initial PNPI responsibilities. As the first stage, it was decided to build a system for 2000 channels in 2007 with further extension up to 4000 channels. The designed HV system provides in each channel the voltage control with 1 V resolution and the current control with a resolution of 2 nA (for $I < 1$ μA) and 100 nA (for $I > 1\mu$A). The maximal current in one channel is 100 μA. During 2006, a 108-channel prototype of the HV system was constructed at PNPI and tested at CERN. Construction of the 2000-channel system is planned to be completed by the end of 2007. A block scheme of this HV system is presented in Fig. 17.

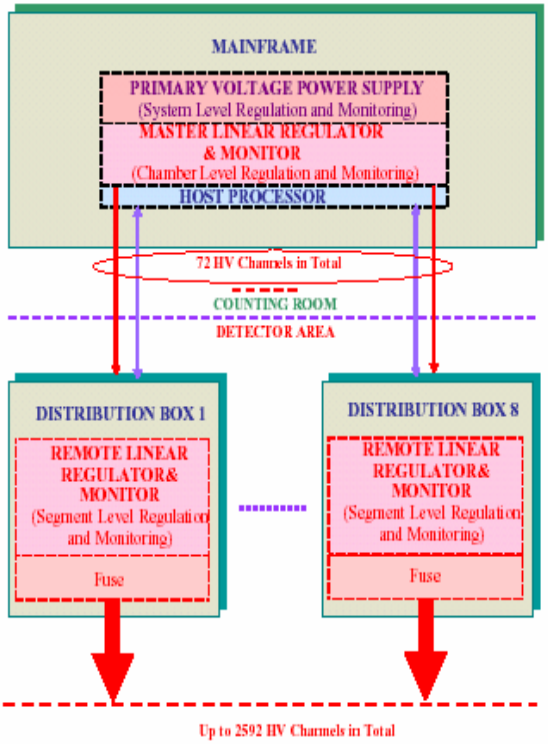

Fig. 17. Block scheme of designed multi-channel HV system for the LHCb Muon detector.

References

1. LHCb Reoptimized Detector Design and Performance Technical Design Report, CERN/LHCC 2003-30, LHCb TDR9, 9 September 2003.
2. M. Borkovsky, A. Tsaregorodtsev and A. Vorobyov, LHC-B 97-007 TRIG, 1997; M. Borkovsky, G. Gorti, B. Cox, A. Tsaregorodtsev, K. Nelsen and A. Vorobyov, LHC-B 98-002 TRIG/MUON, 1998.
3. LHCb Muon System. Technical Design Report, 28 May 2001.
4. N. Sagidova, A. Tsaregorodtsev and A. Vorobyov, LHC-B 97-009 EXPT; LHC-B 97-011 EXPT; LHC-B 97-012 EXPT; LHC-B 98-059 EXPT.
5. B. Bochin, S. Guets, V. Lazarev, N. Sagidova, E. Spiridenkov, An.Vorobiev and A.Vorobyov, LHCb 2000-003 MUON, 14 February 2000; LHCb 2000-102 MUON, 24 Octjber 2000; LHCb 2001-025 MUON, 28 March 2001; LHCb 2002-025 MUON, 19 April 2002.

PNPI IN ALICE

V.M. Samsonov, V.A. Evseev, V.V. Ivanov, A.V. Khanzadeev, E.L. Kryshen, N.M. Miftakhov, V.N. Nikulin, V.V. Polyakov, E.V. Roschin, V.I. Ryazanov, O.P. Tarasenkova, M.B. Zhalov

1. Introduction

The ALICE detector is designed to study heavy ion collisions at the energies of several TeV per nucleon by detecting hadrons, electrons, photons, and muons produced in these collisions. A special feature of such collisions is high multiplicity – up to several thousand particles per event per rapidity unit. This feature demands high granularity in the detector systems. The ALICE detector consists of a central (barrel) part embedded in a large solenoid magnet (L3 magnet) and a forward muon spectrometer (Fig. 1).

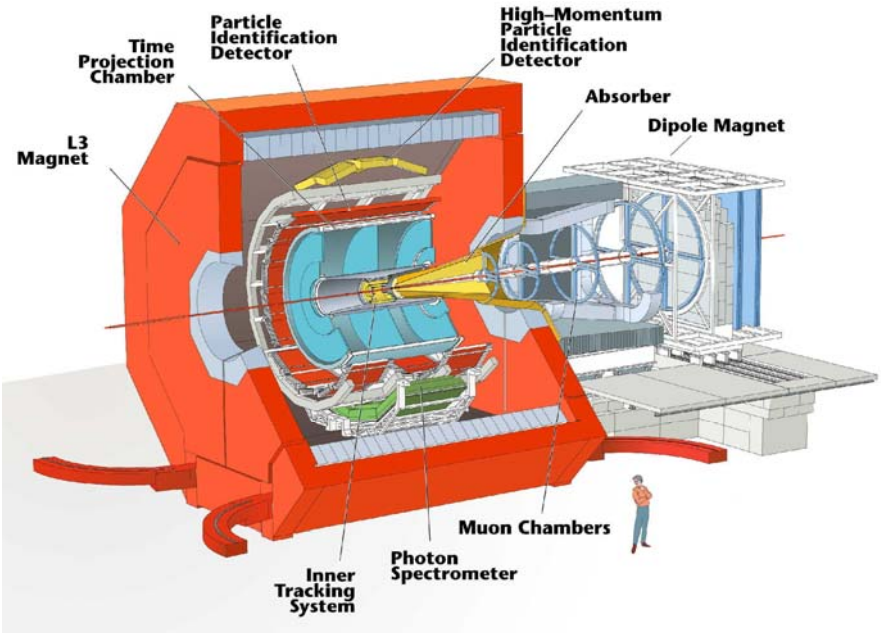

Fig. 1. The layout of the ALICE detector. The muon spectrometer arm is depicted on the right side of the figure

The barrel part comprises the Inner Tracking System (based on Si-detectors), the Time Projection Chamber, the Particle Identification System (consists of a time-of-flight detector, transition radiation detector and a ring imaging Cherenkov detector), and the Photon Spectrometer based on scintillating $PbWO_4$ crystals. There are also several small forward detectors (not shown in Fig.1): ZDC (zero degree calorimeter), EMD (forward multiplicity detector), TO (collision timing detector), and VO (centrality and collision vertex detector).

PNPI participates in design and construction of the muon spectrometer. This spectrometer consists of a large dipole magnet, absorbers, five tracking stations, the muon filter and trigger chambers. It is aimed to study the heavy quark resonances, *i.e.* J/ψ, ψ', Υ, Υ', Υ'' identified by their decay into muon pairs. The estimated mass resolution is of the order of 100 MeV at 10 GeV, sufficient to distinguish the fine structure of the Υ resonances.

The physics interests of the PNPI team are concentrated on studies of the ultraperipheral collisions and polarization effects in production of the heavy quarkonia. We exploit the unique features of the muon spectrometer – high mass resolution and capabilities to produce various trigger signals. It has been demonstrated that minor modifications of the standard trigger algorithm may allow to obtain valuable information on gluon density behavior.

2. Tracking chambers for the Muon Spectrometer

2.1. Tracking chamber design

In order to achieve the required mass resolution the tracking stations of the ALICE Dimuon arm should satisfy several main requirements:

- They must be thin enough in order to introduce negligible deterioration to the muon track (average X/X_0 of the station is less than 3%),
- They should be able to operate in high hit density environment (up to 0.01 hits per cm^2), and
- To measure the track position with the precision of about 100 μm in bending plane and about 1 mm in non-bending one.

Moreover, the stations cover large sensitive area (up to 5×5 m^2). The cathode pad chambers (CPC) were chosen for this purpose.

Following suggestions of the PNPI group [1], the rear tracking stations (stations 3, 4 and 5) have a slat structure, *i.e*. they are composed of the overlapping rectangular CPC modules (also called as slats). The length of the modules varies from 80 cm to 240 cm with the constant height of 40 cm.

Several CPC prototypes were constructed and tested, and the assembling technology was developed. The CPC body built of two carbon-fiber/honeycomb sandwiches with the PCB cathodes glued onto them. The cathode segmentation (length of the pads) varies with the behavior of the expected hit density. The signal wires (made of tungsten, diameter of 18 microns, without gold plating) are glued between the spacers made of Noryl. The materials were carefully chosen in order to minimize the detector ageing. The front-end electronics cards are plugged into connectors in the peripheral area of the slats. Special attention has been paid to perform permanent in-production quality control of the modules from the very beginning of the assembly till the final tests, to maintain the cathode planarity, uniformity of the anode-cathode distance, the stress of anode wires, to achieve the correct position of each pad. The special tooling has been developed at PNPI for this purpose.

The assembly of 38 CPC modules (a quarter of the total number) has been accomplished at PNPI. For this task, a clean assembly area was prepared and equipped with specially developed tooling and with testing setups.

2.2. Tooling for production of the tracking chambers

The PNPI team was responsible for design and construction of the tooling for production of the tracking chamber modules. The PCB trimming machine, the high voltage test bed, the β-source test bench and the devices to measure the wire tension were developed at PNPI and provided to all teams in the collaboration involved in production of the tracking chambers for stations 3-4-5 of the ALICE Muon spectrometer.

PCB trimming device

The high spatial resolution requires a precise (about ±40 microns) positioning of the cathode pads. In order to accomplish this task, the sides of the PCBs were trimmed and the fiduciary holes were punched. The typical linearity of the trim was ±15 microns, the trim line being positioned with respect to the pads within ±20 microns. The same precision was achieved in positioning of the fiduciary holes. This device (see Fig. 2, left) has been used to treat all the PCBs used in the tracking chambers for stations 3, 4, and 5.

A simplified option of the device (Fig. 2, right) has been developed and produced at PNPI for our colleagues at Saha Institute (Kolkatta, India). In this case the chamber assembling technology did not require the fiduciary holes, the cathode pads are aligned using the high quality of the PCB edge trimming. The device has been successfully used in production of the chambers for the tracking station 2.

Fig. 2. The PCB trimmers developed for preparation of the slats for stations 3, 4, 5 (left) and for station 2 (right) at PNPI

β-source test bench

Special attention was paid to monitoring the gas gain uniformity. The variations of the gas gain reflect defects of planarity of the cathode planes, resulting in degradation of the chamber spatial resolution. We controlled the gas gain by measuring the current induced in the chambers by a β-source. The constructed test bench (Fig. 3) performs movement of the collimated β-source across the sensitive area with simultaneous measurement of the current. The observed irregularities of the 2-dimensional gas gain distribution do not exceed 30% with typical dispersion around 10% [2].

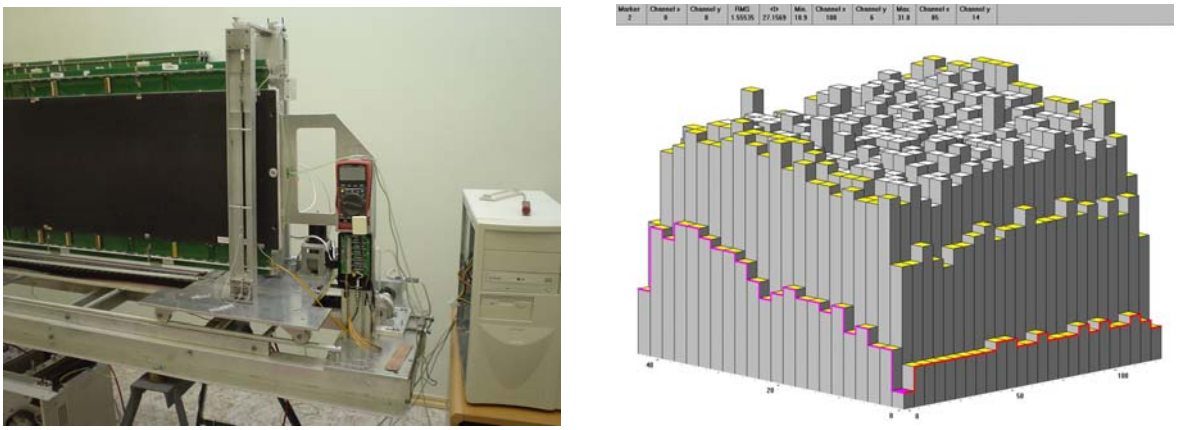

Fig. 3. β-source test bench and an example of gas gain homogeneity distribution in a tracking chamber

High voltage test bed

The High Voltage Test Bed (HVTB) was build to check the quality of assembled chamber wire planes [3]. The HVTB is a leak-proof box with a transparent cover (see Fig. 4). The cover has a translucent cathode grid and spacers attached to it. The HVTB is equipped with a pneumatic system which lifts up the wire plane and presses it to the cover spacers to reproduce the HV geometry close to that of the real slat chamber. The HVTB is filled with nitrogen – a spark-resistant gas. The applied HV induces corona discharge around the anode wires. The glow is brighter near locations with abnormally strong electric field, as motes, sharp burrs, loose wires etc. This makes the chamber defects visible. The small motes and burrs can be burnt out after 6–7 hours of the corona discharge. Such devices were shipped to all teams which produced chambers for tracking stations 3-4-5.

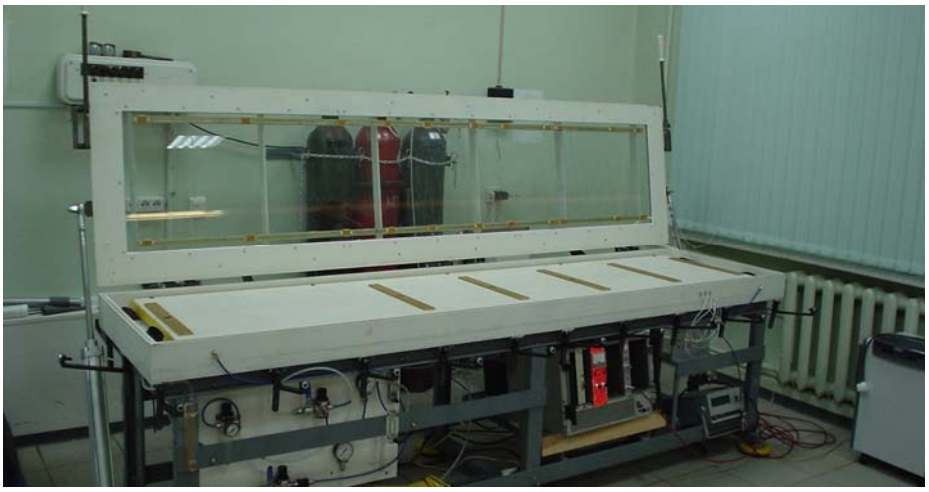

Fig. 4. A view of the high voltage test bed

Measurement of wire tension in tracking chambers

The total number of wires in the tracking system is of the order of 100,000. All wires must be stressed; otherwise the system would be mechanically unstable due to electrostatic repulsion (so-called staggering effect). For the chosen wire parameters the minimal tension (staggering limit) is estimated to be 17 grams, while the wire elasticity limit is about 70 grams. The nominal wire tension was chosen to be 40 grams. In order to guarantee the quality of the wiring, it was foreseen that each individual wire tension should be measured during the chamber production. Two kinds of devices for measurements of the wire tension have been built. The first one (see Fig. 5) is designed for use during the chamber production and the other one to check the fully assembled chambers. Both devices use the relation between the wire tension and its resonance frequency. Capacitive sensors are used to catch the free wire oscillations, and the Fourier procedure is used to find the resonance frequency. The difference between the setups is the wire excitation method: while the in-production procedure uses electrostatic pulses, the assembled chambers are checked using the mechanical tap.

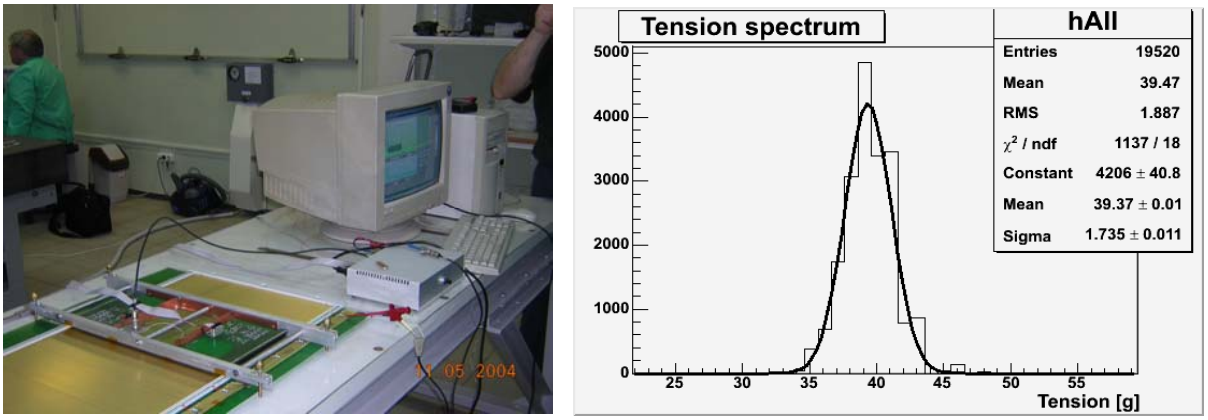

Fig. 5. The equipment for wire tension measurement and the wire tension distribution measured for about 20,000 wires in the chambers produced at PNPI

Both devices can measure the wire tension with the tolerance of ±0.5 g within reasonable time (about 20 minutes per 80 wires) [4]. The results of the measurements with the first device are filled in the production database. The second device is used during the chamber commissioning and in periodical checks during the LHC shutdowns.

Beam tests results

The prototypes of the tracking chambers were tested at CERN using the pion beam at PS with the momentum of 7 GeV/c and the muon beam at SPS with the momentum of 120 GeV/c. An array of 10 silicon strip detectors (pitch of 50 microns) has been used to reconstruct the track parameters. The beam test data has been analyzed by several teams. The analyses gave consistent results: the spatial resolution had a narrow component with sigma of about 70 microns at PS and about 50 microns at SPS (the difference is caused by the multiple scattering) at the efficiency of 96% (inefficiency is caused by the distribution tails). The PNPI analysis [5] featured a readout/decoding subroutine, several new methods for the position reconstruction, wide-range parameterization of the realistic residual distribution (see Fig. 6), and parameterization of the resolution angular dependence.

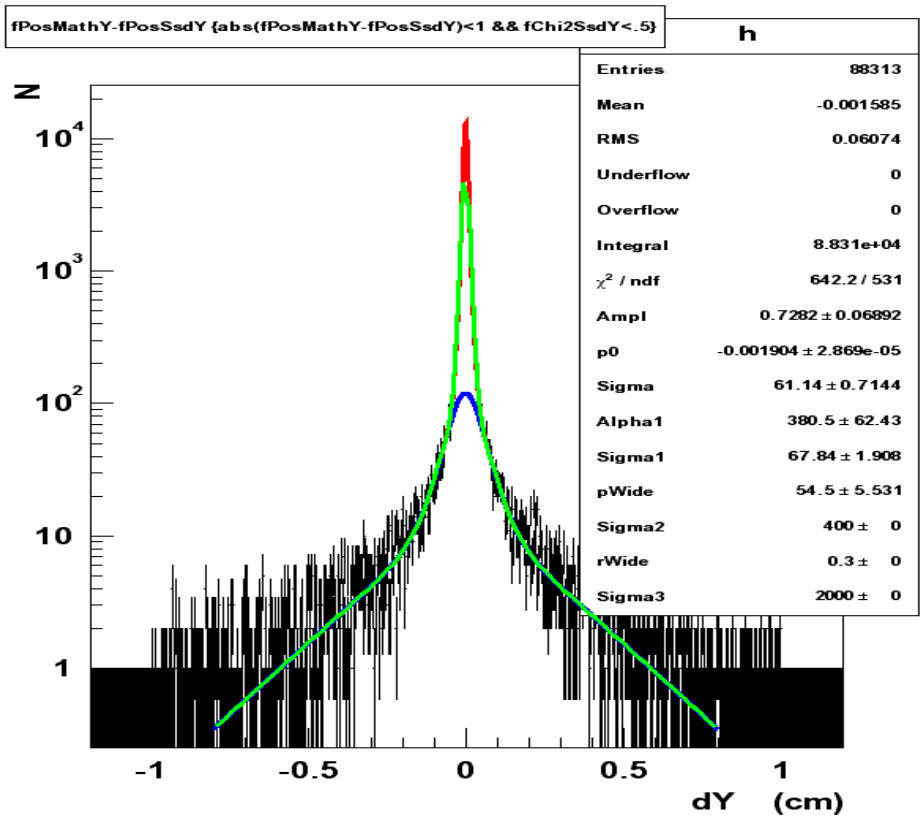

Fig. 6. Parameterization of the residual distribution measured at PS, one can see narrow (~70 microns) and wide (~300 microns) components of the distribution

2.3. Assembling, tests and commissioning of the tracking chambers

To perform the slat production of the tracking chambers, a dedicated assembling site was organized at PNPI (Fig. 7). It includes a clean room (equipped with necessary tooling with a climate control) and several auxiliary rooms.

The final assembling of the tracking stations took place at CERN; the PNPI representatives participated in this activity (see Fig. 8). During the chamber assembling, the slats were tested for gas tightness and high voltage, they were equipped with electronics; the electronics was burned and the readout has been tested. By mid of 2007 the Muon Spectrometer assembling is nearly completed, most of the chambers are equipped with electronics and installed in the ALICE cave. The time before the run will be devoted to the commissioning: final installation of the services, tests of the readout, *etc.*

Fig. 7. A view of clean assembling room (a), gluing of the PCB to the composite sandwiches (b), wiring machine (d), and installation of the signal wires on a wire plane (c)

Fig. 8. Tests of tracking chambers at CERN (left) and the assembled half of the tracking station (right) at CERN

3. Mechanical design of the setup

The PNPI team contributed to mechanical design of the muon spectrometer parts: the muon filter and the superstructure. The design includes a complete set of the engineering drawings and the finite element analysis (stress and buckling analysis, simulation of the earthquake). The design was adapted to the capabilities and features of Russian plants. Unfortunately the price tag proposed by Russian industry was too high, so the muon filter has been redesigned in order to build elsewhere. The design of the superstructure did not affected significant changes; it was built at CERN (Fig. 9).

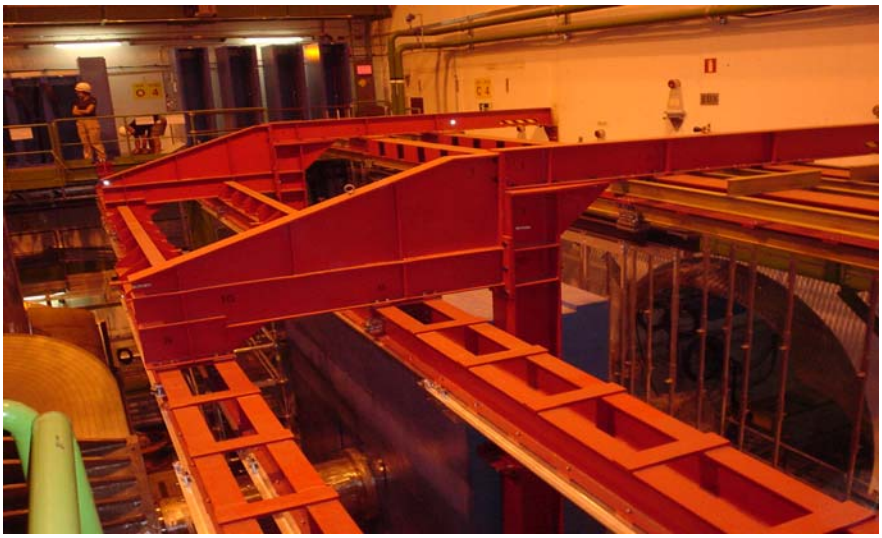

Fig. 9. Superstructure for support of the tracking and trigger chambers designed by the PNPI group

It has also been demonstrated that the requirements to the quality of the gaps between the elements of the muon filter could be rather loose [6].

The members of the PNPI team (Fig. 10) also participated in magnetic field mapping, geometry survey of the detectors and pulling of the cables (together with colleagues from JINR, Dubna).

Fig. 10. Geometrical survey (left) and cabling activity (right) at ALICE

4. Physics activities

Heavy quarkonia photoproduction

In their pioneering article [7], L. Frankfurt, M. Strikman and M. Zhalov demonstrated that the coherent photoproduction of heavy quarkonia in Pb-Pb collisions at LHC has considerable total cross section and is sensitive to the small-x behavior of the gluon density. We found that the Level-0 trigger in the muon spectrometer, with minor modifications, could be used to study the coherent quarkonia photoproduction (Fig. 11). The two cases were considered: when both muons are detected by the muon spectrometer, and also

when one muon hits the muon arm while another one is detected in the barrel. In the first case the standard muon trigger could be used with T0 and V0 decisions excluded. In the second case an additional pre-selection of the events of interest could be achieved including a veto from the Photon Spectrometer. Later, more sophisticated L0 triggers from the pixel Inner Tracking System and from the Time-of flight detectors could be implemented. The additional clean-up could be done at Level-1 analyzing the (ZDC) information. The off-line quarkonia p_t analysis will make a final selection of the coherent events. The estimated counting rates are order of 20,000 events in both cases for J/ψ and few hundreds for the case of Upsilon per heavy ion running year [8].

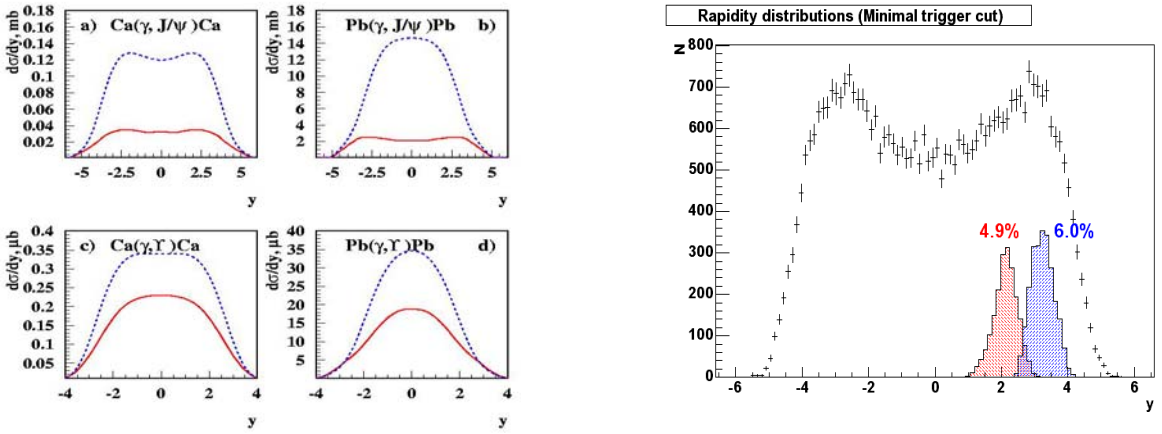

Fig. 11. The theoretical predictions (left) and the AliRoot simulation of the coherent J/ψ photoproduction (right) in function of rapidity; the blue peak corresponds to the case when both muons are detected in the muon arm, the red peak corresponds to the case when one muon is detected in the muon arm, and another one is detected in the barrel

Heavy quarkonia polarization

We considered the possibility of the J/ψ polarization measurements in the barrel part of ALICE [9]. The quarkonium polarization is an important test for understanding the quarkonium production mechanisms and heavy ion collision dynamics. The simulations were carried out within the *AliRoot* framework. An event generator has been developed; the 3D acceptance analysis (p_t, y, $\cos\theta$) has been carried out. It has been demonstrated that the polarization parameter can be extracted in five p_t bins, with the statistical uncertainties on the reconstructed parameter ranging from 0.02 to 0.13.

References

1. V. Nikulin, A. Vorobyov *et al.*, ALICE internal note ALICE-INT/DIM-99-41.
2. V. Baublis, A. Khanzadeev, V. Nikulin *et al.*, ALICE internal note ALICE-INT/DIM-2003-044.
3. A. Khanzadeev, V. Polyakov, E. Rostchin *et al.*, ALICE internal note ALICE-INT/DIM-2004-003.
4. V. Ivanov, V. Nikulin, E. Rostchin, V. Samsonov and E. Vznuzdaev, "Wire tension measurements for ALICE muon arm slat chambers", submitted as ALICE note.
5. A. Khanzadeev, V. Nikulin, V. Samsonov *et al.*, ALICE internal note ALICE-INT/DIM-2003-048.
6. V. Nikulin *et al.*, ALICE internal note ALICE-INT/DIM-2002-021
7. L. Frankfurt, M. Strikman and M. Zhalov, Phys. Lett., B **540**, 220 (2002).
8. V. Nikulin and M. Zhalov, ALICE internal note ALICE-INT/DIM-2003-043.
9. E. Kryshen, PWG-3 Report, 18 April 2006.

STUDY OF CHANNELING AND VOLUME REFLECTION EFFECTS IN BENT CRYSTALS

PNPI participants of the Russia-Italy-USA-CERN Collaboration:
Yu.M. Ivanov, N.F. Bondar, Yu.A. Gavrikov, A.S. Denisov, A.V. Zhelamkov, V.G. Ivochkin, S.V. Kosyanenko, L.P. Lapina, A.A. Petrunin, V.V. Skorobogatov, V.M. Suvorov, A.I. Shchetkovsky

1. Introduction

In the last years it has been shown that short bent silicon crystals can be used efficiently to extract beam particles out of the accelerators. This crystal extraction was applied to the main beam and also to the halo particles. The idea of crystal based collimation for the Large Hadron Collider (LHC) at CERN is to use bent crystals for deflecting the halo protons at 6σ from the central beam orbit onto a special absorber where they hit with large impact parameters. Due to large deflection angles and high impact parameters the halo protons can be efficiently removed using crystals from the LHC beams that should reduce background in detectors and avoid quenches of superconducting magnets at highest luminosities. Below we describe our recent studies of silicon properties and beam-crystal interactions performed at PNPI, IHEP, and CERN with the aim to develop high efficient crystal collimation system for the LHC.

2. Observation of elastic quasi-mosaicity effect in silicon

Multiple scattering of high energy charged particles in material restricts an efficiency of the crystals as beam deflectors. Estimations show that optimal size of the bent silicon crystals in beam direction should lie in millimeter or sub-millimeter region with the bending angles of the atomic planes not exceeding one-two hundred microradians. We found that such requirements can be met using elastic quasi-mosaicity effect in bent silicon plates.

This effect is well-known in crystal-diffraction γ- and X-rays spectrometry after studies carried out by O.I. Sumbaev in 60-es. He showed that bending of quartz plate results in the curving of atomic planes coinciding with normal cross sections of the plate. It broadens the diffraction profiles of γ-lines as if the plate was the mosaic crystal. In 70-es, A.V. Tyunis, V.M. Samsonov and O.I. Sumbaev generalized the theory of the effect and predicted that some other materials (*i.e.* silicon) should reveal elastic quasi-mosaicity behavior.

We investigated with X-rays the properties of silicon plates cut under different angles with respect to the crystallographic axes and observed the elastic quasi-mosaicity effect for the (111) atomic planes [1]. The plate orientation respect to the crystallographic planes corresponding to the largest elastic quasi-mosaicity effect in silicon is shown in Fig. 1.

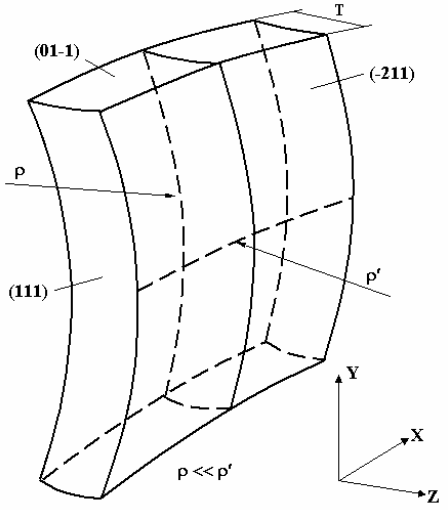

Fig. 1. Elastic quasi-mosaicity effect in bent silicon plate: the bending of the plate to a cylinder of radius ρ results in curving of the (111) crystallographic planes along thickness T. The radius ρ' characterizes the curvature induced by anticlastic forces

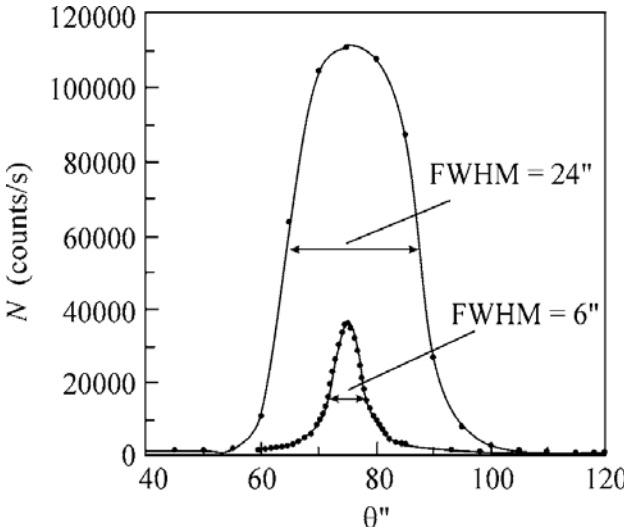

Fig. 2. Rocking curves before and after bending of the sample (FWHMs are 6″ and 24″, respectively)

Using double crystal *X*-rays diffractometer in the transmission mode we measured rocking curves of the sample with sizes 20(X) × 60(Y) × 0.43(Z) mm^3 before and after bending. The measurement results are shown in Fig. 2, where both rocking curves are presented. The FWHM of the rocking curve for unbent plate is equal to 6″ and close to the width from two ideal crystals. After the bending of the sample to a radius of ρ = 92 cm in vertical plane, the rocking curve width and amplitude increase by a factor of 4. The width of the rocking curve directly characterizes a bending angle of the (111) atomic planes along plate thickness. It is equal to 24″ that means bending angle 120 μrad per 0.43 mm. Due to anticlastic forces a shape of the bent plate is similar to the "saddle" with a radius of ρ' = 410 cm in the horizontal plane.

The control experiment was made with another plate cut from the same ingot. This plate was identical to the studied above but differed in the cut angle in the (111) plane by 30°. After the bending of the control plate, its rocking curve practically did not change.

The measured bending angles of atomic planes in silicon were found to be in a good agreement with the updated theory predictions and close to values needed for crystal collimation.

3. Observation of volume reflection effect in bent silicon crystal with 70 GeV proton beam at IHEP

Using elastic quasi-mosaicity effect in silicon we prepared a series of bent crystals with sub-millimeter lengths along beam and studied them at the Institute for High Energy Physics (Protvino) with 70 GeV protons. In the experiment, besides channeling, we observed a volume reflection of protons in the bent crystal [2, 3], the new effect essential for development of crystal applications at accelerators predicted by A.M. Taratin and S.I. Vorobiev in 80-es. This phenomenon arises from the coherent interaction of proton with a bent atomic plane in the tangency point of the plane with the proton trajectory and results in a small angular deflection of the reflected particle opposite the atomic plane bending.

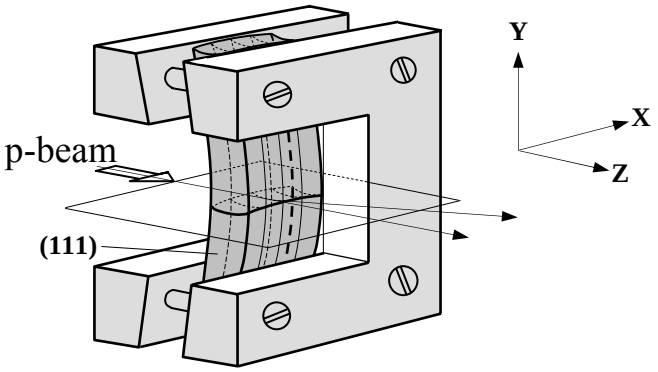

Fig. 3. Bending method of Si (111) planes (coinciding with vertical narrow face of crystal plate)

Silicon plate used in experiment had sizes 20(X) × 60(Y) × 0.72(Z) mm^3 with channeling (111) planes parallel to the YZ plane. The plate was bent in the YZ plane using method of applied moments (Fig. 3) to a radius of 48 cm that induced a quasi-mosaic bending of the (111) planes in the XZ plane to a radius of 1.7 m with a full bending angle of ~420 μrad. The saddle radius in the XZ plane was found to be about 3.2 m in the center of the crystal with increasing to the clamping areas.

The crystal was mounted on a turntable providing 4 mm overlapping with the proton beam in the X-direction (Fig. 4). Alignment of the crystal was done using a reflection of laser beam from crystal faces to the marks related with proton beam. Channeling orientation of the crystal was found as an angular position with maximal coincidence rate between narrow scintillation counters S1 and S2 placed in and out of the primary beam, respectively. A large counter S3 was used as a primary beam monitor.

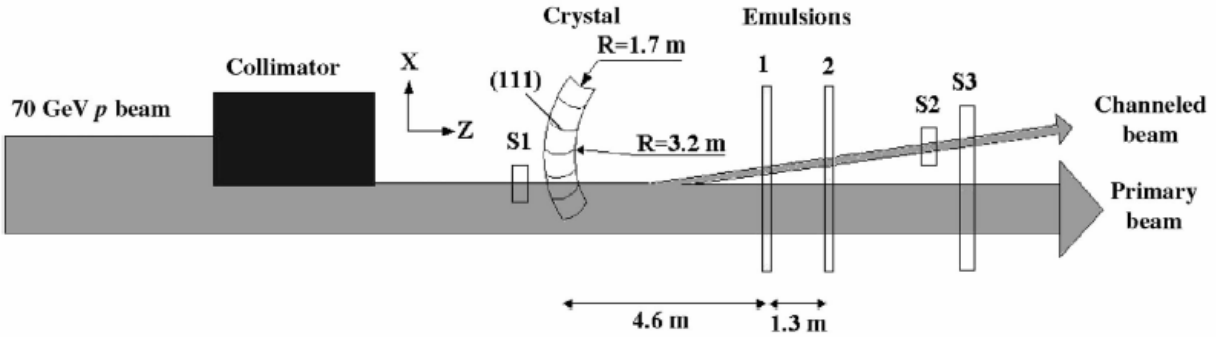

Fig. 4. Layout of the experiment. S1, S2, S3 – scintillation counters

In the experiment we used a small-divergent (~15 μrad), low intensity (~10^5 s^{-1}), external 70 GeV proton beam. The angular spreading of the beam induced by the multiple scattering in the crystal plate was 13.5 μrad. Both the divergence of the incident beam and the multiple scattering in the crystal were small with respect to the critical angle for channeling θ_c equal to 24 μrad in our case.

The profile of the beam transmitted through the oriented crystal was measured using emulsions of the R-100 type located 4.6 m and 5.9 m downstream. They were exposed to an integrated flux of about 5 particles/(μm)^2 and displayed three slightly distinct curved lines A, B, and C. The lines were well visible in a wide background spot from primary beam having a semicircle shape due to cutting a beam by collimator. The measured profiles were similar in both emulsions, but separation of lines was largest in the most distant emulsion, which is shown in Fig. 5. For both emulsions we determined the relative positions and widths of the observed lines in the X-direction of the crystal mid-plane with a microscope (along the white dashed line in Fig. 5).

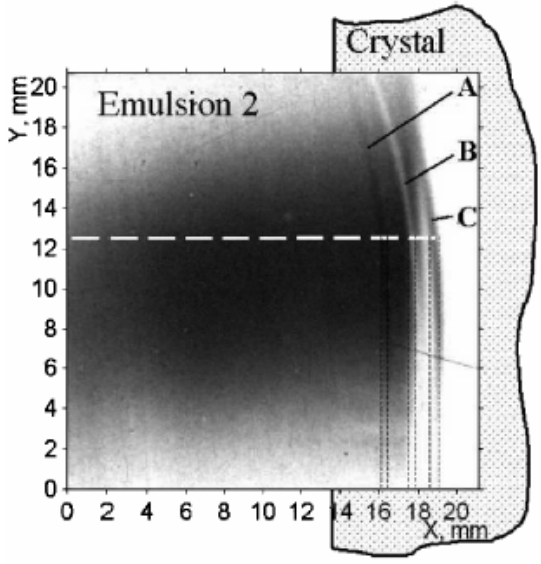

Fig. 5. Part of emulsion 2 with the profile of the proton beam. The white dashed line indicates the trace of the measurement with a microscope. The black dashed lines show X-readings, which correspond to the borders of the lines A, B, and C

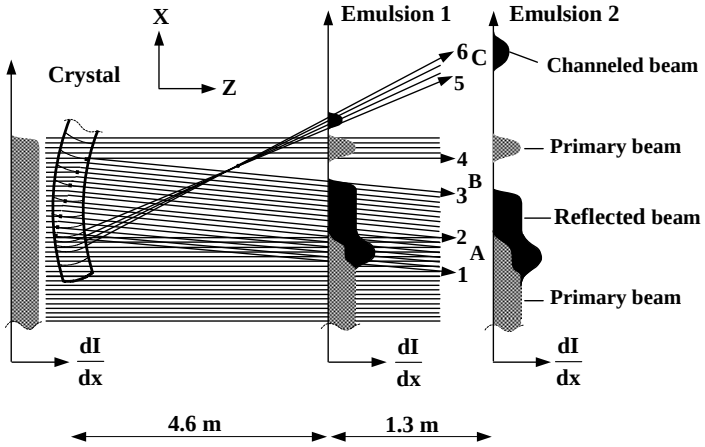

Fig. 6. Proton trajectories crossing the crystal and emulsions in the horizontal plane (top view). The incident beam is shown as parallel (distance between the effective ''source'' of the beam and the crystal is much larger than a saddle radius of the crystal) with a uniform intensity distribution along the X-direction. The dots within the crystal indicate the tangency points of the incident proton trajectories with the (111) atomic planes where the volume reflection takes place

An explanation of the beam intensity distribution observed in emulsions is given in Fig. 6 where proton trajectories in the horizontal XZ-plane are shown. The crystal has curvature in this plane due to anticlastic forces so the (111) planes change orientation along the X-direction. In a small X-range, where incident protons are tangent to the (111) planes on the entry face, part of the protons transiting through this range are captured in the channeling along the (111) planes (rays between 5 and 6) producing a spot C. For points at larger X-coordinates, the conditions are adequate for volume reflection, since the trajectories of the incident protons are tangent to the atomic (111) planes somewhere inside the crystal (rays in between 1 and 3). Out of the X-ranges for the channeling and volume reflection, incident protons pass through the crystal and experience only multiple scattering (rays above ray 4 and below 2). In this case, there is an area depleted of protons in between the reflected and primary beams, denoted by B, and another area where primary and reflected protons mix, denoted by A.

Above or below the mid-plane, we have the same picture of the proton-crystal interactions, except that the vertical dependence of the anticlastic curvature produces a continuous shifting of the projected spots. As result, a joint pattern comprises three lines (two black lines A and C and one light line B) of the same slightly curved shape.

The deflection angle of the channeled protons is estimated from the ratio of the distance between lines A and C to the distance between the crystal and the corresponding emulsion. Averaging over two emulsions, we found a value of 435 ± 6 μrad that coincides with the bending angle of the (111) planes measured with *X*-rays.

The deflection angle $2\theta_R$ of the reflected protons is estimated from the angular width of lines A and B, defined as the ratio of the line width to the distance from the crystal to each emulsion. Averaging the widths of A and B, we found $2\theta_R$ equal to 39.5 ± 2.0 μrad, or $(1.65 \pm 0.08)\cdot\theta_c$ in terms of the critical angle for channeling.

The dark color of the line A shows that probability of the reflection is larger than probability of the channeling. The widths of the reflected and channeled beams demonstrate that an angular acceptance of the volume reflection determined by a bend angle of the atomic planes is larger than an angular acceptance of the channeling restricted by a critical angle θ_c.

4. Study of volume reflection effect in bent silicon crystals with 1 GeV proton beam at PNPI

In the experiment with emulsion detectors, only a qualitative estimate for the reflection probability was obtained. In the next experiment with the use of electronic detectors the channeling and reflection effects were registered separately providing accurate estimates for the probabilities of the processes [4, 5].

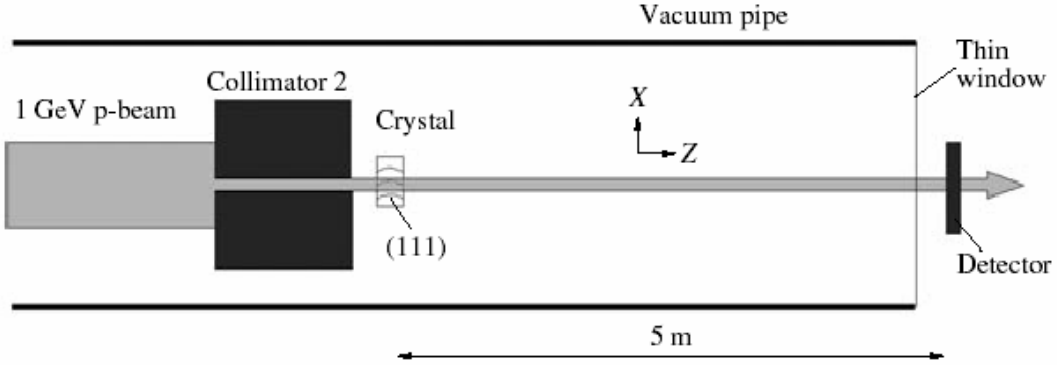

Fig. 7. Layout of the experiment on the observation of volume reflection with the 1 GeV proton beam

This experiment was carried out at the 1 GeV proton synchrocyclotron. The method (Fig. 7) involved the formation of a narrow, almost parallel, proton beam incident on a crystal and measurement of the distribution of the protons deflected by the crystal using fast-response detectors with high position resolution.

The beam was formed by means of two collimators near 1 m in length and separated by a distance of 31 m from one to another with a deflecting magnet between them. The adjusted proton beam had half-width in the horizontal plane at the exit of the second collimator equal to 80 ± 20 μm with the angular divergence of 160 ± 20 μrad and intensity of about 2×10^4 protons per second.

A silicon plate similar to the shown in Fig. 1 was used as the working crystal. The thickness of the plate was 30 μm that corresponds to the multiple scattering angle of 105 μrad (smaller than a critical angle for channeling equal to 170 μrad for the (111) silicon planes and 1 GeV protons). The plate was bent with a radius of 22 mm in the vertical plane by means of clamping in cylindrical mirrors with a hole with a diameter of 3 mm at the center for passing the proton beam. The quasi-mosaic bending of the (111) planes measured with *X*-rays was found to be 380 ± 20 μrad. The bent crystal was mounted on the rotary table attached to the exit end of the second collimator so that the center of the crystal coincided with the proton beam axis. Position-sensitive detectors were placed at a distance of 5 m from the crystal outside the vacuum channel.

One of the detectors was a parallel plate gas counter with linear position sensitivity (due to dividing anode plane into 64 elements with 200 μm pitch), the other was a cross of two scintillation counters (with 80 μm widths) placed on a linear carriage and working in coincidence. The both detectors had detection area for protons limited in the vertical direction and allowed measurements of the beam profile in the horizontal plane.

Figure 8 shows the typical angular scan with the parallel plate counter. The X-axis is the anode-strip coordinate in millimeters, zero corresponds to the position of the primary beam axis. The θ-axis is the

crystal angle in microradians, zero corresponds to the tangency of the primary-beam axis with the (111) planes on the entrance face of the crystal. The color of a point corresponds to the number of protons, the color scale is shown on the right-hand side from the plot. Two effects are clearly seen in the plot, which cause particles to deviate oppositely with respect to the initial direction. The right and left spots are easily identified as the regions of the channeling effect and the volume reflection effect, respectively. The lower and upper spots correspond to the primary beam passing through the non-oriented crystal.

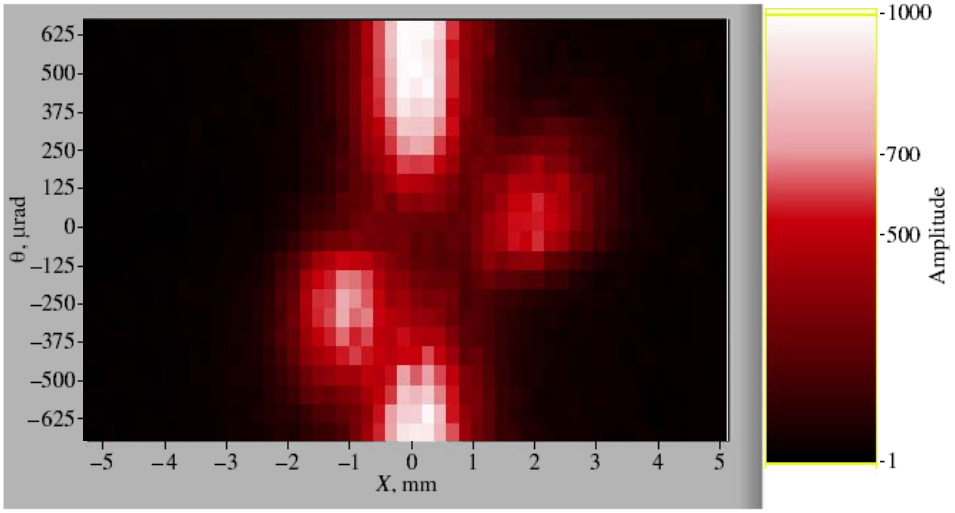

Fig. 8. Beam profile *vs* the angular position of the crystal as measured using the parallel plate position sensitive gas counter

Figures 9 and 10 show the profiles of the beam passed through the crystal in the angular positions corresponding to the centers of the channeling and volume reflection regions measured with the scintillation detector. The dashed line presents the beam profile corresponding to the non-oriented crystal.

From fitting of the peaks, the probability of the volume reflection equals to 0.71 ± 0.03 that is higher than probability of the channeling equal to 0.63 ± 0.03. The deflection angle of protons reflected inside the crystal is equal to 1.39 ± 0.04 in terms of the critical angle for channeling. The width of the reflected peak is equal to 1.76 ± 0.04 in the same units.

The protons that are not involved in channeling undergo volume reflection and are deflected by an angle of 1.01 ± 0.05 in terms of the critical angle for channeling, and the width of the reflected peak is equal to 1.94 ± 0.08 in the same units.

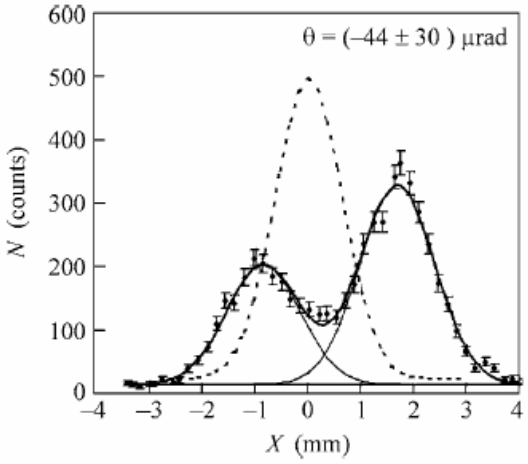

Fig. 9. Beam profile in the angular position of the crystal that corresponds to the maximum channeling as measured by means of the scintillation detector. The collection time at each point is equal to 10 s

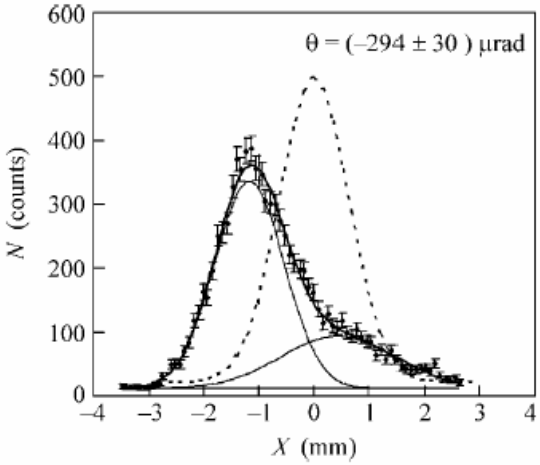

Fig. 10. Beam profile in the angular position of the crystal that corresponds to the maximum volume reflection as measured by means of the scintillation detector. The collection time at each point is equal to 10 s

5. Study of volume reflection effect in bent silicon crystals with 400 GeV proton beam at CERN

The experiment [6] was carried out with a 400 GeV proton beam from the CERN Super Proton Synchrotron H8 external line, which had a low divergence and an intensity near 10^4 particles per second. An experimental layout is shown in Fig. 11. It consisted of a high precision goniometer (G), where the crystals under investigation were mounted, and of various detectors to track particles. They were positioned along the beam line in the vicinity of the crystal and in an experimental area at about 70 m downstream.

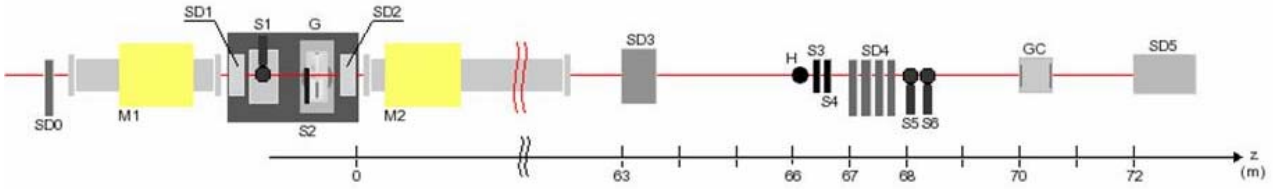

Fig. 11. Sketch of the H8-RD22 experimental setup. M1 and M2 are two bending magnets, part of the H8 beam transport line with no specific function for this experiment. See the text for more details

For the experiment, several quasi-mosaic and strip silicon crystals were prepared. In fact, the results of the measurements with all these crystals turned out to be very similar. Below a result from one of the strip crystals is presented. This crystal had (110) channeling planes bent (due to anticlastic effect) at an angle of 162 μrad along its 3 mm length in the beam direction. The multiple scattering angle of 400 GeV protons in this crystal was equal to 5.3 μrad and small with respect to the critical angle equal to 10.6 μrad. The proton beam had a divergence of 8 ± 1 μrad, also smaller than the critical angle. The beam spot size was of about 1 mm close to the strip crystal thickness.

The goniometer consisted of three high precision motion units, two linear and one angular. With the linear motions, the crystals were positioned with respect to the beam center with an accuracy of several micrometers. With angular scans, the crystals were aligned with respect to the beam axis with an accuracy of 1.5 μrad.

Six scintillator counters were used to determine the beam transverse offset with respect to the crystal (S1−S2), to provide the basic trigger signal for silicon detectors (S3−S4), and to measure the beam divergence and the beam profile (S5–S6). A scintillation hodoscope (H) and a position-sensitive gas chamber (GC) were operated in self-triggering mode for a fast prealignment of the crystal. High statistical runs were taken instead with a set of silicon microstrip detectors (SDn) of spatial resolution in the range 10–30 μm.

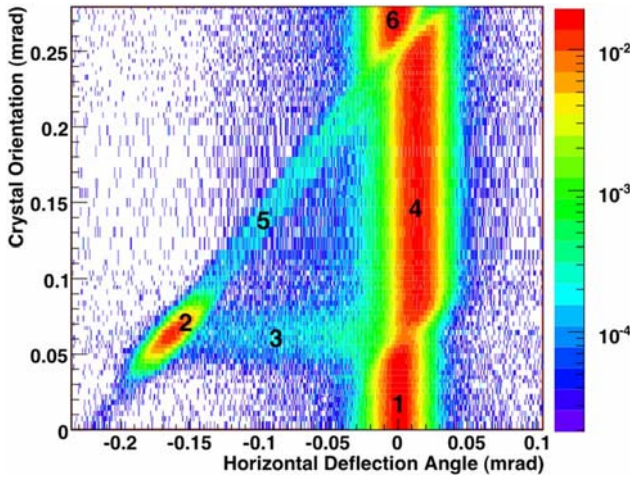

Fig. 12. Beam intensity recorded by the silicon microstrip detectors as a function of the horizontal deflection angle (X-axis) and the crystal orientation (Y-axis). Six regions can be distinguished: (1) and (6) non-channeling mode; (2) channeling; (3) dechanneling; (4) volume reflection; (5) volume capture. The wider angular acceptance of volume reflection compared to channeling is clearly visible in the figure

Figure 12 shows a summary plot of a scan performed with the crystal. A deflection angle of the channeled beam is equal to 165 ± 2 μrad in agreement with the value of the bending angle of the crystal. An efficiency of the channeling is about 55%. A deflection angle of the volume reflected beam is equal to 13.9 ± 0.2_{stat} ± 1.5_{syst} μrad, which is in agreement with the theory predictions. The volume reflection efficiency has been estimated to exceed 95%. This high efficiency is by far greater than the maximal theoretical single-pass efficiency for channeling.

6. Observation of double volume reflection of proton beam by a sequence of two bent crystals

Using the beam and setup described in previous section we have carried out an experiment on double volume reflection in two quasi-mosaic crystals [7]. Experimental layout is shown schematically in Fig. 13.

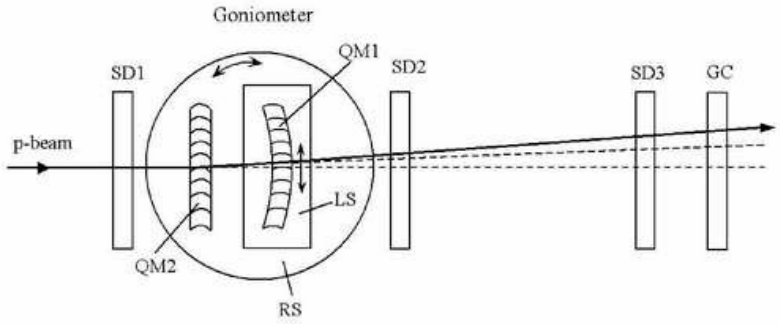

Fig. 13. Schematic top view of the experimental layout in the horizontal plane. QM1 and QM2 are two quasi-mosaic crystals installed on the rotational stage RS of the goniometer. The QM1 crystal is placed on the additional linear stage LS that allows to align QM1 with QM2. SD1, SD2, SD3 are silicon microstrip detectors, GC is a position-sensitive gas chamber. The lines represents the trajectories of the protons after the crystals, the unperturbed beam (lower dashed) crossing the crystals both in amorphous position, the beam reflected by the first crystal only (upper dashed), and the double-reflected beam (solid)

Two silicon plates QM1 and QM2 with the (111) atomic planes bent of ~70 μrad along the plate thickness of ~0.8 mm were installed on a goniometer. The (111) planes of QM1 plate were fan-shaped that made possible to align them with respect to the QM2 plate within the proton beam spot using the transverse linear motion of the QM1 support.

In Fig. 14 the angular scans performed before (a) and after (b) the fine relative alignment of the two crystals are shown. The channeling peaks for both QM2 and QM1 crystals are visible as the two isolated spots at negative values of the beam deflection angles in Fig. 14a. This scan was obtained before the alignment and, therefore, the two peaks appear at different angular positions of the goniometer.

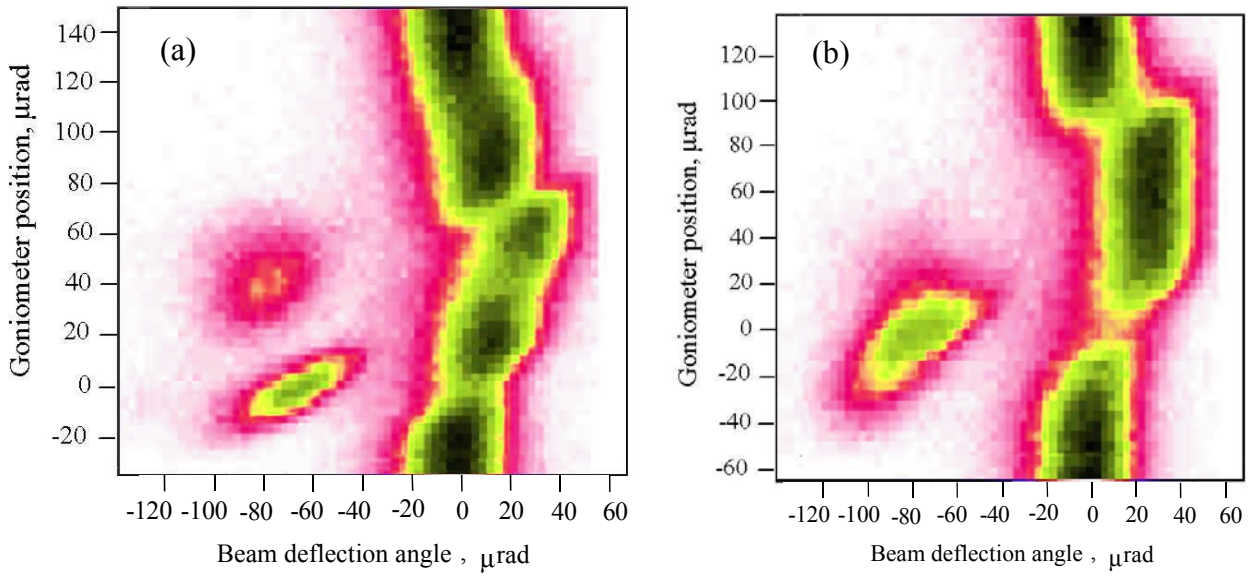

Fig. 14. Angular scans performed before (a) and after (b) the fine alignment of the crystals. On the Y-axis the angular position of the goniometer is shown while on the X-axis the beam deflection angle of the particle measured with the GC detector is reported. The origin of the X-axis corresponds to the direction of the incident beam. The origin of the Y-axis corresponds to the angular position of the goniometer when the channeling effect in QM2 crystal is maximal. In (a) both channeling peaks due to QM1 and QM2 are visible. In (b) the two channeling peaks coincides at about the same goniometer angle and are followed by the double reflection. The color scale indicates the beam intensity at a given deflection angle for various angular positions of the goniometer

The mean deflection angles of the channeled protons are measured with the SD2 and SD3 detectors to be 68.6 ± 0.9 μrad and 78.1 ± 4.8 μrad for the QM2 and QM1 crystals, respectively: they are equal to the bending angles of the (111) atomic planes in the crystals. The region of the scan with the proton beam

deflected to the opposite direction with respect to the channeled protons is due to the volume reflection effect. The deflection angle and efficiency of a single reflection are found to be 11.70 ± 0.51 μrad and (98.27 ± 0.50)% for QM2 and 11.90 ± 0.59 μrad and (97.80 ± 0.64)% for QM1, respectively.

The volume reflection regions corresponding to the QM2 and QM1 crystals in Fig. 14a are partly superimposed resulting in the deflection of the proton beam at larger angles than in the case of a single reflection. The angle and efficiency of double reflection were accurately measured with finally aligned crystals, the result is shown in Fig. 14b.

Figure 15 shows the beam profiles for three different cases corresponding to amorphous scattering, single, or double reflections of protons in the crystals. The deflection angle of the double reflected beam is found to be equal to $23.23 \pm 0.18_{stat} \pm 0.09_{syst}$ μrad, that is twice larger than in the single reflection. The efficiency of the double reflection is equal to $(96.73 \pm 0.38_{stat} \pm 0.50_{syst})$%.

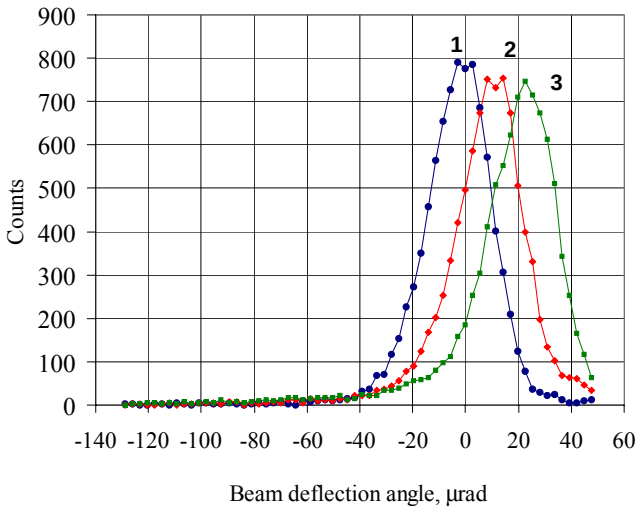

Fig. 15. The beam profiles corresponding to amorphous scattering of protons in both crystals (1), the reflection case in one of the crystal (2) and in both crystals – double reflection (3)

Thus, the experiment demonstrated a feasibility of multiple volume reflections in a sequence of short bent crystals with high efficiency and with beam deflection angle proportional to the number of reflections. This result opens new ways to develop crystal optics for the manipulation of high-energy charged particle beams.

7. Conclusion

In conclusion, the volume reflection exhibits high performance compared to channeling in terms of efficiency and angular acceptance, sheds new insight into the physics of interaction of charged particles with crystals, and suggests new applications in the next generation of experiments in both accelerators and high-energy physics.

References

1. Yu.M. Ivanov, A.A. Petrunin and V.V. Skorobogatov, Pis'ma v ZhETF **81**, 129 (2005) [JETP Lett. **81**, 99 (2005)].
2. Yu.M. Ivanov, A.A. Petrunin, V.V. Skorobogatov *et al.*, Preprint PNPI-2649, Gatchina, 2005. 22 p.
3. Yu.M. Ivanov, A.A. Petrunin and V.V. Skorobogatov *et al.*, Phys. Rev. Lett. **97**, 144801 (2006).
4. Yu.M. Ivanov, N.F. Bondar, Yu.A. Gavrikov *et al.*, Preprint PNPI-2687, Gatchina, 2006. 22 p.
5. Yu.M. Ivanov, N.F. Bondar, Yu.A. Gavrikov *et al.*, Pis'ma v ZhETF **84**, 445 (2006) [JETP Lett. **84**, 372 (2006)].
6. W. Scandale, D.A. Still , A. Carnera *et al.*, Phys. Rev. Lett. **98**, 154801 (2007).
7. W. Scandale, A. Carnera, G. Della Mea *et al.*, submitted to Phys. Lett. B (2007).

ELEMENTARY PARTICLES PHYSICS

PRECISION MEASUREMENT OF THE RATE OF MUON CAPTURE IN HYDROGEN GAS AND DETERMINATION OF THE PROTON'S PSEUDOSCALAR COUPLING g_P

PNPI participants of the MuCap Collaboration[*)] :
V.A. Andreev, V.A. Ganzha, P.A. Kravtsov, A.G. Krivshich, E.M. Maev, O.E. Maev, G.E. Petrov, G.N. Schapkin, G.G. Semenchuk, M.A. Soroka, A.A. Vasilyev, A.A. Vorobyov, M.E. Vznuzdaev

*) *Petersburg Nuclear Physics Institute, 188300, Gatchina, Russia*
Paul Scherrer Institute, CH-5232, Villigen, PSI, Switzerland
University of California, Berkeley, and LBNL, Berkeley, CA 94720, USA
University of Illinois at Urbana-Champaign, Urbana, IL 61801, USA
Universite Catholique de Louvain, B-1348, Louvain-la-Neuve, Belgium
University of Kentucky, Lexington, KY 40506, USA
Boston University, Boston, MA 02215, USA

1. Introduction

Here we report the first result of the MuCap experiment for the rate Λ_S of the semileptonic weak process of the ordinary muon capture (OMC) by the proton from the singlet ground state of the $\mu^- p$ atom:

$$(\mu^- p)_{1S} \to n + \nu_\mu , \quad BR = 0.16\% . \tag{1}$$

In the framework of the Standard Model, this reaction is parameterized by six induced form factors g_V, g_M, g_A, g_P, g_S, g_T evaluated at the relevant value of the four-momentum transfer $q_c^2 = -0.88\ m_\mu^2$, where m_μ is the muon mass. The second-class (scalar and tensor) form factors g_S and g_T vanish in the limit of exact G-parity invariance. The other three form factors $g_V(q_c^2)$, $g_M(q_c^2)$, $g_A(q_c^2)$ are accurately determined by experimental data and Standard Model symmetries. According to the conserved vector current (CVC) theorem, the vector and magnetic form factors $g_V(q^2)$ and $g_M(q^2)$ are identical to corresponding electromagnetic form factors which are determined by the nucleon magnetic moments and by the *ep*-scattering data:

$$g_V(q_c^2) = 0.976 \pm 0.001, \quad g_M(q_c^2) = 3.583 \pm 0.003.$$

The axial form factor $g_A(0)$ is determined from the neutron β-decay, and its extrapolation to $q^2 = q_c^2$ can be done using *νN*-scattering data (Congleton and Truhlik, 1996)

$$g_A(q_c^2) = -1.245 \pm 0.004.$$

The neutron beta decay is sensitive only to the $g_V(0)$ and $g_A(0)$ form factors. On the contrary, due to its larger momentum transfer $q_c^2 = -0.88\ m_\mu^2$, the muon capture reaction (1) is also sensitive to the magnetic and pseudoscalar form factors $g_M(q_c^2)$ and $g_P(q_c^2)$ which vanish at $q^2 \to 0$. That is why the OMC reaction (1) is considered as a source of information on the pseudoscalar form factor $g_P(q_c^2)$. In particular, $g_P(q_c^2)$ can be obtained from measurements of the muon capture rate Λ_S from the $1S$ ground state of the $\mu^- p$ atom. One should point out, however, that such measurements should be very accurate as a 1% error in Λ_S results in a 6.5% error in $g_P(q_c^2)$. In principle, $g_P(q_c^2)$ could be measured also in the radiative muon capture (RMC) reaction

$$\mu^- + p \to n + \nu_\mu + \gamma, \quad BR = 10^{-8}. \tag{2}$$

Though the sensitivity of the RMC rate to $g_P(q^2)$ is by a factor of 3 higher than in OMC, however the RMC studies are complicated by the very low branching ratio and some difficulties in interpretation of the experimental data.

The form factor $g_P(q_c^2)$ arises mainly from the coupling of the weak leptonic current to the nucleon via an intermediate pion, which generates a pole term that dominates at q_c^2. Early theoretical expressions for $g_P(q_c^2)$

were derived using current algebra techniques; now $g_P(q_c^2)$ can be systematically calculated within the heavy baryon chiral perturbation theory (HBChPT) up to two-loop order. The precise QCD result $g_P(q_c^2) = 8.26 \pm 0.23$ (V. Bernard *et al.*, 2002) follows from the basic concepts of explicit and spontaneous chiral symmetry breaking, and thus its experimental confirmation is an important test of the QCD symmetries. The observed deviation of the experimental data on $g_P(q_c^2)$ from the theoretical prediction might be also an indication of the "new physics" beyond the Standard Model.

Experimental OMC efforts span a period of more than forty years, and more recently one RMC experiment was performed at TRIUMF (Joukmans *et al.*, 1996). However, as shown in Fig. 1, the situation prior to the present experiment was inconclusive, as the results lacked sufficient precision due to ambiguities in the interpretation as well as to technical challenges.

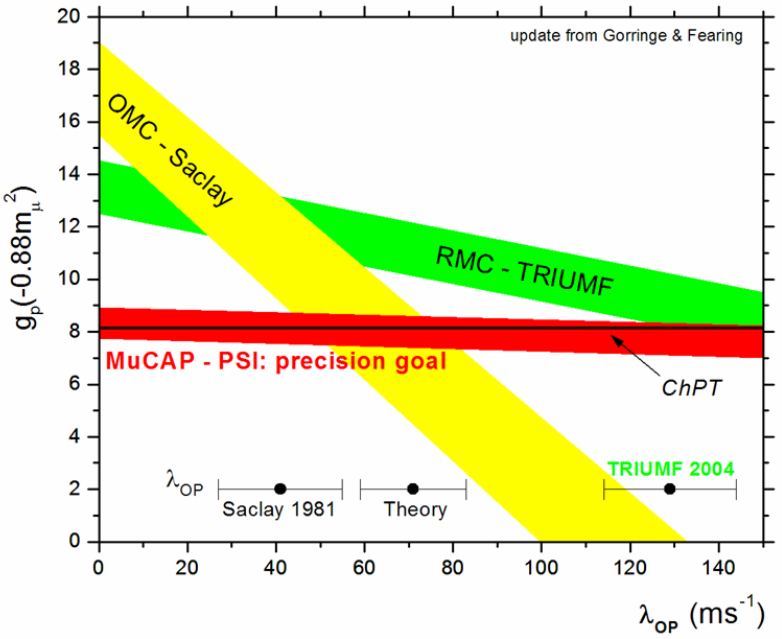

Fig. 1. Experimental and theoretical determinations of $g_P(q_c^2)$ presented *vs* the ortho-para transition rate λ_{op} in the *pμp* molecule. The most precise previous OMC experiment (Saclay, 1981) and the RMC experiment (TRIUMF, 1996) both depend significantly on the value of λ_{op}, which itself is poorly known due to mutually inconsistent experimental (λ_{op}^{Ex1}, λ_{op}^{Ex2}) and theoretical (λ_{op}^{Th}) results. In contrast, the MuCap result for $g_P(q_c^2)$ is nearly independent of molecular effects

Table 1 presents the experimental data on the OMC rates available prior to our experiment. Two experimental methods were applied to measure the OMC rate:

• detection of neutrons from the reaction (1);

• lifetime measurements of μ^- in hydrogen by detecting electrons from the muon decay, $\mu^- \to e^- + \nu_\mu + \tilde{\nu}_e$.

A serious limitation of the neutron detection method is an inevitable uncertainty in determination of the neutron detector efficiency. This leads to an error in measurements of muon capture rates $\delta\Lambda_c/\Lambda_c \geq 9\%$ that corresponds to too high error ($\geq$60%) in the determination of $g_P(q_c^2)$. The lifetime method has no such limitations. In this method, the muon capture rate is determined by the difference between the measured μ^- lifetime in hydrogen, τ_{μ^-}, and the known μ^+ lifetime, τ_{μ^+}, assuming that free μ^- and μ^+ decay with identical rates according to the *CPT* theorem. The contribution of the muon capture rate to the total muon disappearance rate being quite small (0.16%), this requires very high precision in measurements of τ_{μ^-}. For example, in order to reach ~1% precision in determination of the muon capture rate, one should measure τ_{μ^-} with a precision of $\Delta\tau_{\mu^-}/\tau_{\mu^-} \approx 10^{-5}$. This method was used in the Saclay experiment resulting in the most precise measurement of the OMC rate (Table 1). Unfortunately, this experiment was performed with a liquid hydrogen target where unambiguous derivation of $g_P(q_c^2)$ from the measured τ_{μ^-} was not possible.

Table 1

Status of $p\mu$-capture measurements prior to MuCap experiment

Year	Exptl. place	H_2-target	$\Lambda_c \pm \delta\Lambda_c$, s^{-1}	$\delta\Lambda_c/\Lambda_c$	Method
1962	Chicago	liquid	428±85	20%	neutron detection
1962	Columbia	liquid	515±85	17%	-"-
1962	CERN	liquid	450±50	11%	-"-
1963	Columbia	liquid	464±42	9%	-"-
1969	CERN	gas, 8 atm	651±57	9%	-"-
1974	Dubna	gas, 41 atm	686±88	13%	-"-
1981	Saclay	liquid	460±20	4.5%	lifetime measurement
1981	Saclay	liquid	531±33*)	6%	-"-

*) corrected for ortho-para transitions in the $pp\mu$ molecule

The problems of interpretation of the experimental data can be explained by considering the chain of reactions (Fig. 2) possible for negative muons after stopping in a hydrogen target of density ϕ relative to liquid hydrogen (LH_2). Stopped muons immediately form ground state μp atoms whose hyperfine states are populated in a statistical manner.

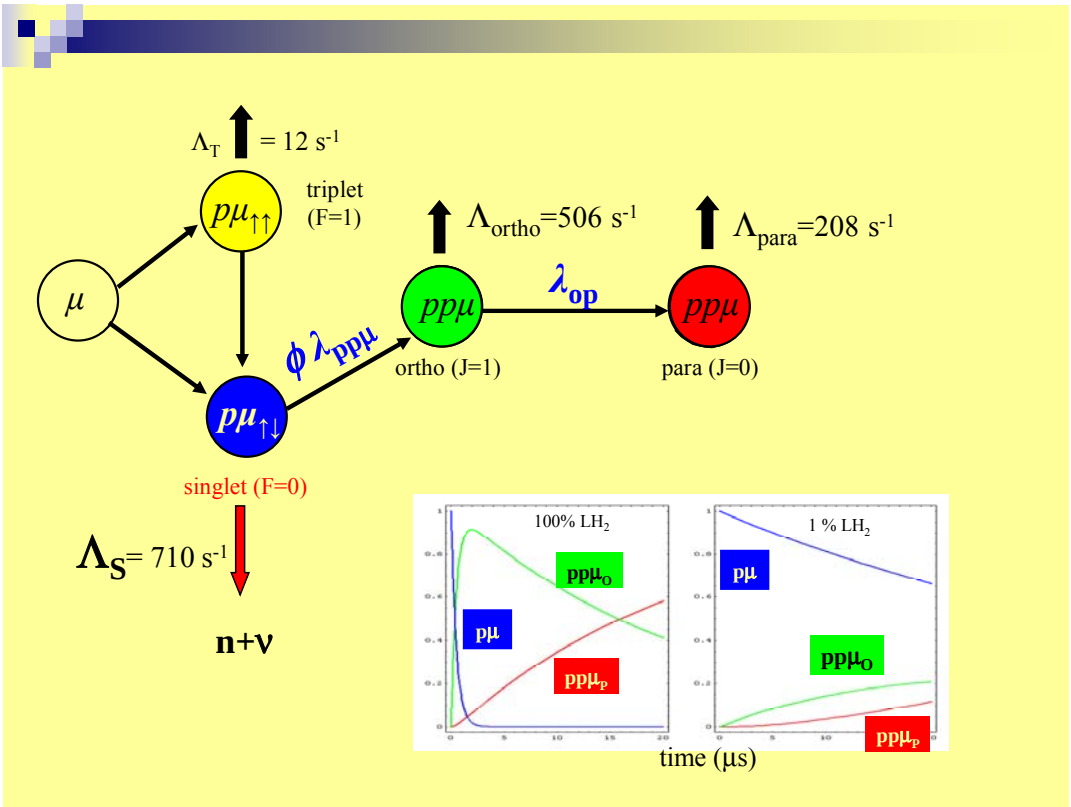

Fig. 2. Scheme of reaction after stopping of negative muons in a hydrogen target. Panels in the right-down corner show percentage of the muon captures from various molecular states for two target densities (LH_2 and 0.01 LH_2) in function of time after the muon stop

The upper triplet spin state is rapidly depopulated in collisions with H_2 molecules, and for densities $\phi \geq 0.01$ all muons reach the μp singlet state $1S$ well before 100 ns. From there, muons can either decay with a rate close to $\lambda_\mu^+ \equiv 1/\tau_\mu^+ \approx 0.455 \times 10^6$ s^{-1} or be captured *via* reaction (1) at the predicted rate $\Lambda_S \approx 710$ s^{-1}. Complications arise at higher densities, however, as the μp atoms increasingly collide with target H_2 molecules to form $p\mu p$ molecules. The $p\mu p$ molecules are initially created in the ortho state at the density-dependent rate $\phi\lambda_{of}$, where $\lambda_{of} \approx 2.3 \times 10^6$ s^{-1}, and then de-excite to the para state at rate λ_{op}. The nuclear capture rates from the ortho and para states, $\Lambda_{om} \approx 506$ s^{-1} and $\Lambda_{pm} \approx 208$ s^{-1} are quite different from each other and from Λ_S, so knowledge of the relative populations of the μp and $p\mu p$ states is crucial for a correct determination of $g_P(q_c^2)$. Alas, λ_{op} is poorly known. The available experimental and theoretical data are mutually inconsistent. This prevents a clear interpretation of the Saclay OMC experiment which was performed on LH_2 target where muon capture occurs predominantly in $p\mu p$ molecules (Fig. 1).

The RMC process is less sensitive to λ_{op}, but it difficult to draw firm conclusions from the RMC experiment, whose results suggested a nearly 50% higher value for $g_P(q_c^2)$ than predicted (Fig. 1).

2. Strategy of the MuCap experiment

The MuCap experiment employs a new experimental method, first suggested at PNPI [1], aimed to avoid the described above problems. The main features of this method are as follows.

- The capture rate is determined by measuring the μ^- lifetime in ultra-clean deuterium-depleted hydrogen gas at relatively low density $\phi \approx 0.01$, where the formation of $p\mu p$ molecules is slow and 96% of all captures proceed from the μp singlet state. The hydrogen contamination by impurities with $Z > 1$ should be on a level of $C_Z \leq 10^{-8}$ to avoid the muon disappearance due to capture by these impurities. The concentration of deuterium in hydrogen should be $C_d \leq 10^{-6}$ to prevent the formation of $d\mu$ atoms which could diffuse far from the muon stop.
- The muons are detected in an active target consisting of a hydrogen time projection chamber (TPC) which determines the muon stopping point well isolated of all materials of the chamber [1]. The trajectory and the emission time of the muon decay electrons are measured with an external detector. The space-time correlation of the muon stops and the electron trajectory serves to reduce the accidental background. TPC also provides a self-control for presence of $Z > 1$ impurities on a level of 10^{-8} by detecting recoil nuclei from the μZ capture.
- The high intensity muon beam in combination with fast read out electronics enables collection of the required statistics ($\sim 10^{10}$ events) for reasonable running time to provide measurements of the muon capture rate Λ_S with a precision of 10^{-5} or better.

The experiment was planned to be carried out at a muon beam at the Meson Factory of Paul Scherrer Institute. The proposal was presented and approved with the high priority in 1997 [2]. The first physics run was performed in 2004. Then measurements were going on in 2005, 2006 and 2007 with continuous improvements of the experimental setup and the muon beam line. This report contains the results of analysis of the 2004 data set. The analysis of the data obtained in 2005–2007 runs will require some more time.

3. The MuCap experimental setup

The MuCap experiment was conducted in the πE3 beam line at Paul Scherrer Institute, using $a \approx 20$ kHz DC muon beam tuned to a central momentum of 32.6 MeV/c. As illustrated in Fig. 3, incident muons first traverse a plastic scintillator (μSC) and a multiwire proportional chamber (μPC), and then pass through a 0.5-mm-thick hemispherical beryllium window to enter an aluminum pressure vessel filled with ultra-pure, deuterium-depleted hydrogen gas at a pressure of 1.00 MPa and at ambient room temperature. In the center of the vessel is the TPC (sensitive volume $15 \times 12 \times 28$ cm^3), which tracks incoming muon trajectories and thus enables the selection of muons that stop in the gas at least 15 mm away from chamber materials. Approximately 65% of the muons passing through the μSC stop within this fiducial volume. The ionization electrons produced by incoming muons drift downwards at velocity 5.5 mm/μs at applied field of 2 kV/cm,

towards a multiwire proportional chamber containing perpendicular anode and cathode wires. The anode plane consists of wires with 25 μm diameter and 4 mm spacing, and a high voltage of 5.0 kV across the 3.5 mm half-gaps provides a moderate gas gain of ~100 in hydrogen. Digital signals from three-level discriminators are recorded, with the energy thresholds adjusted to trigger on (i) the fast muons, (ii) the Bragg peaks near the muon stopping points and (iii) the larger energies that may be deposited by recoiling nuclei following muon capture by gas impurities.

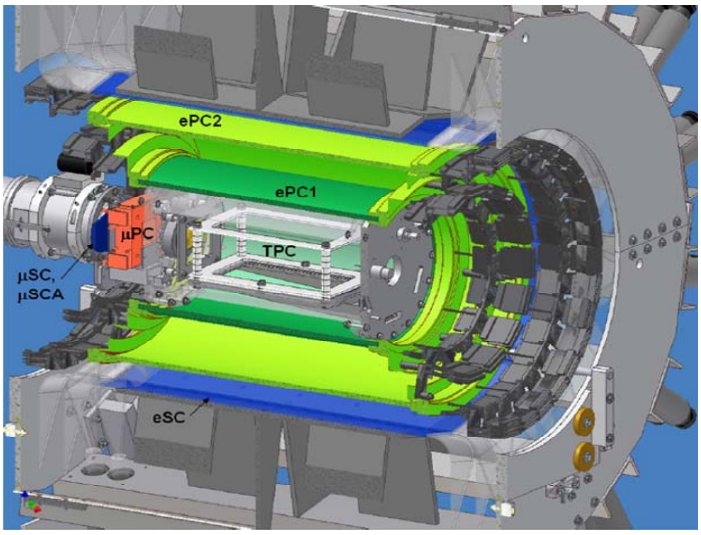

Fig. 3. Simplified cross-sectional diagram of the MuCap detector. The detector components are described in the text

The TPC is surrounded by two cylindrical wire chambers (*e*PC1, *e*PC2), each containing anode wires and inner/outer cathode strips, and by a hodoscope barrel (*e*SC) consisting of 16 segments with two layers of 5-mm-thick plastic scintillator. This tracking system detects outgoing decay electrons with 3π solid angle acceptance. All data are recorded in a trigger-less, quasi-continuous mode to avoid dead time distortions to the lifetime spectra. Custom-built time-to-digital converters (TDCs) digitize hit times for the TPC and the electron wire chambers. The muon and electron times t_μ and t_e are established by the μSC and *e*SC detectors, and recorded in separate CAEN V767 TDC modules. Figure 4 shows a general view of the MuCap experimental setup.

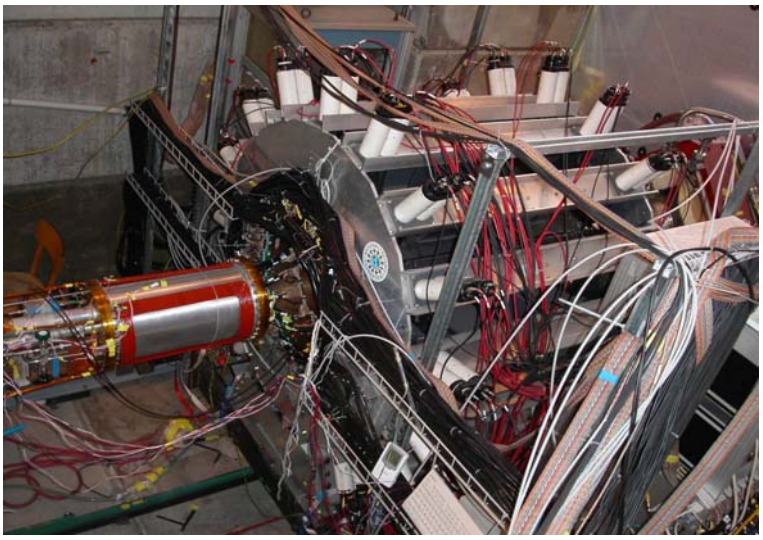

Fig. 4. General view of the MuCap experimental setup

4. Purity of hydrogen gas in TPC

All TPC materials were carefully selected for high vacuum operation. Prior to the run, the TPC system was heated to 115°C under vacuum for several weeks to remove impurities. The system was filled with deuterium-depleted hydrogen through a palladium filter. However, these precautions were not enough to provide the high gas purity during the run. It was found that, due to outgasing of the TPC materials, the impurity concentration (N_2, H_2O) increased in time with the rate of $dC_Z/dt = 10^{-7}$ per day. Therefore, a special gas circulation/purification system was designed and constructed at PNPI [3], and implemented into the MuCap setup. During data taking, the gas was continuously circulated *via* an adsorption cryopump system and cleaned by cooled Zeolite filters, which achieved an equilibrium concentration of $C_Z < 5 \times 10^{-8}$, as monitored by direct TPC detection of recoil nuclei from muon capture by impurities. The primary contaminant was H_2O outgasing, while concentration of N_2 was below 10^{-8}, as shown by gas chromatography measurements.

The isotopic purity of the hydrogen is critical. Muons preferentially transfer from μp to μd at the rate $\phi C_d \cdot \lambda_{pd}$, where C_d is the deuterium concentration and $\lambda_{pd} \approx 1.4 \times 10^{10}$ s^{-1}. Whereas the μp diffusion is of the order of mm, μd atoms can diffuse cm-scale distances due to a Ramsauer-Townsend minimum in the $\mu d + p$ elastic scattering cross section. As a result, the μd atoms can drift sufficiently far away from the muon's original stopping point so that the decay event will be rejected by the μ-e vertex reconstruction cut in a time-dependent manner. In addition, the μd atoms can drift into surrounding materials and be captured there. Our target gas was produced *via* electrolysis of deuterium-depleted water, provided by Ontario Power Generation Company (Canada). The accelerator mass spectrometry (AMS) analysis of this gas determined that $C_d = (1.44 \pm 0.13) \times 10^{-6}$, roughly 100 times below deuterium's natural abundance. This was the best deuterium-depleted hydrogen available on market, and it was used in our 2004 and 2005 runs. Later, a new cryogenic isotopic exchange column was designed and constructed at PNPI [4], which was able to reduce the deuterium concentration in hydrogen down to $C_d < 0.06 \times 10^{-6}$. This highly deuterium-depleted hydrogen was used in our 2006 run.

5. Measurements and results

The time differences between muon arrivals and decay electron emission, $\Delta t = t_e - t_\mu$, are histogrammed into lifetime spectra (Fig. 5). Only muons that are separated in time by ± 25 μs from other muon arrivals are accepted. While this condition reduces considerably the usable statistics, it is essential for avoiding ambiguities in resolving multiple muon tracks in the TPC. Note, that this pile up protection was not needed in our 2006 run when the so-called "muon-on-request" facility was put into operation on the muon beam at PSI. This facility deflected the muon beam for a requested time as soon as a signal on the muon stop in the TPC was registered. Implementation of this method in our experiment allowed to increase the data taking rate by a factor of 3 and also helped to reduce the background. As shown in Fig. 4, the background suppression can be improved by performing a vertex cut on the impact parameter between each decay electron's trajectory and its parent muon's stopping point. In the final analysis of the 2004 run data we employ a loose impact parameter cut of 120 mm as an optimal compromise between the competing demands for a good signal-to-background ratio and minimization of losses due to μd diffusion out of the cut volume.

We fit μ^- lifetime spectra with a simple exponential function $f(t) = N \cdot \omega \cdot \lambda \cdot e^{-\lambda t} + B$, where the free parameters are the number of reconstructed decay events N, the disappearance rate λ, and the accidental background level B; ω is the fixed 40 ns histogram bin width. The typical time range was 0.1–24 μs. The result was stable under variation of different cuts with typically χ^2/dof = 0.95–1.02 for 600 degrees of freedom. The main corrections to λ were derived directly from experimental data, with some additional information from external measurements and literature. These corrections are summarized in Table 2.

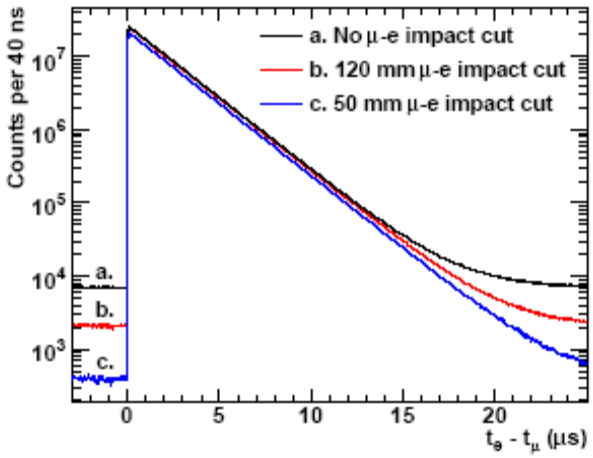

Fig. 5. Lifetime spectra of negative muons. The signal-to-background rate is improves with tighter cuts on the μ-e vertex

Table 2

Systematic corrections and uncertainties applied to the observed μ^- disappearance rate λ

Source	Correction, s^{-1}	Uncertainty, s^{-1}
$Z > 1$ impurities	–19.2	5.0
μd diffusion	–10.2	1.6
μp diffusion	–2.7	0.5
$\mu + p$ scattering		3.0
μ pileup veto efficiency		3.0
Analysis methods		5.0
Total	–32.1	8.5

The final result for the μ^- disappearance rate in pure hydrogen, based on $N = 1.6 \times 10^9$ fully tracked, pileup-protected decay events from our 2004 data set, is $\lambda_\mu^- = 455851.4 \pm 12.5_{stat} \pm 8.5_{syst}$ s^{-1}. As a consistency check, we also measured the μ^+ decay rate from $N = 0.5 \times 10^9$ events to be $\lambda_\mu^+ = 455164 \pm 28$ s^{-1}, in agreement with the world average.

The observed μ^- disappearance rate can be written as

$$\lambda_\mu^- = (\lambda_\mu^+ + \Delta\lambda_{\mu p}) + \Lambda_S + \Delta\Lambda_{p\mu p} \, . \qquad (2)$$

Here $\Delta\lambda_{\mu p} = -12.3$ s^{-1} describes a small reduction in the muon decay rate in the bound μp system (H.C. von Baeyer and D. Leiter, 1979). The term $\Delta\Lambda_{p\mu p} = -23.5 \pm 4.3 \pm 3.9$ s^{-1} accounts for captures from $p\mu p$ molecules and is calculated from the full μ^- kinetics in pure hydrogen. Its error terms come from our estimates $\lambda_{of} = (2.3 \pm 0.5) \times 10^6$ s^{-1} and $\lambda_{op} = (6.9 \pm 4.3) \times 10^4$ s^{-1} , respectively, which cover most of the existing literature values. Using the new world average $\lambda_\mu^+ = 455162.2 \pm 4.4$ s^{-1} (μLAN experiment, to be published), we determine the rate of muon capture by the proton to be

$$\Lambda_S^{MuCap} = 725.0 \pm 13.7_{stat} \pm 10.7_{syst} \ s^{-1} \, . \qquad (3)$$

To compare with theory we consider the two recent NNLO calculations of Λ_S: 687.4 s^{-1} (V.Bernard *et al*., 2001) and 695 s^{-1} (S. Ando *et a*l., 2000) here are averaged to 691.2 s^{-1}. Adding the very recently calculated radiative correction $\Delta_R = 19.4\ s^{-1}$ (A. Czarnecki, W.J. Marciano, A. Sirlin, to be published) increased from $\Delta_R = 4.5\ s^{-1}$ (M.R. Goldman, 1972) yields the value $\Lambda_S^{\rm Th} = 710.6\ s^{-1}$ and enables us to calculate

$$g_P^{\rm MuCap}(q_c^2) = g_P^{\rm Th}(q_c^2) + (dg_P/d\Lambda_S)(\Lambda_S^{\rm MuCap} - \Lambda_S^{\rm Th}) = 7.3 \pm 1.1\ , \qquad (4)$$

where $g_P^{\rm Th}(q_c^2) = 8.26$ (V. Bernard *et al*., 2002), $dg_P/d\Lambda_S = -0.065$ s (J. Govaerts and J.L. Lucio-Martinez, 2000), and only experimental uncertainty from Eq. (3) is propagated. The linear expansion in Eq. (4) is valid because of the small difference $\Lambda_S^{\rm MuCap} - \Lambda_S^{\rm Th}$.

The current information on $g_P(q_c^2)$ is summarized in Fig. 1; the constraints (T. Gorringe and H.W. Fearing, 2004) from the Saclay OMC experiment (G. Bardin *et al*., 1981) are updated to reflect the larger Δ_R. The situation before the MuCap experiment was inconclusive and exhibited mutually inconsistent theoretical predictions and experimental determinations of both $g_P(q_c^2)$ and $\lambda_{\rm op}$. The low gas density in the MuCap experiment renders our result relatively insensitive to $\lambda_{\rm op}$ and thus avoids most model dependence, enabling us to report the first unambiguous, precise determination of $g_P(q_c^2)$. This experimental result agrees with present theory to within 1σ and does not support a dramatic deviation from the chiral prediction as the RMC result originally had implied.

6. Conclusion

We should point out that analyzed up to now the 2004 data set constitutes only 10% of the statistics collected in the 2004–2007 runs. Moreover, the 2006 and 2007 runs, besides the largest statistics, had other important advantages (reduced deuterium concentration, $C_d < 0.06$ ppm, and the "muon-on-request" mode) which should help to reduce the background and possible systematic errors. So one could expect that the presented in this report error in $g_P(q_c^2)$ will be reduced by a factor of three in the final analysis of all MuCap data.

Earlier, in 1998, we have studied the muon capture on ^{3}He [5]. The muon capture rate in the channel $\mu^- + {}^3\mathrm{He} \rightarrow {}^3\mathrm{H} + \nu_\mu$ was measured with a high precision: $\Lambda_c = 1496.0 \pm 4.0\ s^{-1}$. This result have been used in some theoretical analyses (T. Gorringe and H.W. Fearing, 2004) for deriving the proton's pseudoscalar coupling $g_P(q_c^2)$. They applied the microscopic theory based on impulse approximation supplemented by explicit calculations of the meson exchange corrections. Their result was $g_P(q_c^2) = 8.77 \pm 1.58$. Though this result was considered as the best measurement at that time, however, it is model-dependent, its precision depends to a large extent on calculations of the meson exchange corrections. Now one can reverse the task, using our direct measurement of $g_P(q_c^2)$, to control various aspects of the microscopic theory of μ^3He capture.

References

1. E.M. Maev *et al*., Nucl. Instr. Meth. A **478**, 158 (2002).
2. MuCap collaboration, PSI Proposal R-97-05.1 (1997), PSI Technical Proposal R-97-05.2 (2001).
3. B.M. Bezymyannykh, A.A. Vasilyev *et al*., Preprint PNPI-2611, Gatchina, 2005. 32 p.
4. I.A. Alekseev *et al*., Preprint PNPI-2702, Gatchina, 2006. 26 p.
5. P. Ackerbauer *et al*., Phys. Lett. B **417**, 224 (1998).

NEW RESULTS FROM SELEX

PNPI participants of the SELEX Collaboration:
G.D. Alkhazov, V.L. Golovtsov, V.T. Kim, A.G. Krivshich, P.V. Neustroev, L.N. Uvarov, A.A.Vorobyov

1. Introduction

The SELEX experiment (E781) at Fermilab is a fixed target experiment aimed at studying charm baryon production in the forward hemisphere and charm baryon spectroscopy. However**,** the versatility of the apparatus also allowed for the study of such reactions as elastic scattering of electrons on Σ^- hyperons (in inverse kinematics), Primakoff scattering of π^- mesons, and some others. The data were taken in 1996–1997. Results on charm-anticharm production asymmetries, Λ_c^+ production x_F-dependence in different beams, the Λ_c^+ lifetime, the total cross section for interaction of π^-, Σ^- and protons with nucleons at ~600 GeV, the charge radius of the Σ^- hyperon, and some other results have already been reported [1]. Since then, new results from the SELEX data have been obtained. The polarizations of the Σ^+ hyperons produced by 800 GeV/c protons on Be and Cu targets have been determined [2]. An upper limit on the width of the radiative decay of $\Sigma(1385)^-$ to $\Sigma^-\gamma$ has been set, and the cross section for the reaction $\gamma\Sigma^- \to \Lambda\pi^-$ at $\sqrt{s} \approx 1.4$ GeV has been evaluated [3]. In this report, the most interesting recent SELEX results on observation of the doubly charmed baryon Ξ_{cc}^+ [4, 5] and of a narrow charm–strange meson D_{sJ}^+ (2632) [6] are presented and discussed.

2. Experimental setup

The SELEX experiment used the Fermilab charged Hyperon beam which is composed of 50 % Σ^- and 50 % π^- with the energy of about 600 GeV for negative polarity and 92 % p and 8 % π^+ with the energy of 540 GeV for positive polarity. The beam was run at the forward production angle (Θ = 0°). Beam particles were identified by beam Transition Radiation Detectors (TRD). The experiment was designed to have high acceptance and resolution in x_F region $0.1 < x_F < 1$. The spectrometer schematic layout is shown in Fig. 1.

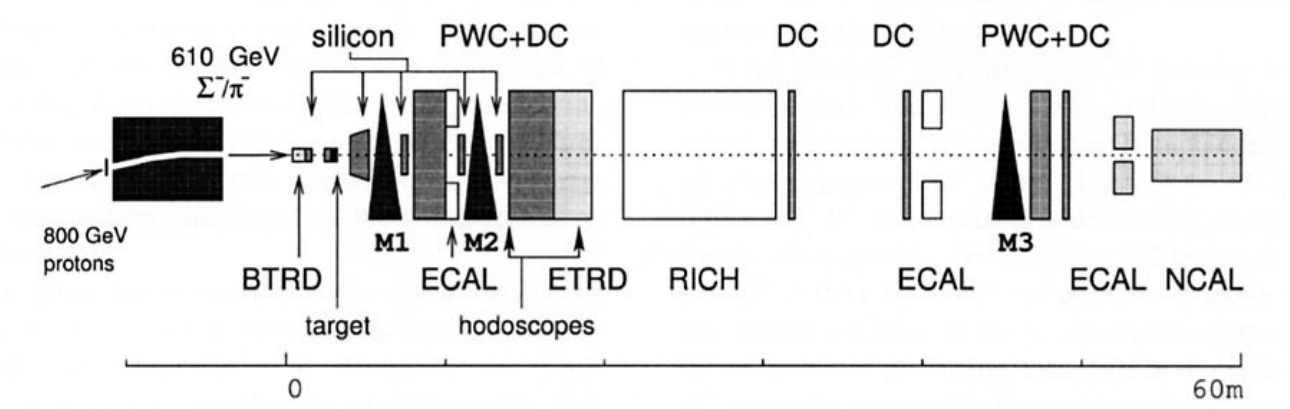

Fig. 1. Schematic view of the experimental setup. BTRD – beam transition radiation detector, ETRD – electron transition radiation detector, ECAL – electromagnetic calorimeter, PWC – proportional wire chambers, DC – drift chambers, RICH – ring image Cherenkov detector, NCAL – neutron calorimeter, M1, M2, and M3 – analyzing magnets

Interactions occurred in a target stack of 5 foils: 2 made of copper and 3 made of carbon. The total interaction length of all targets was about 5% for protons. Each foil was spaced by 1.5 cm from its neighbors. An additional Pb target was also employed in some runs. Trigger requirements (for charm physics) were: ≥ 4 charged tracks in the forward 150 mrad cone and ≥ 2 hits in a counter hodoscope located behind the second analyzing magnet. Triggering took place for about 30% of inelastic interactions.

Downstream of the target region, charged reaction products were measured in 20 vertex silicon planes having the position resolution of 4 μm for high momentum tracks. Beam tracks were measured in 8 planes of 2 μm pitch beam silicon. The downstream tracking system included 18 silicon planes for precise measurement of high momentum (100–600 GeV) tracks. In total, the SELEX silicon system had 74,000 strips with analog and digital information.

Another distinct feature of SELEX was an extensive particle identification system, which included 3,000 phototubes Ring Imaging Cherenkov detector (RICH) with K/π separation up to 165 GeV, beam TRD for beam tagging (Σ^-/π^-, p/π^+), downstream electron TRD to identify secondary $e^\pm$, 3 lead-glass photon calorimeters covering the forward hemisphere. The downstream tracking system had 3 analyzing magnets, 26 Proportional Wire Chamber (PWC) planes with position resolution ~0.8 mm, and 3 vector drift chamber (DC) stations with 24 ~100 μm resolution planes each.

PNPI has made a significant contribution to the apparatus of the SELEX experiment, providing good particle identification (Beam and Electron Transition Radiation Detectors, BTRD and ETRD) and tracking capabilities (Proportional Wire Chambers). The readout electronics (CROS) for these detectors and also for other detectors (RICH, NCAL) – 11,000 channels in total – was fabricated at PNPI as well. Another important contribution of PNPI was the design and commissioning of 60,000 FASTBUS readout channels for the Si vertex detector. PNPI has also provided SELEX with the front-end electronics for the drift chambers, as well as with the electronics for BTRD.

3. First observation of the doubly charmed baryon Ξ_{cc}^+

In the SELEX experiment, a signal was observed [4] which was interpreted as due to the doubly charmed baryon Ξ_{cc}^+ in the charged decay mode $\Xi_{cc}^+ \to \Lambda_c^+ K^-\pi^+$. The experiment selected charm candidate events using an online secondary vertex algorithm. A scintillator trigger demanded an inelastic collision with at least four charged tracks in the interaction scintillators and at least two hits in a positive particle hodoscope after the second analyzing magnet. Event selection in the online filter required full track reconstruction for the measured fast tracks ($p \geq 15$ GeV/c). These tracks were extrapolated back into the vertex silicon planes and linked to silicon hits. The beam track was measured in upstream silicon detectors. A full three-dimensional vertex fit was then performed. In the course of the experiment, data from 15.2×10^9 inelastic interactions were recorded and 1×10^9 events were written to tape using both positive and negative beams. 67% of events were induced by Σ^-, 13% by π^-, and 18% by protons.

The Ξ_{cc}^+ analysis began with a sample of Λ_c^+ single-charm baryons decaying to $pK^-\pi^+$ [1]. Candidates were selected with a topological identification of three-prong positively-charged secondary vertices, requiring a momentum measurement for each track. The RICH identification of the proton and kaon was required. Charged tracks with reconstructed momenta which traversed the RICH ($p \geq 22$ GeV/c) were identified as protons or kaons if those hypotheses were more likely than the pion hypothesis. The other positive track was identified as a pion when possible; otherwise, it was assumed to be a pion. The primary vertex was refit using all other found tracks.

A Cabibbo-allowed decay of a doubly charmed baryon must have a net positive charge and contain a charmed quark, a strange quark, and a baryon. In the discussed work, a search for decay modes such as $\Xi_{cc}^+ \to \Lambda_c^+ K^-\pi^+$ with an intermediate $K^-\pi^+$ secondary vertex between the primary vertex and the Λ_c^+ vertex was performed.

Events were analyzed for evidence of a secondary vertex composed of an opposite-signed pair between the primary and the Λ_c^+ decay point. All tracks not assigned to the Λ_c^+ candidate were used in the search.

A new primary vertex was formed from the beam track and tracks assigned to neither the Λ_c^+ nor the $K^-\pi^+$ vertices. The new secondary vertex had to have an acceptable fit χ^2 and a separation of at least 1σ from the new primary one. The $\Lambda_c^+ K^-\pi^+$ transverse momentum with respect to the incident beam direction was required to be in the range $0.2 < p_t$ [GeV/c] < 2.0.

Most tracks from the $K^-\pi^+$ vertex have insufficient momentum to reach the RICH. Masses were assigned according to topology. For the signal channel, negative tracks were assigned the kaon mass and positive tracks the pion mass. A candidate event from the $\Lambda_c^+ K^-\pi^+$ sample is shown in Fig. 2.

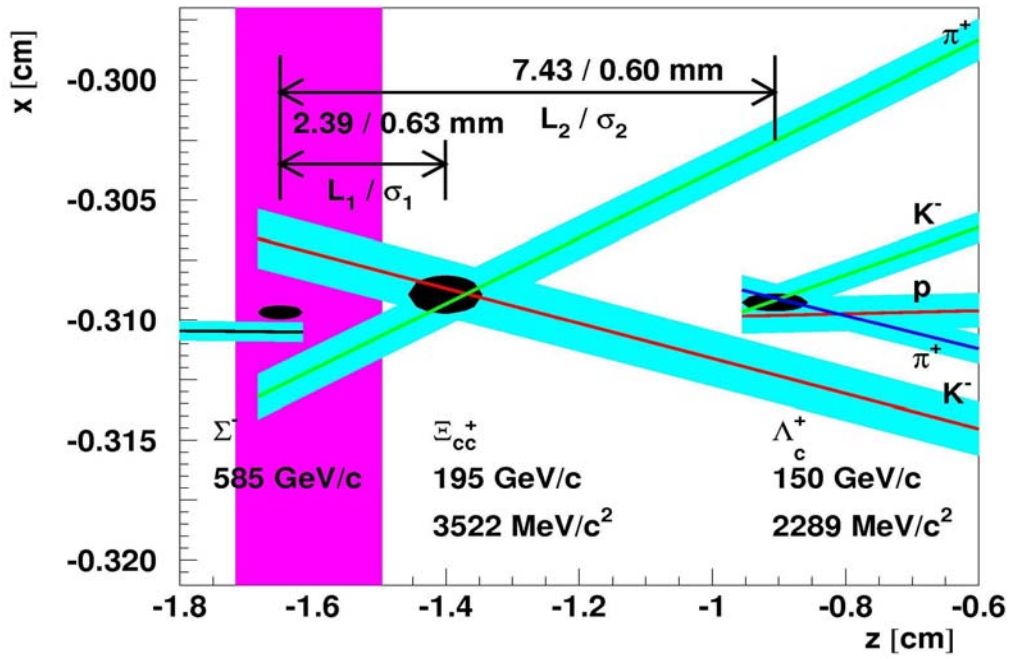

Fig. 2. A candidate event with the production target, 1σ track error corridors, and vertex error ellipses. This is a plan view of three-dimensional tracks and vertices. Three additional found tracks which form the primary vertex with the beam track are not shown

Figure 3a shows the invariant mass of the $\Lambda_c^+ K^-\pi^+$ system, the Λ_c^+ mass being fixed at 2284.9 MeV/c^2. The data, plotted in 5 MeV/c^2 bins, exhibit a large, narrow excess at 3520 MeV/c^2. This excess is stable for different bin widths and bin centers. Figure 3b shows the wrong-sign invariant mass distribution of the $\Lambda_c^+ K^+\pi^-$ system with the same binning as in Fig. 3a. There is no significant excess.

In Fig. 3c the shaded region from Fig. 3a is replotted in 2.5 MeV/c^2 bins and fit with a maximum likelihood technique to a Gaussian plus linear background. The fit has χ^2/d.o.f. = 0.45, indicating that the background is linear in this region.

The combinatorial background under the signal peak was determined under an assumption of the linearity of the background, which is justified by the fit. Two symmetric regions of the mass plot are defined in Fig. 3c: (i) the signal region 3520 ± 5 MeV/c^2 with 22 events and (ii) 115 MeV/c^2 sideband regions above and below the signal region, containing 162 – 22 = 140 events. The estimated number of expected background events in the signal region from the sidebands is $140 \times 5/(115) = 6.1 \pm 0.5$ events. This determination has a (Gaussian) statistical uncertainty, solely from counting statistics. The single-bin significance of this signal is the excess in the signal region divided by the total uncertainty in the background estimate: $15.9/\sqrt{6.1+0.5^2} = 6.3\sigma$. The Poisson probability of observing at least this excess, including the Gaussian uncertainty in the background, is 1.0×10^{-6}.

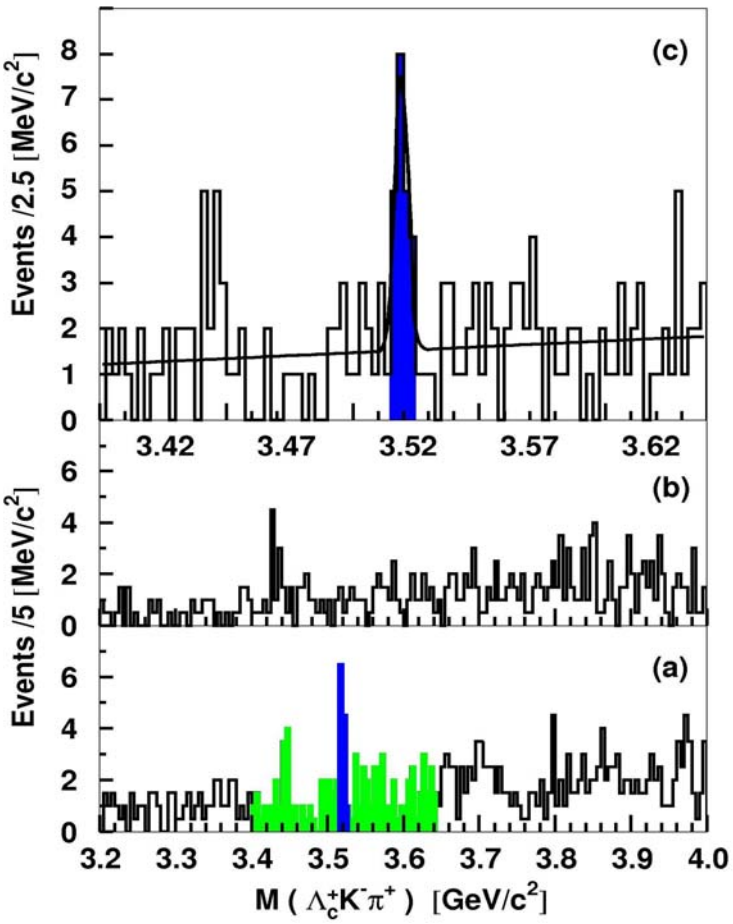

Fig. 3. (a) The mass distribution $\Lambda_c^+ K^- \pi^+$ in 5 MeV/c^2 bins. The shaded region 3.40–3.64 GeV/c^2 contains the signal peak and is shown in more detail in (c). (b) The wrong-sign combination $\Lambda_c^+ K^+ \pi^-$ mass distribution in 5 MeV/c^2 bins. (c) The signal (shaded) region (22 events) and sideband mass regions with 162 total events in 2.5 MeV/c^2 bins. The fit is a Gaussian plus linear background

The reconstruction mass window is 3.2 –4.3 GeV/c^2 with 110 bins of width 10 MeV/c^2 in this interval. The overall probability of observing an excess at least as large as the one which is seen anywhere in the search interval is 1.1×10^{-4}. The width of the observed state is consistent with the experimental resolution, less than 5 MeV/c^2. An analysis of the flight path from the primary vertex to the Ξ_{cc}^+ decay point indicates that the lifetime of Ξ_{cc}^+ is very short, smaller than 33 fs (at 90% confidence level).

Thus, the narrow state seen in this experiment at 3520 MeV/c^2 is interpreted as the doubly charmed baryon Ξ_{cc}^+ which decays into $\Lambda_c^+ K^- \pi^+$. This is the first observation of doubly charmed baryons. In order to confirm the interpretation of this state as a doubly charmed baryon, it is essential to observe the same state in some other way, in particular in a different decay mode. The further analysis of the SELEX data has allowed to see Ξ_{cc}^+ in the channel $\Xi_{cc}^+ \to pD^+K^-$ [5]. This study was begun with the SELEX $D^\pm$ sample that was previously used in lifetime and hadro-production studies [1]. Intermediate vertices were looked for using all charge zero pairs of tracks from the set of reconstructed tracks not assigned to the *D*-meson candidate. The additional positive track in this final state had to be RICH-identified as a proton if it traversed the RICH. The negative track in the new vertex was assigned the kaon mass. The Ξ_{cc}^+ signal search was based on a 10 MeV/c^2 window centered on the Ξ_{cc}^+ mass 3519 MeV/c^2 from Ref. [4]. The expected mass resolution for the decay $\Xi_{cc}^+ \to pD^+K^-$ was 4 MeV/c^2. The right-sign mass combinations in Fig. 4a show an excess of 5.4 events over a background of 1.6 events. The wrong-sign mass combinations ($\bar{c}$ quark in the decay) for the $pD^-\pi^+$ final state are also plotted in Fig. 4b, scaled by 0.6 for the D^+/D^- ratio. The wrong-sign background shows no evidence for a significant narrow structure near 3519 MeV/c^2. The average wrong-sign occupancy

is 0.4 events/bin, exactly the background seen in the right-sign channel. This confirms the combinatoric; character of the background population in the right-sign signal. All possible permutations of particle assignments were investigated. The only significant structure observed is in the channel $\Xi_{cc}^{+} \to pD^{+}K^{-}$, the place where the decay of a doubly charmed baryon can occur.

The estimated single significance is 4.8σ. The Poisson probability of observing at least this much excess, including the Gaussian uncertainty in the background, is 6.4×10^{-4}.

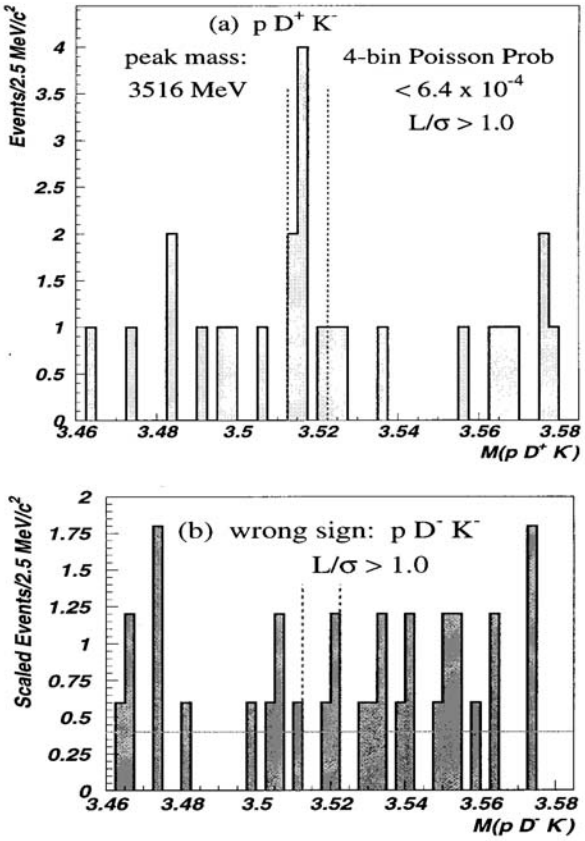

Fig. 4. (a) $\Xi_{cc}^{+} \to pD^{+}K^{-}$ mass distribution for right-sign mass combinations. Vertical dashed lines indicate the region of smallest fluctuation probability as described in the text. (b) Wrong-sign events with a $pD^{-}K^{+}$, scaled by 0.6 as described in the text. The horizontal line shows a maximum likelihood fit to the occupancy

In order to estimate the mass of the $\Xi_{cc}^{+} \to pD^{+}K^{-}$ state in light of the sparse statistics in Fig. 4a, the width of the Gaussian was fixed to 4 MeV/c^2 and the data distribution was fit around the signal peak. The fit mass was 3518 ± 3 MeV/c^2. This result agrees with the measurement of 3519 ± 2 MeV/c^2 from the original doubly charmed baryon report [4]. The weighted average mass is 3518.7 ± 1.7 MeV/c^2. The observation of the Ξ_{cc}^{+} decay into the $pD^{-}K^{+}$ final state is an independent confirmation of the doubly charmed baryon Ξ_{cc}^{+} previously seen [4] in the $\Xi_{cc}^{+} \to \Lambda_c^{+} K^{-} \pi^{+}$ decay mode.

4. Observation of a narrow charm-strange meson D_{sJ}^{+} (2632)

In 2003, the BABAR Collaboration reported the first observation of a massive, narrow charm-strange meson $D_{sJ}^{+}(2317)$ below the *DK* threshold. Confirmations quickly followed from CLEO and BELLE. The CLEO Collaboration showed that a higher-lying state, suggested by BABAR, existed and was a partner to $D_{sJ}^{+}(2317)$. A number of theory papers suggested different explanations for the unexpectedly low mass of the state which had been thought to lie above the *DK* threshold. It was predicted that the pattern of parity-

doubled states is expected to continue to higher excitations with similar splittings. In the SELEX experiment, a search for D_{sJ}^{+} with higher masses was undertaken [6]. This search was begun with the SELEX $D_s^{\pm} \to K^+K^-\pi^{\pm}$ sample used in lifetime and hadro-production studies [1]. The D_s meson momentum vector had to point back to the primary vertex with $\chi^2 < 8$, and its decay point must have a vertex separation significance of at least eight from the primary. Tracks that traversed RICH ($p \geq 22$ GeV/c) were identified as kaons if this hypothesis was most likely. The pion was required to be RICH-identified if it went into its acceptance.

Because of high-multiplicity, the photon detection in an open charm-trigger is challenging. SELEX has three lead glass calorimeters covering much of the forward solid angle. The energy scale for the detector was set first by using electron beam scans. Then π^0 decays were reconstructed from exclusive trigger data, which selected low-multiplicity radiative final states: $\eta \to \gamma\gamma$ and $\pi^+\pi^-\pi^0$, $\omega \to \pi^+\pi^-\pi^0$ as well as η' and $f(1285)$ mesons. The final energy scale corrections were developed using π^0 decays from the high multiplicity charm-trigger data. Further checks in the charm data set were made using single photon decays, *e.g.* $\Sigma^0 \to \Lambda\gamma$. The uncertainty in the photon energy scale was less than 2 %. Candidates for $\eta \to \gamma\gamma$ were selected in the $\gamma\gamma$ mass range 400–800 MeV/c^2. Each photon of the pair had $E_\gamma > 2$ GeV. The photon pair had $E_\gamma > 15$ GeV. The $\gamma\gamma$ mass distribution from 10^6 charm-trigger events (0.1% of the data) is shown in Fig. 5 where the η signal over a large combinatorial background is seen. A fit to a Gaussian plus an exponentially falling background yields an η mass of 544.8 ± 2.9 MeV/c^2 consistent with the PDG value. The observed resolution of 28 ± 4 MeV/c^2 is consistent with the SELEX simulation result, 30 MeV/c^2.

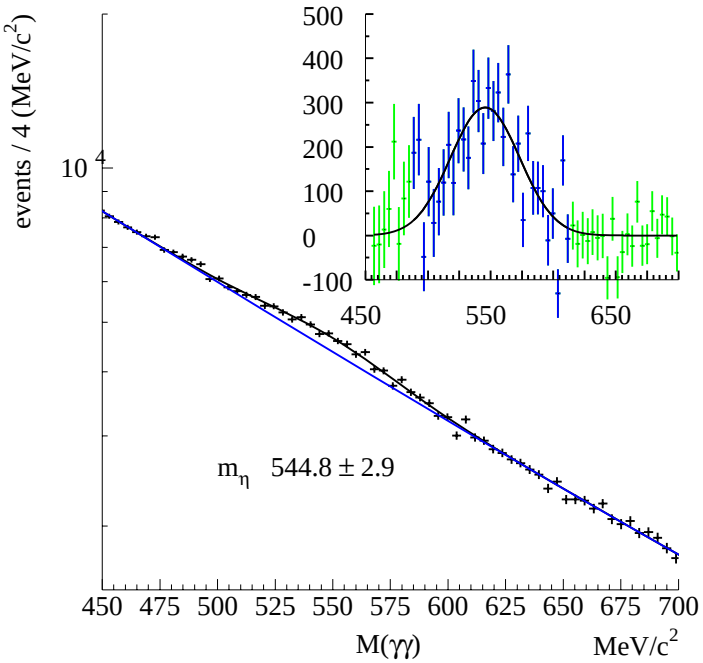

Fig. 5. $M(\gamma\gamma)$ distribution for photon pairs in the η mass region from 0.1% of the data sample. The inset shows the background subtracted η signal. The dark points indicate the η signal region

High-mass charm-strange decays that followed the pattern D_s plus pseudoscalar meson were searched. The event selection used included the η selection discussed above and the D_s selection described previously. The η signal region is shown in Fig. 5. The results of the D_{sJ} search are shown in the $M(KK\pi^{\pm}\eta) - M(KK\pi^{\pm})$ mass-difference distribution in Fig. 6. The η four vector was defined in this plot with the measured η momentum and the PDG η mass. A clear peak is seen in Fig. 6 at a mass difference of 666.9±3.3 MeV/c^2.

To estimate the combinatoric background, each D_s candidate was matched with η candidates from other sample events to form an event-mixed sample representing the combinatoric background of true single charm production and real η candidates. As can be seen in Fig. 6, the event-mixed background models the background shape very well, but does not produce any signal peak.

To estimate the signal yield, the combinatoric background (light shaded area) was subtracted from the signal data. The resulting difference histogram is plotted in the inset in Fig. 5 in the mass-difference range appropriate to the D_{sJ} search (D_{sJ}^{+} masses up to 2900 MeV/c^2). Outside the peak region the data scatter about 0. The difference histogram was fit with only a Gaussian with no residual back-ground terms. The Gaussian width was fixed at the simulation value of 10.9 MeV/c^2. The fit yield is 43.4 ± 9.1 events at a mass of 2635.4 ± 3.3 MeV/c^2.

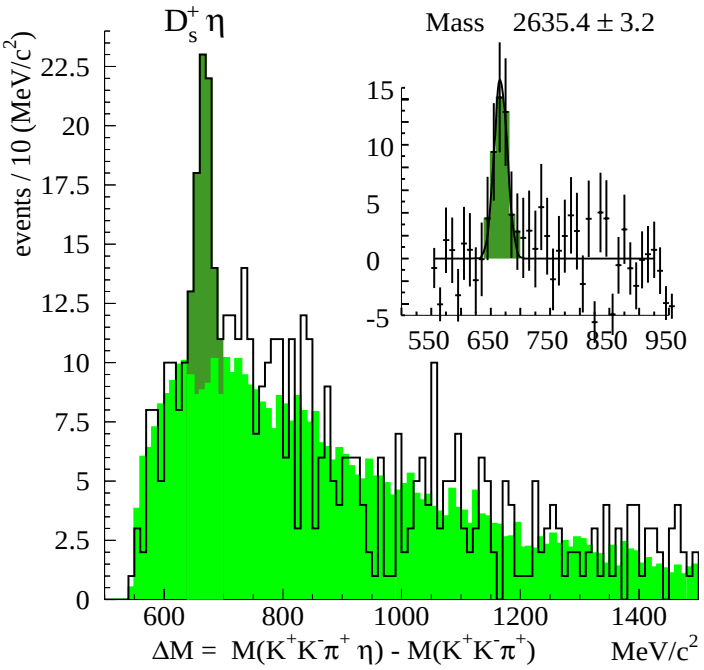

Fig. 6. $M(KK\pi^{+}\eta) - M(KK\pi^{+})$ mass-difference distribution. Charged conjugates are included. The darker shaded region is the events excess used in the estimation of signal significance. The lighter shaded region is the event mixed combinatoric background described in the text. The inset shows the difference of the two with a Gaussian fit to the signal

The Poisson fluctuation probability for this excess is 3×10^{-7} including the uncertainty in the background. A conservative estimate of the fluctuation probability anywhere in the search region (up to 2900 MeV/c^2) is 6×10^{-6}.

The decay $D_{sJ}^{+}(2632) \to D^0 K^+$ is kinematically allowed. After the $D_{sJ}^{+}(2632) \to D_s^{+}$ the η signal had been found, this second decay mode was searched for as confirmation. The D^0 sample was the Σ^-- induced $D^0 \to K^-\pi^+$ subset of the sample used in the SELEX measurement of the D^0 lifetime [1].

The results are shown in Fig. 7a, where both the known $D_{sJ}^{+}(2573)$ state and another peak above the $D_{sJ}^{+}(2573)$ are clearly seen. Each peak was fit with a Breit-Wigner convoluted with a fixed width Gaussian plus a constant background term (as suggested from the wrong-sign data discussed below). The Gaussian resolution was set to the simulation value of 4.9 MeV/c^2. The mass difference and width of the $D_{sJ}^{+}(2573)$ returned by the fit, $\Delta M = 705.4 \pm 4.3$ MeV/c^2 and $\Gamma = 14^{+9}_{-6}$ MeV/c^2, respectively, agree well with the PDG values of $\Delta M = 707.9 \pm 1.5$ MeV/c^2 and $\Gamma = 15^{+5}_{-4}$ MeV/c^2. The fitted mass difference of the second Breit-Wigner is 767.0 ± 2.0 MeV/c^2, leading to a mass for the new peak of 2631.5 ± 2.0 MeV/c^2. The fitted yield is 13.2 ± 4.9 events. The signal spread is consistent with the Gaussian resolution, even when plotted in 2.5 MeV/c^2 bins, limiting the possible natural width. For the Breit-Wigner fit, a limit for the width of < 17 MeV/c^2 at 90% confidence level was found. This signal has a significance of 5.3σ in a ± 15 MeV/c^2 interval. The mass difference between this signal and the one seen in the $D_s^{+}\eta$ mode is 3.9 ± 3.8 MeV/c^2, statistically consistent with being the same mass. The combined measurement of the mass of this state in the studied decay modes is 2632.5 ± 1.7 MeV/c^2. Unlike the D_s case, the D^0K^+ decay contributes a small fraction to the SELEX D^0 sample.

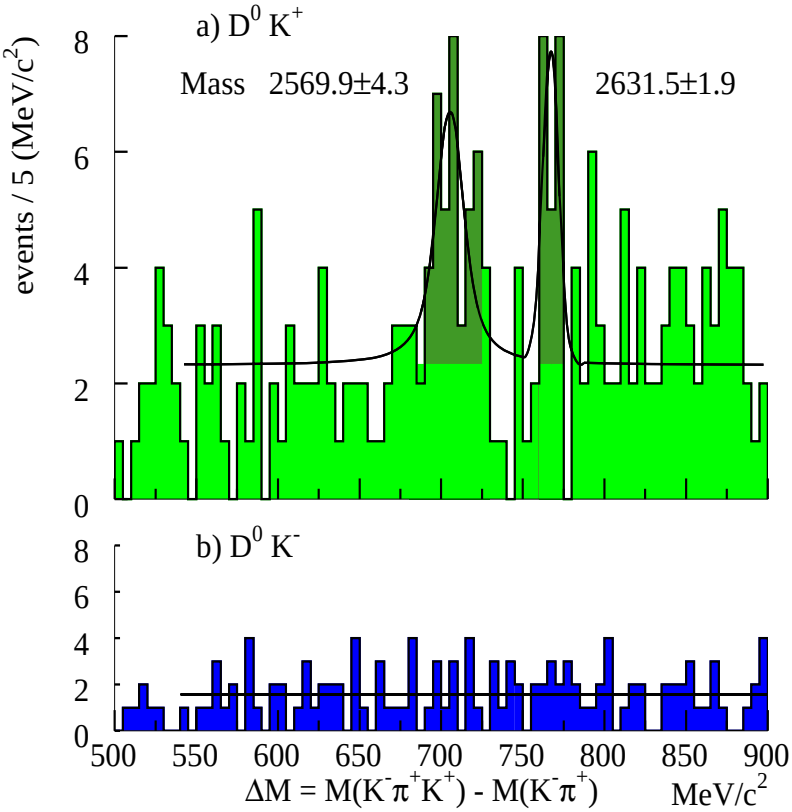

Fig. 7. (a) $D_s(2632)\to D^0K^+$ mass-difference distribution. Charged conjugates are included. The shaded regions are the events excesses used in the estimation of signal significances. (b) Wrong-sign background D^0K^- events, as described in the text

The combinatorial background will be equally likely to produce a D^0K^- combination (wrong-sign kaon) as a D^0K^+. The wrong-sign combinations are shown in Fig. 7b. There is no structure in these data which fit well to a constant background. Therefore, it may be concluded that the peak at 2631.5 MeV/c^2 is real and confirms the observation in the $D_s^+\eta$ mode.

The relative branching ratio $\Gamma(D^0K^+)/\Gamma(D_s^+\eta)$ was estimated to be 0.14 ± 0.06. The observed $D_{sJ}(2632)$ state is very narrow, consistent with a width due only to the resolution in the D^0K^+ decay mode. The mechanism that keeps this state narrow is unclear. The D^0K^+ channel is well above the hreshold, with a Q value ~275 MeV. The branching ratios for this state are also unusual. The $D_s^+\eta$ decay rate dominates the D^0K^+ rate by a factor of ~7 despite having half the phase space.

References

1. G.D. Alkhazov, N.K. Terentyev and A.A. Vorobyov, in *PNPI-XXV, High Energy Physics Division. Main Scientific Activities 1997–2001*, Gatchina, 2002, p. 104.
2. P. Pogodin *et al*. (the SELEX Collaoration), Phys. Rev. D **70**, 112005 (2004).
3. V.V. Molchanov *et al*. (the SELEX Collaboration), Phys. Lett. B **590**, 161 (2004).
4. M. Mattson *et al*. (the SELEX Collaboration), Phys. Rev. Lett. **89**, 112001 (2002).
5. A. Ocherashvili *et al*. (the SELEX Collaboration), Phys. Lett. B **628**, 18 (2005).
6. A.V. Evdokimov *et al*. (the SELEX Collaboration), Phys. Rev. Lett. **93**, 242001 (2004).

RECENT PHYSICS RESULTS FROM THE D0 EXPERIMENT

PNPI participants of the D0 Collaboration:
G.D. Alkhazov, V.T. Kim, A.A. Lobodenko, P.V. Neustroev, G.Z. Obrant, Yu.A. Scheglov, L.N. Uvarov, S.L. Uvarov

1. Introduction

D0 is an international collaboration of about 670 physicists from 83 institutions, who have designed, built and are operating a collider detector at the Fermilab Tevatron.

Main physics goals are precision tests of the Standard Model (SM), the weak bosons physics, top quark physics, QCD, *B* physics and a search for particles and forces beyond the SM: super-symmetric (SUSY) particles, gravitons, candidates for the cosmic dark matter, and a search for extra dimensions.

During Run II, the Tevatron is operated at an increased $p\bar{p}$ center-of-mass energy of 1.96 TeV. The luminosity has been increased by a factor more than ten, to $\geq 10^{32}$ $cm^{-2}\,s^{-1}$.

PNPI has been involved in the D0 project through the design and programming of the electronic readout for mini drift tubes (50,000 channels) and operation of the Forward Muon System [1]. PNPI physicists take part in the data analysis, including QCD, *B* physics, and Electroweak physics studies. Main D0 physics results are the top-quark mass, B_s mixing frequency, cross section for single top-quark production and inclusive cross section.

2. The D0 detector

The Run II D0 detector (Fig. 1) [2] consists of a central tracking system, a liquid-argon/uranium sampling calorimeter and an iron toroid muon spectrometer.

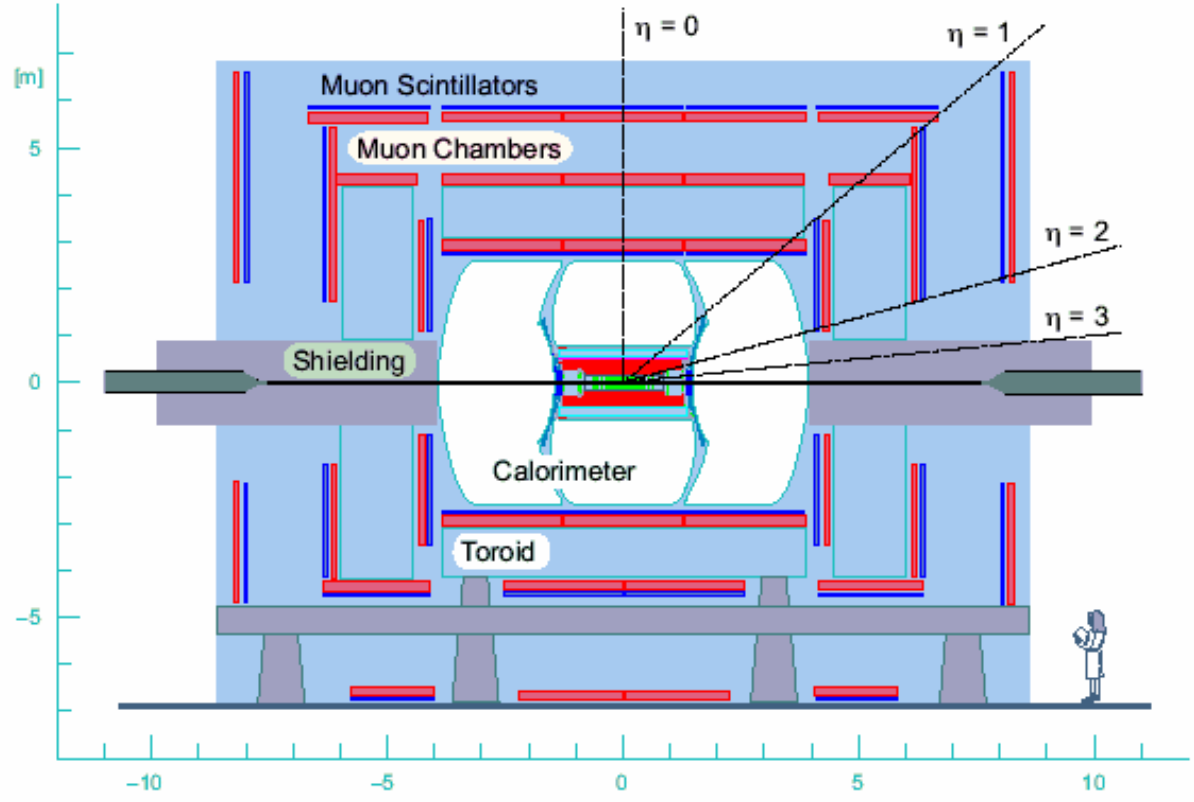

Fig. 1. A schematic view of the D0 detector

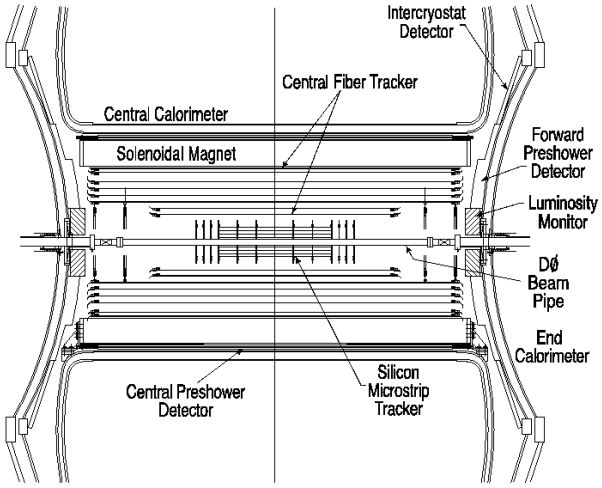

Fig. 2. Cross-sectional view of the new central tracking system in the XZ plane

The central tracking system (Fig. 2) is composed of a silicon microstrip tracker (SMT) and a central fiber tracker, both located into a 2T superconducting solenoidal magnet. The SMT detector has about 800,000 individual strips, and its design is optimized for tracking and vertexing capabilities allowing heavy flavor tagging. The calorimeter is longitudinally segmented into electromagnetic and hadronic layers and is housed into three cryostats. The muon system [3] resides beyond the calorimeter and consists of a layer of tracking detectors and scintillation counters before the toroidal magnet, followed by two similar layers after the toroid. Tracking in the muon system relies on wide or mini drift tubes depending on the acceptance. The Run II D0 detector allows to work at the luminosity of $>10^{32}$ cm^{-2} s^{-1}. The D0 detector is described in detail in Ref. [2]. Most important recent physics results are presented below.

3. Top quark production cross section and mass

The t quark, the heaviest particle known, was discovered at the Tevatron in 1995. Since then, the study of the top quark was one of important directions of investigations at D0. In the triggering and analysis, the event selection was done with high p_T leptons, high E_T multiple jets, large missing energy E_T and displaced vertices for b-jets. The cross section for the $t\bar{t}$ production was measured by several methods. Two most precise results [4] for the $t\bar{t}$ production cross section are derived from the lepton + jets channel: $\sigma_{t\bar{t}} = 7.2 \pm 1.2 + 1.9 - 1.4$ pb, with an impact parameter tagging, and $\sigma_{t\bar{t}} = 8.2 \pm 1.3 + 1.9 - 1.8$ pb, using a vertex tagging.

Last measurements using the vertex tagging combines the μ + jets and e + jets channels, using 422 pb^{-1} and 425 pb^{-1} of data. The measured $t\bar{t}$ production cross section for a top-quark mass of 175 GeV is $\sigma_{t\bar{t}} = 6.6 \pm 0.9\,(\text{stat} + \text{syst}) \pm 0.4\,(\text{lum})$ pb.

The top-quark mass is a fundamental SM parameter. Together with the W mass, it provides a constraint on the Higgs mass. Different methods were used at D0 to derive the top-quark mass. The combined result for the top-quark mass, obtained by the D0 and CDF collaborations from the data of Run I and Run II, is [5]: $m_t = 172.5 \pm 2.3$ GeV/c^2 (Fig. 3). This is the most accurate measurement of the top-quark mass by now.

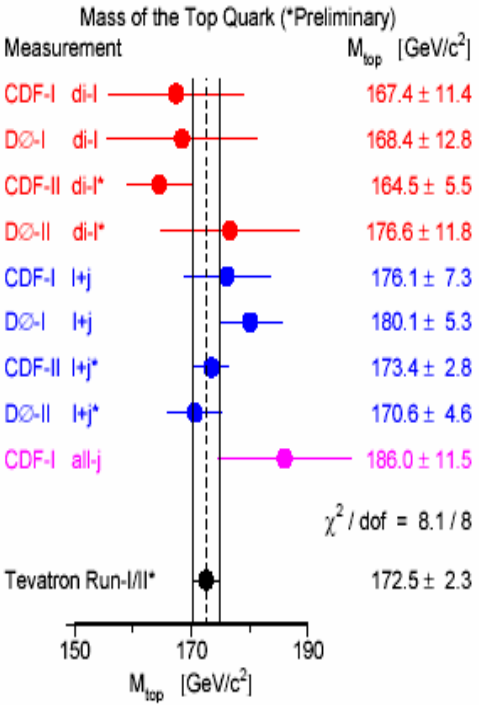

Fig. 3. Results of the t-quark mass measurements in the experiments D0 and CDF

4. Search for single top-quark production

For the first time, the top quark was observed in its $t\bar{t}$ production mode. The single top-quark production with the *tb* or *tqb* final states is possible *via* the electroweak interaction. A measurement of the single top-quark production cross section can be used to constrain the magnitude of the CKM matrix element V_{tb} and study the *Wtb* coupling. An events selection in the search for single top quarks is similar to the search for the top-quark pairs in the *l* + jets mode. Backgrounds of *W* + jets, $t\bar{t}$ and dibosons are substantial.

The D0 Collaboration presents a first evidence for the production of single top quarks at the Fermilab Tevatron $p\bar{p}$ collider. Using a 0.9 fb^{-1} data set and applying a multivariate analysis to separate signal from background, the cross section for the production of single top quarks in the reactions $p\bar{p} \to tb + X$, $p\bar{p} \to tqb + X$ was measured to be 4.9 ± 1.4 pb [6] (Fig. 4). The probability to measure a cross section at this value or higher in the absence of signal is 0.035%, corresponding to a 3.4 standard deviation significance. The measured cross section was used to directly determine the CKM matrix element that describes the *Wtb* coupling. The found value of V_{tb} is $0.68 < |V_{tb}| \leq 1$ at the 95% CL, which agrees with the SM.

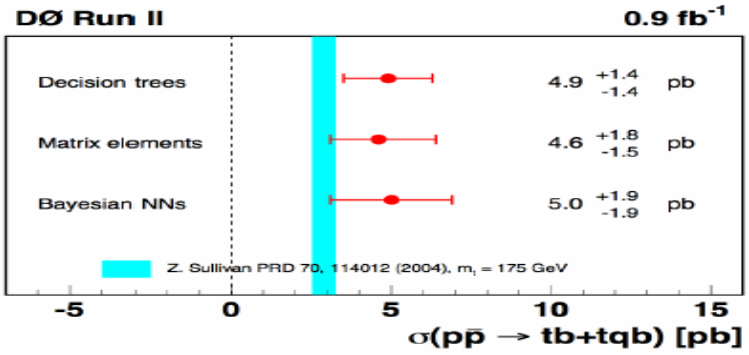

Fig. 4. Single top-quark production cross section, *s* + *t* channels

5. QCD studies

Motivations of the QCD studies are to use the strong interaction processes for an investigation of the internal proton structure, a search for the quark substructure, a study of the diffractive and heavy flavor production, a study of new objects, like *X*(3872), and for the understanding of backgrounds to the physics beyond the SM.

The D0 Run II results [7] cover the QCD cross section which changes up to 8 orders of magnitude. One of the most new QCD results is the inclusive photon cross section in the central rapidity region for p_T range of $23 < p_T$ [GeV/c] < 300 (Fig. 5). The dominant source of the photon production for $p_T < 150$ GeV/c is the prompt Compton quark-gluon scattering. The cross section for the inclusive photons is sensitive to the gluon parton distribution function. The gamma p_T values measured at D0 are much higher than those covered in previous experiments. The NLO QCD predictions describe the data within the experimental uncertainties in the whole p_T range considered.

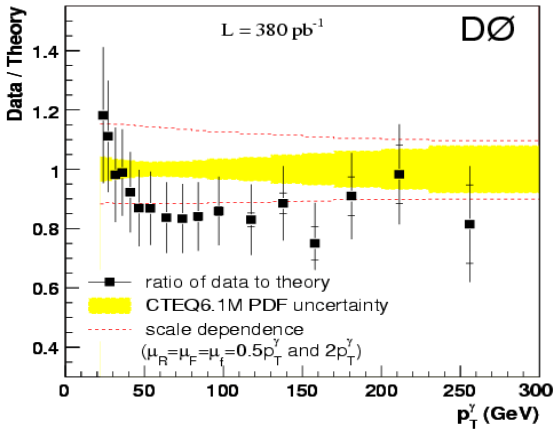

Fig. 5. Inclusive photon cross section in the central rapidity region: ratio of the experimental data to theory

6. Electroweak physics. Diboson production

One of the main motivations of the electroweak physics is to constrain indirectly new physics by means of precision measurements of electroweak parameters. The experimental cross sections for WW, WZ, ZZ, $W\gamma$ and $Z\gamma$ production provide a test of the SM and give information about boson self-coupling. Besides, the electroweak processes are backgrounds to many interesting searches, like $H \rightarrow WW$.

Measurements of a single and multi-boson production, a W production asymmetry, a forward-backward asymmetry in the Z-boson production and other electroweak processes are underway at D0 [8]. New experimental limits on Anomalous Couplings are set (Fig. 6) for $ZZ\gamma$ and $Z\gamma\gamma$: $|h_{30}^{\gamma}|<0.23$, $|h_{40}^{\gamma}|<0.019$, $|h_{30}^{Z}|<0.23$, $|h_{40}^{Z}|<0.20$ at the 95% CL for Λ=1 TeV, where Λ is a form factor scale displaying the scale of new physics. All cross sections are in good agreement with the SM.

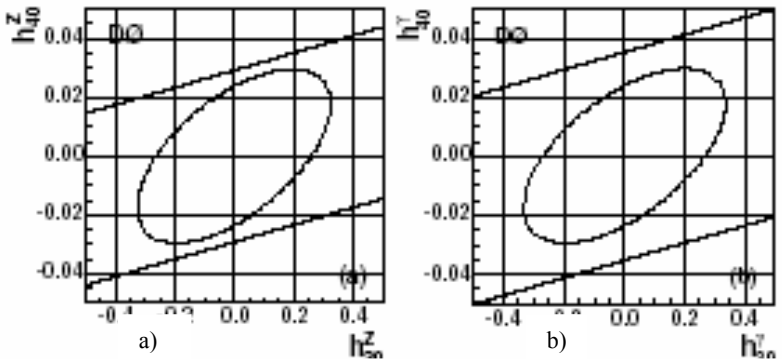

Fig. 6. The 95% CL two-dimensional exclusion limits for CP-conserving (a) $ZZ\gamma$ and (b) $Z\gamma\gamma$ couplings for Λ = 1 TeV. Straight lines illustrate the unitarity constraints

7. Search for the $B_s \rightarrow 2\mu$ decay

B physics is one of the important directions of studies at D0 [9]. A search for $B_s \rightarrow 2\mu$ of the flavor-changing neutral current decay helps to find an evidence of possible SM enhancements – the MSSM , SUSY, *etc*. The decay $B_s \rightarrow 2\mu$ is strongly suppressed in the SM. A contribution from all possible $B_s \rightarrow 2\mu$ SM diagrams gives the branching ratio ~3.5×10^{-9}. At the same time, in the MSSM this branching ratio can be up to 10^{-7}.

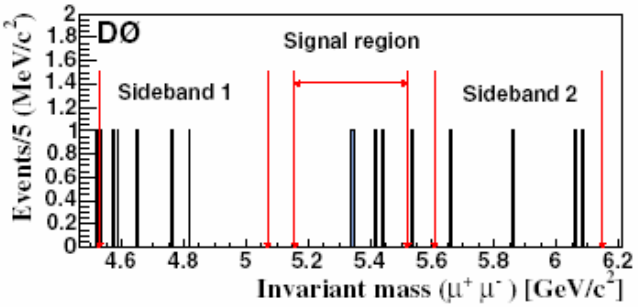

Fig. 7. Invariant mass of the remaining events of the full data sample after optimized requirements on discriminating variables

The silicon microstrip tracker allows to realize a search for the $B_s \rightarrow 2\mu$ rare decay. Since τ_{Bs} = 1.46 ps (400 μm), the secondary vertices of the B_s decay could be selected from the primary vertices. Figure 7 shows an invariant mass spectrum of $(\mu^{+}\mu^{-})$ events in the search region of the $B_s \rightarrow 2\mu$ decay. The D0 published an upper limit for this process: $BR\,(B_s \rightarrow 2\mu) < 5.0 \times 10^{-7}$ at the 95% CL [10]. A very recent new D0 preliminary result is: $BR\,(B_s \rightarrow 2\mu) < 1.1 \times 10^{-7}$ at the 95% CL.

The obtained results provide restrictions to many SUSY models. For example, last D0 and CDF results (the CDF result is $BR\,(B_s \rightarrow 2\mu) < 1.0 \times 10^{-7}$ at 95% CL) provide very strong restrictions to the parameters of the minimal supergravity scenario model mSUGRA and SO(10) SUSY symmetry breaking model.

8. B_s oscillations

One of the most interesting topics in B physics is the B_s^0 oscillations (or B_s^0 mixing – a transition of neutral B_s mesons between particle and antiparticle) and measurement of the oscillation frequencies Δm_s and Δm_d (correspondingly of B_s and B_d mesons). The values of Δm_s and Δm_d provide powerful constraints to the V_{td} and V_{ts} elements of the CKM matrix. The oscillation frequency Δm_d for B_d mesons was measured previously in the D0 and CDF experiments. As for B_s mesons, they are expected to oscillate much faster than B_d mesons. Consequently, their oscillations are more difficult to detect. Note that the ratio of the frequencies Δm_s and Δm_d is free of several theoretical uncertainties.

A search for the B_s^0 oscillations was performed at D0 using a semileptonic decay $B_s \to \mu D_s X$. D_s mesons were reconstructed *via* their decay channel $D_s \to \varphi\pi$, $\varphi \to KK$. As a result of this search, the D0 collaboration determined not only the lower boundary, but also the upper boundary of possible values of the B_s^0 oscillation frequency. The amplitude fit method of the data analysis gives a lower limit on the B_s^0 oscillation frequency at 14.8 ps^{-1} at the 95% CL. At Δm_s = 19 ps^{-1}, the amplitude deviates from the hypothesis of an oscillation amplitude of zero by 2.5 standard deviations (Fig. 8), corresponding to a two-sided CL of 1%. A likelihood scan over the oscillation frequency Δm_s gives a most probable value of 19 ps^{-1} and a range of $17 < \Delta m_s < 21$ ps^{-1} at the 90% CL [11]. This is the first direct two-sided bound on the B_s^0 oscillation frequency measured by a single experiment. The D0 result was confirmed shortly after by the CDF precise measurement: $\Delta m_s = 17.3 - 0.2 + 0.4 \pm 0.1$ ps^{-1}.

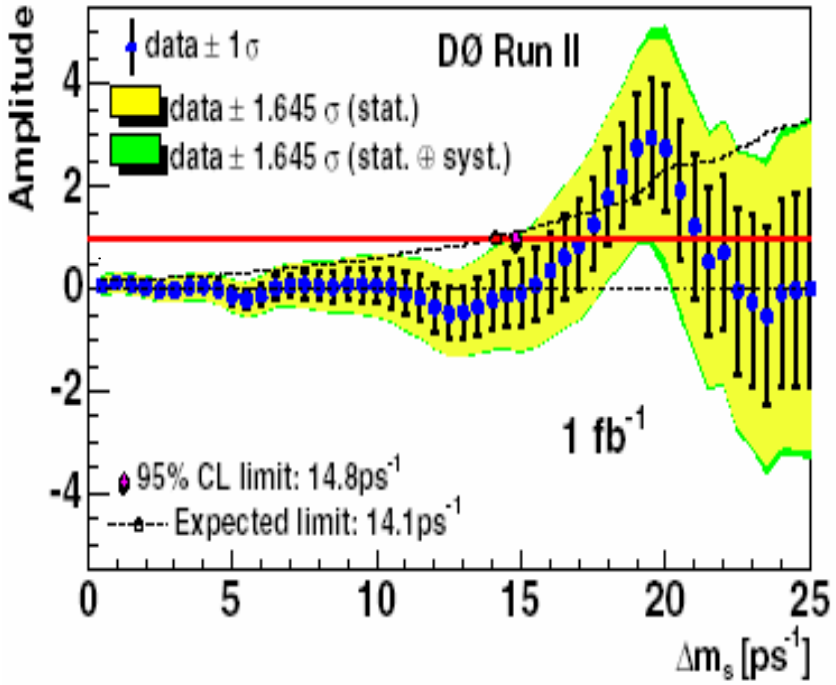

Fig. 8. B_s oscillation amplitude as a function of oscillation frequency Δm_s. The solid line shows the A = 1 axis for reference. The dashed line shows the expected limit including both statistical and systematic uncertainties

Systematic uncertainties of these measurements were addressed by varying inputs for a fitting procedure, cut requirements, branching ratios, and probability density function modeling. The branching ratios were varied within known uncertainties and large variations were taken for those not yet measured. The K-factor distributions were varied within uncertainties, using measured instead of generated momenta in the Monte Carlo simulation. The fractions of peaking and combinatorial backgrounds were varied within uncertainties. The lifetime of B_s^0 was fixed to its world average value, and $\Delta\Gamma_s$ was allowed to be nonzero. The scale factors on the signal and background resolutions were varied within uncertainties, and typically generated the largest systematic uncertainty.

9. Search for extra dimensions

A search for a virtual graviton exchange in Kaluza-Klein modes and Large Extra Dimensions in the channel of a real graviton emission is underway. A signal would be an excess of ee, $\mu\mu$ or $\gamma\gamma$ events at large invariant masses due to the virtual graviton exchange (Fig. 9). The latest D0 limit from the $p\bar{p} \to ee, \mu\mu$ and $\gamma\gamma$ events is MS (GRW) > 1.43 TeV at the 95% CL. This result is the most stringent limit to date on the Large Extra Dimensions [12].

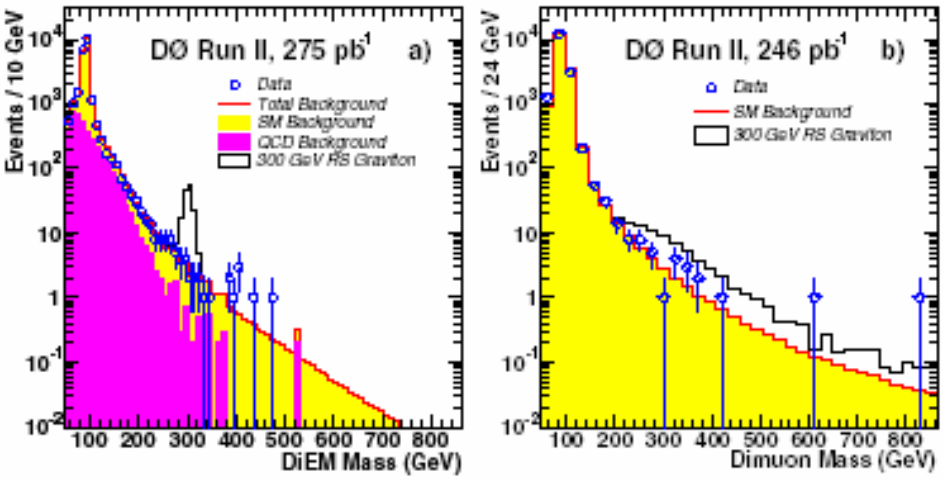

Fig. 9. Invariant mass spectrum in the (a) diEM and (b) dimuon channels. An open histogram is the signal from an RS graviton with the mass M_1 = 300 GeV and coupling k/M_{Pl}= 0.05

10. Search for SUSY particles

SUSY solves the "Hierarchy Problem" and provides the Grand Unification on the energy scale less than 10^{16} GeV. SUSY particles are good Dark Matter candidates. The D0 experiment realizes a search for the Chargino/Neutralino production in the $3l$ + missing E_T-channel and a search for Squarks and Gluinos (Fig. 10) in the channel jets + missing E_T. The Run II D0 data have allowed to improve the Run I limit of 1.6 pb in the 3-lepton search to 0.26 pb and to extend the LEP mSUGRA search [13].

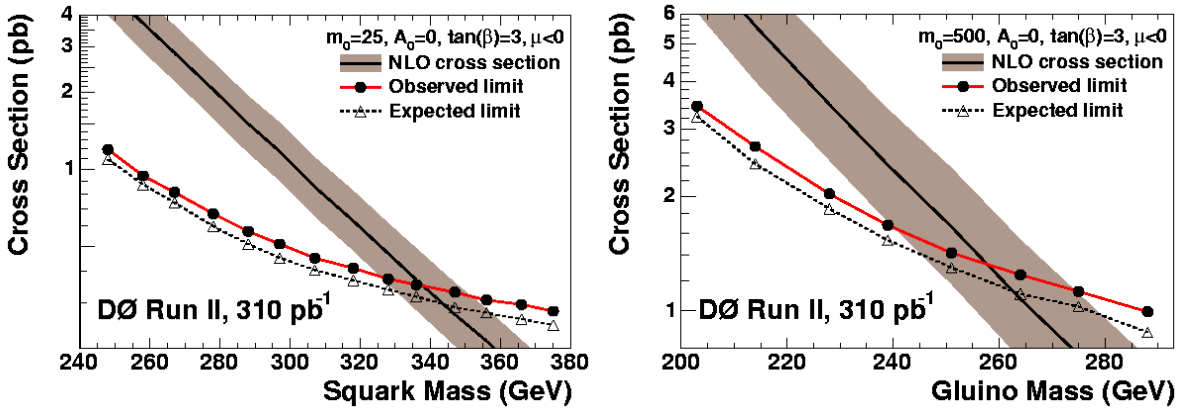

Fig. 10. D0 Run II observed limit for squark and gluino in comparison with the NLO production cross-section

11. Standard Model Higgs search

In the SM, the Higgs boson is crucial to the understanding of electroweak symmetry breaking and the mass generation of electroweak gauge bosons and fermions. However, this particle has not yet been observed. The mass of the Higgs boson is not predicted in the SM. Precision measurements in particle physics constrain the Higgs mass to $114 < m_H$ [MeV/c^2] < 260. The low mass region of 120–130 GeV/c^2 is available to a search for the Higgs at the Tevatron. Therefore, a search for the Higgs boson is one of the most important goals of the D0 experiment.

In 2003, the Tevatron Higgs sensitivity study was updated for the low Higgs mass region. The full detector simulation was used and an optimization of the analysis was done. Several searches for the SM Higgs boson have been performed using the D0 data from Run II. In particular, the Higgs boson was searched in the $p\bar{p} \to WH \to Wb\bar{b}$ [14] and $p\bar{p} \to H \to WW^{(*)}$ [15] channels. No evidence for the Higgs particle has been found. The number of events observed is consistent with the expectation from the background. Upper limits on the production cross section times the branching ratio have been derived: $\sigma(p\bar{p} \to WH) \times BR(H \to b\bar{b}) \leq 9.0$ pb and $\sigma(p\bar{p} \to H) \times BR(H \to WW^{(*)}) \leq 5.6$ pb at the 95% CL for the expected Higgs mass 115 and 120 GeV/c^2, respectively.

12. Conclusion

The D0 detector is working well with a high data taking efficiency. A number of physics results have been obtained recent years. New results in *B* and Top quark physics based on higher statistics are anticipated. New measurements in QCD and electroweak physics are planned. The SM Higgs and new phenomena physics searches are in progress.

During the D0 detector upgrade in 2006, a new silicon tracker Layer "0" was installed with improvements in *b*-tagging. The Tevatron luminosity is planned to be still further increased. The Tevatron operation and data taking at D0 and CDF will continue to 2009.

References

1. G.D. Alkhazov, V.L. Golovtsov, V.T. Kim, A.A. Lobodenko, P.V. Neustroev, G.Z. Obrant, Yu.A. Scheglov, N.K. Terentyev, L.N. Uvarov, S. L. Uvarov and A.A. Vorobyov, in *PNPI-XXV, High Energy Physics Division. Main Scientific Activities 1997–2001*, Gatchina, 2002, p. 124.
2. V.M. Abazov *et al*., Nucl. Instr. Meth. A **565**, 463 (2006).
3. V.M. Abazov *et al*., Nucl. Instr. Meth. A **552**, 372 (2005).
4. V.M. Abazov *et al*., Phys. Lett. B **626**, 35, 45, 55 (2005); Phys. Rev. D **74**, 112004 (2006).
5. CDF and D0 Collaborations and Tevatron Electro-Weak Working Group, hep-ex/0603039 (2006).
6. V.M. Abazov *et al*., Phys. Lett. B **622**, 265 (2005).
7. V.M. Abazov *et al.*, Phys. Rev. Lett. **93**, 162002 (2004) ; **94**, 221801 (2005); V.M. Abazov *et al*., Phys. Lett. B **639**, 151 (2006).
8. V.M. Abazov *et al.*, Phys. Rev. Lett. **94**, 151801, 152002, 161801 (2005) ; **95**, 051802, 141802 (2005); V.M. Abazov *et al.*, Phys. Rev. D **71**, 072004 (2005); Phys. Rev. D **71**, 091108(R) (2005).
9 V.M. Abazov *et al*., Phys. Rev. Lett. **94**, 042001, 102001, 182001, 232001 (2005), **97**, 241801 (2006); V.M. Abazov *et al*., Phys. Rev. D **74**, 031107(R) (2006).
10. V.M. Abazov *et al*., Phys. Rev. Lett. **94**, 071802 (2005).
11. V.M. Abazov *et al*., Phys. Rev. Lett. **97**, 021802 (2006).
12. V.M. Abazov *et al*., Phys. Rev. Lett. **95**, 091801, 161602 (2005).
13. V.M. Abazov *et al*., Phys. Rev. Lett. **93**, 141801 (2004) ; **94**, 041801 (2005) ; **95**, 151801, 151805 (2005); V.M. Abazov *et al*., Phys. Rev. D **71**, 071104(R) (2005).
14. V.M. Abazov *et al*., Phys. Rev. Lett. **94**, 091802 (2005).
15. V.M. Abazov *et al*., Phys. Rev. Lett. **96**, 011801 (2006).

STUDY OF LIGHT VECTOR MESONS AT RHIC BY PHENIX

PNPI participants of the PHENIX Collaboration:
V.V. Baublis, D.A. Ivanischev, A.V. Khanzadeev, B.G. Komkov, V.G. Ryabov, Yu.G. Ryabov, V.M. Samsonov, E.A. Vznuzdaev, M.B. Zhalov

1. Introduction

Light vector mesons are among the most interesting probes of the matter created in relativistic heavy ion collisions. The simultaneous measurement of meson properties in *p*+*p*, *d*+Au and Au+Au collisions provides a basis for the observation of anomalous features specific to heavy ion collisions and allows separation of cold and hot nuclear effects affecting particle production.

One of the most exciting measurements performed by all experiments at RHIC was the observation of suppression of high transverse momentum hadrons in central Au+Au collisions. Later it was found that baryons (protons) and light mesons (π^0) have different suppression tendencies that brought up the "baryon puzzle" [1]. Measurement of nuclear modification factors for vector mesons adds to the picture of particle suppressions and their dependence on particle mass and composition supporting hydrodynamics or recombination models.

Properties of the light vector mesons are sensitive to the chiral symmetry restoration expected to occur at sufficiently high temperatures achieved in heavy ion collisions. Short lifetimes of ω and φ-mesons (Γ_ω = 8.5 MeV, Γ_φ = 4.3 MeV) presuppose that significant part of them decays inside the hot and dense nuclear matter produced in heavy ion collisions. Theoretical models predict that basic properties of the light vector mesons such as mass, width and branching ratios can be modified in presence of this media. Such modifications can be studied by comparison of meson properties measured in leptonic and hadronic decay modes in different collision systems.

2. Experimental setup and data samples

The two central spectrometers of the PHENIX experiment [2] each covering 90° in azimuth and ±0.35 in pseudorapidity have a capability to measure both neutral and charged particles produced in RHIC collisions (see Fig. 1). Beam-Beam Counters and Zero Degree Calorimeters provide the minimum bias trigger and are

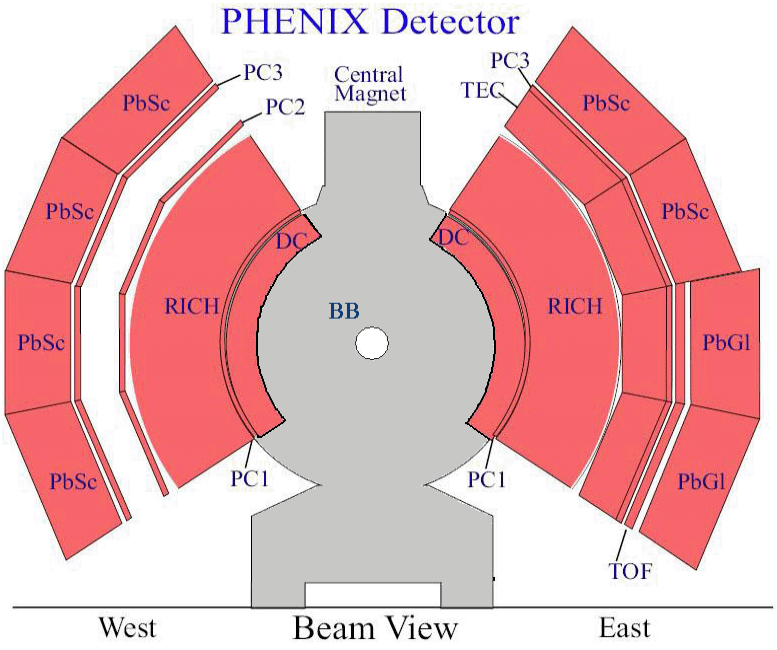

Fig. 1. Layout of the PHENIX central spectrometer

used to determine Z-coordinate of the collision vertex and the event centrality. The momentum of charged particles is measured with the Drift Chamber (DC) and the first layer of the Pad Chamber (PC1). In some cases the third layer of the Pad Chambers (PC3) is used for track confirmation. For hadron identification PHENIX has a high resolution TOF subsystem covering about half of the East arm ($|\eta| < 0.35$ and $\Delta\varphi \sim 45°$) and an Electromagnetic Calorimeter (EMC: PbSc and PbGl) covering both arms. The TOF subsystem and time of flight of the EMC identify kaons within $0.3 < p$[GeV/c] < 2.0 and $0.3 < p$[GeV/c] < 1.0, respectively. The electrons are identified with a Ring Imaging Cherenkov Detector (RICH) and by matching of energy measured in the EMC and momentum measured in the DC for the charged track. The EMC is also used as a primary detector for the reconstruction of photons and π^0-mesons [3].

For hadron decays of ω-mesons minimum bias and ERT data samples are used. The latter sample was accumulated with high-p_T online trigger realized by adding together amplitudes in 4 × 4 adjacent EMC towers and comparing them to a threshold of 1.4 GeV in p+p and 2.4 GeV in d+Au collisions. Analyzed decays, basic analysis cuts and data samples are presented in Table.

Table

Decay	Vertex, cm	PID	Data Sample, events
$\varphi \to e^+e^-$	$-28 < Z < 26$	RICH, EMC	Run 4, (Au+Au, 200 GeV): 9×10^8 MinBias
$\varphi \to K^+K^-$	$-30 < Z < 30$	TOF (EMC)	Run 4, (Au+Au, 200 GeV): $4.1\ (1.1) \times 10^8$ MinBias Run 3, (p+p, 200 GeV): 4.3×10^7 MinBias Run 3, (d+Au, 200 GeV): 5.4×10^7 MinBias
$\omega \to e^+e^-$	$-25 < Z < 25$	RICH, EMC	Run 4, (Au+Au, 200 GeV): 8×10^8 MinBias
$\omega \to \pi^0\pi^+\pi^-$	$-30 < Z < 30$	No PID	Run 5, (p+p, 200 GeV): 1.5×10^9 MinBias and 10^9 ERT (5.7×10^{10} sampled MinBias) Run 3, (d+Au, 200 GeV): 2.1×10^7 ERT (3.1×10^9 sampled MinBias)
$\omega \to \pi^0\gamma$	$-30 < Z < 30$	No PID	Run 5, (p+p, 200 GeV): 1.5×10^9 MinBias and 10^9 ERT (5.7×10^{10} sampled MinBias) Run 4, (Au+Au, 200 GeV): 7.8×10^8 MinBias Run 3, (d+Au, 200 GeV): 2.1×10^7 ERT (3.1×10^9 sampled MinBias)

3. Analysis

For the reconstruction of $\varphi(\omega) \to e^+e^-$ and $\varphi \to K^+K^-$ decays we combine oppositely charged identified particles to form unlike sign invariant mass spectra containing both the signal and combinatorial background of uncorrelated pairs. The shape of the uncorrelated combinatorial background is estimated in mixed event technique where identified particles of one sign are combined with particles of the opposite sign taken from several other events having the same centrality and collision vertex. The mixed event invariant mass distribution is then normalized to the value of $2\sqrt{N_{++}N_{--}}$ where N_{++} and N_{--} are the measured integrals of like-sign yields. The validity of this method of event mixing was confirmed by comparing the like-sign invariant mass spectra from mixed events [4]. Raw yields are extracted by the subtraction of mixed event distributions from invariant mass spectra and counting the particle yields around the known masses of particles. In the hadronic decay modes one can see a prominent peak in the mass distributions of the measured mesons but in the di-electron modes it is challenging because of huge combinatorial background originating primarily from the conversion and Dalitz decays of π^0-mesons. For example, in Run 4 data sample the signal-to-background ratio in the range of ω and φ-meson masses is about 1:500.

To measure hadron decays of the ω-mesons we start with reconstruction of π^0-mesons in the $\pi^0 \to \gamma\gamma$ decay channel using EMC. For the $\omega \to \pi^0\gamma$ decay we combine selected π^0-candidates with all other photons from the same event. In case of the $\omega \to \pi^0\pi^+\pi^-$ decay we combine π^0-candidates with any pair of negatively

and positively charged tracks assuming them to be π-mesons. Integrals of peaks reconstructed in invariant mass distributions are extracted by fitting since mixed event technique does not reproduce background shape due to presence of residual correlations [5]. In Au+Au collisions we loose the possibility to detect ω-meson in the $\omega \to \pi^0\pi^+\pi^-$ channel because four particles in the final state produce too much combinatorial background. However even in the most central collisions we can still extract ω-meson yield in the $\omega \to \pi^0\gamma$ decay at very high p_T.

Extracted raw yields of vector mesons are corrected for detector acceptance and trigger efficiencies evaluated with full Monte Carlo simulation of the PHENIX layout, detector responses, kinematics of particular decays and online trigger settings. For three-body decay of ω-meson we also take into account a non-uniform population of the phase space.

4. Results

The invariant m_T spectra of the φ-mesons in p+p, d+Au and Au+Au collisions at $\sqrt{s_{NN}}$ = 63 and 200 GeV are shown in Fig. 2. The PHENIX has an extensive set of $\varphi \to K^+K^-$ measurements in time-of-flight region for different collision systems and event centrality bins and also has a preliminary measurement of φ-meson production in the $\varphi \to e^+e^-$ channel with the results consistent with the hadronic channel. The latter, however, is rather limited because of small signal-to-background ratio.

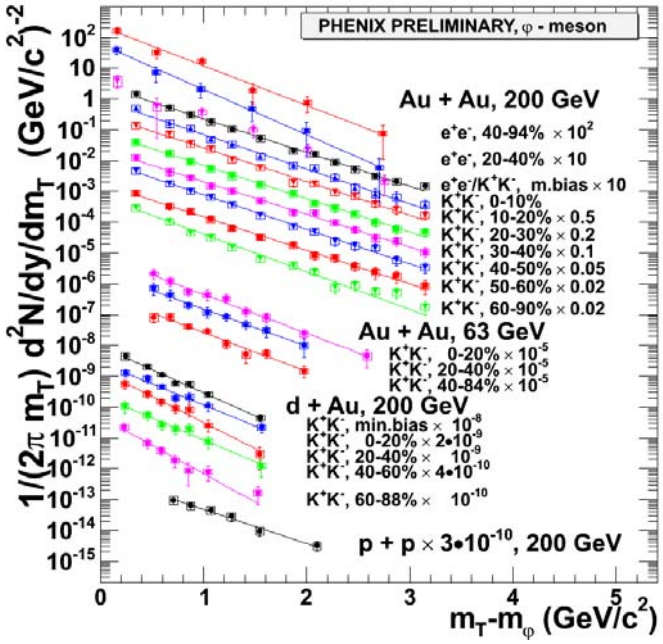

Fig. 2. Transverse mass spectra measured for φ-mesons in p+p, d+Au and Au+Au collisions at $\sqrt{s_{NN}}$ = 63 GeV and $\sqrt{s_{NN}}$ = 200 GeV

The measured m_T spectra were fit to the exponential function to extract integrated yields (dN/dy) and temperatures (T):

$$\frac{1}{2\pi m_T}\frac{d^2N}{dm_T\,dy} = \frac{dN/dy}{2\pi T(T+M_\phi)}\exp\frac{-(m_T-M_\phi)}{T},$$

Dependence of the measured temperature and integrated yield per pair of participating nucleons on the system size is shown in Fig. 3. The extracted temperatures do not change among different collision systems at the same energy and only slightly grow between 63 GeV and 200 GeV. Also there is no indication that the measured temperature is different in hadronic and leptonic channels. The integrated φ-meson yield per participant increases by approximately a factor of two from peripheral to central collisions at full RHIC

energy. Similar growth is also observed at $\sqrt{s_{NN}}$ = 63 GeV. Preliminary measurement of the yields in the leptonic channel looks higher than in $\varphi \to K^+K^-$ channel. However, statistical and systematic uncertainties prevent us from making a conclusive statement on this subject.

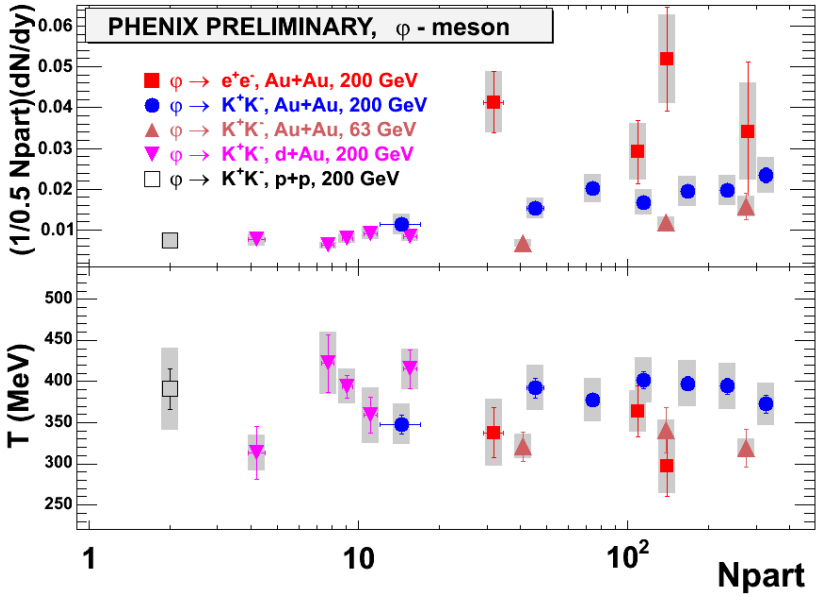

Fig. 3. φ-meson inverse slop (bottom panel) and integrated yield per pair of participants (top panel) as a function of centrality

The invariant p_T spectra measured for ω-mesons in p+p, d+Au and Au+Au collisions at $\sqrt{s_{NN}}$ = 200 GeV are shown in Fig. 4. For two hadronic decays $\pi^0\pi^+\pi^-$ and $\pi^0\gamma$ having different kinematics and reconstruction efficiencies we have a very good agreement in p+p and d+Au. In Au+Au collisions we measured three p_T points in each most central, minimum bias and peripheral collisions in the $\pi^0\gamma$ channel. In the di-electron channel the PHENIX has preliminary measurement of ω-meson production at low p_T.

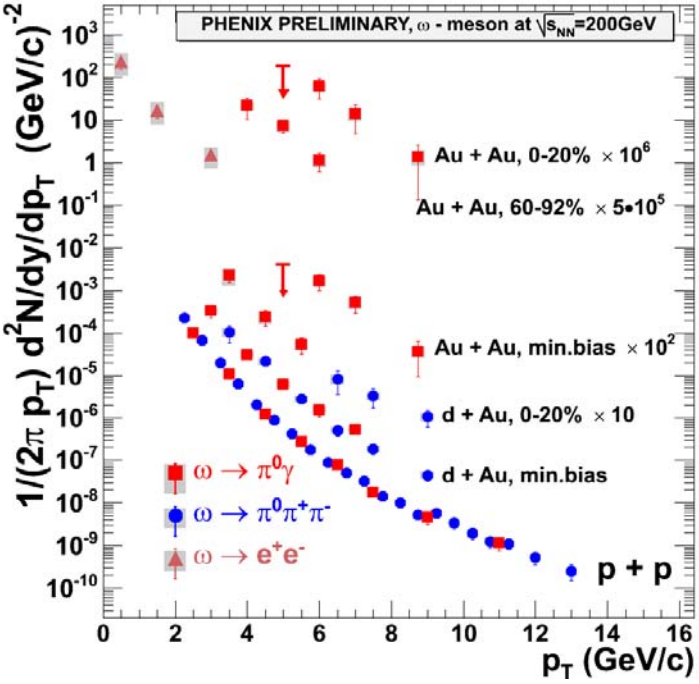

Fig. 4. ω-meson p_T spectra measured in p+p, d+Au and Au+Au collisions at $\sqrt{s_{NN}}$ = 200 GeV

Figure 5 shows nuclear modification factors (R_{AA}) defined as the ratio of particle yields in Au+Au and p+p collisions scaled by the number of binary collisions, measured for ω and φ-mesons. In peripheral Au+Au collisions meson yields scale from p+p yields by the number of binary collisions. But in most central collisions we observe a suppression on the level of 3–5. Such a suppression pattern is consistent within errors with results previously obtained for π^0 mesons [6].

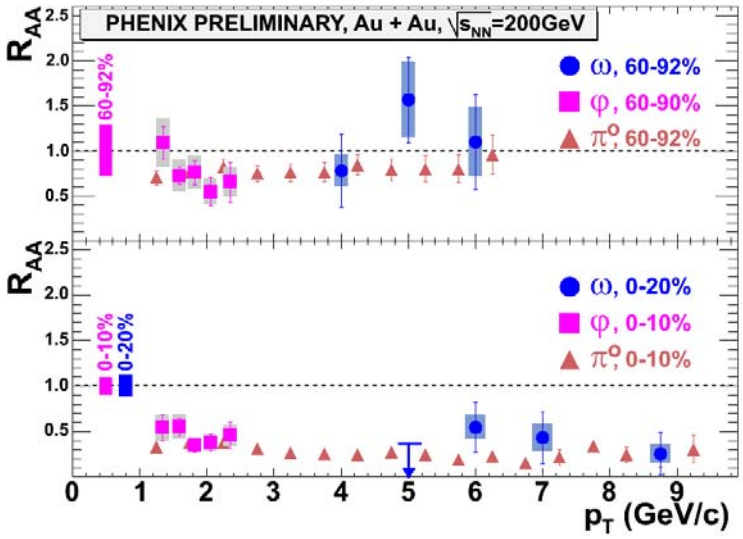

Fig. 5. R_{AA} for φ and ω mesons in Au+Au collisions at $\sqrt{s_{NN}}$ = 200 GeV

Short living light mesons are considered a good probe of chiral symmetry restoration which can be seen as modification of meson properties in leptonic channels in heavy ion collisions [7, 8]. Besides, some recent publications suggest that modification of meson masses can also be observed in hadronic decays and not only in heavy ion but also in p+p collisions. Dependence of the mass and width of φ-mesons reconstructed in the $\varphi \to K^+K^-$ decay channel on the centrality in d+Au and Au+Au collisions at $\sqrt{s_{NN}}$ = 200 GeV is shown in Fig. 6. The PHENIX experiment sees no modification of the φ-meson mass or width measured in

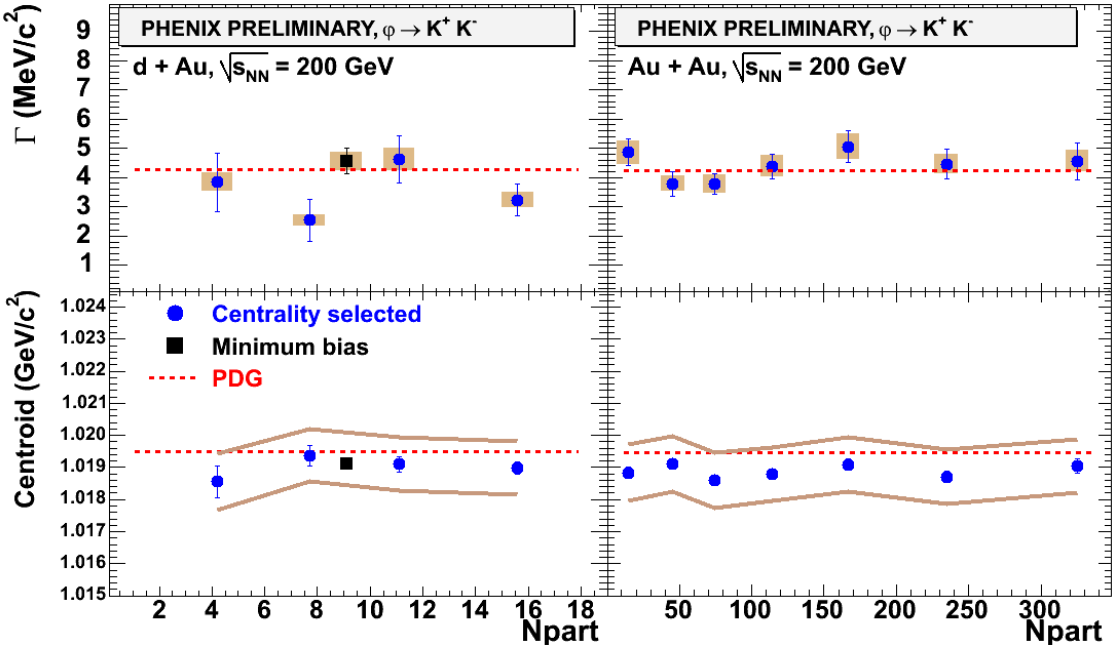

Fig. 6. φ-meson mass and width *vs* centrality in d+Au and Au+Au collisions at $\sqrt{s_{NN}}$ = 200 GeV

hadronic channels. In *p*+*p* and *d*+Au collisions within the errors of the measurement [4] we find that the reconstructed ω-meson mass is in agreement with PDG value at p_T > 2.5 GeV/c (Fig. 7).

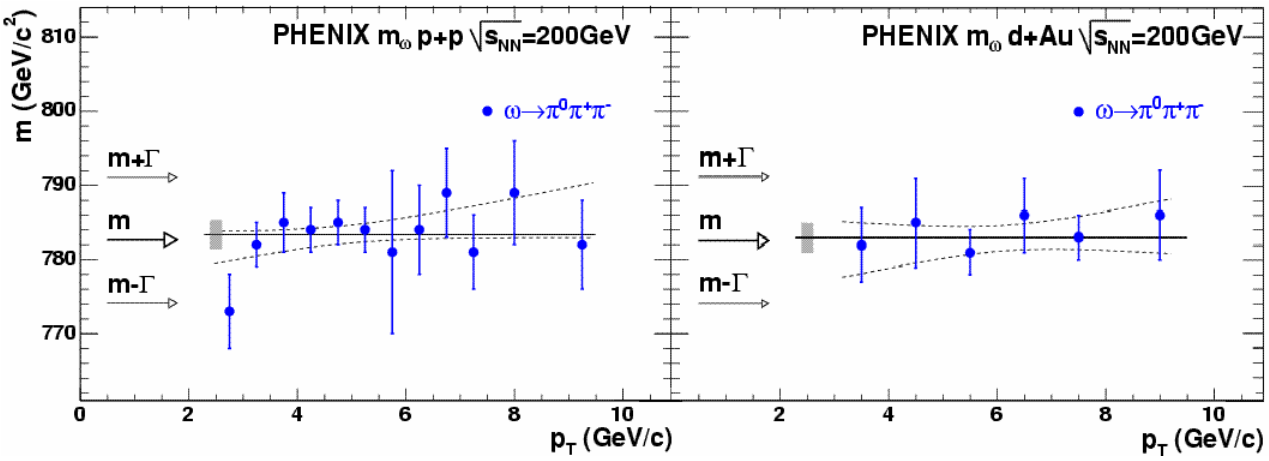

Fig. 7. Reconstructed in *p*+*p* (lower panel) and *d*+Au (upper panel) collisions ω-meson mass versus p_T

References

1. S.S. Adler *et al.*, Phys. Rev. Lett. **91,** 172301 (2003).
2. K. Adcox *et al.*, Nucl. Instr. Meth. A **499**, 469 (2003).
3. S.S. Adler *et al.*, Phys. Rev. Lett. **96**, 032302 (2006).
4. A. Toia and the PHENIX Collaboration, Nucl. Phys. A **774,** 743 (2006).
5. V. Ryabov and the PHENIX Collaboration, Nucl. Phys. A **774**, 735 (2006).
6. S.S. Adler *et al.*, Phys. Rev. Lett. **96**, 202301 (2006).
7. J. Adams *et al.*, Phys. Rev. Lett. **92**, 092301 (2004).
8. M. Naruki *et al.*, Phys. Rev. Lett. **96**, 092301 (2006).

HERMES EXPERIMENT AT DESY: SELECTED ANALYSIS RESULTS

PNPI participants of the HERMES Collaboration:
S.L. Belostotski, G.E. Gavrilov, A.A. Izotov, A.A. Jgoun, A.Yu. Kisselev, P.V. Kravchenko, S.I. Manaenkov, O.V. Miklukho, Yu.G. Naryshkin, D.O. Veretennikov, V.V. Vikhrov

1. Introduction

The HERMES experiment at DESY studies the spin structure of hadrons. In the experiment, the 27.6 GeV longitudinally polarized positron beam of the HERA *e-p* collider is passed through an open-ended tubular storage cell in which polarized (longitudinally or transversely) or unpolarized target atoms in undiluted gaseous form are continuously injected. An average beam polarization is typically 55%. The beam helicity is reversed every month during the period of data taking. The target polarization is about 90%, being reversed every 90 seconds. The secondary particles are detected with a large acceptance forward spectrometer described in details in paper of K. Ackerstaff *et al.*, Nucl. Instr. Meth. A **417**, 230 (1998). Briefly, the HERMES spectrometer consists of multiple tracking stages before and after a 1.3 T·m dipole magnet. Electrons and positrons are identified by the combination of a lead-glass calorimeter, a scintillation hodoscope preceded by two radiation lengths of lead (the pre-shower detector), and a transition-radiation detector (TRD). A Ring-Imaging Cherenkov detector (RICH) allows separation of pions, kaons and protons. Due to reliable particle identification and relatively large acceptance the HERMES experiment measures not only inclusive reactions in deep-inelastic scattering (DIS), where only the scattered lepton is detected, but also semi-inclusive DIS events (SIDIS), where hadrons are detected in coincidence with the lepton.

The HERMES experiment started data taking in the year 1995. By the end of 2006, 7.5×10^7 inclusive DIS events (with $Q^2 > 1$ GeV^2 where Q^2 is the negative four-momentum transfer squared for virtual photon) were accumulated at the integrated luminosity of 1505 pb^{-1}. Most of the data were collected from the hydrogen and deuterium targets but in order to study nuclear effects the ^{4}He, ^{14}N, ^{20}Ne and ^{84}Kr targets were also used. The polarized target data amount about 1/4 of the whole HERMES data set.

The PNPI is involved in the HERMES since its design phase with a substantial contribution to the hardware and software of the experiment, spectrometer maintenance and data analysis. In this paper selected analysis topics, in which PNPI plays a leading (or significant) role, are presented.

2. Quark helicity distributions from semi-inclusive deep-inelastic scattering

The HERMES experiment has measured double-spin asymmetries in deep-inelastic semi-inclusive scattering (SIDIS) [1] in which both scattered electron and produced hadron are well identified. The double-spin asymmetry is defined as a fractional difference of the cross sections with beam and target helicities anti-parallel and parallel. It is proportional to the sum over flavor q:

$$\sum_q P_h^q(x)\frac{\Delta q(x)}{q(x)}. \qquad (1)$$

Here, the polarized quark density Δq is the difference $q^+ - q^-$ between quark densities with positive and negative helicities with respect to the helicity of the target nucleon (in the infinite momentum frame), the unpolarized quark density is given by $q \equiv q^+ + q^-$, and x is the Bjorken variable. In the lab frame $x = Q^2/2M\nu$, where ν is the photon energy and M is the mass of target nucleon. All quantities in Eq. 1 are averaged over Q^2 and $z = E_h/\nu$, the fractional energy of the detected hadron, where E_h is the energy of the produced hadron h. The ratio $\Delta q/q$ represents polarization of a quark with the flavor q. The purity P_h^q describes the probability that the hadron h originates from interaction of the virtual photon with a quark of flavor q (struck quark). The purities were extracted using Monte Carlo simulations with the spectrometer acceptance taken into account. The CTEQ5L parametrization was used for the unpolarized quark distributions. Figure 1 shows semi-inclusive asymmetries for pions and kaons produced on the deuteron target within a momentum range of $4 < p_h < 13.8$ GeV [2]. The SIDIS asymmetries are measured at $Q^2 > 1$ GeV^2 and $0.2 < z < 0.8$. The lower z

cut suppresses hadrons from the target fragmentation region. Except for negative kaons, all asymmetries are positive and rising with x. Since a negative kaon is a sea-only object $\bar{u}s$, its asymmetry is most sensitive to the sea quark polarizations, and thus, it is expected to be small.

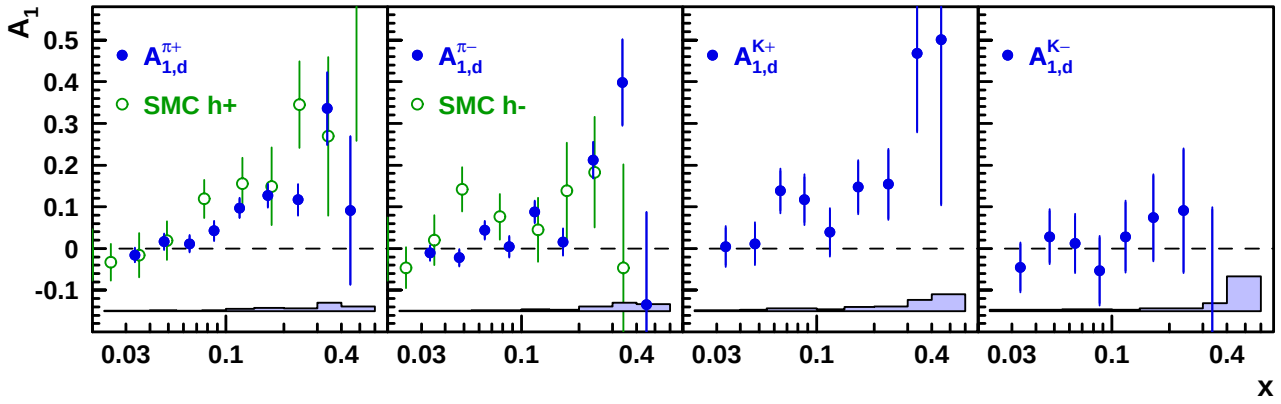

Fig. 1. The HERMES results on semi-inclusive asymmetries on deuterium target for identified charged pions (compared to all charged hadrons from SMC in the x-range of HERMES) and for identified charged kaons. The error bands represent the systematic uncertainties

Figure 2 shows the x-weighted distributions $x\cdot\Delta q(x)$ extracted using purity formalism (Eq. 1). Note that in contrast to the LO QCD fits to inclusive data overlaid in Fig. 2 in the HERMES analysis the only assumption made on the sea flavor polarization is that $\Delta\bar{s}/\bar{s} = 0$. The systematic error bands include systematic uncertainties of the extracted $x\cdot\Delta q(x)$ distributions dominated by the uncertainties in purity calculations.

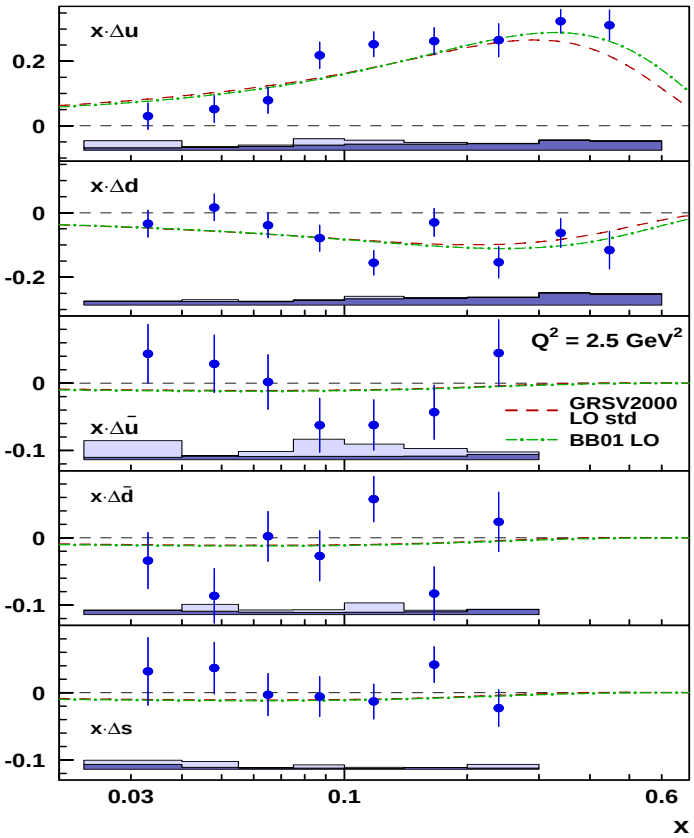

Fig. 2. The quark helicity distributions $x\cdot\Delta q(x,Q^2)$ evaluated at an average value of Q^2 = 2.5 GeV^2 as a function of x. The dashed line is the GRSV2000 parametrization (LO, valence scenario) scaled with $1/(1+R)$, where R is a kinematical factor ranging from 0 to 0.4, and the dashed-dotted line is the Blümlein-Böttcher (BB) parametrization (LO, scenario 1)

Averaged over HERMES kinematics, the quark contributions to the nucleon spin are summarized as follows:

$\Delta u + \Delta\bar{u} = 0.599 \pm 0.022 \pm 0.065$

$\Delta d + \Delta\bar{d} = -0.280 \pm 0.026 \pm 0.065$

$\Delta s = 0.028 \pm 0.033 \pm 0.009$

$\Delta\bar{u} = -0.002 \pm 0.036 \pm 0.023$

$\Delta\bar{d} = -0.054 \pm 0.033 \pm 0.011$

$\Delta\bar{s} \equiv 0$ (*assumed*)

Overall contribution Σ of the quarks dominated by the valence u and d quarks amounts $\Sigma = 0.330 \pm 0.011_{\text{theo}} \pm 0.025_{\text{exp}} \pm 0.028_{\text{evol}}$ [3].

3. Hyperon production at HERMES

Hyperon yields and fragmentation functions. In the HERMES experiment the $\Lambda\left(\bar{\Lambda}\right)$ hyperons are identified through their $p\pi^-(\bar{p}\pi^+)$ decay channel. Heavier than Λ charged hyperons ($\Xi^-, \Sigma^+_{1393}, \Sigma^-_{1388}$) and their antiparticles are identified through their $\Lambda\pi$ decay channels, and Σ^0_{1116} through the $\Lambda\gamma$ decay. The hyperon yields accumulated at the integrated luminosity of 791.4 pb^{-1} are listed in Table.

Table

Yields of hyperons detected at integrated luminosity of 791.4 pb^{-1}

Hyperon	Decay mode, %	Hyperon yield	Antihyperon yield
Λ^0_{1116}	$p\pi^-$ (63.9)	386000	72000
Σ^0_{1193}	$\Lambda^0\gamma$ (100)	19000	5200
Ξ^-_{1321}	$\Lambda^0\pi^-$ (99)	2500	650
Σ^{*+}_{1393}	$\Lambda^0\pi^+$ (88)	5700	820
Σ^{*-}_{1388}	$\Lambda^0\pi^-$ (88)	6300	1200

In the DIS regime the virtual photon γ^* emitted with the energy ν by the charged lepton is absorbed by a quark in the target nucleon ("struck quark"). The struck quark forms a string (or cluster) with the target remnant (Lund fragmentation model). The final hadrons are produced due to hadronization of this string. The multiplicity z distribution describing the number of hadrons h per inclusive DIS event is given by:

$$n_h(z) = \frac{1}{Ne}\frac{dN^h}{dz} = \sum_f \omega_f D_f^h(\overline{Q^2}, z), \qquad (2)$$

where we omit a weak dependence on Q^2 replacing it by its average value. Here ω_f is the fractional contribution of a quark flavor f to the inclusive DIS cross section .The fragmentation function $D_f^h(z)$ reflects the probability that the hadron h is produced due to the fragmentation of a struck quark of flavor f. In the current fragmentation regime interaction with the target remnant can be neglected and one may assume that $D_u^\Lambda = D_d^\Lambda$ due to the isospin symmetry. When extracting D_u^Λ from Eq. 1, it is not specified whether the final Λ hyperon is related to the struck quark (current fragmentation) or it is produced *via* remnant diquark (target fragmentation). At high energy these two mechanisms are usually separated with the help of Feynman variable x_F. At the moderate energy of the HERMES experiment the distinction between the current and target fragmentation domains is not very sharp. Nevertheless, with the requirement $x_F > 0$ imposed the remnant contribution is assumed to be reduced. In order to suppress the target remnant contribution even more, the data were analyzed under the requirement $x_F > 0.3$. Besides, the fractional z variable was redefined as follows: $z \to z^* = (E^\Lambda - M^\Lambda)/\nu$ [4]. The hadron production in DIS is dominated by the $u(d)$ quark, *i.e.* the contribution from the $\bar{u}, \bar{d}$ quarks and from the strange quarks is small ($\omega_u + \omega_d \approx 1$). Due to this fact, the multiplicity distribution and fragmentation function D_u^Λ are very close one to another.

Figure 3 shows the $n^\Lambda(z)$ (or $D_u^\Lambda(z)$) distributions measured by the HERMES together with the results of other experiments [4].

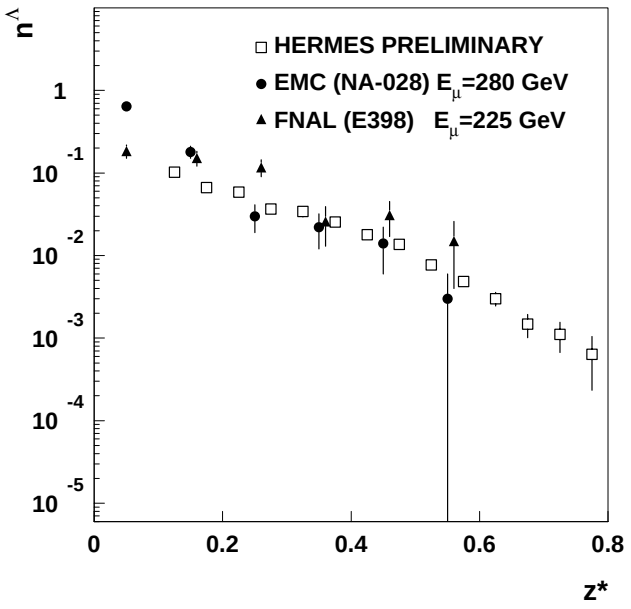

Fig. 3. World data on multiplicity distribution function for Λ hyperons produced in lepton DIS experiments

Longitudinal spin transfer. The longitudinal spin transfer D_{LL} to the Λ hyperon has first been studied by the LEP experiments OPAL and ALEPH at an energy corresponding to the Z_0 pole. In these experiments the hyperons are predominantly produced *via* the strange quark antiquark decay channel in which the primary strange quarks initiating the hadronization process were negatively polarized at the level of 91%. The OPAL and ALEPH (LEP) data show a significant polarization transfer $D_{LL} \approx 0.3$ from the $s(\bar{s})$ quark to the $\Lambda(\bar{\Lambda})$ hyperon at $z > 0.3$, thus confirming that the s quark dominates the spin of the Λ hyperon. In contrast to the LEP experiments, as it has been mentioned above, the production of Λ hyperons in DIS is

originated predominately from the struck u or d quark emitted from the target nucleon, the contribution from the strange quark being small.

The HERMES collaboration has preliminary reported on measurements of the spin transfer D_{LL} to the Λ hyperon in DIS [5, 6]. Here we present the final results based on a semi-inclusive DIS data sample containing about 8000 Λ events [7, 8].

If the longitudinal polarization of the beam is given by P_b and the target is unpolarized, the struck quark will acquire a polarization $P_q = P_b \cdot D(y)$. Here $y = \nu/E_e$ is the fractional energy carried by the photon and $D(y)$ gives the "depolarization" of the virtual photon as compared to the incident electron. The component of polarization transferred along the direction L' from the virtual photon to the produced Λ hyperon is given by $P_{L'} = P_b \cdot D(y) \cdot D_{LL'}$, where L is the primary quantization axis directed along the virtual photon momentum. The spin transfer coefficient $D_{LL'}$ describes the probability that the polarization of the struck quark is transferred to the Λ hyperon along the secondary quantization axis L'. In the final analysis, the quantization axis L' was chosen along the direction of the Λ-hyperon momentum (not affected by the relativistic transformation to the Λ rest frame).

The spin-transfer coefficient extracted from the data with the requirement $x_F > 0$ is found to be $D_{LL'} = 0.11 \pm 0.10_{\text{stat}} \pm 0.03_{\text{syst}}$. The dependence on x_F is presented in Fig. 4 together with those of the NOMAD and COMPASS experiments at CERN and E665 at FNAL.

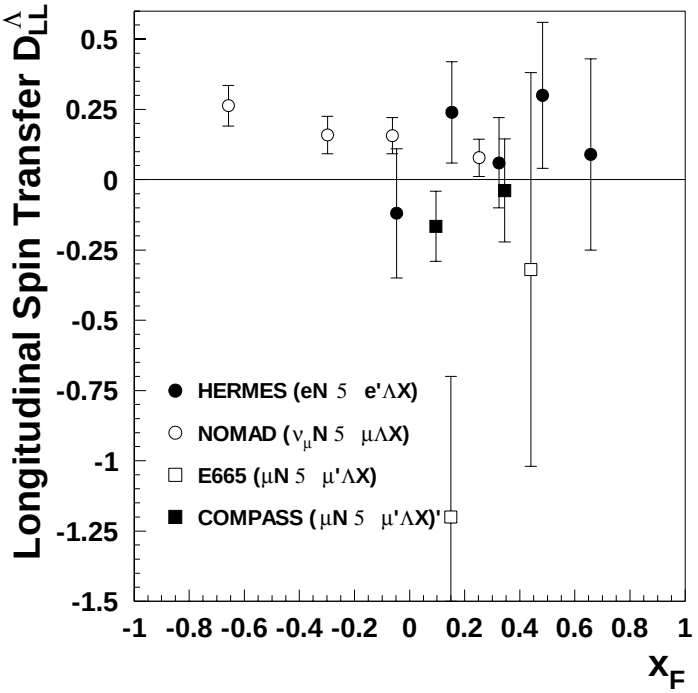

Fig. 4. Longitudinal spin transfer to the Λ hyperon in DIS. Compilation of world data

Most of NOMAD data have been obtained at negative x_F. At $x_F > 0$ NOMAD has measured $D_{LL'} = 0.09 \pm 0.06_{\text{stat}} \pm 0.03_{\text{syst}}$, which is in a very good agreement with the HERMES result averaged in the $x_F > 0$ domain. The average COMPASS number is −0.12 ± 0.10. Therefore, for positive x_F all existing to date experimental results indicate that the $D_{LL'}$ is compatible with zero within the statistical uncertainty of ±0.10. The observation of a small (or equal to zero) value of $D_{LL'}$ points to the dominance of scattering from u or d quarks whose polarization within the Λ hyperons is small. On the other hand, the condition $\Delta q_u^{\Lambda} = \Delta q_d^{\Lambda} \equiv 0$ does not necessarily mean that the $D_{LL'}$ vanishes. In order to produce the Λ hyperon, a polarized struck (current) u quark picks up a ds diquark from the string. If the helicity of the u quark is +,

then the d quark helicity must be –, which fixes the helicity of the s quark depending on the spin state of the ds diquark. If probability to find the singlet diquark is higher than that for the triplet diquark, one would expect predominantly positive helicity for the s quark and for the Λ hyperon and, thus, the positive spin transfer $D_{LL'}$. Further, the fraction of Λ hyperons produced *via* heavier hyperon decays is significant: only about 40% of the Λ hyperons are produced directly from the string fragmentation. The contribution from heavier hyperons Σ^0, Σ^* or Ξ, which may decay into the polarized Λ hyperons and thus modify the $D_{LL'}$, can be taken into account with the help of the Lund-based polarized Monte Carlo simulations.

Transverse Λ and $\bar{\Lambda}$ polarization in photoproduction. The transverse (spontaneous) polarization of Λ particles and other hyperons has been observed in many high-energy scattering experiments, with a wide variety of hadron beams and kinematical settings. While the transverse hyperon polarization has been intensively studied in hadron interactions, very little information exists about this effect in photo- and electroproduction. Here we present first statistically significant experimental results on the Λ-hyperon polarization measured inclusively in the photoproduction regime [9, 10]. Since the scattered positron was not detected, the final data set of the Λ events is dominated by the photo-production kinematics with $Q^2 \approx 0$ and an average photon energy about 16 GeV.

The extraction of the Λ polarization P_n is based on the moment method and up/down symmetry of the HERMES spectrometer using recently developed iteration procedure [10]. The measured polarizations P_n versus P_T, where P_T is the transverse Λ momentum, are shown in Fig. 5 for $\varsigma \approx p_z / p_e < 0.25$ and $\varsigma > 0.25$, respectively. Here p_z is the longitudinal Λ or $\bar{\Lambda}$ momentum and p_e is the beam momentum.

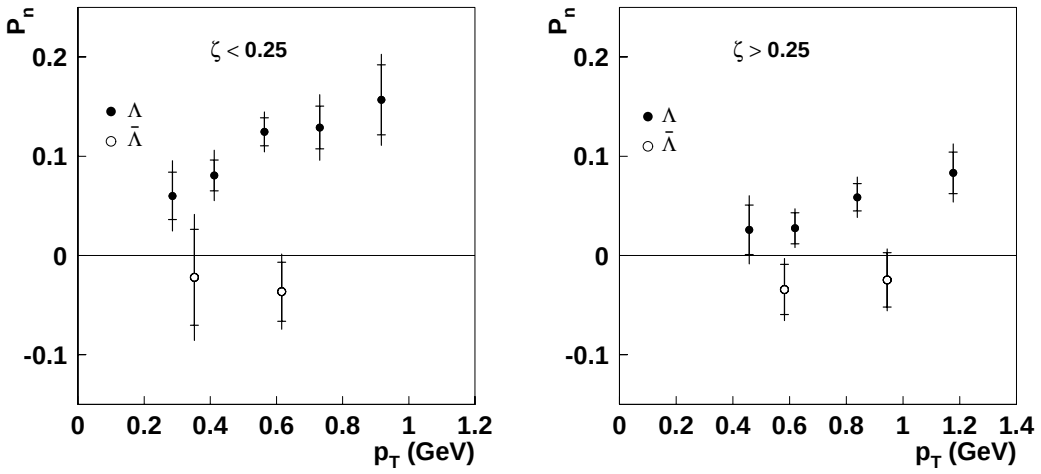

Fig. 5. Transverse polarization of low momentum (left panel) and high momentum (right panel) Λ hyperon

Combining all kinematical points together, the average transverse polarization is found to be $P_n = 0.078 \pm 0.006_{\text{stat}} \pm 0.012_{\text{syst}}$ for the Λ hyperon and $P_n = 0.025 \pm 0.015_{\text{stat}} \pm 0.018_{\text{syst}}$ for the $\bar{\Lambda}$ hyperon. As suggested by the PYTHIA Monte Carlo, the mechanism, when the target diquark picks up a strange quark from the string and fragments into a hyperon, dominates at low Λ momenta ($\varsigma < 0.25$). At higher Λ momenta the contribution from this mechanism is decreasing while the mechanism, when a photon quark, *i.e.* a quark from the photon $q\bar{q}$ dissociation, picks up a diquark from the string, becomes dominating. As follows from the data, the first variant results in higher polarization. This is also confirmed by the fact that the polarization of the $\bar{\Lambda}$ hyperons is found to be compatible with zero.

An overview of hyperon physics at HERMES can be found in Ref. [11].

4. Exclusive diffractive ρ-meson production at HERMES

Exclusive diffractive ρ-meson production in deep-inelastic lepton-nucleon scattering provides the unique information both on the structure of involved hadrons and the reaction mechanism. The spin density matrix of the "heavy" photon is well known from quantum electrodynamics, and the spin density matrix of produced vector mesons can be experimentally reconstructed by measuring the angular distributions of pions in the self-analyzing $\rho^0 \to \pi^+ + \pi^-$ decay. This allows, in principle, to extract the helicity amplitudes $T_{\lambda_V \lambda_\gamma}$ of the process $\gamma^* + N \to \rho + N'$ in the $\gamma^* N$ rest frame. Here λ_γ and λ_V are helicities of the virtual photon γ^* and the vector meson, respectively, and represents the target (recoil) nucleon. At high energies, a mechanism, in which the created vector meson (pre-hadron) interacts with the target nucleon through the two gluon exchange (Pomeron exchange), dominates. In the HERMES kinematics with moderate Q^2 the reaction mechanism is more complicated. In addition to the two gluon exchange, the quark exchange (or equivalent subleading reggeon exchange [12]) plays a significant role and the helicity amplitudes should be calculated with both gluon and quark exchanges taken into account.

The spin density matrix of the vector meson is usually decomposed into a standard set of matrices r^α and the results are presented as spin density matrix elements $r^\alpha_{\lambda_V \lambda'_V}$ (SDMEs). The matrix elements $r^\alpha_{\lambda_V \lambda'_V}$ are expressed through bi-linear combinations of the helicity amplitudes $T_{\lambda_V \lambda_\gamma}$. As it was established experimentally, the dominant contributions to SDMEs come from the diagonal transitions $\lambda_\gamma = \lambda_V$ (*S*-channel helicity conservation, SCHC), *i.e.* the only nonzero helicity amplitudes in this case are T_{11}, T_{00} and T_{-1-1}. If SCHC is valid, the $r^{04}_{00}, r^1_{1-1} = -\mathrm{Im}\{r^2_{1-1}\}, \mathrm{Re}\{r^5_{10}\} = -\mathrm{Im}\{r^6_{10}\}$ are nonzero of 15 SDMEs measured in experiments with the unpolarized lepton beam ("unpolarized" SDMEs), and two matrix elements ($\mathrm{Re}\{r^8_{10}\} = \mathrm{Im}\{r^7_{10}\}$) are nonzero of 8 "polarized" SDMEs related to experiments with the longitudinally polarized beam.

The spin-flip amplitudes T_{01} and T_{10} are small at low momentum transfer to the nucleon *t* and $|T_{01}| > |T_{10}|$ at high Q^2. These amplitudes vanish if quark Fermi motion in the ρ meson is neglected. The double spin-flip amplitude T_{1-1} gives information on soft gluon contribution to the gluon density in the target. Therefore investigation of these small amplitudes and hence SDMEs, which are zero in SCHC approximation, is of particular interest. *S*-channel helicity violation (SCHV) was experimentally observed for the first time at HERA collider experiments where r^5_{00} ($\sim \mathrm{Re}\, T_{01} T^*_{00}$) was found to be nonzero. The HERMES experiment measured more nonzero SCHV matrix elements due to high statistical accuracy of the data and due also to that for the HERMES kinematics with moderate Q^2 $|T_{00}| \sim |T_{\pm 1 \pm 1}|$, while at collider experiments $|T_{00}| >> |T_{\pm 1 \pm 1}|$, thus giving access only to those SCHV matrix elements which contain the product $T_{01} T^*_{00}$.

The HERMES experiment has measured for the first time all 23 SDMEs including 8 polarized ones. The SDMEs measured under the following kinematical conditions: $1 < Q^2 < 5$ GeV^2 and $-t < 0.4$ GeV^2 for mean $\gamma^* N$ center-of-mass energy $W = 5$ GeV are depicted in Fig. 6 [13], where both results obtained from the hydrogen and deuterium targets are presented. The vertical line is broken for those SDMEs which are nonzero in the SCHC approximation. The SCHV matrix elements which deviate significantly (> 2σ effect) from zero are shown with enlarged points. As follows from Fig. 6, the SCHV is well established at HERMES kinematics. There is no noticeable difference between SDMEs of ρ-meson production on the proton and deuteron. This means that the contribution from isovector $q\bar{q}$ exchanges with natural parity is not important. The HERMES measured for the first time the signal of unnatural parity exchange (UPE) which is very likely pion exchange. The combination of SDMEs $U_1 = 1 - r^{04}_{00} + 2r^{04}_{1-1} - 2r^1_{11} - 2r^1_{1-1}$ is zero if UPE is absent.

Having combined the HERMES results for the proton (U_1 = 0.132 ± 0.026$_{stat}$ ± 0.043$_{syst}$) and for the deuteron (U_1 = 0.094 ± 0.020$_{stat}$ ± 0.041$_{syst}$), one may state that the UPE signal is seen on the 3σ level.

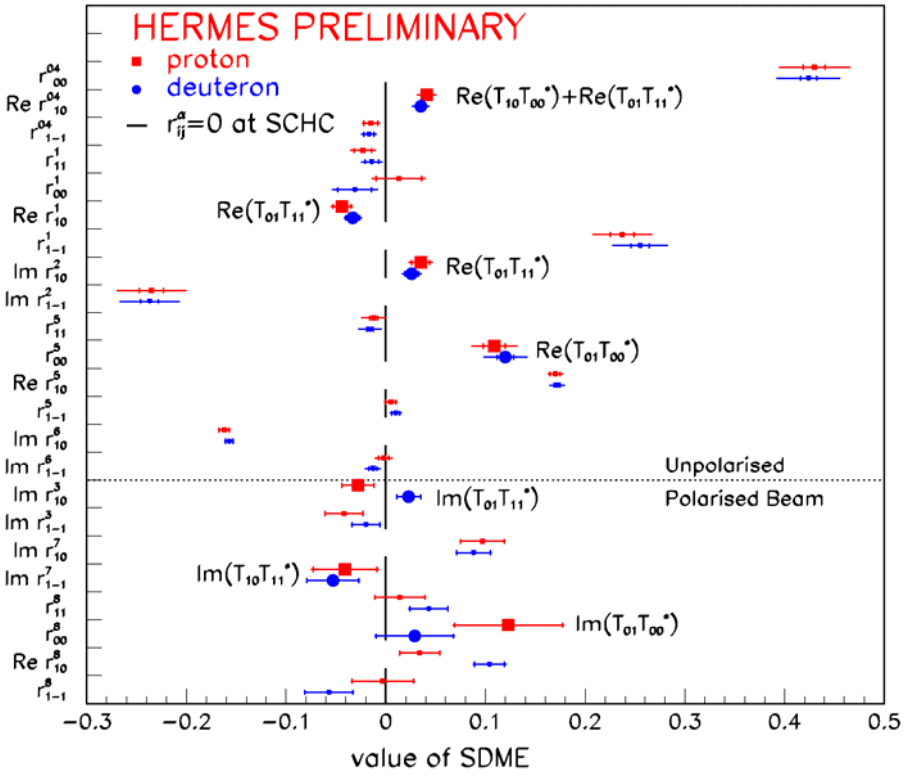

Fig. 6. The SDMEs measured under the following kinematical conditions: $1 < Q^2 < 5$ GeV^2 and $-t < 0.4$ GeV^2 for mean $\gamma^* N$ center-of-mass energy $W = 5$ GeV. Each vertical division corresponds to one SDME

5. Mean hadron transverse momenta and quark transverse motion

In terms of the Quark-Parton Model (QPM) the mean value of the squared transverse momentum of a hadron produced in DIS on a nucleon can be written as

$$\left\langle P_\perp^2 \right\rangle \cong z^2 \cdot \left\langle q_\perp^2 \right\rangle + \left\langle k_\perp^2 \right\rangle + \left\langle p_\perp^2 \right\rangle^{QCD} + \left\langle p_\perp^2 \right\rangle^{soft},$$

where $q_\perp$ is the transverse momentum of a quark in the nucleon, $k_\perp$ is the transverse momentum related to the fragmentation process, $\left\langle p_\perp^2 \right\rangle^{QCD}$ is the contribution from hard QCD processes and $\left\langle p_\perp^2 \right\rangle^{soft}$ is the contribution from soft gluon emission.

Most of existing to date experimental studies report on much higher values of the $\left\langle P_\perp \right\rangle$ for high z region in comparison with any conservative theoretical estimates. This might be an indication of either a large quark transverse momentum ($\left\langle q_\perp^2 \right\rangle \approx 0.65\,\text{GeV}^2$) or presence of a significant soft gluon emission term $\left\langle p_\perp^2 \right\rangle^{soft}$, the quark transverse momentum $\left\langle q_\perp^2 \right\rangle$ being in latter case at a reasonable level of $0.1-0.2$ GeV. Unfortunately, because of lack of statistical accuracy, available experimental data cannot unambiguously point out at a unique relevant scenario. Thus, the question of transverse quark motion in the nucleon is still open.

The HERMES experiment has measured hadron transverse momentum distributions with unprecedented statistical accuracy using hydrogen, deuterium and, also, heavy gaseous target (^{3,4}He, ^{14}N, ^{20}Ne, ^{84}Kr and ^{132}Xe) [14]. The HERMES data are corrected for the acceptance effect, the radiation of soft photons and the contribution from $\rho^0 \to \pi^+ + \pi^-$ decay. In Fig. 7, left panel, the hadron transverse momentum versus z is

shown for positive and negative hadrons, and also for K_S^0 meson. The data presented in Fig. 7 were accumulated on the hydrogen target in 1996-1997 years, being a fraction of the presently existing data sample still to be analyzed. As one can see, for $z < 0.6$ the z-dependence of $\langle P_\perp \rangle$ is universal, while for $z > 0.6$ the $\langle P_\perp \rangle$ depends strongly on the charge (type) of the hadron. As hard and soft gluon emission is independent on the quark charge, the difference between positive and negative hadrons can originate either from the different patterns of the fragmentation or from the different internal transverse momentum distributions of the u and d quarks. The fragmentation process for a positive hadron (*e.g.* pion) is straightforward: the struck u quark picks up a sea quark from the string. In contrast, the negative hadron fragmentation cannot be done in one step. For example, as the pion is $d\bar{u}$ object, it cannot be directly produced by the struck u quark. This would result in larger $k_\perp$ and, respectively, in larger $\langle P_\perp \rangle$. The experiment, however, shows the opposite trend. Then one has to assume that the average primordial momentum $q_\perp$ for the u quark in the proton is indeed much larger than that for the d quark which would explain the experimental result. As for the K_S^0 data, the very large $\langle P_\perp \rangle$ in the region of z around 0.7 might be explained by the necessity to pick up the heavy s quark and a multi-step fragmentation process. Following to the assumption of a large difference in the internal u and d quark distributions, one would expect that the ratio of $\langle P_\perp \rangle$ for the hydrogen target to that for the deuterium target ($\langle P_\perp^H \rangle / \langle P_\perp^D \rangle$) must be larger than unity for the positive hadrons and smaller than unity for the negative hadrons. This is confirmed by Fig. 7, right panel.

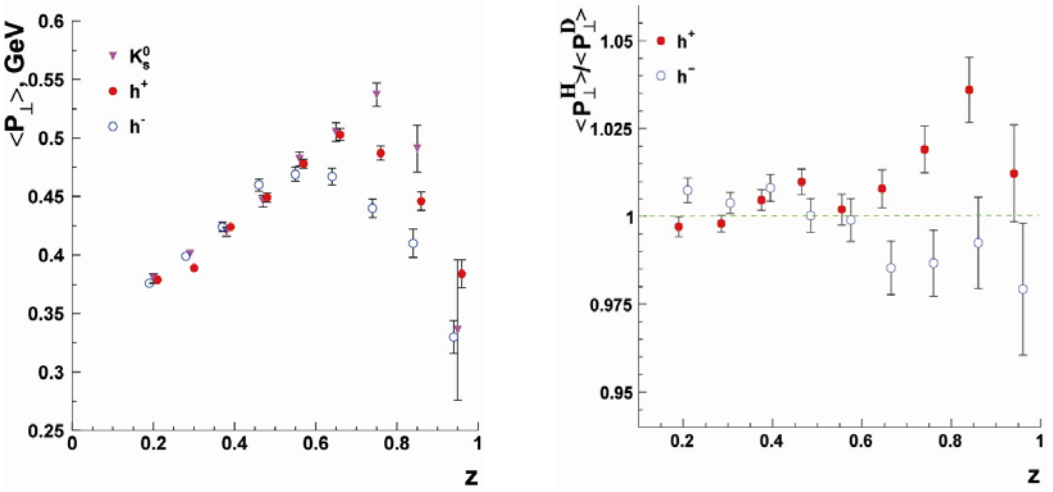

Fig. 7. Dependence of mean transverse momentum of the K_S^0 mesons, positive charged hadrons and negative charged hadrons on z (left panel). Ratio of the mean hadron transverse momentum from DIS on hydrogen target to that on deuterium target (right panel)

Results of investigations of the heavy gaseous target are presented in Fig. 8 where the ratio $Y_h^A = \langle P_h^A \rangle / \langle P_h^D \rangle$ is shown versus the hadron momentum p. Surprisingly, this ratio is going below unity at large hadron momenta for all investigated nucleus. The curves shown in Fig. 8 are obtained by fit to the data performed taking into account that the formation length at the high hadron momenta (~15 GeV) is larger than the nuclear radius and, thus, the nucleus is transparent for propagation of the pre-hadron state. Under this assumption it has been obtained $\langle q_\perp \rangle^A / \langle q_\perp \rangle^D = 0.95 \pm 0.02$ which may be explained by the hypothesis that the size of the nucleon in a nucleus is somewhat larger than that in loosely bound deuteron ("swelled" nucleons). This gives more space freedom for the transverse quark motion in a nucleus which makes more compact the internal quark transverse momentum distribution.

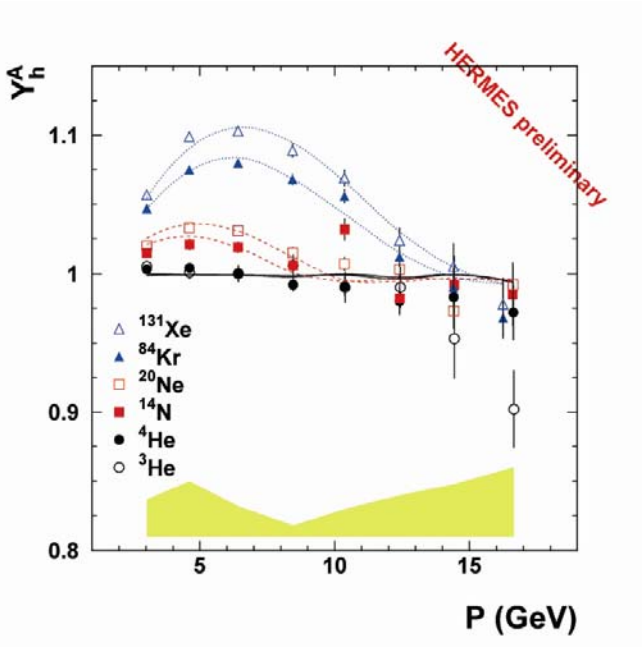

Fig. 8. Ratio of mean transverse momentum of the charged hadrons produced from a nuclear target to that from the deuterium target

Acknowledgements

We gratefully acknowledge our colleagues from the HERMES collaboration for their valuable contribution to this field. This work was supported by the Russian Academy of Science and the Russian Federal Agency for Science and Innovations.

References

1. A. Airapetian *et al.* (the HERMES Collaboration), Phys. Rev. D **71**, 012003 (2005).
2. P.V. Kravchenko, in *Proceedings.of the Workshop "Symmetries and Spin"* (Prague, Czech Republic, 27 July – 3 August 2005), Czech. J. Phys. **56**, Suppl. C, 317 (2006).
3. A. Airapetian *et al.* (the HERMES collaboration), Phys. Rev. D **75**, 012007 (2007).
4. S. Belostotsky, O. Grebenyuk and Yu. Naryshkin, in *Proceedings of the 10th International Workshop on Deep Inelastic Scattering* (Cracow, Poland, 30 April – 4 May 2002), Acta Phys. Polon. B **33**, 3785 (2002)
5. A. Airapetian *et al*. (the HERMES Collaboration), Phys. Rev. D **64**, 112005 (2001).
6. S.L. Belostotsky, in *Proceedings of the 9th Workshop on High Energy Spin Physics* (*Dubna-SPIN-2001*), JINR E1,2-2002-103,192 (2002).
7. A. Airapetian *et al.* (the HERMES Collaboration), Phys. Rev. D **74**, 072004 (2006).
8. Yu. Naryhskin, Nucl. Phys. B (Proc. Suppl.) **167**, 62 (2007).
9. S. Belostotsky, in *Proceeding of the 16th International Spin Physics Symposium SPIN-2004* (Trieste, Italy, 6 – 10 October 2004), World Scientific Publishing Co., Trieste/Mainz, 2005, p. 400.
10. A. Airapetian *et al.* (the HERMES Collaboration), Preprint DESY-HERMES-07-036; submitted to Phys. Rev. D.
11. S. Belostotski, lecture prepared for *the 58th Scottish Universities Summer School in Physics (SUSSP58)*, Preprint DESY-HERMES-06-57, 30 p.
12. S.I. Manayenkov, Eur. Phys. J. C **33**, 397 (2004).
13. S.I. Manayenkov for the HERMES Collaboration, talk at *the 13th International Conference QCD06*, (Montpellier, France, 3 – 7 July 2006); A. Airapetian *et al.*, to be published in Eur. Phys. J.
14. A. Jgoun on behalf of the HERMES Collaboration, talk at *the 36th Rencontrence de Moriond on QCD and High Energy Hadronic Interactions* (Moriond, France, 17 – 24 March 2001), hep-ex/0107003.

RESULTS OF ELECTROWEEK INTERACTION FROM LEP-II EXPERIMENT AT CERN

V.A. Schegelsky

1. Introduction

Experiments with the Large Electron-Positron Collider at CERN have been started in 1989. Four large detectors have been constructed at LEP: ALEPH, DELPHI, L3, and OPAL. The simultaneous operation of all these detectors provided powerful cross checks of the obtained results that made them highly reliable. PNPI took an active part in construction and operation of the L3 detector. In the first period of 1989 – 1995, LEP operated at the center-of mass energy of m_z (LEP-I phase). The main motivation was investigations of electroweak (EW) processes and verification of the validity of the most complete theory – the Standard Model (SM). The first target was the intermediate neutral vector boson, already experimentally discovered, Z boson. In the six years period several millions of Z's was produced, its mass and widths (total and partial), branching ratios into all possible final states were measured. The SM parameters were determined with high accuracy. There was no evidence of deviations from the SM predictions. Some free parameters of the theory were estimated. The number of leptons families was established to be equal to three, the same as the number of quarks families in the strong interaction sector of the SM. The high precision reached provided a possibility to constrain the mass of not yet discovered top quark from the calculations of the loop correction to the bare Z-boson mass using in the calculations the value of the charged vector boson mass m_w, already observed in the experiments on hadron colliders. The correction is rather strongly, quadratically, depends on the quark mass, but there are also contributions from the scalar bosons. To explain the mass splitting of the EW intermediate bosons – photon, Z and W – there should be at least one scalar Higgs boson (H), which also enters into the loop calculations. It was not found any scalar boson in the experiments, *i.e.* the mass of the boson is high ($m_H > 58$ GeV), moreover the loops correction from this source is only weakly (logarithmically) dependent on the Higgs boson mass. For this reason, the prediction of the mass of top quark was rather accurate ($m_t = 197^{+30}_{-16}$ GeV). Such low limit gave a chance to observe the top quark production on the proton-antiproton collider at Fermilab[1,2]. After several years of very difficult studies the top quark was discovered by Fermilab experiments, confirming once more the high predictive power of the SM. The main results of the L3 experiments during LEP-I operation have been already presented in the previous reports [1, 2].

Already at the early stage of the LEP project, it was decided to rise up the beam energy to 100 GeV (LEP-II). At this energy the EW cross section of production of the W pairs is rising first and then is flattened out. Copious W production studies make possible to determine the parameters of the W boson with higher accuracy, making the theoretical constraints much tougher, in particular predicting the range of the Higgs boson mass.

The data taking on LEP-II was terminated in 2000 but sophisticated analysis is still under way. For example, during last 5 years the L3 collaboration has published more than 30 papers with the final results. At the same time, all four LEP experiments – ALEPH, DELPHI, L3, and OPAL – in the frame of the LEP Working groups (WG) – carried out combined studies of different topics of the SM, with consideration of all available data including the relevant Fermilab results. Some of the WG reports are already published or presented during international conferences. In this report, the most spectacular results from the LEP-II experiments on the SM verifications will be reviewed [3].

[1] F. Abo *et al.* (CDF Collaboration), Phys. Rev. Lett. **79**, 4327 (1997).
[2] B. Abbott *et al.* (D0 Collaboration), Phys. Rev. Lett. **80**, 2051 (1998).

2. e^+e^--annihilation into two photons or two fermions

During 1996-2000 LEP was running at the center-of-mass energies above the Z pole 130–209 GeV (LEP-II), and the total luminosity per experiment of 700 pb^{-1} has been collected.

The reaction $e^+e^- \to \gamma\gamma(\gamma)$ provides a clean test of the theory (QED) up to the highest energy available, and it can be a good tool for search of non-standard physics signals. The total cross sections measured were found to be in a good agreement with the QED. Table 1 shows the results.

Table 1

Cross section ratios $\sigma_{meas}/\sigma_{QED}$ of the process $e^+e^- \to \gamma\gamma(\gamma)$ from the LEP experiments

Experiment	cross-section ratio
ALEPH	0.953±0.024
DELPHI	0.976±0.032
L3	0.978±0.018
OPAL	0.999±0.016
global	0.982±0.010

The differential cross sections are also in good agreement with QED (Fig. 1).

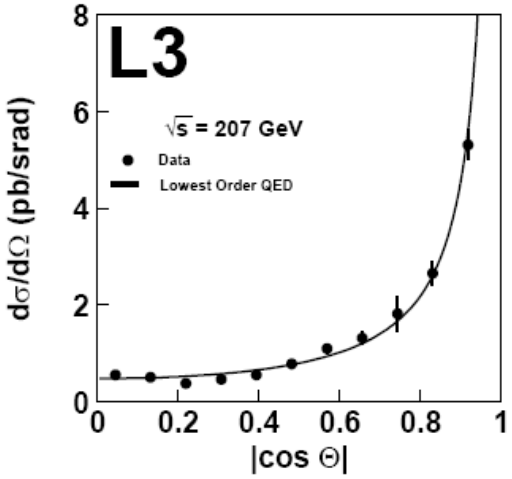

Fig. 1. An example for photon angular distribution of the process $e^+e^- \to \gamma\gamma(\gamma)$, total energy 207 GeV

The modification of the QED model for two photon annihilation is a short-range exponential deviation from the Coulomb field with the cut-off parameters $\Lambda_{\pm}$:

$$\left(\frac{d\sigma}{d\Omega}\right)_{\Lambda_\pm} = \left(\frac{d\sigma}{d\Omega}\right)_{\text{Born}} \pm \frac{\alpha^2 \pi s}{\Lambda_\pm^4}(1+\cos^2\theta)\,.$$

The combined fit of the four LEP experiments provides limits for these parameters $\Lambda_+ > 392$ GeV and $\Lambda_- > 364$ GeV.

The process of two fermions production is interesting in particular for a search of new objects, outside of the SM: an additional heavy vector boson Z', leptoquark, influence of the extra dimensions. Different models of the new physics have different sensitivity to such objects**.** The lower limit of Z' mass is 340–1800 GeV, depending on the model; the leptoquark mass should be higher than 100–1000 GeV for different quark type. Limit on the scale of gravity in models with large extra dimensions is higher than 1 TeV.

3. *W*-boson production and its properties

LEP-II operated above the *W*-pair production threshold. The *W*-pair cross sections and the *W*-decay branching ratios have been measured in the whole energy range of LEP-II. Figure 2 shows the comparison of the SM prediction with the experimental data with the *W*-mass fixed at 80.35 GeV.
There is good agreement: $\sigma^{meas}/\sigma^{theo} = 0.995 \pm 0.009$.

Close to the threshold, the cross section is sensitive to the W boson mass. Such estimates are summarized in Table 2. At higher energies, the cross section has little sensitivity to m_W. For these energies, the direct reconstruction of the *W* boson invariant mass was done from the observed jets and leptons. At the same time the *W* width was also estimated. Tables 3 and 4 show the results.

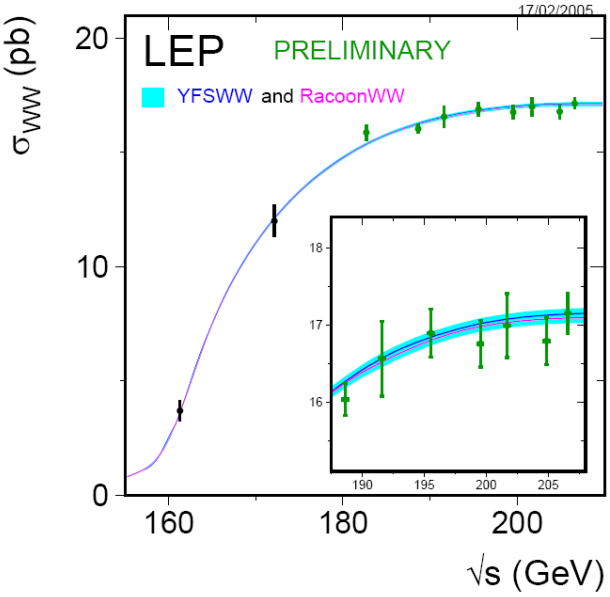

Fig. 2. Measurement of the *W*-pair production cross section compared with the SM prediction

Table 2

The *W* mass measurement from *W*-pair threshold cross section

Experiment	m_W(threshold)/GeV
ALEPH	80.14 ± 0.35
DELPHI	80.40 ± 0.45
L3	$80.80^{+0.48}_{-0.42}$
OPAL	$80.40^{+0.46}_{-0.43}$

Table 3

The *W* mass measurements from direct reconstruction

	DIRECT RECONSTRUCTION		
	$W^+W^- \to q\bar{q}\ell\bar{\nu}_\ell$	$W^+W^- \to q\bar{q}q\bar{q}$	Combined
Experiment	m_W/GeV	m_W/GeV	m_W/GeV
ALEPH	80.429 ± 0.059	80.475 ± 0.082	80.444 ± 0.051
DELPHI	80.340 ± 0.076	80.310 ± 0.102	80.330 ± 0.064
L3	80.213 ± 0.071	80.323 ± 0.091	80.253 ± 0.058
OPAL	80.449 ± 0.062	80.353 ± 0.081	80.415 ± 0.052

Table 4

The W width estimations

Experiment	Γ_W (GeV)	Γ_W (GeV)
	published	common
ALEPH	2.14 ± 0.11	2.14 ± 0.11
DELPHI	2.40 ± 0.17	2.39 ± 0.17
L3	2.18 ± 0.14	2.24 ± 0.15
OPAL	2.00 ± 0.14	2.00 ± 0.14

The 'published' column is taken from the individual publications. In the last column, final state interaction correction common for all experiment was applied.

The combined LEP results for m_W and Γ_W are :

$$m_W = 80.376 \pm 0.033 \text{ GeV},$$
$$\Gamma_W = 2.196 \pm 0.083 \text{ GeV}.$$

The branching ratios measured are presented in Table 5. As one can see, the probability of the W decay into τ lepton is more than 2 standard deviations above the SM prediction (10.83%) for all **four** LEP experiments. However, the averaged leptonic branching ratio $\boldsymbol{BR(W \rightarrow \text{leptons}) = (10.84 \pm 0.08)\%}$ in a good agreement with the SM value.

Within the SM, the W branching fractions are determined by 6 matrix elements $|V_{qq'}|$ of the Cabibbo-Kabayashi-Maskava (CKM) quark mixing matrix. Using the strong coupling constant $\boldsymbol{\alpha_s(M_W) = 0.119 \pm 0.002}$ and the sum $\boldsymbol{|V_{ud}|+|V_{us}|+|V_{ub}|+|V_{cd}|+|V_{cb}| = 1.0476 \pm 0.0074}$ one can get an estimate of $\boldsymbol{|V_{cs}| = 0.976 \pm 0.014}$, where the dominant contribution into the error is statistical.

Table 5

Summary of W branching fractions

	Lepton non–universality			Lepton universality
Experiment	$\mathcal{B}(W \rightarrow e\overline{\nu}_e)$ [%]	$\mathcal{B}(W \rightarrow \mu\overline{\nu}_\mu)$ [%]	$\mathcal{B}(W \rightarrow \tau\overline{\nu}_\tau)$ [%]	$\mathcal{B}(W \rightarrow \text{hadrons})$ [%]
ALEPH	$10.78 \pm 0.29^*$	$10.87 \pm 0.26^*$	$11.25 \pm 0.38^*$	$67.13 \pm 0.40^*$
DELPHI	$10.55 \pm 0.34^*$	$10.65 \pm 0.27^*$	$11.46 \pm 0.43^*$	$67.45 \pm 0.48^*$
L3	$10.78 \pm 0.32^*$	$10.03 \pm 0.31^*$	$11.89 \pm 0.45^*$	$67.50 \pm 0.52^*$
OPAL	10.40 ± 0.35	10.61 ± 0.35	11.18 ± 0.48	67.91 ± 0.61
LEP	10.65 ± 0.17	10.59 ± 0.15	11.44 ± 0.22	67.48 ± 0.28
χ^2/d.o.f.	6.3/9			15.4/11

In addition to the total W^+W^- cross section, the differential cross sections were also measured (Fig. 3). The data are described rather well by the SM predictions.

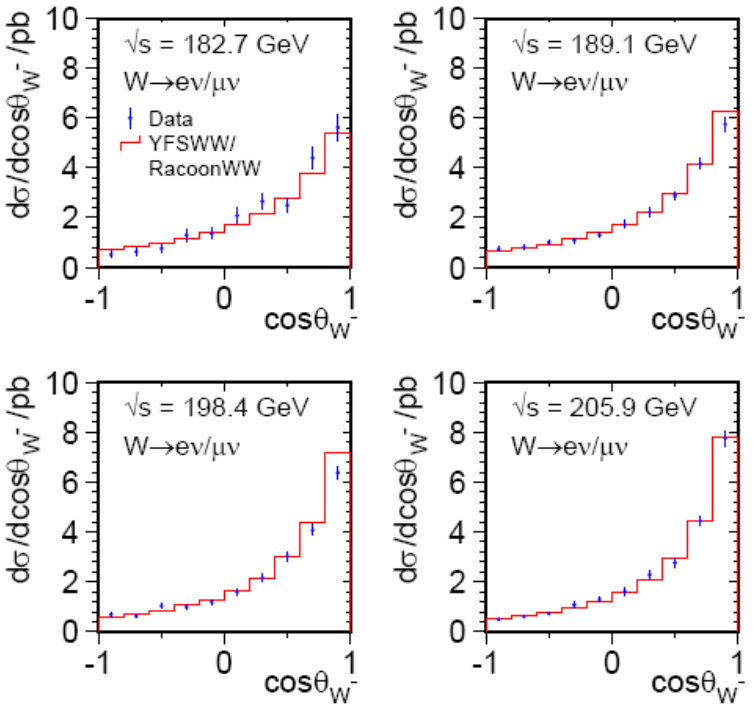

Fig. 3. Differential cross sections for the W-pair production. 4 different energy regions are selected. OPAL,DELPHI and L3 results are combined and compared with the SM predictions

4. Triple gauge boson coupling and search for anomalous vertices

The measurement of gauge boson couplings and the search for possible anomalous contributions are among the main goals of LEP-II. The *W*-pair production process involves charged triple gauge boson vertices – W^+W^-Z and $W^+W^-\gamma$. Single *W* and single photon production is also sensitive to these couplings. The most general description of the triple gauge coupling (TGC) includes 14 complex constants. The electromagnetic gauge invariance and *C* and *P* conservation decrease this number to five: g_1^Z, κ_Z, κ_γ, λ_Z, λ_γ. In the SM $g_1^Z = \kappa_Z = \kappa_\gamma = 1$, $\lambda_Z = \lambda_\gamma = 0$. In the LEP analysis, 3 real parameters g_1^Z, κ_γ, λ_γ are used. Moreover, only one- and two-parameter fits are done (Tables 6 and 7). No deviations from the SM predictions are found.

Similar analysis has been done for reactions with production of $Z\gamma$ and *Z*-pair. In these cases, neutral gauge vertices do not occur in the SM. Within SM quadric gauge boson vertices exist, but effects of such couplings are below experiments sensitivities.

Anomalous vertices search has been performed with the negative results.

Table 6

Results of one parameter fit for charged triple gauge boson couplings

Parameter	ALEPH	DELPHI	L3	OPAL
g_1^Z	$1.026^{+0.034}_{-0.033}$	$1.002^{+0.038}_{-0.040}$	$0.928^{+0.042}_{-0.041}$	$0.985^{+0.035}_{-0.034}$
κ_γ	$1.022^{+0.073}_{-0.072}$	$0.955^{+0.090}_{-0.086}$	$0.922^{+0.071}_{-0.069}$	$0.929^{+0.085}_{-0.081}$
λ_γ	$0.012^{+0.033}_{-0.032}$	$0.014^{+0.044}_{-0.042}$	$-0.058^{+0.047}_{-0.044}$	$-0.063^{+0.036}_{-0.036}$

Table 7

Results of two parameters fit for charged triple gauge boson couplings

Parameter	68% C.L.	95% C.L.	Correlations	
g_1^Z	$1.004^{+0.024}_{-0.025}$	[+0.954, +1.050]	1.00	+0.11
κ_γ	$0.984^{+0.049}_{-0.049}$	[+0.894, +1.084]	+0.11	1.00
g_1^Z	$1.024^{+0.029}_{-0.029}$	[+0.966, +1.081]	1.00	-0.40
λ_γ	$-0.036^{+0.029}_{-0.029}$	[−0.093, +0.022]	-0.40	1.00
κ_γ	$1.026^{+0.048}_{-0.051}$	[+0.928, +1.127]	1.00	+0.21
λ_γ	$-0.024^{+0.025}_{-0.021}$	[−0.068, +0.023]	+0.21	1.00

5. Constraints of the Standard Model

The precise measurements performed at LEP-I and LEP-II together with results from other colliders (SLC and Tevatron) allow to check the SM and to make some predictions for the mass of the Higgs boson m_H. Figure 4 illustrates the results of the combined analysis.

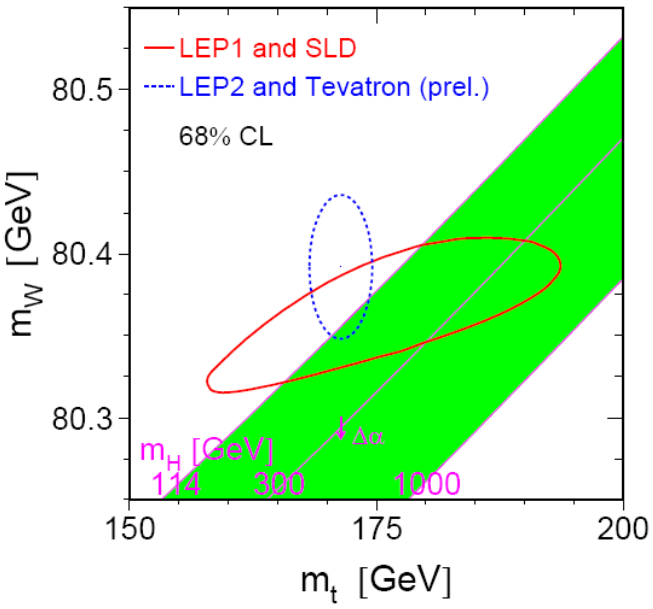

Fig. 4. The comparison of indirect measurements of m_W and m_t (LEP-I and SLD) and direct mass reconstruction (LEP-II and Tevatron). Correlation of these quantities with the SM Higgs boson mass is also shown. The arrow indicates the change of the correlation if $\alpha(m_Z)$ is changed by one standard deviation.

References

1. A.A. Vorobyov, A.G. Krivshich and V.A. Schegelsky, in *PNPI-XXV, High Energy Physics Division. Main Scientific Activities 1971–1996*, Gatchina, 1998, p. 65.
2. V.A. Andreev *et al.*, in *PNPI-XXX, High Energy Physics Division. Main Scientific Activities 1997–2001*, Gatchina, 2002, p. 82.
3. The LEP Electroweak Working Group, hep-ex/0612034, 14 December 2006.

QUARCONIUM PHOTOPRODUCTION IN ULTRAPERIPHERAL ION COLLISIONS WITH THE ALICE DETECTOR AT LHC

V.N. Nikulin, V.M. Samsonov, M.B. Zhalov

We analyze possibility to study the small Bjorken variable x behavior of nuclear gluon density and other features of small x QCD dynamics measuring the cross section of photoproduction of heavy quarkonia in the ultraperipheral ion collisions with the ALICE detector at LHC.

At high energies the theory of strong interactions, Quantum Chromodynamics (QCD), enters a new regime characterized by strong coherent gluon fields. The QCD cross sections are driven by gluons in the hadron wave functions carrying the very small fraction x of the hadron longitudinal momentum. It was discovered at HERA that the density of soft gluons rapidly grows with a decrease of x down to a value of about 10^{-4} at fixed momentum transfer Q^2 and with an increase of Q^2 at fixed x. The HERA data are obtained in the $x - Q^2$ domain where the evolution of the parton distributions can be still described within perturbative QCD (pQCD) by DGLAP (Dokshitzer-Gribov-Lipatov-Altarelly-Parisi) and by Leading Order (Balitsky-Fadin-Kuraev-Lipatov) + Next-to-Leading Order (Ciafalloni *et al.*) BFKL evolution equations. In nucleus-nucleus collisions at energies around $3A$ TeV the essential value of x can be, at least, by one order smaller than those at the HERA energies. The behavior of the gluon density in this region of x is still not well understood theoretically and is not studied, in particular for nuclear target, experimentally. Asymptotically ($x \to 0$) the growth of gluon density is limited by the unitarity of the S matrix but already at LHC one can expect revealing of strong gluon shadowing, parton recombination and gradual onset of the gluon density saturation which could be responsible for the probability conservation within the regime of strong gluon fields. Understanding of these phenomena is very important for successful realization of the high energy nuclear physics program with ALICE detector at the LHC focused on creation and characterization of new extreme forms of a quark-gluon matter where the chiral symmetry is restored and color is not confined within hadrons.

Our goal is to demonstrate that the detector ALICE can be used without significant modifications to study the photoproduction of heavy quarkonia in the ultraperipheral ion collisions and, hence, to investigate the small x QCD dynamics of high energy interactions. The ultrarelativistic heavy ions produce a significant flux of quasireal photons. The photon wave function contains the hadron components (vector dominance) as well as the direct quark-antiquark components with sizes which are controlled by the quark mass, $r \propto m_q^{-1}$. Hence, the coherent photoproduction of heavy flavor vector mesons by quasireal photons off nuclei provides unique opportunities. Selecting a particular final state which contains, for example, $c\bar{c}$ or $b\bar{b}$ pairs, one can *postselect* a small size initial state thus justifying analysis of the process within the framework of perturbative QCD. The QCD factorization theorem for the hard exclusive coherent heavy flavor vector meson (V) photoproduction off particular target (T) implies that the cross section is proportional to the square of the corresponding gluon density $G_T(x, Q^2)$:

$$\sigma_{\gamma T \to VT}(s_{\gamma T}) \propto \left| x G_T(x, M_V^2/4) \right|^2, \tag{1}$$

where $x = \frac{M_V^2}{s_{\gamma T}}$. Our analysis of the ALICE capability to study the coherent photoinduced processes in ultrarelativistic peripheral AA collisions at LHC is based on the predictions of Refs. [1-3] where the cross section was calculated using the Weizsacker-Williams approximation:

$$\frac{d\sigma(AA \to VAA)}{dy} = N_\gamma(y)\sigma_{\gamma A \to VA}(y) + N_\gamma(-y)\sigma_{\gamma A \to VA}(-y). \tag{2}$$

Here $y = \ln(\frac{1}{x}\frac{M_V}{2\gamma_L m_N})$ is the rapidity, γ_L is the Lorentz factor and $N_\gamma(y)$ is the flux of the equivalent photons emitted by nucleus which can be calculated with a reasonable accuracy. The cross section

of the process $\gamma A \to VA$ was considered in the Leading Twist Approximation (LTA) for the nuclear gluon shadowing:

$$\sigma_{\gamma A\to VA}(y) = \frac{d\sigma_{\gamma N\to VN}(\omega, t_{min})}{dt}\left[\frac{G_A(x,\frac{M_V^2}{4})}{G_N(x,\frac{M_V^2}{4})}\right]^2 \int\limits_{-\infty}^{t_{min}} dt\left|\int d^2bdze^{i\vec{q}_t\cdot\vec{b}}e^{-q_l z}\rho(\vec{b},z)\right|^2. \qquad (3)$$

Here $-t = |\vec{q}_t|^2 + |q_l|^2$ is the square of the vector meson transverse momentum and $\sqrt{-t_{min}} = q_l = \frac{M_V^2}{2\omega}$ is the minimal longitudinal momentum transfer in the photoproduction vertex, $\rho(\vec{b},z)$ is the nuclear density normalized by the condition $\int d^2bdz\rho(\vec{b},z) = A$.

The key characteristics of the nuclear shadowing in the photoproduction of the hidden heavy flavor vector mesons is the ratio of the gluon density distribution in nucleus, $G_A(x,Q^2)$, to that in proton, $G_N(x,Q^2)$. At $x \geq 0.01$ the nuclear gluon density $G_A(x,Q^2) \approx AG_N(x,Q^2)$, and a distance on which the squeezed $q\bar{q}$ pair transforms into the "ordinary" meson is large at high energies. Hence, one should expect the revealing of the Color Transparency (CT) effect when small colour singlet dipole $q\bar{q}$ passes through the nuclear medium. With a decrease of x ($x < 0.01$) the nuclear gluon shadowing ($G_A(x,Q^2)/AG_N(x,Q^2) < 1$) should lead to a gradual disappearance of color transparency and to the onset of a new regime – *the perturbative color opacity* in photoproduction of heavy quarkonium off nuclei.

The total cross sections for the coherent J/ψ and Υ production in the ultraperipheral ion collisions calculated in Refs. [1-3] are given in Table 1. From comparison of calculations performed in the LTA with estimates in the Impulse Approximation it follows that the Υ yield is expected to be suppressed by a factor of 2 at central rapidities due to the leading twist shadowing. The suppression of the J/ψ cross section is much stronger, by a factor of 4–6. In principle, the multiple eikonal type rescatterings of the small color singlet dipole (squeezed $q\bar{q}$ pair) off nucleus could also result in suppression of the heavy quarkonium photoproduction. This mechanism predicts significantly smaller suppression than the leading twist gluon shadowing, at least for $x \leq 0.001$.

Experimentally, the coherent quarkonium photoproduction in the ultraperipheral ion collisions has clearly distinguishable signature. The dimuon decay mode could be used to tag effectively the reaction of interest. The ALICE muon arm provides the Level 0 triggers in the situations when one or two fast ($p > 5$ GeV/c) muons are within its acceptance ($2^\circ < \Theta < 8^\circ$). The reconstructed equivalent mass of the muon pair identifies the parent particle (the dimuon arm mass resolution is about 100 MeV at Υ mass). Since the ions in the coherent photoproduction remain intact, only muon pair should be detected and nothing else. The photon spectrometer PHOS covers approximately 10% of the barrel solid angle. The grazing ion collision results in strong nucleon-nucleon interactions with production of some number of hadrons that hit the PHOS with a large probability. That is why a veto from the PHOS subsystem could be used to preselect very peripheral events. This signal is implemented in the PHOS Level 0 trigger electronics on our request. We expect that the PHOS veto will reduce the single muon trigger rate to affordable level. The inefficiency estimated for such kind of trigger (the muon hit in the PHOS) is expected to be at a level of 3%.

Table 1

Total cross sections of J/ψ and Υ production in ultraperipheral collisions at LHC

Colliding ions	CaCa, $\gamma = 3500$		PbPb, $\gamma = 2700$	
Quarkonium	J/ψ	Υ	J/ψ	Υ
Impulse	0.6 mb	1.8 μb	70 mb	133 μb
Leading Twist	0.2 mb	1.2 μb	15 mb	78 μb

Further improvement could be achieved at trigger level 1 applying the decision of the Zero Degree Calorimeters (ZDC). The coherent photoproduction of vector mesons in the ultraperipheral collisions can be accompanied by some number of neutrons emitted due to decays of one or both nuclei excited by additional photon exchanges. These neutrons with high efficiency will be detected by the ZDC placed on the axis of the ALICE detector at large distances from the interaction point. Detecting of the dimuon pair in combination with the vetoes of hadron detector systems and ZDCs will effectively select the coherent photoproduction events.

At the same time, it was recently shown [3] that the ultraperipheral heavy ion collisions can be used to measure not only the nuclear gluon densities but also the nucleon gluon density almost in the same kinematical conditions. To achieve these aims, one has to study quasielastic quarkonium photoproduction off the nuclear nucleon at momentum transfer more than a few hundreds MeV. In this case one of the colliding nuclei which emits the photon remains intact. The nucleon of another nucleus, participating in the process of photoproduction, will interact with other nucleons of target nucleus. As a result, the nucleus becomes excited and decays emitting a few neutrons [3] which will be registered by ZDC. The cross section of this incoherent process is proportional to the squared nucleon gluon density and the mass number of the target nucleus. The experimental signature of such events is signal from one side ZDC detecting a few neutrons in direction opposite to the direction of quarkonium produced with transverse momentum $p_t \geq 200$ MeV. Similar type of events can be due to the physical background – coherent production of heavy quarkonia in strong interactions, however the probability to keep, at least, one of the colliding ions intact in such processes is expected to be very small.

An estimate of the total yields is not sufficient to prove the feasibility of the experimental studies. The sub-detectors, capable to detect heavy quarkonia through their dimuon decay, should be able to produce trigger for the coherent J/ψ and Υ production in the ultraperipheral collisions ; also the acceptances of these sub-detectors may cut significantly the phase space of the reaction. The acceptances were estimated using the approximative method and with the detailed `AliRoot` simulation code – both approaches give similar results. No detailed event reconstruction was done. In the approximate simulation we *assume* that the muon in angular range $2^\circ < \Theta < 8^\circ$ and $p > 5$ GeV/c is detected by the muon arm and the muon in the range of $45^\circ < \Theta < 135^\circ$ is detected in the barrel detectors (ITS + TPC). In the `AliRoot` simulation we assume that once the muon passed through the detector (10 Tracking chambers + 4 Trigger chambers of the dimuon arm and/or has hits both in ITS and TPC), the detector response could be successfully analyzed. The muon trigger efficiencies were taken into account.

The machine-induced background (beam-gas interactions) is expected to be negligible.

Another source of physical background is the muon pair production in $\gamma\gamma$ interactions. The total number of these triggers could be significant. The studies of the muon pair production in $\gamma\gamma$ interactions have a special interest, this well understandable process could be used for the calibrations of the detector.

The signal-to-background ratio in the mass range of interest (in the vicinity of the J/ψ peak) is expected to be of the order of one. The significance (signal/$\sqrt{\text{signal} + \text{background}}$) of the data collected during standard LHC heavy ion year (running time of 10^6 sec at mean luminosity of $\mathcal{L}_{mean} = 0.5 \times 10^{27}\text{sec}^{-1}\text{cm}^{-2}$) is estimated to be about 100 in a case of J/ψ and of the order of 1 in a case of Υ. The mass ranges of interest have been chosen depending on the estimated mass resolution: the resolution is better in case when second muon is detected in the barrel part because the vertex position can be reconstructed.

The acceptances for the heavy quarkonia photoproduction in the ultraperipheral lead-lead collisions are presented in Figs. 1, 2.

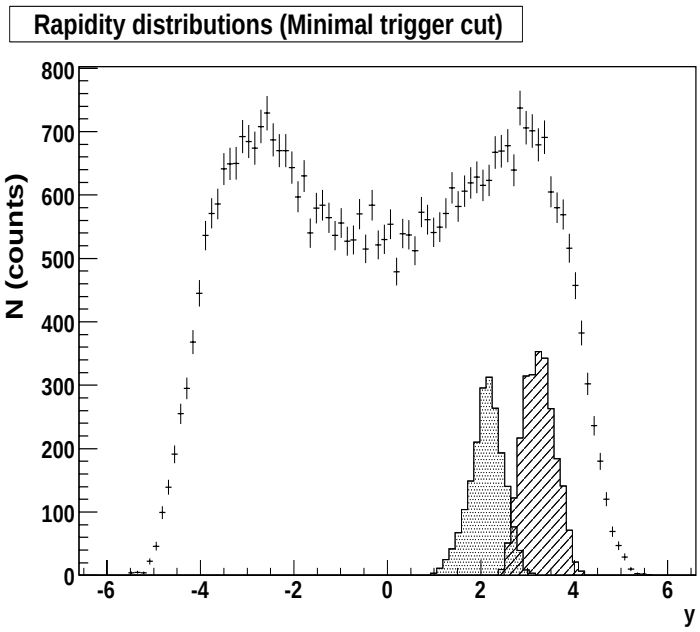

Fig. 1. The J/ψ coherent photoproduction acceptance, the `AliRoot` estimation within *Minimal* trigger p_T cut. The left (grey) peak corresponds to the case when one muon is triggered by the dimuon spectrometer, the other one is detected by the barrel. The right (hatched) peak is formed of the muon pair detected by the dimuon arm. Pb-Pb collision case

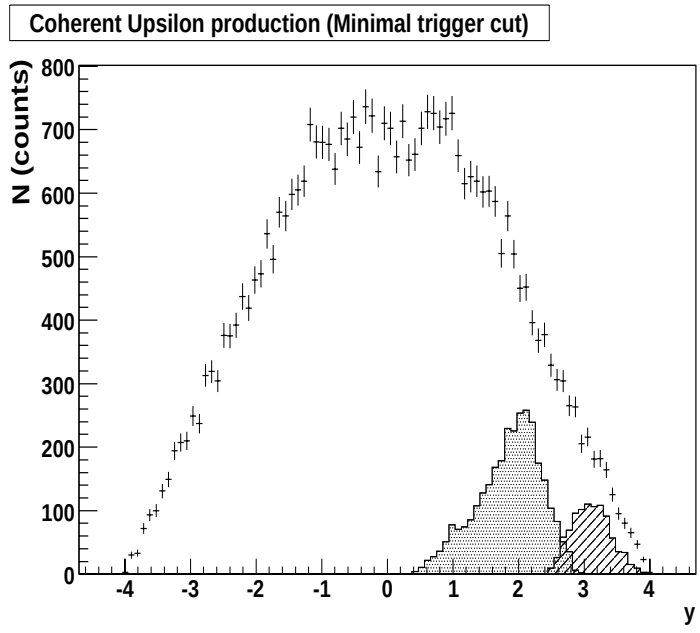

Fig. 2. The Υ coherent photoproduction acceptance, the `AliRoot` estimation within *Minimal* trigger p_T cut. The left (grey) peak corresponds to the case when one muon is triggered by the dimuon spectrometer, the other one is detected by the barrel. The right (hatched) peak is formed of the muon pair detected by the dimuon arm. Pb-Pb collision case

Table 2

Acceptance A, statistics N, signal-to-background ratio N/Bg and significance ($S = N/\sqrt{N + Bg}$) to be accumulated during heavy ion running year for the coherent J/ψ photoproduction in ALICE subsystems in the Pb-Pb collisions

	Acceptance	Statistics	N/Bg	Significance
$\mu\mu$-channel	5.29%	23300	1.27	122
$B\mu$-channel	4.86%	12200	0.57	80

Table 3

Acceptance A, statistics N, signal-to-background ratio N/Bg and significance ($S = N/\sqrt{N + Bg}$) to be accumulated during heavy ion running year for the coherent Υ photoproduction in ALICE subsystems in the Pb-Pb collisions

	Acceptance	Statistics	N/Bg	Significance
$\mu\mu$-channel	2.45%	24	0.05	1.1
$B\mu$-channel	6.02%	78	0.05	1.8

The corresponding numerical results are given in Tables 2, 3 ($\mu\mu$ stands for the case when both muons are detected in the dimuon arm; $B\mu$ denotes the case when one muon has been detected in the barrel part, while another one passed through the muon spectrometer). These results show that the ALICE detector can be used without significant modifications to study the behavior of the nucleus gluon density distributions at small x and to observe the transition from the nuclear color transparency to regime of the color opacity in the ultrarelativistic peripheral ion collisions. The counting rate for the coherent J/ψ photoproduction is reasonable (order of thousand of $\mu^+\mu^-$ pairs per day within the dimuon arm acceptance). In a case of Υ photoproduction the counting rate is about of one hundred per heavy ion running year (including those detected in dimuon trigger and in the barrel-dimuon coincidence). The information which can be obtained from studying the heavy quarkonium photoproduction in ultraperipheral ion collisions will be undoubtedly useful for the reliable interpretation of the experimental data on study of the central heavy ion collisions aimed at the investigation of the quark-gluon plasma formation at LHC.

References

1. L. Frankfurt, M. Strikman and M. Zhalov, Phys. Lett. B **540**, 220 (2002).
2. L. Frankfurt, V. Guzey, M. Strikman and M. Zhalov, JHEP **0308**, 043 (2003).
3. M. Strikman, M. Tverskoy and M. Zhalov, Phys. Lett. B **626**, 72 (2005).

EXPERIMENTS OF CRYSTAL BALL COLLABORATION AT BNL

PNPI participants of the Crystal Ball Collaboration:
V.V. Abaev, V.S. Bekrenev, N.G. Kozlenko, S.P. Kruglov, A.A. Kulbardis, I.V. Lopatin, A.B. Starostin

1. Introduction

The experimental program "Baryon spectroscopy with the Crystal Ball" was under way in 1998–2002 at the Alternating Gradient Synchrotron AGS of Brookhaven National Laboratory, USA. The main goal of this program was to map up the existence of all baryon resonances and to study their characteristics with a high precision. The program has been carried out with the team, the Crystal Ball Collaboration, including 14 institutions from 5 countries. Physicists of PNPI participated in this collaboration playing an essential role.

Almost all our information on the N and Δ resonances comes from πN data, mainly from elastic scattering, in the form of cross section and polarization measurements. The data are synthesized by a partial-wave analysis. The end products are the various partial waves; the Argand diagram and speed plot of each wave are used to identify the resonances. Till starting the experiments at BNL, the πN data sets in certain energy regions were incomplete and it was easy for a resonance with a small elasticity to be missed. One of the most evident shortcomings of the existed data-base was a lack of precise and systematic data on $\pi^- p$ reaction with neutral particles in the final state: $\pi^- p \to \gamma n$, $\pi^- p \to \pi^0 n$, $\pi^- p \to \pi^0 \pi^0 n$, $\pi^- p \to \eta n$.

The experiment E913 at the AGS was concerned with the systematic measurement of neutral final states in $\pi^- p$ interactions in the region of low-lying πN resonances; the experiment covered the N and Δ resonances using π^--beams.

The multi-photon Crystal Ball detector was used for registering photons and neutral mesons in this experiment. This detector has a good energy and angular resolution. The Crystal Ball made it possible to study neutral baryon spectroscopy on a scale not seen before.

2. The Crystal Ball detector

The Crystal Ball is a highly segmented, total absorption electromagnetic calorimeter and spectrometer, covering over 94% of 4π steradian. The Crystal Ball detector was installed at the C6 beam line of the AGS at Brookhaven National Laboratory. The ball proper is a sphere with an entrance and exit opening for the beam and an inside cavity for the target. The ball (see Fig. 1) is constructed of 672 optically isolated NaI(Tl) crystals, 15.7 radiation length thick. Each crystal is viewed by its own photomultiplier tube.

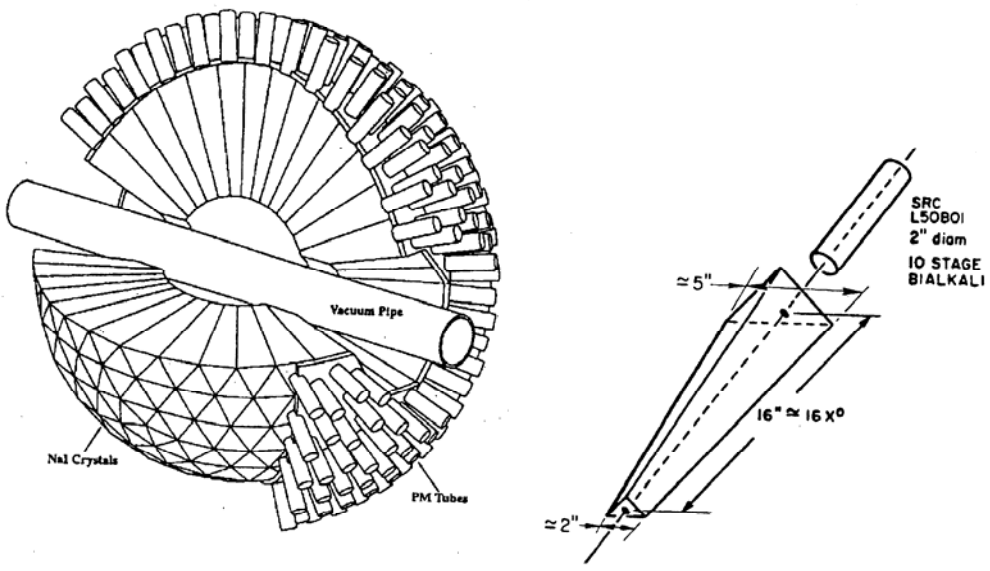

Fig. 1. Left: the Crystal Ball detector. Right: the typical Crystal Ball crystal

The counters are arranged in a spherical shell with an inner radius of 25.3 cm and an outer radius of 66 cm. The sphere is approximated by an icosahedron, a figure consisting of 20 equivalent equilateral triangles called as "major" triangles. Each major triangle is divided into 4 "minor" triangles and each minor triangle consists of 9 crystals. While majors are similar, there are 2 types of minors – the central minor is slightly different from the corners. The Crystal Ball consists of 11 types of slightly different shaped crystals. The crystals are about 41 cm long truncated triangular pyramids about 14 cm across at the outer and about 5 cm at the inner radius.

An electromagnetic shower from a single photon deposits energy in several crystals, called a cluster. The present cluster algorithm sums the energy from the crystal with the highest energy with that from the twelve nearest neighbors. Shower directions are measured with the resolution in polar angle $\sigma_\theta = 2^\circ$–3° for energies in the range 50–500 MeV; the resolution in azimuthal angle is $\sigma_\varphi = 2^\circ/\sin\theta$. The energy resolution was $\sigma_E/E = 2.0\%/E^{0.36}$ with E given in GeV. The Crystal Ball is also ia useful detector of neutrons. Neutrons with a kinetic energy of 10–250 MeV are detected with an efficiency of 20–40%.

A liquid hydrogen target LH_2 (a 10 cm diameter horizontal cylinder with spherical endcaps and total thickness along the beam axis being equal to 10.56 cm) was installed inside a vacuum pipe. A veto barrel consisting of four 120 cm long plastic scintillation counters surrounding the vacuum pipe was used to identify neutral (no signal in the veto barrel) and charged (at least one veto barrel signal) triggers.

In an experiment, the coordinates and momenta of beam particles were determined using a set of seven drift chambers. Three drift chambers were used to measure the horizontal coordinates, three chambers were used to measure the vertical coordinates and one chamber situated upstream of the beam bending magnet aimed to determine the beam particle's momentum. An eight element horizontal hodoscope was mounted immediately upstream of the first drift chamber at the point of maximum horizontal momentum dispersion of the beam.

3. Study of $\pi^- p$ charge exchange scattering $\pi^- p \to \pi^0 n$

In experiments with the liquid hydrogen target over 42×10^6 triggers for $\pi^- p \to$ *neutrals* were collected at 22 beam momenta over a range of 150–760 MeV/c; additional runs with an empty target were taken at each momentum. This momentum range includes four low-lying resonances: $P_{33}(1232)$, $P_{11}(1440)$, $D_{13}(1520)$ and $S_{11}(1535)$.

When studying the $\pi^- p$ charge exchange (CEX) reaction, two- and three-cluster events were used to select this reaction and to calculate differential cross sections. The π^0 meson from the CEX reaction decays into two photons immediately, and the showers from these two photons give clusters in the Crystal Ball NaI(Tl) crystals. The cluster finding program finds the crystal with maximum deposited energy, adds the energies from adjoining crystals and then zeroes the energies in those crystals. After that the program finds the next crystal with the maximum energy to form the next cluster and so on until all the clusters are found. Events containing clusters with the maximum energy in a crystal at the beam entrance or exit holes were rejected. For two-cluster events the invariant mass was calculated in assumption that both clusters are from photons. If the invariant mass coincides with the mass of π^0 meson and the kinematics of the CEX reaction is fulfilled, then the event was accepted. For three-cluster events the analysis is more complicated – it is not known which cluster is produced by the neutron, so all possible combinations must be examined.

The Crystal Ball acceptance was determined on the base of the Monte Carlo simulation of the experiment. The acceptance value rapidly decreased when $\cos\theta_{cm} > 0.5$ because of the beam-exit tunnel.

At the first stage of data processing, results for the CEX reaction $\pi^- p \to \pi^0 n$ are obtained for eight momenta in the range from 147 to 322 MeV/c [1, 2]; the momentum spread (σ) varied from 1.5% to 1.0%, respectively. When carrying out the experiment, the beam contamination was determined using the time-of-flight (TOF) technique on the base of about 9 meters. As an example, the μ/π fraction was evaluated to be 3.5% and e/π was 5.9% at 300 MeV/c using this technique.

As a result of data processing, the center-of-mass scattering angle θ_{cm} was calculated for each CEX event and the data were histogrammed into 20 bins $\Delta\cos\theta_{cm} = 0.1$. Yields taken with the empty target were

subtracted then from the data taken with the full target, and the differential cross sections were calculated at each angular bin. In total, 160 new experimental points were obtained. The statistical errors are typically 2–6% except forward-angle points at three lowest momenta where the cross sections decrease to a few tenths of millibarn. Systematic uncertainties increase from 3% to 6.5% as the beam momentum decreases.

The differential cross sections were integrated to obtain the total charge-exchange cross sections at eight momenta. In Fig. 2 the results are presented in comparison with the predictions of the FA02 partial-wave analysis (PWA) and with previous data. As with the differential cross sections, the total cross sections are in a good agreement with the FA02 PWA.

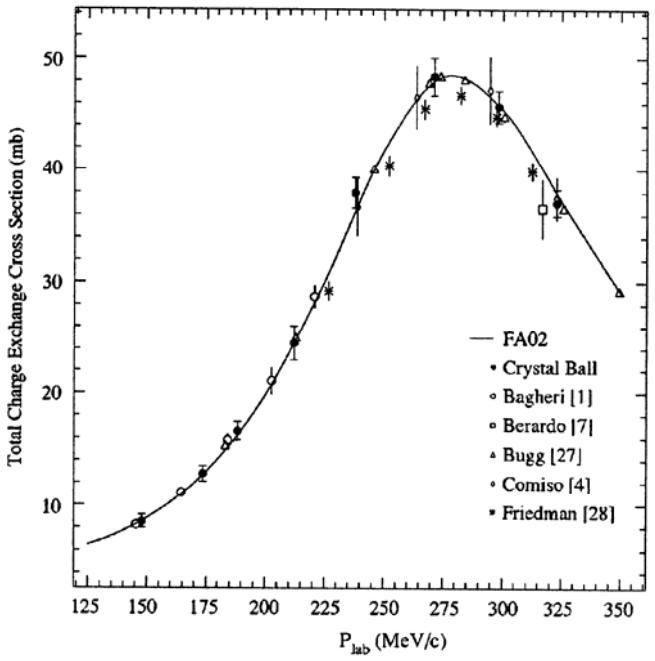

Fig. 2. The total cross sections obtained from integrating the differential cross sections. The results are compared to the FA02 PWA and to previous data

At the next stage of data processing, the differential cross sections of the CEX reaction were obtained [3] for momenta in the vicinity of the η-production threshold – from p_π = 649 MeV/c to 752 MeV/c. Since the TOF-technique is not appropriate to determine lepton contamination in the beam in such high momenta, a cylindrical gas Cherenkov counter was used to measure the electron contamination. This experiment used a pion beam with a momentum spread of $\sigma \approx 1\%$. The momentum dispersion of the beam on the hodoscope plane was used to split the beam distribution into narrower momentum intervals, which have a typical resolution of $\sigma \approx 5$ MeV. Each fraction of the beam passing through one of the hodoscope counters was analyzed independently. The mean value of the beam momentum for each individual hodoscope counter was obtained from the momentum spectrometer. As a result, the differential cross sections of the CEX reaction were calculated in 27 momentum bins. The full covered angular range (from –1 to +1 in $\cos\theta_{cm}$) was divided into 24 angular bins. In total, 648 new experimental points were obtained in this experiment. A value of the statistical error varies from 5% to 15% – depending on the momentum and angle. The overall systematic uncertainty that affects the normalization of the differential cross sections is estimated to be 4% for the momenta below 689 MeV/c and 6% for the momenta above.

Shown in Fig. 3 are three examples of the CEX differential cross sections. A comparison is made with the predictions of the FA02 PWA. There is good agreement between the PWA results and experimental data at p_π = 661 MeV/c and p_π = 705 MeV/c. The PWA results agree with our data at these momenta in both the absolute magnitude and the shape of the distribution over the full angular range. At p_π = 742 MeV/c, the PWA results deviate from our data by 10–15% at backward angles.

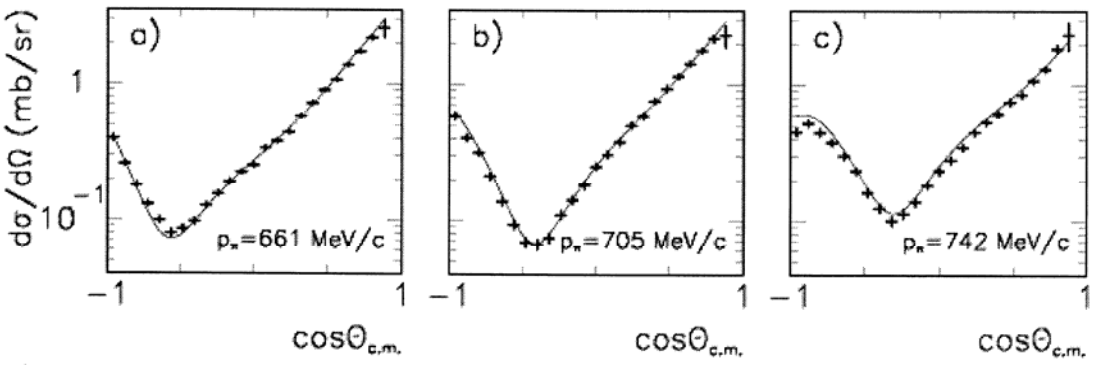

Fig. 3. The differential cross sections of the CEX reaction at selected momenta compared to the FA02 PWA (solid line). The ordinates of the histograms are logarithmic

In 2002, a separate experiment was carried out in which the liquid hydrogen target was replaced with a thin polyethylene (CH_2) target, 10 cm in diameter; the monitor counter was placed immediately in front of this target. Several data sets were obtained with both CH_2 and carbon (C) targets at nine incident beam momenta between 547 and 750 MeV/c. When carrying out this experiment, a lead plate of 3-mm thickness was inserted upstream of the second dipole magnet to eliminate most of electron component by radiation losses, so the electron contamination for the CH_2 – C data (measured using the gas Cherenkov counter) was about 6%.

The differential cross sections for CH_2 – C were calculated after subtracting the normalized carbon data from the CH_2 data. The typical carbon contribution was 30%. For calculating the differential cross sections the full angular range (from –1 to +1 in $\cos\theta_{cm}$) was divided into 24 angular bins. In total, about 200 new experimental points were obtained [4]. The statistical errors are at a level of 5–15%, the systematic uncertainties are estimated to be equal to 6%. A comparison of obtained differential cross sections with the predictions of the FA02 PWA shows their general agreement within 5%, although remarkable deviations are observed at momenta higher than 675 MeV/c and at angles $\cos\theta_{cm} < -0.45$ – see Fig. 4.

At the beam momentum of 720 MeV/c the differential cross sections were obtained in measurements with both the liquid hydrogen and polyethylene targets – the electron contamination in the beam was 6% in both cases. A comparison shows that the results agree within 3%.

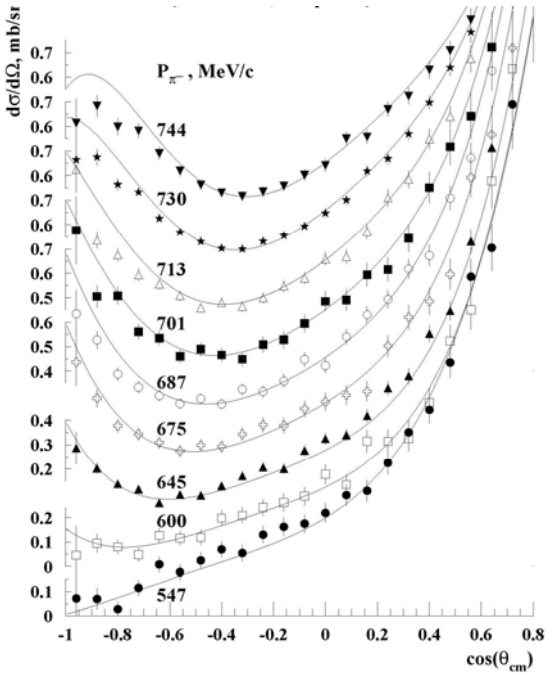

Fig. 4. The differential cross sections of the CEX reaction measured using the CH_2 target. Shown by curves are the predictions of the FA02 PWA

4. Study of the η-production process $\pi^- p \to \eta n$

At the incident pions momenta higher than the η-production threshold accumulated data were used to obtain cross sections of the reaction $\pi^- p \to \eta n$. Until now existing experimental information on the cross sections of this reaction has been very scarce and contradictory, especially near the threshold. At the same time, obtaining accurate experimental data in the near-threshold region is very important for verifying theoretical models of η-production. Such data will also be useful for extracting the ηN scattering length and understanding properties of the $S_{11}(1535)$ resonance.

Cross sections of the reaction $\pi^- p \to \eta n$ were determined in the momentum range from the threshold (685 MeV/c) up to 750 MeV/c. The η meson produced in this reaction has – as distinct from the $\pi^- p$ charge exchange scattering – two decay modes with approximately equal branching ratios: $\eta \to \gamma\gamma$ and $\eta \to 3\pi^0$. Evidently, in this case the candidates for the $\pi^- p \to \eta n \to 2\gamma n$ and $\pi^- p \to \eta n \to 3\pi^0 n \to 6\gamma n$ channels are the neutral two-cluster and six-cluster events, respectively, assuming that each cluster is because of a photon shower in the Crystal Ball. The neutron is assumed to be the missing particle. Because the $\pi^- p \to \eta n$ reaction is studied near the production threshold, only a few percent of all events have the final-state neutron entering the crystals of the Crystal Ball, *i.e.* almost all events have the neutrons escaping through the downstream tunnel. So events in which there was an extra cluster from a neutron were not taken into account.

At the first stage of data processing, only events caused by the $\eta \to \gamma\gamma$ decay were considered – see Refs. [5, 6]. Both the differential and total cross sections were obtained as a result of this work. The differential cross sections were fitted with Legendre polynomials: $d\sigma/d\Omega = a_0 + a_1 P_1(\cos\theta_{cm}) + a_2 P_2(\cos\theta_{cm})$. It appeared that at momenta up to 705 MeV/c the *S*-wave amplitude gives the main contribution to the cross sections, while for momenta from 705 to 750 MeV/c the contribution of higher waves becomes essential. The total cross sections obtained by integrating $d\sigma/d\Omega$ are in a general agreement with results of previous experiments but exceed them in statistical accuracy.

More detailed data analysis was performed some later [7]. The two sets of results for the differential cross sections for the reaction $\pi^- p \to \eta n$ using $\eta \to \gamma\gamma$ and $\eta \to 3\pi^0$ decays are shown in Fig. 5.

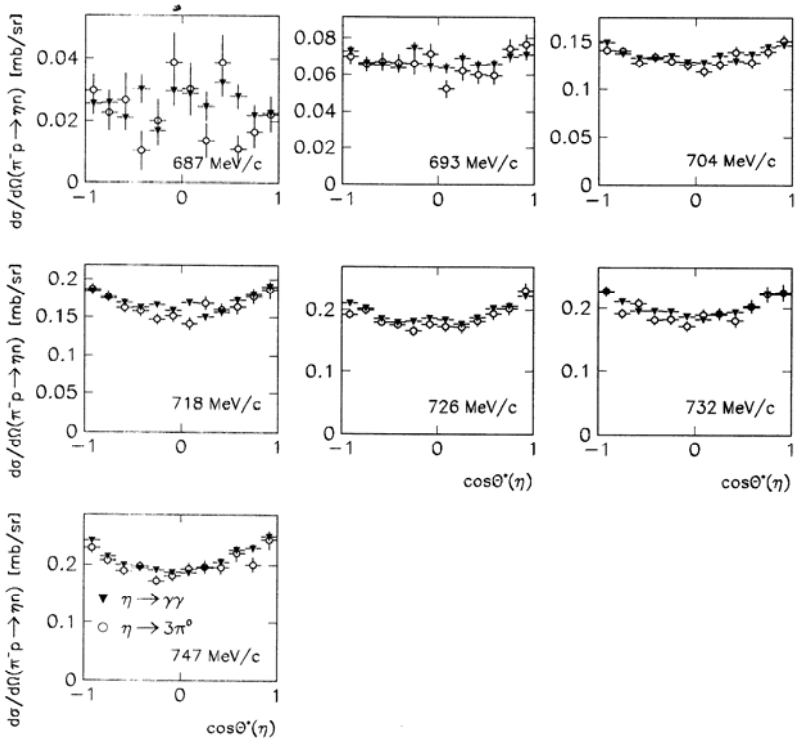

Fig. 5. Differential cross sections for $\eta \to \gamma\gamma$ (filled triangles) and $\eta \to 3\pi^0$ (open circles) decays

Inspection of this figure reveals that results obtained using $\eta \to \gamma\gamma$ decay is smoother than ones obtained using $\eta \to 3\pi^0$. This can be explained by the fact that the number of $\eta \to \gamma\gamma$ decays detected in the Crystal Ball is 3.5 times the number of $\eta \to 3\pi^0$ ones.

The systematic uncertainty in $d\sigma/d\Omega$ is dominated by two sources: the uncertainty in the η decay branching ratio and the uncertainty in the determination of the lepton contamination of the incident π^- beam. The absolute uncertainty in the value of $BR(\eta \to \gamma\gamma)$, which has been determined directly, is only 0.9%. In contrast, $BR(\eta \to 3\pi^0)$ has been determined only relatively. For this reason, authors of Ref. [7] preferred to use the $d\sigma/d\Omega$ data set obtained using $\eta \to \gamma\gamma$ rather than taking the weighted average of the two sets. As to the systematic uncertainty in the determination of the lepton contamination in the beam, it was taken to be 6% – in accordance with the procedure described in Ref. [3].

The $d\sigma/d\Omega$ angular distribution for two lowest momenta looks isotropic confirming that near the threshold the η-production process goes through formation of the $S_{11}(1535)$ resonance. For $p_\pi \geq 704$ MeV/c these angular distributions are bowl shaped. This is consistent with no *P*-wave and a modest *D*-wave production of order 5–10% and *S*-*D* interference. This conclusion coincides with that made in Refs. [5, 6].

The total cross section increases immediately and rapidly from the η-production threshold at 685 MeV/c, reaching 2.6 mb at $p_\pi = 750$ MeV/c.

3. Study of forbidden and rare decays of η meson

The Crystal Ball collected approximately 30×10^6 η mesons from the reaction $\pi^- p \to \eta n$ using a liquid hydrogen target at a beam momentum of 720 MeV/c.

An important goal of this experiment was to improve the present values of branching ratios for rare and forbidden decays of the η meson. Besides the most intense neutral decays $\eta \to 2\gamma$ and $\eta \to 3\pi^0$ having branching ratios of 39.4% and 32.5%, accordingly, the following neutral decay modes forbidden for different reasons were investigated using the Crystal Ball: $\eta \to 3\gamma$, $\eta \to \pi^0\gamma$, $\eta \to 2\pi^0\gamma$, $\eta \to 3\pi^0\gamma$, $\eta \to 4\pi^0$.

The decay $\eta \to 3\gamma$ is forbidden by *C* invariance. Besides, there exist several additional factors which suppress this decay. The decay to three photons is an electromagnetic interaction of the 3rd order proportional to $\alpha^3 \approx 4 \times 10^{-7}$. The decay is suppressed even more by the limitations of the phase space and by the centrifugal barrier. The upper limit for this decay measured in this experiment for the first time is $BR(\eta \to 3\gamma) < 4 \times 10^{-5}$ at the 90% CL [8]. Candidates for the $\pi^- p \to \eta n \to 3\gamma n$ process were searched for in the three-cluster data set, which comprised 18.4×10^6 events. The mostly significant experimental background is due to the decay $\eta \to 3\pi^0 \to 6\gamma$, when photon showers overlap in the detector.

A spin-zero to spin-zero transition by the emission of a real photon is forbidden by conservation of angular momentum. Thus, the decay mode $\eta \to \pi^0\gamma$ should be absolutely forbidden. Furthermore, this decay is not allowed by gauge invariance and by *C* invariance. Possible candidates for the $\pi^- p \to \eta n \to \pi^0\gamma n \to 3\gamma n$ process were searched for in the same three-cluster data set that was used for the determination of the upper limit in $BR(\eta \to 3\gamma)$. This process has the same background sources as the $\pi^- p \to \eta n \to 3\gamma n$ process. The number of effective constraints that apply to the $\pi^- p \to \pi^0\gamma n \to 3\gamma n$ hypothesis is one more than for $\pi^- p \to 3\gamma n$, namely the mass of the π^0 meson. The obtained upper limit $BR(\eta \to \pi^0\gamma) < 9 \times 10^{-5}$ at the 90% CL [8] is about two times larger than the one for $BR(\eta \to 3\gamma)$.

The decay modes $\eta \to 2\pi^0\gamma$ and $\eta \to 3\pi^0\gamma$ are strictly forbidden both by charge conjugation invariance. The five-cluster data set of 5.2×10^6 events was used to search for $\pi^- p \to \eta n \to 2\pi^0\gamma n \to 5\gamma n$ candidates. The background for this decay is determined mainly by evens from the decay $\eta \to 3\pi^0$ in cases when two single-photon showers overlap or one photon is not detected in the Crystal Ball. Another source of background is the reaction $\pi^- p \to 2\pi^0 n$ when either a single-photon splits off or the neutron is detected in the Crystal Ball. The obtained upper limit is $BR(\eta \to 2\pi^0\gamma) < 5 \times 10^{-4}$ at the 90% CL [9]. Using the value $\Gamma(\eta \to all) = 1.29 \pm 0.07$ keV, the *BR* was converted to the decay-width upper limit: $\Gamma(\eta \to 2\pi^0\gamma) < 0.64$ eV. No searches for this decay mode have been reported earlier. To search for the reaction $\pi^- p \to \eta n \to 3\pi^0\gamma n \to 7\gamma n$ the sample of seven-cluster events was used, which has 0.168×10^6 entries. The main source of background here is $\eta \to 3\pi^0 \to 6\gamma$ events with seventh cluster produced by a one-photon shower split-off or an occasional

cluster from a pile-up event. To suppress this background, the several selection cuts were applied. The obtained upper limits are $BR(\eta \to 3\pi^0\gamma) < 6 \times 10^{-5}$ at the 90% CL and $\Gamma(\eta \to 3\pi^0\gamma) < 0.077$ eV [10].

The decay $\eta \to 4\pi^0$ is forbidden by *CP* conservation, so it provided a test for strong *CP*-violating amplitudes down to a level of about 10^{-7} where weak interactions come into play. This decay mode requires 8 neutral clusters in the Crystal Ball which must be reconstructed to four π^0 mesons which together have the invariant mass of the η meson. This enables also to eliminate the expected background from the $\eta \to 3\pi^0$ decay in which there are two extra clusters from photon showers which breakup into separate clusters. The main limitation of the $4\pi^0$ decay mode is its small phase space, the maximum π^0 momentum in $\eta \to 4\pi^0$ is only 39 MeV/c, as compared to the π^0 momentum in $\eta \to 2\pi^0$ of 238 MeV/c. The eight-cluster data set contained 14804 experimental events. These events were subjected to a constrained least square fit satisfying the $\pi^- p \to \eta n \to 4\pi^0 n \to 8\gamma n$ reaction hypothesis with a confidence level > 2% With no 8-cluster event from $\eta \to 4\pi^0$ found, the upper limits become $BR(\eta \to 4\pi^0) < 6.9 \times 10^{-7}$ at the 90% CL and $\Gamma(\eta \to 4\pi^0) < 8.3 \times 10^{-4}$ eV [10].

All above considered decays of the η meson are forbidden – in the framework of the Standard Model – by the fundamental conservation laws, and a stimulus for the investigation of branching ratios of such decays is the search for such decay mechanisms which were outside the Standard Model. However, there is another category of decays (so called rare decays) values of branching ratios for which are predicted by existing theoretical models, and experiments on measuring these branching ratios are important for testing these models. The η-meson decays $\eta \to \pi^0\gamma\gamma$, $\eta \to \pi^0\pi^0\gamma\gamma$ belong just to this category. For example, measurement of the decay rate for $\eta \to \pi^0\gamma\gamma$ is a direct test of the correctness of calculations of the third order χPTh, the first order being zero and the second order being very small. The experimental determination of the $BR(\eta \to \pi^0\gamma\gamma)$ is a rather complicated task, mainly because of the contribution of background from the decay $\eta \to 3\pi^0 \to 6\gamma$ and the reaction $\pi^- p \to 2\pi^0 n \to 4\gamma n$. As a result of multi-step procedure of processing four-cluster data set about 1600 events attributed to the decay $\eta \to \pi^0\gamma\gamma$ were obtained. This gives $BR(\eta \to \pi^0\gamma\gamma) = (3.5 \pm 0.7_{stat} \pm 0.6_{syst}) \times 10^{-4}$ and $\Gamma(\eta \to \pi^0\gamma\gamma) = 0.45 \pm 0.09_{stat} \pm 0.08_{syst}$ eV [11]. This result agrees well with the theoretically calculated value $\Gamma(\eta \to \pi^0\gamma\gamma) = 0.47 \pm 0.10$ eV but lower by a factor of 2 in comparison with the experimental value obtained in 1982 at the setup GAMS.

There are χPTh theoretical predictions for the probability of the decay $\eta \to \pi^0\pi^0\gamma\gamma$, but estimations of the *BR* values given by theoreticians are too low (at a level of 10^{-6}–10^{-7}) to be confirmed or rejected on the base of existing experimental data. For the time present, an analysis of data obtained using the Crystal Ball has given only the upper limit for the *BR* of this decay: $BR(\eta \to \pi^0\pi^0\gamma\gamma) < 1.2 \times 10^{-3}$ [8].

References

1. A.A. Kulbardis for the Crystal Ball Collaboration, in *Proceedings of the 9th International Conference on Hadron Spectroscopy* (Protvino, Russia, 26 August – 1 September 2001), AIP Conference Proceedings, **619**, 701 (2002).
2. M.E. Sadler, A.A. Kulbardis *et al.*, Phys. Rev. C **69**, 055206 (2004).
3. A. Strarostin *et al.*, Phys. Rev. C **72**, 015205 (2005).
4. N.G. Kozlenko *et al.*, Preprint PNPI-2684, Gatchina, 2006. 56 p.
5. N.G. Kozlenko *et al.*, Phys. Atom. Nucl. **66**, 110 (2003).
6. N.G. Kozlenko for the Crystal Ball Collaboration, in *Proceedings of the 9th International Conference on Hadron Spectroscopy* (Protvino, Russia, 26 August – 1 September 2001), AIP Conference Proceedings, **619**, 697 (2002).
7. S. Prakhov *et al.*, Phys. Rev. C **72**, 015203 (2005).
8. B.M.K. Nefkens *et al.*, Phys. Rev. C **72**, 035212 (2005).
9. B.M.K. Nefkens *et al.*, Phys. Rev. Lett. **94**, 041601 (2005).
10. S. Prakhov *et al.*, Phys. Rev. Lett. **87**, 192001 (2000).
11. S. Prakhov *et al.*, Phys. Rev. C **72**, 025201 (2005).

STUDY OF PHOTOPRODUCTION OF NEUTRAL MESONS USING THE CRYSTAL BARREL AT ELSA

PNPI participants of the CB@ELSA Collaboration:
D.E. Bayadilov, Yu.A. Beloglazov, A.B. Gridnev, I.V. Lopatin, D.V. Novinsky, A.K. Radkov, V.V. Sumachev

1. Introduction

Due to their substructure, nucleons exhibit a rich spectrum of excited states. In spite of considerable theoretical achievements, attempts to model the nucleon spectrum with three constituent quarks and their interactions still fail to reproduce experimental findings in important details. In most quark-model based calculations, more resonances are found than have been observed experimentally. However, the quark model is only an approximation and may overpredict the number of states. Alternatively, these *missing resonances* could as well have escaped experimental observation due to a weak coupling to $N\pi$ which makes them unobservable in elastic πN scattering.

Resonances with small $N\pi$ coupling are predicted to have sizable photocouplings. Thus, the photoproduction of baryon resonances provides an alternative tool to study nucleon states. New facilities at ELSA in Bonn, GRAAL at Grenoble, CLAS at Jefferson Lab, MAMI-C at Mainz, and Spring-8 (Hyogo) offer the possibility to investigate photoproduction for $E_\gamma > 1$ GeV and to study nucleon resonances above the first and second resonance region.

Good angular coverage is needed to be able to extract the resonant and non-resonant contributions. The Crystal Barrel detector at ELSA is thus an ideal tool for studying nucleon resonances.

2. Experimental setup

The experiment was carried out at the electron accelerator ELSA. The maximum available electron energy is 3.2 GeV. The experimental setup is shown in Fig. 1.

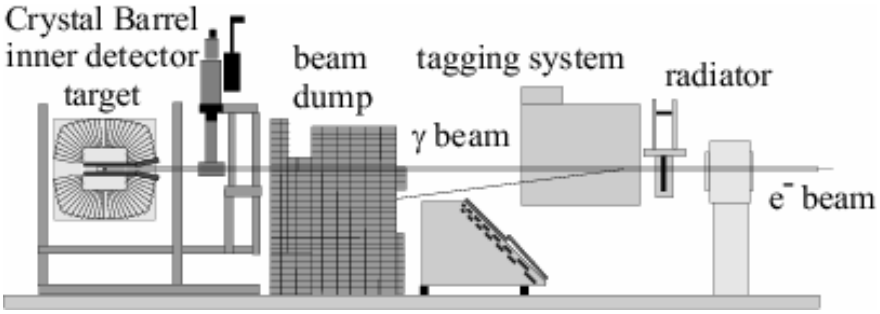

Fig. 1. Experimental setup at ELSA in Bonn

The electrons hit a radiator target, where they produce bremsstrahlung. The energy of photons, in the range between 25% and 85% of the primary electron energy, was determined *via* the detection of the corresponding scattered electrons in the tagging system ("tagger") consisting of a dipole bending magnet and two detecting parts – an array of fourteen scintillation counters to provide fast timing information and two multiwire proportional chambers (MWPCs) with a total of 348 channel to provide information about trajectories of the scattered electrons. Each scintillator of the array was read out *via* two photomultiplier tubes attached from both sides. A logical OR of the left-right coincidence from all scintillators was required in the first-level trigger.

The tagger was calibrated by direct injection of a very low intensity e^--beam of 600 or 800 MeV, after removing the radiator. Variation of the magnetic field of the tagging dipole magnet enabled a scan of several spatial positions over MWPCs. For a given wire, the electron momentum is proportional to the magnetic

field strength. The calibration was checked [1] by a Monte Carlo simulation of electron trajectories through the tagger. Geometry of the setup, dimensions of the electron beam, angular divergences, multiple and Møller scattering in the radiator foil and air were taken into account. From these simulations, the energy corresponding to each MWPC wire was obtained by a polynomial fit. The uncertainty of the simulation was estimated to be of the same order of magnitude as the "energy width" of the respective wire.

The Crystal Barrel forms the central component of the experiment. It consists of 1380 CsI(Tl) crystals with a length of 30 cm (16 X_0) and has an excellent photon-detection efficiency. The large solid-angle coverage (the 12° opening on either side of the barrel is necessary for technical reasons) and the high granularity allow for reconstruction of multi-photon final states. The spatial resolution determined by the size of individual crystal is at a level of 20 mrad (≈1.1°); it allows the separation of two photons stemming from the decay of π^0 meson with a maximum momentum 1 GeV/c corresponding to a minimum opening angle of 16.6°. The energy resolution of the calorimeter is empirically described by $\sigma_E/E = 2.5\%/[E(\mathrm{GeV})]^{0.25}$.

The three-layer scintillating fiber detector was inserted into the inner cavity of the Crystal Barrel to identify charged particles leaving the target and to determine their intersection point with the detector. The fibres are 2 mm in diameter; one of the layers was straight, the fibers of other two layers encircled the target with ±25° with respect to the first layer. The innermost layer corresponds to a solid angle of 92.6% of 4π.

The coincidence between tagger and scifi detector provided the first-level trigger of the experiment. From the hit pattern in the Crystal Barrel, a fast cluster logic determined the number of "particles" defined by clusters of contiguous crystals with individual energy deposits above 15 MeV. A second-level trigger was generated for events with two or more particles in the cluster logic. In the data analysis, clusters with two local maxima were split into two particles sharing the total energy deposit. The offline threshold for accepted particles was set to 20 MeV. The proton kinetic energy had to exceed 35 MeV to traverse the inner two scifi layers and to produce a trigger. A proton of 90 MeV was needed to reach the barrel calorimeter and to deposit the minimum cluster energy of 20 MeV.

The Crystal Barrel acceptance was determined from the Monte Carlo simulation. It vanishes for forward protons leaving the Crystal Barrel through the forward hole and for protons with very low energies.

3. The reaction $\gamma p \to p\pi^0$

Differential cross sections of the π^0 photoproduction were determined [2, 3] in two run periods with different primary electron energies of 1.4 and 3.2 GeV providing a total range of photon energies from 0.3 to 3 GeV. The π^0 mesons were reconstructed from their $\pi^0 \to \gamma\gamma$ decays. The compatibility of events with the hypothesis $\gamma p \to p\gamma\gamma$ was tested in a one-constraint kinematical fit imposing energy and momentum conservation but leaving the proton 3-momentum as adjustable quantity. Figure 2 shows the $\gamma\gamma$ invariant mass spectrum after a 10^{-4} confidence level cut in the 1C kinematical fit. The π^0-meson and η-meson signals are observed above a small residual background. There are 2.6×10^6 events due to $\gamma p \to p\pi^0$.

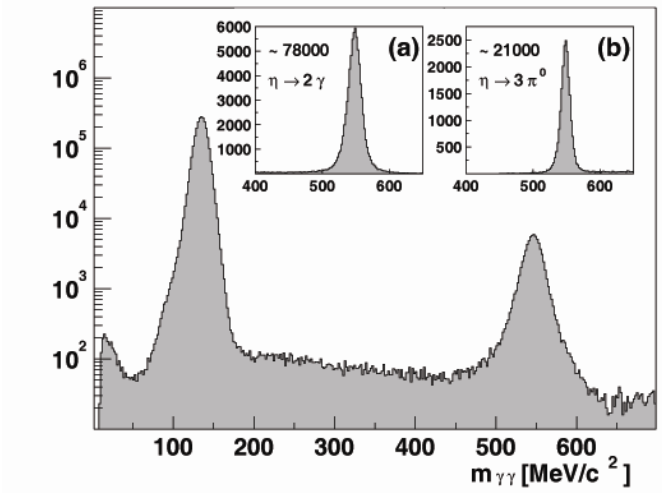

Fig. 2. Spectra of invariant $\gamma\gamma$ masses. Inserted in the top are spectra for the two different modes of the η decay

The differential cross sections can be calculated from the number of data events identified in the respective E_γ channel using the relation

$$\frac{d\sigma}{d\Omega} = \frac{N_{\pi^0\to 2\gamma}}{A_{\pi^0\to 2\gamma}} \cdot \frac{1}{N_\gamma N_p} \cdot \frac{1}{\Delta\Omega} \cdot \frac{\Gamma_{total}}{\Gamma_{\pi^0\to 2\gamma}}, \quad (1)$$

where the quantities are:

$N_{\pi^0\to 2\gamma}$ – the number of events in (E_γ, $\cos\theta_{cm}$) bin;

$A_{\pi^0\to 2\gamma}$ – the angular acceptance in (E_γ, $\cos\theta_{cm}$) bin;

N_γ – the number of primary photons in E_γ bin;

N_p – the number of protons in the target (in $1/cm^2$);

$\Delta\Omega$ – the solid-angle interval;

$\frac{\Gamma_{\pi^0\to 2\gamma}}{\Gamma_{total}}$ – the decay branching ratio.

The solid-angle interval is $\Delta\Omega = 2\pi\cdot\Delta(\cos\theta_{cm})$ where $\Delta(\cos\theta_{cm}) = 0.1$ gives the bin width of the angular distributions, subdividing $\cos\theta_{cm}$ into 20 bins. Photon-energy bins of 25 MeV were chosen for the 1.4-GeV data set. The 3.2-GeV data are presented in bins of about 50 MeV, 100 MeV and 200 MeV in the intervals $E_\gamma \in$ [750, 2300], [2300, 2600], [2600, 3000], respectively. In total, approximately 1500 experimental points were obtained.

From the differential cross sections, the total cross section was determined by integration. The integration was performed by summing over the differential cross sections and using extrapolated values from the fit for angular bins with no data. In the total cross section, shown in Fig. 3, clear peaks are observed for the first, second, and third resonance regions. The fourth resonance region exhibits a broad enhancement at W about 1900 MeV. The decomposition of the peaks into partial waves was based on a coupled-channel partial-wave analysis (PWA) in the framework of an isobar model. Resonances are described by Breit-Wigner amplitudes, except for strongly overlapping states which are described in K-matrix formalism. In total, the masses, widths, helicity ratios, and contributions to the cross section for π^0 photoproduction were determined for twelve N-resonances and for seven Δ-resonances as a result of such analysis.

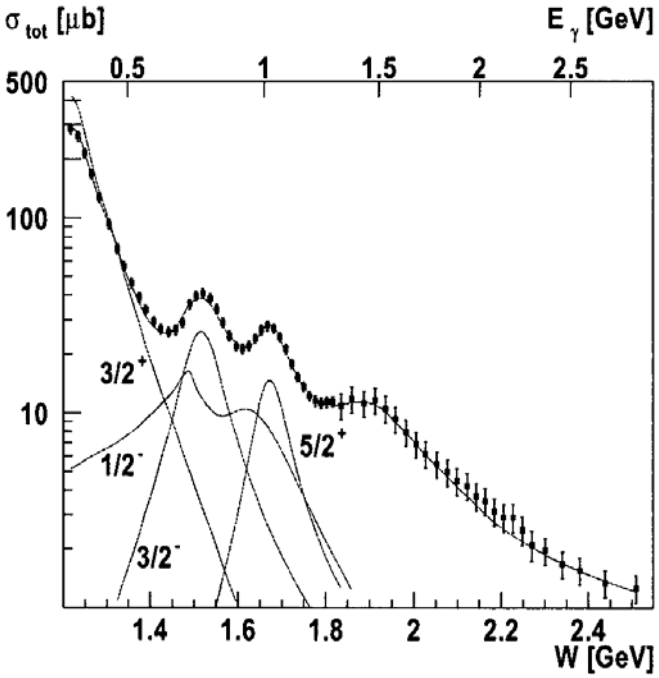

Fig. 3. Total cross section (logarithmic scale) for the reaction $\gamma p \to p\pi^0$ obtained by integration of angular distributions of the CB-ELSA data. The solid line represents the results of the PWA. Four individual contributions to the cross section are also shown

4. The reaction $\gamma p \to p\eta$

Differential cross sections of η photoproduction were determined [4, 5] in the run with primary electron energy of 3.2 GeV providing a total range of photon energies from the threshold (0.75 GeV) to 3 GeV. The η meson was reconstructed from two different modes of its decay: $\eta \to 2\gamma$ with BR = (39.4 ± 0.3)% and $\eta \to 3\pi^0 \to 6\gamma$ with BR = (32.5 ± 0.3)%. The 2γ invariant mass spectrum from events with two photons detected (after a kinematical fit to $\gamma p \to p\gamma\gamma$) and the $3\pi^0$ invariant mass distribution for events with six photons detected (after a kinematical fit to $\gamma p \to p3\pi^0$) are shown in the top part of Fig. 2. In both cases the η meson is observed above a small background which was subtracted in further processing.

The angular bin was chosen to be equal $\Delta(\cos\theta_{cm}) = 0.1$, photon-energy bins varied from 50 MeV at the lowest E_γ to 200 MeV at highest E_γ. The ratio $\eta \to 3\pi^0$ to $\eta \to 2\gamma$ was determined for each bin and histogrammed, giving $\Gamma_{\eta\to 3\pi^0}/\Gamma_{\eta\to 2\gamma} = 0.822 \pm 0.002_{stat} \pm 0.004_{syst}$. This value agrees well the Particle Data Group value and demonstrates the good understanding of the detector response. It is thus justified to add the data from the two channels $\eta \to 2\gamma$ and $\eta \to 3\pi^0 \to 6\gamma$. In total, approximately 700 experimental points were obtained.

The total cross section was determined by integrating the differential cross sections. The obtained total cross sections are shown in Fig. 4 *vs* photon energies in comparison with the results of earlier experiments. The new CB-ELSA data extends the covered angular and energy range significantly compared to previous measurements.

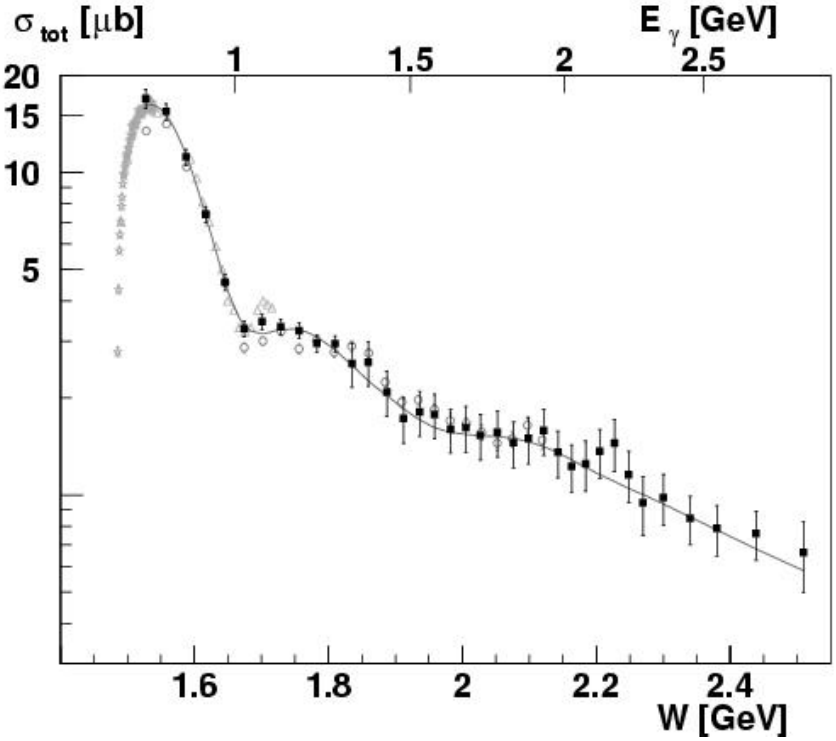

Fig. 4. Total cross section (logarithmic scale) for the reaction $\gamma p \to p\eta$ obtained by integration of angular distributions of the CB-ELSA data (squares) are shown in comparison with results of earlier experiments

The data obtained are interpreted using a coupled-channel PWA in the framework of an isobar model. This analysis determines parameters (masses, widths, and contributions to the total cross section) of eleven N resonances coupling to $N\eta$. A new state coupling strongly to the η-channel was found, an $D_{15}(2070)$ with a mass of 2068 ± 22 MeV/c^2 and a width of 295 ± 40 MeV/c^2. In addition, an indication for a possible new $D_{13}(2200)$ state with a mass of 2214 ± 28 MeV/c^2 and a width of 360 ± 55 MeV/c^2 was given also by this analysis. No evidence was found for a third S_{11} resonance for which claims have been reported at masses of 1780 MeV/c^2 and 1846 MeV/c^2.

5. The reaction $\gamma p \to p\pi^0\pi^0$

At higher energies, multi-meson final states play a role of increasing importance. Above 1900 MeV the spectrum and properties of resonances are rather badly known. Calculations showed that many of these states should have a strong coupling to $\Delta\pi$ and a non-vanishing coupling to γN and hence photoproduction experiments have a good chance to discover such states. Within different $\gamma\, p \to N\, 2\pi$ channels, the $\gamma p \to p\pi^0\pi^0$ channel is the one best suited to investigate the $\Delta\pi$ decay of baryon resonances. Compared to other isospin channels, many non-resonant "background" amplitudes do not contribute, and this leads to a high sensitivity of the $\gamma p \to p\pi^0\pi^0$ channel on baryon resonances decaying into $\Delta\pi$.

To investigate the reaction $\gamma p \to p\pi^0\pi^0$, events with 4 photons are selected [6]. In Fig. 5 the invariant $p\pi^0$-mass is shown for two $\sqrt{s}$-bins. At low $\sqrt{s}$ only a peak due to the $\Delta(1232)$ resonance is observed, at higher energies additional structures became visible. In addition to the $\Delta(1232)$, contributions from the D_{13} (1520) and a further state around 1660 MeV are observed. To extract the properties of contributing resonances from the data, a PWA has been performed. Resonances with different quantum numbers were

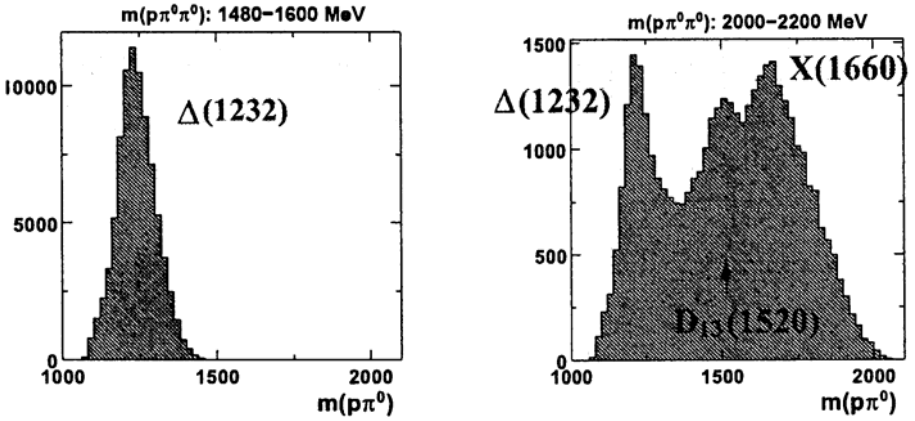

Fig. 5. $p\pi^0$ invariant mass for events with $\sqrt{s}$ = 1480–1600 MeV (left) and $\sqrt{s}$ = 2000–2200 MeV (right)

introduced in different combinations allowing for the following decay modes: $\Delta(1232)\pi$, $N(\pi\pi)_s$, $P_{11}(1440)\pi$, $D_{13}(1520)\pi$ and $X(1660)\pi$. The $\Delta(1232)$ resonance clearly dominates the $p\pi^0$ invariant mass. The PWA attributes most of these events to the $\gamma p \to D_{13}(1520) \to \Delta\pi$ amplitude. Another result of the PWA is the observation of baryon cascades.

Shown in Fig. 6 is the total cross section of the reaction $\gamma p \to p\pi^0\pi^0$ [7] for the two run periods with primary electron energies of 1.4 and 3.2 GeV. For comparison results of earlier measurements are given also. Our data confirms the cross section in the energy range between 700 and 1200 MeV and extends the energy range up to 3 GeV. Deviations are visible between 500 and 700 MeV and at energies above 1200 MeV.

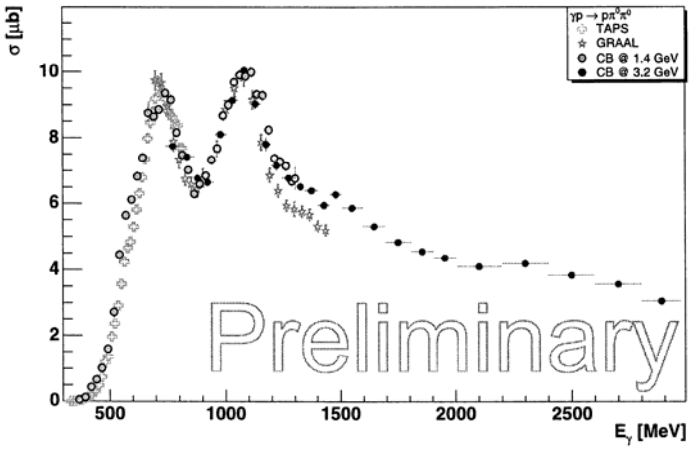

Fig. 6. Total cross section of the reaction $\gamma p \to p\pi^0\pi^0$ with statistical errors only

6. The reaction $\gamma p \to p\pi^0\eta$

The reaction $\gamma p \to p\pi^0\eta$ gives another interesting final state. Here, *e.g.*, the decay of Δ^* resonances into $\Delta\eta$ can be investigated. This decay had the advantage of being isospin selective; no N^* resonances can be produced.

This reaction is well suited to investigate the existence of the negative parity Δ^*-states around 1900 MeV/c^2. These states would, if they exist, pose a problem for quark model calculations because of their low mass. But so far an evidence for their existence is weak. Only one of the three states, the $D_{35}(1930)$, has 3 stars in the PDG notations. The 1-star $D_{33}(1940)$ resonance can decay with orbital angular momentum zero into $\Delta\eta$, which makes the $p\pi^0\eta$ final state a good place to investigate the existence of this resonance.

With the Crystal Barrel detector at ELSA this final state has been investigated from the threshold up to photon energy of 3 GeV [8]. In Fig. 7 the invariant $p\pi^0$-masses are shown for three $\sqrt{s}$-bins. The spectra may be explained by the $\Delta(1232)$ resonance which appears in each $\sqrt{s}$-bin, indicating possible decay mode *via* $\Delta(1232)\eta$. At two lower $\sqrt{s}$ the $\Delta(1232)\eta$ intermediate state could come from the sequential decay of the

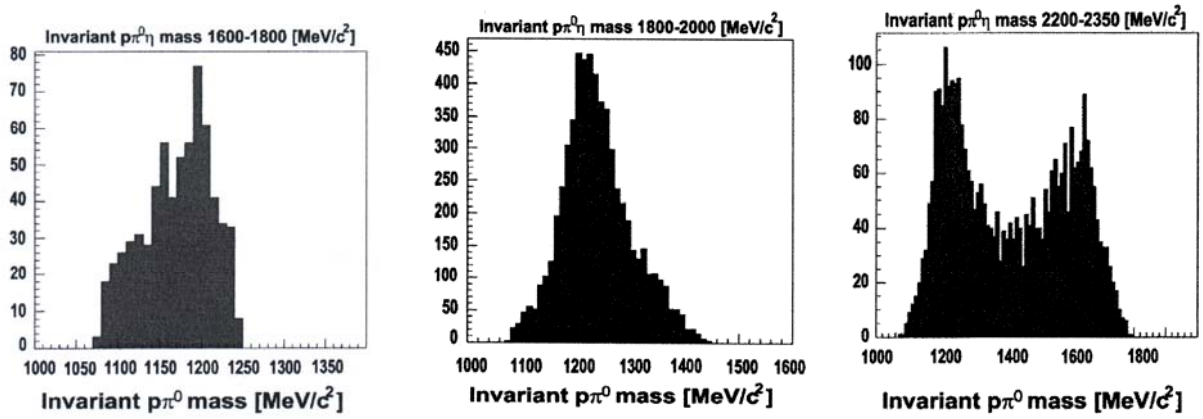

Fig. 7. $p\pi^0$ invariant mass for events with $\sqrt{s}$ = 1600–1800 MeV, $\sqrt{s}$ = 1800–2000 MeV and $\sqrt{s}$ = 2200–2300 MeV

negative parity $D_{33}(1940)$ resonance. In the third case, higher mass contributions at about 1600 MeV/c^2 become obvious in the $p\pi^0$ subsystem. In addition to the $\Delta(1232)$ resonance there are other interesting structures observed, such as the $a_0(980)$ in the $\pi^0\eta$ invariant mass or the $S_{11}(1535)$ in the Dalitz plot.

To extract the resonance contributions from the data a PWA of the $p\pi^0\eta$ final state has been performed. Three ambiguous solutions were found, which resulted in a similar likelihood being based, at the same time, on quite different sets of contributing amplitudes. All three solutions do need a $D_{33}(\approx 1900)$ state and show indications to baryon cascades

Figure 8 shows the total cross sections of the reactions $\gamma p \to p\pi^0\pi^0$ and $\gamma p \to p\pi^0\eta$. Above 2 GeV both cross sections are almost equal in magnitude.

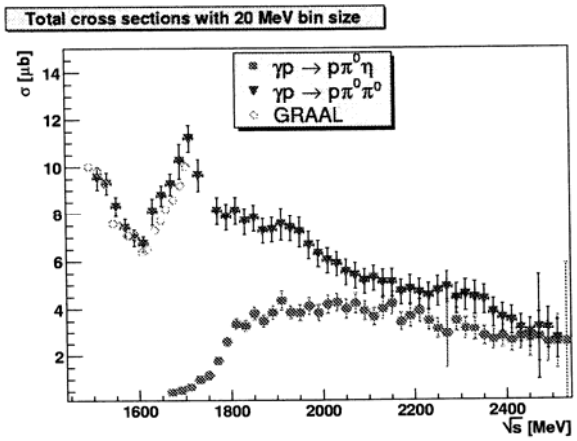

Fig. 8. Total cross sections of the reactions $\gamma p \to p\pi^0\pi^0$ and $\gamma p \to p\pi^0\eta$

7. Upgrade of experimental setup

At the next stage of experiments on photoproduction of neutral mesons, measurements of the double polarization parameters of reactions under study are planned. Such kind of measurements provide physicists with a unique information for identification of different baryonic states, especially in the region of overlapping resonances where "missing" baryonic states could be found.

These rather complicated experiments need both a beam of polarized photons and a polarized proton target. To realize this, the upgrade of the experimental setup was performed during 2005–2006. First of all, the Crystal Barrel was moved to another beam-line – Fig. 9. The tagging system installed earlier at this line was modified being equipped with 96 new scintillation counters (with overlapping scintillators of

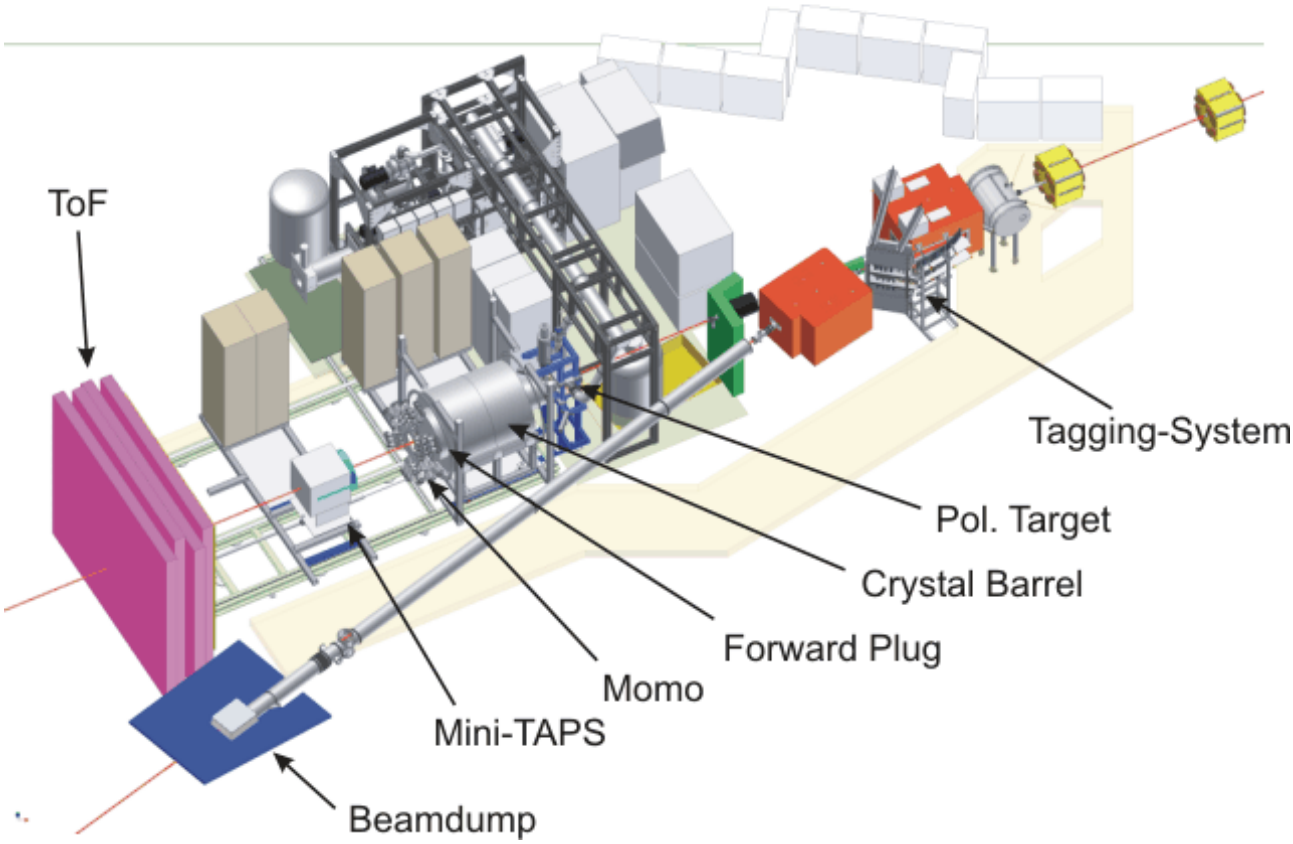

Fig. 9. Disposition of the experimental setup after its upgrading and replacing to another beam-line

varying width) and with an array of 480 scintillating fibres (two layers of 2 mm diameter fibres arranged with overlap). This will allow to tag photons with 18% to 95% of the incoming electron energy with an energy resolution between 0.2% and 2.2%. Linearly polarized photons will be produced by coherent bremsstrahlung at a 100 μm thick diamond crystal, circularly polarized photons – *via* incoherent bremsstrahlung of longitudinally polarized electrons off an amorphous radiator.

Displacement of the Crystal Barrel to another beam-line allowed to insert a longitudinally polarized proton target into the Crystal Barrel inner cavity and to arrange its operation in the "frozen spin" mode by locating a system of polarization "pumping" outside the Crystal Barrel. This system consists of a horizontal dilution refrigerator and a 5 T superconducting polarization magnet, which will be used in the polarization phase together with a microwave system for dynamical nuclear polarization. The polarization will be preserved in the "frozen spin" mode at temperature of about 50 mK by a very thin superconducting solenoid

located within the target cryostat, which will produce a 0.5 T longitudinal holding magnetic field. In general, maximum polarization of 90% is possible. The relaxation time of the target is in the order of 200 hours.

In order to have a possibility to detect photons and charged particles emitted from the target at small angles, the main detector of the setup – the multi-crystal photon spectrometer Crystal Barrel – was equipped in addition with two forward detectors (see Fig. 10) created specially for this purpose. One of them (so called Forward Plug) assembled of 90 CsI(Tl) crystals was inserted into the open forward cone of the Crystal Barrel for registering particles emitted at angles from 10° to 30° and, thus, for increasing the total covered solid angle. 180 overlapping veto-counters made of thin scintillators were placed in front of the CsI(Tl) crystals in order to determine the kind of particle (photon or proton) entering each crystal. Another forward detector (Mini-TAPS) is a "wall" consisting of 216 BaF_2 crystals and 216 veto-counters located in front of crystals; the central crystal was removed to make a hole for the photon beam. The Mini-TAPS registers particles (photons and protons) emitted at angles from 1° to 10°

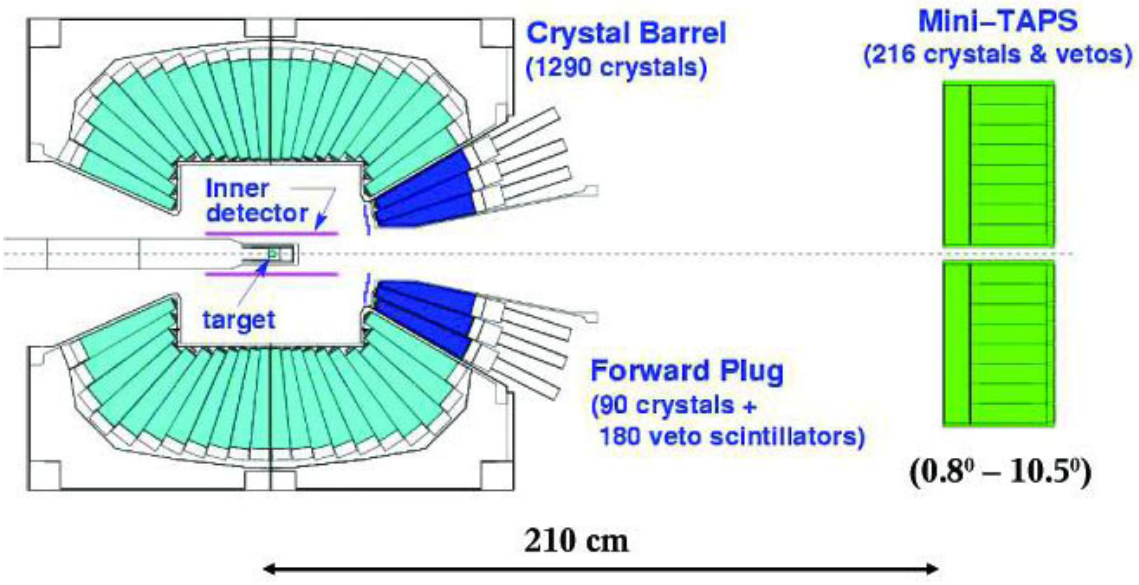

Fig. 10. Schematic drawing (cross section) of two forward detectors

The mostly essential PNPI contribution to the above described upgrade was manufacturing and tuning the system of veto-counters for the Forward Plug. In particular, 180 thin scintillators for these counters were manufactured at PNPI. In Bonn, PNPI physicists participated in assembling the whole system of veto-counters and in tuning the associated electronics.

The new series of experiments with the polarized proton target and polarized photons started in 2007.

References

1. D. Bayadilov *et al.*, Preprint PNPI-2520, Gatchina, 2003. 27 p.
2. O. Bartholomy, … , Yu.Beloglazov *et al.*, Phys. Rev. Lett. **94**, 012003 (2005).
3. H. van Pee, …, Yu. Beloglaziov *et al.*, Eur. Phys. J. A **31**, 61 (2007).
4. V. Crede, … , Yu. Beloglazov *et al*., Phys. Rev. Lett. **94**, 012004 (2005).
5. O. Bartholomy, … , Yu.Beloglazov *et al.*, Eur. Phys. J. A **33**, 133 (2007).
6. U. Thoma for the CB/ELSA Collaboration, in *Proceedings of the Workshop on the Physics of Excited Nucleons* (Tallahassee, USA, 12 – 15 October 2005), World Scientific Publishing Co., 2006, p. 108.
7. M. Fuchs for the CB/ELSA Collaboration, in *Proceedings of the Workshop on the Physics of Excited Nucleons* (Tallahassee, USA, 12 – 15 October 2005), World Scientific Publishing Co., 2006, p. 324.
8. V. Crede for the CB/ELSA Collaboration, in *Proceedings of the 10th International Conference on Hadron Spectroscopy* (Aschaffenburg, Germany, 31 August – 6 September 2003), AIP Conference Proceedings, **717**, 236 (2004).

STUDY OF BINARY $\pi^- p$ REACTIONS WITH NEUTRAL PARTICLES IN THE FINAL STATE AT THE PION CHANNEL OF THE PNPI SYNCHROCYCLOTRON

D.E. Bayadilov, Yu.A. Beloglazov, E.A. Filimonov, N.G. Kozlenko, S.P. Kruglov, I.V. Lopatin, D.V. Novinsky, A.K. Radkov, V.V. Sumachev

1. Introduction

During several years, the Meson Physics Laboratory performs at the pion channel of the PNPI synchrocyclotron a wide program of investigation pion-nucleon scattering in the region of low-lying πN resonances. At the first stages of this program, precision measurements of the differential cross sections, polarization parameters P and spin rotation parameters A and R were made for $\pi^{\pm} p$ elastic scattering at energies of incident pions in the range from 300 to 600 MeV (corresponding values of the incident pions momenta being from 417 to 725 MeV/c). In total, more than 400 new experimental points were obtained, which served – together with the results of experiments carried out at the Los-Alamos Meson Facility LAMRF – as a base of the new phase shift analysis PNPI-94. It became evidently in the course of performing this analysis that the mostly serious obstacle for determining phase shifts (and, consequently, partial amplitudes of πN scattering) with a higher precision is a lack of systematic data on $\pi^- p$ charge exchange scattering and η-production process. That is why the investigation of reactions $\pi^- p \to \pi^0 n$ and $\pi^- p \to \eta n$ has become a logical continuation of earlier experiments on the study of $\pi^{\pm} p$ elastic scattering.

For performing this new series of experiments, the Neutral Meson Spectrometer was designed and created at PNPI.

2. Neutral Meson Spectrometer

The main principle of the Neutral Meson Spectrometer (NMS) – determining the total energy of produced π^0 meson (η meson) E_{π° and the angle θ_{π° under which it produced on the base of measuring energies of two photons from the decay of π^0 meson (η meson) $E_{\gamma 1}$, $E_{\gamma 2}$ and angles of their emission $\theta_{\gamma 1}$, $\theta_{\gamma 2}$ (all values are in the lab. system):

$$E_{\pi^o} = \left[\frac{2M_{\pi^o}^2}{\left(1-\cos\Psi_{\gamma\gamma}\right)\cdot\left(1-X^2\right)} \right]^{1/2} , \qquad (1)$$

$X = (E_{\gamma 1} - E_{\gamma 2})/(E_{\gamma 1} + E_{\gamma 2})$ – the parameter which characterizes the sharing π^0 meson (η meson) energy among the two photons, $\Psi_{\gamma\gamma}$ – the angle between directions of emitted photons,

$$\cos\theta_{\pi^o} = \frac{E_{\gamma 1}\cos\theta_{\gamma 1} + E_{\gamma 2}\cos\theta_{\gamma 2}}{\left(E_{\gamma 1}^2 + E_{\gamma 2}^2 + 2E_{\gamma 1}E_{\gamma 2}\cos\Psi_{\gamma\gamma}\right)^{1/2}} . \qquad (2)$$

The schematic drawing of the NMS is shown in Fig. 1, the photo of its disposition at the experimental hall of PNPI synchrocyclotron is presented in Fig. 2. The NMS consists of two total absorption electromagnetic calorimeters, each being an array of 24 CsI(Na) crystals. The size of each crystal – $60 \times 60 \times 300$ mm^3; the last figure – thickness, it corresponds to 16.2 radiation lengths. Also shown (conditionally in Fig. 1) are a liquid hydrogen target and two veto counters intended for rejecting those events when a charged particle (but not a photon) enters the calorimeter.

For readout a pulse from each crystal, photomultiplier tubes (PMT) of type FEU-97 were used. For each of 48 PMTs a special stabilized high-voltage supplier was created the main principle of which is a voltage multiplication; each supplier was mounted directly on the PMT base. Signals from the output of each PMT were split – the anode signal was fed to a Charge-to-Digital Converter (CDC) and was used,

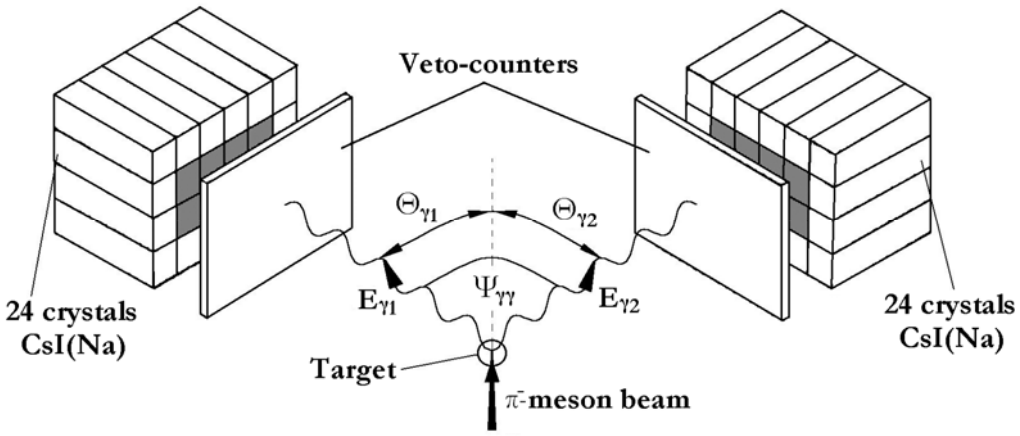

Fig. 1. Schematic drawing of the NMS

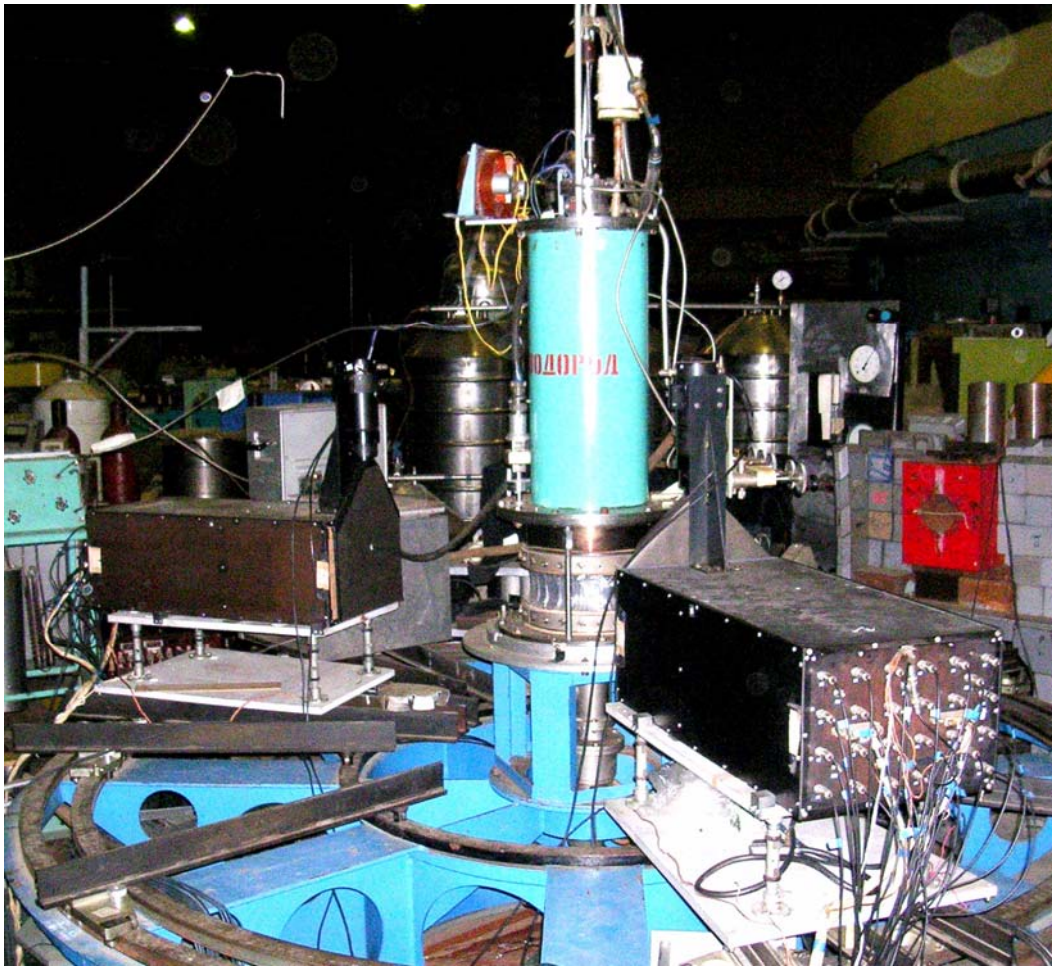

Fig. 2. General view of the experimental setup including the NMS and the liquid hydrogen target

consequently, for getting information about the energy deposited in the crystal, the signal from the last dynode was used for forming a fast trigger. In order to minimize an uncertainty in the determination of photon energy due a side leakage of the shower energy, the trigger was formed only in the case when energy deposited in eight inner crystals of each calorimeter exceeded some fixed value. For this purpose, dynode signals from 8 inner crystals were added up and after that the summed signal was fed to a shaper with the

threshold corresponding minimal required energy deposit. Surrounding 16 crystals played a role of somewhat like “guard ring” in which the shower energy carried out of central part of the calorimeter was registered.

The typical trigger to initiate a setup was formed as a coincidence of fast logical signals from the two calorimeters and from monitor counters provided there was no signal from veto counters placed in front of the calorimeters.

3. Energy calibration of spectrometer

In order from CDC readings one can determine the energy deposited in different crystals, it is necessary to perform the energy calibration of each chain crystal + PMT + CDC. In another words, it is necessary to find the dependence between the energy E_γ^i deposited in the crystal “*i*” and the number of corresponding CDC channel N_γ^i (after subtracting the pedestal which is located in the channel approximately 20). If this dependence is linear one (it will be shown below that it is actually so), E_γ и N_γ are connected by a simple proportion

$$E_\gamma^i = K^i N_\gamma^i, \tag{3}$$

and the task is to determine calibration coefficients K^i for all 48 chains crystal + PMT + CDC.

In principle, coefficient K^i can be determined by registering signals generated in the crystal due to the energy E_μ^i deposited by cosmic muons (*via* ionization losses) when traversing the crystal:

$$E_\mu^i = K^i N_\mu^i \ . \tag{4}$$

However, it is difficult to calculate the deposited energy E_μ^i with a high accuracy since the cosmic muons cross the crystal in different directions and their energy spectrum depends on the angle of incidence.

That is why for reliable determining the value E_μ^i a special experiment was carried out, in which several central crystals were irradiated by electrons; these electrons are available in the beam of negatively charged particles formed by the pion channel of the PNPI synchrocyclotron. To select electrons in the beam from pions we used a gas Cherenkov counter filled with CO_2 at 4 atm pressure; the counter was placed in the beam line just upstream of the liquid hydrogen target. During the calibration procedure, a narrow electron beam (defined by a small counter with the 2 cm diameter scintillator) was injected into the center of the crystal under investigation. The calibration was made at electron energies of 70, 120, 200, 300, 400, and 500 MeV. For each energy a position of a peak in the pulse height spectrum was determined. Because the lateral spreading of the electromagnetic shower a part of energy leaks from the injected crystal, so the energy deposited in this crystal is less than the energy of the incident electron. Corresponding correction was calculated using a Monte Carlo simulation, its value is about 15%. After introducing this correction, the positions of peaks in the pulse height spectra (measured in CDC channels) were plotted against the energy deposited in the crystal. Obtained dependence is described with a good accuracy by a straight line the slope of which determines the value of calibration coefficient K^i [1]. If we use now this dependence for determining the energy deposit corresponding to the number of CDC channel N_μ^i, we shall obtain $E_\mu^i = 36$ MeV. The similar result was obtained for all four central crystal irradiated by electrons.

Thus, the calibration coefficient is defined by the relation

$$K^i = 36 / N_\mu^i . \tag{5}$$

Just this coefficient K^i is used for determining the energy deposited in the crystal “*i*” in case when photon enters this crystal:

$$E_\gamma^i = K^i N_\gamma^i = (36 / N_\mu^i) \cdot N_\gamma^i . \tag{6}$$

---

[1] Since at rather high energies electromagnetic showers initiated by photons and by electrons develop in the matter almost identically, this coefficient may be considered equal to the coefficient K^i in the formula (3).

4. Measurements of differential cross sections of $\pi^- p$ charge exchange scattering at small angles

The first experiment [1–3] carried out using the NMS was aimed at measurements of differential cross sections of $\pi^- p$ charge exchange scattering $\pi^- p \to \pi^0 n$ at small angles. The measurements were made at ten momenta of incident pions in the range from 417 to 710 MeV/c (corresponding values of kinetic energy of pions – from 300 to 585 MeV); at each momentum the data acquisition was performed for both a hydrogen-filled and an empty target. A momentum distribution in the incident beam had the Gaussian form, the full width at half-maximum being 6%. The central value of the momentum was determined by readings of a Hall probe placed at the gap of the last bending magnet of the π-meson channel and was known with an accuracy of ±0.5%. The flux of pions incident on the target was about 10^5 1/s.

When carrying out the experiment, for each event energies and emission angles of two photons from the decay $\pi^0 \to \gamma\gamma$ were measured; after that the angle, at which π^0 meson was produced in the laboratory frame, could be determined using the relation (2). The main feature of the decay $\pi^0 \to \gamma\gamma$ is that it occurs with the most probability symmetrically in respect to the direction of π^0 meson. Since it was proposed in this experiment to detect only events with small scattering angles (*i. e.* small angles between the directions of produced π^0 mesons and incident pions), it is evidently that the two calorimeters of the NMS should be placed symmetrically (on the right and on the left) relatively to the beam axis. For the momenta of incident pions in the range from 417 to 710 MeV/c, π^0 mesons produced at small angles have the kinetic energy from 300 to 590 MeV, respectively; the angle between the two photons emitted symmetrically in respect to the direction of π^0 meson varies from 18° to 11°. Having this in mind and taking into account the size and construction of the NMS, we located the calorimeters at angles ±16° relatively to the beam axis; a distance from the center of the target to faces of the calorimeters was 101 cm.

To identify that in the considered event with two registered photons just π^0 meson was produced, the invariant mass of these two photons should be reconstructed; it must be equal to the rest mass of π^0 meson. The energies $E_{\gamma 1}$, $E_{\gamma 2}$ of both photons and the angle $\Psi_{\gamma\gamma}$ between them being known on the base equations (1) and (2), the invariant mass of the two photons can be calculated by formula:

$$M_{\gamma\gamma}^2 = 2E_{\gamma 1}E_{\gamma 2}(1-\cos\psi_{\gamma\gamma}). \tag{7}$$

As an example, in Fig. 3 the distribution of events by the invariant mass of the two photons is shown for the momentum of the incident pions 614 MeV/c. A clear peak corresponding to the π^0 meson mass is seen.

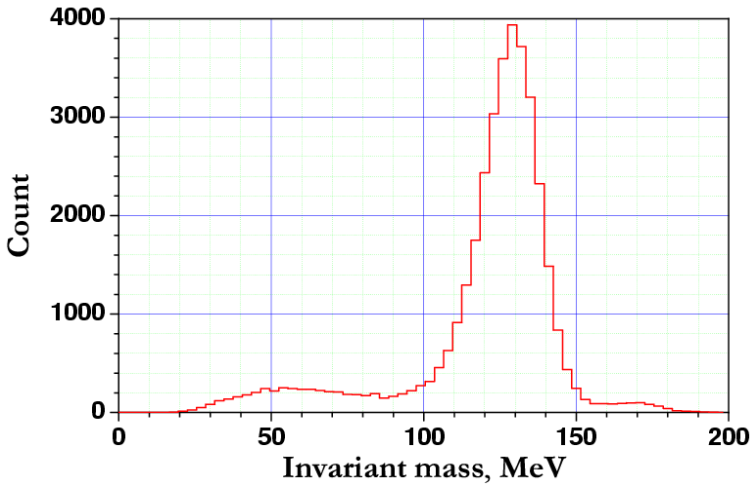

Fig. 3. Invariant $\gamma\gamma$-mass distribution for the incident pion momentum of 614 MeV/c

After the invariant mass is calculated, the next step of processing is the reconstruction of the missing mass. For the reaction $\pi^- p \to \pi^0 n$ it is the mass of the recoil neutron. For the analysis of accumulated data it is convenient to plot a two-dimensional distribution of events – the correlation between the missing mass and

the invariant mass; Fig. 4 illustrates a character of such distribution. Events caused by the charge exchange (CEX) reaction on the target's protons are concentrated in this Figure inside a dark spot of elliptical form. Also seen are background events due to the CEX reaction on nuclei of a monitor counter and of a mylar foil closing target's windows (points in the left upper part) as well as to the reaction of two π^0 production.

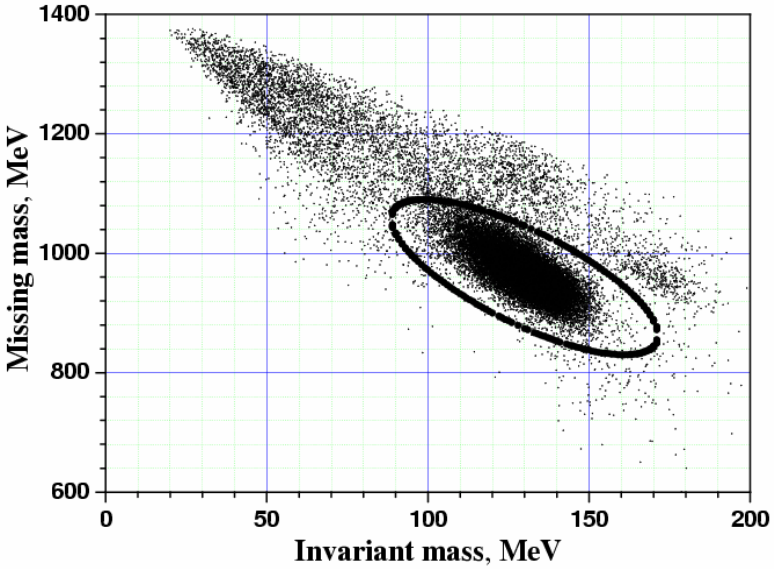

Fig. 4. Two-dimensional plot missing mass *vs* invariant mass for the incident pions momentum of 614 MeV/c

In further processing, only those events were considered "useful" (*i. e.* caused by the CEX reaction on protons of the target) which lay within the ellipse shown in Fig. 4. Using a Monte Carlo simulation, the correct shape and size of the ellipse were chosen so that 99% of all "useful" events were within this ellipse.

The "useful" events registered by the NMS cover the angular range from $\cos\theta^{cm}_{\pi^0}$=0.98 to $\cos\theta^{cm}_{\pi^0}$=1.00. To calculate differential cross sections, it is necessary to determine the angular distribution of these events. When plotting such distribution, the value of one angular bin was chosen to be equal $\Delta\cos\theta^{cm}_{\pi^0}$=0.002 taking into account the angular resolution of the NMS.

The differential cross section was calculated for each angular bin using the equation:

$$\frac{d\sigma^{cm}}{d\Omega} = \frac{N_{\pi^0}}{N_{\pi^-}\cdot A\cdot N_p\cdot 2\pi\cdot\Delta\cos\theta^{cm}\cdot BR(\pi^0\to 2\gamma)}. \qquad (8)$$

Notations in this expression are as follows. N_{π^0} is the number of π^0 mesons produced in the reaction $\pi^-p\to\pi^0 n$, which are detected by the NMS during the experiment; N_{π^-} is the number of pions passed through the target in the course of the experiment; N_p is the number of protons in the target per cm^2; A is the angular acceptance obtained by a Monte Carlo simulation for the definite angular interval $\Delta\cos\theta^{cm}_{\pi^0}$; $2\pi\cdot\Delta\cos\theta^{cm}_{\pi^0}$ is the covered c.m.s. solid angle; $BR\ (\pi^0\to 2\gamma)$ is the branching ratio of the decay $\pi^0\to 2\gamma$ equal to (98.80 ± 0.03)%. It should be mentioned here that in the beam formed by the pion channel there exists also an admixture of muons and electrons, and an appropriate correction has to be introduced into the monitor counts when determining the number N_{π^-}.

As an example, the angular dependence of the differential cross section for the incident pions momentum of 614 MeV/c is presented in Fig. 5. One can see that the angular dependence is very weak in this range.

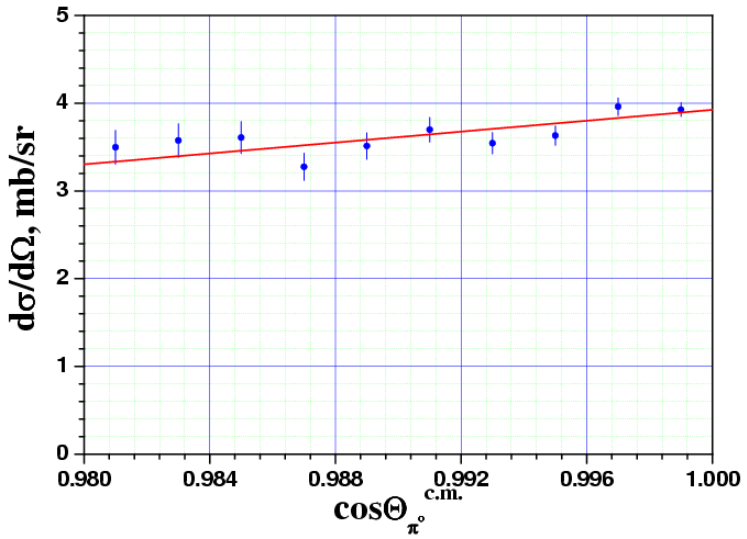

Fig. 5. Angular dependence of differential cross section for the incident pions momentum of 614 MeV/c

The value of differential cross section at zero degree was obtained by the extrapolation of this angular dependence to the point $\cos\theta_{\pi^0}^{cm}$=1.00. To do it, we used the least squares method in a linear approximation.

In Fig. 6 the obtained values $\frac{d\sigma}{d\Omega}(0^\circ)$ are plotted as a function of the incident pions momentum. Also shown are the results of previous experiments and the predictions of the partial-wave analyses (PWA) KH-80 (Karlsruhe-Helsinki) and SM-02 (the George Washington University, USA). One can see that our experiment is the mostly full and essentially more precision in the range of the incident pions momenta from 417 to 710 MeV/c. Experimental points obtained at PNPI have statistical uncertainties at a level of 2% exceeding significantly an accuracy of other experiments. The comparison with the predictions of different PWAs demonstrates that the new data obtained does not agree fully with the shown PWA predictions, although when comparing the momentum dependences some preference can be given to the PWA SM-02.

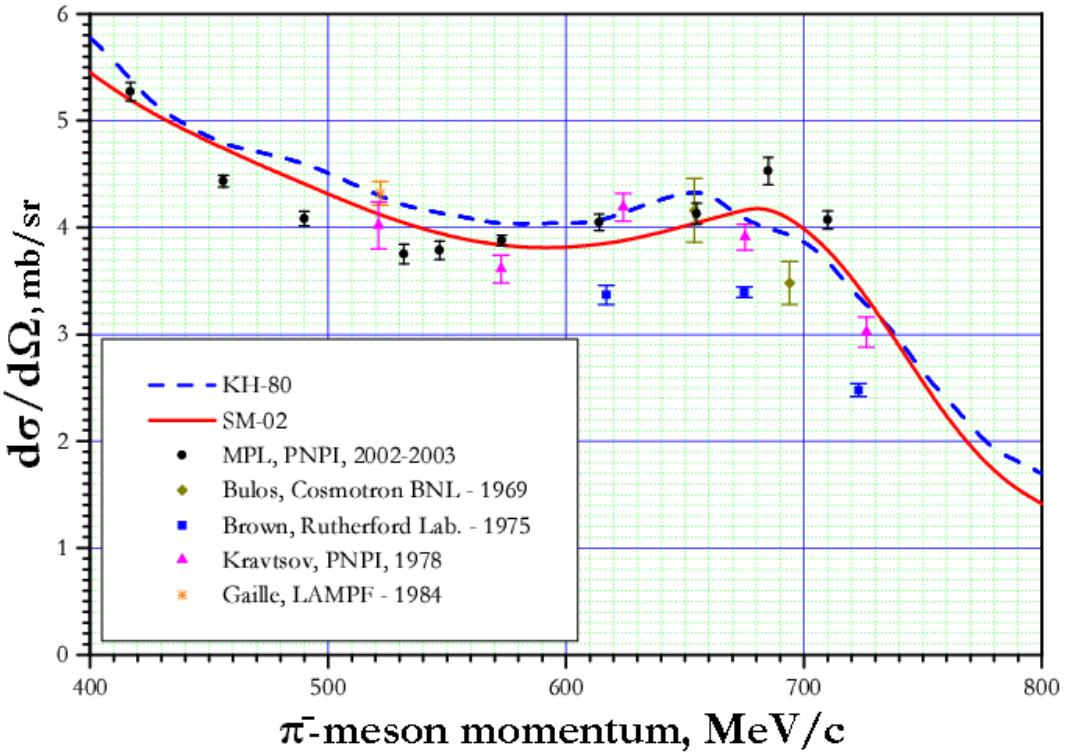

Fig. 6. Experimental results of this work (black circles) are given in comparison with data of previous experiments

5. Measurement of cross sections of the η-production process in the near-threshold region

In the next series of experiments, the NMS is used [4, 5] for measuring the cross section of the η-production in the reaction $\pi^- p \to \eta n$ at the incident pions momenta close to the threshold of this reaction (685 MeV/c). Since the cross section of this reaction rises sharply with the momentum in the near-threshold region, the momentum spread of particles in the beam was decreased down to 1.5% by putting a special vertical narrow beam slit in that part of the pion channel where the momentum dispersion is maximal.

The experimental layout was similar to that used for studying $\pi^- p$ charge exchange scattering at small angles, the main distinction – the calorimeters were placed at the distance 65 cm from the target center at the angles ±66° relatively to the pion beam axis – was dictated by the specific kinematics of the η-production process in the near-threshold region. The main peculiarity is that η mesons, which produced in the center-of-mass system in a wide angular range from $\theta_\eta^{cm} = 0°$ to $\theta_\eta^{cm} = 180°$, concentrate in a narrow angular cone after transferring to the laboratory system. So, at the incident pions momentum of 710 MeV/c the opening angle of this cone is ±23.5°. In the subsequent η-decay $\eta \to 2\gamma$, photons are emitted in the angular range from 0° to 180° (relatively to the momentum of the η meson), but their symmetrical emission ($\theta_{\gamma 1} \approx \theta_{\gamma 2}$) is mostly probable. These kinematical features allow to measure the differential cross sections of the reaction $\pi^- p \to \eta n$ in the full angular range from $\theta_\eta^{cm} = 0°$ to $\theta_\eta^{cm} = 180°$ using the NMS with a rather restricted angular acceptance.

In the course of the experiment on studying the reaction $\pi^- p \to \eta n$ the NMS detects in coincidence two photons produced after the η-decay. However the η meson can decay not only by the channel $\eta \to 2\gamma$ with the branching ratio BR=(39.38 ± 0.26)% but also by the channel $\eta \to 3\pi^0 \to 6\gamma$ with BR=(32.51 ± 0.28)%. The Monte Carlo simulation of the experiment shows that the most effective method of selecting events of the η-production process with the subsequent decay $\eta \to 2\gamma$ is to use the two-dimensional distribution in which the energy $E_{\gamma 1}$ deposited in one calorimeter is plotted *vs* the energy $E_{\gamma 2}$ deposited in another calorimeter. The result of such simulation is demonstrated in Fig. 7. A "banana"-shape spot clearly seen at photon energies from 200 to 400 MeV is due to photons from the decay $\eta \to 2\gamma$. On the base of such distribution cuts were chosen later on for the selection of "useful" events (*i. e.* events attributed to the η-production process with the subsequent decay $\eta \to 2\gamma$) – these cuts are shown in Fig. 7 as an ellipse within which 99% of the "useful" events are contained.

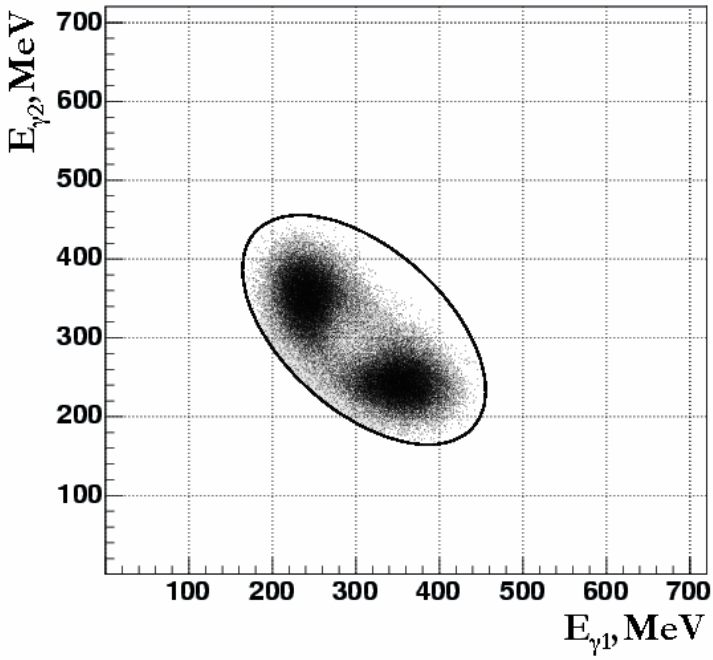

Fig. 7. Two-dimensional distribution $E_{\gamma 1}$ *vs* $E_{\gamma 2}$ obtained by the Monte Carlo simulation

Just such ellipse-shape cut was put after that on the similar two-dimensional distribution of real events obtained in the experiment. And all events inside this ellipse were considered to be "hydrogen" ones. Then the full angular range (from $\cos\theta_\eta^{cm} = -1$ to $\cos\theta_\eta^{cm} = +1$) was divided into 10 bins $\Delta\cos\theta_\eta^{cm} = 0.2$ and the differential cross sections for each bin were calculated using the formula similar (8).

The differential cross sections of the reaction $\pi^- p \to \eta n$ measured at the incident pions momenta of 700, 710, and 720 MeV/c are presented in Fig. 8. Shapes of the differential cross sections distinguish essentially

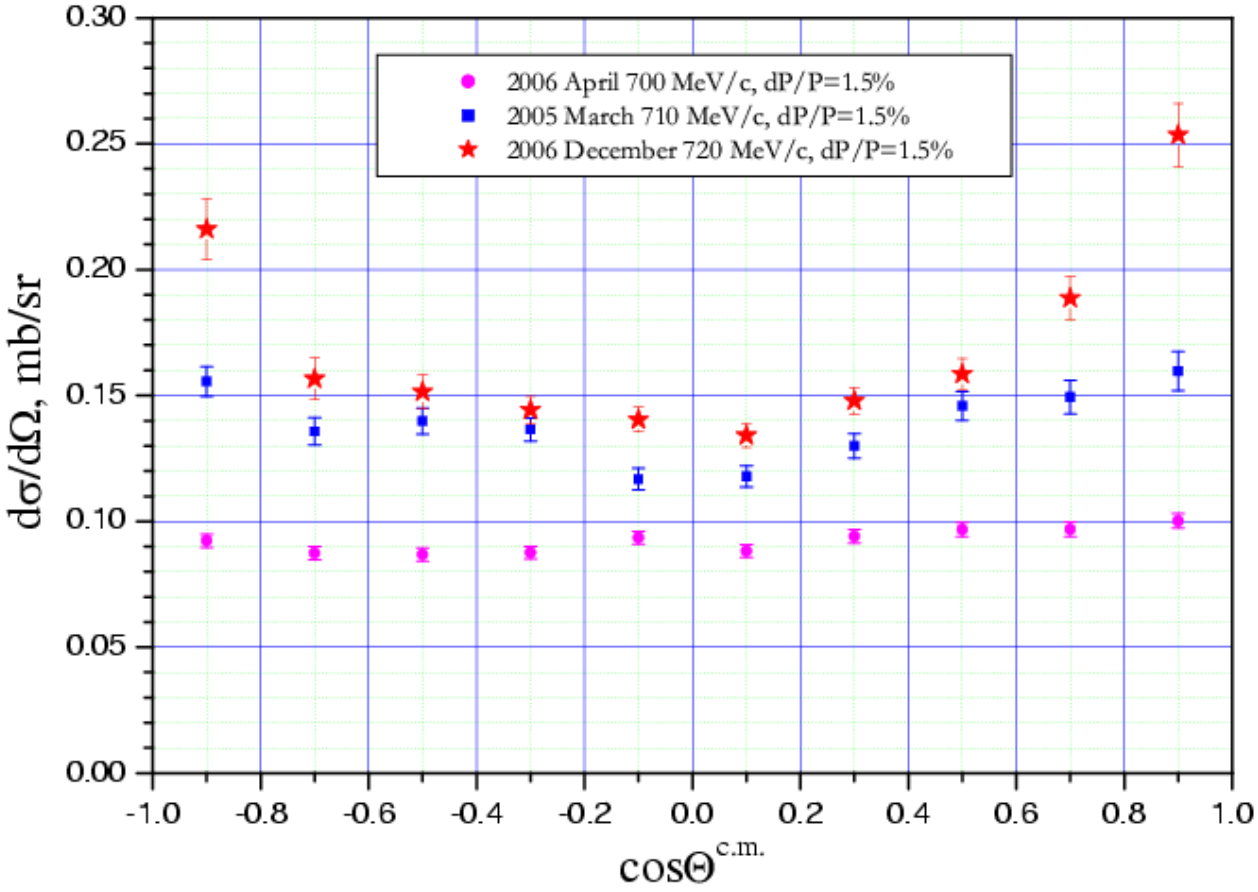

Fig. 8. Differential cross sections of the reaction $\pi^- p \to \eta n$ measured using the Neutral Meson Spectrometer

at different momenta – if at 700 MeV/c the angular dependence is practically flat, at 710 and 720 MeV/c it looks like a bowl profile. It may be considered as an evidence that at the momentum of 700 MeV/c only *S*-wave plays a role in the η-production process (*i.e.* this process goes through the formation of the $S_{11}(1535)$ resonance) but at higher momenta the contribution of *D*-wave became essential – it means that the η-production process goes partly through the formation of the $D_{13}(1520)$ resonance.

References

1. D.E. Bayadilov *et al.*, Preprint PNPI-2530, Gatchina, 2003. 20 p.
2. D.E. Bayadilov *et al.*, in *Proceedings of the 10th International Conference on Hadron Spectroscopy* (Aschaffenburg, Germany, 31 August – 6 September 2003), AIP Conference Proceedings **717**, 270 (2004).
3. D.E. Bayadilov *et al.*, Yad. Fiz. **67**, 512 (2004) [Phys. Atom. Nucl. **67**, 493 (2004)].
4. D.E. Bayadilov *et al.*, Preprint PNPI-2612, Gatchina, 2005. 34 p.
5. D.E. Bayadilov *et al.*, Preprint PNPI-2719, Gatchina, 2007. 13 p.

MEASUREMENT OF THE SPIN ROTATION PARAMETERS *A* AND *R* IN πp ELASTIC SCATTERING AT THE PION CHANNEL OF THE ITEP ACCELERATOR

PNPI participants of the PNPI-ITEP collaboration:
A.I. Kovalev, S.P. Kruglov, D.V. Novinsky, V.A. Shchedrov, V.V. Sumachev, V.Yu. Trautman

1. Introduction

This experiment is from the series of the spin rotation parameter measurements performed by the PNPI-ITEP collaboration during the last decade [1–5]. The main goal of this studies was to enrich the experimental data base of partial-wave analyses (PWA) with qualitatively new information on the spin rotation parameters, which have never been measured in the incident pion momentum interval under consideration.

2. Formalism

The importance of measurements of the *A* and *R* spin rotation parameters becomes clear from the expressions below, where the observed parameters are expressed in terms of the complex spin-nonflip amplitude *f* and spin-flip amplitude *g*:

$$F = f + ig\,(\boldsymbol{\sigma}\boldsymbol{n}),$$

where $\boldsymbol{\sigma}$ is the Pauli spin operator, $\boldsymbol{n}$ is a unit vector normal to the scattering plane. The relations connecting the observables with the amplitudes *f* and *g* have the following form:

$$d\sigma/d\Omega = |f|^2 + |g|^2,$$

$$P = \frac{1}{|f|^2 + |g|^2}\, 2\,\mathrm{Im}(f g^*),$$

$$R = \frac{1}{|f|^2 + |g|^2}\left[(|f|^2 - |g|^2)\cdot\cos(\theta_p^{cm} - \theta_p^{\ell ab}) + 2\,\mathrm{Re}(fg^*)\cdot\sin(\theta_p^{cm} - \theta_p^{\ell ab})\right],$$

$$A = \frac{1}{|f|^2 + |g|^2}\left[(|f|^2 - |g|^2)\cdot\sin(\theta_p^{cm} - \theta_p^{\ell ab}) - 2\,\mathrm{Re}(fg^{\bullet})\cdot\cos(\theta_p^{cm} - \theta_p^{\ell ab})\right],$$

where θ_p^{cm} and θ_p^{lab} are the angles of the recoil proton emission in the center-of-mass system and in the laboratory system, respectively. The parameters *A*, *R*, *P* are connected by the quadratic equation:

$$A^2 + R^2 + P^2 = 1.$$

3. Experimental layout

To determine the spin rotation parameters *A* and *R* in $\pi^{\pm}p$ elastic scattering, it is necessary to measure the polarization of the recoil protons produced by pions on a proton target polarized in the scattering plane. The polarization of the recoil protons is measured through the asymmetry of their secondary scattering on nuclei of a substance with known analyzing power (usually carbon).

The apparatus is shown in Fig. 1. Its basic elements are:

(i) polarized proton target (PT);
(ii) proton polarimeter including carbon filter (C), four sets of magnetostrictive chambers (MSC) to detect the recoil proton before and four sets of MSC to detect the recoil proton after *p*C-scattering;
(iii) six sets of MSC to detect the scattered pions;
(iv) six pion beam MSCs ;
(v) scintillation counters C1-C9 to provide the trigger and to identify pions in the beam by the time of flight.

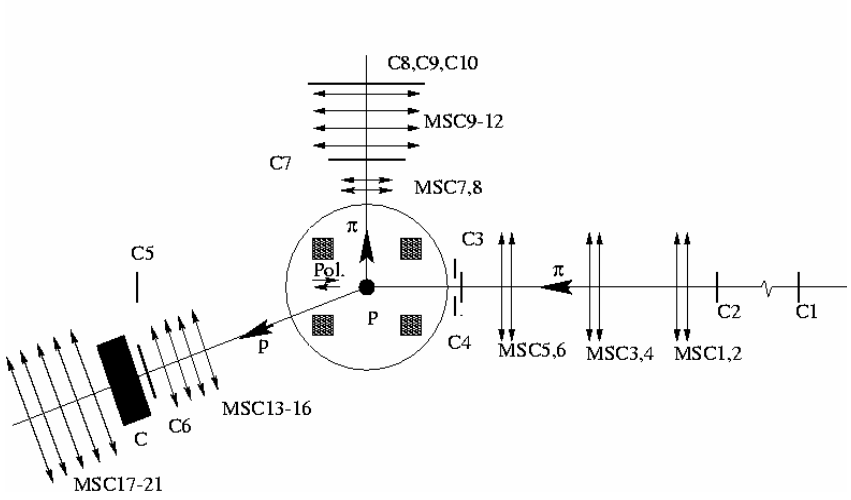

Fig. 1. Experimental setup for the spin rotation parameter *A* and *R* measurement

3.1. Polarized target

The polarized proton target with arbitrary spin orientation in the horizontal plane has been built at PNPI especially for the measurements of the spin rotation parameters in πp elastic scattering (Fig. 2.). A container filled with the target material (propanediole $C_3H_8O_2$ doped by Cr^V complexes) is placed into magnetic field of 2.5 T created by a Helmholtz pair of superconductive coils[1].

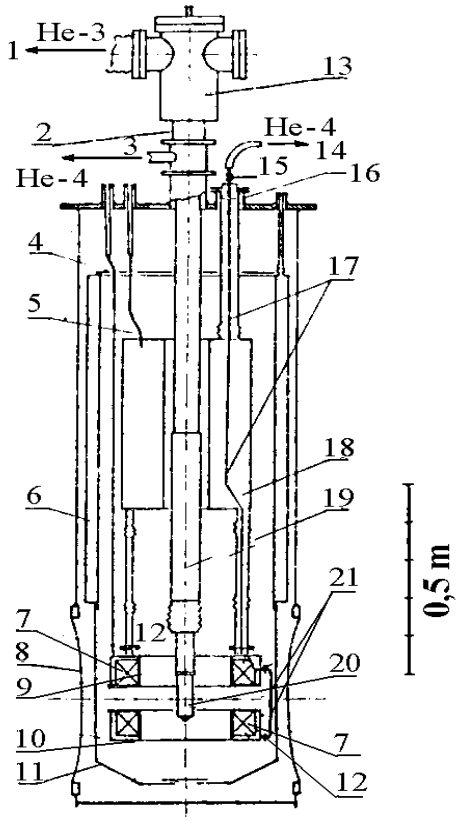

Fig. 2. Target in the vertical sectional view

3 – helium-4 pump-out
4, 11 – nitrogen screens
5, 21 – helium inputs
6 – nitrogen tank
7 – magnet
8 – window
9 – magnet frame
10 – housing
12 – indium compaction
13 – rotating tee-joint
14 – helium-4 output through current-input
15 – connection to current source
16 – current-input compaction and helium-4 output
17 – current input
18 – helium tank (at 4.2 K)
19 – refrigerator
20 – appendix with target matter ($C_3H_8O_2$)

[1] E.I. Bunyatova *et al*., Preprint LNPI-1191, Leningrad, 1986.

The container has a cylindrical form with vertical size and diameter of 30 mm × 30 mm. Cooling of the target down to 0.5K is provided by an evaporation-type ^{3}He-cryostat.The polarization is pumped by the dynamic nuclear orientation method up to the absolute value of 70–80% with an uncertainty of 1.5%. The method of nuclear magnetic resonance (NMR) is used for measuring the polarization value. These measurements are based on the calculations of area under the NMR curve. The equipment (Fig. 3) is calibrated on the equilibrium target polarization at temperature of 0.8 K. To measure the area under the NMR curve the system containing *Q*-meter with sequential contour, analogous integral-synchronize detector and digital device made in CAMAC standard was used.

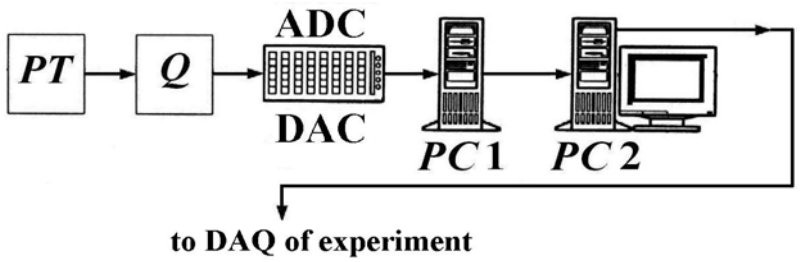

Fig. 3. Electronics for measuring the polarization value

3.2. Recoil proton polarimeter

The recoil proton polarimeter consists of two sets of MS chambers (four chambers in each set) and a carbon block in between. The accuracy of determination of the secondary scattering angle is near 1°.

For realization of present experiment, it is necessary to have a possibility to measure the normal components of recoil proton polarization in the proton energy range from 100 to 1600 MeV and to know the *p*C analyzing power in this energy region. The PNPI-ITEP collaboration performed the associated investigations. At the first step the existing world experimental data were collected and *p*C analyzing power has been systematized[2] as a function of proton scattering angle θ_{pC}, proton kinetic energy T_p and energy losses in the process of *p*C-scattering in the investigated energy range. At the next step the *p*C analyzing power for polarized protons has been experimentally measured[3] by the PNPI-ITEP collaboration for proton beam momenta of 1.36, 1.60, 1.78 and 2.02 GeV/c and for carbon scatterer thicknesses of 4.9, 19.4 and 36.5 g/cm^2. These data have been compared with previous results and used to fit analyzing power obtained for various proton energies and scattering angles. For measurements of the spin rotation parameters *A* and *R* the thickness of carbon blocks should be optimized in accordance with the recoil proton energy and range.

The purity of the carbon (graphite GMZ) in current use is 99.9%.

3.3. Scattered pion registration

Scattered pions are registered by the set of six two-coordinate MS chambers. Two chambers are placed immediately near the polarized target and four chambers out of the magnetic field of the target solenoid. The sensitive area of each module is 400 × 600 mm^2. The expected coordinate accuracy is near 0.5 mm.

3.3. Beam MS chambers

The pion beam of ITEP synchrotron has intensity up to 10^6 π/sec. On this account six MS chambers are used for the determination of beam pion direction.

3.4. Scintillation counters and trigger

The scintillation counters use the photomultiplier tubes FEU-97. The polystyrene is used as scintillation material. The sizes of the counter scintillators are defined by the pion beam sizes and by the acceptance

[2] N.G. Kozlenko *et al.*, Preprint PNPI-2145, St.-Petersburg, 1997.
[3] I.G. Alekseev *et al.*, Nucl. Instr. Meth. A **434**, 254 (1999).

angles for the scattered pions and recoil protons. Scintillation counters are C1–C9 (see Fig. 1). Beam is defined by counters C1, C2, C3 and C4. A veto counter C5 excludes non-scattered beam particles. The recoil protons in the polarimeter and the scattered pions are specified by counters C6 and C7, C8, C9, respectively.

The trigger pulse that initiates readout from MS chambers is generated by coincidence of counter signals: C1×C2×C3×C6×C7×(C8+C9) and anticoincidence of counters C4 and C5 signals.

3.5. Electronics

The electronics of this experiment includes:
– trigger signal from the scintillation counters;
– data from the Personal Computer handling the polarized target;
– electronics and its power supply for the MSC signal digitization.

The trigger production makes a start of the experimental setup. Each event includes the next information:
– beam particle coordinates;
– coordinates of the particles which passed through the polarimeter;
– scattered pion coordinates;
– information about the target polarization.

The event information is analyzed to make a preliminary data selection and to estimate at real-time the setup efficiency.

4. Data processing

The processing of the data is performed at three steps:
(i) The second scattering events in the polarimeter are analyzed and their (second) vertex and other parameters are determined. The events with recoil proton-carbon scattering angle 6°–20° are selected for further processing. From them only those events are taken for which all the azimuthal angles are allowed by the MS chambers geometry. The proton energy T_2 at the second vertex is calculated for each event and the analyzing power P_C is obtained from the empirical expression $P_C = f(T_2,\theta)$ which has been fitted to all available data on proton-carbon scattering between 100 and 1600 MeV.
(ii) The first scattering is reconstructed and the elastic events on free protons of the target are selected. Since trajectories of both particles are bent by the magnetic field of the polarized target and their momenta (and, hence, the curvatures of the trajectories) are not known beforehand, an iteration method is used for the reconstruction of the first vertex. The kinematical criteria of coplanarity and of correlation between polar angles of the scattered pions and the recoil protons are used for the selection. The background of quasi-elastic events on bound protons of target nuclei is known to be (from our previous measurements) not more than 20–30%, and it is taken into account in the data processing.
(iii) The selected events are divided into several angular bins corresponding approximately to $\Delta\cos\theta^{cm} = 0.1$ and in each bin the values of the polarization parameters A, P, R are calculated. The method of the maximum likelihood is used in this calculation. The experimental errors are defined according to the method described J. Bystricky *et al.* – see footnote [4].

At this processing one of two spin rotation parameters (A or R) and, respectively, the absolute value ($|R|$ or $|A|$) of another parameter are defined. Simultaneously the polarization parameter P value is obtained to compare with the existing data to estimate roughly systematical errors.

5. Results and systematic errors

Results of measurement of the parameters A and P for $\pi^- p$ elastic scattering at 1.43 MeV/c [5] are presented in Table and in Fig. 4.

The most important sources of the A parameter systematic errors are the uncertainties in the polarimeter analyzing power (~ 4%) and in the measurement of the target polarization (~2%). The contribution of the

[4] J. Bystricky *et al.*, Nuovo Cim. A **1**, 601 (1971).

background polarization is negligible. This fact was checked by varying the value of the background polarization from 0 to the normal polarization in πp elastic scattering. The final value of the ratio of the background polarization to the normal polarization in πp elastic scattering was taken equal to 0.7, similar to the ratio of polarizations in the elastic and quasi-elastic pp scattering (see footnote [3]).

The combined estimate for the systematic error of the A parameter is ~8%.

As it was stressed above, there are no ways to eliminate the false asymmetry in the direction of the P parameter measurement ($\varphi_2 = 0, \pi$ plane) using our experimental data. Consequently, the systematic error of P cannot be reliably evaluated. Thus the results on this parameter can be used only for qualitative comparison with the main features of PWA solutions, for example: strong angular dependence, angular position of the polarization minimum and the value at the minimum close to –1.

Table

Polarization parameter A and P in the $\pi^- p$ elastic scattering at 1.43 GeV/c

$\Delta\theta$, degrees	θ_{mean}	A	ΔA	P	ΔP	N_{events}
155.0–162.2	160.4	–0.152	0.251	–1.150	0.166	2355
162.2–165.6	163.9	–0.360	0.260	–1.039	0.170	2259
165.6–172.0	167.4	–0.131	0.264	–0.501	0.175	2163
155.0–172.0		–0.219	0.149	–0.91	0.10	6787

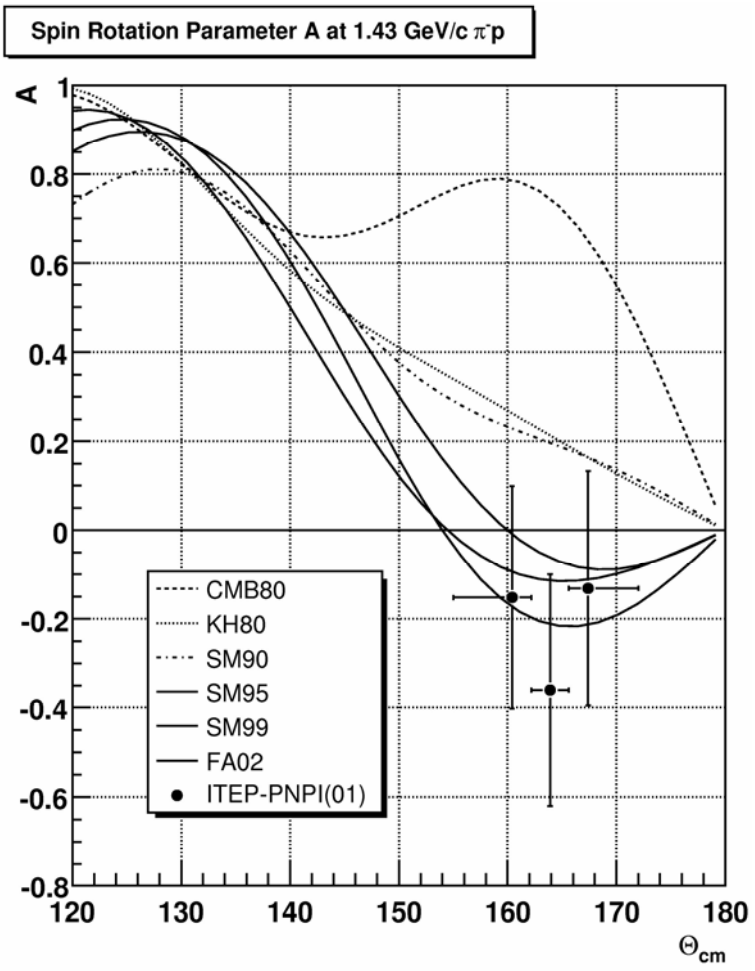

Fig. 4. Comparison of results for the A parameter with PWA predictions

6. Conclusion

Measurements of the polarization parameters were performed in the region of backward scattering where the predictions of various PWA have maximum discrepancy. The data on *A* parameter agree well with SM95 and FA02 PWA solutions of the GWU-VPI group[5]. They contradict to the predictions of the CMB80 analysis[6] while the deviation from KH80[7] is three standard errors. The data on *P* parameter are consistent with the main features of the latest analyses of the GWU group. The results of this experiment along with our previous measurements of the spin rotation parameters indicate that CMB80 and KH80 analyses do not reconstruct properly the relative phase of the transverse amplitudes for scattering to the backward hemisphere. This conclusion together with the fact that the latest analysis of the GWU group confirms only 4-stars resonances (and only one 3-stars resonance $D_{35}(1930)$) impose serious doubts about the present-day spectrum given in the Review of Particle Physics and properties of the light baryon resonance. The development of a new energy independent partial-wave analysis.

Acknowledgments

Our thanks are to Prof. G. Höhler for the interesting and fruitful discussion. We are grateful to the staff of the ITEP accelerator for the excellent beam quality.

This work was partially supported by the Russian Foundation for Basic Research (grants 99-02-16635 and 00-15-96545) and by the Russian State program "Fundamental Nuclear Physics".

References

1. V.V. Abaev *et al.* (PNPI-ITEP Collaboration), Yad. Fiz. **58**, 1635 (1995) [Phys. Atom. Nucl. **58**, 1542 (1995)].
2. I.G. Alekseev *et al*. (PNPI-ITEP Collaboration), Phys. Lett. B **351**, 585 (1995).
3. I.G. Alekseev *et al*. (PNPI-ITEP Collaboration), Phys. Lett. B **485**, 32 (2000).
4. I.G. Alekseev *et al.* (PNPI-ITEP Collaboration), Eur. Phys. J. A **12**, 117 (2001).
5. I.G. Alekseev *et al.* (PNPI-ITEP Collaboration), Eur. Phys. J. C **45**, 383 (2006).

[5] R.A. Arndt *et al*., Phys. Rev.C **69**, 035213 (2004).
[6] R.E. Cutkosky *et al*., Phys. Rev. D **20**, 2839 (1979).
[7] G. Höhler, Handbook of Pion Nucleon Scattering, Physics Data No.12-1 (Fachinformtionzentrum, Karlsruhe 1979).

TWO-PION PRODUCTION IN αp SCATTERING AT 1 GeV/NUCLEON IN THE ENERGY REGION OF THE $P_{11}(1440)$ RESONANCE EXCITATION

G.D. Alkhazov, A.V. Kravtsov , A.N. Prokofiev

1. Introduction

A study of inelastic αp scattering at an energy of ~1 GeV/nucleon is of significant interest since it is related to the problem of the $P_{11}(1440)$ (Roper) resonance. This reaction was investigated in an inclusive experiment at the Saturne–II accelerator in Saclay using the SPES4 magnetic spectrometer. The energy distribution of the scattered α-particles from the $p(\alpha, \alpha')X$ reaction was studied, and a strong excitation of the $P_{11}(1440)$ resonance was discovered. Two peaks were observed in the reaction cross section *vs* the missing energy $\omega = E_{\alpha'} - E_{\alpha}$ distribution (see Fig. 1). A large one, in the region of small energy transfers $\omega \simeq -0.25$ GeV, was evidently due to the $P_{33}(1232)$ (Δ) resonance excitation in the α-particle, and a smaller one, in the region of $\omega \simeq -0.55$ GeV, was interpreted as a signal of the $P_{11}(1440)$ resonance excitation in the target proton. This interpretation was confirmed later by more detailed theoretical considerations. According to theory, only three diagrams (see Fig. 2) dominate in αp inelastic scattering at this energy. The first diagram (*a* in Fig. 2) corresponds to excitation of the Δ resonance in the α-particle projectile, while the second and third diagrams (*b* and *c* in Fig. 2) correspond to excitation of the Roper resonance in the target proton mainly through an exchange of a neutral isoscalar "sigma meson" between the α-particle and the proton. The contribution of all other possible diagrams is practically negligible.

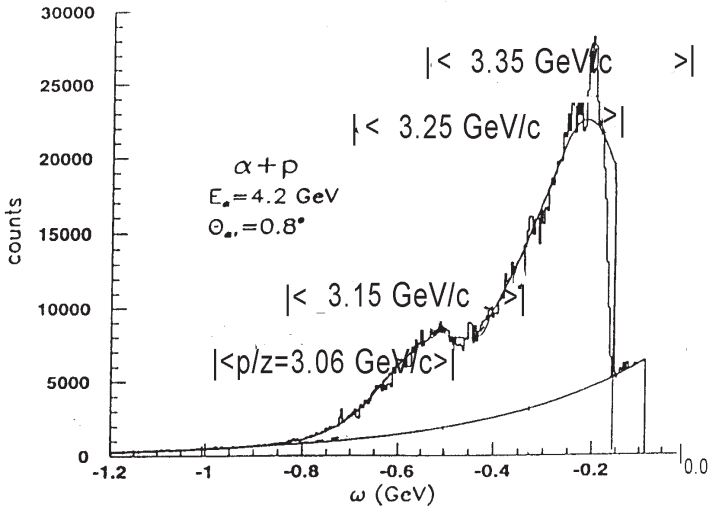

Fig. 1. Inclusive missing energy spectrum of inelastic αp scattering. The acceptance boundaries of the four different $q_{\alpha'}/Z$ momentum settings of the present SPES4-π experiment are marked

Note that due to the isoscalar nature of α-particles and isospin conservation, a direct excitation of the Δ resonance in the proton is forbidden. The decay products from the $p(\alpha, \alpha')X$ reaction may be either a nucleon (proton or neutron) and one pion resulting from the decay of the Δ or Roper resonances (diagrams *a* and *b* in Fig. 2), or a nucleon and two pions resulting from the decay of the Roper resonance (diagram *c* in Fig. 2).

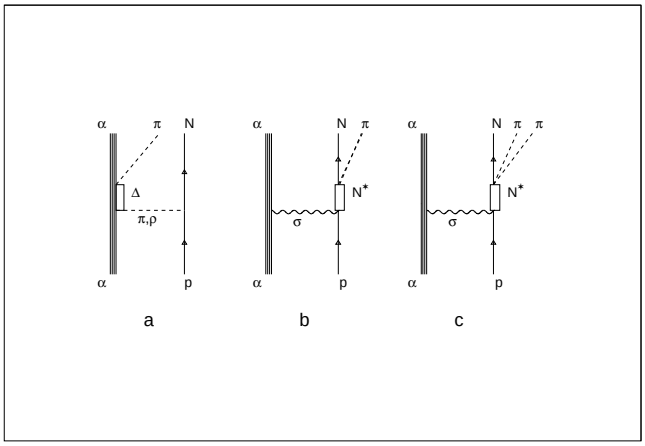

Fig. 2. Main diagrams contributing to the $p(\alpha,\alpha')X$ reaction: (a) Δ excitation in the projectile, (b) N^* excitation in the target with the following one-pion ($N\pi$) decay, and (c) N^* excitation in the target with the following two-pion ($N\pi\pi$) decay

The Roper resonance is the lowest positive parity excited state N^* of the nucleon and is in many respects a very intriguing and important object. This resonance is important in many intermediate-energy processes and also may play a significant role in the three-body nuclear forces and in the swelling of nucleons in nuclei. The result of the inclusive $p(\alpha,\alpha')X$ experiment was interpreted as an observation of the scalar excitation of the $P_{11}(1440)$ resonance which is a breathing mode monopole ($L=0$) excitation of the nucleon. In this interpretation, the $P_{11}(1440)$ resonance mass can be related to the compressibility of the nuclear matter (on the nucleonic level). Some authors have also supposed that the Roper resonance is in fact a superposition of two structures, one being understood as the nucleon breathing mode and the other as double excitation of the Δ resonance. The first structure is strongly excited by scalar probes, like in αp scattering, whereas the second one is excited in spin-isospin flip reactions, like in πN scattering.

An advantage of studying the Roper resonance in an αp-scattering experiment, as compared to πN, NN and γN experiments, is that in the case of αp scattering, as it has already been mentioned, the number of the reaction channels is rather limited. At an energy of $\sim$1 GeV/nucleon, the Roper resonance is strongly excited in αp scattering, whereas the contribution from excitation of higher baryon resonances should be expected small. A deficiency of the inclusive αp experiment was that only the momentum of the scattered α-particles was measured, while other reaction products were not detected. In order to get more information on the resonance excited in the αp-scattering reaction, an exclusive (or semi-exclusive) experiment at the Saturne II accelerator (Saclay) has been performed. Here, we present the results of this experiment in respect to the two-pion production reaction $p(\alpha,\alpha')p\pi\pi$.

Note that the channel of one-pion decay of the Roper resonance strongly interferes with the channel of decay of the Δ resonance, the latter decaying in practically pure one-pion decay mode. This interference makes the separation of the channel of one-pion decay of the Roper resonance from the channel of decay of the Δ resonance to be a complicated task. As for the channel of two-pion decay of the Roper resonance, the contribution of other possible two-pion production channels and interference with them are expected to be small and this allows one to extract much less ambiguous results.

2. Experiment and data analysis

The experimental study of the $p(\alpha,\alpha')pX$ reaction discussed in the present paper was carried out at the Saturne-II accelerator (CE Saclay, France) at a beam of α-particles with a momentum of q_α= 7 GeV/c (E_α=4.2 GeV) [1]. The scattered α-particles and the charged reaction products (p, π^+ or π^-) were registered with the SPES4-π setup (Fig. 3). The installation [2, 3] included the high resolution magnetic spectrometer SPES4, which was used in earlier experiments, and a wide-aperture non-focusing Forward Spectrometer (FS). FS consisted of an analyzing large-gap dipole magnet TETHYS,

a drift chamber telescope and a hodoscope of scintillation counters. A liquid hydrogen target, 60 mm in length, was located inside the TETHYS magnet.

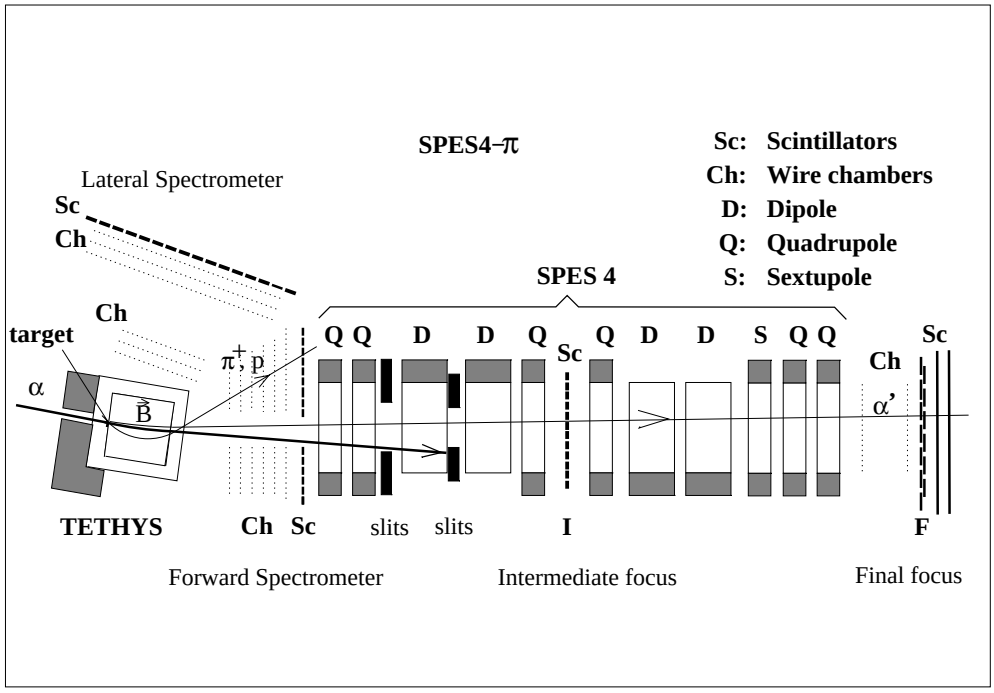

Fig. 3. Schematic view of the SPES4-π setup. TETHYS – large-gap dipole magnet; D,Q,S – magnetic elements of the SPES4 spectrometer; Ch – wire chambers; Sc – hodoscope of scintillation counters

The measurements were carried out at four magnetic rigidity settings of the SPES4 spectrometer. The central values of $q_{\alpha'}$/Z=3.35, 3.25, 3.15, and 3.06 GeV/c (where $q_{\alpha'}$ is the momentum of the scattered α-particle, and Z=2 is the α-particle charge) were chosen to allow the study of the reaction at the values of the energy transfer ω from –0.15 GeV to –0.9 GeV. The ω-intervals accepted at different momentum settings of SPES4 are indicated in Fig. 1. In this paper, the data obtained by detecting the scattered α-particles with SPES4 and only protons with FS are discussed. The measured momenta $\mathbf{q}_{\alpha'}$ and $\mathbf{q}_p$ of the scattered α-particle and secondary proton allowed us to determine the missing mass[1] $M_{\rm miss}$ and the invariant masses $M(p\pi\pi)$ and $M(\alpha'\pi\pi)$.

2.1. Intermediate state excitation

Two-pion events were separated from one-pion events in the analysis of the experimental data by making use of the determined values of the squared missing mass $M^2_{\rm miss}$. Figure 4 shows the distributions of $M^2_{\rm miss}$ for the four momentum settings of SPES4. The spectra include the sum of the events from the one-pion and two-pion production channels.

[1]The missing mass $M_{\rm miss}$ is defined in the present paper as the mass of the object X in the $p(\alpha,\alpha')pX$ reaction, the object X consisting of one or two pions. The number of the emitted pions could be, in principle, more than two. However, the probability that the number of pions is more than two in this reaction at the considered energy is expected to be very small.

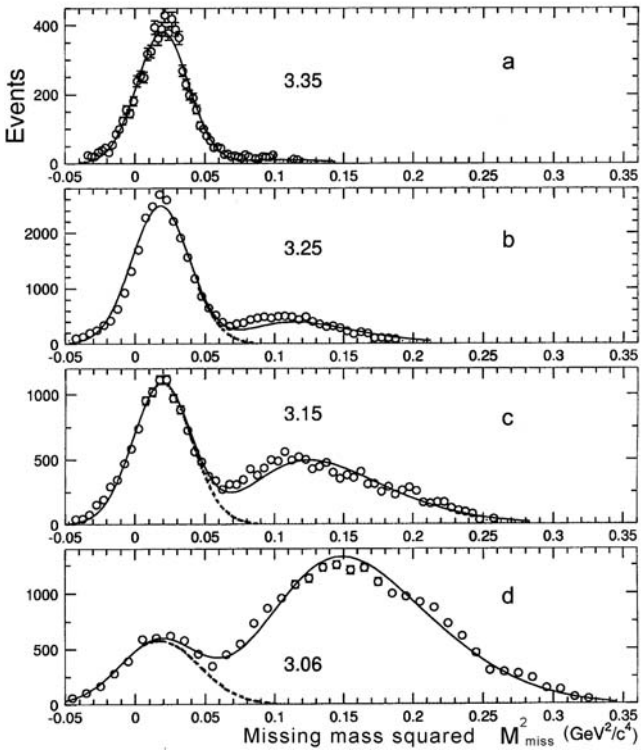

Fig. 4. Missing mass squared spectra $M^2_{\rm miss}$ for the $p(\alpha,\alpha')pX$ reaction for different SPES4 momentum settings. The open points are the experimental data. The solid lines are the sums of the one-pion production distributions, parametrized by Gaussians (dotted lines), and the two-pion production distributions, calculated taking into account the $p(\alpha,\alpha')p\pi\pi$ phase space, α-particle form factor and SPES4-π acceptance

It is seen (Fig. 4a) that for the SPES4 setting $q_{\alpha'}$/Z=3.35 GeV/c, corresponding to small values of $|\omega|$ (see Fig. 1), a peak at $M^2_{\rm miss} \simeq 0.02$ $(\mathrm{GeV/c^2})^2$ (that is at $M_{\rm miss} \simeq 0.14$ $\mathrm{GeV/c^2}$) dominates in the spectrum. Evidently, this peak is due to one-pion events production mostly from the decay of the Δ resonance excited in the scattered α-particle, as it was discussed before. A slight tail at high masses in this spectrum is presumably due to a small contribution of two-pion events from the low-mass tail of the Roper resonance excited in the proton. The width of the peak at $M^2_{\rm miss} \simeq 0.02$ $(\mathrm{GeV/c^2})^2$ reflects the resolution of the reconstructed values of $M^2_{\rm miss}$. This resolution was practically identical for all SPES4 settings. For the SPES4 momentum setting $q_{\alpha'}$/Z=3.25 GeV/c, the contribution from two-pion events (at $M^2_{\rm miss} \geq 0.09$ $(\mathrm{GeV/c^2})^2$) is more prominent (Fig. 4b). In the interval of 0.04 $(\mathrm{GeV/c^2})^2 \leq M^2_{\rm miss} \leq 0.09$ $(\mathrm{GeV/c^2})^2$, the one-pion and two-pion events are not resolved. As for the settings $q_{\alpha'}$/Z=3.15 GeV/c and $q_{\alpha'}$/Z=3.06 GeV/c, the data show (Figs. 4c,d) that the two-pion production is an important channel of the $p(\alpha,\alpha')pX$ reaction at the energy under study.

While comparing the numbers of the registered two-pion and one-pion events it should be kept in mind that the acceptance for registration of two-pion events in our experiment is higher than that for registration of one-pion events, since the protons to be registered by FS are emitted in the forward direction in a more narrow angular cone in the first case in comparison with the second one. Note also that the registered one-pion events are from the reaction $p(\alpha,\alpha')p\pi^0$, while the two-pion events are from the reactions $p(\alpha,\alpha')p\pi^0\pi^0$ and $p(\alpha,\alpha')p\pi^+\pi^-$, the last two channels being not separated in this study.

We can suppose that the detected two-pion events are due to the excitation and decay of the Roper resonance in the target proton. In order to check this conjecture, we have simulated the spectra of the invariant squared masses $M^2(\alpha'\pi\pi)$ and $M^2(p\pi\pi)$ for the $p(\alpha,\alpha')p\pi\pi$ reaction, and compared them with the experimental data. The simulated spectra are compatible with the data, as it is demonstrated in Fig. 5, for the assumed channel of the two-pion production *via* excitation in the target proton of the $P_{11}(1440)$ resonance and its decay to a proton and two pions.

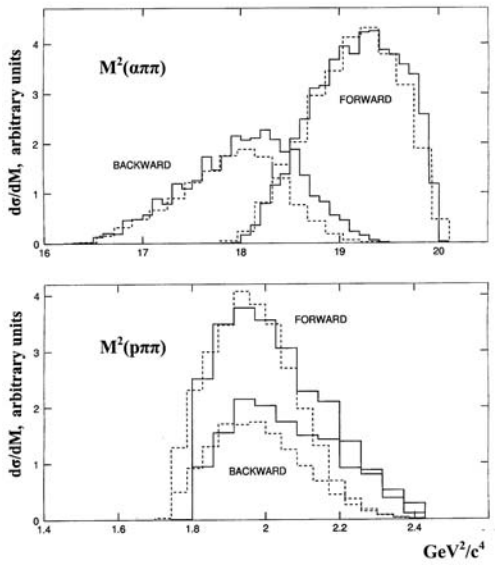

Fig. 5. Invariant mass squared $M^2(\alpha'\pi\pi)$ and $M^2(p\pi\pi)$ distributions of the reaction $p(\alpha,\alpha')p\pi\pi$ for forward and backward emitted protons in the N^* center-of-mass system at p/Z=3.06 GeV/c. Solid line – experimental data; dashed line – Monte Carlo (MC) simulation for the case of N^* excitation in the target

In Fig. 5, a comparison of the simulated spectra with the experimental data is presented for the SPES4 momentum setting $q_{\alpha'}$/Z=3.06 GeV/c. Similar results are also obtained for the setting $q_{\alpha'}$/Z=3.15 GeV/c. Note that the theoretical considerations predict that the contributions from the Roper excitation in the α-particle and from the double excitation of the Δ resonance are relatively small in the $p(\alpha,\alpha')p\pi\pi$ reaction and they may be neglected.

Fig. 6 presents a comparison of the simulated spectra for the invariant mass $M(p\pi\pi)$ with the corresponding experimental spectrum obtained from the properly combined data of the SPES4 momentum settings $q_{\alpha'}$/Z=3.25 GeV/c, $q_{\alpha'}$/Z=3.15 GeV/c and $q_{\alpha'}$/Z=3.06 GeV/c. In the simulations, the $P_{11}(1440)$ resonance parameters from different analyses were assumed. One can see (Fig. 6a) that the simulated spectrum of $M(p\pi\pi)$ is in reasonable agreement with the experimental data when the standard parameters (M_R = 1440 MeV, Γ_R = 359 MeV) of the Roper resonance are assumed[2]. We have also performed a simulation under an assumption that two-pion events are produced *via* excitation and decay of the higher mass $D_{13}(1520)$ baryon resonance. In this case, the results of the simulations are in drastic disagreement with the data (Fig. 6b). At the same time, it is seen that a small admixture of events from the D_{13} resonance in the experimental spectrum of $M(p\pi\pi)$ is possible. Adding to the simulated spectrum a small contribution of events from the decay of the D_{13} resonance can improve the agreement of the simulated spectrum with the data in the region of high masses ($M(p\pi\pi) \simeq$1.5 GeV).

Thus, we see that our data are consistent with the scenario that two-pion events are produced mostly *via* the excitation of the Roper resonance in the target proton with its following decay into a proton and two pions. It should, however, be admitted that the shape of the simulated $M(p\pi\pi)$ spectrum is practically also consistent with the data for the case of non-resonant two-pion production (see Fig. 6a). This may be explained by the fact that the width of the Roper resonance is large and the Roper resonance propagator exerts very little influence on the shape of the simulated $M(p\pi\pi)$ spectrum. An estimate of the non-resonant contribution has been made by the Valencia University theory group for the case of pp inelastic scattering at 1 GeV. It has been shown that the non-resonant contribution should be about two orders smaller than the resonant one. The same should be also for αp scattering. Therefore, the non-resonant contribution may be neglected. Taking this statement

[2]Due to insufficient precision of the experimental data obtained and in view of an uncertainty in the contribution of events from the decay of the $D_{13}(1520)$ resonance, we cannot exclude a possibility that the Roper resonance has other parameters, a slightly smaller mass and a smaller width.

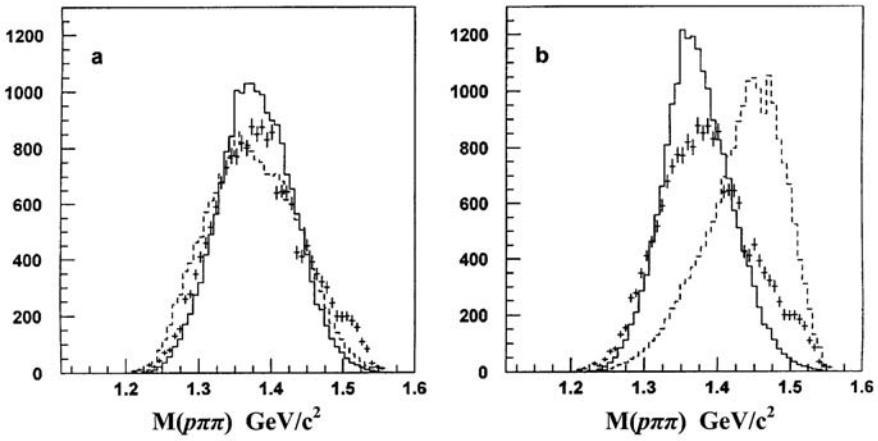

Fig. 6. Experimental and simulated invariant mass distributions for $M(p\pi\pi)$. Experimental data are shown by crosses. a) Dotted line – phase space calculations; solid line – excitation of the Roper resonance with $M = 1440$ MeV, $\Gamma = 350$ MeV (from PDG). b) Solid line – excitation of the P_{11} resonance with $M = 1390$ MeV, $\Gamma = 190$ MeV (from H.P. Morsch and P. Zupranski, Phys. Rev. C **61**, 024002 (1999)), dotted line – excitation of the D_{13} resonance with $M = 1520$ MeV, $\Gamma = 120$ MeV. The α-particle form factor and the spectrometer acceptance are included. The data from all momentum settings are combined. The simulated spectra are normalized to the experimental one

for granted and taking into account our previous considerations, we conclude that the $p(\alpha, \alpha')p\pi\pi$ reaction (at an energy of ~1 GeV/nucleon) proceeds mainly through the intermediate state which is the $P_{11}(1440)$ resonance excited in the target proton. Due to the isoscalar nature of α-particles, the Roper resonance, as it has been already mentioned, may be excited in this reaction *via* an exchange between the projectile α-particle and the target proton of a σ meson, which is a coupled pion pair in the isospin I=0, S-wave state (Fig. 2c).

2.2. Intermediate state decay

In πN scattering, according to Particle Data Group, the two-pion decay of the Roper resonance occurs mainly either as a simultaneous emission of two pions in the I=0 isospin, S-wave state, $N^* \to N(\pi\pi)^{I=0}_{S-wave}$ or as a sequential decay through the Δ resonance, $N^* \to \Delta\pi \to N\pi\pi$, with branching ratios of ~10% and ~30%, respectively. The σ (or ϵ in different notation) meson was introduced as a S-wave isoscalar $\pi\pi$ interaction in a partial-wave analysis of the $\pi N \to N\pi$ and $\pi N \to N\pi\pi$ scattering data. It was discussed whether this σ state is in fact a genuine meson or just some effective meson simulated by the reaction dynamics effects. In the present analysis, we consider two possible channels of the Roper resonance two-pion decay, namely, through the Δ resonance and through the real (or effective) σ meson (Fig. 7).

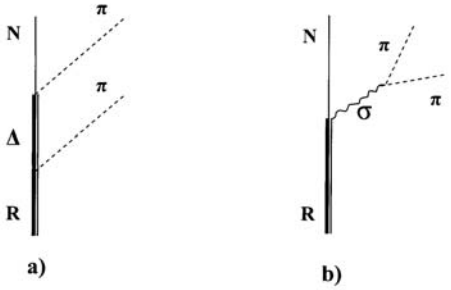

Fig. 7. Diagrams for the Roper resonance decay into two pions: a) sequential decay through Δ: $N^* \to \Delta\pi \to N\pi\pi$; b) decay through the $\sigma(\epsilon)$ meson: $N^* \to N\sigma(\epsilon)$

As follows from theory, the shapes of the spectra of the invariant mass $M(\pi\pi)$ of the pions emitted in the Roper resonance decay are essentially different for these two-pion production channels (Fig. 7). Therefore, a comparison of our experimental data with theoretical predictions can be used to find out what process is more important for the decay of the Roper resonance excited in inelastic αp scattering. In πN scattering, the sequential decay of the Δ resonance (Fig. 7a) is dominant. This should be the same in αp scattering if the same resonance is excited in both reactions. On the other hand, according to the two-resonance picture, the breathing mode of the nucleon is strongly excited in αp scattering, and a different decay pattern (shown in Fig. 7b) is expected.

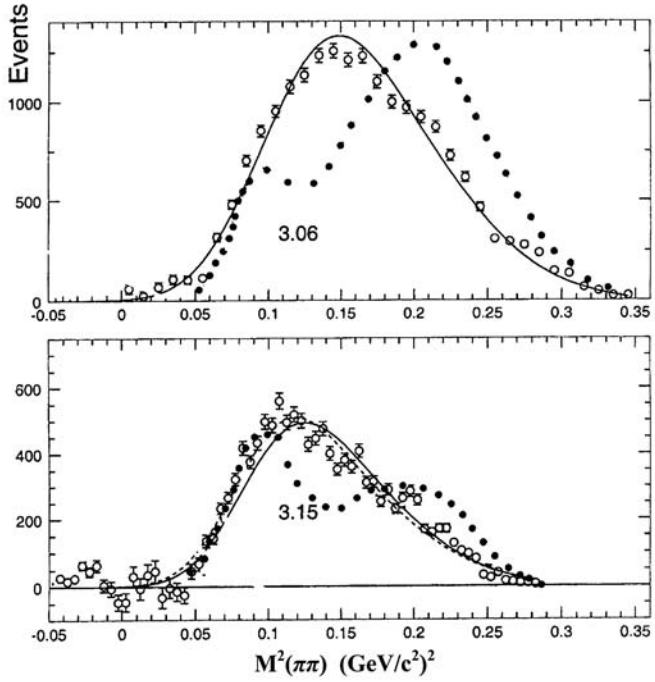

Fig. 8. Invariant mass squared $M^2(\pi\pi)$ distribution for the two-pion production channel in the $p(\alpha,\alpha')p\pi\pi$ reaction. Open points – experimental data. Solid lines – the results of the MC phase space simulations assuming $N^* \to p\sigma \to p\pi\pi$ decay. Dotted curves – the results of the MC simulations assuming $N^* \to \Delta\pi \to p\pi\pi$ decay. Dashed line in the lower plot – the result of the MC simulation assuming the decay through the σ meson with a small admixture of the decay through the Δ resonance

In Fig. 8, the simulated $M^2(\pi\pi)$ spectra are compared with the experimental data for the SPES4 momentum settings $q_{\alpha'}$/Z= 3.06 and 3.15 GeV/c, which have high acceptance for the events of the two-pion production channel of the $p(\alpha,\alpha')pX$ reaction. The experimental spectra $M^2(\pi\pi)$ are obtained from the missing mass squared $M^2_{\rm miss}$ spectra shown in Fig. 4 by subtracting the one-pion production contributions $M^2(\pi)$, which are parametrized by Gaussians (see dotted curves in Fig. 4). In the presented simulation, the σ meson and Δ resonance are described by the Breit-Wigner distributions. The α-particle form factor and the SPES4-π acceptance are also taken into account. Furthermore, the simulated spectra are smeared to take into account the experimental resolution of $M^2(\pi\pi)$, which is estimated from the width of the $M^2(\pi)$ spectra (see Fig. 4). The following parameters for the Δ resonance and σ meson are used: M_Δ = 1232 MeV, Γ_Δ = 120 MeV, and M_σ = 600 MeV, Γ_σ = 600 MeV. It should be noted, however, that due to the large width Γ_σ of the σ meson the specific parameters of the σ meson exert practically no influence on the simulated spectra. As for the channel of the decay through the intermediate Δ-resonance state, the amplitude of this process is strongly influenced by the following kinematical factor [3]

$$A(\mathbf{q}_{\pi_1}, \mathbf{q}_{\pi_2}) \sim \mathbf{q}_{\pi_1} \cdot \mathbf{q}_{\pi_2}, \tag{1}$$

where $\mathbf{q}_{\pi_1}$ and $\mathbf{q}_{\pi_2}$ are the pion momenta in the N^* center-of-mass system. As a result of this factor influence, the simulated spectra of $M^2(\pi\pi)$ have two maxima, at small values of $M(\pi\pi)$ (at $M(\pi\pi)$ close to 0.3 GeV/c^2) and at large values of $M(\pi\pi)$. The first peak corresponds to the events when

[3] We have neglected small spin terms in Eq. (1).

both emitted pions fly in the N^* center-of-mass system with similar momenta in the same direction, while the second peak corresponds to the events when the pions are emitted in opposite directions.

As one can see in Fig. 8, the shapes of the $M^2(\pi\pi)$ spectra simulated for the channel of the Roper resonance decay through the Δ resonance are in evident disagreement with the experimental data for both SPES4 momentum settings. Differently, the shape of the simulated spectrum $M^2(\pi\pi)$ assuming the Roper resonance decay through the intermediate σ meson is in perfect agreement with the data for the SPES4 setting $q_{\alpha'}$/Z= 3.06 GeV/c. A similar spectrum for the SPES4 setting $q_{\alpha'}$/Z= 3.15 GeV/c is also in fairly good agreement with the data[4]. Thus, the $M^2(\pi\pi)$ spectra measured in this experiment suggest that the $P_{11}(1440)$ resonance excited in the $p(\alpha,\alpha')pX$ reaction at an energy of $\sim$1 GeV/nucleon decays mainly as $N^* \to p\sigma \to p\pi\pi$.

This result is also supported by the extracted angular distribution of the emitted protons in the N^* center-of-mass system. This distribution is close to isotropic (see Fig. 9) and therefore agrees with the assumed picture of the decay of the Roper resonance (with the spin 1/2) to a nucleon and a scalar meson.

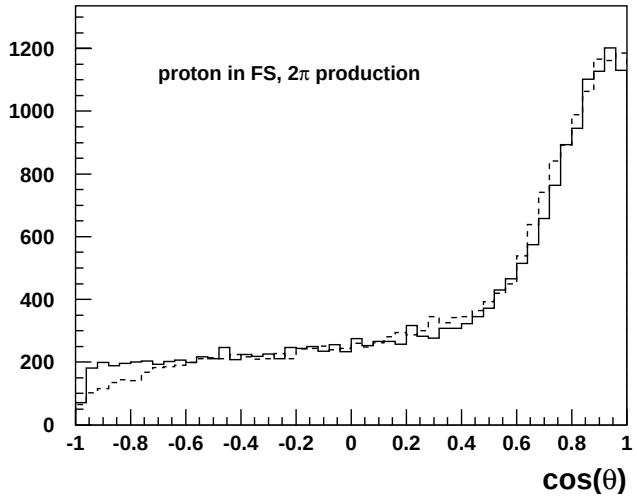

Fig. 9. Angular distribution of the protons in the N^* center-of-mass system (not corrected for the SPES4-π acceptance). θ is the angle between the proton and the momentum transfer $\mathbf{q}_\alpha - \mathbf{q}_{\alpha'}$ in the rest frame of N^*. Solid line – experimental data, dashed line – normalized MC calculation assuming isotropic N^* decay. The data from settings 3.06, 3.15 and 3.25 GeV/c are included

Our conclusion that the $P_{11}(1440)$ resonance excited in αp scattering decays predominantly through the $N^* \to p\sigma \to p\pi\pi$ channel is very different from the πN scattering result. On the other hand, our result nicely correlates with recent investigations of the two-pion production in pp inelastic scattering experiments at energies of 0.650–0.775 GeV (J. Petzold *et al.*, Phys. Rev. C **67**, 052202R (2003)). The authors of these studies come to the conclusion that the two-pion production in pp scattering at these energies proceeds mainly through the excitation of the Roper resonance which decays predominantly through the intermediate σ meson. Note that in a recent analysis of the $\pi N \to N\pi\pi$ data it has been also found by L.Ya. Glozman and D.O. Riska (Phys. Rep. **268**, 263 (1996)) – in contrast to the earlier $\pi N \to N\pi\pi$ analyses conclusion – that the σN channel is more important than the $\pi\Delta$ channel.

3. Conclusion

The two-pion production in the inelastic $p(\alpha,\alpha')p\pi\pi$ reaction was studied in a semi-exclusive experiment at the Saturne-II accelerator (Saclay) at an energy of $\simeq$1 GeV/nucleon with the registration of the scattered α-particle and the secondary proton. The invariant mass distributions $M(\alpha'\pi\pi)$, $M(p\pi\pi)$ and $M(\pi\pi)$ were obtained and analyzed. The results are compatible with the assumption that the studied $p(\alpha,\alpha')p\pi\pi$ reaction proceeds *via* scalar excitation in the target proton of the Roper

[4]Better agreement with the data can be achieved in this case (see Fig. 8) if a small admixture of events corresponding to the Roper resonance decay through the intermediate state of the Δ resonance is added to the simulated spectrum.

resonance as an intermediate state which decays predominantly through the $N^* \to p\sigma \to p\pi\pi$ channel. The obtained results are in favor of the statement that the resonance excited in αp scattering at the excitation energy around 1440 MeV is the breathing excitation mode of the nucleon.

This work has been performed by the SPES4-π collaboration. The PNPI participants are: G.D. Alkhazov, A.V. Kravtsov †, V.A. Mylnikov, E.M. Orischin, A.N. Prokofiev, B.V. Razmyslovich, I.B. Smirnov, I.I. Tkach †, S.S. Volkov, A.A. Zhdanov.

Acknowledgments

The authors are indebted to the LNS directorate and the Saturne-II accelerator staff for their help and support during all phases of the program. The authors are also grateful to Prof. A. A. Vorobyov for his support and fruitful discussions. This work was partly supported by INTAS-RFBR grant 95-1345 and by the Russian Fundamental Nuclear Physics grant.

References

1. G.D. Alkhazov *et al.*, in *"Juelich 2000, Baryon Excitation"*, Juelich, Germany, 2001. p. 53.
2. G.D. Alkhazov and A.N. Prokofiev, in *"PNPI-XXX, High Energy Physics Division. Main Scientific Activities 1997–2001*, Gatchina, 2002, p. 136.
3. G.D. Alkhazov *et al.*, Nucl. Instr. Meth. A **551**, 290 (2005).

STRANGENESS PRODUCTION IN HADRON-INDUCED REACTIONS

S.G. Barsov, A.A. Dzyuba, V.P. Koptev, S.M. Mikirtychyants, M.E. Nekipelov, Yu.V. Valdau

After the experimental program "Subthreshold K^+ production in proton-nuclear interactions" has been successfully finished, a new program has been initiated at the Cooler Synchrotron COSY-Jülich — a storage ring for (un-)polarized proton and deuteron beams up to 3.7 GeV/c — to investigate K and $\bar{K}$ mesons production in pp, pn and dd interactions. These are new studies of hyperon-production ($pN \to KYN$, where $Y = (\Lambda, \Sigma)$, in particular reaction $pp \to K^+ n\Sigma^+$) as well as measurements of the production of kaon pairs in reactions: $pp \to ppK^+K^-$ above the ϕ-threshold, $pn \to dK^+K^-$ to study a_0, f_0, ϕ-production on the neutron, $pp \to dK^+\bar{K}^0$ for kaon-pair production in the "a_0^+-channel" and $dd \to {}^4\mathrm{He}K^+K^-$ which filters kaon pairs in the f_0-channel

ANKE, a magnetic spectrometer at an internal target position of COSY (Fig. 1), is equipped with detector systems which consist from scintillator counters and multiwire proportional chambers for registration positively and negatively charged particles. They can do spectroscopy of K^+, K^-, p, d, ${}^{3,4}\mathrm{He}$ in the momentum range 200–2500 MeV/c with the momentum resolution (FWHM) about 1.5%, so that one can reconstruct the intermediate $K\bar{K}$-states by their invariant mass or find by the missing-mass technique not-detected particles such as neutral kaons and spectator protons. The missing-mass resolution (FWHM) is better than 10 MeV/c^2 and the resolution for kaon-pair invariant-mass spectrum is about 3 MeV/c^2.

Up to now, more states with $J^P = 0^+$ have been observed than it is necessary to form the scalar nonet. This initiated the discussion about the nature of the $a_0/f_0(980)$ resonances. The naive constituent quark model treats the scalar mesons as qq states. However, a_0/f_0 can be also identified with $K\bar{K}$ molecules or compact $qq - \bar{q}\bar{q}$ states. The possible observation of the a_0/f_0-mixing (which can violate isospin conservation) is very interesting because this symmetry plays an important role in

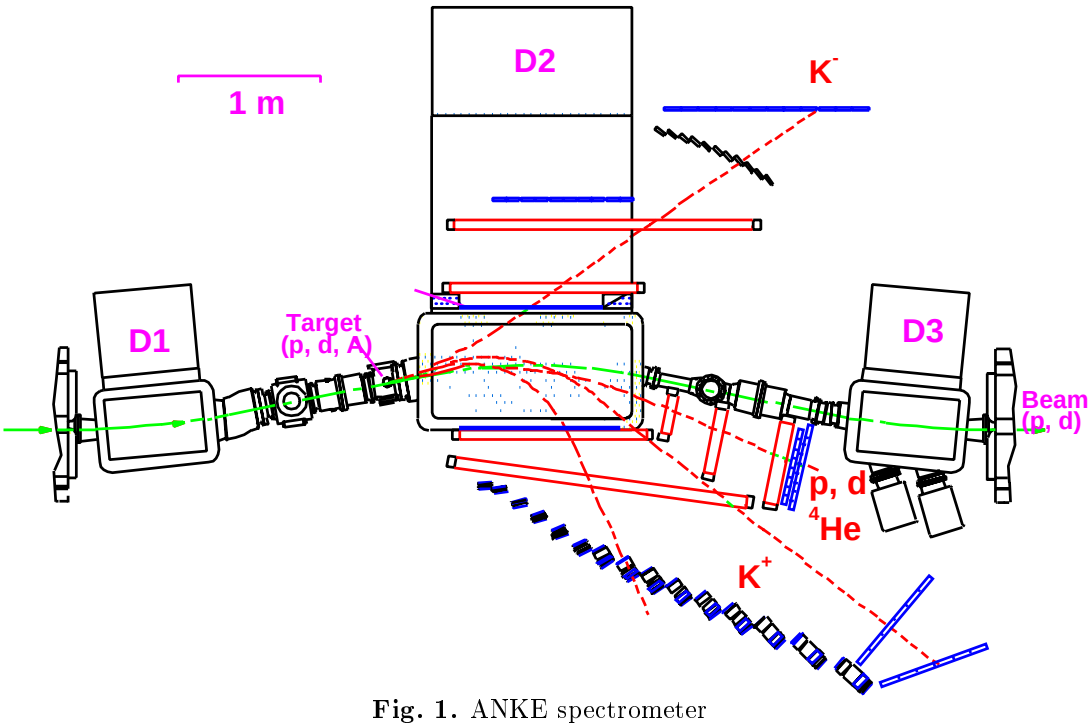

Fig. 1. ANKE spectrometer

QCD and such a measurement can provide a new observable which is sensitive to unknown structures of the light scalar mesons.

Two experiments on $a_0^+(980)$ production have been performed in pp collisions at $T_p = 2.65$ GeV [1] and $T_p = 2.83$ GeV [2] (corresponding to 47.4 and 104.7 MeV excess energy (Q) with respect to the $K^+\bar{K}^0$ threshold). The advantage of this reaction is that it contains no physical background (ϕ-meson). Contribution from background accidental events, which are of the order of 13%, have been subtracted in the differential spectra (Fig. 2). In order to improve the invariant-mass and angular resolutions, a kinematical fit has been applied to the data. As a result of the fit, the $K\bar{K}$ invariant-mass resolution is less than 3 MeV/c^2 for $Q = 47.4$ MeV data and less than 10 MeV/c^2 for $Q = 104.7$ MeV. In the experiment both momentum and angular distributions of K^+ and d were measured.

Since the data have been obtained close to threshold, the model analysis has been restricted to the lowest allowed partial waves, *i.e.* s-wave in the $K\bar{K}$ system accompanied by a p-wave of the deuteron with respect to the meson pair ("$a_0^+(980)$-channel"[1]), and p-wave $K\bar{K}$ production with s-wave deuteron (non-resonant channel). Under this assumption the square of the spin-averaged transition matrix element can be written as:

$$|\bar{\mathcal{M}}|^2 = C_0^q q^2 + C_0^k k^2 + C_1(\hat{\vec{p}}\cdot\vec{k})^2 + C_2(\hat{\vec{p}}\cdot\vec{q})^2 + C_3(\vec{k}\cdot\vec{q}) + C_4(\hat{\vec{p}}\cdot\vec{k})(\hat{\vec{p}}\cdot\vec{q}) \ . \quad (1)$$

Here $\vec{k}$ is the deuteron momentum in the overall c.m. system, $\vec{q}$ denotes the K^+ momentum in the $K\bar{K}$ system, and $\hat{\vec{p}}$ is the unit vector of the beam momentum. Only $K\bar{K}$ p-waves contribute to C_0^q and C_2, only $K\bar{K}$ s-waves to C_0^k and C_1, and only s-p interference terms to C_3 and C_4. The coefficients C_i can be determined from the data by a simultaneous fit of Eq.(1) to the six measured differential distributions (two invariant-mass spectra and four angular distributions) which are not corrected for the ANKE acceptance. ANKE events uniformly distributed over reaction phase space and traced through the GEANT simulation have been used for the fit. The coefficients C_i can be directly related to the different partial waves. They contain even more information than a Dalitz plot, particularly for the interference of $[(K\bar{K})_s d]_p$ and $[(K\bar{K})_p d]_s$ contributions. The fit for the $K^+\bar{K}^0$ invariant-mass spectrum demonstrates the dominance of the "a_0-channel" (around 90% of $[(K\bar{K})_s d]_p$ configuration).

The coefficients C_i define the initial differential distributions. These allow one to calculate the total acceptance and the total and differential cross sections (see Fig. 2). Values of $\sigma(pp \to dK^+\bar{K}^0) = (38 \pm 2_{\rm stat} \pm 14_{\rm syst})$ nb and $(190 \pm 4_{\rm stat} \pm 39_{\rm syst})$ nb have been obtained for 47.4 and 104.7 MeV excess energy. The energy dependence of the total cross section can be described by phase space with the above mentioned partial wave restrictions.

In principle, the contribution of the $a_0^+(980)$ resonance should be visible in the invariant mass distribution of the scalar $K\bar{K}$ channel. In Fig. 2a the $K\bar{K}$ invariant-mass distribution is shown for Q=104.7 MeV. A Flatte distribution is added to the $a_0^+(980)$-channel ($[(K\bar{K})_s d]_p$ partial wave configuration). The mass of the $a_0(980)$ meson has been taken as 984.7 MeV. From this figure one can see that in order to describe our experimental data a rather large width of $a_0(980)$ resonance is needed. Another possibility to explain experimental data is a mixture of a_0 with non-resonant production of kaon-pair in s-wave (α – fraction of resonance). One can conclude that either the $a_0^+(980)$ has a large width or it has a very week coupling to the scalar $K\bar{K}$ channel, at least for the investigated reaction.

Another interesting topic is the properties of light vector mesons ($J^P = 1^-$) ρ, ω and ϕ, such as their coupling constants, production mechanisms close to thresholds and in particular the so-called Okubo-Zweig-Iizuka (OZI) rule. This rule states that processes with disconnected quark lines between initial and final states are suppressed. As a result, the production of ideally mixed ϕ-mesons (quark content $s\bar{s}$) in a reaction $AB \to \phi X$ is reduced compared to $AB \to \omega X$ (ω is a linear combination of $u\bar{u} + d\bar{d}$) under similar kinematical conditions. Calculations by Lipkin predict ratio of single ϕ to

[1] Due to selection rules the $a_0^+(980)$ can contribute only to this channel.

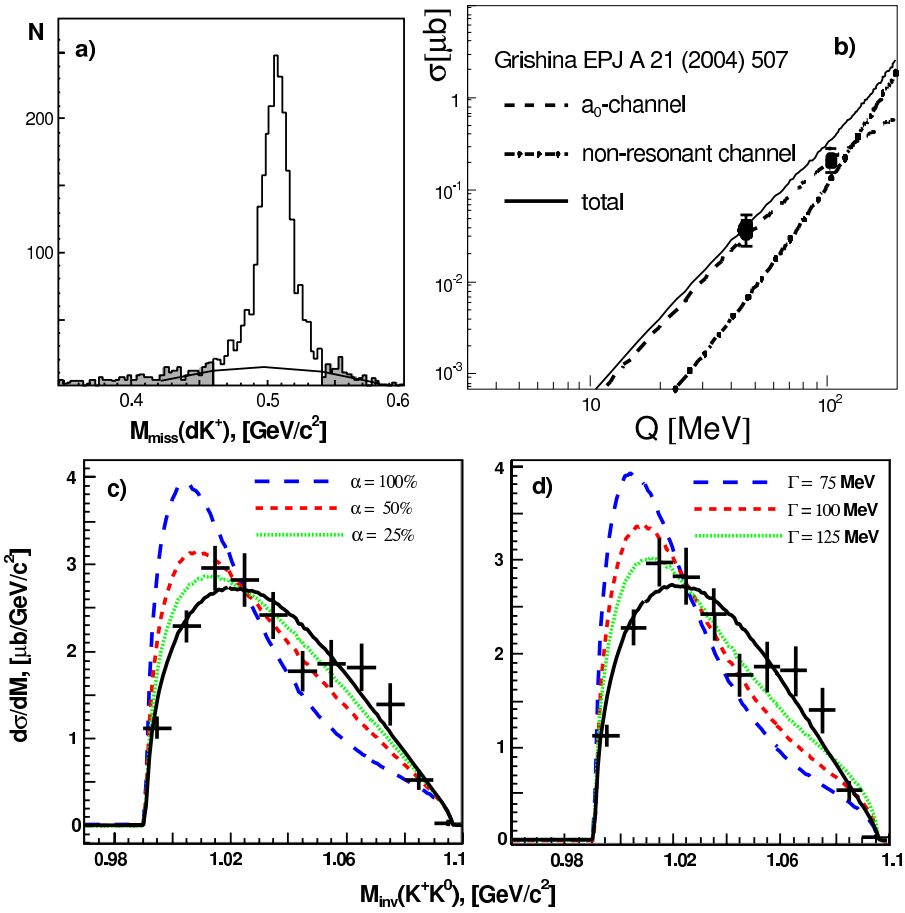

Fig. 2. a) Missing-mass $m(pp, dK^+)$ distribution of the $pp \to dK^+\bar{K}^0$ events for $T_{beam} = 2.83$ GeV. The line shows the background distribution (polynomial fit) and the shaded area indicates the events used for background subtraction. b) Total cross section for the reaction $pp \to dK^+\bar{K}^0$. Lines indicate theoretical predictions. c) $K^+\bar{K}^0$ invariant-mass spectrum and models with different fractions (α) of resonance contribution to kaons s-wave. d) Fit result plus Flatte distribution to the $[(K\bar{K})_s d]_p$ term with different widths of $a_0^+(980)$. Black solid line coresponds to our best fit result without a_0^+

ω production of $R_{\phi/\omega} = 4.2 \times 10^{-3} \equiv R_{OZI}$. However, experimentally measured $R_{\phi/\omega}$ is strongly enhanced in comparison with this prediction, for example in $p\bar{p}$ interactions where $R_{\phi/\omega}$ can be as large as $\sim 100 \times R_{OZI}$.

The reaction $pp \to pp\phi$ has been studied at three beam energies 2.65, 2.70 and 2.83 GeV which correspond to 18.5, 34.5 and 75.9 MeV excess energies above ϕ-production threshold (ϵ) [3]. At the K^+K^- invariant-mass spectra the peaks around ϕ-meson mass are clearly visible for the all data sets (see Fig. 3a-c). In order to extract the ϕ-contribution, a fit of the K^+K^- invariant-mass spectra has been performed for these three data samples. The distributions have been described by a Breit-Wigner function for ϕ and four-body phase-space for non-ϕ part.

Using the number of ϕ-mesons from the fit, the integral luminosity for the measurements, and the efficiencies and acceptances of the ANKE detectors, the total ϕ-meson production cross section has been deduced for the three energies, taking into account the branching ratio in ϕ-meson decay $\Gamma_{K^+K^-}/\Gamma_{tot} = 0.491$. The results plotted in Fig. 3d show a good agreement with those obtained by the DISTO collaboration [Phys. Rev. C **63**, 024004 (2001)] data point at $\epsilon = 83$ MeV. The cross section for the two low energy data points is higher than predicted by a pure phase space extrapolation

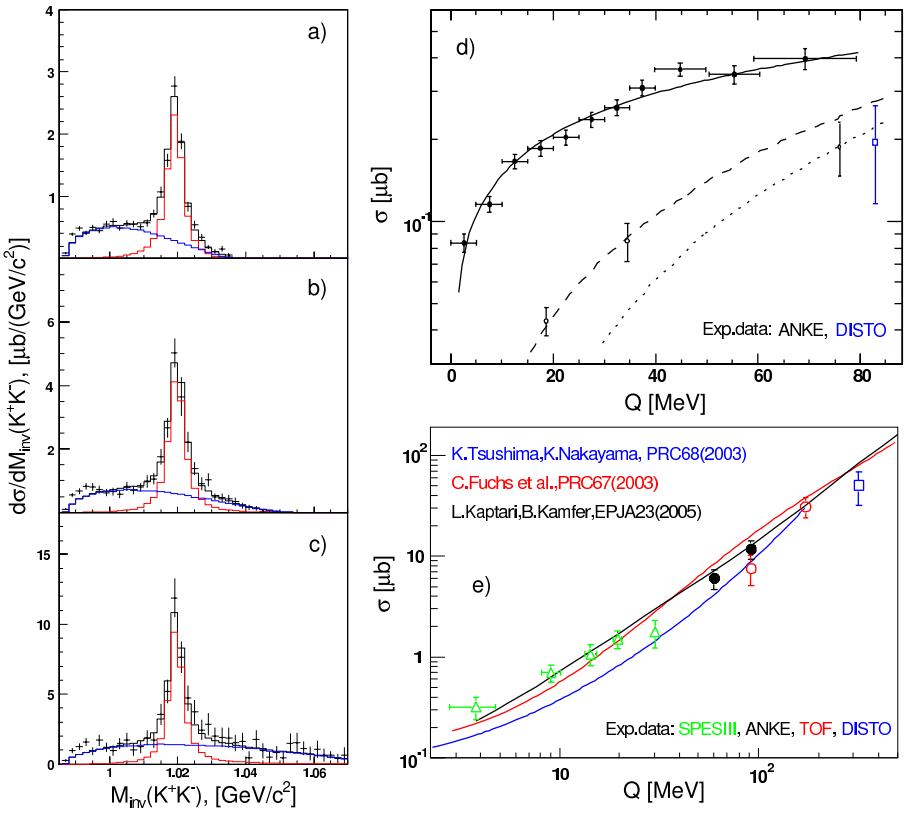

Fig. 3. a, b, c) Invariant-mass of K^+K^- pair for the reaction $pp \to ppK^+K^-$ at three beam energies 2.65 (a), 2.70 (b) and 2.83 GeV (c). Lines indicate ϕ and non-ϕ contributions. d) Total cross section of the reactions $pn \to d\phi$ (filled circles) and $pp \to pp\phi$ (open circles for ANKE and open box for DISTO) as a function of their excess energies. On-neutron ϕ-production can be described by 2-body ($\sim \sqrt{\epsilon}$) phase space (solid line). In pp case the pure 3-body $\sim \epsilon^2$ (dotted line) curve have been modified by a Jost-function, in order to include an effect of the protons FSI (dashed line). e) Total cross section for the reaction $pp \to pp\omega$ and different theoretical predictions

normalized to the 75.9 MeV point, but this enhancement can be explained by the final state interaction between the two protons in the $^1S_0$-state. The same effect is also visible in the differential spectra [3].

The pilot measurement of cross sections of the reaction $pn \to dK^+K^-$ at $T_{beam} = 2.65$ MeV [4] has been performed on deuteron as an effective neutron target. Such measurements have the advantage that the c.m. excess energy of the neutron in deuteron varies due to the Fermi-motion. Thus, even in an experiment with fixed beam momentum the energy dependence of the total cross section for a quite large ϵ region can be measured. In order to confirm the spectator hypothesis, a Monte Carlo simulation has been performed, in which the momentum of neutron in the target deuteron has been derived from the Bonn potential. The energy dependence of the $pn \to d\phi$ cross section is assumed to follow the phase space. This assumption is consistent with the results to be shown later – see Fig. 3d. After including the detector response, the simulation fits the shape of the data for momenta very well at least up to 150 MeV/c.

K^+K^- invariant-mass distribution is dominated by the ϕ-meson peak on the top of a slowly varying background from direct K^+K^- production. This has been estimated by a three-body phase-space simulation (effected by deuteron wave-function) which, together with the ϕ contribution, is fitted to the overall spectra.

The world data on $pp \to pp\omega$ had a gap between 20 and 200 MeV excess energies. Our study of

this reaction [5] has removed this uncertainty. The first measurement of the total cross section for the reaction $pn \to d\omega$ has been also performed at ANKE spectrometer [6]. These production cross sections have been used to determine $R_{\phi/\omega}$.

We have obtained $R_{\phi/\omega} = (33\pm6)\times10^{-3} \approx 8\times R_{OZI}$ in proton-proton and $R_{\phi/\omega} = (40\pm19)\times10^{-3} \approx 9 \times R_{OZI}$ in proton-neutron collisions indicating that the enhancement of the ratio is independent of isospin. It may be a signal for additional and, as yet non-understood, dynamical effects related to the role of strangeness in few-nucleon systems.

We are currently working on a joint analysis of the reactions $pp \to ppK^+K^-$, $pn \to dK^+K^-$ and $pp \to dK^+\bar{K}^0$ in order to separate different isospin fractions and in particular to search for contributions from $a_0/f_0(980)$ and K^-p FSI.

A measurement of the isoscalar $K\bar{K}$ production in the isospin selective reaction $dd \to {}^4\mathrm{He}K^+K^-$ has been performed in April 2006. In order to suppress the huge background from breakup protons, the energy losses of the high momentum particles in the forward detector have been included into the on-line trigger. According to a first rough analysis we expect less than 100 $dd \to {}^4\mathrm{He}K^+K^-$ events in the data.

Another direction of PNPI group activity is the production of light hyperons in proton-proton collisions in the close-to-threshold region. Nowdays not much data about $pp \to K^+n\Sigma^+$ reaction are available, moreover existing information is very inconsistent.

A model independent estimate for $R(\Sigma^+/\Sigma^0)$ might be obtained from the isospin relation linking the different Σ-production channels, the amplitudes satisfy equation:

$$f(pp \to K^+n\Sigma^+) + f(pp \to K^0p\Sigma^+) + 2f(pp \to K^+p\Sigma^0) = 0. \qquad (2)$$

This leads to so-called triangle inequality between the total cross sections (Fig. 4). But recent experiments in the close-to-threshold region give surprisingly high total cross sections for this process and breaking this triangle inequality.

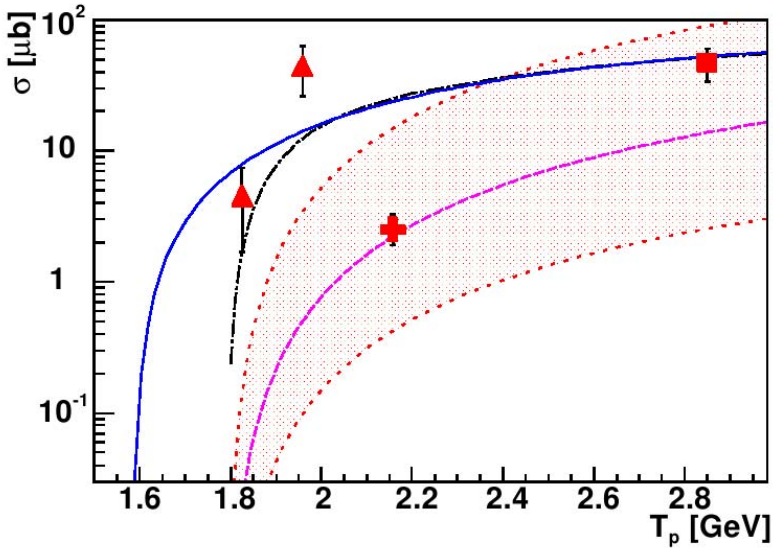

Fig. 4. Total cross section for the reaction $pp \to K^+n\Sigma^+$. Triangles shows data obtained by T. Rozek *et al.* [Phys. Lett. B **643**, 251 (2006)], cross – the value from Ref. [7], box – bubble-chamber data [Phys. Rev. **123**, 1465 (1961)]. Shaded area shows the region restricted by triangle inequality. Lines show the behaviors of total cross sections $pp \to pK^+\Lambda$ (solid), $pp \to pK^+\Sigma^0$ (dashed), $pp \to K^+n\Sigma^+$ (chain line)

Since one cannot *a priori* exclude an anomalous threshold behavior associated with $I = \frac{1}{2}$ K^+n-system, further experimental studies for this reaction are necessary in order to clarify the situation. We have obtained the total cross section at a proton beam energy of T_p =2.16 GeV which corresponds to 128 MeV excess energy [7].

Information about the Σ^+ production was determined from three simultaneously measured observables, *viz* the K^+ inclusive double differential cross section, and the K^+p and $K^+\pi^+$ correlation spectra. The most important is the last one because there is only one more physical source of K^+ and π^+ coincidence – reaction $pp \to K^+n\Lambda\pi^+$ which has much smaller total cross section. The accidental background contribution is also small.

The measured missing-mass spectrum of detected K^+p pairs as well as the inclusive K^+ double differential cross section also allow to fix strength (upper limit for total cross section) of $pp \to K^+n\Sigma^+$. For it they have been compared with multichannel model traced through the GEANT simulation program.

Obtained total cross section $\sigma(pp \to K^+n\Sigma^+) = (2.3{\pm}0.6_{\rm stat}{\pm}0.4_{\rm syst})$ μb is significantly smaller than that presented in [Phys. Lett. B **643**, 251 (2006)] at lower excess energy. The important point is that simultaneously measured total cross sections for $pp \to pK^+\Lambda$ and $pp \to pK^+\Sigma^0$ reactions are in good agreement with world data.

In order to confirm this result, a new experiment on Σ^+ production has been performed in September 2007. Data have been taken at four beam energies – 1.83, 1.92, 1.95 and 2.02 GeV. Data analysis is going on now.

References

1. V. Kleber *et al.*, Phys. Rev. Lett. **91**, 172304 (2004).
2. A. Dzyuba *et al.*, Eur. Phys. J. A **29**, 245 (2006).
3. M. Hartman *et al.*, Phys. Rev. Lett. **96**, 242301 (2006).
4. Y. Maeda *et al.*, Phys. Rev. Lett. **97**, 142301 (2006).
5. S. Barsov *et al.*, Eur. Phys. J. A **21**, 521 (2004).
6. S. Barsov *et al.*, Eur. Phys. J. A **31**, 95 (2007).
7. Yu.Valdau *et al.*, Phys. Lett. B **652**, 245 (2007).

INVESTIGATION OF THE $pp \to pp\pi^0$ REACTION AT TWO ENERGIES NEAR 1 GeV

V.V. Sarantsev, K.N. Ermakov, V.I. Medvedev, O.V. Rogachevsky, S.G. Sherman

1. Introduction

The pion production in the NN interactions is the main inelastic process at the energies below 1 GeV. Despite the fact that a lot of experiments have been performed, many questions on this process are not yet answered. One of them is a question of the contribution of the isoscalar ($I = 0$) channel to the inelastic neutron-proton collisions. Since the neutron-proton scattering amplitude contains both isoscalar and isovector ($I = 1$) parts, a detailed investigation of the neutral pion production in the pp collisions (isovector contribution only) might give the most accurate information on the isovector channel that, in a combination with the neutron-proton data, would allow one to extract more correctly the contribution of the isoscalar channel.

Various theoretical models, more or less successful, arose while the data on the pion production in NN collisions were accumulated. Most of them work for pion production near the production threshold and are not applied at higher energies.

For the energy range 1–3 GeV an earlier peripheral or one-pion exchange (OPE) model suggested by E. Ferrary and F. Selleri assumed the dominance of the one-pion exchange term in the inelastic amplitude. Pole diagram matrix elements were calculated using the uncertain beforehand form factor, the interference between diagrams being neglected. The form factor function was obtained then by fitting to experimental data, so in fact this was a semiphenomenological model. Its predictions were in a good agreement with rather rough measurements of the differential cross sections in the energy range 800–1300 MeV.

The later modifications of the one-pion exchange model have described rather well (with the accuracy 5–10%) the differential spectra for the $pp \to pn\pi^+$ reaction which provided the largest piece of experimental information that time. The total cross sections were predicted to be a little lower than the observed ones. For other reactions, *e.g.* for $pp \to pp\pi^0$, the discrepancies between the theory and experiment were even larger.

It should be noted that the experimental data on the $pp \to pp\pi^0$ reaction near the energy of 1 GeV are much more scarce than those for $pp \to pn\pi^+$ channel. The KEK data contain the information on total cross sections only. The only data on the spectra of secondaries at the energy 970 MeV were provided by D.V. Bugg *et al.*, the statistics being rather poor. For this reason it would be important to perform more accurate measurement of the cross sections in this energy region and to compare carefully the differential distributions of the final particles in the $pp \to pp\pi^0$ reaction with the predictions of the modern OPE model. Such a comparison would allow one to see the strong and weak aspects of this simplest theoretical model, as well as to judge about the necessity of some additional nonperipheral mechanisms of the pion production in NN collisions. The results on the study of neutral pion production in the energy range below 900 MeV were published earlier in our work [1]. Here we present the results [2] of the investigation of differential spectra at two higher momenta (1581 and 1683 MeV/c) and their comparison with the OPE-model advanced by V.K. Suslenko *et al.*

2. Experiment

The experiment was performed at the PNPI 1 GeV synchrocyclotron with the help of the 35 cm hydrogen bubble chamber disposed in the 1.48 T magnetic field. The proton beam (after corresponding degrader for the momentum 1581 MeV/c) was formed by three bending magnets and by eight quadrupole lenses. The incident proton momentum value was defined independently by the kinematics of the elastic scattering events. The accuracy of the incident momentum value was about 0.5 MeV/c, the momentum spread being 25 and 7 MeV/c (FWHM) at 1581 and 1683 MeV/c, respectively. A total

of 10^5 stereoframes were obtained at both proton momenta.

According to kinematics of the pion production in NN collisions, the laboratory angles of secondary protons are in the forward hemisphere, maximum angle being not larger than 60° at our energies. For this reason we selected two-prong events with track angles in the plane of the film not larger than 60°.

The events selected so can belong not only to the neutral pion production but also to the elastic pp scattering or to the π^+ production reactions. The events in the fiducial volume of the chamber were measured and geometrically reconstructed. The identification of the events was performed on the strength of the χ^2 criterion, the confidence level being equal to 1%. If the event had a good χ^2 for the elastic version (4C-fit), it was considered as elastic one. If several inelastic versions revealed a good χ^2, we used visual estimate of the ionization density to distinguish between the proton and pion.

The standard bubble chamber procedure was used to obtain absolute cross sections. Absolute values were measured with an accuracy about 4%.

3. One-pion exchange model

According to the OPE model, the main role in the reaction $NN \to NN\pi$ is played by the pole diagrams (Fig. 1). The matrix element of any diagram in Fig. 1 can be presented as a product of three factors: the propagator, the amplitude of the πN scattering and the πNN vertex function

$$M_i \sim \frac{1}{k_i^2 + \mu^2} \Im(z_i, y_i^2; k_i^2) G(k_i^2), \tag{1}$$

where z_i is the total energy of the πN system, y_i^2 is the four-momentum transfer square in the πN scattering vertex, k_i^2 is the four-momentum square of the virtual pion and μ^2 is the pion mass squared.

The form factor function of the πNN vertex taking into account the nonpole diagram contributions was not determined in the frame of the OPE model. The following expression was suggested for the form factor

$$G(k_i^2) = \alpha\mu^2/[k_i^2 + (\alpha + 1)\mu^2]. \tag{2}$$

The choice of α in the range 8–9 gave a good description of the experimental data on the $pp \to pn\pi^+$ reaction in the energy range 600–1000 MeV.

The πN scattering amplitude $\Im(z_i, y_i^2; k_i^2)$ and its off-shell behavior were taken according to the paper of E. Ferrary *et al.*, where the off-shell corrections were introduced into partial waves. We confined ourselves to the P_{33} wave only in the partial wave expansion, assuming the leading role of the Δ_{33} resonance in the πN scattering.

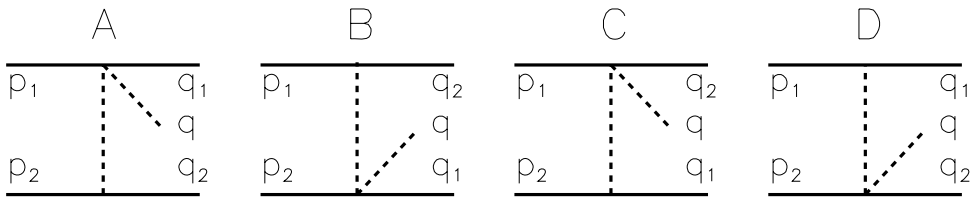

Fig. 1. Feynman diagrams of the OPE model for the $NN \to NN\pi$ reaction

The reaction matrix element is the sum of matrix elements of diagrams of Fig. 1

$$M = M_A - M_B - M_C + M_D, \tag{3}$$

where the choice of signs is determined by the Pauli principle. All possible interference terms were taken into account.

We used a FOWL simulation program in order to obtain all necessary distributions at once.

4. Experimental results and discussion

The main evidence for the pole diagram contribution would definitely be the observation of a peak in the momentum transfer distribution from the target particle to the secondary proton (*e.g.*, for the diagram A – in the distribution on $\Delta^2 = -(p_2 - q_2)^2$) at low momenta. But since there is no difference between the final protons in the $pp \to pp\pi^0$ reaction, it is difficult to separate the contribution of a certain diagram experimentally. The whole Δ^2 distribution is rather complex, because other diagrams have singularities on their own variables which spread the studied one. So the contribution of the diagram A really contains the low momentum peak, while the B diagram contribution has a maximum at high Δ^2. It is quite natural because the diagram B has a singularity in $\bar{\Delta}^2 = -(p_1 - q_2)^2$ distribution, so for this diagram the beam proton is a spectator and Δ^2 is not small (p_2 is the nucleon mass in the laboratory system and q_2 is almost equal to p_1). The contributions of diagrams C and D are similar to those of B and A, respectively, but more spread out.

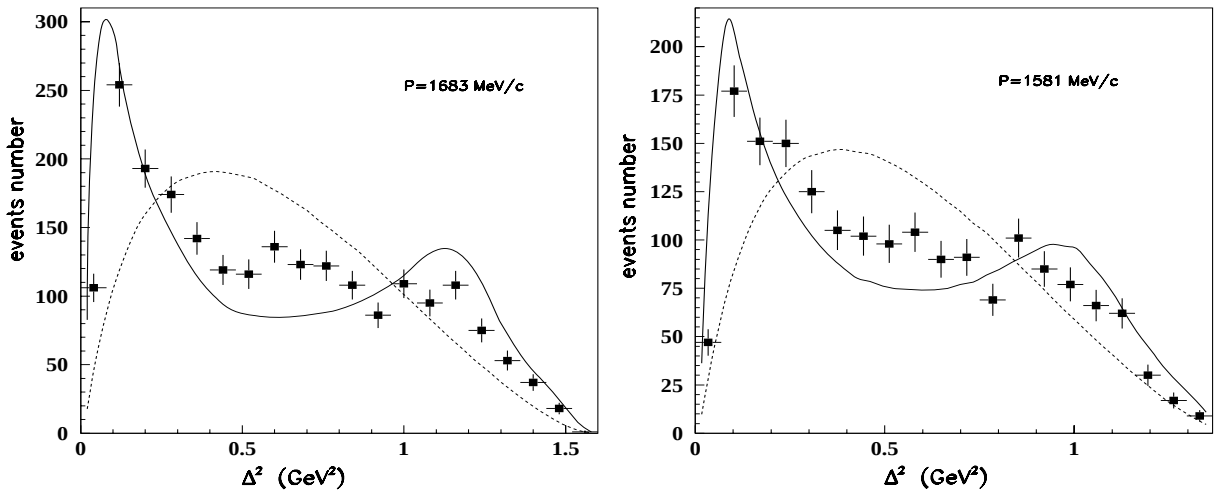

Fig. 2. The four-momentum transfer Δ^2 distributions. The solid and dotted curves are the calculations of the OPE model and the phase space normalized to the total experimental number of events

Figure 2 shows the Δ^2 distributions for our energies together with the OPE model predictions (solid lines) and phase space calculations (dotted lines) normalized to the total experimental number of events, because the absolute values of the OPE model calculations do not agree with the experiment. We shall return to this question later when we will discuss the energy dependence of the cross sections.

Forgetting for a while the underestimated absolute cross section values, we can see that the OPE model describes qualitatively well the data on Δ^2 at both energies studied. It is remarkable because one should bear in mind that only the P_{33} wave was taken into account in the πN scattering.

Perhaps, the Δ^2 distribution is mainly sensitive to the pole diagram propagator, and the dependence on the πN amplitude manifests itself in other distributions.

Figure 3 shows the laboratory momentum spectra of final protons of the $pp \to pp\pi^0$ reaction. In the proton spectra one can see two peaks, one in the region 300–400 MeV/c (independently of the

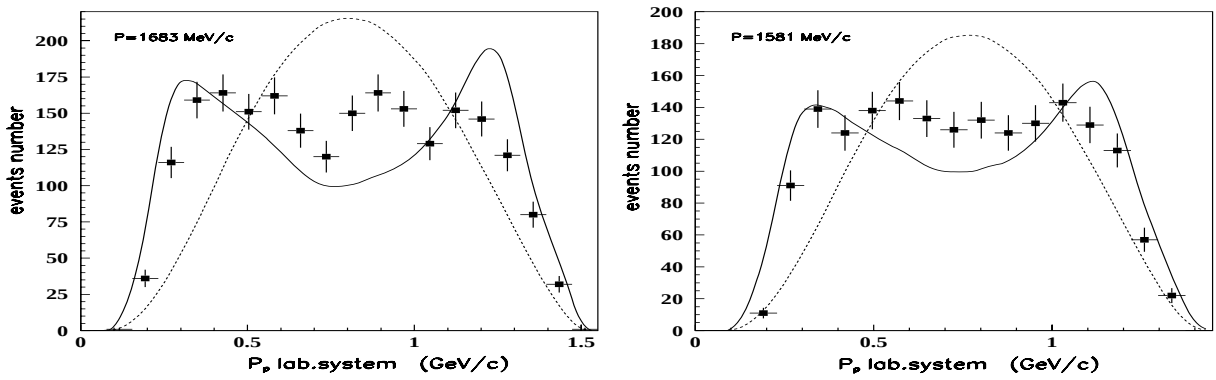

Fig. 3. The laboratory momentum spectra of final protons. The curves have the same meaning as in Fig. 2

incident energy) and the second moving to the left with the decrease of beam energy. The low-energy peak corresponds to the target spectator proton, while the high-energy one corresponds to the incident proton being a spectator. The OPE calculations describe the experiment satisfactorily, contrary to the phase space ones. The pion spectra calculated are close to the phase space and experimental distributions.

Figure 4 shows the $M_{p\pi^0}$ effective mass distributions. It looks like that the distributions on $M_{p\pi^0}$ consist of two parts: one is the phase space distribution, while the other has the form of a peak with the width $\sim$100 MeV/c^2. The peak location corresponds to the Δ_{33} mass. The origin of these two contributions is quite clear in the frame of the OPE model, if one keeps in mind that the πN scattering comes from the P_{33} wave only. When the $M_{p\pi^0}$ is calculated for the spectator proton, (*e.g.*, q_2 in the diagram A, Fig. 1) one has the phase space distribution. When the proton comes from the πN scattering block the resulting $M_{p\pi^0}$ distribution corresponds to the Δ_{33} isobar peak. As can be seen in Fig. 4, OPE calculations are in qualitative agreement with the experiment at both energies studied.

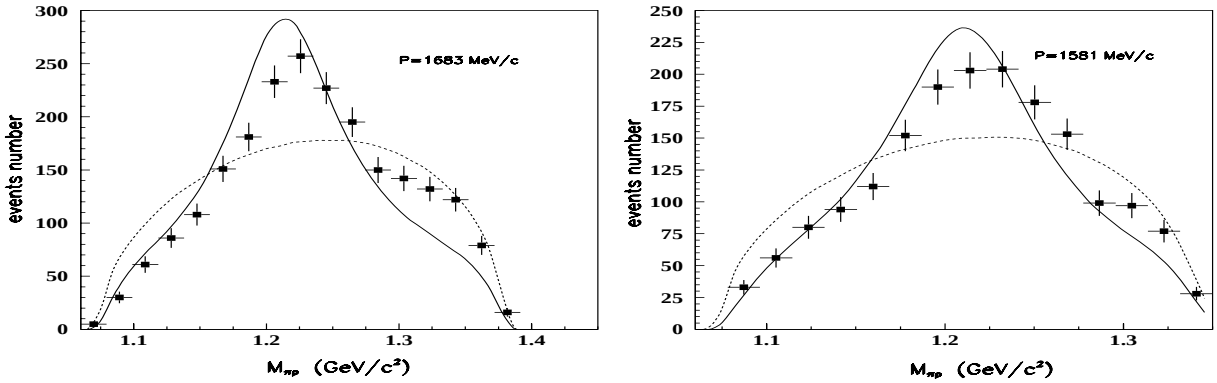

Fig. 4. $M_{p\pi^0}$ effective mass spectra. The curves have the same meaning as in Fig. 2

The c.m.s. angular distributions of protons are given in Fig. 5. OPE calculations are in rather good agreement with the experimental data, with the exception for the small proton scattering angles. A possible explanation of this discrepancy is the presence of the sole P_{33} wave in the πN scattering amplitude. It is clear that a small admixture of other waves interfering with the main one should manifest itself mainly in the angular distributions.

The angular distributions of pions together with the OPE predictions are given in Fig. 6. One

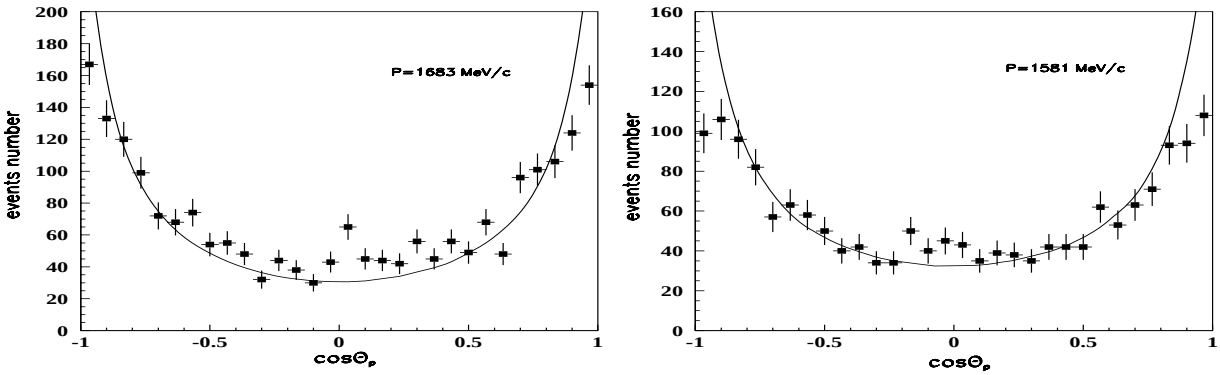

Fig. 5. Proton angular distributions (c.m.s.). The curves have the same meaning as in Fig. 2

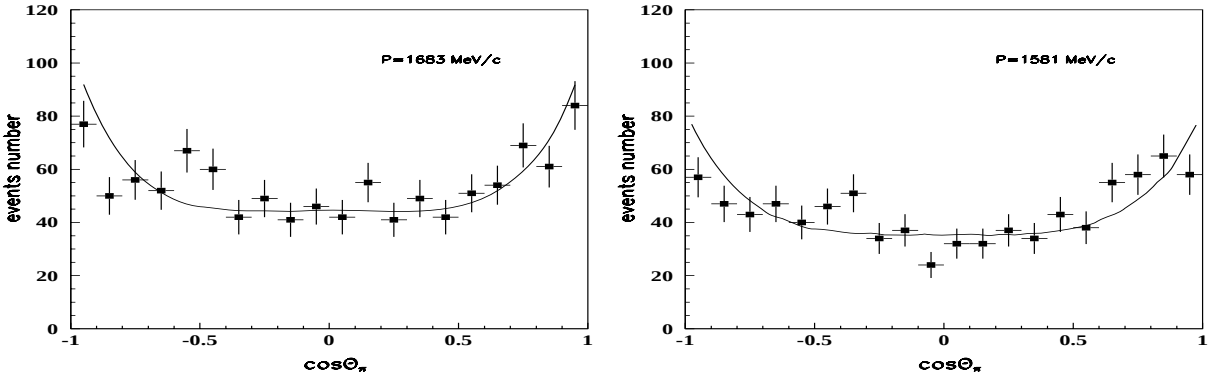

Fig. 6. π^0-meson angular distributions (c.m.s.). The curves have the same meaning as in Fig. 2

should say that the distributions are far from being isotropic. Since the c.m.s. angular distributions of pions should be symmetrical, we tried fitting to them by the formula

$$\frac{d\sigma}{d\Omega^*_{\pi^0}} \sim \frac{k}{2\pi}(1/3 + b\cos^2\theta^*_{\pi^0}). \tag{4}$$

The results of such a fit are shown in Fig. 7 together with the values found by other authors. The problem is important, being connected with the attempts to estimate the contribution from the isoscalar channel to the inelastic np-interaction. If this contribution is zero, the angular distributions of charged pions in the $np \to pp\pi^-$ $(nn\pi^+)$ reactions should be simular to those of π^0 mesons in the $pp \to pp\pi^0$ reaction. The presence of terms linear in $\cos\theta^*_{\pi^\pm}$ in the angular distribution of np-reactions might be considered as an indication to the isoscalar contribution. It is clear that to catch a small contribution of the isoscalar channel one needs to know well enough a form of the isovector contribution for which the $pp \to pp\pi^0$ reaction provides better opportunity.

As it is seen in Fig. 7, the anisotropy factor b is rather badly determined and a scatter of values is fairly large. Nevertheless one can see that b increases gradually together with the energy and starting with the momentum of ~1.2 GeV/c it is in the range 0.2–0.4.

As one can see in the above-given Figures, there is a good qualitative agreement of the OPE model with experimental differential spectra while the predictions for the total cross sections underestimate the data. The existing experimental data on the total cross sections are shown in Fig. 8 together with the model predictions. It is seen that there is an obvious discrepancy between the OPE model

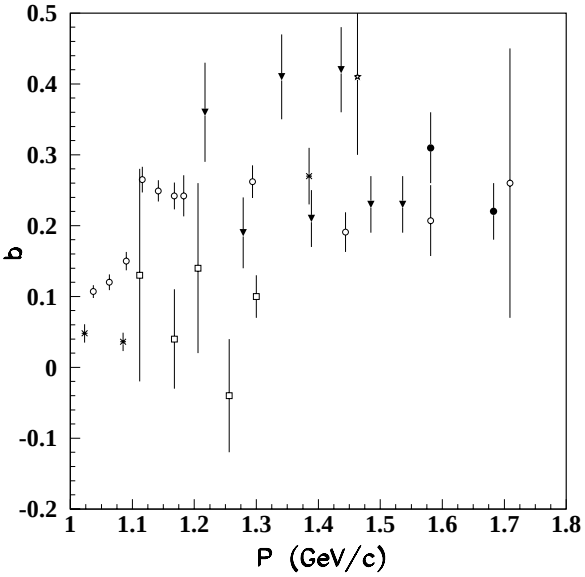

Fig. 7. The values of the parameter b from the fit of the experimentally measured angular distributions of the π^0 mesons: • – this work, ∘ – Ref. [1]

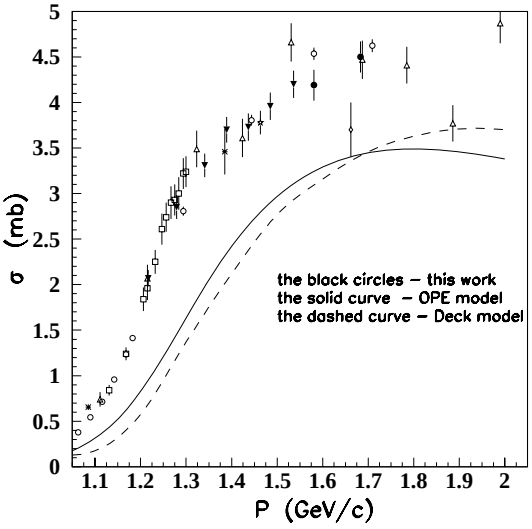

Fig. 8. Cross section of the $pp \to pp\pi^0$ reaction

calculations (solid curve) and experimental cross sections. Why does the OPE model fail to describe the cross section values for the $pp \to pp\pi^0$ reaction? One can obtain better agreement with a proper choice of the form factor, but such a choice destroys the agreement with total cross sections of the $pp \to pn\pi^+$ reaction, as was shown in Ref. [1]. One might guess that the reason for such a situation is that the πN amplitude is not good enough because only the P_{33} wave was taken into account. The dashed curve in Fig. 8 corresponds to the predictions of the Deck model, where the πN vertex includes all the waves obtained in the partial-wave analysis of Karlsruhe group. One can see that this does not change the situation significantly. One should keep in mind, however, that, with an exception for P_{33} wave, there is no good prescription for the calculation of the off-shell correction being very important. So the question is still open.

The present measurements together with our previous data at lower energies [1] as well as measurements of cross sections of the $pn \to pp\pi^-$ reaction[1] allow one to obtain the energy dependence of the isoscalar inelastic cross section

$$\sigma(I=0) = 3[2\sigma(pn \to pp\pi^-) - \sigma(pp \to pp\pi^0)] \ . \tag{5}$$

Figure 9 shows one third of the isoscalar inelastic $NN\pi$ cross section for the energies at which the reaction $pp \to pp\pi^0$ was investigated by us [1, 2] and also by G. Rappenecker *et al.* The values of $\sigma(np \to pp\pi^-)$ were obtained by the interpolation to the same final kinetic energy in the center-of-mass system.

One can see that the isoscalar cross section is close to zero up to the momentum 1.4 GeV/c, and furthermore it rises in agreement with the prediction of the Deck model (solid curve).

[1] L.D. Dakhno *et al.*, Phys. Lett. B **114**, 409 (1982).

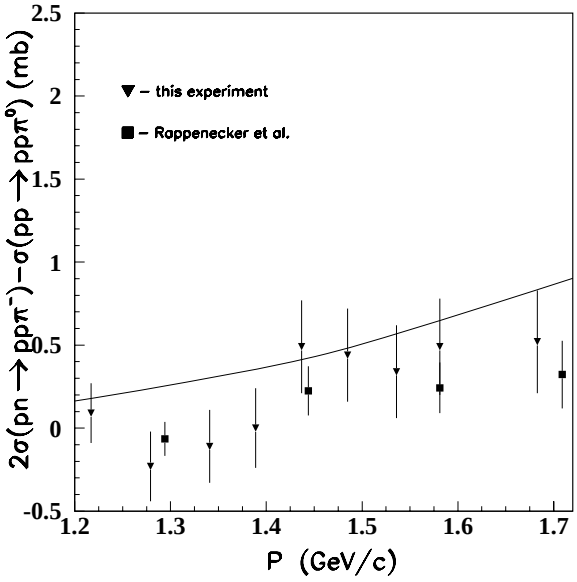

Fig. 9. Isoscalar inelastic cross section. The curve is the calculation of the Deck model

5. Conclusion

A detailed study of differential cross sections of the $pp \to pp\pi^0$ reaction has been performed at two incident energies near 1 GeV. The shape of the distributions is described by the OPE model quite well, in spite of the fact that the P_{33} wave only is used in the πN scattering amplitude. On the other hand, the OPE model fails to predict the correct total cross sections and it cannot be improved by the simple choice of the form factor.

We would like to express our gratitude to the bubble chamber staff as well as to the laboratory assistants, which toiled at the film scanning and measuring. A half of measurements of selected two-prong events at one momentum was carried out on the "Elit" device in the Institute of Nuclear Physics of Moscow State University. We would like to express our deep acknowlegement to Prof. P.F. Ermolov for supporting this work as well as to N. Grishin and the staff of engineers of the INP MSU without whom this work could not be completed.

References

1. V.P. Andreev *et al.*, Z. Phys. A **329**, 371 (1988); V.P. Andreev *et al.*, Phys. Rev. C **50**, 15 (1994).
2. V.V. Sarantsev *et al.*, Eur. Phys. J. A **21**, 303 (2004).

EXTRACTION OF THE $\pi^- n \to \pi^- \pi^- p$ CROSS SECTION FROM THE MEASUREMENT OF THE $\pi^- d \to \pi^- \pi^- pp$ REACTION AT ENERGY 430 MeV

S.G. Sherman, K.N. Ermakov, V.I. Medvedev, O.V. Rogachevsky, V.V. Sarantsev

1. Introduction

Recent few years have brought a number of measurements of the $\pi N \to \pi\pi N$ reaction at energies close to the threshold. One of the main goals of these investigations was the extraction of the S-wave, isospin–0, 2 $\pi\pi$-scattering lengths. In addition, these production processes certainly are of interest due to their important role in the low-energy physics of elementary particles and nuclei. It was shown that the low-energy experimental data for $\pi N \to \pi\pi N$ are consistent with the assumption of isospin symmetry as well as threshold predictions of chiral perturbation theory. An important progress in the understanding of $\pi N \to \pi\pi N$ reactions was due to Olsson and Turner, who calculated the leading contributions near threshold using an almost model-independent Lagrangian. The chiral perturbation theory (and its extensions) is applied strictly at the threshold of the single pion production reactions, where as a rule the statistics is rather poor because of a smallness of the cross sections. Experimentalists are forced to move to the above threshold region of energies because the pion production cross section grows faster than T^2, where T is the energy above the threshold in c.m.s. In this case an accurate extraction of scattering lengths in the large extent depends on a correct understanding of the production mechanism in the above-threshold region, because here other diagrams together with pole and contact terms contribute into the reaction amplitude.

It is important here to know the role of contributions from tails of the $N^*(1440)$ and $\Delta(1232)$ baryon resonances, which determine almost wholly the mechanism of the process at higher energies. Hence in this region the experimental data are needed too. In addition, the certain models developed for the pion production above threshold pretend to describe the experimental data up to incident pion kinetic energy 400 MeV.

In the energy range 400–600 MeV, experimental data on the reaction $\pi^+ p \to \pi^+ \pi^+ n$ are rather scarce and the statistics consists of tens of events. The poor statistical accuracy is due to experimental difficulties: apart from a smallness of the cross section, the single pion production reaction has a strong background of the elastic $\pi^+ p$ scattering which also has two positive charged particles in the final state.

Due to these reasons we investigated [1] the charge-conjugated reaction

$$\pi^- n \to \pi^- \pi^- p \tag{1}$$

using the bubble chamber filled with deuterium as a neutron target.

2. Measurements and experimental results

To determine the cross section of the process $\pi^- n \to \pi^- \pi^- p$ we have selected in the deuterium bubble chamber the events for the reaction

$$\pi^- d \to \pi^- \pi^- pp\ . \tag{2}$$

Experimentally the presence of more than two charged particles in the final state is an advantage in using this reaction for it enables us to separate it unambiguously from the background (elastic and quasi-elastic processes) at the first stage of the film processing.

The experiment was carried out at the pion channel of the PNPI synchrocyclotron. A 35 cm bubble chamber filled with deuterium was exposed to the π^--meson beam at the momentum of 555 MeV/c with the spread 25 MeV/c (FWHM). The muon and electron contamination was determined from the time-of-flight spectrum and found to be negligible. The average number of incident particles per picture was about 10. A total number of 225 000 pictures was taken.

Monte Carlo simulation of the reaction (1) with the use of the FOWL code for a generation of events according to the phase space as well as the GEANT21 for particle tracking through the chamber showed that among the events generated there was none with a length of any negative track of the unmeasured curvature. On the other hand, there were the events without one proton track that corresponded to the case when one of the protons (the proton-spectator for the pion production reaction off a neutron) with a momentum smaller than 80 MeV/c is not visible in the chamber. To select the necessary three- and four-prong events with two negative charged tracks in the final state all films were scanned twice. The efficiency of the double scanning was 99.5%.

The selected events could belong not only to the negative pion production but also to processes with Dalitz pairs in the final state (*e.g.*, the neutral pion production). The events found were measured on semi-automatic measuring devices and geometrically reconstructed. To select the events for the reaction (2) the χ^2-criterion was used with 1% confidence level. Dalitz pair events were rejected by kinematical and ionization criteria. A total number of 207 events of the type (2) was selected.

To obtain the absolute cross section value, the total length of the beam tracks in the fiducial volume of the chamber was determined. To this aim the number of the beam tracks was counted in ten pictures taken from every fifty ones all along the exposure and the mean length of beam tracks was measured. The deuterium density was taken to be 0.136 g/cm^3 with the 4% accuracy. The error given below for the cross section value consists of the statistical one as well as errors of the measurement of the average track length (1%), track density per picture (3%), total number of useful pictures (1%) and deuterium density. The cross section value for the reaction (2) has been found to be

$$\sigma(\pi^- d \to \pi^- \pi^- pp) = 0.194 \pm 0.016 \text{ mb}. \tag{3}$$

The purpose of the present experiment is to determine the cross section of the reaction (1). So it is necessary to discuss the influence of Fermi motion of the neutron in the deuteron and the Pauli exclusion principle for identical protons in the reaction (2) as well as to take into account screening effects.

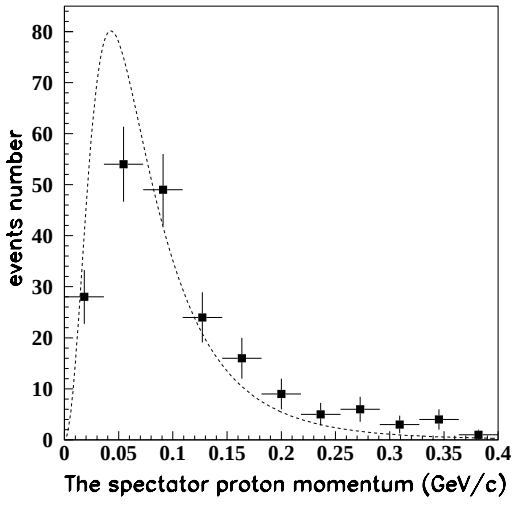

Fig. 1. Momentum distribution of the slow proton. Curve is corresponding distribution for the Hulthen wave function

The Fermi motion of the neutron in the deuteron could change the mean value of the effective incident pion momentum for the reaction (1) as well as the momentum distribution form. Figure 1 shows the momentum distribution of the slowest proton in the final state of the reaction (2) together with the Hulthen deuteron wave function distribution. One can see that the impulse approximation is valid with an exception for the region of large momenta. The momentum distribution of effective incident pion from the reaction (1) calculated from the final state of (2) taking into account two pions and fast proton only has the same mean value as that of the pion beam. But the first distribution has the gaussian width three times larger. Since the cross section of the reaction (1) grows linearly with the energy, this increase of the width has nothing to do with the mean energy for which we intend to give a value of the cross section of the reaction (1).

The Pauli principle is important mainly at low energies when two low-energy protons have rather large probability to be in the same state. The simple estimates of the Pauli effect were made in the framework of the isobar model of the single pion production. Such an estimate showed that Pauli principle could result in less than 2–4% decrease

of the cross section value. These estimates are model-dependent and, since the total error of the cross section $\sigma(\pi^- d \to \pi^-\pi^- pp)$ measured in this experiment is above 8%, the last correction was not included in the magnitude of the cross section off the free neutron.

The screening effect for the neutron in the deuteron was estimated in the framework of Glauber theory. It was assumed that screening corrections are identical for any channel of πN-collisions. Following the receipt given by Glauber theory, the negative pion production cross section on the deuteron is connected with that on the free neutron as follows:

$$\sigma_{\pi^- d} = \sigma_{\pi^- n} - \frac{1}{4\pi}\sigma_{\pi^- n}\sigma^{tot}_{\pi^- p} < \frac{1}{r^2} >, \tag{4}$$

where the second term is the screening correction, $\sigma_{\pi^- n}$ and $\sigma^{tot}_{\pi^- p}$ are the cross section sought on the free neutron and the total cross section on the proton, respectively, and $< r^2 >$ is the mean distance squared between the proton and neutron in the deuteron.

The distance between the proton and neutron in the deuteron is the double deuteron matter radius. The mean square matter radius (rms) equal to 1.967 fm was taken from the paper of Friar *et al.*, where this value was obtained from the isotope-shift measurements. The total cross section of the $\pi^- p$ scattering was taken to be 27.8 mb. Substituting these values and $\sigma(\pi^- d \to \pi^-\pi^- pp)$ into (3) one obtains that the screening correction to the deuteron cross section amounts to 1.5% and is equal to 0.003 mb. Then the cross section of the single pion production off the free neutron is

$$\sigma(\pi^- n \to \pi^-\pi^- p) = 0.197 \pm 0.016 \text{ mb}. \tag{5}$$

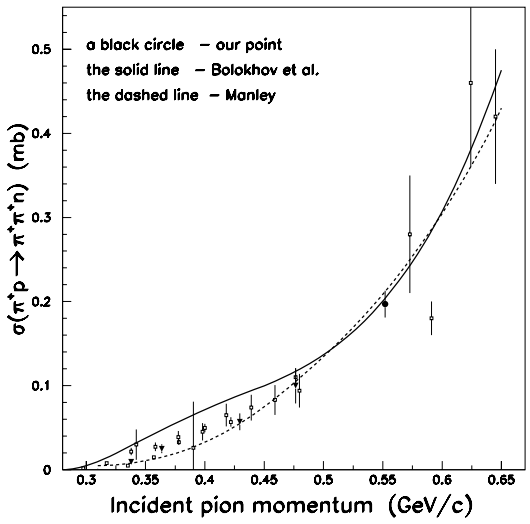

Fig. 2. Total cross section for the $\pi^+ p \to \pi^+\pi^+ n$ ($\pi^- n \to \pi^-\pi^- p$) reaction as a function of incident pion momentum

In Fig. 2, this value (black circle) is shown together with the data of others experiments for $\pi^+ p \to \pi^+\pi^+ n$ as well as the data for the reaction (1) obtained by us earlier [2] for four lower energies (black triangles). Curves in Fig. 2 correspond to the isospin analysis by Manley and to calculations carried out in the framework of the model of Bolokhov *et al.*[1] Among all diagrams considered in this model, only those shown in Fig. 3 are needed for a satisfactory description of the experimental data. They include one-pion exchange diagram and those at tree level with the nucleon, $\Delta(1232)$ and $N^*(1440)$ baryons in the intermediate states. The parameters of the model were obtained by fitting to five total cross section for five pion production reactions in the energy points near 430 MeV as well the differential distributions obtained by Kirz *et al.* at 357 MeV and those of this experiment, which are presented below.

In the papers by Bernard *et al.* and Jensen *et al.*, the single pion production was studied in the frame of relativistic baryon chiral perturbation theory at tree level, with the $\Delta(1232)$ and $N^*(1440)$ baryon resonances in the intermediate states. In the first of them the exchanges by heavy mesons (σ, ρ) were also taken into account. In both papers, it was declared that they can describe satisfactorily the majority of existing data for total and differential cross sections for incident pion energies up to 400 MeV. Since the cross sections were calculated only for the region below 400 MeV, we may compare our experimental value with those given by them on the edge of this energy range. In both papers, a slow growth was predicted for the $\pi^+ p \to \pi^+\pi^+ n$

[1] A.A. Bolokhov *et al.*, Nucl. Phys. A **530**, 660 (1991); Preprint PNPI-2197, Gatchina, 1997.

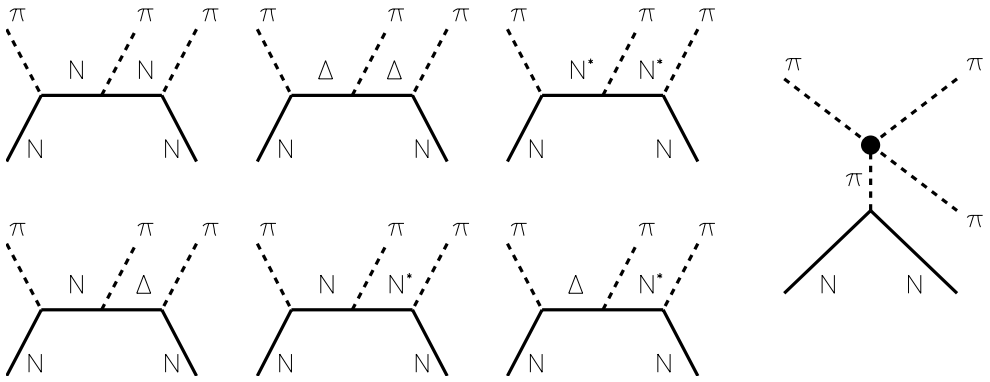

Fig. 3. Feynman diagrams taken into account in the framework of the model of Bolokhov *et al.*

reaction cross section, and the values given for 400 MeV are about 0.4 mb and 0.35 mb, respectively, that is much larger than the value measured by us for 430 MeV.

So the predictions of the chiral perturbation theory for the cross section of this reaction are obviously overestimating. Of course, it is possible that the energy above 400 MeV is too high, and these approaches are not applicable here. An analysis of pion production through the baryon resonance formation in the intermediate states is more appropriate here. Such is the model of Bolokhov *et al.*

As it was mentioned above, the statistics for the reaction $\pi^+ p \to \pi^+\pi^+ n$ ($\pi^- n \to \pi^-\pi^- p$) in the energy range 400–600 MeV amounted to tens of events only. Therefore so far it was impossible to investigate the differential spectra and compare them to the theoretical calculations. Although the statistics for the present experiment is not large too, still it allowed us to carry out the analysis of one-dimensional spectra.

Figure 4 shows the distributions of the events as a function of the pion and proton momentum in the c.m.s. of the $\pi^- n \to \pi^-\pi^- p$ reaction at 430 MeV.

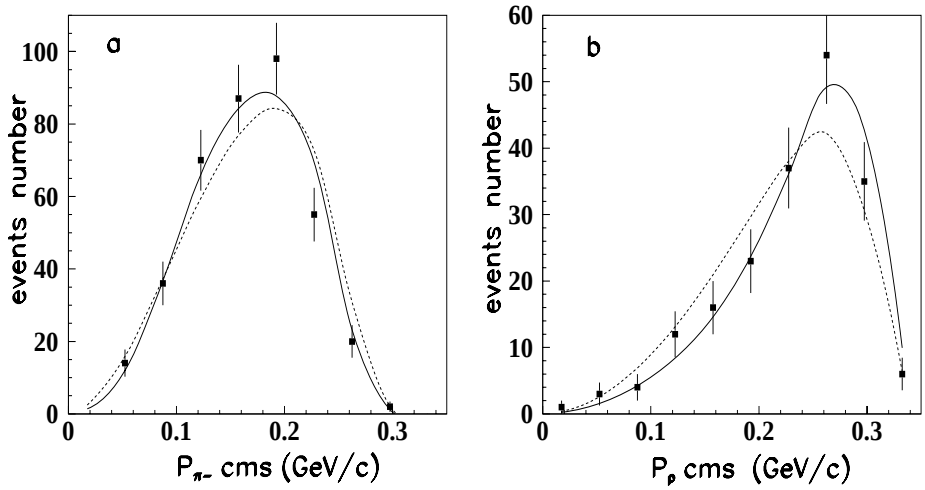

Fig. 4. The center-of-mass momentum spectra of pions and proton of the $\pi^- n \to \pi^-\pi^- p$ reaction. Dashed curve is the phase space distribution and the solid one is calculated in the framework of the model of Bolokhov *et al.*

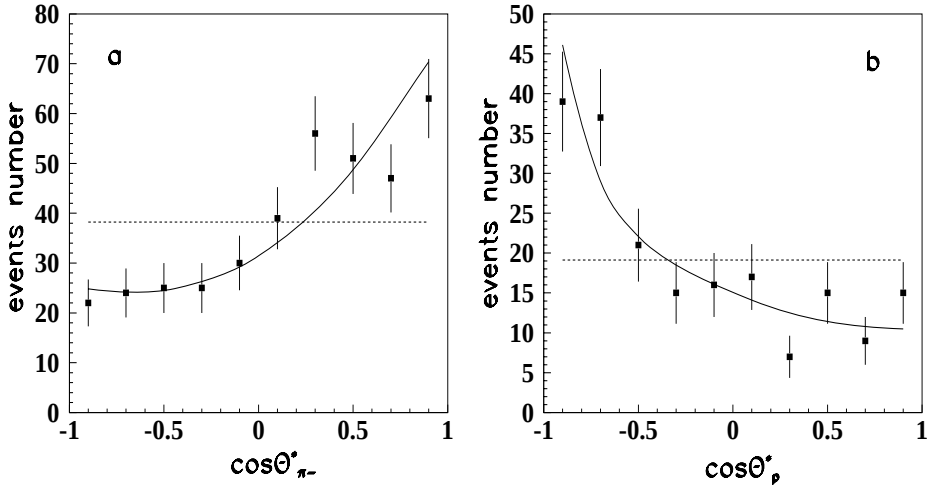

Fig. 5. Distributions of events as functions of the π^--meson and proton angles in c.m.s. The curves are the same as in Fig. 4

The curves normalized to the total number of events represent the phase space (dashed curve) and the results of the fit (solid one) carried out in the framework of the model of Bolokhov *et al.* with the use of diagrams of Fig. 3. Although the curves differ a little from each other, the calculations within the model of Bolokhov *et al.* reproduce more correctly the behavior of experimental spectra. The c.m.s. angular distributions of pions and the proton are shown in Fig. 5 together with curves presenting the results of above-mentioned fit. It is worth noting that the observed behaviour of the differential cross section of this experiment is similar to that observed by Kirz *et al.* at 357 MeV. The calculations of the Bolokhov *et al.* model for angular distributions agree excellently with both set of data of these experiments.

Figure 6a shows the distribution of events as a function of the relative pion momentum $K_{\pi\pi}$ in the

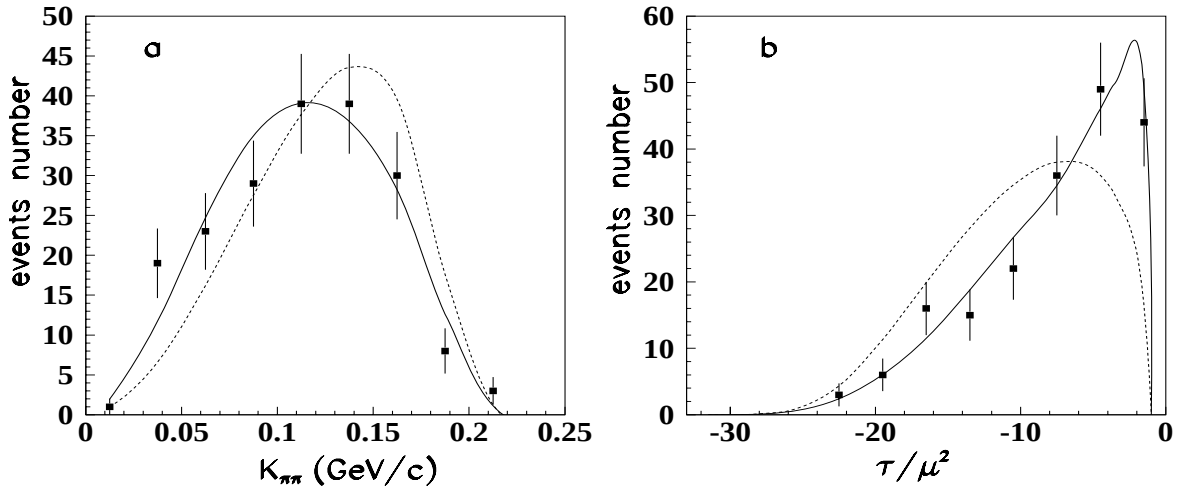

Fig. 6. a) Distribution of events as a function of the relative pion momentum in the dipion c.m.s. b) Distribution of events as a function of the square of momentum transfer. The curves are the same as in Fig. 4

dipion c.m.s. The phase space distribution and the calculation within the model of Bolokhov *et al.* are similar here, though the latter is closer to the experimental distribution. In Fig. 6b one can see the distribution of the events as a function of the momentum square τ transferred to the proton, in the m_π^2 units. Again, the dashed line represents the phase space, whereas solid line shows the calculation within the model of Bolokhov *et al.*

So the comparison of the various differential spectra with calculations in the frame of the model by Bolokhov *et al.* shows that to reach the agreement of the theory with experimental data in the energy range 450–550 MeV/c one needs to include into theory not only one-pion exchange but also diagrams with the nucleon, $\Delta_{33}(1232)$ and $N^*(1400)$ in the intermediate states. The exclusion from the fit any of baryon resonances shown in Fig. 3 results in a considerable disagreement between experimental data and the theory.

3. Conclusion

We have studied the single pion production $\pi^- n \to \pi^- \pi^- p$ reaction, using the bubble chamber filled with deuterium as a neutron target. The obtained cross section value coincides fairly well with the prediction of the isospin analysis by Manley but disagrees with models developed for the description of the energy region of single pion production a little bit above the threshold. As a rule, the predicted values are much higher than experimental magnitude. The fitting of various differential spectra obtained by Kirz *et al.* and in the present experiment allowed us to find parameters of the model of Bolokhov *et al.*, so that the theory describes quite well experimental data in energy range 450–550 MeV/c.

We would like to acknowledge a personnel of the cryogenic division for excellent operation of the bubble chamber and to thank the scanners and measurers for their painstaking efforts.

References

1. K.N. Ermakov *et al.*, Eur. Phys. J. A **23**, 345 (2005).
2. A.V. Kravtsov *et al.*, Nucl. Phys. B **134**, 413 (1978).

NUCLEAR AND ATOMIC PHYSICS

EXPERIMENTAL STUDY OF THE NUCLEAR SPATIAL STRUCTURE OF NEUTRON-RICH He AND Li ISOTOPES

G.D. Alkhazov, A.V. Dobrovolsky, A.V. Khanzadeev, G.A. Korolev, A.A. Lobodenko, D.M. Seliverstov, A.A. Vorobyov

1. Introduction

To understand the evolution of sizes and shapes of nuclei in the nuclear chart from the valley of β-stability to the drip-line is one of the central questions of modern nuclear structure physics. Recent technique with radioactive beams has made it possible to reach the limit of the neutron drip-line for relatively light nuclei. Experimental studies have led to a discovery of significant neutron halos (skins) in these neutron-rich exotic nuclei. In nuclei near the drip-line, the separation energy of the last nucleon(s) becomes small. The valence nucleons of such loosely bound nuclei may have a very extended density distribution, called "halo". The necessary conditions for the halo formation have been intensively discussed. It was concluded that the nuclear states with small binding energy and low angular moment may form halos. The halo structure manifests itself in different types of reactions, in particular, by a large interaction cross section and by narrow momentum distributions of the reaction products in the processes of nuclear breakup and Coulomb dissociation. Note that the term "neutron skin" is used to describe an excess of neutrons over protons at the nuclear surface. It should be admitted however that a uniquely strict definition of the terms "skin" and "halo" does not exist. Some nuclei, such as ^{6}He and ^{8}He, are often referred to as neutron-skin as well as neutron-halo nuclei.

Experimental methods applied for studying halo nuclei were mainly measurements of the total interaction cross sections and investigations of momentum distributions of the reaction products after fragmentation. The spatial structure of exotic nuclei was proposed at PNPI to be studied by small-angle proton elastic scattering on nuclei. The proton-nucleus elastic scattering at intermediate energy is known to be an efficient means for studying the matter distributions in stable nuclei. This method can also be used in the inverse kinematics to study unstable short-lived nuclei. An advantage of proton scattering experiments at intermediate energy as compared to similar experiments at low energy is that at intermediate energy there exists a rather accurate multiple scattering theory of Glauber, which can relate the measured cross sections with the studied density distributions in quite an unambiguous way. The scattering of protons from the nuclear halo is confined to small scattering angles. Therefore, in order to study the spatial structure of halo nuclei it is important to measure with high accuracy the differential cross sections for proton scattering at small momentum transfers. The recoil detector IKAR, developed and built at PNPI [1], was adapted as an active hydrogen target in combination with a spectrometer for measurement of projectile scattering angles. Previously, IKAR was successfully used for investigation of small-angle hadron elastic scattering.

In experiments performed at GSI (Darmstadt) by the PNPI-GSI Collaboration, precise data on absolute differential cross sections for proton elastic scattering on stable ^{4}He, ^{6}Li and neutron-rich ^{6}He, ^{8}He, ^{8}Li, ^{9}Li, and ^{11}Li nuclei have been obtained in the inverse kinematics at an energy of about 0.7 GeV/nucleon at near-forward angles [2–4].

The matter radii and the radial structure of nuclear matter were derived from the data using the Glauber multiple scattering theory. Combining these results with results of other experiments permits one to obtain more details on the nuclear spatial structure.

2. Experimental setup and procedure

For the experiments, primary ^{18}O beams were extracted from the heavy-ion synchrotron SIS and focused on an 8 g/cm^2 beryllium production target at the entrance of the fragment separator FRS. Isotopes of helium and lithium nuclei produced by fragmentation of ^{18}O entered the FRS and were separated according to their magnetic rigidity. In some cases the separation power of the FRS was enhanced by inserting an achromatic (20 g/cm^2) aluminum degrader at the dispersive central focal plane for achieving isotopically pure beams. Beam intensities were generally 10^3 s^{-1} with the duty factor between 25% and 50%.

The arrangement of detectors for the scattering experiment is shown in Fig. 1. The main constituent of the setup was the hydrogen-filled ionization chamber IKAR at a pressure of 10 bar, which served simultaneously as a gas target and a recoil proton detector. The recoil protons were registered in IKAR in coincidence with the scattering projectiles. The momentum transfer could be determined either from the measured energy of the recoil protons or from the value of the scattering angle Θ_s of the projectiles which was measured by a tracking detector consisting of 2 pairs of two-dimensional multiwire proportional chambers (PC1-PC2 and PC3-PC4), arranged upstream and downstream with respect to IKAR. A set of scintillation counters (S1, S2 and S3) were used for triggering and identification of the beam particles *via* time-of-flight and *dE/dx* measurements, and a circular-aperture scintillator VETO was used to select projectiles that entered IKAR within an area of 2 cm in diameter around the central axis. In the experiment with the secondary beams of the lithium isotopes, the experimental setup was supplemented with a magnetic-rigidity analysis of the scattered particles (with the help of a dedicated dipole magnet ALADIN and a scintillator wall behind it) for the reliable separation of the projectile break-up channels. The quality of the isotope separation achieved is demonstrated in Fig. 2 for the case of the ^{11}Li scattered beam, where the ejectile horizontal plane X-coordinate measured at the scintillator wall is plotted *vs* the horizontal plane scattering angle Θ_x for the Li isotopes, these measurements being performed in coincidence with the IKAR signals corresponding to scattering events. It is seen that the projectile breakup channels could easily be discriminated.

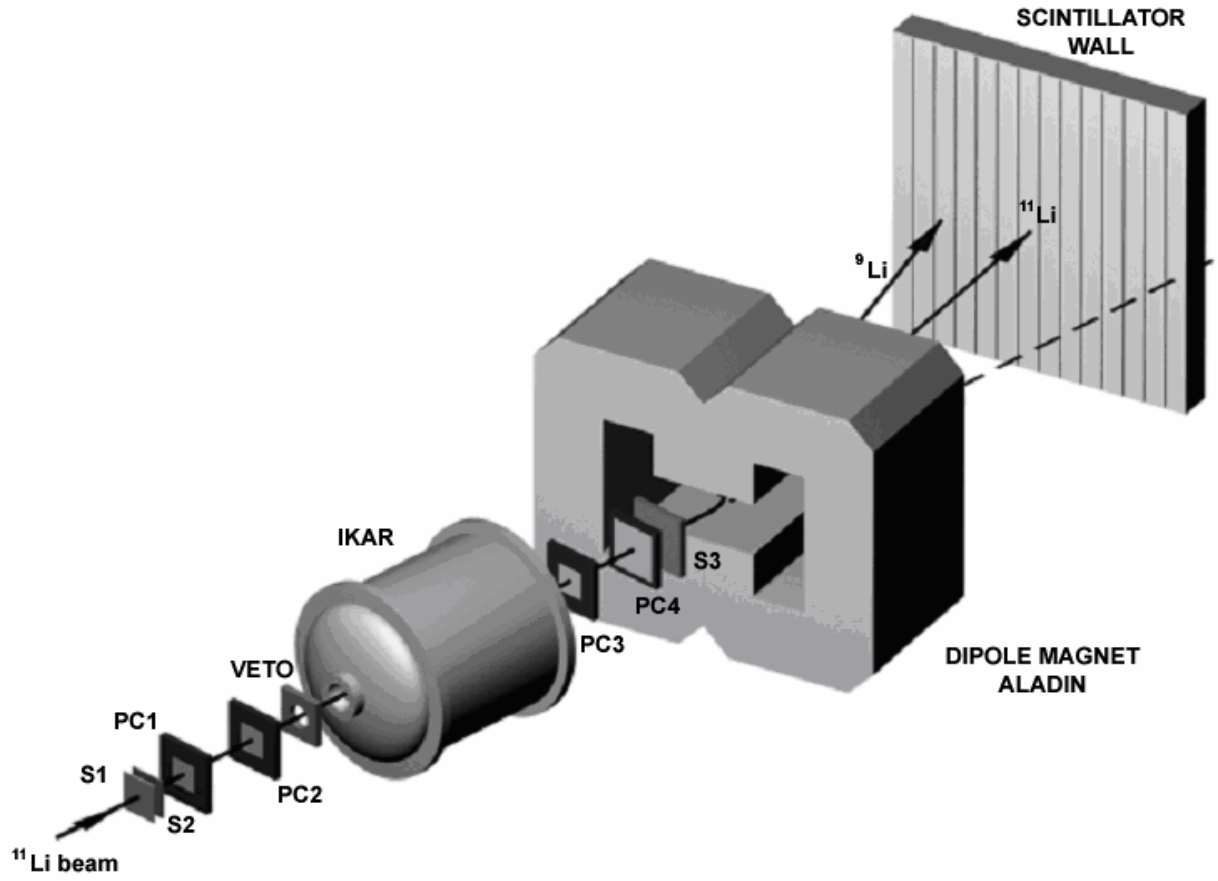

Fig. 1. Schematic view of the experimental setup for small-angle proton elastic scattering on exotic nuclei in the inverse kinematics. The central part shows the hydrogen-filled ionization chamber IKAR, which serves simultaneously as gas target and detector system for recoil protons. In six independent sections of this detector the recoil energy T_R, the recoil angle Θ_R and the vertex point Z_v are determined. The forward spectrometer consisting of four multi-wire proportional chambers PC1–PC4 determines the scattering angle Θ_S of the projectile. The scintillation counters S1–S3 and VETO are used for beam identification and triggering. The dipole magnet ALADIN with a position-sensitive scintillator wall behind allows to identify the scattered beam particle and to discriminate breakup channels

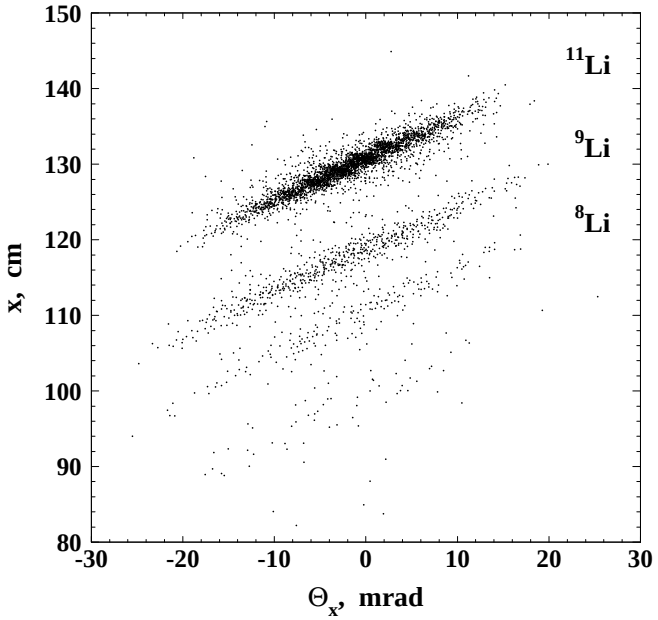

Fig. 2. Correlation between the measured ejectile horizontal X-coordinate behind the ALADIN magnet and the scattering angle Θ_x for the case of the ^{11}Li beam

The absolute differential cross section $d\sigma/dt$ is determined from the relation

$$\frac{d\sigma}{dt} = \frac{dN}{dt \cdot Mn \cdot \Delta L} \ . \qquad (1)$$

Here, dN is the event rate of elastic pHe or pLi scattering in the interval dt of the four-momentum transfer squared, and M is the corresponding rate of beam particles hitting the target. The quantity n is the density of the target nuclei known from the measured H_2 gas pressure and temperature, and ΔL denotes the effective target length. The differential cross section for proton scattering at the energy of E_p= 0.7 GeV from the ^{4,6,8}He and ^{6,8,9,11}Li nuclei were measured in the t-range of 0.002 $(\text{GeV/c})^2 \le |t| \le 0.05$ $(\text{GeV/c})^2$ (Fig. 3). The systematic error of the cross section normalization was ~3%, while the uncertainty in the t-scale calibration was about 1.5%.

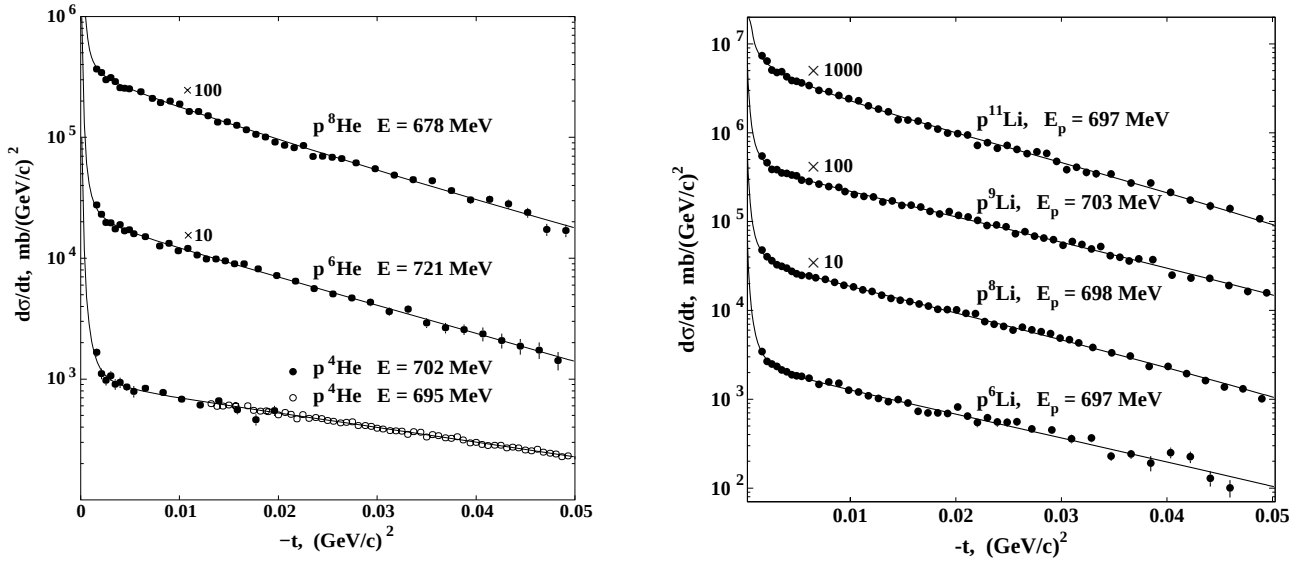

Fig. 3. Absolute differential cross sections $d\sigma/dt$ *vs* the four momentum transfer squared t for p^4He, p^6He, and p^8He (left side), and p^6Li, p^9Li, and p^{11}Li (right side) elastic scattering measured in the present experiment (full dots). For p^4He scattering, the open dots show the data of Ref. [5]. Plotted lines are obtained by calculations using the Glauber multiple scattering theory

The measurement of $d\sigma/dt$ for p^4He scattering was carried out for the main purpose of providing a reference to the known precise data of the IKAR experiment [5] performed in the direct kinematics. Good agreement between both sets of data (see Fig. 3) gives confidence to the novel experimental approach applied in this work.

For establishing the nuclear density distributions from the measured cross sections, the Glauber multiple scattering theory was applied. Calculations were performed using the basic Glauber formalism for proton-nucleus elastic scattering and taking experimental data on the elementary proton-proton and proton-neutron scattering amplitudes as input. In the analysis, four parameterizations for phenomenological nuclear density distributions have been applied, labeled as SF (symmetrized Fermi), GH (Gaussian-halo), GG (Gaussian-Gaussian) and GO (Gaussian-oscillator). Each of these parameterizations has two free parameters. While the SF and GH parameterizations do not make any difference between the neutron and proton distributions, the GG and GO parameterizations assume that the nuclei consist of core nucleons and valence nucleons with different spatial distributions. The core distribution is assumed to be a Gaussian one in both the GG and GO parameterizations. The valence nucleon density is described by a Gaussian or a 1p shell harmonic oscillator-type distribution within the GG or GO parameterizations, respectively. The free parameters in the GG and GO parameterizations are the r.m.s. radii R_c and R_v of the core and valence nucleon distributions. It was assumed that the considered nuclei have one (^{8}Li), two (^{6}He, ^{6}Li, ^{9}Li, ^{11}Li) or four (^{8}He) valence nucleons. The free parameters of the model density distributions have been deduced by fitting the calculated cross sections to the experimental ones in the t-range covered by the experiment. For p^4He scattering, the data of this experiment and those of Ref. [5], measured in a wider t-interval, were analyzed together.

3. Results on the matter density distribution and radii

The solid curves in Fig. 3 represent the results of the calculations performed using phenomenological density distributions with fitted parameters. At very small values of $|t|$, the steep rise of the cross sections with $|t|$ decreasing is due to the Coulomb scattering. As for the cross sections at larger values of $|t|$ (at $|t| > 0.005$ (GeV/c)^2 where the contribution from the Coulomb scattering is small), at first glance the measured cross sections plotted in the logarithmic scale look like straight lines, that is the cross sections seem to have an exponential t-dependence. However, at closer examination it is possible to see that the t-dependence of the cross sections at 0.005 (GeV/c)$^2 < |t| < 0.05$ (GeV/c)^2 in the cases of p^4He and $p^{8,9}$Li scattering is indeed very close to the exponential one, whereas the shape of the cross sections in the cases of $p^{6,8}$He and $p^{6,11}$Li scattering deviates noticeably from the exponential form. This deviation can be seen if one plots the cross sections divided by exponential functions. Such a plot is presented in Fig. 4. It is seen that the p^{11}Li, p^6He, p^8He and p^6Li cross sections are not consistent with the exponential form, that can be explained by the fact that the contributions to the cross section of proton scattering from the core and from the halo of these nuclei have different angular dependences, the contribution of scattering from the halo decreasing with $|t|$ increase faster than that from the core. The fact that halo nuclei demonstrate positive curvature in log ($d\sigma/dt$) was supported by simulation calculations [2, 4] for the cases of ^{6}He and ^{11}Li.

The parameterizations SF and GH applied for ^{4}He allowed us to describe the data equally well and have yielded identical values of the matter radius. The experimental differential cross sections for the case of ^{6}He, ^{6}Li, ^{8}He, ^{8}Li, and ^{9}Li are well described with the four density parameterizations used, the reduced value of χ^2 being around unity. For these nuclei, the matter density distributions obtained with the GG and GO parameterizations are very similar to those obtained with the SF and GH parameterizations, the deduced r.m.s. matter radii being practically the same for the four versions of the analysis. All versions of the analysis also resemble each other in reproducing extended matter distributions in ^{6}He and ^{8}He, the matter density decreasing with the radial distance r increase much slower than that for ^{4}He.

A simple geometrical classification scheme has been suggested by theorists, where the ratio of the valence nucleon to core nucleon radii $\kappa = R_v/R_c$ is used as a gauge for the halo. For light neutron-rich nuclei close to the valley of β-stability theory predicts typically $\kappa \sim 1.20$–1.25, while for halo nuclei this values can be essentially larger, up to $\kappa \geq 2$. Fig. 5 shows for the case of p^{11}Li scattering the value of χ^2, which serves as a quantitative criterion for the quality of the theoretical description of experimental data, the fitted cross sections being

calculated with different values of the assumed ratio R_h/R_c of the halo (R_h) and core (R_c) r.m.s. radii. It is seen that good data description is achieved only in the case when the halo radius is significantly larger than that of the core, the fitted value of R_h/R_c being 2.46 (17). This figure demonstrates high sensitivity of the proton scattering cross sections at small momentum transfers to the halo structure of exotic nuclei.

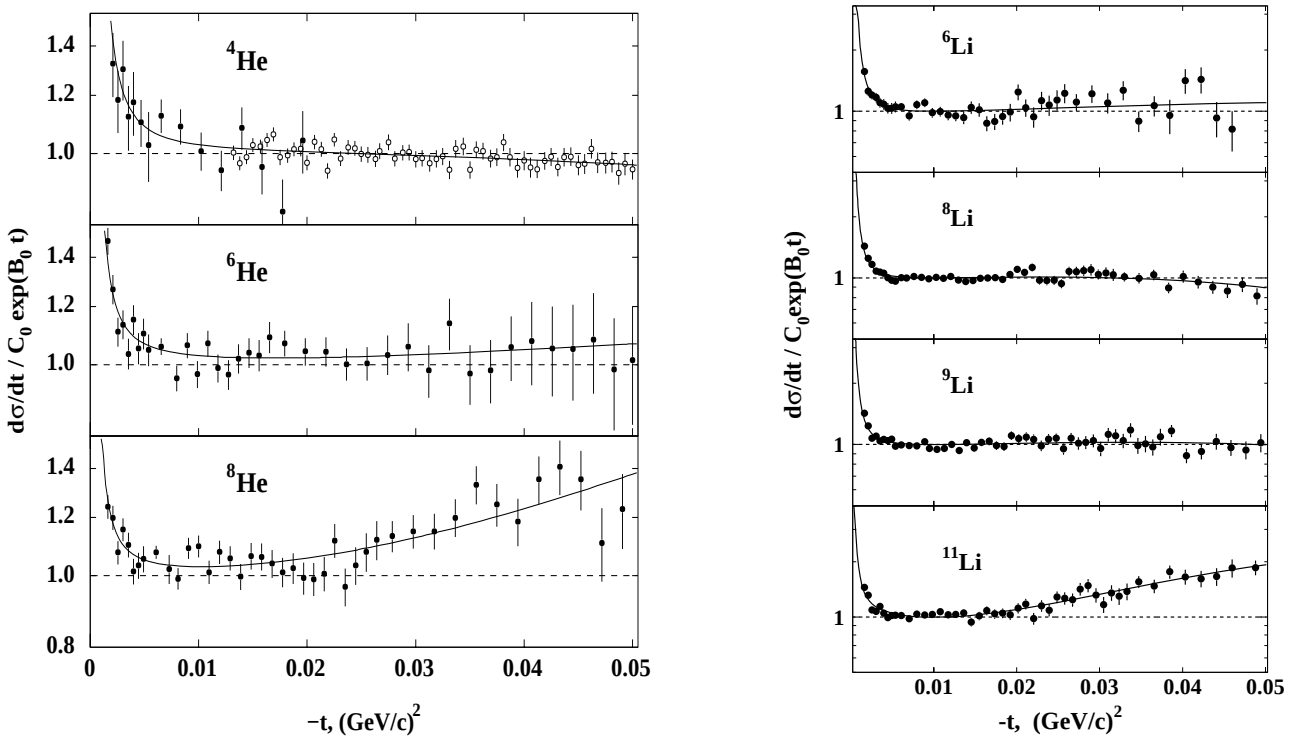

Fig. 4. Measured differential cross sections for He and Li isotopes divided by an exponent. The positive curvature in $\log(d\sigma/dt)$ is a fingerprint of isotopes with an extended density distribution. The ^{11}Li nucleus with the largest halo shows the most pronounced positive curvature

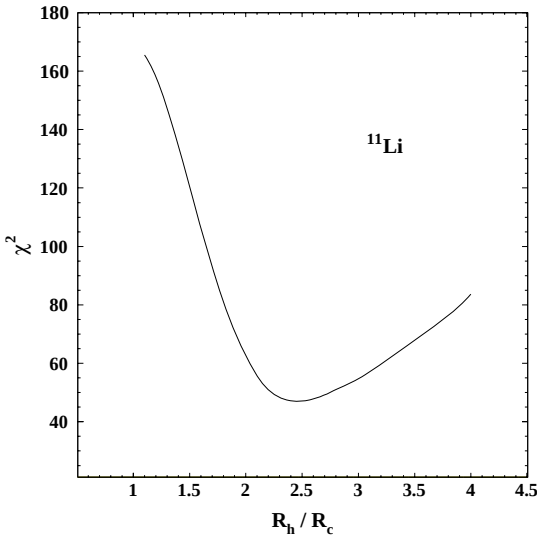

Fig. 5. The value of χ^2, serving as quantitative criterion for the quality of p^{11}Li differential cross section description, as a function of the assumed ratio R_h/R_c of the halo and core radii of ^{11}Li.

It should be noted that the data on small-angle proton scattering have low sensitivity to a possible contribution of long halo density tails, which are predicted by theory for nuclei with low binding energy. Taking such tails from theory may increase the deduced radii by 0.1–0.2 fm in the case of ^{6}He and ^{8}He [2] and by ~0.3 fm in the case of ^{11}Li [4].

The results obtained for helium and lithium isotopes in this experiment are presented in Table 1. This table presents the r.m.s. radii R_m, R_c, and R_v of the matter, core and valence nucleon distributions, and the ratio $\kappa = R_v/R_c$ deduced from the data. It is seen that the matter radii of the ^{6}He, ^{8}He and ^{11}Li nuclei are significantly larger that those of the lighter He and Li isotopes. In the case of ^{4}He and ^{6}Li, which are the $N = Z$ nuclei, the matter density distributions and radii determined from the data on proton scattering are in good agreement with the proton distributions deduced from the known data on electron scattering. The ^{8}Li and ^{9}Li nuclei do not have noticeable signatures of the halo-like structure. However ^{6}He, ^{8}He and ^{11}Li exhibit a halo-like structure, the ^{11}Li nucleus having the most pronounced halo.

Table 1

Summary of the results obtained for helium and lithium isotopes in the present experiment. The values R_m, R_c and R_v denote the r.m.s. radii of the matter, core and valence nucleon(s) distributions, κ is the ratio R_v/R_c. As mentioned in the text, R_m (and R_v) for ^{6}He, ^{8}He and ^{11}Li are deduced taking into account long density tails predicted by theory at the nuclear far periphery

Nucleus	R_m, fm	R_c, fm	R_v, fm	$\kappa = R_v/R_c$
^{4}He	1.49 (3)	–	–	–
^{6}He	2.45 (10)	1.88 (12)	3.31 (28)	1.76
^{8}He	2.53 (8)	1.55 (15)	3.22 (14)	2.08
^{6}Li	2.44 (7)	2.11 (17)	3.00 (34)	1.42
^{8}Li	2.50 (6)	2.48 (7)	2.58 (48)	1.03
^{9}Li	2.44 (6)	2.20 (6)	3.12 (28)	1.41
^{11}Li	3.71 (20)	2.53 (3)	6.85 (58)	2.71

The matter distributions deduced for ^{8}Li and ^{9}Li turn out be quite similar to each other (Fig. 6). Within the quoted errors the matter radii of ^{8}Li and ^{9}Li are equal to that of ^{6}Li. This means that ^{8}Li and especially ^{9}Li are more dense nuclei than ^{6}Li, the latter being considered to have an $\alpha + d$ spatial structure.

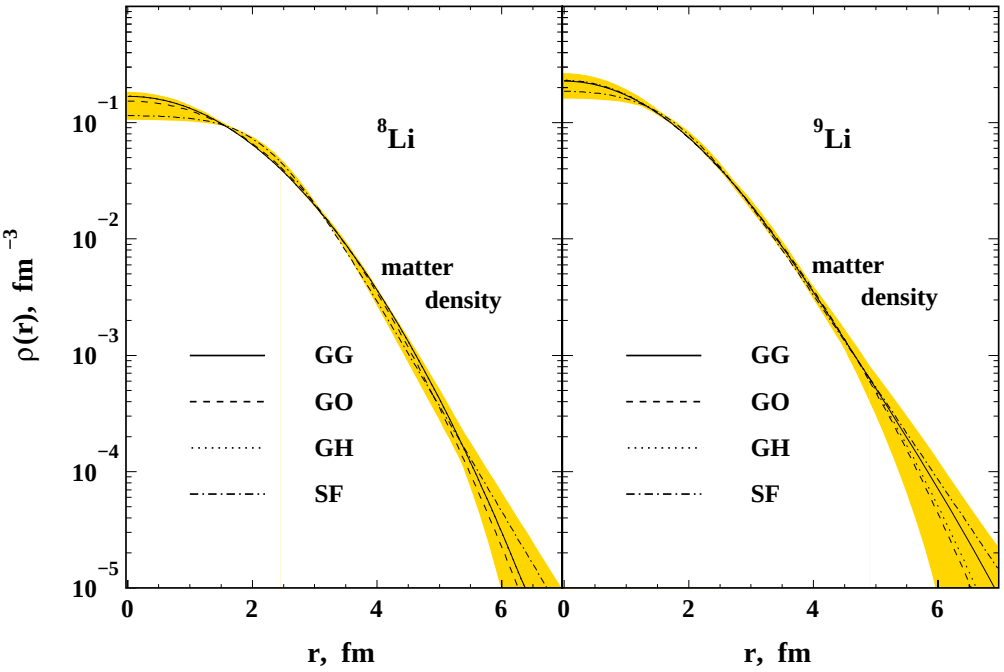

Fig. 6. Nuclear matter density distributions in ^{8}Li and ^{9}Li deduced from the present data. Solid, dashed, dotted and dash-dotted lines correspond to the densities obtained using the SF, GH, GG and GO density distribution parameterizations, respectively. The shaded areas represent the envelopes of the density variation within the model parameterizations applied, superimposed by the statistical errors. The nuclear density distributions are normalized to the total number of nucleons

Figure 7 shows the core and total matter density distributions derived for ^{11}Li and ^{8}He using phenomenological density distributions. It is seen that while in the case of ^{8}He it might be still questionable whether the valence neutron distribution should be called halo or skin, the observed extended valence neutron distribution in ^{11}Li at the nuclear far periphery is decidedly an outstanding neutron halo.

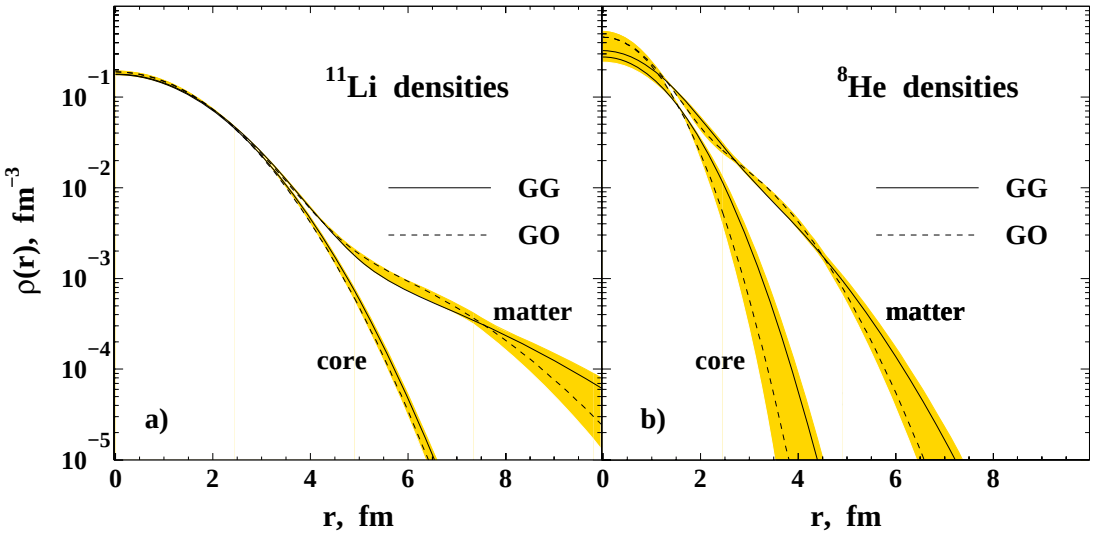

Fig. 7. (a) Nuclear core and total matter density distributions in ^{11}Li deduced from the present data using the GG and GO density distribution parameterizations. (b) Similar distributions in ^{8}He. The shaded areas represent the envelopes of the matter and core density variations within the model parameterizations applied, superimposed by the statistical errors

Recent precise measurements of the charge radii by the laser spectroscopy for ^{6}He and ^{8,9,11}Li permit to extract the r.m.s. radii R_p of proton distributions (see Table 2). Combining these values and the value of R_m deduced from the data on proton elastic scattering, it is easy to obtain the radii of the neutron distributions R_n of these nuclei. The thickness of the neutron skin $\delta_{np} = R_n - R_p$ can also be determined (Table 2).

In the experiment on the Coulomb dissociation of ^{6}He performed recently at GSI, new information on the structure of the ground state wave function was obtained. It was found that the mean square distance between the center-of-mass (CM) of the ^{6}He system and that of the α-particle core is $R_{\alpha}^{CM} = 1.12\ (13)$ fm, while the distance between the CM of the ^{6}He system and that of the two halo neutrons is $R_{2n}^{CM} = 2.24\ (26)$ fm. Combining these values with the radii from Table 2 it is possible to find for ^{6}He the radius of the proton distribution in the core center $R_p^* = [R_p^2 - (R_{\alpha}^{CM})^2]^{1/2} = 1.55\ (10)$ fm and the radius of the di-neutron cluster $R_{dn}^* = [R_h^2 - (R_{2n}^{CM})^2]^{1/2} = 2.45\ (48)$ fm. The determined size of the di-neutron cluster (or the distance between the two neutrons $R_{nn} = 2\,R_{dn}^*$) denotes a weak attractive correlation between the halo neutrons. It means that the di-neutron configuration of halo neutrons in ^{6}He predominates over cigar-like configuration [6].

Table 2

Neutron radii R_n and neutron skin thicknesses $\delta_{np} = R_n - R_p$, derived from matter radii R_m (present experiment) and proton radii R_p (laser spectroscopy experiments)

Nucleus	R_m, fm	R_p, fm	R_n, fm	δ_{np}, fm
^{6}He	2.45 (10)	1.91 (2)	2.68 (13)	0.77 (13)
^{8}Li	2.50 (6)	2.16 (3)	2.68 (9)	0.52 (10)
^{9}Li	2.44 (6)	2.09 (4)	2.60 (8)	0.51 (9)
^{11}Li	3.71 (20)	2.37 (4)	4.10 (25)	1.73 (25)

4. Conclusion

A new method to study the nuclear spatial structure of exotic nuclei by small-angle proton elastic scattering in the inverse kinematics has been proposed and developed at PNPI. The positive curvature in log $d\sigma/dt$ at small momentum transfers can be used as a qualitative indication of a possible halo existence. The method also permits to obtain from the data the matter, core and valence nucleon r.m.s. radii. The ratio of the valence nucleon to core nucleon radii gives a parameter for the quantitative measure for the halo structure.

Successful measurements of p^4He, p^6He, p^8He, p^6Li, p^8Li, p^9Li, and p^{11}Li elastic scattering were performed at an energy of 0.7 GeV/u at GSI, Darmstadt. Absolute differential cross sections were obtained with the experimental setup where the main constituent was an active target-recoil detector IKAR. The obtained results clearly demonstrate the halo structure of ^{6}He, ^{8}He and ^{11}Li, the most prominent halo being observed for ^{11}Li.

New measurements with the same experimental techniques were performed on B and Be ion beams at GSI in 2005 and 2006. Small-angle proton elastic scattering from the ^{7}Be, ^{9}Be, ^{10}Be, ^{11}Be, ^{12}Be, ^{14}Be and ^{8}B nuclei was studied. The most interesting among these nuclei are ^{8}B, for which the proton halo existence is expected, and ^{11}Be and ^{14}Be, for which significant neutron halos are expected. An analysis of the experimental data is in progress.

The data presented in this article have been measured and analyzed by the IKAR Collaboration:
G.D. Alkhazov, M.N. Andronenko, A.V. Dobrovolsky, G.E. Gavrilov, A.V. Khanzadeev, G.A. Korolev, A.A. Lobodenko, D.M. Seliverstov, N.A. Timofeev, A. A.Vorobyov, V.I .Yatsoura (PNPI, Gatchina), A. Baucher, P. Egelhof, S. Fritz, H. Geissel, C. Gross, H. Irnich, G. Kraus, G. Münzenberg, S. R .Neumaier, T. Schäfer, C. Scheidenberg, W. Schwab, T. Suzuki (GSI, Darmstadt), M. Mutterer (IKP TU, Darmstadt).

References

1. A.A. Vorobyov, G.A. Korolev, V.A. Schegelsky *et al*., Nucl. Instr. Meth. **119**, 509 (1974).
2. G.D. Alkhazov, A.V. Dobrovolsky, P. Egelhof *et al*., Nucl. Phys. A **712**, 269 (2002).
3. S.P. Neumaier, G.D. Alkhazov, M.N. Andronenko *et a*l., Nucl. Phys. A **712**, 246 (2002).
4. A.V. Dobrovolsky, G.D. Alkhazov, M.N. Andronenko *et al*., Nucl. Phys. A **766**, 1 (2006).
5. O.G. Grebenyuk, A.V. Khanzadeev, G.A. Korolev *et al*., Nucl. Phys. A **500**, 637 (1989).
6. G.D. Alkhazov, A.V. Dobrovolsky and A.A. Lobodenko, Yad. Fiz. **69**, 1157 (2006) [Phys. Atom. Nucl. **69**, 1124 (2006)].

INVESTIGATION OF NUCLEAR MEDIUM EFFECT ON CHARACTERISTICS OF PROTON-PROTON SCATTERING AT 1 GeV

O.V. Miklukho, S.L. Belostotski, K. Hatanaka[1)], A.Yu. Kisselev, T. Noro[2)], H. Sakaguchi[3)]

[1)] *Research Center for Nuclear Physics, Osaka University, Ibaraki, Japan*
[2)] *Department of Physics, Kyushu University, Fukuoka, Japan*
[3)] *Department of Physucs, Kyoto University, Kyoto, Japan*

1. Introduction

The modification of basic properties of nucleons and mesons in nuclear fields is one of the most interesting current topics in nuclear and hadron physics. It has been predicted in the framework of quantum chromodynamics that nucleon and meson masses are modified as a result of the partial restoration of chiral symmetry in nuclear media. From a different point of view, it has been conjectured that a nucleon Dirac spinor is modified in nuclear matter due to the large scalar potential in the framework of quantum hadrodynamics. This modification, a lower-component enhancement of the Dirac spinor, is also expressed as a decrease of nucleon masses in a nuclear field. Because nucleon-nucleon (NN) interactions are described as meson exchange forces between mucleons, it is expected that such medium effects at the hadron level cause the modification of NN interactions that is detectable with some nuclear reactions.

Intensive efforts have been continued to study NN interactions in the nuclear field and to investigate the effects of possible modification of hadron properties. In the study of nucleon elastic scattering, significant success has been realized with the relativistic impulse approximation, in which a modification of the Dirac spinor is implicitly taken into account. The effect of meson-mass modification on proton-nucleus scattering has been investigated by Brown *et al.*, and they found that the theoretical prediction is improved when this effect is taken into account. Recently, Sakaguchi *et al.* [1] studied this effect experimentally and concluded that modifications of the coupling constants and meson masses in the NN interaction are necessary in order to obtain predictions consistent with their experimental data in the case that the relativistic impulse approximation is employed.

Another type of nuclear reaction suitable for studying in-medium NN interactions is nucleon quasifree scattering which is, in a simple picture, NN scattering in nuclear field. It was first pointed out clearly by Horowitz that the analyzing power A_y values measured at LAMPF in inclusive experiment are smaller than those predicted using the free NN interaction. It has been suggested that this decrease in A_y is a signature of the relativistic effect mentioned above. This decrease has also been found to be much more distinct for a $(p, 2p)$ reaction corresponding to proton knockout from the S-shell of ^{16}O target in a TRIUMF experiment with incident energy of 500 MeV. Maxwell and Cooper analyzed these data with a relativistic distorted wave impulse approximation (RDWIA) formalism that includes both dynamic and kinematical recoil effects. Although their formalism exactly includes the relativistic effect, the calculated A_y values for knockout from the S-shell and the experimental data are in significant disagreement yet. They also found that the elimination of the spin-orbit parts of the Schrodinger phase-equivalent distortion potential gives moderate outgoing-proton energy dependence of the calculated A_y for knockout from S-shell, which is closer to the experimental data. On the other hand, Krein *et al.* have investigated the effects of modifications of meson masses and coupling constants on NN interactions in nuclear field. They have found that the effective polarizations of the target nucleons derived from TRIUMF data for $^{16}\mathrm{O}(p, 2p)$ reactions at proton energy of 200 MeV leading to $3/2P$ and $1/2P$ hole states can be consistently accounted for if such modified NN interactions are employed.

The $(p, 2p)$ experiments have been made for several types of target nuclei at RCNP at proton energy of 392 MeV [2]. As in the case of the TRIUMF data mentioned above, the A_y data for knockout of protons from the S-shells of nuclei were found to be smaller than those estimated by using NN interactions in free space. In addition, it was found that the decreasing rates are significantly target dependent. There was defined an effective mean density that provides a good measure of the sensitivity of $(p, 2p)$ reaction to the density-dependent term of NN interactions and showed that the observed decrease of A_y depends monotonically on the mean density. It has also been shown that this density-dependent reduction can not be accounted for by a medium effect in the nonrelativistic framework, which is inclusion of the Pauli-blocking effect [3]. In a recent paper, Miller *et al.* compared the TRIUMF data with results of "the best available DWIA reaction models". They concluded that the existing density-dependent NN interactions are not adequate for nucleon knockout reactions and the possibility of a more interesting mechanism, such as a hadron level medium effect, is implied.

At PNPI the polarization P of both secondary protons from the $(p, 2p)$ reaction with the ^{7}Li nucleus has been measured at proton energy of 1 GeV. The reduction of the measured polarizations of both protons in comparison with the polarization in the free elastic proton-proton scattering was observed, a value of the reduction being especially significant for the reaction with the S-shell protons [4]. It has also been shown that this effect can not be related to depolarization of the secondary protons due to proton-nucleon rescatterings in nucler matter, since the values of the reduction for these protons, which had essentially different energies, are close to each other.

In this paper, we present new results obtained in joint PNPI–RCNP $(p, 2p)$ experiment at 1 GeV.

The main goal of the experiment is to investigate the target dependence of the polarization in the $(p, 2p)$ reactions with the unmoved S-shell protons of nuclei ^{4}He, ^{6}Li, ^{12}C and ^{40}Ca at 1 GeV, which is an essentially higher energy than those at TRIUMF and RCNP. To study the nuclear medium effect comprehensively, we have measured the angular distribution of the polarization for ^{12}C and ^{6}Li targets for an angular range where energies of secondary protons change considerably and for ^{4}He target for an angular range where a value of residual nucleus momentum K_R changes from 0 to 150 MeV/c. These angular distributions permit to control contributions from so called multistep processes which are believed to vary significantly with kinematical conditions of the $(p, 2p)$ experiment. These angular distributions give the polarizations for a more wide range of the recoil momentum values compared with the scale of typical meson-mass values in the meson exchange model of the NN interaction and can be used for the examination of theoretical models that predict modification of the in-medium NN interaction, which may be related to medium effects at the hadron level.

2. Experimental method

The experimental method is described in details in Refs. [5–7]. The $(p, 2p)$ experiment was performed at non-symmetric scattering angles $\Theta_1 = 13.2°$–$26.1°$, $\Theta_2 = 53.1°$–$64.0°$ of the final protons under the conditions of a practically coplanar quasi-free scattering geometry and a complete reconstruction of the reaction kinematics.

External proton beam of the PNPI synchrocyclotron was focused onto a target of two-arm spectrometer (the magnetic spectrometers MAP and NES). The solid targets from CH_2, ^{6}Li, ^{12}C, ^{40}Ca and liquid helium (^{4}He) target [8] were used in present experiment.

The polarizations of secondary protons from the $(p, 2p)$ reaction P_1 and P_2 were measured by polarimeters located in the region of focal planes of spectrometers MAP and NES.

In measurements of the target dependence of polarization, the recoil spectrometer NES was installed at a fixed angle of around $\Theta_2 = 53.3°$. The momentum settings of the spectrometers NES and MAP and an angular position Θ_1 of the latter for each target corresponded to kinematics of the $(p, 2p)$ reaction with the $1S$-shell proton (with the $2S$-shell proton for the ^{40}Ca target) in which the nuclear proton momentum K ($\vec{K} = -\vec{K}_R$) has a value close to zero. This is the condition for which the cross section for the S-shell knockout is maximal and the reaction mechanism is expected

to be the simplest. At this kinematical condition, the dependences of polarization for ^{6}Li and ^{12}C targets as functions of an angular position of the NES spectrometer in the range of Θ_2 from 53.3° to 63.9° were measured. In the case of ^{4}He nucleus, the dependence of polarization as a function of an angular position of the MAP spectrometer in the range of $\Theta_1 = 24.21°–18.0°$ was measured, angle Θ_2 (53.22°) and momentum settings of both spectrometers being fixed. In this angular range, a value of the residual nucleus momentum K_R changes from 0 to 150 MeV/c.

The proton separation energy spectra for solid targets, presented in Fig. 1, allow to estimate the experimental energy resolution in this work.

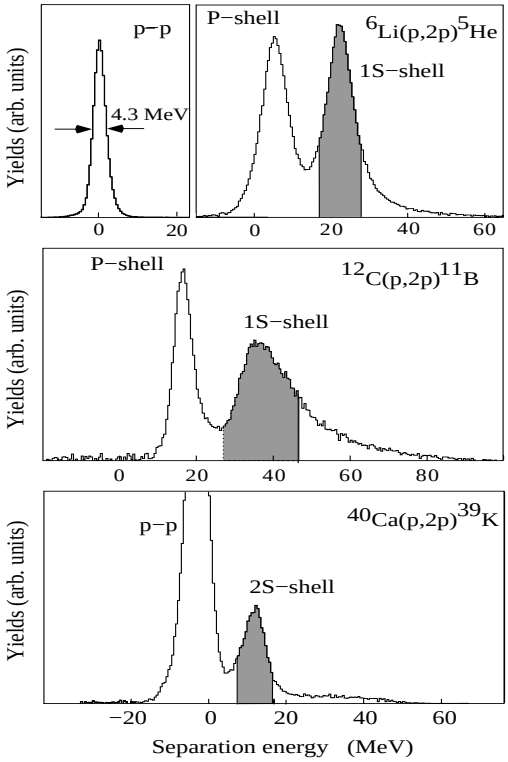

Fig. 1. Proton separation energy spectra for pp scattering and $(p, 2p)$ reactions. The shaded areas were used for data analysis

3. Experimental results

In Figs. 2–5 the results of present $(p, 2p)$ experiment are compared with various theoretical calculations. The experimental free elastic pp scattering points are also shown in these Figures with the open and closed square (or triangle) points for the scattered forward and recoil protons, respectively.

In Fig. 2 the polarizations P_1 and P_2 of secondary protons from the $(p, 2p)$ reactions with S-shell protons of the nuclei investigated are plotted *versus* the effective mean nuclear density $\bar{\rho}$ (given in units of the saturation nuclear density $\rho_0 \approx 0.19$ fm^{-3}) and the average binding energy E_s of the S-shell protons. These experimental data were obtained in the kinematical conditions in which the nuclear S-shell proton before the interaction had the momentum close to zero and the momentum q, transferred to a nucleus, depended weakly on the type of nuclear target. The actual calculation of the effective mean nuclear density, which is determined by absorptions of the incident and both outgoing protons, was carried out following a procedure described in Ref. [2] using the computer code THREEDEE.

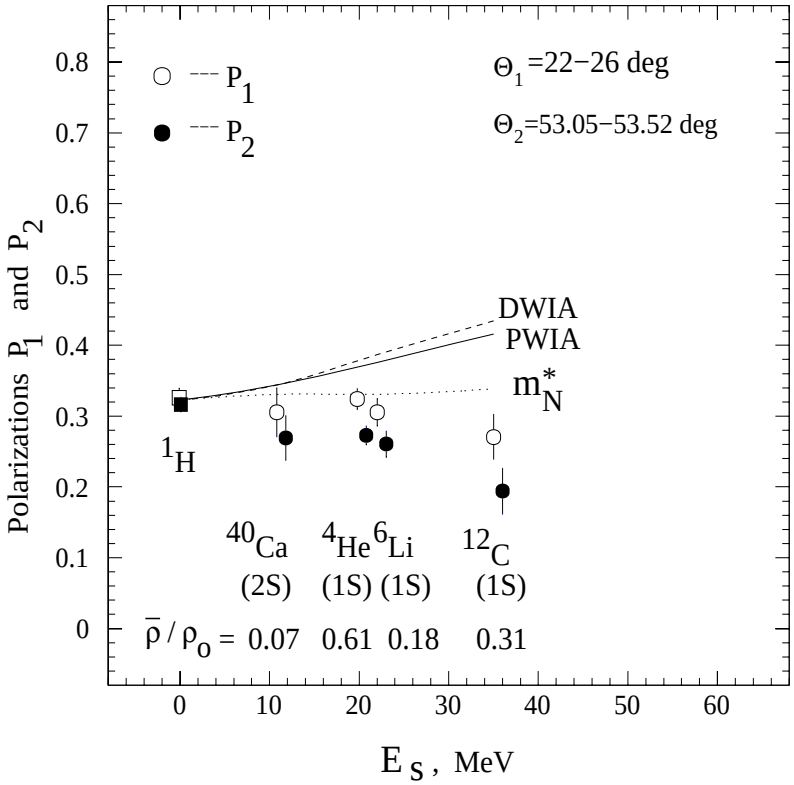

Fig. 2. Target dependence of the polarization data for pp scattering and $(p, 2p)$ reactions. The polarizations of forward and recoil outgoing protons are denoted by P_1 and P_2, respectively. The data points are plotted as functions of the effective mean nuclear density $\bar{\rho}$ and the average binding energy E_s of the S-shell protons. The dashed curve and the solid curve represent results of the DWIA and PWIA calculations with the NN interaction in free space, respectively. The dotted curve is the DWIA result in which the relativistic effect is taken into account in a Schrodinger-equivalent form

Figures 3–4 display the angular dependences of the polarization for the ^{12}C$(p, 2p)$ reaction and free elastic pp scattering, and for the ^{6}Li$(p, 2p)$ reaction, respectively. The data corresponding to NES angle in the range of $\Theta_2 = 53.1°$–$64.0°$ are plotted as functions of the momentum q transferred to a nucleus. These dependences were also obtained at zero values of the momentum of nuclear proton before the interaction. In this case the q is equal to the momentum K_2 of the recoil proton scattered to the NES spectrometer.

In Fig. 5 the polarization in the reaction ^{4}He$(p, 2p)^3$H is presented as a function of the MAP angle in the range of $\Theta_1 = 24.21°$–$18°$. The NES angle ($\Theta_2 = 53.22°$) and the momentum settings of both spectrometers were fixed in these measurements, the momentum of a nuclear proton before the interaction being zero at the angular position of the MAP spectrometer of $\Theta_1 = 24.21°$.

For free elastic pp scattering, the polarization of forward outgoing protons P_1 should be the same as that of backward (recoil) outgoing protons P_2. As seen in Fig. 3, at each value of q considered the measured values of P_1 and P_2 for elastic pp scattering are equal within the statistical errors of 0.01–0.02. Moreover, these data are consistent with the result of a phase shift analysis, that is represented by the dot-dashed curve in Fig. 3. The agreement found between these results indicates that the effective analyzing power of the both polarimeters is sufficient and that systematic errors are not dominant.

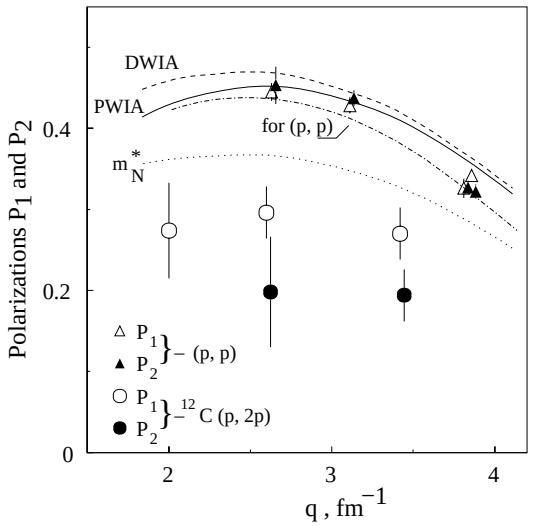

Fig. 3. Angular dependence of the polarization for pp scattering and the $(p, 2p)$ reaction with $1S$-shell proton of the ^{12}C nucleus. P_1 and P_2 are the polarizations of forward and recoil outgoing protons, respectively. The data are plotted as functions of the momentum q transferred to the nucleus. The dot-dashed curve represent the result of a phase shift analysis for free elastic pp scattering. The identifications of the other curves are the same as those in Fig. 2

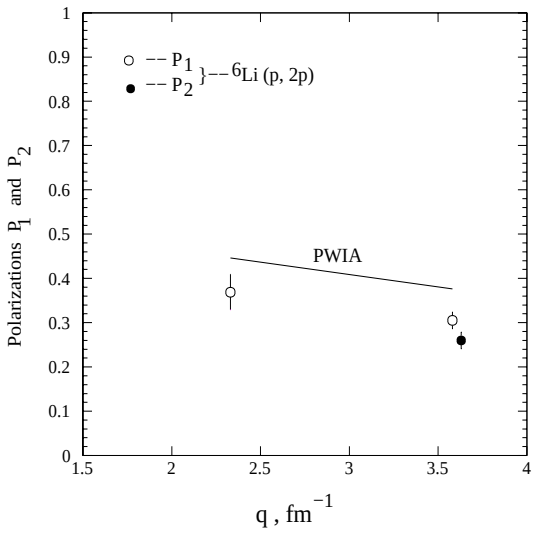

Fig. 4. Angular dependence of the polarization for the $(p, 2p)$ reaction with $1S$-shell proton of the ^{6}Li nucleus. P_1 and P_2 are the polarizations of forward and recoil outgoing protons, respectively. The data are plotted as functions of the momentum q transferred to the nucleus. The solid curve is the PWIA result

4. Comparison with theoretical predictions and discussion

In this section, first the experimental data are compared with the results of calculations in the framework of nonrelativistic plane wave impulse approximation PWIA [6] (solid curves in Figs. 2–5) and distorted wave impulse approximation DWIA employing an on-shell factorized approximation. The dashed curves, corresponding DWIA, represent the results of the calculations for nuclei ^{6}Li, ^{12}C and ^{40}Ca. These results were obtained using the computer code THREEDEE [5]. A global optical potential, parametrized in the relativistic framework and converted to the Schrodinger-equivalent form, was used to calculate the distorted waves of incident and outgoing protons, and a conventional

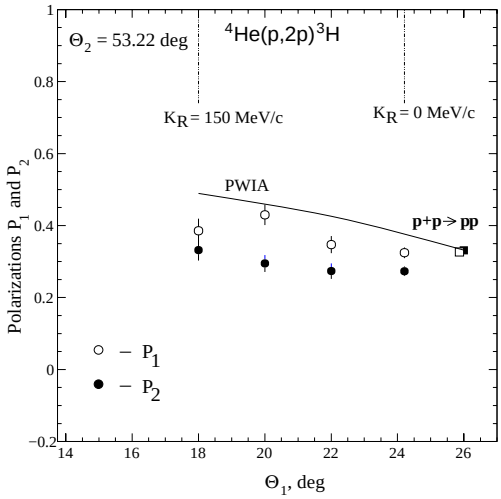

Fig. 5. Angular dependence of the polarization for the $(p, 2p)$ reaction with $1S$-shell protons of the ^{4}He nucleus. P_1 and P_2 are the polarizations of forward and recoil outgoing protons, respectively. The solid curve is a result the PWIA calculations in the range of the residual nucleus momentum K_R = 0–150 MeV/c

well-depth method was used to construct bound-state wave functions. Because the difference between polarizations P_1 and P_2 values in the DWIA calculations was found to be small, typically smaller than 0.01 and no more than 0.02, only the P_1 values obtained from DWIA are plotted in these Figures. As seen in Figs. 2–3, the difference between the PWIA and DWIA results is quite small. This result suggests that the distortion, in a conventional nonrelativistic framework, does not play an essential role in the polarization for the kinematical conditions employed in the present work. The observed experimental fact that the polarizations in both spectrometer arms are close to each other speaks also that depolarization effect (distortion), due to proton-nucleon rescattering in nuclear matter, is small. The final energy prescription was used for the impulse approximation (IA) calculations. It was found that the difference between the initial and final prescriptions was small in the kinematics investigated. The strong positive slope of the polarizations predicted by these calculations in Fig. 2 is caused by the kinematical effects of the binding energy of the struck proton.

The difference between the polarization values from the IA calculations and the measured values, both of P_1 and P_2, for all nuclei investigated excluding the ^{4}He nucleus are monotonically increasing functions of the effective mean nuclear density. This result is similar to the corresponding result obtained at 392 MeV [2] with regard to the analyzing power, and it provides the further evidence that there exists a medium effect. As seen in Figs. 3–4, a value of the difference for the reactions ^{12}C$(p, 2p)$ and ^{6}Li$(p, 2p)$ is essentially constant over the entire range of the momentum q transferred to the nucleus, where the effective mean density for each nucleus is also almost constant. Note here that there is a systematic difference between the P_1 and P_2 values, though they have the same value in the case of free elastic pp scattering, as it was mentioned above. Possible origins of the finite difference between these values include nonrelativistic and relativistic distortions (though the former is excluded if the present DWIA calculations are valid), multistep processes (contributions, for instance, from $(p, 2pN)$ reactions), and even a nontrivial modification of nucleons in the nuclear field. However, the differences are within twice of the magnitude of the statistical errors and are considerably smaller than the differences between either dataset and the results of the IA calculations.

In Figs. 2–3, the polarizations P_1 and P_2 observed in the $(p, 2p)$ experiment with the nuclei ^{6}Li, ^{12}C and ^{40}Ca are also compared with a theoretical result (the dotted curve) obtained in the framework of the Horowitz and Iqbal relativistic treatment of proton nucleus scattering [5]. In this approach a

modified NN interaction in nuclear medium is assumed due to the effective nucleon mass (smaller than the free mass) which affects the Dirac spinors used in the calculations of the NN scattering matrix. A linear dependence of the effective mass of nucleons on the nuclear density was assumed in the calculations. As seen in Figures, the discrepancy between the predictions obtained with the in-medium NN interaction and the experimental values is roughly half as large as that between the predictions obtained with the free NN interaction and the experimental values. The result is also similar to that found at 392 MeV in RCNP for the analyzing power A_y and thus it implies that the same kinds of mechanism causes the density-dependent modification of these observables at both energies. It is also to be emphasized that this relativictic approximation gives an almost constant reduction rate in Fig. 3, where the effective mean nuclear density is practically the same.

Another possible medium effect is the modifications of exchanged meson masses and meson-nucleon coupling constants in the NN interaction. Krein *et al.* have shown in the relativistic Love-Franey model (RLF) that these modifications cause significant changes in spin observables which include suppression of A_y. Because parameter values for the RLF model valid in the 1 GeV region are not known yet, such a calculation is not presented in this paper, but this medium effect is expected to lead also to smaller predicted values of polarization P.

As seen in Fig. 2, the ^{4}He nucleus breaks the correlation observed for other nuclei between a value of the polarization reduction measured in comparison with the polarization obtained in the IA and a value of the effective mean nuclear density $\bar{\rho}$. This reduction in the case of the ^{4}He nucleus having the largest value of the $\bar{\rho}$ is close to that for the ^{6}Li nucleus and is small in comparison with that for the ^{12}C nucleus. The $\bar{\rho}$ for the ^{4}He nucleus was calculated as well as for other, more heavy, nuclei following a procedure described in Ref. [2] using the computer code THREEDEE. Note that a result of such calculations based on the DWIA is not reliable in the case of very light nuclei as ^{4}He. Moreover, the bound state wave function of ^{4}He generated and used in these calculations, parameters of which are tuned to get a reasonable mean square radius (1.47 fm) of the nucleus, gives a value of the proton separation energy E_s much larger than the experimental value ($\approx$ 20 MeV). However, according to studies of elastic nucleon-nucleus scattering, the ^{4}He nucleus has the largest mean nuclear density, only a part of which ($\bar{\rho}$), having unexpectedly small value, manifests itself in a $(p, 2p)$ experiment because of absorption effects. It is possible that in light nuclei, where nuclear matter is strongly heterogeneous and clusterized, the $\bar{\rho}$ does not reflect quite properly the scale of nuclear medium effect on hadron properties and NN interaction. The important result of the present work including experiment with the ^{4}He nucleus (see Fig. 2) is that the polarization reduction mentioned above keeps to be a monotonous function of the S-shell proton binding energy E_s, which for light nuclei at least may also be a measure of influence of nuclear matter on protons and, as consequence, on characteristics of the pp interaction. In 2006 year there was carried out the $(p, 2p)$ experiment in which the polarization of the secondary protons produced in the reaction with protons of the very deep shell ($1S$) of the ^{40}Ca nucleus was measured. The experiment was aimed to identify whether a value of nuclear density or proton separation energy determines the scale of the nuclear medium effect in heavy nuclei.

The second important significance of the $(p, 2p)$ experiment with the ^{4}He nucleus, all nucleons of which being at $1S$-state, is a possibility to see the medium effect without any contribution from the multistep processes, which can take place when there are nucleons of outer shells as in other nuclei. Figure 4 shows that a value of the polarization reduction for the ^{4}He nucleus does not depend on kinimatical conditions of the $(p, 2p)$ experiment in a wide range of the residual nucleus momentum K_R. This also confirms that there is a medium effect related to the modification of NN scattering matrix in nuclear field.

5. Conclusion

The reduction of both P_1 and P_2 polarizations of the secondary protons from $(p, 2p)$ reactions with the S-shell protons of nuclei ^{4}He, ^{6}Li, ^{12}C and ^{40}Ca in comparison with the polarization calculated with free NN interaction in the framework of the PWIA and DWIA was observed. A value of the reduction does not depend on kinematical conditions of the experiment and for nuclei with atomic number $A > 4$ monotonically increases with the effective mean nuclear density. This indicates a modification of the proton-proton scattering matrix in nuclear medium. The experiment with the ^{4}He nucleus showed that the magnitude of the reduction, in light nuclei at least, is determined rather by the mean binding energy of the S-shell proton of a nucleus than by the effective mean nuclear density. The calculations in the relativistic approximation, in which a modification of nucleon Dirac spinor is taken into account, reproduce only a half of magnitude of the reduction. These results are similar to the results of the RCNP experiment in which the analyzing power for the same reactions at the incident protons energy of 392 MeV was measured. From the fact that essentially the same reduction rate has been observed over a wide range of incident and outgoing protons, in which contributions of multistep processes are expected to vary significantly, it is concluded that this phenomenon does not originate from the reaction mechanism. In order to extract a definitive conclusion regarding the medium modification of interactions, more theoretical works are needed. The data presented here should provide a good test for such works.

The list of participants of the present work:
V.A. Andreev, G.M. Amalsky, S.L. Belostotski, Yu.V. Elkin, O.Ya. Fedorov, K. Hatanaka, A.A. Izotov, A.A. Jgoun, J. Kamia, A.Yu. Kisselev, L.M. Kotchenda, A.I. Kovalev, M.P. Levchenko, O.V. Miklukho, T. Noro, E. Obayashi, Yu.G. Naryshkin, A.N. Prokofiev, D.A. Prokofiev, H. Sakaguchi, A.V. Shvedchikov, H. Takeda, V.Yu. Trautman, V.A. Trofimov, S.I. Trush, V.V. Vikhrov, T. Wakasa, Y. Yasuda, H.P. Yoshida, and A.A. Zhdanov

References

1. H. Sakaguchi *et al.*, Phys. Rev. C **57**, 1749 (1998).
2. K. Hatanaka *et al.*, Phys. Rev. Lett. **78**, 1014 (1997).
3. T. Noro *et al.*, Nucl. Phys. A **663-664**, 517c (2000).
4. O.V. Miklukho *et al.*, Nucl. Phys. A **683**, 145 (2001).
5. V.A. Andreev *et al.*, Phys. Rev. C **69**, 024604 (2004).
6. O.V. Miklukho *et al.*, Preprint PNPI-2614, Gatchina, 2005. 22 p.
7. O.V. Miklukho *et al.*, Phys. Atom. Nucl. **69**, 474 (2006).
8. L. Kotchenda *et al.*, in *Main Results of Scientific Research at PNPI RAS in 2000-2004*, Gatchina, 2005, p. 221.

STUDY OF ENERGY DEPENDENCE OF PROTON-INDUCED FISSION CROSS SECTIONS FOR HEAVY NUCLEI IN THE ENERGY RANGE 200–1000 MeV

L.A. Vaishnene, V.G. Vovchenko, Yu.A. Gavrikov, A.A. Kotov, V.V. Polyakov, M.G. Tverskoy, O.Ya. Fedorov, Yu.A. Chestnov

The need for the information concerning fission reactions induced in heavy nuclei by intermediate energy projectiles has been obvious. The interest in this process emerges from both fundamental and applied problems of nuclear physics. In spite of extensive experimental efforts, the fission process of nuclei induced by intermediate energy projectiles remains insufficiently understood in many aspects. The proposed measurements of the energy dependence of total fission cross sections of heavy nuclei induced by intermediate energy protons will add to our understanding of the fission process in terms of nuclear properties of highly excited nuclei, such as temperature dependence of level density and fission barriers of excited nuclei. For physics applications, the nuclear data are required for new energy production concepts with the help of accelerator driven system (ADS), for nuclear waste transmutation technologies, for accelerator and cosmic device radiation shields. All the above-mentioned problems require fission cross section data of high accuracy and reliability. Unfortunately, most of experimental data have been obtained in various experiments by using different methods of registration. That is why available data on the fission cross section are dispersed in the range which exceeds the declared accuracy of measurements, not allowing to determine reliable energy dependence of the fission cross section on proton energy. High accuracy of the fission cross section measurements may be achieved only by the use of modern electronic methods of the registration of the both fission fragments in coincidence together with high precision monitoring of a proton flux on the studied target. In the present experiment the method based on the use of gas parallel plate avalanche counters for the registration of complementary fission fragments in coincidence and a telescope of scintillation counters for direct counting of the incident protons on the target has been applied. This method allowed us to measure the absolute proton induced fission cross sections of ^{239}Pu, ^{237}Np, ^{238}U, ^{235}U, ^{233}U, ^{232}Th, ^{209}Bi and ^{nat}Pb in the energy range from 200 to 1000 MeV with the step of 100 MeV, and results on the energy dependence of total fission cross sections are presented.

The experiment has been performed at 1-GeV PNPI synchrocyclotron. Since an external proton beam of the PNPI synchrocyclotron has a fixed energy of 1 GeV, in order to obtain proton beams with energies in the range from 200 to 900 MeV a method of energy decrease by the beam absorption in a copper degrader was applied [1]. The proton energy was measured by the time-of-flight method. The TOF spectra analysis showed that π^+ mesons were practically absent. The beam diameter at the target chamber location for all proton energies did not exceed 40 mm. The beam profile was measured by a thin scintillation counter which scanned the beam in two orthogonal directions. The beam divergence was determined by measuring the beam profile at the chamber inlet, outlet and in its center at each proton energy variation. The beam intensity distribution on the target was a bi-dimensional normal distribution with the FWHM not larger than ~18 mm.

In the present experiment the fission fragment detector comprised an assembly of two identical gas parallel plate avalanche counters (PPAC) with the target to be studied in between. The PPAC had a high efficiency for the fragment detection and good time characteristics (better than 300 ps time resolution for fission fragments). The latter property, together with the PPAC insensitivity to neutrons, photons and light charged particles with minimal energy loss in the matter, makes the PPACs extremely favorable tool for accelerator experiments, allowing one to place them in the direct proton beam, that provides the large solid angle for the fragment registration [1].

The PPAC pulse amplitude is determined both by the specific energy losses of the detected particles in heptane and by the gas amplification value. The latter depends on the voltage value between the anode and cathode, so the detection efficiency could be controlled by voltage choosing. By the appropriate choice of the

[1] A.A. Kotov, W. Neubert, L.N. Andronenko, B.L. Gorshkov, G.G. Kovshevy, L.A. Vaishnene and M.I. Yazikov, Nucl. Instr. Meth. **178**, 55 (1980).

voltage value one can introduce a threshold selection criterion which is especially important when detecting the fission fragments from nuclei with a high level of α-activity, such as ^{233}U, ^{237}Np and ^{239}Pu.

Nevertheless, it is not sufficient to employ only the threshold selection criterion when using the PPAC directly in the proton beam. In fact, the amplitude spectrum of the detected particles contains, together with the fission fragments, a considerable contribution of low-amplitude background events. These events are caused by various proton-induced nuclear reactions in the matter along the beam line. Such a low-energy component is strongly suppressed after a coincidence criterion is switched on. Moreover, the analysis of amplitude correlations of the coinciding fragments allowed us to exclude all background events almost thoroughly.

Thus, in our experiment we used three criteria to select the binary fission events: the threshold criterion, the coincidences, and the criterion of the total kinetic energy of detected coincident particles (the amplitude correlations).

The PPAC is so thin that it does not harm practically the beam characteristics when located into the beam. For this reason several assemblies with various targets could be readily placed into the beam. This allowed us to diminish considerably the measurement time. In the real experiment up to six assemblies were used simultaneously. The layout of the setup including the reaction chamber with the fission event detectors and proton monitoring system is shown in Fig. 1. The main part of the setup is a hermetic chamber with six detector assemblies, each assembly comprising the two PPACs and the target in between.

Before entering the reaction chamber the proton beam passed three scintillation counters (S1&S2&S3), combined *via* the coincidence scheme and performed direct proton counting. Just downstream of the reaction chamber the polyethylene target $(CH_2)_n$ was placed. The protons elastically scattered from this target were detected by a two-arm scintillation telescope (S4&S5&S6), which served as a secondary beam monitor.

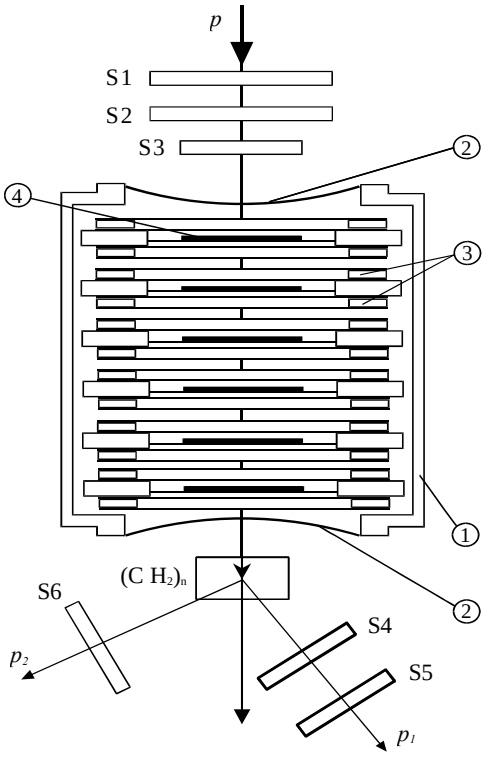

Fig. 1. Experimental setup: 1 – chamber filled with heptane; 2 – entrance window; 3 – PPACs, 4 – target; S1, S2, S3, S4, S5, S6 – scintillation counters

Direct counting of the incident protons with a scintillation counter telescope was used for beam monitoring. This method provides good monitoring accuracy only for low intensity beams, up to $\sim 10^5$ s^{-1}. However, for bismuth and lead nuclei with the fissionability is about an order of magnitude lower than for actinide nuclei one needs much higher intensity. For this reason the measurements were performed at two intensity values of

the proton beam: ~10^5 s^{-1} and 10^6–10^7 s^{-1}. In the latter high intensity case the beam monitoring was done by two methods: 1) by detecting the fission events from the calibration target of ^{238}U residing in the reaction chamber, and 2) by detecting the events of the *pp* scattering on the auxiliary $(CH_2)_n$ target with the two-arm scintillation telescope (S4&S5&S6). Both methods were previously calibrated at low intensity ($< 2 \times 10^5$ s^{-1}) with the direct monitoring telescope (S1&S2&S3). The comparison of both methods at high intensity showed the agreement of results within ~3% at all energies from 200 to 1000 MeV. The calibration procedure for secondary monitoring is described in detail in Ref. [2].

The target to be investigated was a thin layer of material laid by vacuum evaporation on a thin 50 mm in diameter backing foil made of alumina (Al_2O_3). The thickness of actinide targets, their composition and the uniformity of the evaporated layer were determined by measuring the α-activity and energy spectra of the α-particles. For the lead and bismuth targets the thickness of the backings and targets was determined by measuring the energy losses of α-particles passing through the target.

So, using the methods of detection of the binary fission events and beam monitoring described in Ref. [2] we have measured the fission cross sections for each target at nine proton energies.

The cross section calculation procedure comprised the following steps.

1. Background subtraction after the analysis of the bi-dimensional amplitude distribution of the detected events. The number of the background events amounted to 2–3% of the total number of the detected events.
2. Determination of the solid angle for the fission event detection for each assembly. The calculation was done by a Monte Carlo simulation which took into account: the proton beam profile on the target; the detection geometry for the fission fragments, their mass and energy distributions as well as the anisotropy of fragment angular distribution in the laboratory frame due to the longitudinal momentum component of the fissioning nucleus. The statistical accuracy of the solid angle calculations amounted to 0.1%.
3. Estimation of the undetectable portion of the fission events caused by the energy loss of the fission fragment in the target, its backing and in the PPAC electrodes. The undetectable part of the events depended on the target nucleus and thickness and amounted to 3–8%.
4. Determination of the integral proton flux through the target, with the account of the scintillation telescope efficiency and the probability of the appearance of more than one proton in a microbunch at low intensity.
5. Determination of the normalizing coefficients to calculate the proton flux at high intensity *via* the counting rate of the *pp*-scattering monitor and the fission counting rate from the calibration target.

The measured fission cross sections for ^{239}Pu, ^{237}Np, ^{233,235,238}U, ^{232}Th, ^{209}Bi and ^{nat}Pb nuclei are shown in Table. For the most of nuclei the data presented are averaged over the results of several measurements, the errors being determined mainly by the monitoring errors and the uncertainty in the target thickness.

The energy dependence of the fission cross sections obtained in the present experiment for the mentioned nuclei is shown in Fig. 2. Also presented are the results of previous experiments extracted from compilations [2,3] as well as the JINR data on the fission of ^{237}Np, ^{235,238}U, ^{232}Th and ^{209}Bi nuclei induced by 1000 MeV protons. In the compilation [2] a parameterization of all the world fission cross section data was proposed after the critical analysis and data selection for the actinide and pre-actinide nuclei for proton energies up to 10–30 GeV. The results of this cross section estimation are also given in Fig. 2 by dashed lines.

As seen in Fig. 2, the energy dependence of the fission cross sections for all actinide nuclei is characterized by common regularities demonstrating the rise of the cross sections in the energy range from 200 to ~400 MeV with the following plateau up to 1000 MeV. Such a behavior is not consistent with estimations of compilation [2] (dashed lines) which predict smooth decrease of the cross sections with energy in the range 200–1000 MeV. Our experimental results for actinide nuclei together with the previously available data at low energies (below 200–300 MeV) form a certain picture of the energy behavior of the fission cross sections in the whole energy range from the threshold up to 1000 MeV. In fact, a large body of the data indicates (at least for ^{237}Np, ^{238}U, ^{235}U and ^{232}Th nuclei) the presence of the maximum in the energy dependence near several tens MeV, followed by the cross section decrease up to the energy of ~200 MeV. Then after the indistinct minimum near 200–300 MeV the cross sections rise again till

[2] A.V. Prokofiev, Nucl. Instr. Meth. A **463**, 557 (2001).
[3] A.I. Obukhov, Particles & Nuclei **32**, 319 (2001).

~ 400 MeV reaching a plateau which continues up to the maximum energy of 1000 MeV. The change of the energy behavior of the fission cross sections near 200 MeV resembles a characteristic minimum of the total inelastic cross section of the proton-nucleus interaction in the same energy region.

Table

Fission cross sections, mb

Energy, MeV	^{239}Pu	^{237}Np	^{238}U	^{235}U
207	1260 ±126	1187 ± 81	1352 ± 68	1464 ± 83
302	1339 ±134	1438 ± 98	1470 ± 68	1562 ± 94
404	1585 ±158	1624 ± 88	1527 ±104	1626 ±138
505	1613 ±161	1607 ± 98	1491 ± 78	1592 ±102
612	1628 ±163	1647 ±100	1499 ± 72	1610 ±124
702	1700 ±170	1674 ±102	1518 ± 76	1620 ±131
802	1672 ±167	1629 ± 88	1503 ± 63	1571 ± 90
899	1688 ±168	1673 ±114	1490 ± 63	1592 ± 96
1000	1592 ±159	1568 ± 96	1489 ± 64	1591 ±113
Energy, MeV	^{233}U	^{232}Th	^{209}Bi	^{nat}Pb
207	1625 ±162	1144 ± 90	136 ± 13	60.5 ± 3.5
302	1651 ±115	1200 ± 91	178 ± 17	84 ± 4.5
404	1767 ±124	1236 ± 91	207 ± 21	110 ± 6
505	1818 ±123	1239 ± 61	227 ± 23	118.5 ± 6
612	1763 ±123	1268 ± 80	233 ± 23	127 ± 6.5
702	1798 ±126	1285 ± 81	235 ± 23	132.5 ± 9.5
802	1778 ±124	1247 ± 54	229 ± 23	131 ± 8.5
899	1779 ±122	1252 ± 58	239 ± 24	133.5 ± 7.5
1000	1745 ±122	1245 ± 85	235 ± 23	129 ± 8.5

The energy behavior of the cross sections for pre-actinide nuclei ^{209}Bi and ^{nat}Pb demonstrates sharp increase in the range 200–400 MeV changing gradually to plateau at higher energy, at about 500 MeV for ^{209}Bi and ~700 MeV for ^{nat}Pb. Our data for ^{209}Bi nuclei are in a good agreement with the previous experiments in the energy range 200–600 MeV, while for ^{nat}Pb our data in the range 200–400 MeV lie somewhat lower than the previous experimental results.

Theoretical calculations of fission cross sections were carried out [3, 4] in the framework of the two-step cascade evaporation model. At the first stage of the reaction, when the mean range of the incident protons in the nucleus is comparable with the nucleus diameter, the interaction of the nucleon with the nucleus may be considered as a cascade of binary collisions of the incident nucleon with separate nucleons of the initial nucleus. During this fast stage ($\tau \sim 10^{-22}$ s) some part of fast nucleons leaves the nucleus taking away a considerable part of energy. The rest of the energy is transformed into the excitation energy of the residual nucleus which nucleon composition differs from that of the initial nucleus. So, after the cascade stage of the reaction a residual nucleus appears with wide spectra of the nucleon composition and excitation energies, which depend on the incident nucleon energy. At the second (slow) stage of the reaction ($\tau \sim 10^{-16} - 10^{-19}$ s) the highly excited nucleus either emits nucleons or undergoes the fission. The calculation of the cascade stage of the interaction was done by us with the help of the modified version of the model of the intranuclear cascade [4], in which a Fermi-gas model of the nucleus was used with the account of the nucleon density spread at the border of the nucleus. This version of the cascade-evaporation model was successfully used earlier to analyze the reactions of deep disintegration and fission [5] induced by 1-GeV protons. At the stage

[4] V.E. Bunakov, M.M. Nesterov and N.A. Tarasov, Phys. Lett B **73**, 267 (1978).

[5] L.N. Andronenko, A.A. Kotov, M.M. Nesterov, V.F. Petrov, N.A. Tarasov, L.A. Vaishnene and W. Neubert, Z. Phys. A **318**, 97 (1984).

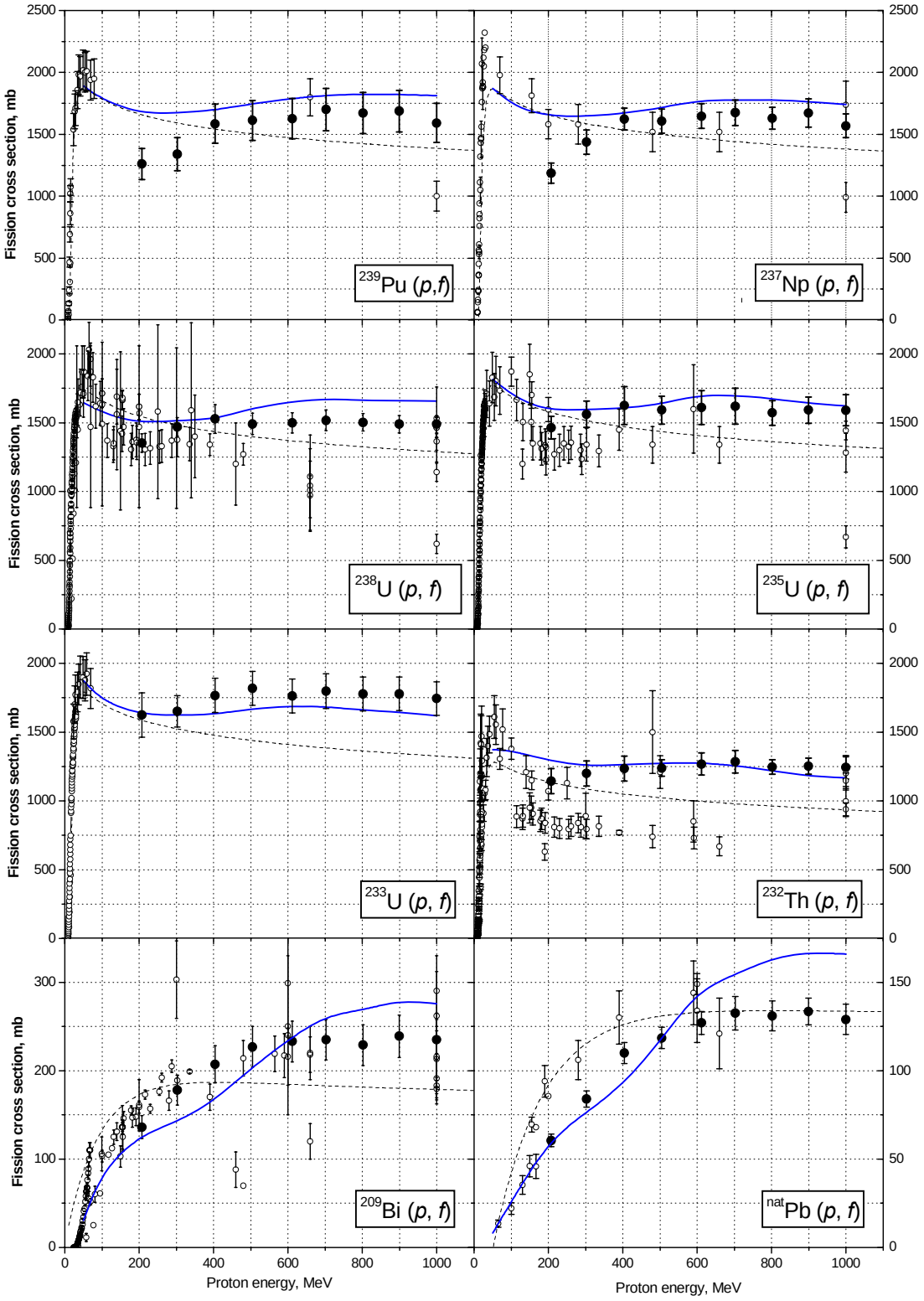

Fig. 2. Energy dependences of the fission cross sections. Black circles – our data, open circles – data from the compilation [2]. Dashed line – parameterization from the compilation [2], solid line – theoretical calculations

of the decay of the highly excited nucleus the fission cross section is determined mainly by the ratio of the fission probability to the probability of the neutron emission . The probability of the neutron emission was calculated in the frame of the statistical theory of Weisskopf, the fission probability being considered in the Bohr-Wheeler approach. When calculating the fission cross sections, one needs, as a rule, to vary the nuclear level density at the equilibrium deformation a_n and at the saddle point of the fissioning nucleus a_f, as well as the fission barrier value B_f. It was supposed that at high excitation energy nuclear shell effects in the fission barriers may be neglected, the ratio of the level density parameters a_f/a_n being supposed to be independent of the excitation energy of the decaying nucleus. In our calculations the level density parameter a_n was taken to be $A/10$ MeV^{-1} for all actinide nuclei and $A/16$ for pre-actinide nuclei of Bi and Pb, the ratio of the level density parameters a_f/a_n being equal to 1.1. The fission barriers calculated in the liquid drop model were taken for B_f. The results of the calculations are presented by solid lines in Fig. 2. It is seen that the calculations reproduce qualitatively the general behavior of the cross sections in the range 50–1000 MeV, with a minimum near 200–300 MeV and a plateau above 400 MeV for actinide nuclei. However, our experimental data for ^{239}Pu and ^{237}Np at 200 and 300 MeV and for ^{nat}Pb at 700–1000 MeV lie considerably lower than the calculated cross sections.

The dependences of the total fission cross sections on the parameter Z^2/A of the target nucleus are shown in Fig. 3 at the proton energies of 207 and 1000 MeV. It is seen that the total fission cross section is an increasing function of the Z^2/A parameter only up to ^{233}U nucleus, while for ^{237}Np and ^{239}Pu the cross sections are equal but lower than that for ^{233}U. Besides, the fission cross sections for uranium isotopes in the whole energy range demonstrate systematically (despite considerable experimental uncertainties) the rise of the cross section when going from ^{238}U to lighter isotopes – see Fig. 4.

The isotope dependence of the fission cross sections for uranium was observed earlier in the experiments on the fission induced by neutrons and photons [6,7] of intermediate energies. The cross section values for uranium fission induced by neutrons of 100–300 MeV energy are in a good agreement with our data in the corresponding energy region.

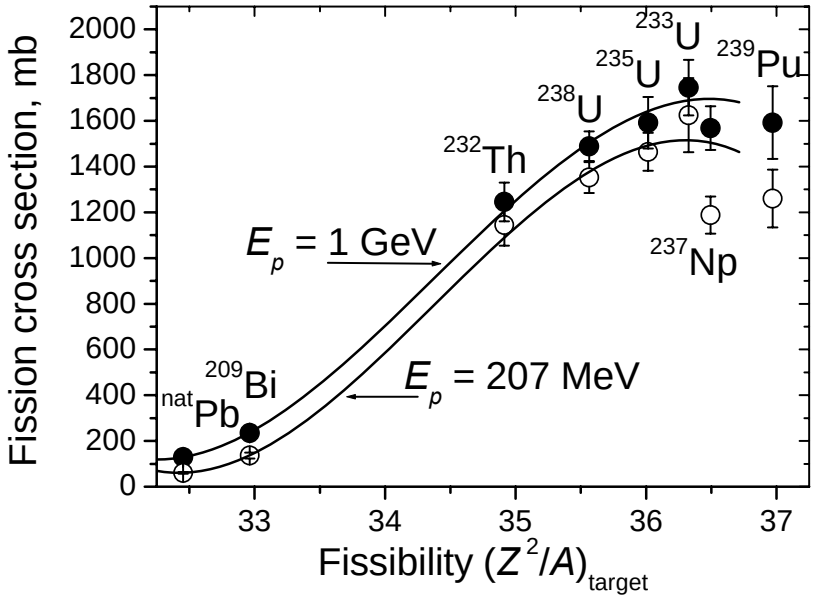

Fig. 3. Dependences of the total fission cross sections on the parameter Z^2/A of the target nucleus

[6] P.W. Lisowski *et al.*, in *Proceedings of the International Conference on Nuclear Data for Sciences and Technologies* (Juelich, Germany, 13 – 17 May 1991), p. 731.
[7] J.C. Sanabria *et al.*, Phys. Rev. C **61**, 426 (2000).

However, the existence of the isotope dependence of the uranium fission cross sections for higher energies looks unexpected and strange from the point of view of the cascade evaporation model for two reasons. First, as it was written above, the cascade stage of the proton-nucleus interaction results in the formation of the wide isotope spectrum of the residual excited nuclei, that should lead to the "loss of the memory" about the nucleon composition in the input channel reaction (nucleon composition of the initial nucleus).

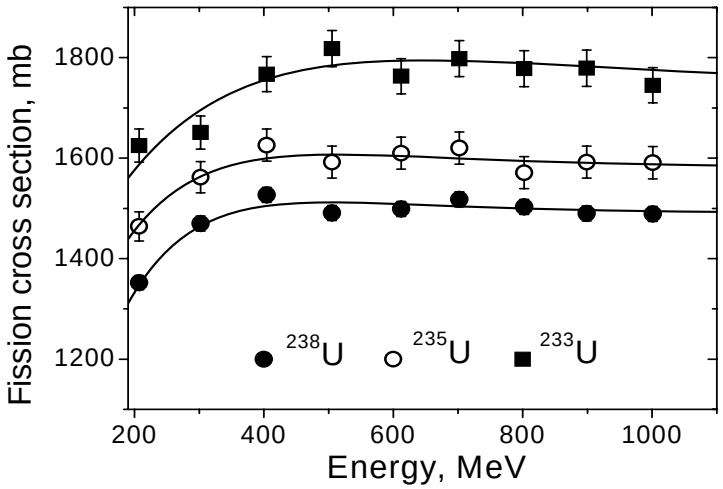

Fig. 4. Fission cross sections for uranium isotopes

Second, the fission barriers B_f for the uranium nuclei calculated in the liquid drop model amount to less than 10 MeV, the difference in the B_f values for a series of the residual nuclei not exceeding several MeV. So the version of the cascade evaporation model we used cannot reproduce the isotopic dependence of the fission cross sections for uranium nuclei.

The analysis of the dependence of the total fission cross sections on the parameter Z^2/A of the actinide nucleus in proton energy region of 200–1000 MeV shows that decreasing uranium mass number on one neutron or proton is accompanied by changing the fission cross section by ~3%. The fission cross sections increase or decrease proportionally to the parameter Z^2/A (Fig. 5).

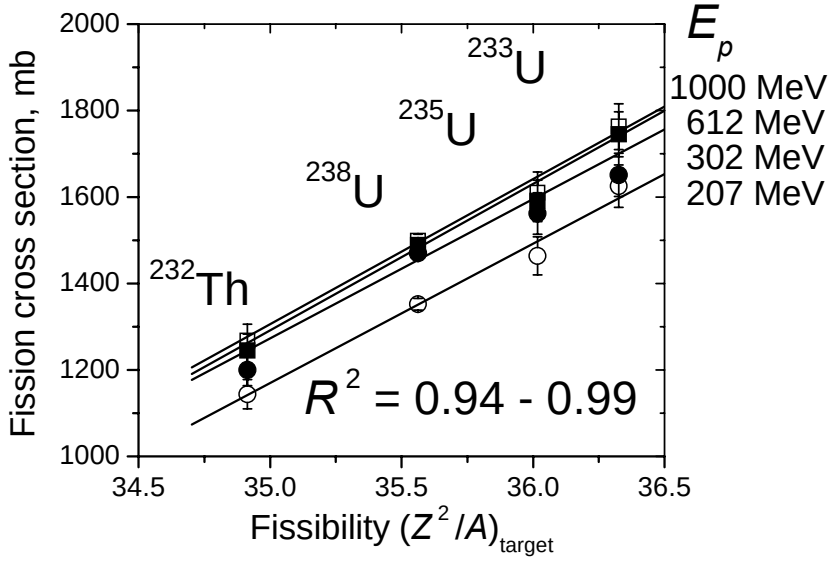

Fig. 5. Dependences of the fission cross sections on the parameter Z^2/A for various energies

To resume, we can formulate a summary.

For the first time in one and the same experimental technique the cross sections of proton-induced fission for ^{nat}Pb, ^{209}Bi, ^{232}Th, ^{233}U, ^{235}U, ^{238}U, ^{237}Np and ^{239}Pu nuclei have been measured in the wide energy range from 200 to 1000 MeV. The analysis of the results and comparison with the previous experimental data allows one to come to the following conclusions.

The cross sections for all actinide nuclei have similar energy dependences characterized by the rise of the cross sections in the range from 200 to ~400 MeV followed by a plateau which continues up to at least 1000 MeV.

For pre-actinide nuclei Bi and Pb the increase of the cross sections for energies above 200 MeV is faster. The rise then changes to a plateau which begins at ~500 MeV for ^{209}Bi and at ~600 MeV for ^{nat}Pb and continues till 1000 MeV.

The calculations of the fission cross sections in the framework of the cascade evaporation model allow one to reproduce qualitatively the cross section behavior.

The data for uranium isotopes in the whole energy range demonstrate the systematic rise (despite considerable experimental uncertainties) of the cross section when going from ^{238}U to lighter isotopes.

The total fission cross section in the saturation region (at the proton energy of 1000 MeV) is an increasing function of the Z^2/A parameter only up to ^{233}U nucleus, while the cross section values for ^{237}Np and ^{239}Pu are approximately equal to the cross section for ^{235}U.

References

1. N.K. Abrossimov, V.G. Vovchenko, V.A. Eliseev, E.M. Ivanov, Yu.T. Mironov, G.A Riabov, M.G. Tverskoy and Yu.A. Chestnov, Preprint PNPI-2525, Gatchina, 2003. 31 p.
2. V.G. Vovchenko, L.A. Vaishnene, Yu.A. Gavrikov, A.A. Kotov, V.I. Murzin, V.V. Poliakov, S.I. Trush, O.Ya. Fedorov, Yu.A. Chestnov, AV. Shvedchikov and A.I. Shchetkovski, Preprint PNPI-2532, Gatchina, 2003.
3. A.A. Kotov, L.A. Vaishnene V.G. Vovchenko, Yu.A. Gavrikov, A.Yu. Doroshenko, V.I. Murzin, V.V. Poliakov, M.G. Tverskoy, O.Ya. Fedorov, T. Fukahori, Yu.A. Chestnov and A.I. Shchetkovski, Izvestiya RAN, ser. fiz., **70**, 1602 (2006).
4. A.A. Kotov, L.A. Vaishnene, V.G. Vovchenko, Yu.A. Gavrikov, V.V. Poliakov, M.G. Tverskoy, O.Ya. Fedorov, Yu.A. Chestnov, A.I .Shchetkovskiy, A.V. Shvedchikov, A.Yu. Doroshenko and T. Fukahori, Phys. Rev. C **74**, 034605 (2006).

MECHANISMS OF NUCLEAR DISINTEGRATIONS INDUCED BY RELATIVISTIC PROJECTILES

B.L. Gorshkov, A.V. Kravtsov, V.R. Reznik, G.E. Solyakin

1. Introduction

During the time of 2001–2006 years investigations on the fission and multifragmentation induced by relativistic projectiles remained at the focus of experimental activity of many world accelerator centers. These both nuclear disintegrations as yet were treated in the frames of two distinct models, the first as a division of a nuclear drop and the second as a decomposition representing the specific nuclear liquid-fog phase transition. Meanwhile binary fission fragments very often were accompanied by large nucleon losses what was a reason for lower fragment masses. Such fission fragments might be attributed to the category of intermediate mass fragments (IMF) which is an important signature of the multifragmentation. Thus there are some common features of two processes in spite of the fact that the binary fission is possible at a low excitation energy and can take place even spontaneously, while the multifragmentation requires high excitation. Our intention is to make an attempt to connect the fission and multifragmentation by the introduction of the intermediate process of collinear three-body disintegration which was the main goal of experimental studies in 2001–2006.

Though the detection of two massive fragments which separate collinearly seems to confirm unambiguously the two-body character of the nuclear fission reaction, it is clear, however, that this experimental result is a necessary but not a sufficient sign of the two-body kinematics. To be consistent with experimental observation of the two collinear fragments, one could consider a more general case, when the classical liquid drop was fissioning into three fragments, the third fragment remaining at rest. The nuclear fission reaction should be written then as

$$^{M_0}Z_0 \rightarrow {}^{M_1}Z_1 + {}^{M_3}Z_3 + {}^{M_2}Z_2 , \tag{1}$$

where M_i and Z_i are the mass numbers and the electric charges of the initial fissioning nucleus and of three fragments. The conservation of the mass and of the charge leads to

$$M_0 = \sum_{i=1}^{3} M_i \text{ and } Z_0 = \sum_{i=1}^{3} Z_i . \tag{2}$$

The fragment $^{M_3}Z_3$, being located between the two others, will not move, if the two repulsive forces from its partners are equal. The detected fragments $^{M_1}Z_1$ and $^{M_2}Z_2$ in this case will separate from each other in the collinear geometry. This generalization of the nuclear fission concept implies the binary process as a result of the ultimate disintegration of the binary configuration which is only a limit of previous successive three-body configurations. Then three-body disintegrations would take place at the earlier stages of the nuclear deformation of the fissioning nucleus. If the collinear three-body configuration loses its unstable equilibrium, a coplanar disintegration will be seen in the experiment. Thus coplanar three-body disintegrations have their origin from the collinear three-body nuclear configurations. A certain part of disintegrations could preserve their primary collinearity. It goes without saying that the concept of the collinear three-body disintegration needs its experimental verification.

2. Nuclear fission experimental studies beyond two-body kinematics

Experimental studies of the nuclear fission beyond two-body kinematics were first of all performed with ^{238}U target nuclei irradiated by 1 GeV protons. Using (2*E*, 2*V*)-measurement method, a comparison of kinematics of two complementary fragments was carried out for events detected in collinear and non-collinear geometries. Signs of collinear three-body disintegrations were observed with respect to the third

nuclear-unstable slowly moving fragment. Further possibilities for the investigation of the collinear nuclear three-body disintegrations at low and high excitation energies were discussed in details. Then the experimental search for the spontaneous collinear tripartition of ^{252}Cf nuclei gave an upper limit of 7.5×10^{-6} to the probability of the binary fission process for $M_3 > 75$ u. Later studies lowered the limit for M_3 mass to 18 ± 3 u [1].

Experiments with relativistic light projectiles could be more favorable for the search for the collinear three-body disintegrations. The important premise for this conclusion was the observation of the momentum compensation of the primary projectile interacting with heavy and medium-heavy nuclei. As a result of such interaction, a residual nucleus remains at rest in the laboratory frame [2]. The same recoil-free kinematics was observed also in experiments where deeply bound pion states in several nuclei were detected. The first stage of the interaction of a relativistic projectile with a target nucleus of mass M_T presents itself as a reaction

$$m_p + M_T \rightarrow M_0^* + m_e \tag{3}$$

on the condition that the projectile momentum is compensated by the ejectile momentum. Excitation states of the residual nucleus with mass M_0 receive significant energy only if the mass of the ejectile m_e is larger than the mass of the projectile m_p, *i. e.* $m_p < m_e$ [2].

In the experiment on the search for the collinear three-body disintegrations a method of (2*E*, 2*V*)-measurements of the two complementary fragments was used at the 1 GeV proton beam of the PNPI synchrocyclotron. A tungsten target enriched by ^{184}W isotope of 270 μg/cm^2 thickness was irradiated by the stretched in time 1 GeV proton beam with the intensity of 5×10^{11} s^{-1}. Two massive complementary fragments were detected within narrow cones whose common axis was orthogonal to the proton beam direction. The two-arm time-of-flight angle-velocity-energy correlation spectrometer (SAVEC) shown in Fig. 1 comprises a vacuum chamber with two time-of-flight tubes. In the end of each tube at the distance of 70 cm a mosaic of eight semiconductor surface-barrier silicon detectors was located. An independent start signal device (SSD) was placed at the fixed arm close to the target for time-of-flight measurements. The ^{252}Cf source was used for energy and time calibrations.

As it follows from Fig. 1, in the experiment $8 \times 8 = 64$ spectrometers were used. Various combinations of the address pairs (A_1, A_2) of the semiconductor surface-barrier detectors were possible as a characteristic of the average folding angle $\langle\theta\rangle$ between the two detected fragments. Two angular diapasons I and II were easily distinguished in the experiment according to Table.

Table

Collinear geometry	Angular diapason I	Angular diapason II
$\langle\theta\rangle$, deg.	180–177.5	176.5–172.9
Number of addresses combinations	28	36

The first angular diapason I covers an interval of 180°–177.5° with the average value $\langle\theta\rangle_I = 178.2°$. The second angular diapason II covers an interval of 176.5°–172.9° with the average value $\langle\theta\rangle_{II} = 175.3°$. Two mosaics of the semiconductor surface-barrier silicon detectors in combination with the start signal device made it possible to measure kinetic energies E_i and times of flight T_i for both $(i = 1, 2)$ complementary fragments. So each of the registered events has been characterized by the collection of six measured quantities $(A_1, E_1, T_1; A_2, E_2, T_2)$ related to the two detected fragments.

3. Observation of collinear three-body disintegrations induced in tungsten nuclei by 1 GeV protons

When kinetic energy E_i and time-of-flight T_i for each of the two complementary fragments are measured simultaneously, one can determine, unlike in $(2E)$ or in $(2V)$-measurement methods, their absolute masses $M_i \sim E_i \cdot T_i^2$ and momenta $P_i \sim E_i \cdot T_i$. However, as a consequence of the enlargement of the experimental merits of the SAVEC, there arises an unavoidable problem of background events. They have their origin mainly from two independent sources. The first one is accidental coincidences and the second – fragment scatterings on details of the experimental equipment. In the following analysis a useful dimensionless parameter of the background elimination was proposed. It looks like

$$\lg \frac{E_1 + E_2 - E_{rec}}{E_{rec}} = \lg \frac{TKE}{E_{rec}}, \tag{4}$$

where measured sum of two kinetic energies E_1 and E_2 is compared with the calculated recoil energy of the disintegrating nucleus

$$E_{rec} = \frac{(\vec{P}_1 + \vec{P}_2)^2}{2(M_1 + M_2)}. \tag{5}$$

As a rule, the background events group at low TKE and smaller values of the chosen parameter (4).

Figure 2 shows the distribution on $\lg \frac{TKE}{E_{rec}}$-values for all the registered experimental events with the tungsten target at the proton beam.

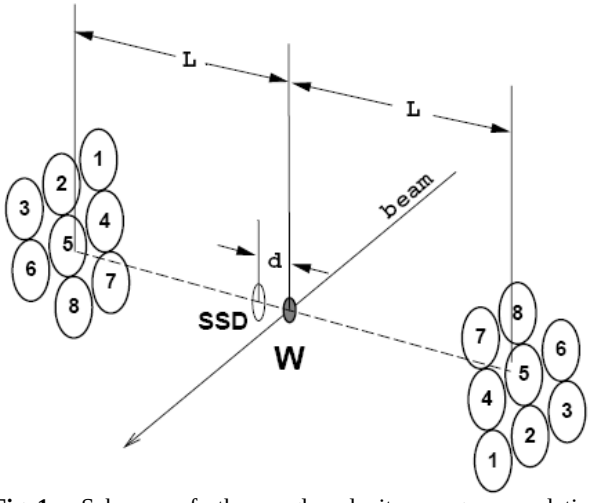

Fig. 1. Scheme of the angle-velocity-energy correlation spectrometer (SAVEC). The length of the time-of-flight base L = 70 cm. The distance between the sources of fission fragments (proton beam targets or a source of spontaneous decay of ^{252}Cf) and the foil of the start-signal device (SSD) d = 3.7 cm

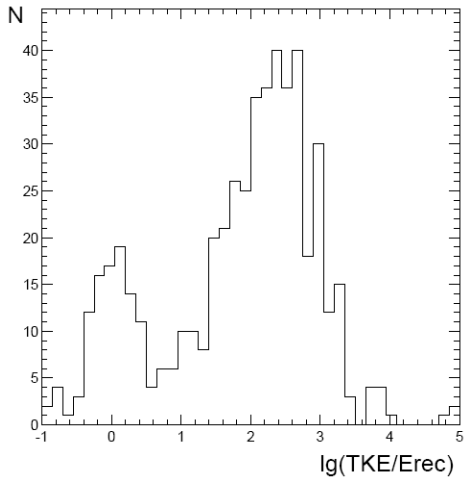

Fig. 2. Distribution of all experimentally registered events on the value of elimination criterion. The right large peak is originated from disintegrations of tungsten target nuclei induced by 1 GeV protons, while the smaller left peak- from random background coincidences

A portion of almost one fifth of the total statistics belonging to the left-hand part of the distribution was eliminated from the further analysis as originated from accidental coincidences. The rest events were considered as those from disintegrations induced in tungsten nuclei by 1 GeV protons.

The correlated mass distribution (M_1, M_2) for complementary fragments of these disintegrations is shown in Fig. 3 which demonstrates the efficiency of the chosen elimination criterion. Disintegration events from the angular diapason I are shown by stars and those from the angular diapason II – by full points. There is no real difference for the correlated mass distributions between the two angular diapasons. In both cases together with fission events, disintegrations were registered in a wide variety of nucleon losses in total mass of two detected fragments. This means that in the experiment collinear disintegrations had various values of ξ. The last were calculated for each experimental event according to the expression

$$\xi = \frac{M_3}{M_0} = 1 - \frac{M_1 + M_2}{M_T - (m_e - m_p)}. \tag{6}$$

In this formula M_T is a target nuclear mass, m_p and m_e are masses of a light projectile and of an ejectile compensating projectile momentum. The value of $(m_e - m_p)$ is always positive and small with respect to M_T, so hereafter the denominator in formula (6) is put equal to 182 u. The introduced ξ-value is a significant characteristic of the third fragment in the collinear three-body reaction (1). During the time of the nuclear disintegration reaction (1) it varies from 1 for the initial nucleus to 0 for the two-body configuration of the binary fission. A certain interval of ξ-values close to 0 should also satisfy to the binary fission process while the intermediate values between 0 and 1 could be inherent for the collinear three-body configuration. The particular interval of ξ-values would be revealed in experiments with different target nuclei.

Every collinear three-body configuration possesses its own potential Coulomb energy which is transformed into fragment kinetic energies at the latest stage of the nuclear reaction. A slowly moving third fragment initially has to be located at the point between its partners where both repulsive forces are equal. This condition permits to write an expression for the potential energy of the three collinearly situated charged bodies:

$$U_3(\rho,\xi) = \frac{e^2 Z_0^2}{D_3(\rho,\xi)} \frac{\rho(1-\xi)}{(1+\rho)^2} \left\{1 + \xi\left[(1+\rho^{1/2}+\rho^{-1/2})^2 - 2\right]\right\}. \tag{7}$$

In formula (7) besides above introduced values of Z_0 and ξ also used are e – electron charge, $\rho = M_1/M_2$ – mass ratio of detected fragments, and D_3 – initial distance between the centers of fragment charges Z_1 and Z_2. In the evolution of formula (7) the equality for mass and charge ratios of all the fragments was supposed. When ξ goes to 0, formula (7) transforms into a well known expression for the two-body configuration:

$$U_2(\rho) = \frac{e^2 Z_0^2}{D_2} \frac{\rho}{(1+\rho)^2}. \tag{8}$$

Two variables ρ and ξ represent a minimal set for the description of the nuclear collinear three-body configuration.

The next step of the analysis is to use the equality of the potential configuration energy with the total kinetic energy of all the fragments. From this equality one can get an independent of ρ parameter

$$\eta(\xi) = \frac{e^2 Z_0^2}{D_3} = \frac{(1+\rho)^2}{\rho(1-\xi)} \times \frac{E_1 + E_2 + E_3}{\{1 + \xi[(1+\rho^{1/2}+\rho^{-1/2})^2 - 2]\}}. \tag{9}$$

When calculating $\eta(\xi)$, values of ξ, ρ, E_1 and E_2 are taken directly from the experimental data. The kinetic energy of the third fragment E_3 can be obtained if one takes into account the momentum imbalance of the two detected fragments

$$E_3 = \frac{(\vec{P} + \vec{P}_2)^2}{2M_3}. \tag{10}$$

As a rule, E_3 represents a small addition to the sum $E_1 + E_2$. The $\eta(\xi)$-values determined from experimental events are shown by stars for the angular diapason I and by full points for the angular diapason II in Fig. 4 for ξ up to 0.7. A few events at small negative ξ-values are accounted for by the finite experimental mass resolution of the SAVEC. In the range from $\xi = 0$ up to 0.15–0.20 experimental events in Fig. 4 are concentrated as a whole sample having origin from the same disintegration reaction. It is binary nuclear fission with a certain amount of nucleon losses before and after the neck scission. Three separated branches of events are clearly seen in the range $0.2 \le \xi \le 0.7$. And what is of a great importance, the first upper branch consists only of star events. Two others the second and the third branches are mixtures of stars and points in comparable quantities. This experimental result emphasizes the importance of three-body configurations for different kinds of deep inelastic reactions depending on the collinearity of the detected fragments. Each of the reactions proceeds having its own three-body $(\rho, \xi$ and $\eta)$ parameters.

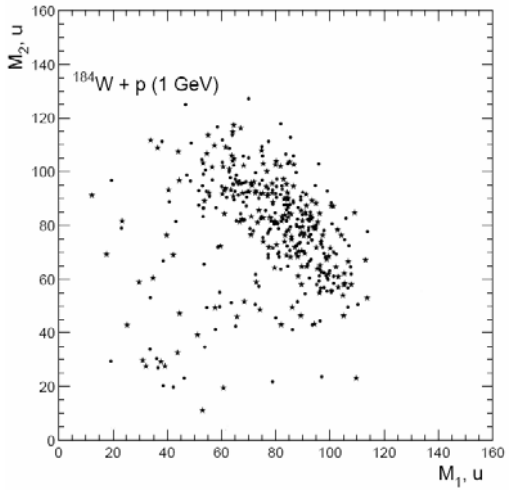

Fig. 3. Correlated mass distribution (M_1, M_2) for complementary fragments from disintegrations of tungsten target nuclei induced by 1 GeV protons. Stars are events from the angular diapason 180°–177.5° and points are events from the angular diapason 176.5°–172.9°

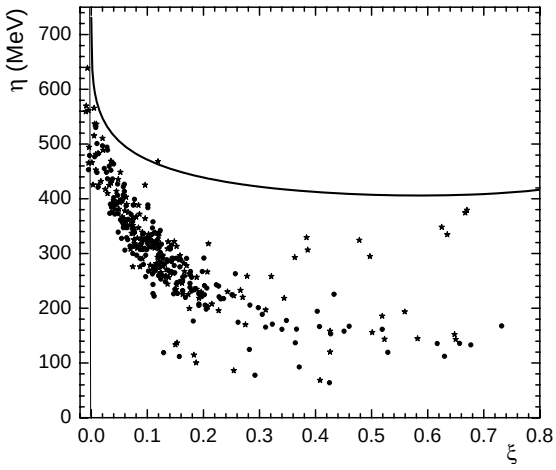

Fig. 4. Distribution of experimental events from disintegrations of tungsten nuclei induced by 1 GeV protons in the frame [$\xi, \eta(\xi)$] for the folding angular diapason 180°–177.5° marked by stars and for the angular diapason 176.5°–172.9° marked by points. The meaning of variables and of a solid curve is explained in the text

It follows from Fig. 4 that there is an angular dependence of $\eta(\xi)$-parameter. Its upper branch is preserved only for the diapason I and achieves maximum proximity to the solid curve which represents the electrostatic potential energy $\eta_0(\xi)$-parameter for the most compact configuration of collinear three contiguous spherical bodies

$$\eta_0(\xi) = \frac{e^2 Z_0^2}{D_{30}} = \frac{e^2 Z_0^2}{1.2 M_0^{1/3}} \times \left[(1+\rho^{1/3}) \left(\frac{1-\xi}{1+\rho} \right)^{1/3} + 2\xi^{1/3} \right]^{-1} \tag{11}$$

taken at $\rho = 1$. In the expression (11) the distance D_{30} between the charge centers Z_1 and Z_2 was used in the form

$$D_{30}(\rho,\xi) = R_0\left[\left(1+\rho^{1/3}\right)\left(\frac{1-\xi}{1+\rho}\right)^{1/3} + 2\xi^{1/3}\right], \tag{12}$$

where the radius of the initial nucleus is expressed as

$$R_0 = 1.2\times M_0^{1/3}. \tag{13}$$

Numerical value of the multiplier for the solid curve was evaluated at $Z_0 = 74$ and $M_0 = 182$ u. If one suggests that Fig. 4 demonstrates all possible disintegration reactions induced in tungsten nuclei by 1 GeV protons then it is convenient to distribute and to discuss their mechanisms according to different ξ intervals.

4. Discussion

The binary fission registered in the present experiment is the most prominent process which comprises experimental events with $0 \le \xi < 0.2$. The mass distribution from these events for the single of complementary fragments is shown in Fig. 5 by closed circles, the most probable mass corresponding to the nucleon losses ΔM = (20 ± 2) u. The FWHM value of the mass spectrum amounts to 40 u what is almost twice as large as the value (23 ± 2) u measured for fission of rhenium and iridium nuclei induced by ^{4}He ions with energies of 40.9 and 42.2 MeV, respectively. References on the original experimental results are provided in Ref. [3]. Nucleon losses were negligible, evaluated as (1 ± 1) u in the fission of rhenium and (2 ± 1) u in the fission of iridium. Broadening of the mass spectra of the fission fragments with increasing the projectile energy indicates the increase of the mass range for the two-body configurations, *i. e.* the significant change in the variations of ρ-parameter. At the same time larger projectile kinetic energy gave rise to the increase of the binary fission cross section by two orders of magnitude. Together with the variation of ρ-parameter, assumingly between 1 and 2, changes of ξ-parameter in the limits $0 \le \xi < 0.2$ also took place due to nucleon evaporation processes.

Depending on the collinearity of the detected fragments each of the disintegration reactions in the interval $0.2 \le \xi \le 0.7$ proceeds having specific excitation energy and its own shape elongation of the collinear three-body configuration. The first upper branch is characterized by the minimal excitation energy, the second and most prominent branch originates from disintegration events with the moderate excitation energy. The largest excitation energy is inherent to experimental events from the third lower branch. The shape elongation of three-body configurations is also changed, being minimal for the first upper branch and becoming larger for the second and especially for the third branches. It is possible to calculate ratios $\beta = D_3(\xi)/D_{30}(\xi)$ which distinguish experimental elongations $D_3(\xi)$ from those of the collinear three contiguous spheres $D_{30}(\xi)$. Comparing formulas (9) and (11) one obtains

$$\beta = \frac{\eta_{30}(\xi)}{\eta\ (\xi)}. \tag{14}$$

Numerical results, shown in Fig. 6, can be valid only for events from the first branch where the total nuclear charge Z_0 is definitely equal to 74. It should be stressed that according to relation (14) branching inversion takes place. For two other branches the total nuclear charge should be decreased because of the unknown number of emitted secondary charged particles. At the present stage of investigation one may restrict oneself by calculations for all the experimental events choosing Z_0 = 74. Then results of Fig. 6 except those of the

first branch are considered as limitations for values of shape elongation β coefficients. In spite of the rudeness of the evaluations it may be definitely stated that three branches are quite different with respect to shape elongations of collinear three-body configurations.

In the recently published papers [4, 5] we proposed that disintegration events with two detected collinear fragments could reveal specific mechanisms of interaction of a light relativistic projectile with a heavy nucleus. In this respect the three branches of experimental events in Fig. 4 can be treated as those originated from the formation of mesonic states in a fissioning nucleus at the stage of its deformation. This statement is supported by the recoil-free kinematics for collinear fragment disintegrations [2] and for the pion state formation also.

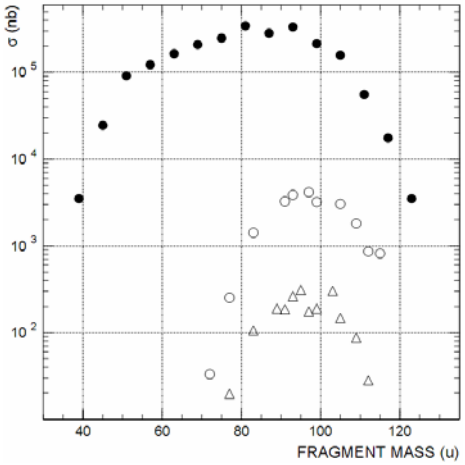

Fig. 5. Comparative single fragment mass distributions for induced binary fission of rhenium + 40.9 MeV ^{4}He ions (open triangles), of iridium + 42.2 MeV ^{4}He ions (open circles) and of tungsten + 1 GeV protons (closed circles)

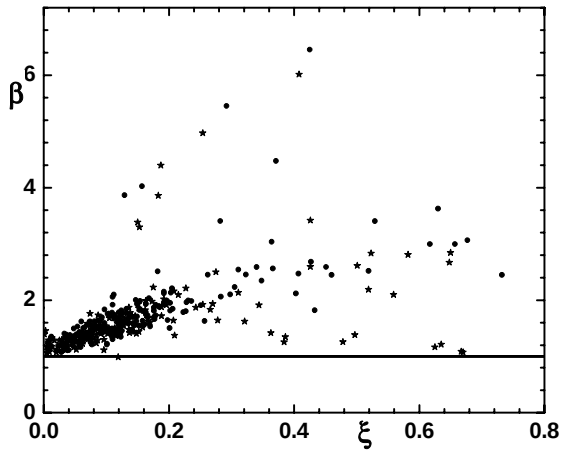

Fig. 6. Distribution of experimental events in the [$\xi - \beta$] frame. The straight horizontal line $\beta = 1$ represents the lower possible limit for shape elongation parameter. The largest measured beta values are forming its upper limit

The only difference is in the excitation energies of the residual nuclei. In the case of tungsten disintegrations induced by 1 GeV protons the excitation energy exceeds 300 MeV [2] which is more than two pion masses.

Thus three branches of experimental events may correspond to different kinds of pion absorption in or emission from the fissioning nucleus, when the total pion number is equal to 2. Then there are three variants to distribute emission and absorption of two mesons. They are (2,0) – two emitted and nought absorbed, (1,1) – one emitted and one absorbed, and (0,2) – nought emitted and two absorbed. The detailed picture is shown in a special preprint [4].

It is of interest to perform experiments with the excitation energy sufficient for the formation only one pion in the primary interaction. In this case two possibilities would exist for the pion emission from or its absorption in the fissioning nucleus. Such experiments can be carried out at the PNPI synchrocyclotron if instead of the proton one would use a deuteron beam with the same initial momentum. The primary kinetic energy of the deuteron beam would be 653 MeV and the excitation energy of a fissioning nucleus only 180 MeV in the interaction with the recoil free kinematics in the pickup reaction of (d,^{3}He)-type. The evolution of detected events grouping in branches should follow the number of pions produced in experiments with 1 GeV proton and 653 MeV deuteron beams.

5. Conclusion

The first claim of the observation of the collinear three-body disintegration appeared in paper [5]. This was a deliberately planned experiment. But indirect tokens could be found in many previously fulfilled experiments of different authors. A few were mentioned in our preprint [4]. Leaving aside all the examples at relativistic energies of projectiles it is rather instructive to pay attention for quaternary fission and for two-proton radioactivity which were discussed in Ref. [4] as limiting cases of the collinear three-body

disintegration. They differ from others by relatively low excitation energy much less than in experiments with relativistic projectiles.

A distinctive feature of this presentation is the treatment of the nuclear excitation in a number of pions formed in the primary interaction of a projectile with a target nucleus. Temperature concept is not used at any stages of the disintegration. If one continues the tendency, new sorts of nuclear disintegrations could be revealed when the energy of the incoming projectile would increase together with the number of pions. The cardinal intent in this direction may be a complete disintegration of a tungsten nucleus by a relativistic projectile into nucleons and lightest nuclei accompanied by uncertain number of pions.

References

1. A.V. Kravtsov and G.E. Solyakin, Preprint PNPI-2462, Gatchina, 2002. 22 p.
2. L.N. Andronenko, A.A. Zhdanov, A.V. Kravtsov and G.E. Solyakin, Yad. Fiz. **65**, 504 (2002) [Phys. Atom. Nucl. **65**, 478 (2002)].
3. B.L. Gorshkov, A.V. Kravtsov, N.P. Popov, V.R. Reznik, N.G. Soboleva and G.E. Solyakin, Preprint PNPI-2508, Gatchina, 2003. 24 p.
4. B.L. Gorshkov, A.V. Kravtsov, V.R. Reznik and G.E. Solyakin, Preprint PNPI-2686, Gatchina, 2006. 44 p.
5. B.L. Gorshkov, V.R. Reznik and G.E. Solyakin, Pis'ma v ZhETF **84**, 691 (2006) [JETP Lett. **84**, 577 (2006)].

MASS DEPENDENCE OF NUCLEAR ISOTOPE TEMPERATURE IN LOW ENERGY FISSION

M.N. Andronenko, L.N. Andronenko, W. Neubert [1)]

[1)] *Institut für Strahlungsphysik, FZ Dresden-Rossendorf, 01314 Dresden, Germany*

1. Introduction

The nuclear temperature is an important parameter in statistical models of nuclear reactions but this quantity is not directly available in experimental investigations. The reason is that the temperature can be evaluated only from other physical observables. A promising situation has arisen as several approaches were available to determine the nuclear temperature which allowed to minimize systematic errors of this parameter. We point to some examples which show the preference of the nuclear temperature as an essential physical quantity. The temperature is in relationship with the nuclear excitation energy, the nuclear phase transition and the time scale of the investigated processes. Furthermore, the nuclear temperature is important for the choice of theoretical models to describe the physical process of interest. During the last decade, this has provided the opportunity of an extended use of isotope thermometry in investigations of multifragmentation at intermediate energies. At the same time, in nuclear fission experiments the temperature was rarely explored, apart from traditional measurements in which the slope of neutron time-of-flight spectra were determined. Here we present an analysis of available low energy fission data (see Refs. in [1, 2]) to extract isotope temperatures with a view to confront it with the corresponding results of nuclear fragmentation [3] at intermediate energies.

2. Method of tempearture extraction

The method of isotope temperatures (or **D**ouble yield **R**atio **T**emperatures (DRT)) allows for the determination of the nuclear temperature related to the moment of the formation of reaction products. The so called "apparent" temperature can be obtained from the relation

$$T_{app} = B \,/\, \ln(a \cdot R_{app}) \;, \tag{1}$$

where the double ratio $R_{app} = R_1/R_2$ is defined by the isotope yields (Y) as

$$R_1 = Y(A_i, Z_i) \,/\, Y(A_i + \Delta A, Z_i + \Delta Z), \qquad R_2 = Y(A_j, Z_j) \,/\, Y(A_j + \Delta A, Z_j + \Delta Z),$$

where ΔA=1, 2, 3, ... and ΔZ=0, 1, 2, ... may be used. The parameter a includes the spin degeneration factor and mass numbers of the considered isotopes. The numerator B in Eq. (1) is determined by the binding energies BE: $B = BE(A_i,Z_i) - BE(A_i+\Delta A,Z_i+\Delta Z) - BE(A_j,Z_j) + BE(A_j+\Delta A,Z_j+\Delta Z)$. Eq. (1) is valid if the fragments with mass A_i, A_j and nuclear charge Z_i, Z_j are produced in their ground states. Each combination of (R, a, B) in Eq. (1) terms a *thermometer* which allows to find the corresponding temperature related to the fragment formation.

The relation (1) must be modified for "sequential decays", *i.e.* if fragment decays from higher lying states of the same and other isotopes contribute to the yields. An empirical correction for such decays was given by M.B. Tsang *et al.* [Phys. Rev. Lett. **78**, 3836 (1997)] for the special case of thermometers selected by $B \geq 10$ MeV

$$\frac{1}{T_{app}} = \frac{1}{T_o} + \frac{\ln \kappa}{B}, \tag{2}$$

where T_o is the unknown intrinsic equilibrium temperature. The correction factor κ is defined by $R_{app}=\kappa \cdot R_o$ where R_{app} is the measured double isotope yield ratio and R_o is the corresponding one for isotopes produced at equilibrium.

For the beginning we compare isotope temperatures for nucleon-induced reactions with different beam energies but nearly the same targets and the same range of the emitted fragments (Z≤5). A scatter plot of T_{app} *versus* B presented in Fig. 1, taken from Ref. [4], shows a similar behavior in p(1 GeV)+^{238}U fragmentation and **T**ernary **C**harged **P**article (TCP) accompanying neutron-induced fission of ^{239}Pu. In spite of this similarity, both the absolute values of T_{app} and the fluctuations from thermometer to thermometer are obviously different.

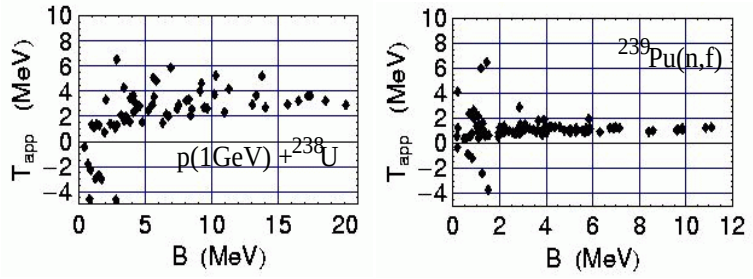

Fig. 1. Scatter plots of T_{app} *versus* the difference of the binding energies for p(1 GeV) + ^{238}U collisions (left panel) and TCP accompanied n-induced fission of ^{239}Pu (right panel)

According to the number of available thermometers, N_{th}, we used three methods ((i)–(iii) below) to extract the temperature dependence on the target mass. A first inspection of the obtained temperatures [3, 4] suggested a linear dependence on the target mass A_T:

$$T_{app} = c_1 + c_2 \cdot A_T. \tag{3}$$

Method (i): $N_{th} \sim$ 1, 2, ... up to 10, utilizes simple fits of T_{app} *versus* A_T [3].

Method (ii): $N_{th} \sim 10^2$, after fits of the dependence for individual thermometers the average value of the parameter $\langle c_2 \rangle$ has been obtained [1].

Method (iii): $N_{th} \sim 10^3 - 10^5$, in this case the average values of isotope temperatures, $\langle T_{app} \rangle$, have been extracted from temperature distributions as described below (see Refs. [2, 5, 6])

3. Results of fission data analysis

3.1. Ternary fission

Recently we analyzed more than 10^3 thermometers, which are available for TCP accompanied fission, and then the dependence on the target mass A_T was evaluated [1, 5]. Data related to fragment production at E_p=1 GeV provided more than 10^2 thermometers [3]. The temperatures extracted from the considered processes have confirmed that a linear relation like Eq. (3) can be used to parametrize the dependence of T_{app} on A_T. An example of case (ii) is shown in Fig. 2, taken from Ref. [1], where a detailed comparison of isotope temperatures evaluated for different reaction types is given, namely for neutron-induced ternary fission and for 1 GeV proton-induced fragmentation. Figure 2 demonstrates that the temperatures T_{app} differ considerably in the two interaction mechanisms with regard to the absolute value. Here we selected thermometers with the same $\Delta A = \Delta Z$=1 where the influence of the chemical potentials cancels out. A slight increase of T_{app} in Fig. 2 is observed with increasing A_T of the fissioning nuclei whereas proton-induced fragmentation shows an opposite behavior.

3.2. Temperature distribution method

The case (iii) is appropriate for processes characterized by low excitation energy, *e.g.* in low-energy fission. In this case a large number of isotope thermometers can be considered, and one may expect that small fluctuations from sequential decays of different origin are partly canceled out. Therefore, we propose to use the whole ensemble of available isotope combinations to obtain **T**emperature **D**istributions (TD). Then the average of the distribution and its variance are supposed to be related to the intrinsic temperature and its dispersion, respectively.

Figure 3 implements these ideas and demonstrates how we get a temperature distribution using the measured TCP yields for ^{242}Am(n,f). Every point on the scatter plot T_{app} *versus* B represents

an individual thermometer with its error bar (left panel, top). Some points, which are scattered away from the region where the bulk of thermometers is located, have usually the largest errors caused by experimental uncertainties. This observation is sufficiently confirmed by the plot T_{app} *versus* relative errors $\Delta T_{app}/T_{app}$ (left panel, bottom). Values T_{app} with large *relative errors* can be removed by a simple cut set in the projection onto the axis $\Delta T_{app}/T_{app}$ (right panel, top). After this selection, the reduced TD represented by the hatched histogram is obtained (right panel, bottom). The mean value $\langle T_{app} \rangle$ of this distribution was found to be insensitive to the chosen cut. Therefore, it is possible to apply any relevant cut in the relative errors to remove the unphysical negative tail of the TD.

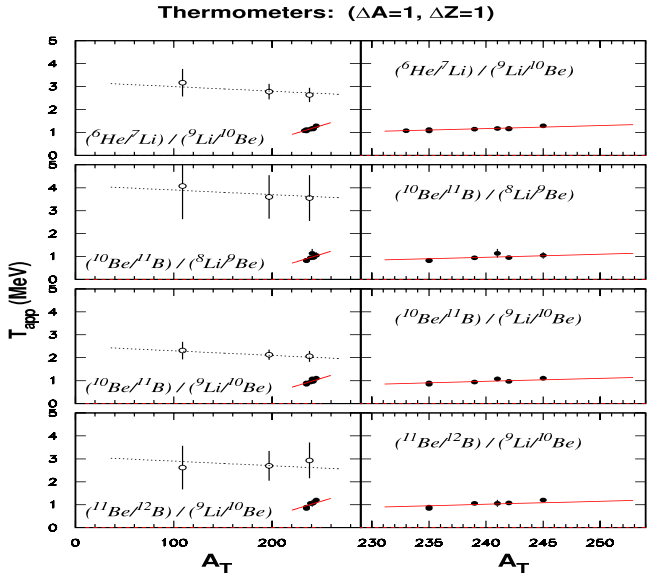

Fig. 2. T_{app} as function of the target mass A_T. Open circles: p(1 GeV)+A fragmentation, full circles: TCP accompanied fission. The right panels give the close-packed T_{app} (dots) on an expanded mass scale. The solid lines show the applicability of the obtained slope parameter $\langle c_2 \rangle$ to various isotope thermometers

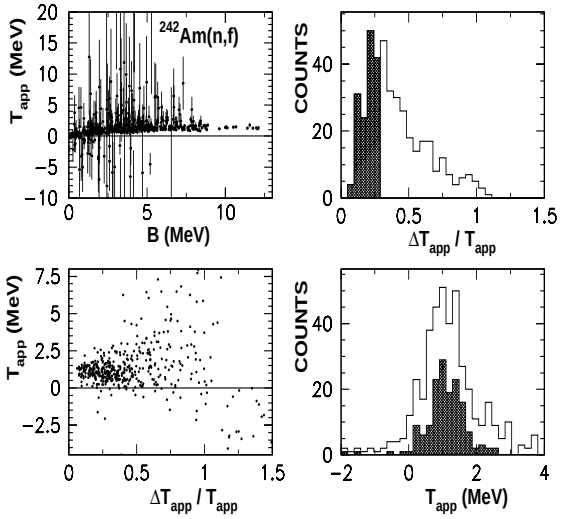

Fig. 3. Extraction of T_{app} distributions on the base of TCP's accompanying n-induced fission of ^{242}Am. Left panel, top: T_{app} *versus* difference of the binding energies, bottom: T_{app} *versus* the $\Delta T_{app}/T_{app}$. Right panel: projections onto the axes $\Delta T_{app}/T_{app}$ and T_{app}. Details are described in the text

The small value of c_2 (see Eq. (3)) for ternary fission gives us the opportunity to combine isotope temperatures T_{app} evaluated for target nuclei from ^{229}Th to ^{245}Cm into one temperature distribution. Sufficient statistics allows to select isotope combinations with Z$\geq$3 to avoid distortions of light particle yields by decay modes like ^{5}He$\rightarrow^4$He + n and ^{7}He$\rightarrow^6$He + n, which cannot be distinguished from the intrinsic yields of the He isotopes. As shown in Fig. 4 this selection leads to a slightly reduced average

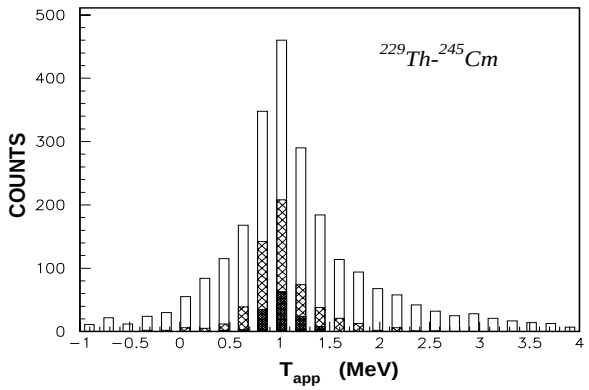

Fig. 4. Summary temperature distribution obtained from TCP in low-energy neutron-induced fission of heavy nuclei from ^{229}Th to ^{245}Cm (see Ref. [1]). Only TCP with Z$\geq$3 were selected (see text). Open bar histogram: no cut in $\Delta T_{app}/T_{app}$. Hatched histogram: cut at $\Delta T_{app}/T_{app} \leq 0.10$. Black histogram: cut at $\Delta T_{app}/T_{app} \leq 0.05$

temperature of $\langle T_{app} \rangle$ = 1.00 MeV. We emphasize that the mean value $\langle T_{app} \rangle$ obtained from such distributions is stable for different cuts even if we consider the summary TD for all targets.

3.3. Binary fission

It should be noted that the DRT method was suggested for light fragments, but it was shown later [2, 5, 6] that it can be applied properly also to heavy products like fission fragments. The analysis of binary fission is based on the Evaluated Nuclear Data File (ENDF-349) from which data for nuclei from ^{238}U to ^{256}Fm are presented here. First of all we mention that the 2-dimensional plot (Fig. 5), obtained for fission fragments from the spontaneous fission of ^{238}U, is very similar to that presented in Figs. 1 and 3. The main dissimilarity is the number of available thermometers N_{th}.

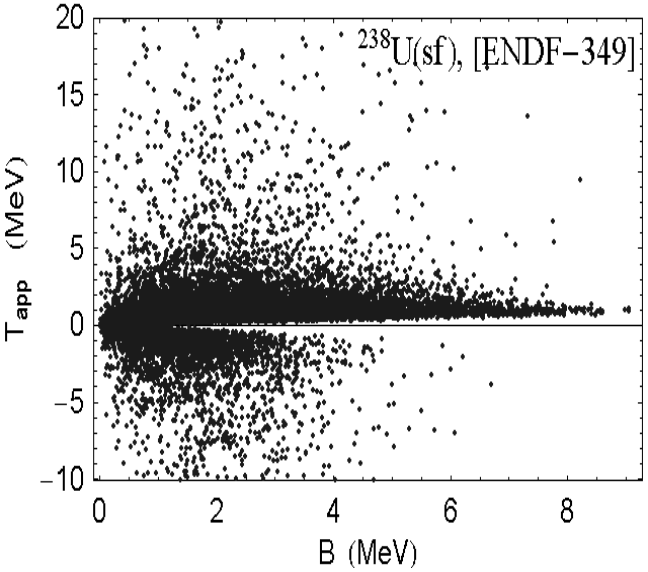

Fig. 5. A scatter plot of T_{app} *versus* B for binary fission of ^{238}U(sf) obtained using thermometers including the yields of isotopes As−Nb and Sb−Pr [6]

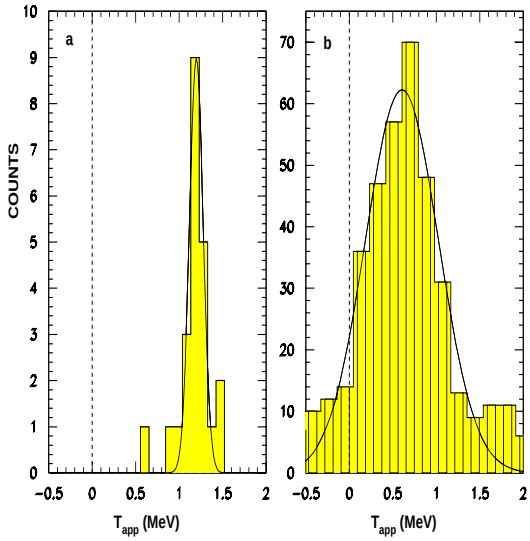

Fig. 6. Temperature distributions obtained for ^{252}Cf(sf): **a** - from TCP's accompanying fission and **b** - from binary fission fragment yields [5]

Concerning TD's related to ternary and binary fission, we present in Fig. 6a corresponding comparison for one of the fissioning nuclei. Figure 6**a** shows the TD derived from TCP's associated to the *spontaneous* fission of ^{252}Cf. Data on neutron decay of these TCP's [M. Mutterer, in *"Seminar on Fission, Pont d'Oye IV"* edited by C. Wagemans, O. Serot and P. D'Hondt, World Scientific, Singapore, 95 (1999)] allow to correct the yields of He isotopes for contributions from decay modes like ^{5}He→^{4}He+n and ^{7}He→^{6}He+n. The resulting TD delivers $\langle T_{app} \rangle$ = 1.20 ± 0.15 MeV in agreement with T=1.1 ± 0.2 MeV obtained from the spectrum of neutrons accompanying the ternary fission of ^{252}Cf [A.P. Graevsky *et al.*, Pis'ma Zh. Eksp. Teor. Fiz. **15**, 572 (1972)]. The TD in Fig. 6**b** extracted from isotopically resolved yields of fission fragments in the *binary* spontaneous fission of ^{252}Cf [G.M. Ter-Akopyan *et al.*, Part. and Nucl. **28**, 1357 (1997)] delivers $\langle T_{app} \rangle \simeq 0.6$ MeV. This value is close to the temperatures obtained from the neutron spectra associated with the most cold fission fragments [C. Budtz-Jörgensen and H.H. Knitter, Nucl. Phys. **A 490**, 307 (1988)]. It should be mentioned that the temperatures obtained from TCP yields in ternary fission are related to the moment of TCP's escape, *i.e.* can be assigned to the local nuclear temperature. In the binary fission mode it will be the scission-point temperature.

3.4. Target mass dependence of isotope temperatures

Various temperatures (and the corresponding excitation energies) which are responsible for ternary and binary fission modes can be obtained by the data analysis for one target. In order to establish the dependence of the nuclear temperature on the target mass a sufficient data base is required which

provides isotopically resolved yields of reaction products for a number of target nuclei. In the case of ternary fission we made use of TCP yields ($Z \leq 14$) available for the targets from ^{229}Th to ^{245}Cm and ^{252}Cf (see Refs. in [1]) The method labeled (ii) was applied to $\sim 10^2$ thermometers to determine the dependence on the target mass and then the corresponding slope parameter c_2. Afterwards this dependence was normalized to $\langle T_{app} \rangle$=1.2 $\pm$ 0.15 MeV obtained for ^{252}Cf. The top line in Fig. 7 shows this result. The large error bars for ^{252}Cf are due to the limited number of available thermometers and large experimental errors of the measured yields. In order to demonstrate the common fit–quality for ternary fission, some points which represent the temperatures evaluated using the special double-yield ratio (^{6}He/^{7}Li)/(^{9}Li/^{10}Be) for 6 targets, are also given here. The lower points and line in Fig. 7 show the temperature $\langle T_{app} \rangle$ obtained by the method (iii) for the binary mode of spontaneous fission and the fit to these data. The applicability of the ENDF-349 data base was verified by comparison with independent measurements of fragment yields for ^{252}Cf [G.M. Ter-Akopyan *et al.*] and thereby the same set of thermometers was exploited. The temperatures obtained from both data sets are in agreement within the error bars. Thus, Fig. 7 demonstrates in this way convincingly the dependence of the temperature, extracted by the DRT method, on the target mass for both TCP accompanied

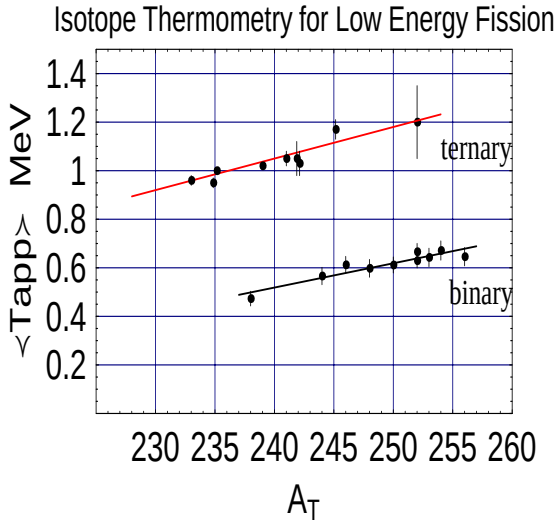

Fig. 7. Dependence of isotope temperatures on target mass A_T in spontaneous and neutron-induced fission. Top line – fit of $\langle T_{app} \rangle$ *versus* A_T for ternary fission for targets from ^{229}Th to ^{252}Cf [1]. Bottom line – fit of $\langle T_{app} \rangle$ *versus* A_T for spontaneous binary fission (black points) in the target mass range ^{238}U – ^{256}Fm [2]

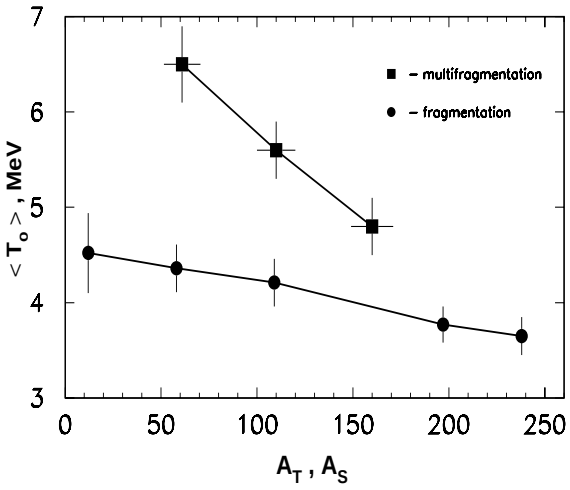

Fig. 8. Corrected temperatures $\langle T_o \rangle$ as function of A_T (or A_S) evaluated from isotope production cross sections. Dots: p(1 GeV)+nucleus fragmentation [3], squares: multifragmentation in 1A·GeV Au, La and Kr collisions with carbon. A_S is are the remnant mass in the multifragmentation reaction

and binary fission modes. This result seems to be a nontrivial one because a number of authors suggest a non-adiabatic TCP production (neck rupture) in the ternary fission mode. But, on the other hand, isotope thermometry is generally applicable to systems in thermal and chemical equilibrium. In order to approve the obtained isotope temperatures, we compared our results with temperatures obtained by other methods. The temperatures evaluated from the slope of the spectrum of neutrons accompanying the ternary fission of ^{252}Cf (T = 1.1(2) MeV) and the temperatures derived from the population of excited states of ^{7}Li produced in n_{th}-induced fission of ^{234}U (T = 0.80(9) MeV), ^{236}U (T = 0.87(6) MeV) and ^{252}Cf(sf) (T = 0.98(12) MeV) [P. Jesinger *et al.*, Eur. Phys. J. **A 24**, 379 (2005)] show a similar dependence on the target mass and they are comparable with our results. Hence it follows that for ternary fission both the values of isotope temperatures and the dependence of these temperatures on the target mass are supposed to be confirmed.

3.5. Comparison with p(1 GeV)+A fragmentation

The dependence of the temperature on the target mass, which was found for low-energy fission, may be compared with that observed for nuclear fragmentation at intermediate energies. In the discussion regarding Fig. 2 we mentioned already the different sign of the slope parameters c_2 found by the method (ii) for low-energy ternary fission and nuclear fragmentation. The characteristic dependence of T *versus* A (see Fig. 8), obtained by the standard procedure (i) applied to fragmentation of nuclei induced by 1 GeV protons [3], can be also verified when extending this method to multifragmentation of 1A·GeV Au, La and Kr projectiles on carbon nuclei [B.K. Srivastava *et al.*, Phys. Rev. **C 65**, 054617 (2002)]. We mention that in this case the temperature T_o was obtained by using empirical correction according to Eq. (2) but not by averaging of T_{app}. It is remarkably that such dependence, *i.e.* the decrease of T with increasing A, was predicted by theoretical models assuming that the long-range (Coulomb) force dominates in the fragmentation. This conclusion is also supported by Hartree-Fock calculations. On the other hand, models based on short-range forces (Ising and percolation models) show the opposite slope.

3.6. Comparison with p(1 GeV)+A fragmentation

The analysis of TCP data [1] showed that the temperature increases with the mass number A of the fissioning nuclei like Eq. (3), where $\langle c_2 \rangle$=0.013 ± 0.004 MeV. An additional check of the obtained results can be performed by comparing the dependence of T_{app} as function of A with theoretical calculations of released energies in binary and ternary fission. For this purpose we converted the values $T_{app}(A)$ into the corresponding excitation energies (supposing the same $\langle c_2 \rangle$ for binary and ternary fission). At this we used in a first approximation the Fermi-gas relation $E_{exc} = a \cdot T^2$ with level density parameters a for low-lying levels evaluated from neutron resonances [W. Dilg *et al.*, Nucl. Phys. **A 217**, 269 (1973)] in ^{230,231,233}Th, $^{233-237,239}$U, $^{239-241}$Pu and $^{245-247,249}$Cm. The results are shown as open symbols in Fig. 9 (taken from Ref. [5]).

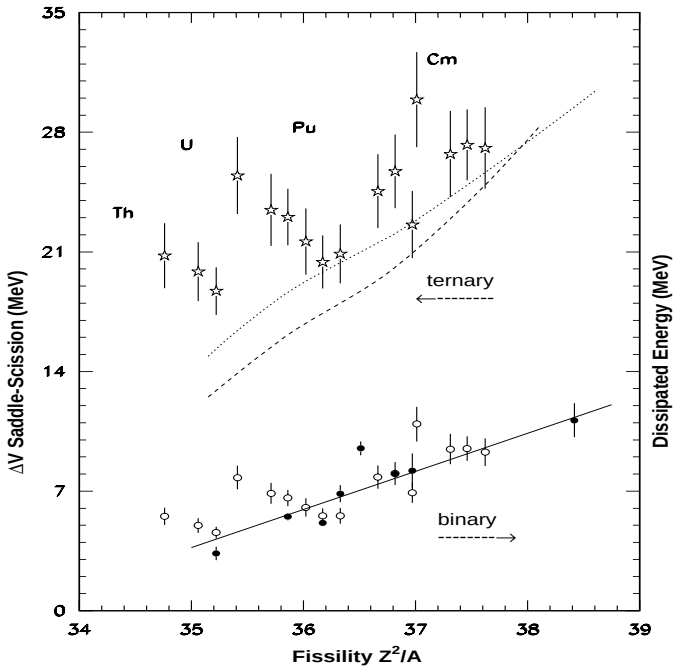

Fig. 9. Comparison of available data related to excitation energies derived for ternary and binary fission of heavy nuclei. Open symbols represent E_{exc} evaluated in this work for binary (open circles) and ternary fission (open stars). Dashed and dotted lines show two versions of theoretical predictions of the potential energy gains ΔV [M. Asghar *et al.* and G. Adeev *et al.* in *The Nuclear Fission Process*, edited by C. Wagemans (CRC Press, Inc., Boca Raton, 1991)]. Black dots are dissipated energies in binary fission taken from the review of F. Gönnenwein [see in C. Wagemans, *ibid.*]

The dissipated energies extracted earlier from the odd-even effects in the abundance of binary fission fragments are shown in Fig. 9 as black dots together with the corresponding linear fit.

The overall trend of our estimated values E_{exc}, related to binary fission, is an increase with Z^2/A guided by the fit to the earlier data points (black dots). On the other hand, the values of E_{exc} referring to TCP data (open stars) are closer to the difference ΔV of the potential energy jump from the saddle to the scission points predicted by theoretical calculations (dashed and dotted lines). Thus, both the temperatures evaluated for the two fission modes and the value of the slope parameter $\langle c_2 \rangle$ in the temperature dependence on the target mass don't contradict to earlier estimations of energy release and its global dependence on Z^2/A.

However, it is worthy of note that E_{exc} related to a chain of fissioning isotopes steeply increases if the mass number A raises (open symbols in Fig. 9). Formerly, the limited number of data (black dots in Fig. 9) relevant to some isotopes of one element did not allow to observe this tendency. Our evaluation, *i.e.* the observed tendency for fixed Z, is nothing else as a consequence of the dependence $T_{app}(A)$ displayed in Fig. 7. This observation is evidently confirmed by the data shown in Fig. 10

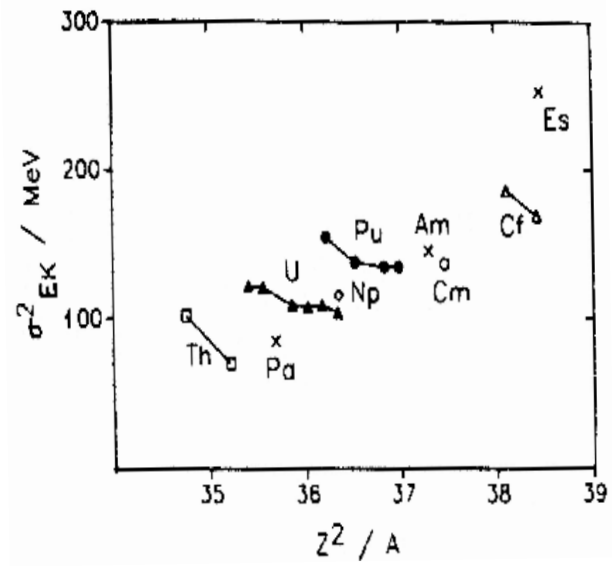

Fig. 10. Variance $\sigma^2_{E_k}$ of total kinetic energy distributions *versus* Z^2/A of fissioning nuclei for near-barrier fission

(taken from the earlier cited review ed. by C. Wagemans, there it is numbered as Fig. 27). In this figure the dependence of the variance σ^2_{Ek} of the total kinetic energy of fission fragments on the fissility Z^2/A is given. A comparison of Figs. 9 and 10 suggests for binary fission that the higher the temperature of fissioning nuclei the higher the variance σ^2_{Ek}.

4. Summary

In this contribution we show that

- the determination of the nuclear temperature from double yield-ratios of isotopically resolved reaction products can be applied to quite different reaction types as low-energy fission and fragmentation induced by intermediate energy projectiles.
- The mean temperatures in the spontaneous and low-energy fission, related to ternary charged-particle emission or to the binary fission modes, differ in a factor of two. In the case of ^{252}Cf these mean temperatures amount to $\sim$1.2 MeV and $\sim$0.65 MeV, respectively.
- The dependence of the temperature on the masses of the fissioning nuclei shows the same behavior for the binary and the TCP accompanied fission modes. In particular, the temperature increases with increasing mass of the target nucleus. We notice about the different behavior of

the analog dependence for nuclear fragmentation at intermediate energies which was also obtained by isotope thermometry. The consideration of such dissimilarities may be appropriate to the choice and parametrization of theoretical models to describe the mentioned processes.

Finally, we point out that the presented results are in agreement with other experimental data regarding temperature evaluation by other methods as well as with results of calculations in the framework of theoretical models.

Acknowledgments

We would like to thank D.M. Seliverstov for encouragement in our work.

References

1. M.N. Andronenko *et al.,* Eur. Phys. J. **A 12**, 185 (2001).
2. M.N. Andronenko, L.N. Andronenko and W. Neubert, Preprint PNPI-2643, Gatchina, 2005. 21 p.
3. M.N. Andronenko *et al.,* Eur. Phys. J. **A 8**, 9 (2000).
4. M.N. Andronenko *et al.,* in *Abstracts of the International Conference "Structure of the Nucleus at the Dawn of the Century"* (Bologna, Italy, 29 May – 3 June 2000), A-83.
5. M.N. Andronenko, L.N. Andronenko, and W. Neubert, in *"Clustering Aspects of Quantum Many-Body Systems"* ed. by A. Ohnishi *et al.*, World Scientific Publishing Co. (2002), p. 223.
6. M.N. Andronenko, L.N. Andronenko, and W. Neubert, in *Proceedings of the 16th International Workshop on Nuclear Fission* (Obninsk, Russia, 7 – 10 October 2003).

LASER SPECTROSCOPIC STUDIES OF NEUTRON-DEFICIENT EUROPIUM AND GADOLINIUM ISOTOPES

A.E. Barzakh, D.V. Fedorov, A.M. Ionan, V.S. Ivanov, F.V. Moroz, K.A. Mezilev, S.Yu. Orlov, V.N. Panteleev, Yu.M. Volkov

1. Introduction

The region of nuclei near $Z = 64$ and $N < 82$ is of great interest for nuclear physics. It has been established that closed sub-shell $Z = 64$ considerably influences on the regime of the entrance into the deformation region at $N > 82$. Nuclei with Z close to $Z = 64$ keep their spherical form up to $N = 88$. Then the sudden jump of deformation takes place. For nuclei with Z as far from $Z = 64$ as five and more protons, the deformation is changing smoothly and reaches the maximum at $N = 90–92$ [1].

The region of nuclides at $N < 82$ was systematically investigated at the IRIS facility for a long time. Studies of the deformation behavior for Eu ($Z = 63$), Sm ($Z = 62$) and Nd ($Z = 60$) isotope chains point to the smooth change of deformation, growing right after $N = 81$, without any jump-like effects.

In this report the recent development of the laser ion source spectroscopy technique and the results of the very neutron-deficient Eu isotope shift measurements are presented.

To complete these investigations, the isotope change of deformation for Gd ($Z = 64$) isotope chain has to be studied. For Gd the stabilizing influence of the closed sub-shell should be maximal, if it takes place. It is of importance also to extend our knowledge of the deformation behavior in the adjacent isotopic chains (for example, for Eu isotopes) as far as possible.

2. Experimental method

Method of the resonance laser photoionization in the laser ion source proves to be one of the most efficient for isotope shift and hyperfine structure investigations [2]. The essential point of the experimental method is step-by-step resonant laser excitation to autoionization states or continuum. The ionization schemes for Eu and Gd are shown in Fig. 1. The first experimental techniques based on the resonant ionization of the radioactive atoms at the exit of the mass separator enable one to carry out experiments with the isotopes at a production rate down to 10^4–10^5 atoms per second.

To extend the investigations to the more neutron-deficient isotopes, first of all to the region of neutron-deficient isotopes near and below the magic neutron number $N = 82$, the method of photoionization spectroscopy inside the laser ion source has been proposed and applied at the IRIS facility [2]. The experimental setup is presented in Fig. 2. Nuclides under study are produced in the target of the mass-separator by 1 GeV protons of the PNPI synchrocyclotron. The atoms are thermally released from the target to the ion source cavity. Three beams of pulsed dye lasers are introduced to the same cavity to provide the multistep resonance ionization of the atoms under investigation.

The dye lasers are pumped by three copper vapor lasers (repetition rate 10 kHz). The wavelengths of the dye lasers are tuned to the transitions of the chosen ionization scheme. The radiation frequency of the two broadband lasers (bandwidth 30 GHz) are fixed according to the second and the third transitions. The wavelength of the narrowband laser (bandwidth 1 GHz) is scanned across the first transition. The photoion current in the mass-separator collector increases at the resonance. Thus, the experimental spectra represent the dependence of the ion current on the scanned laser frequency. The detection of ion current is provided by α-, β-, or γ-counting. The corresponding detectors are installed on the tape-driving system.

A part of the scanning laser radiation is directed to the Fabry-Perrot interferometer (free spectral range 5 GHz) to produce frequency marks for the frequency scale calibration. Another part of the laser beam is used in a reference chamber to provide a reference spectrum from the sample of stable isotopes for the isotope shifts measurements.

---

[1] G.D. Alkhazov *et al*., JETP Lett. **37**, 274 (1983).
[2] G.D. Alkhazov *et al*., Nucl. Instr. Meth. B **69**, 517 (1992); A. E. Barzakh *et al*., Phys. Rev. C **61**, 034304 (2000).

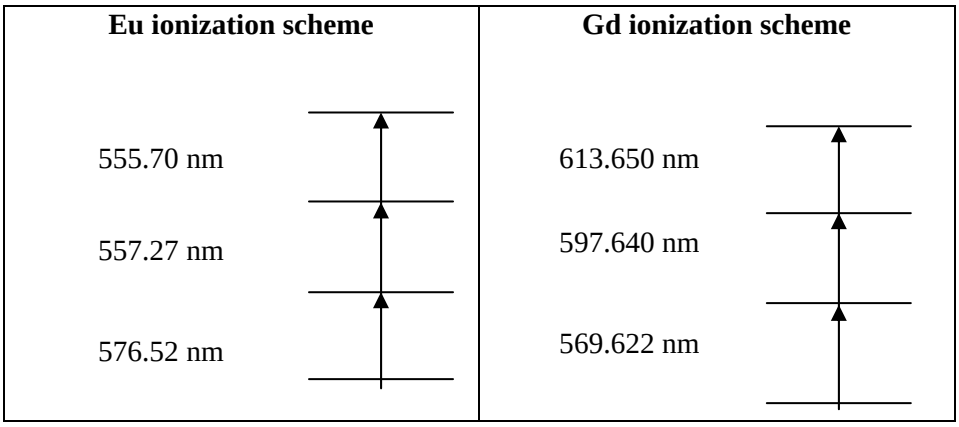

Fig. 1. Ionization schemes of Eu and Gd

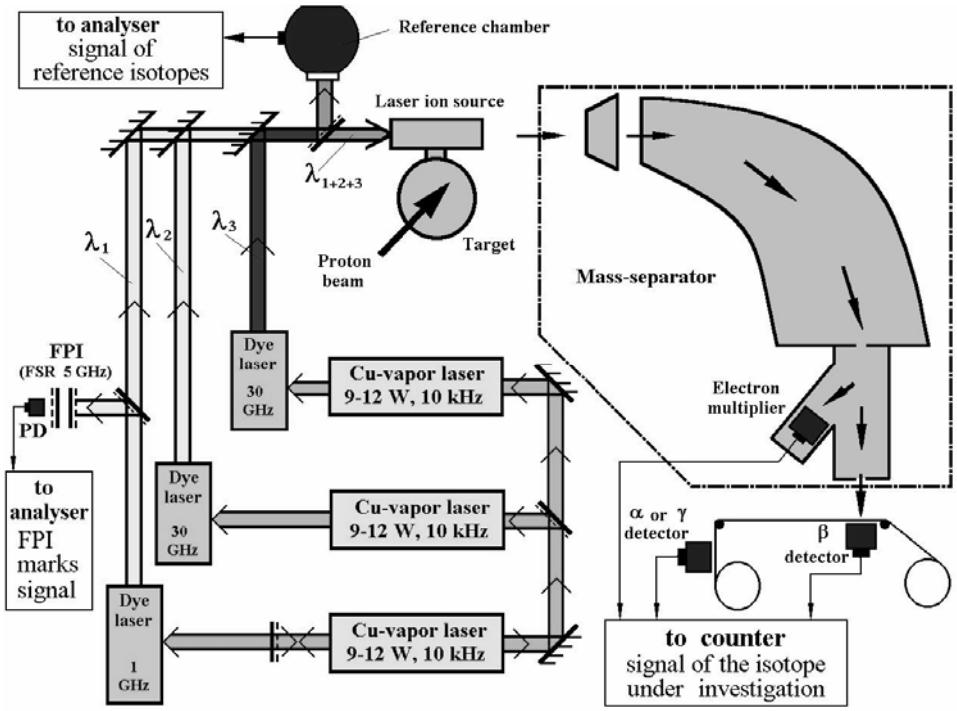

Fig. 2. Experimental setup

Two methods of the multistep resonance ionization at the entrance of the mass-separator have been used in the course of the experiment. The first one is a laser spectroscopy in the laser ion source. This is a traditional for the IRIS facility method, and it was described in details elsewhere [2]. The main point of this method is the multistep resonance ionization of the atoms under investigation directly inside the cavity of the ion source, coupled with the target, irradiated by proton beam. A scheme of this method is presented in Fig. 3 (left).

The second method is based on the resonance ionization directly inside the target, producing the nuclides under study [1]. We call this method as the laser target (LT) in order to emphasize that it differs from the method employing the resonance ionization in the laser ion source (LIS). Schematically this construction is presented in Fig. 3 (right).

For such a hard volatile element as gadolinium (boiling point is 3546°C) an effusion is the main process responsible for the delay of nuclides in the target-ion source system. The newly developed target was specially designed for the production of elements with long sticking time such as Gd to exclude “cold spots” which sometimes exist at the places of the target – transfer tube – ion source connection.

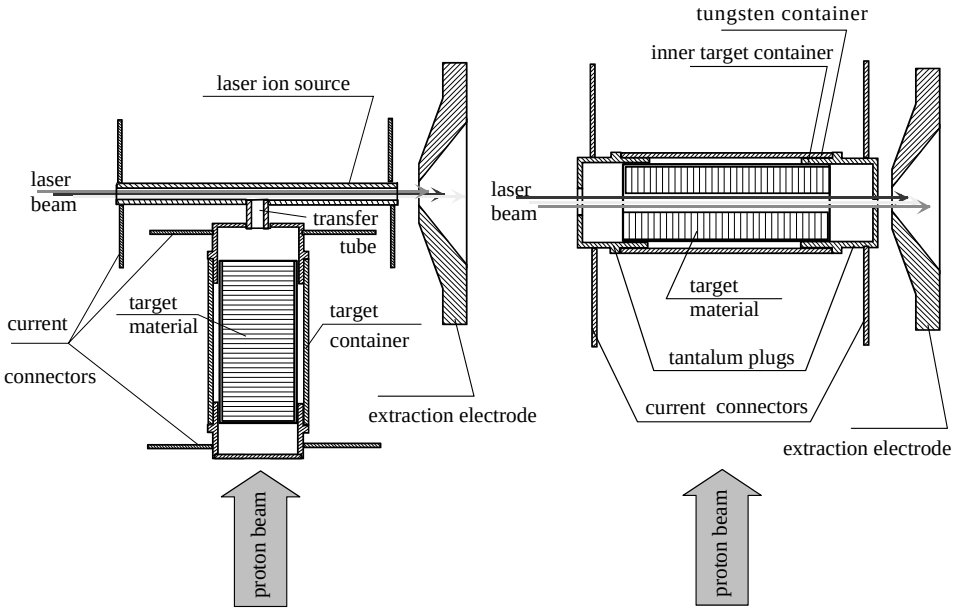

Fig. 3. Scheme of the resonance laser ionization inside the laser ion source LIS used for Eu (left) and the laser high temperature target LT used for Gd (right)

3. Experimental results and discussion

3.1. Europium

Isotope shifts for the chain of europium isotopes have been measured [2]. For ^{142m}Eu, the γ-line with the energy 556.6 keV was used to avoid influence of the short-lived ground state ($T_{1/2}$ = 2.4 s). Table 1 presents the experimental results of the isotope shift measurements for neutron-deficient Eu isotopes.

Table 1

Experimental results for isotope shifts of the neutron-deficient Eu isotope chain

Isotope	$\Delta\nu_{145,A}$, MHz	$\Delta\nu_{145,A}$, MHz, (previous meas.)	$\lambda_{145,A}$, fm^2
^{144}Eu	240(160)	340(200)	–0.039(25)
^{143}Eu	150(160)	200(170)	–0.028(25)
^{142}Eu	20(180)	35(150)	–0.010(28)
^{141}Eu	–260(160)	–300(150)	0.032(25)
^{139}Eu	–590(240)	–750(200)	0.079(37)
^{138}Eu	–880(220)	–500(350)	0.114(34)
^{137}Eu	–730(280)	–	0.096(44)

The results previously obtained by the conventional resonance ionization technique [3] are also shown. They are consistent with the new results within the experimental errors. To extract the parameter $\lambda_{145,A}$ which is connected with the changes of the mean square charge radii $\delta\langle r^2\rangle_{145,A}$ the standard procedure [4] was used (with the electronic factor $F = -6.55$ GHz/fm^2). The specific mass shift for this pure s^2-sp transition was neglected. The errors for $\lambda_{145,A}$ in Table 1 are pure statistical; the uncertainty of the electronic factor is assumed to be about 5%.

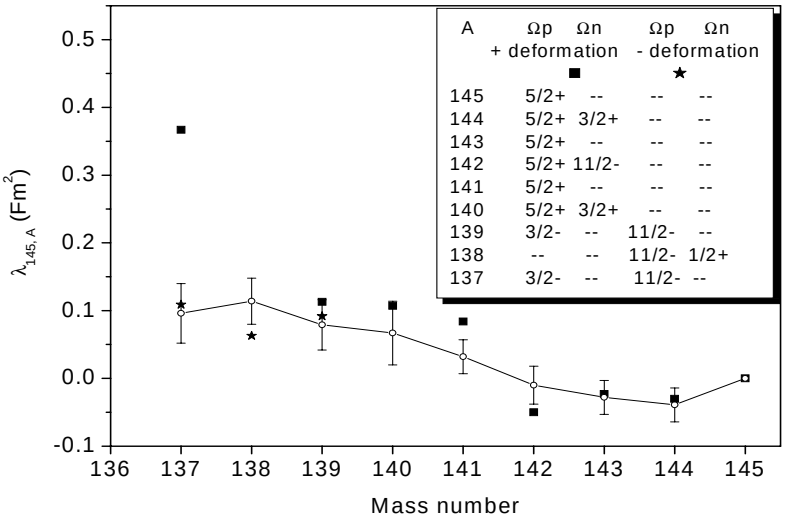

Fig. 4. Hartree-Fock calculations with SkM′ forces for the neutron-deficient Eu isotopes

Hartree-Fock calculations with SkM′ forces for axially deformed nuclei have been performed for neutron-deficient Eu isotopes (see Fig. 4). The states blocked by the last odd particle were fixed in accordance with the known spin and parity of the corresponding nuclei (see Table in Fig. 4). For ^{137}Eu the agreement of the experimental and theoretical data can be obtained only for the negative deformation minimum on the conditions that the proton state with $\Omega^{\pi}=11/2^{-}$ which lies closest to the Fermi level is blocked by the odd proton. The results of the Hartree-Fock calculations for the very neutron-deficient Eu nuclei are crucially dependent on the odd particle states. It should be noted that for the proper theoretical description of $^{137, 138, 139}$Eu a triaxial deformation should be taken into account instead of the negative quadrupole deformation.

3.2. Gadolinium

The isotope shifts of the optical line 569.622 nm for nuclides ^{145}Gd, ^{145m}Gd and ^{143m}Gd have been measured [3]. For ^{145}Gd (I = 1/2) the hyperfine splitting has also been measured. During the data processing, spins for ^{145m}Gd and ^{143m}Gd have been fixed according to known values I = 11/2 because the resolution of the method applied is not sufficient to provide hyperfine splitting measurements for the independent determination of the spin values. The optical line width on the measured spectra is taken as a convolution of the laser linewidth and the Doppler broadening in the target-ion source system. Calculated by this way value of the optical line width (of about 2100 MHz) is in agreement with the width of a separate optical line in the experimental spectrum of ^{145}Gd.

We suppose that ^{145m}Gd with its closed proton sub-shell and one neutron vacancy has an electric quadrupole moment with the absolute value not exceeding 1 barn. The systematics for all known nuclei with

[3] V.S. Letokhov *et al*., J. Phys. G **18**, 1177 (1992).
[4] A.E. Barzakh *et al*., Eur. Phys. J. A **1**, 3 (1998).

the same neutron configuration and spin (for instance ^{147}Dy: Z = 66, N = 81, I = 11/2, Q_s= 0.67(10) barn) sidewards confirm this estimation.

At this supposition, taking into account the optical linewidth and varying the quadrupole moment in the limits mentioned above, the magnetic moment of ^{145m}Gd can be determined from the broadening of the line in the ^{145m}Gd spectrum. In Table 2 the experimental results on isotope shifts and hyperfine structure constants are shown. For ^{143m}Gd there are no reliable limits for the quadrupole moment. Therefore only the isotope shift for this nuclide has been determined as a distance between the centers of gravity of ^{143m}Gd and ^{160}Gd optical lines.

Table 2

Experimental results for isotope shits $\Delta\nu$ and
hyperfine structure constants a in the 569.622 nm line of Gd isotopes

Isotope	$\Delta\nu_{A,160}$, MHz	a, MHz
^{145m}Gd (I=11/2)	–12350(320)	–7.5(1.5)
^{145}Gd (I=1/2)	–12550(190)	–58.8(3.8)
^{143m}Gd (I=11/2)	–12350(350)	–

Table 3 represents the values of the nuclear parameter $\lambda_{A,A'} \approx \delta\langle r^2\rangle_{A,A'}$ and dipole magnetic moments evaluated according to the standard procedure [5].

Table 3

Changes of mean-square charge radii and dipole magnetic moments of Gd isotopes

Isotope	$\delta\langle r^2\rangle_{A,160}$, fm^2	μ, n.m.
^{145m}Gd (I=11/2)	–1.76(5)	–1.0(0.2)
^{145}Gd (I=1/2)	–1.79(3)	–0.74(5)
^{143m}Gd (I=11/2)	–1.69(5)	–

3.3. Changes of mean-square charge radii $\delta\langle r^2\rangle_{A,146}$ of Gd nuclides with I = 11/2 as compared with data for Eu (Z = 63) isotopes with the same neutron numbers

In Fig. 5 the data for $\delta\langle r^2\rangle_{A,146}$ of the Gd nuclides with I = 11/2 are presented as compared with the data for Eu (Z = 63) isotopes with the same neutron numbers. The value of $\delta\langle r^2\rangle_{146,160}$ for Gd has been measured earlier at the IRIS facility [5].

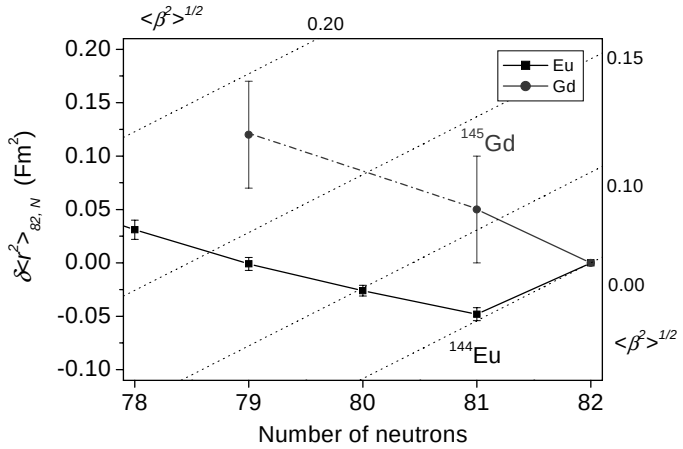

Fig. 5. Changes of mean-square charge radii of Gd nuclides with I =11/2 as compared with data for Eu (Z = 63) isotopes

[5] G.D. Alkhazov *et al*., JETP Lett. **48**, 373 (1988).

Obviously, the deformation for Gd isotopes rises with the decrease of the neutron number from $N = 82$ to $N = 79$ even faster than for adjacent Eu isotopes with the same neutron number. Therefore there is no indication on the stabilization effect of the proton sub-shell $Z = 64$ near the neutron sub-shell $N = 82$. Values of the dipole magnetic moments measured for ^{145}Gd and ^{145m}Gd are close to the values of the dipole magnetic moments for $^{141, 141m}$Sm: ^{141}Sm, $\mu(I = 1/2) = -0.74(2)$ n.m. and ^{141m}Sm, $\mu(I = 11/2) = -0.84(2)$ n.m.

4. Conclusion

The laser ion source has been used for the study of the isotope shifts of neutron-deficient Eu and Gd isotopes. The extension of the region of the applicability of the method by using the γ- and β-radiation detection is reported. We have measured the isotope shifts of the Europium optical line 576.520 nm for $^{137-144}$Eu and 569.622 nm for $^{145, 145m, 143m}$Gd. Changes in mean square charge radii for ^{137}Eu, $^{145, 145m, 143m}$Gd and magnetic moments for $^{145, 145m}$Gd have been determined for the first time.

The resonance ionization directly inside the target (without special ion source unit) was used for producing the Gd nuclides under study. For such a hard volatile element as gadolinium (boiling point is 3546°C) an effusion is the main process responsible for the delay of nuclides in the target–ion source system. The newly developed target was specially designed for the production of elements with long sticking time such as Gd to exclude “cold spots” which sometimes exist at the places of the target – transfer tube – ion source connection. The laser has ensured the resonance count of Gd ions considerably higher than the target system of the usual construction. The most likely explanation of that effect can be a much higher concentration of Gd radioactive neutrals irradiated by the laser beam inside LT than in the volume of the laser ion source.

The gradual transition from the spherical nuclei near the magic neutron number $N = 82$ to the deformed ones near $N = 74$ contrasted with the abrupt increase of deformation on the other side of the same magic neutron number for Eu isotopes at $N = 89$. This different behavior is supposed to be connected with the different influence of the semi-magic number $Z = 64$ on the deformation development for the nuclei with $N > 82$ and $N < 82$.

There is no indication on the stabilization effect of the proton sub-shell $Z = 64$ near the neutron sub-shell $N = 82$ for Gd isotopes as well. Values of the dipole magnetic moments measured for ^{145}Gd and ^{145m}Gd are in a good agreement with magnetic moments of other nuclei with the same neutron number.

References

1. V.N. Panteleev *et al*., Rev. Sci. Instr. **75**, 1585 (2004).
2. A.E. Barzakh *et al*., Eur. Phys. J. A **22**, 69 (2004).
3. A.E. Barzakh *et al*., Phys. Rev. C **72**, 017301 (2005).

NUCLIDES OF ASTROPHYSICS INTEREST WITH MASS NUMBERS CLOSE TO *A*~80

PNPI participants of the IGISOL/JYFLTRAP collaboration[1]
L.Kh. Batist, S.A. Eliseev, Yu.N. Novikov, A.V. Popov, D.M. Seliverstov, G.K. Vorobjev

1. Introduction

Nuclei close to the $N = Z$ line in the region near $A = 80$ play a special role in nuclear astrophysics since the rapid proton (*rp*) capture process is passing right through them (see Fig. 1). The *rp*-process, a sequence of rapid proton captures and β^+-decays, proceeds along the $N = Z$ line up to ^{56}Ni and it can continue ending in a SnSbTe cycle either in explosive *X*-ray bursts or in a steady state burning (*e.g.*, in *X*-ray pulsars). At higher *Z* values, where proton capture rates become smaller, the reaction path can be broader and shifted by about one or two mass units towards the β-stability line. This shift can be even greater for the steady state burning model.

The properties of neutron-deficient nuclei involved in the *rp*-process, especially masses and β-decay half-lives, are needed to perform calculations of *rp*-process nuclear reaction network. These simulations are crucial for the understanding of the energy generation and fuel consumption in the *rp*-process and its potential contribution to galactic nucleosynthesis. The discovery of new long-lived isomeric states in neutron-deficient nuclei is of special interest. Low-lying excited states can therefore alter proton capture rates and β^+/EC decay rates considerably. This is particularly true for isomeric states. Such states typically have different properties than the ground state and therefore potentially different capture and decay rates.

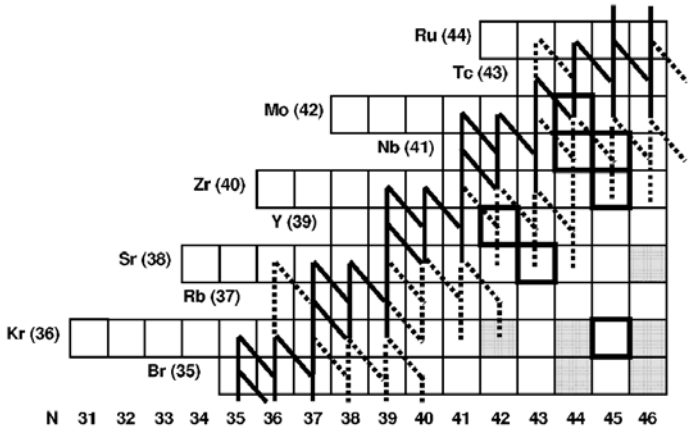

Fig. 1. The *rp*-process path close to $A = 80$ for steady state burning. The reaction flow of more than 10% is shown by the solid line and of 1–10% by the dashed line. The nuclei studied in this work are highlighted by squares

Another problem in astrophysics directly related to our present study is solar neutrino detection. After the experiment using the ^{37}Cl detector had shown the discrepancy between expected and experimental solar neutrino fluxes, it was suggested that the flux should be measured for lower neutrino energies. For this purpose other detectors were proposed, one of which was based on ^{81}Br. Although the solar neutrino flux puzzle has recently been explained by neutrino oscillations, more solar neutrino experiments are required to measure the CNO fusion cycle contribution to the solar luminosity and new types of detectors are very desirable. According to current solar model calculations, 98.5% of the solar luminosity is provided by the *p-p* chain and only 1.5% by CNO reactions. At the moment, solar neutrino experiments have only set an upper limit of 7.8% to the CNO fraction of the Sun's luminosity.

The threshold energy for neutrino capture in the proposed ^{81}Br detector is by a factor of two lower than in ^{37}Cl. It is assumed that a ^{81}Br detector is most sensitive to ^{8}B neutrinos, but ^{7}Be neutrinos as well as neutrinos from ^{13}N and ^{15}O decays from the CNO cycle can also contribute. In radiochemical experiments ^{81}Br can be

[1] This work has been performed at the IGISOL facility of the University of Jyväskylä (Finland)

used for total solar neutrino flux measurements because its energy threshold allows the observation of neutrino-induced events from all main solar neutrino sources mentioned above.

In order to obtain the neutrino capture cross section on ^{81}Br, the probability for the inverse process of electron capture decay of ^{81}Kr has to be measured. As can be seen in Fig. 2, the neutrino capture on ^{81}Br should predominantly populate the isomeric state at 190.5 keV in ^{81}Kr because this allowed transition has to be six orders of magnitude stronger than the capture to the ground state of ^{81}Kr, whose inverse rate is well known. Thus, the rates for all decay branches of ^{81m}Kr, which are electron capture, internal conversion and γ-decay, are needed to derive the electron capture probability. The data for the *K*-electron capture channel, determined independently by two groups, are in satisfactory agreement but the information on the internal transition (γ- and conversion electron branches) is strongly contradictory. Therefore, the electron capture branching ratio has not been obtained with high accuracy and new measurements on the internal decay channel of ^{81m}Kr are needed.

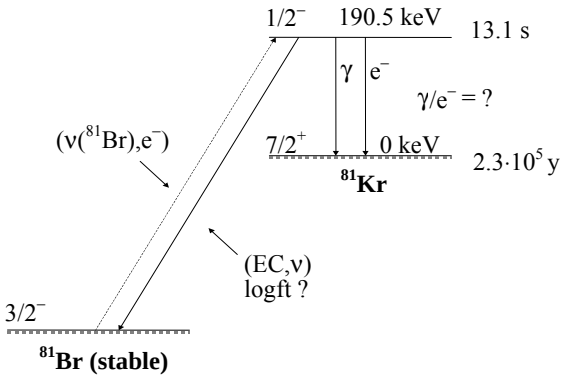

Fig. 2. A decay scheme of the isomeric state ^{81m}Kr (13.1 s)

2. Experimental methods

The experiment was performed using the IGISOL facility at the Jyvaskyla isochronous cyclotron. The isotopes of interest were produced by a 150–170 MeV $^{32}S^{7+}$ beam with an intensity of about 500 nA on ^{nat}Ni (2 mg/cm^2) and ^{54}Fe (1.8 mg/cm^2) targets. The fine tuning of the primary beam energy was performed with degraders of Havar foil and/or ^{nat}Ni. The reaction products passing through a 2.1 mg/cm^2-thick Havar window were stopped in a helium gas cell of the IGISOL facility [1]. After extraction from the gas cell by helium flow and under a small extraction potential (typically 300 V) the ions were accelerated to 40 keV. The accelerated ion beam was mass-separated and used for spectroscopy and mass-spectrometry measurements.

For the aims of spectroscopy measurements the first detector station was situated where the ion beam was implanted into the collector tape (see Fig. 3). It consisted of two HPGe detectors situated face-to-face and a plastic scintillator ($\Delta\beta$) which gated γ-radiation by β-particles. After some time of accumulation at the first station, the tape was moved and the source was delivered to the second detector station where an electromagnetic electron transporter and a low energy Ge detector (LeGe) were installed. The next source was prepared at the first station until the measurements were completed at the second station. Short accumulation and measurement times were optimal for the observation of short-lived nuclei.

Conversion electron decays and low energy γ-radiation were studied at the second detector station. Electron spectra were measured by ELLI, a magnetic conversion-electron transporter spectrometer consisting of two coils. It transported electrons from the implantation point to a cooled Si(Au) surface barrier detector in a remote detection area, that helped to reduce the background. A low energy Ge detector with a very thin entrance window (0.5 mm Be) was placed on the opposite side of the Si detector in a geometry close with respect to the implantation point. The ELLI-spectrometer had a typical efficiency of about 5% at electron energies less than 100 keV in this experiment. With this kind of setup one could measure both the absolute value for α_K and the ratio α_K / α_{L+M}..

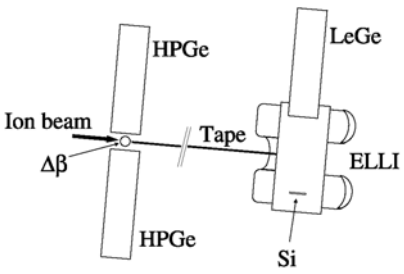

Fig. 3. A schematic view of the detection setup

For mass measurements mass-separated ions of interest were sent to the radiofrequency quadrupole ion beam cooler and buncher. After cooling and accumulating for a short time the ions were extracted as a short bunch and transported to the Penning traps system. JYFLTRAP consists of two cylindrical Penning traps in one superconducting magnet. The traps are placed in the homogeneous regions of the magnet separated by 20 cm. The first trap, the purification trap filled with helium gas at a pressure of about 10^{-4} mbar, is dedicated for isobaric cleaning using mass selective buffer gas cooling technique. The second trap called the precision trap operates in vacuum and is used for high precision mass measurements employing time-of-flight ion cyclotron resonance technique.

In this trap, RF dipole excitations employing the phase locking technique were applied in order to enhance the magnetron radius. Then the RF quadrupole excitations were applied to convert periodically a slow magnetron motion to a fast reduced cyclotron motion with a higher radial energy. An excitation time of 900 ms was chosen with corresponding excitation amplitude which finally allows a full conversion at the resonance frequency. At the end the ions were ejected from the trap. They drift towards the micro channel plate (MCP) detector through a set of drift tubes where a strong field gradient exists. Here the ions experience an axial force which converts the radial kinetic energy of the ions into the longitudinal energy. As a result, an ion in a resonance with the applied quadrupole excitation field moves faster towards the detector than an ion which was off the resonance. By measuring the time of flight as a function of the applied excitation frequency, the cyclotron frequency of the ions under investigation was determined. The mass of an ion can be determined using the equation:

$$\nu_c = \frac{q}{2\pi m} B ,$$

where ν_c is the cyclotron frequency of the ion, m is the mass and q is the charge state of the ion. The magnetic field B is calibrated with a well-known reference mass.

3. Results

Below we would like to illustrate some example spectra. Full information for different nuclides in the region is given in Refs. [2, 3].

A part of the low energy γ-spectrum at mass number $A = 81$ is shown in Fig. 4. The most intense peaks can be seen in this clean spectrum which has no contaminants from neighboring masses.

An internal conversion electron spectrum is shown in Fig. 5. *K*- and *L*-electron lines have been identified for known transitions and the 63.1 keV *K*-electron peak of the 79.2 keV transition in ^{81}Sr has been used for the internal calibration. Conversion electrons from 43.0 keV and 221.0 keV transitions in ^{81}Sr have been observed for the first time. The internal conversion coefficient for the 43.0 keV transition has been determined as $\alpha_K = 1.5 \pm 0.3$ which supports an M1+ E2 multipolarity for the transition.

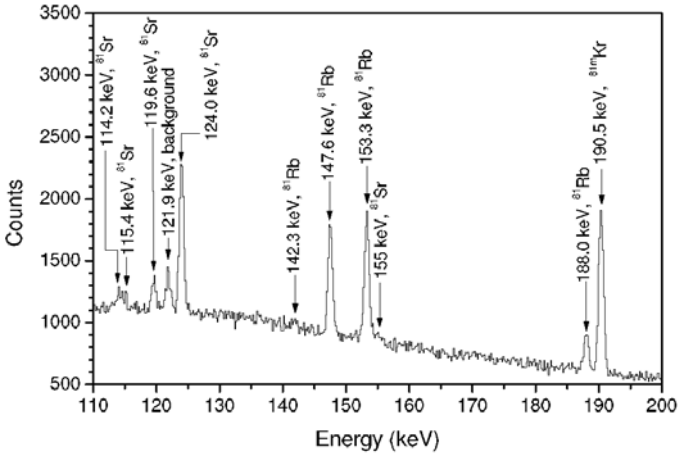

Fig. 4. A low energy part of a γ-spectrum for $A = 81$ measured by the LeGe-spectrometer. The peaks are labeled according to the transitions in daughter nuclei

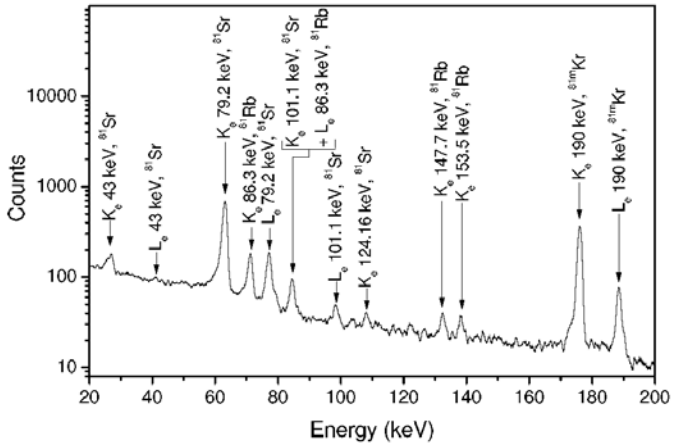

Fig. 5. Internal conversion spectrum measured by the ELLI-spectrometer for the mass number $A = 81$

Strong lines belonging to a 190.5 keV isomeric transition in ^{81}Kr can be observed in γ- and electron spectra (see Figs. 4-5). The previously known experimental values of the ratio α_K/α_{L+M} have been controversial before this experiment, as can be seen in Fig. 6. Hereafter, we have used the latest internal conversion coefficient tables for the multipolarity determination. Our values are $\alpha_K = 0.50 \pm 0.07$ and $\alpha_K/\alpha_{L+M} = 4.7 \pm 0.1$, favor an E3-character for this transition.

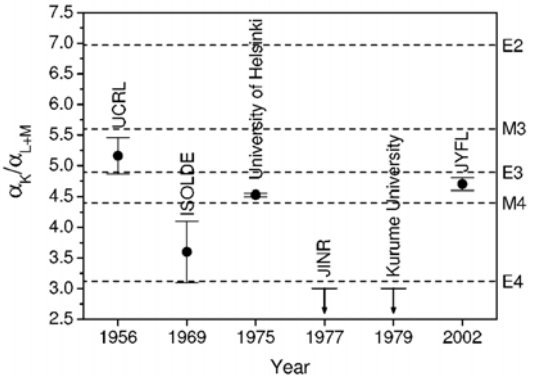

Fig. 6. The values of α_K/α_{L+M} for the 190.5 keV isomeric transition in ^{81}Kr from literature and the one measured in this work. The dashed lines show the theoretical values

Another application of our data in astrophysics concerns the proposed ^{81}Br neutrino detector for which the decay properties of ^{81m}Kr are crucial [2, 3]. The electron capture branching ratio η_ε of the isomeric state ^{81m}Kr, which is inverse to the neutrino capture process (see Fig. 2), can be deduced from the relation:

$$\eta_\varepsilon = \frac{\lambda_\varepsilon}{\lambda_e + \lambda_\gamma + \lambda_\varepsilon} = \frac{\lambda_{\varepsilon K}\left(1 + \frac{\lambda_{(\varepsilon K+\varepsilon M)}}{\lambda_{\varepsilon K}}\right)}{\lambda_{eK}\left(1 + \frac{\lambda_{(eK+eM)}}{\lambda_{eK}}\right)\left(1 + \frac{\lambda_\gamma}{\lambda_e}\right) + \lambda_{\varepsilon K}\left(1 + \frac{\lambda_{(\varepsilon K+\varepsilon M)}}{\lambda_{\varepsilon K}}\right)},$$

where λ_e, λ_γ and λ_ε stand for the internal conversion, gamma transition and electron capture probabilities, respectively. Indices K, L and M label the corresponding atomic shells.

If $\eta_\varepsilon \ll 1$, as it is expected for the decay of ^{81m}Kr, we can deduce the following expression:

$$\eta_\varepsilon = \left(1 + \frac{\lambda_{(\varepsilon K+\varepsilon M)}}{\lambda_{\varepsilon K}}\right) \times \frac{K_X(Br)\varpi_K(Kr)}{K_X(Kr)\varpi_K(Br)} \times \frac{\alpha_K}{1+\alpha_{tot}},$$

where K_X is the intensity of characteristic X-rays corresponding to the K-shell, ω_K stands for the respective K-fluorescence yield and α represents the internal conversion coefficient. As a summary, the electron capture branching ratio depends on the following factors:

– the ratio of electron capture branches $\lambda_{(\varepsilon L+\varepsilon M)}/\lambda_{\varepsilon K}$;
– the intensity ratio of Br K X-rays to Kr K X-rays;
– the ratio $\alpha_K/(1 + \alpha_{tot})$.

We have now calculated the first factor with the literature values and with overlapping and exchange effects taken into account; these calculations have led to $\lambda_{(\varepsilon L+\varepsilon M)}/\lambda_{\varepsilon K} = 0.144$. Groups at Princeton and Argonne have considered the second factor and measured the ratio for *K X*-rays. However, in order to determine the electron capture branching ratio η_ε they used theoretical values for the estimation of the first factor $(\lambda_{(\varepsilon L+\varepsilon M)}/\lambda_{\varepsilon K} = 0.119)$ and for the internal conversion coefficients ($\alpha_K = 0.4$ and $\alpha_{tot} = 0.48$). In the present work we have measured the internal conversion coefficients needed for the third factor, $\alpha_K/(1 + \alpha_{tot})$.

Experimental values for the internal conversion coefficients and for the intensity ratio of *K X*-rays together with a revised value for the ratio of electron capture branches were used to compute the neutrino capture rate of the $3/2^- \rightarrow 1/2^-$ transition in the ^{81}Br detector. The corresponding log *ft* value calculated with the tabulated *f*-values is given in Table 1 in comparison with the averaged literature value. Our value is slightly lower than the earlier value leading to an increased neutrino capture cross section. This supports the conclusion that ^{81}Br can be successfully used as a solar neutrino flux detector.

Table 1

Neutrino capture probability for the ^{81}Br → ^{81m}Kr transition

Group	Argonne	Princeton	This work
η_ε ($\times 10^{-5}$)	3.14 ± 0.58	2.26 ± 0.32	–
Average η_ε ($\times 10^{-5}$)	2.47 ± 0.37		–3.0 ± 0.5
α_K	0.4	0.4	0.50 ± 0.07
α_{tot}	0.48	0.49	0.61 ± 0.09
log ***ft*** (*ν* capture)	5.19 ± 0.07		5.13 ± 0.09

An electron line with an energy of 50 keV observed at the mass number $A = 85$ cannot be attributed to any known transition in the isobaric mass chain $A = 85$. The coincidence of the 50 keV electrons with the Nb *K X*-rays manifests that this electron line belongs to an unknown transition with an energy of 69 keV in ^{85}Nb. The measured half-life of the transition is 3.3 ± 0.9 s.

The new 69 keV transition can originate either from the β^+-decay of ^{85}Mo or from a decay of a new isomeric state in ^{85}Nb. Further analysis showed that there is no coincidence of this peak with the annihilation radiation, which supports the latter option. In addition, the yield of this new transition is 0.8 transitions/s that disagrees strongly with the expected yield of ^{85}Mo and speaks in favor of the identification of ^{85m}Nb. We have also observed a *γ*-transition with an energy of 292 keV belonging to the known isomeric state, ^{85m}Zr.

No indication of the existence of an isomer in ^{86}Nb with a early declared half-life of 56 s has been observed at the mass number $A = 86$.

Examples of the measured time-of-flight resonances are shown for the odd-odd nucleus ^{80}Y (Fig. 7), for the even-even nucleus ^{84}Zr (Fig. 8) and for a reference nucleus ^{98}Mo (Fig. 9).

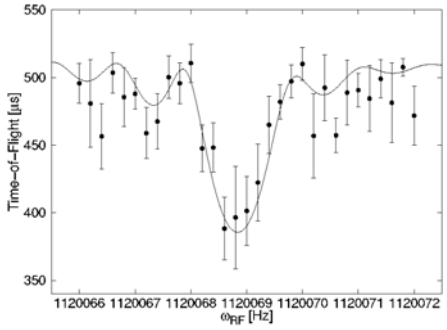

Fig. 7. Time-of-flight resonance of ^{80}Y with an excitation time of 900 ms. The fit on experimental data points is shown by a solid line

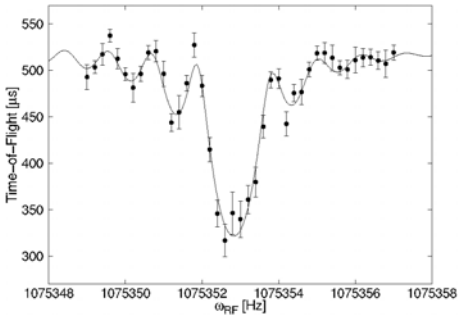

Fig. 8. Time-of-flight resonance of ^{84}Zr with an excitation time of 900 ms. The fit on experimental data points is shown by a solid line

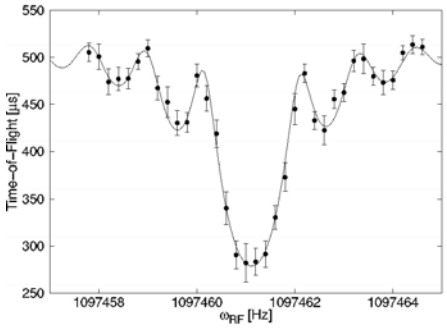

Fig. 9. Time-of-fight resonance of a reference nucleus ^{98}Mo with an excitation time of 900 ms. The fit on experimental data points is shown by a solid line

All measurements were done with 900 ms excitation time in the precision trap. The stable isotopes $^{96-98}$Mo were used as reference masses. Except for the stable Mo references, all nuclides were measured as oxides formed with ^{16}O in the IGISOL. Results for measured mass values are given in Table 2 (see Ref. [4]).

Table 2

Overview of the measured mass excesses (ME) compared to the tabulated values. All masses are for the ground states. The mass excesses are based on the frequency ratio of the reference nucleus to the measured nucleus (ν_{ref}/ν) given in the Table. The error for the difference AME-JYFL is dominated by the uncertainties in the AME-2003 mass excesses

Nuclide	ν_{ref}/ν	ME(JYFL) (keV)	ME(AME) (keV)	AME-JYFL (keV)
^{80}Y	1.00025645(7)	-61144(7)	-61220(180)	-80(180)
^{81}Y	1.00018938(6)	-65709(6)	-66020(60)	-310(60)
^{82}Y	1.00016793(6)	-68060(6)	-68190(100)	-130(100)
^{83}Y	1.01033685(6)	-72170(6)	-72330(40)	-160(40)
^{83}Zr	1.01040553(7)	-65908(7)	-66460(100)	-550(100
^{84}Zr	1.02055911(6)	-71418(6)	-71490(200)	-70(200)
^{85}Zr	1.03075388(7)	-73170(6)	-73150(100)	20(100)
^{86}Zr	1.04091538(7)	-77958(7)	-77800(30)	160(30)
^{88}Zr	1.06128125(7)	83624(7)	-83623(10)	1(12)
^{85}Nb	1.03082952(7)	--66273(7)	-67150(220)	-880(220)
^{86}Nb	1.04101219(6)	-69129(6)	-69830(90)	-700(90)
^{87}Nb	1.05117423(7)	--73868(7)	-74180(60)	-310(60)
^{88}Nb	1.06136322(7)	-76149(7)	-76070(100)	80(100)

The results of the Y isotopes are presented in Fig. 10 in comparison with the earlier results and the AME values (Nucl. Phys. A **729**, 3 (2003)). Most of the masses known so far are based on measurements of end-point energies of β^+-spectra. The corresponding mass excesses have been calculated from the Q_{EC} values with the tabulated mass excesses of the daughter nuclides (^{80,81,82,83}Sr). Our measured mass excesses agree with the AME value only for the isotope ^{80}Y for which a direct time-of-flight measurement has been performed.

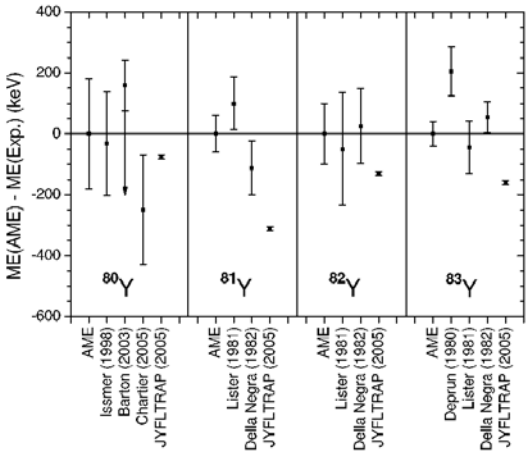

Fig. 10. Mass excesses of the measured Y isotopes relative to AME values. The error bars represent only the uncertainties of the corresponding experiments

In this experiment, the mass of ^{84}Zr was measured for the first time. It agrees with the AME value based on systematics. The measured masses of ^{85}Zr and ^{88}Zr are also in agreement with the AME values (see Fig. 11). However, there are discrepancies in the mass excesses of ^{83}Zr and ^{86}Zr.

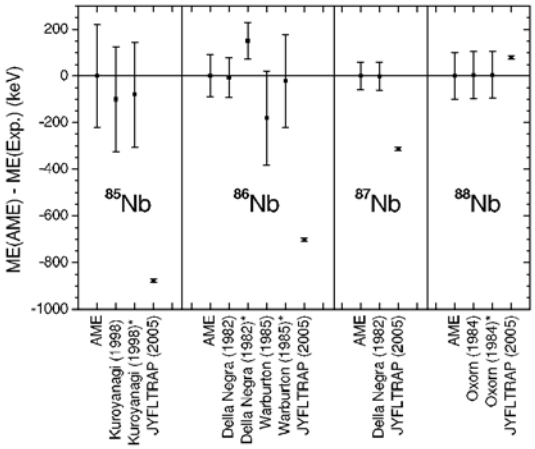

Fig. 11. Mass excesses of the measured Zr isotopes relative to AME values. The error bars represent only the uncertainties of the corresponding experiments

Fig. 12 shows the measured Nb isotopes together with the AME values and previous mass measurements. The large deviations from the AME mass excesses in ^{85}Nb and ^{86}Nb might be explained if the masses of isomeric states instead of ground states had been measured. However, also the mass excess of ^{87}Nb differs significantly from the AME value although the isomeric state should lie at 4 keV which is within the error bars. Only the mass of ^{88}Nb agrees with the AME value. The mass measurements of ^{85,86,88}Zr make it possible to determine Q_{EC} values for ^{85,86,88}Nb. With the mass of ^{84}Zr, a proton separation energy for ^{85}Nb can be experimentally determined for the first time. The measured Zr masses have been taken into account in the derivation of the Nb mass excesses from beta-decay experiments for these nuclides.

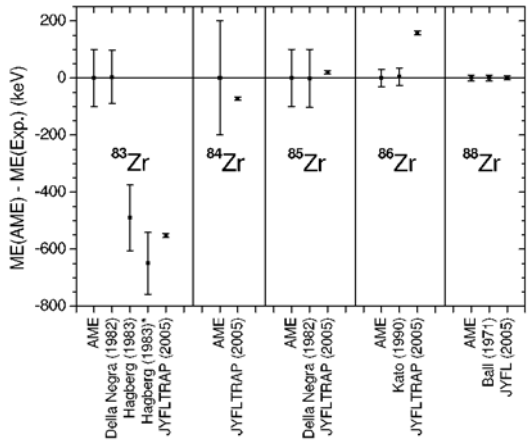

Fig. 12. Mass excesses of the measured Nb isotopes relative to AME values. The error bars represent only the uncertainties of the corresponding experiments. The values of ^{85,85,88}Nb marked with an asterisk have been calculated with the mass excesses of the corresponding daughter nuclei ^{85,86,88}Zr measured in this experiment at the JYFLTRAP. The other mass excesses have been calculated with AME values for daughter nuclides

Almost all of the studied nuclides lie on the path of the *rp*-process and are involved in the proton captures (see Fig. 1). The masses of these nuclides have been measured with uncertainties of less than 10 keV required for detailed *rp*-process calculations. Large deviations (several hundreds of keV) to the adopted AME values have been found except for ^{80}Y, ^{84,85,88}Zr and ^{88}Nb which all agree with the AME values. Many of the AME mass excesses based on beta-decay experiments differ significantly from the directly measured values for these neutron-deficient nuclides. A similar tendency has also been observed for neutron-rich nuclides in direct mass measurements at ESR and at JYFLTRAP. With the measured absolute masses, the accuracies of proton separation energies and Q_{EC} values for 12 neutron-deficient nuclides have been improved substantially (see Tables 3, 4). The Q_{EC} value for ^{84}Zr and proton separation energies for ^{84}Zr and ^{85}Nb have been determined experimentally for the first time.

Table 3

Proton separation energies for the measured nuclides. The mass of the (Z–1,N) nucleus is from this experiment for ^{83}Zr, ^{84}Zr, ^{85}Nb, ^{86}Nb and ^{87}Nb (marked with *). For the others, the AME mass of the (Z–1,N) nucleus is used. Proton separation energies for ^{84}Zr and ^{85}Nb have been experimentally determined for the first time. The last column lists the difference between the determined S_p value and the corresponding AME value

Nuclide	S_p(keV) this work	S_p(keV) AME	Difference (keV)
^{80}Y	2956(11)	3030(180)	-70(180)
^{81}Y	2690(9)	3000(60)	-310(60)
^{82}Y	3821(9)	3950(100)	-130(100)
^{83}Y	3451(9)	3610(40)	-160(40)
^{83}Zr	5137(9)*	5560(140)	-420(140)
^{84}Zr	6536(9)*	6460(200)#	80(200)
^{85}Zr	6300(90)	6280(140)	20(170)
^{86}Zr	7410(20)	7250(40)	160(50)
^{88}Zr	7895(7)	7893(10)	2(12)
^{85}Nb	2144(9)*	2950(300)#	-810(300)
^{86}Nb	3248(9)*	3970(130)	-720(130)
^{87}Nb	3199(9)*	3670(70)	-470(70)
^{88}Nb	4090(11)	4010(100)	80(100)

Table 4

Q_{EC} values for the measured nuclides. The mass of the daughter nucleus from this experiment for ^{83}Zr, ^{85}Nb, ^{86}Nb and ^{88}Nb is marked with *. The last column lists the difference between the determined Q_{EC} value and the adopted AME value

Nuclide	$\boldsymbol{Q_{EC}}$ (keV) this work	$\boldsymbol{Q_{EC}}$ (keV) AME	Difference (keV)
^{80}Y	9164(10)	9090(180)	70(180)
^{81}Y	5819(9)	5510(60)	310(60)
^{82}Y	7948(9)	7820(100)	130(100)
^{83}Y	4625(12)	4470(40)	160(50)
^{83}Zr	6263(9)*	5870(90)	390(90)
^{84}Zr	2740(90)	2670(220)#	70(240)
^{85}Zr	4670(20)	4690(100)	-20(110)
^{86}Zr	1326(16)	1480(30)	-150(40)
^{88}Zr	675(7)	676(10)	-1(12)
^{85}Nb	6898(9)*	6000(200)	900(200)
^{86}Nb	8829(9)*	7980(80)	850(80)
^{87}Nb	5480(11)	5170(60)	310(60)
^{88}Nb	7476(9)*	7550(100)	-70(100)

References

1. J. Huikari *et al*. (IGISOL/JYFLTRAP collaboration), Nucl. Instr. Meth. B **222**, 632 (2004).
2. V.G. Vorobjev *et al.* (IGISOL/JYFLTRAP collaboration), Preprint PNPI-2533, Gatchina, 2003. 27 p.
3. A. Kankainen *et al*. (IGISOL/JYFLTRAP collaboration), Eur. Phys. J. A **25**, 355 (2005).
4. A. Kankainen *et al*. (IGISOL/JYFLTRAP collaboration), Eur. Phys. J. A **29**, 271 (2006).

EXPERIMENTAL ESTIMATION OF THE ^{8}Be YIELD IN THE FRAGMENTATION OF ^{10}B NUCLEI IN PHOTOEMULSION

F.G. Lepekhin

In the identification of ^{8}Be nuclei, the accuracy in estimating the angle θ_{12} between the tracks of particles is important. This accuracy depends not only on the quality of the treatment of the emulsion-chamber layers but also on the energy of particles between which the angles are measured. At the early stage of the development of the photoemulsion method, the tracks of particles were assumed to be rectilinear. However, it was soon experimentally established that, in fact, the particles were subject to multiple Coulomb scattering, false scattering, and distortions. The last two phenomena represent specific distortions of the tracks in an emulsion. Their nature is essentially unknown, but they lead to the fact that trajectories of even high-energy particles are complex curves.

In experiment described in Ref. [1], an emulsion chamber composed of layers of the emulsion BR-2, that were 10×20 cm^2 in area and 500 μm thick, was irradiated along the layer in ^{10}B-ion beam with energy of 10 GeV in the Nuclotron at the Laboratory of High Energies (JINR). We then searched for the events by scanning along a track. The total length of all the portions of the scanned primary tracks before detecting an inelastic interaction with the photoemulsion nuclei or their escape from the layer was equal to 243 m. We found 1823 inelastic interactions at this length. Thus, the mean free path before the interaction is equal to 13.3 ± 0.3 cm. In 217 events containing two doubly charged fragments of ^{10}B nucleus, the x, y, and z coordinates were measured at 11 points with 100 μm intervals along the X axis on both tracks of the doubly charged fragments and the primary-particle track.

If the average values of the coordinates x, y, and z are equal to $< x >$ and $< a >$, where $a = y, z$, the estimate of the tangent of the angle $\varepsilon = \varphi, \alpha$ for $a = y, z$ is equal to

$$\mathtt{tan}\ \varepsilon = \frac{< xa > \ - \ < x >< a >}{< x^2 > \ - \ < x >^2}. \tag{1}$$

By calculating the angles φ and α for the given track, we obtain an estimate of the angle θ:

$$\mathtt{tan}\ \theta = \sqrt{\mathtt{tan}^2\varphi \ + \ \mathtt{tan}^2\alpha}. \tag{2}$$

In spite of the fact that the accuracy in measuring the coordinates along the axes Y and Z are different, the parameters of the distributions for the angles φ and α appeared to be virtually identical for these statistics. As it was expected, both distributions agree with the hypothesis that they are samples of a normal distribution with constant calculated using the ^{10}B-nucleus radius.

It was shown that the angle θ_{12} between the two α-particles produced in the ^{8}Be-fragment decay from a ^{10}B nucleus can be measured with an accuracy of about 1.5 mrad. The maximal value of θ_{12} for the decay $^8\mathrm{Be} \to 2\alpha$ at the energy of 1.0 GeV per nucleon was equal to 5.45 mrad, and its regular bias at the smallest angles was equal to 1.5 mrad. For this reason, it was suggested that the angles θ_{12} smaller than 8.5 mrad are found for the α-particle pairs produced in the ^{8}Be decay, while all the α-particle pairs with angles θ_{12} exceeding this value arise in the $^{10}\mathrm{B} \to 2\alpha$ process.

In Figure below we show the normal-distribution function, with the average equal to zero and the standard deviation equal to 21 mrad, calculated from the value of the constant for the ^{10}B-nucleus radius (the smooth curve) and the empirical distribution function for the angles φ and α.

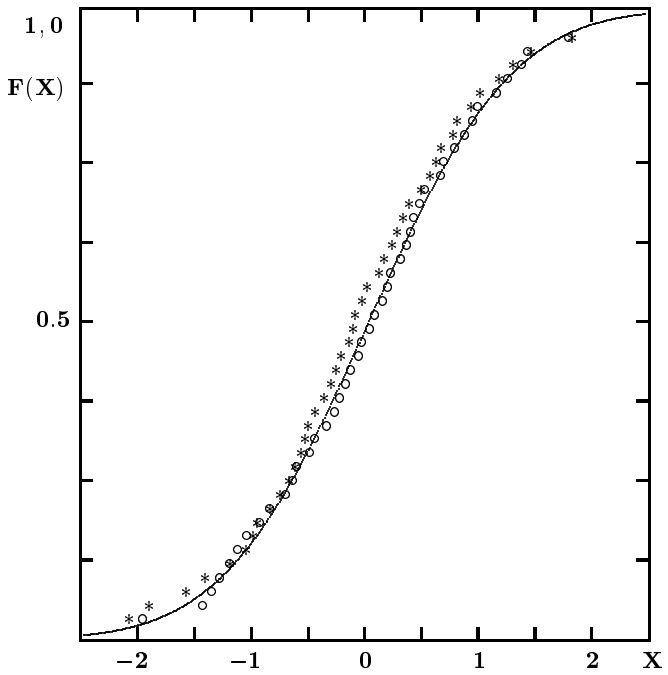

Fig. The smooth curve represents an expected standard normal distribution. The empirical distribution function for the angles φ shown by the asterisks. The empirical distribution function for the angles α is shown by the open circles

The sum of the squares of the differences along the vertical between the smooth curve and empirical distribution function gives the value of ω^2 (Kramers-Mises goodness-of-fit) between the empirical distribution function and the normal distribution. According to our data, this hypothesis is accepted for both φ and α angles at 1% CL.

The value $x = \varphi_1 + \varphi_2 + \alpha_1 + \alpha_2$ for this sample of events is normally distributed with the standard deviation $\sigma_x(\text{exp}) = 39.7 \pm 2.7$ mrad. Therefore, no angular correlations between the particles in the event are experimentally found. Then, it is quite natural that the distributions of the angles $\theta_{12} = x$ between the independent emissions the α-particle pairs should have the distribution function of the form:

$$F(x, \sigma) = 1 - \exp(\frac{-x^2}{2\sigma^2}). \tag{3}$$

When estimating the parameter σ of this distribution from experimental data, it is necessary to exclude the angles θ_{12} that are smaller then a certain value x_{min}. This exclusion is necessary because we are searching for angles θ_{12} arising due to the channels containing $^8\text{Be} \to 2\alpha$. It is also necessary to exclude the angles θ_{12} exceeding a certain value x_{max} because they can correspond to rare events of absolutely different nature, for example, to rescattering of particles in the final state.

Then, the likelihood function for the Rayleigh distribution (3), which is cut off on the left- and right-hand sides by the x_{min} and x_{max} has the form

$$L = \prod_{i=1}^{i=N} f(x_i, \sigma) F(x_{min}, \sigma)[1 - F(x_{max}, \sigma)]. \tag{4}$$

In order to estimate the parameter σ, it is necessary to solve a nonlinear equation that can be derived by setting the derivative of the logarithm of the written likelihood function equal to zero. The peak of L for the given sample is attained for $\sigma = 31.7 \pm 2.0$ mrad.

Table

Calculated and experimental values of different quantities characterizing the ^{10}B-nucleus fragmentation

N	Quantities	Calculated	Experimental
1	$\sigma(\varphi) = \sigma(\alpha)$, mrad	21.011	20.5 ± 0.7
2	$\sigma(Rel, \theta_{12})$, mrad	29.714	31.7 ± 2.0
3	$< \theta_{12} >$, mrad	37.22	34.6 ± 2.2
4	$\sigma(\varphi_1 + \varphi_2 + \alpha_1 + \alpha_2)$, mrad	42.0	39.7 ± 2.7
5	$W(^8\mathrm{Be} \to 2\alpha)$	0.197	0.18 ± 0.03
6	$< \theta_{12} >$ for $\theta_{12} < 8.5$ mrad	6.3	5.6 ± 1.0

Finally, in the experiment 33 events were observed with an angle $\theta_{12} < 8.5$ mrad (instead of the expected 36 events). This number indicates that the probability of observing ^{8}Be nuclei in the fragmentation of a ^{10}B nucleus in this experiment is equal to $(18 \pm 3)\%$ instead of expected 19.7% yielded by the calculation. The principal results of Ref. [1] are summarized in the next Table. All the predictions made before experiment in Ref. [2] have been confirmed.

References

1. F.G. Lepekhin and B.B. Simonov, Yad. Fiz. **68**, 2101 (2006).
2. F.G. Lepekhin, Particles & Nuclei Lett. **3[112]**, 25 (2002).

μSR-INVESTIGATIONS AT PNPI

S.G. Barsov, S.I. Vorobyev, V.P. Koptev, E.N. Komarov, S.A. Kotov, S.M. Mikirtychyants, G.V. Shcherbakov

1. Investigation of the magnetic properties of homogeneous copper-manganese alloys

In this work, the magnetic properties of homogeneous copper-manganese alloys $Cu_{1-x}Mn_x$ were studied [1] by the muon spin relaxation (μSR) technique at the PNPI synchrocyclotron. Samples were homogenized by quenching in water after their heat treatment in a muffle furnace at a temperature of 1100 K for 100 h.

In our experiments, we measured the time distributions of positrons $N_e(t)$ that were formed as a result of the decay $\mu^+ \to e^+ + \nu_e + \tilde{\nu}_\mu$ (the muon lifetime is $\tau_\mu \approx 2.197 \times 10^{-6}$ s) and emitted in the direction of the initial muon polarization (polarized muon beams were used) in a time window $\Delta t \sim 4.5\tau_\mu$ after each muon was stopped in the sample, as well as the integrated yields of these positrons [2]. The time distributions were approximated by the function

$$N_e(t) = N_0 \cdot [1 + a_0 \cdot G(t)] \cdot \exp(-t/\tau_\mu), \quad (1)$$

where the normalization constant N_0 and the maximum asymmetry a_0 characterize the experimental conditions specific for each sample and do not depend on the muon depolarization. The muon spin relaxation function $G(t)$ determined from the time distribution $N_e(t)$ reflects the effect of local magnetic fields on the muon spin at the site of its stopping. In particular, we have $G(t) = 1$ in the absence of depolarization and $G(t) = 0$ for unpolarized muons.

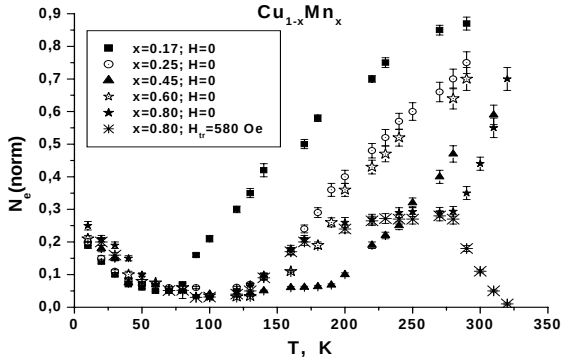

Fig. 1. Temperature dependences of the normalized integrated yield N_e(norm) of positrons for samples with different concentrations of magnetic atoms Mn_x

Figure 1 presents the normalized integrated yields of positrons for samples with different concentrations of magnetic atoms $N_e(\text{norm}) = ((n_e/n_0) - 1)/a_0$. This integrated yield does not depend on the sample geometry, parameters of the muon spin relaxation setup, and muon beam polarization and provides general model-independent information on muon depolarization under local magnetic fields. The parameters n_0 and a_0 were determined at a temperature considerably higher than the temperature of the transition to the magnetically ordered phase.

Specifically, the normalized integrated yield N_e(norm) measured for the $Cu_{0.2}Mn_{0.8}$ sample at temperatures $T > 330$ K in zero magnetic field tends to unity. This circumstance suggests the absence of muon depolarization in the far paramagnetic range in which the frequency of oscillations of electronic moments is too high ($\sim 10^{12}$ Hz) for their magnetic field to change substantially the muon polarization. The paramagnetic state is also indicated by the complete depolarization of muons in a relatively weak transverse external magnetic field of ~580 Oe. In the temperature range 290−320 K, the normalized integrated yield N_e(norm) changes drastically and then reaches a value of ~1/3. This suggests that the sample transforms into a magnetically ordered state with an isotropic (on a local, cluster or domain level) orientation of static internal local magnetic field. This behavior is in good agreement with the phase diagram previously proposed by A. Banerjee and A.K. Majumdar [Phys. Rev. B **46**, 8958 (1992)], according to which the antiferromagnetic transition at $T_N \sim 300$ K occurs in a homogeneous alloy with the concentration $x = 0.8$. The normalized integrated yield N_e(norm) equal to 1/3 is retained to $T \approx 200$ K. With a further decrease in the temperature, the normalized integrated yield N_e(norm) decreases sharply almost to zero. This indicates that in the given temperature range a strong dynamic depolarization of muons arises. The temperature dependence of the normalized integrated yield N_e(norm) in the range 20–200 K is characteristic of frustrated magnets which undergo transition to a low-temperature spin-glass state through an intermediate magnetically ordered phase with a long-range order. In this case, the dynamic polarization is associated with the transformation of the magnetic structure in the transition range [3].

The temperature dependence of the normalized integrated yield N_e(norm) for the samples with the concentration x = 0.17, 0.25, and 0.45 are also plotted in Fig. 1. The normalized integrated yield N_e(norm) for these samples decreases drastically with a decrease in the temperature due to the strong depolarization of muons. Since the normalized integrated yield N_e(norm) decreases almost to zero, the inference can be made that the arising local magnetic fields have a fluctuation character and are rather high. Moreover, the normalized integrated yield N_e(norm) for the sample with the concentration of manganese atoms x = 0.45 initially decreases to a small value and then remains virtually unchanged over a wide temperature range (from 60 to 200 K). This suggests to some extent that, in the given temperature range, the sample is in a specific phase state characterized by a fast spin dynamics. As the temperature decreases (T < 60 K), the normalized integrated yield N_e(norm) increases gradually to the value of ~1/3 which corresponds to the transition of the sample to the isotopic magnetic phase with a slow spin dynamics.

It should be noted that the dependence of the normalized integrated yield N_e(norm) on the concentration x of magnetic manganese atoms exhibits one more feature. The rate of change in the normalized integrated yield N_e(norm) with a variation in the temperature in the high-temperature transition range is identical for all samples with concentrations x = 0.17–0.60. This indicates once again that the same physical processes occur in the alloys and that the characteristics obtained are not associated with the specific quality of the samples. The transition temperature increases with an increase in the concentration of magnetic atoms to x = 0.45. A further increase in the concentration of magnetic atoms is accompanied by a decrease in the transition temperature. For example, the transition temperature for the sample with the concentration x = 0.60 is approximately equal to that for the sample with the concentration x = 0.25. A similar dependence of the transition temperature on the concentration x was observed by Banerjee and Majumdar. This effect was explained by the corresponding change in the size of antiferromagnetic clusters.

The analysis of the time spectra $N_e(t)$ demonstrates that the experimental data cannot be described using simple relaxation functions. In the paramagnetic range, the experimental data are well described by the relaxation function

$$G(t) = \exp(-\lambda \cdot t). \quad (2)$$

However, as the temperature of the first magnetic transition is approached (this can be judged from the drastic increase in the relaxation rate λ), the description of the experimental data requires the use of the relaxation function in the form of the sum of two exponential functions; that is

$$G(t) = a_1 \cdot \exp(-\lambda_D \cdot t) + a_2 \cdot \exp(-\lambda \cdot t), \quad (3)$$

where $a_1 + a_2 = 1$, $G(t)$ is the dimensionless relaxation function varying from 0 to 1, and λ_D and λ are the dynamic relaxation rates for the corresponding exponential function. The experimental data are best described using constant parameters $a_1 = 1/3$ and $a_2 = 2/3$.

At temperatures below 100 K, the experimental data for the samples can be described by the following relaxation function:

$$G(t) = [1/3 + 2/3 \cdot (1 - \Delta \cdot t) \cdot \exp(-\Delta \cdot t)] \cdot \exp(-\lambda_D \cdot t). \quad (4)$$

For $\lambda_D << \Delta$ this form of the relaxation function G is consistent with the spin-glass model. In this case, the parameter λ_D corresponds to the relaxation associated with the occurrence of fluctuating random fields. The parameter Δ is connected to the static fields.

A more complex expression for the relaxation function was proposed by Uemura *et al*. [Phys. Rev. B **31**, 546 (1985)]. However, when describing the time spectra $N_e(t)$ for samples with high manganese concentrations (x >0.2) the form of the relaxation function represented by expression (4) is more preferential.

The behavior of the relaxation functions for the $Cu_{0.55}Mn_{0.45}$ sample with a variation in the temperature is illustrated in Figs. 2, 3. It can be seen from these Figures that a virtually complete depolarization of the muon ensemble is observed in the temperature range 120–240 K. The relaxation function decreases only when the temperature of the sample decreases below a temperature of 100 K. At a temperature of 20 K, the relaxation function asymptotically approaches a value of ~1/3 which corresponds to the isotropic orientation of quasi-static local magnetic fields.

The temperature dependences of the parameters λ, λ_D, and Δ are shown in Fig. 4. There are two magnetic phase transitions. The first transition in the sample is observed at a temperature of ~200 K, and the second transition occurs at temperatures in the range 130–150 K.

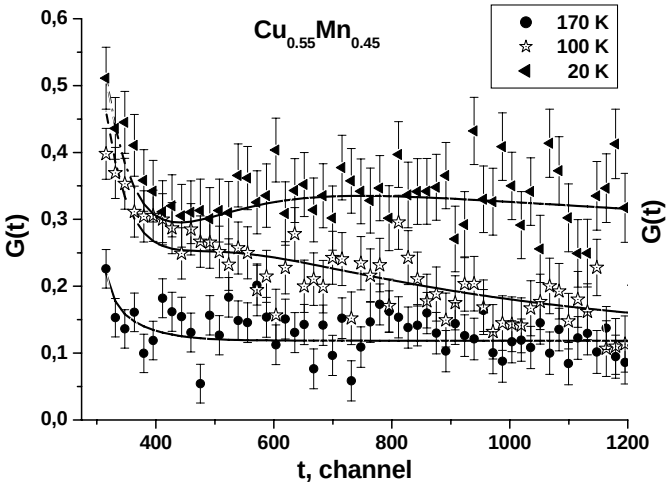

Fig. 2. Relaxation functions for the $Cu_{0.55}Mn_{0.45}$ sample at different temperatures in the range 170–300 K. One channel on the time scale corresponds to 0.625 ns. The origin of the scale is located at the 274th channel

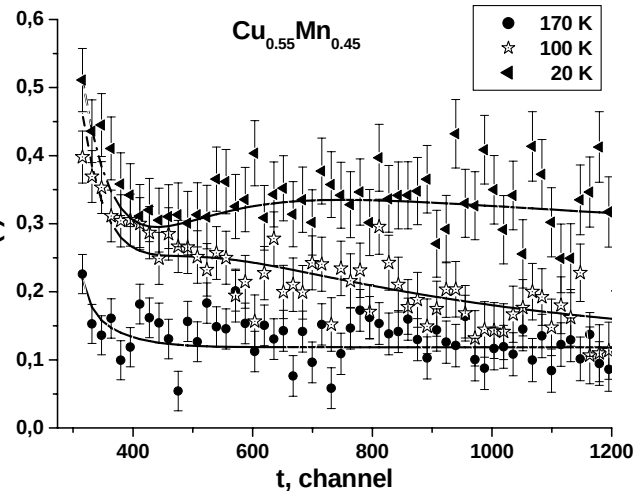

Fig. 3. Relaxation functions for the $Cu_{0.55}Mn_{0.45}$ sample at different temperatures in the range 20–170 K. One channel on the time scale corresponds to 0.625 ns. The origin of the scale is located at the 274th channel

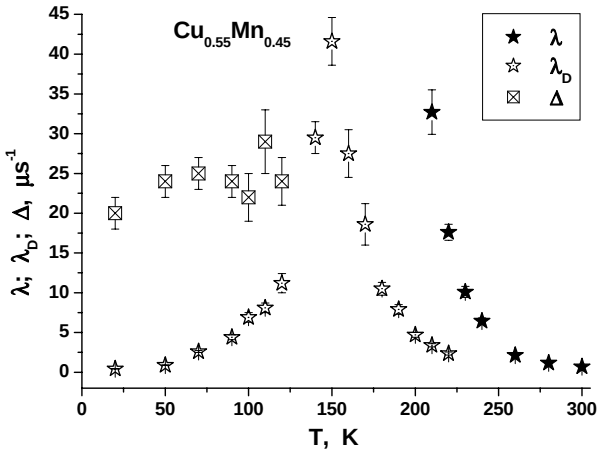

Fig. 4. Temperature dependences of the dynamic (λ, λ_D) and static (Δ) relaxation rates

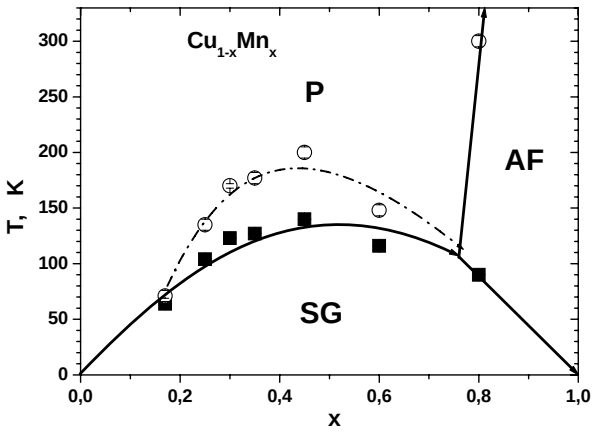

Fig. 5. Phase diagram of the homogeneous copper-manganese alloys $Cu_{1-x}Mn_x$

It should be noted that the static-field parameter Δ can be obtained by processing the experimental data only in the case where $\Delta > \lambda_D$. Note also that a decrease in the parameter λ_D leads to an increase in the reliability for determining the static-field parameter Δ.

Therefore, the results obtained demonstrate that in the homogeneous alloys $Cu_{1-x}Mn_x$ over a wide range of concentrations, there exists a phase transition to a specific magnetic state at temperatures in the range 100–200 K. This phase arises irrespective of the type of the high-temperature state, *i.e.* the paramagnetic or antiferromagnetic state. The new phase is characterized by a considerable non-uniformity of local fields due to the absence of a long-range magnetic order.

Thus, the data obtained make it possible to complement substantially the magnetic phase diagram of the homogeneous copper-manganese alloys $Cu_{1-x}Mn_x$ (Fig. 5). This phase diagram takes the form characteristic of systems with competing exchange interactions [3].

In the phase diagram depicted in Fig. 5 the solid line indicates the boundaries between the paramagnetic (P), antiferromagnetic (AF), and spin-glass (SG) states according to the data available in the literature. Points (○) and (■) correspond to the results obtained in the present work for the high- and low- temperature

transitions, respectively. The dot-dashed line represents the conventional boundary of the existence of the new phase state between the paramagnetic and spin-glass phases. As can be seen in Fig. 5, the concentration dependence $T(x)$ does not contradict the tendency of the change in the temperature T_G of the transition to the spin-glass state for concentrations $x < 0.15$. The largest temperature range between two transitions is observed at concentrations $x \sim 0.5$. The experimental results indicate that the new phase is characterized by a fast spin dynamics not only in the vicinity of the transition but also at lower temperatures down to the temperature of the transition to the spin-glass state. The analysis of the experimental data obtained allows us to assume that two magnetically ordered phases can be formed in the $Cu_{1-x}Mn_x$ binary alloys at relatively high concentrations of magnetic manganese atoms in the temperature range from 20 to 250 K. At temperatures below ~180 K there arises a state with a fast spin dynamics and fluctuating random fields. In this state, the parameters λ_D and Δ are of the same order of magnitude. The experimental data obtained can be described using complex relaxation functions $G(t)$ [expressions (3), (4)]. At a temperature of ~100 K the transition to the spin-glass phase without fluctuating random fields, *i.e.* the conventional spin-glass phase, is observed in the alloys for all the concentrations under investigation.

2. The study of the magnetic properties of the $(Pd_{1-x}Fe_x)_{0.95}Mn_{0.05}$ alloy

The measurements were performed both in a zero external magnetic field and in various transverse magnetic fields over the temperature range 10–300 K [4, 5]. The behavior of the relaxation parameter λ allows determination of the phase transition point, since a sharp increase in λ is observed near this point due to critical fluctuations. Figure 6 shows the temperature dependence of the dynamic relaxation rate $\lambda(T)$; we can see a pronounced peak in λ at $T_C = 39.5$ K which suggests that critical fluctuations develop near this temperature.

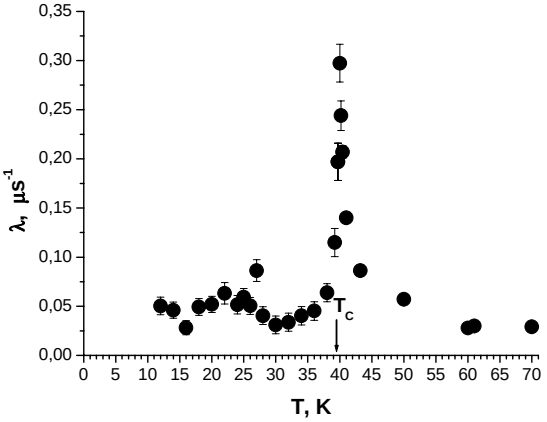

Fig. 6. Temperature dependence of the dynamic relaxation rates λ

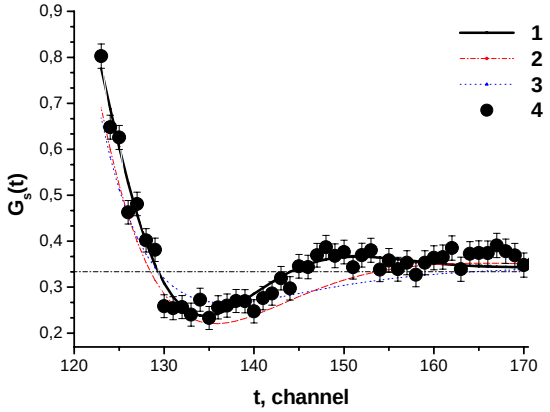

Fig. 7. Muon spin relaxation function: (1) processing within the CFM model with χ^2=1.02, (2) processing within the ASM model with χ^2=2.26, (3) processing within the SG model with χ^2=2.6, and (4) experimental points obtained at T = 28 K in a field H_{ext} = 0. One channel on the time axis corresponds to 5 ns

A further analysis of the experimental data showed that, below $T_C = 39.5$ K, the description of $G(t)$ will have the best value of χ^2 in the collinear-ferromagnet (CFM) model (Fig. 7)

$$G(t) = [1/3 + 2/3\ (\cos(\Omega \cdot t) \cdot \exp(-\Delta \cdot t))] \cdot \exp(-\lambda \cdot t). \quad (5)$$

The distribution function of local static fields is a Lorentzian with the average magnetic field H and the magnetic field variance Δ (Fig. 8); the temperature dependence at $T > 25$ K can be described by the relation $H \sim H_{max}(1 - T/T_C)^{\beta}$, where the value $\beta \approx 0.40 \pm 0.02$ corresponds to the model of the Heisenberg-type 3D magnet.

As the temperature decreases further (below 25 K), the χ^2-parametr changes and the confidence level decreases down to zero. The experimental data in Fig. 8 significantly deviate from the fitting curve and are poorly described by the model based on relation (5). None of the hypotheses proposed in Ref. [2] (CFM, asperomagnet (ASM), and spin glass (SG)) yields a more or less adequate description of the G function. The value $\chi^2 = 1$ at 97% confidence level

was achieved only in the case when the experimental data are processed using the sum of two functions, CFM+SG (Fig. 9),

$$G(t)=(a_{CFM}\cdot(1/3 + 2/3\cdot\cos(H_0\cdot t)\cdot\exp(-\Delta_{CFM}\cdot t))+a_{SG}\cdot(1/3 + 2/3\cdot(1-\Delta_{SG}\cdot t)\cdot\exp(-\Delta_{SG}\cdot t)))\cdot\exp(-\lambda\cdot t), \quad (6)$$

where $a_{CFM} + a_{SG} = a_S$ is the initial decay asymmetry.

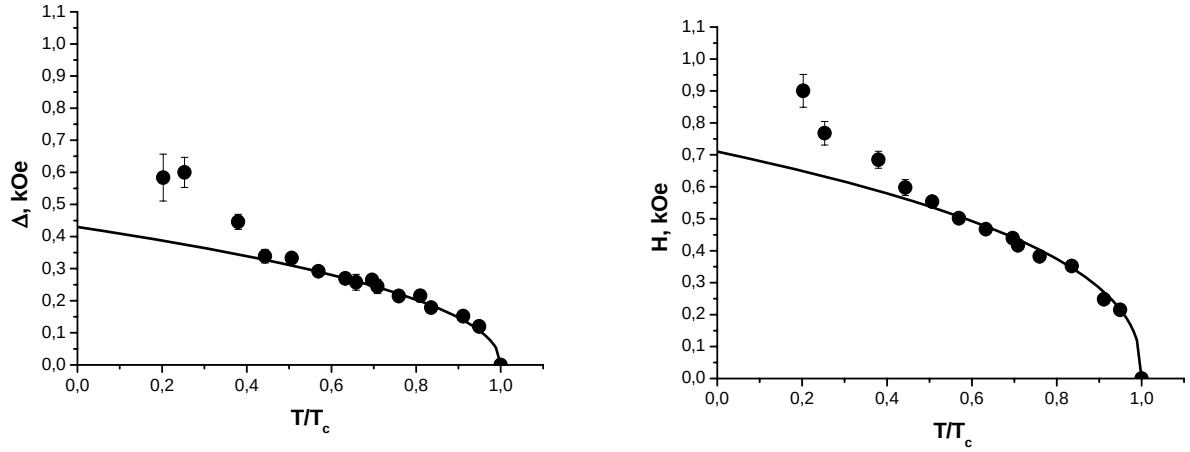

Fig. 8. Temperature dependence of the variance Δ of static fields and the average field H. The curves are fitting of the experimental data using the relation $H \sim H_{max}(1 - T/T_C)^{\beta}$, where $\beta \approx 0.40 \pm 0.02$ corresponds to the model of the Heisenberg-type 3D magnet

By writing the initial decay asymmetry in the form of a sum of two terms describing different states, we can separate both contributions. Thus, we can conclude that two phase states coexist simultaneously in the sample below 25 K; one of these states is ferromagnetic and the other is the spin-glass state. This conclusion is consistent with the model presented by relation (6). Figure 10 shows the temperature dependence of the ratio of the spin-glass fraction asymmetry to the maximum asymmetry. It can be seen that, as the temperature decreases, the spin-glass fraction increases long before the transition to the spin-glass state.

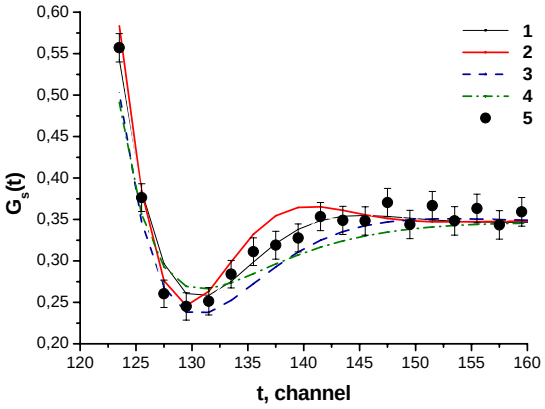

Fig. 9. Muon spin relaxation function: (1) the description by the sum of two functions CFM+SG with χ^2=1.0, (2) processing within the CFM model with χ^2=1.23, (3) processing within the ASM model with χ^2=1.58, (4) processing within the SG model with χ^2=1.85, and (5) experimental points obtained at T=15 K in a zero external field. One channel on the time axis t corresponds to 5 ns

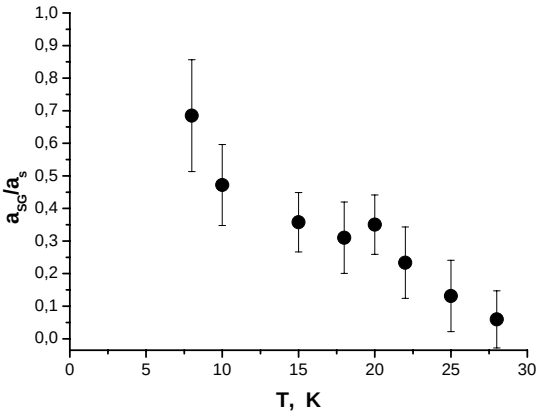

Fig. 10. Temperature dependence of the fraction of the spin-glass contribution to the depolarization of a muon ensemble

An analysis of the distributions of local magnetic fields shows that various magnetic states occur in the $(Pd_{0984}Fe_{0016})_{095}Mn_{005}$ alloy as temperature is varied (Fig. 8). For example, in the temperature range $25 < T < 39$ K this alloy is in the CFM state with a Lorentzian distribution of local magnetic fields. In the temperature range $10 < T < 25$ K, the magnetic structure of the alloy can be considered as a superposition of a collinear ferromagnet

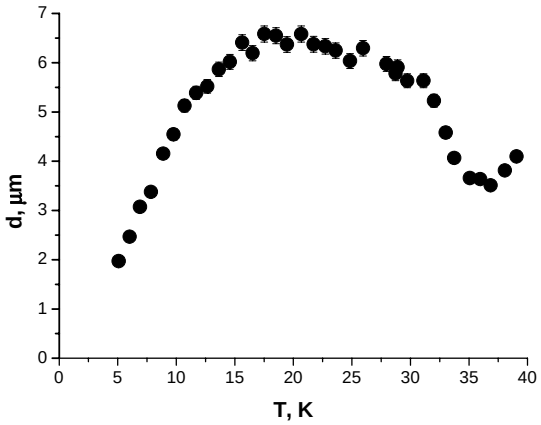

Fig. 11. Temperature dependence of the average size of magnetic inhomogeneities under cooling in a zero field

and a spin glass with a Lorentzian distribution of local magnetic fields. Below T = 10 K, the alloy probably undergoes a transition to the SG phase.

We also calculated the size d of magnetic inhomogeneities. To estimate it, we used the data on neutron depolarization ΔP obtained upon sample cooling under the ZFC conditions. We note that the temperature dependence of the depolarization ΔP under these conditions is characteristic of samples without magnetic anisotropy (the so-called 3/2 rule is valid). The quantity d (the average size of a domain or a cluster) is calculated with allowance for the sample magnetic isotropy and assuming that the average magnetization M_{inh} of inhomogeneities is equal to the average field H (Fig. 8). The results of this calculation are shown in Fig. 11.

3. Muon investigation of $HoMnO_3$ and $YMnO_3$ hexagonal manganites

Manganites $RMnO_3$ exhibit a wide variety of physical properties, depending on the rare-earth element R. Compounds with a large ion radius of the element R (La, Pr, Nd, Sm, Eu, Gd, and Tb) are crystallized in the orthorhombic structure with the space group *Pnma*. Compounds with a smaller ion radius of the element R (Ho, Er, Tm, Yb, Lu, Y, Sc, and In) exhibit the hexagonal crystal structure with the space group $P6_3cm$. The hexagonal manganites belong to ferroelectromagnetic materials in which the transition temperature to the ferroelectric state, $T_C \sim 600-1000$ K, is much higher than the temperature of antiferromagnetic ordering, $T_N \sim 70-130$ K.

This work is devoted to the investigation of local magnetic fields and their distribution in multiferroics $HoMnO_3$ and $YMnO_3$ by the μSR-method of substance investigation [6]. The samples were obtained by the solid-phase synthesis method. The measurements were performed on the muon channel of the PNPI synchrocyclotron using a μSR setup [7].

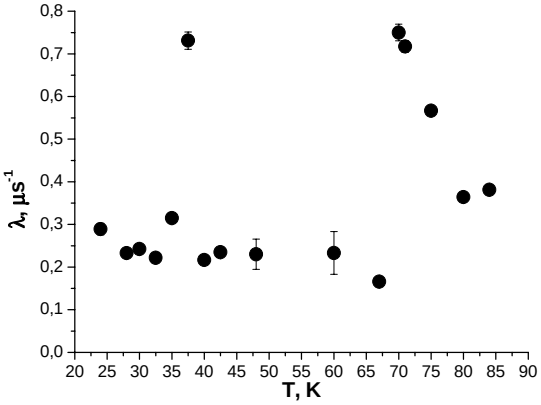

Fig. 12. Relaxation rate of the polarization of muons stopped in the $HoMnO_3$ sample in zero magnetic field

Figure 12 shows the temperature dependence of the relaxation rate λ, of the polarization of muons stopped in the $HoMnO_3$ sample in zero magnetic field. This dependence exhibits two peaks at 76 K and 40 K, which correspond to two phase transitions. The first transition at T = 76 K is a transition from the paramagnetic state to the antiferromagnetic ordering state. The second transition at T = 40 K is associated with the rotation of the spins of Mn by 90° (spin-relaxation transition). This conclusion is in good agreement with results obtained by other methods [B. Lorenz *et al*., Phys. Rev. Lett. **92**, 087204 (2004)].

Detailed analysis of the muon polarization relaxation function G makes it possible to determine the parameters of the distribution of local magnetic fields at various temperatures of the samples under investigation. In particular, the relaxation function of the polarization of muons stopped in the $HoMnO_3$ sample, $G(t)$, in zero magnetic field is described by the expression

$$G(t) = [a_1 \cdot (1/3 + 2/3 \cdot \cos(\Omega_1 \cdot t) \cdot \exp(-\Delta_1 \cdot t)) + a_2 \cdot (1/3 + 2/3 \cdot \cos(\Omega_2 \cdot t) \cdot \exp(-\Delta_2 \cdot t))] \cdot \exp(-\lambda \cdot t), \quad (7)$$

where $a_1 + a_2 = a_S$ is the initial asymmetry of the decay of muons stopped in the sample, λ is the dynamical relaxation rate, $\Omega_{1,2} = 2\pi \cdot F_{1,2}$ are the cyclic frequencies (associated with the mean local field at the muon localization site), and $\Delta_{1,2}$ are the frequency spreads associated with the spread of internal magnetic fields.

Figure 13 shows the temperature dependence of the frequencies of the muon spin precession for the $HoMnO_3$ sample in zero external magnetic field. It is seen that precession at two frequencies, one of which is negligibly low as compared to the other frequency ($F_1 \approx 40$ MHz and $F_2 < 1$ MHz), is observed for sample

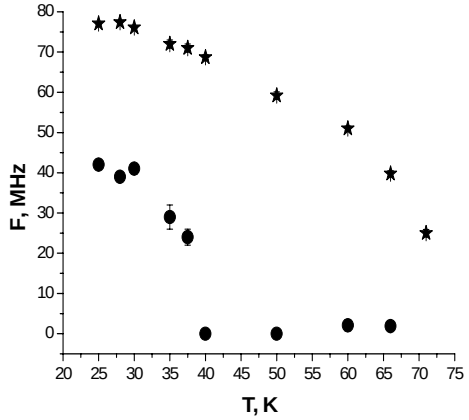

Fig. 13. Temperature dependence of frequencies (stars) F_1 and (circles) F_2 of the precession observed for the $HoMnO_3$ sample in zero field

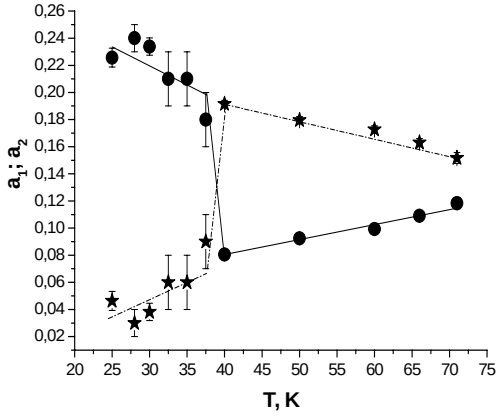

Fig. 14. Temperature dependence of the asymmetry coefficient (stars) a_1 and (circles) a_2, where $a_1 + a_2 = a_S$, for the $HoMnO_3$ sample in zero field. The lines are drawn to guide the eye

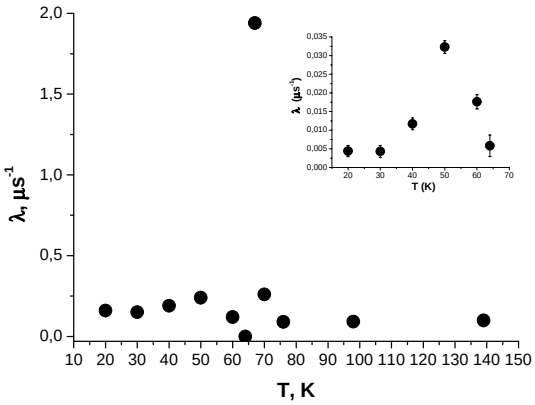

Fig. 15. Temperature dependence of the polarization relaxation rate for muons stopped in the $YMnO_3$ sample in zero field

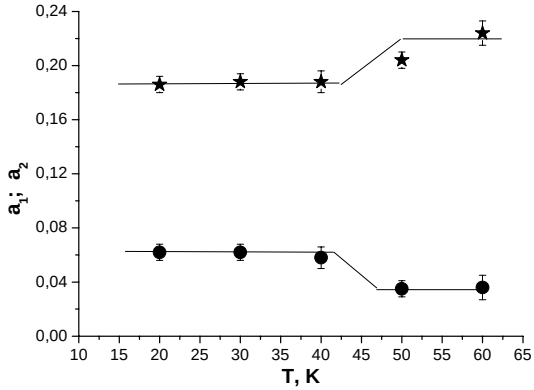

Fig. 16. Temperature dependence of the asymmetry coefficient (stars) a_1 and (circles) a_2, where $a_1 + a_2 = a_S$, for the $YMnO_3$ sample in zero field. The lines are drawn to guide the eye

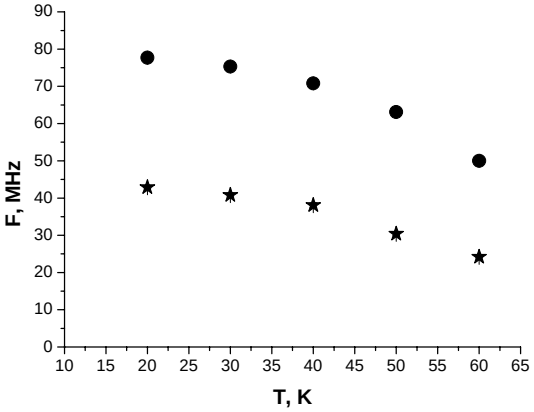

Fig. 17. Temperature dependence of the frequencies (stars) F_1 and (circles) F_2 of the precession observed for the $YMnO_3$ sample in zero field

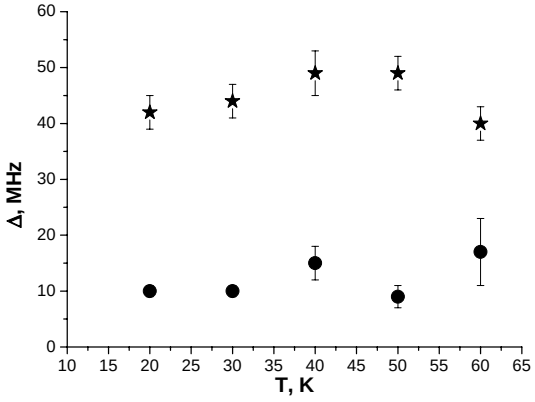

Fig. 18. Temperature dependence of the parameters (stars) Δ_1 and (circles) Δ_2 for the $YMnO_3$ sample

temperatures below $T = 76$ K. As the sample temperature is decreased, F_1 increases monotonically, whereas F_2 decreases. For sample temperatures below the temperature $T_{SR} = 42$ K, the frequency F_2 increases noticeably (almost from zero) and continues to increase monotonically with decreasing the temperature.

Figure 14 shows the temperature dependence of the coefficients a_1 and a_2 (see Eq. (7)). It is seen that the relation between the coefficients a_1 and a_2 changes sharply at the temperature of the spin-rotation transition, $T_{SR} = 42$ K.

Similar investigations were performed for the $YMnO_3$ sample. Figures 15−18 show the results of the processing of the experimental data obtained with the $YMnO_3$ samples. The temperature dependence of the polarization relaxation rate λ for muons stopped in the $YMnO_3$ sample exhibits a peak at a temperature of $T = 66$ K, which corresponds to the paramagnetic-antiferromagnetic phase transition (see Fig. 15). A non-monotonic temperature behavior of the parameter λ is seen in the temperature interval of 45−55 K (see the inset in Fig. 15). The precession at two frequencies F_1 and F_2 is seen in the temperature interval of 20−60 K; the relation between the frequencies, $F_2/F_1 \approx 2$, holds in the indicated temperature interval (Fig. 17).

Figure 18 shows the temperature dependence of the parameters Δ_1 and Δ_2 (frequency spread) in the temperature interval of 20−60 K. Similar results were obtained by T. Lancaster *et al*. [Phys. Rev. Lett. **98**, 197203 (2007)].

Note a feature in the behavior of the partial amplitudes a_1 and a_2 in the temperature interval of 20−60 K. A change in the ratio of these parameters, a_1/a_2, is observed at a temperature of $T \approx 50$ K (see Fig. 16). Thus, the temperature dependences of the relaxation rate of the muon spin (shown in Fig. 15) and partial amplitudes a_1 and a_2 (shown in Fig. 16) for the $YMnO_3$ sample exhibit features at a temperature of ~50 K. This is likely attributed to the partial rotation of the manganese spins in the $YMnO_3$ compound obtained by P.J. Brown and T. Chatterji [J. Phys.: Condens. Matter **18**, 10085 (2006)].

The temperature dependence of the precession frequency for the $HoMnO_3$ and $YMnO_3$ samples is well approximated by the Curie-Weiss curve, $F \sim F_{max}(1 - T/T_N)^{\beta}$ with the value $\beta = 0.39 \pm 0.02$ corresponding to the Heisenberg 3D magnet model.

4. Influence of magnetic nanoparticles on behavior of polarized positive muons in ferrofluid on the Fe_3O_4 base in carrier medium D_2O

The ferrofluid on the basis of the Fe_3O_4 nanoparticles dispersed in heavy water (D_2O) have been investigated by means of the μSR-method. It was revealed that the distinct muonium precession signal is observed simultaneously with the muon (diamagnetic) precession signal. The behaviour of the muon and muonium fractions in the ferrofluid is compared with those in the pure heavy water. The experiment was carried out at temperatures 50−300 K in transverse magnetic fields of 7.76 Oe and 278 Oe. It was observed that the muon (diamagnetic) fraction is created in the ferrofluid approximately in the same proportion as in D_2O, however the muon spin relaxation rate to a considerable extent is higher in the ferrofluid than in D_2O at temperatures $T > 150$ K. A part of the muonium fraction at these temperatures essentially less in the ferrofluid than in D_2O. The precession frequencies of the muon and muonium spins in a ferrofluid is noticeably lower than in D_2O.

References

1. S.G. Barsov, S.I. Vorobyev, V.P. Koptev *et al.*, Physics of Solid State **49**, 1740 (2007).
2. S.G. Barsov, A.L. Getalov, V.P. Koptev *et al.*, Preprint PNPI-1312, Gatchina, 1988. 17 p.
3. S.G. Barsov, A.L. Getalov, S.L. Ginsburg *et al.*, Hyperfine Interactions **64**, 415 (1990).
4. S.G. Barsov, S.I. Vorobyev, V.P. Koptev *et al*., Preprint PNPI-2688, Gatchina, 2006. 17 p.
5. S.G. Barsov, S.I. Vorobyev, V.P. Koptev *et al*., Physics of Solid State **49**, 1492 (2007).
6. S.G. Barsov, S.I. Vorobyev, V.P. Koptev *et al*., JETP Lett. **85**, 658 (2007).
7. S.G. Barsov, S.I. Vorobyev, V.P. Koptev *et al*., Preprint PNPI-2694, Gatchina, 2006. 17 p.

NEW PROJECTS

PNPI PARTICIPATION IN FAIR PROJECTS

1. Introduction

The realization of the new international project, Facility for Beams of Ions and Antiprotons (FAIR), has started at the GSI Laboratory in Darmstadt, Germany. The proposed schedule for building the facility extends over 8 years till 2015. The present estimate of the FAIR construction cost is more than 1 billion €.

The FAIR facility will provide an extensive range of particle beams from protons and antiprotons to ions of all chemical elements up to uranium with in many respects world record intensities. The new facility is built, and substantially expanded, on the present accelerator system at GSI, both in its research goals and its technical possibilities. It consists of a 100/300 T·m superconducting double-ring synchrotron SIS100/300 and a system of associated storage rings for beam collection, cooling, phase space optimization and experimentation (Fig. 1) and uses the present accelerators, a universal linear accelerator (UNILAC) and a synchrotron ring accelerator (SIS18) as injector.

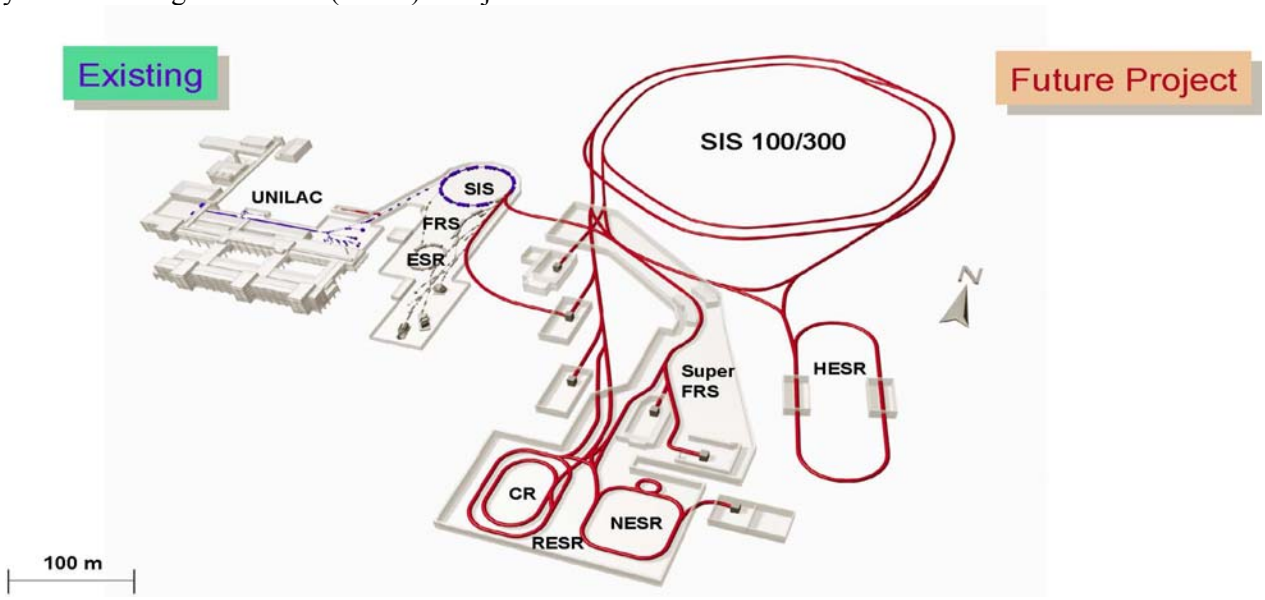

Fig. 1. The existing GSI facility with the linear accelerator UNILAC, the heavy-ion synchrotron SIS18, the fragment separator FRS and the experiment storage ring ESR, and the new project with the double-ring synchrotron SIS100/300, the high-energy storage ring HESR, the collector ring CR, the new experiment storage ring NESR, the super-conducting fragment separator Super-FRS

A key feature of the new facility will be the generation of intense, high-quality secondary beams including beams of short-lived (radioactive) nuclei and beams of antiprotons. Compared to the present GSI facility, a factor of 100 in primary beam intensities and up to a factor of 10000 in secondary radioactive beam intensities are technical goals. The new facility will have possibility to provide beam energies much higher than presently available at GSI for all ions, from protons to uranium.

The beams which can be provided by the proposed synchrotrons and cooler/storage rings are:

Primary Beams
- 10^{12} s^{-1}, 1.5–2 GeV/u, ions up to $^{238}U^{28+}$
- 2×10^{13} s^{-1}, 30 GeV, protons
- up to 90 GeV, protons
- 10^{10} s^{-1}, up to 35 GeV/u, $^{238}U^{73+}$

Secondary Beams
- broad range of radioactive beams, 1.5–2 GeV/u
- antiprotons, 3–30 GeV

Storage and Cooler Rings
- radioactive beams
- *e-A* collider
- 10^{11} s^{-1}, stored and cooled antiprotons, 0.8–14.5 GeV

FAIR will open up unique opportunities for a wide spectrum of research programs including QCD studies with cooled beams of antiprotons, nucleus-nucleus collisions at highest baryon density, nuclear structure and nuclear astrophysics investigations with nuclei far from stability, high density plasma physics, atomic and material science studies, radio-biological investigations and other interdisciplinary studies.

PNPI has a long term cooperation program with GSI. The nuclear spatial structure of the neutron-rich light nuclei by means of the proton elastic scattering in inverse kinematics using a proton recoil detector IKAR developed at PNPI has been investigated over last decade [1]. Worldwide known are the experiments dedicated to mass measurements of exotic nuclides, which were performed with participation of the PNPI group at the ESR of GSI. It is quite natural for PNPI to continue and enforce its research activity at the new GSI facility.

Among the accepted FAIR projects there are NUSTAR, CBM and PANDA where PNPI is taking part. The experiments at FAIR, with PNPI participation, are shortly presented in this report [2].

2. Research with rare-isotope beams – nuclei far from stability

Nuclear Structure and Astrophysics – NUSTAR project

The main studies of nuclei far from stability will be performed in three research areas:

The structure of nuclei towards the limits of stability.

In the past, a major limitation in experiments studying nuclear reactions was that in any reaction both beam and target species needed to be stable. This imposed severe constraints on both the type of information that could be gained, and the region of nuclear chart that could be accessed. An availability of beams of unstable nuclei allows one to interchange the roles of beam and target particles to perform reaction studies in inverse kinematics. In this way many nuclides away from stability become accessible for detailed nuclear structure investigations of these weakly bound nuclei.

The structure and dynamics of such loosely bound nuclei is very different from that of stable nuclei. Rather diffuse surface zones, so-called halos and skins, were observed in neutron-rich unstable isotopes. Among other features unique to such exotic nuclei, one expects to encounter novel types of shell structures, new collective modes, new isospin pairing phases, possibly new decay modes (double proton emission) or regions of nuclei with specific deformations and symmetries. Effects of nucleonic clustering should become prominent, giving rise to unusual nuclear geometries.

Nuclear astrophysics.

The stable, heavy atomic nuclides found in our solar system have been produced in at least three processes, as it was concluded from their abundances. One of them, the slow neutron capture process (*s*-process) creating nuclides at the valley of beta-stability, is believed to be generally understood. Most of the heavy atomic nuclides, however, originate from an explosive process of nucleosynthesis, the so-called rapid neutron capture (*r*-process). A major goal of FAIR is to provide unstable nuclei near and beyond the $N = 126$ closed neutron shell, and to measure their masses, which govern the *r*-process, and their β-decay half-lives, which determine the accumulated abundance pattern along this path. Thereby a long-standing puzzle can be for the first time experimentally addressed, namely in what way the heaviest elements like thorium, uranium and their precursors have been created.

Neutron-deficient nuclides close to the proton drip-line are produced in other explosive scenarios. In these processes, hydrogen is explosively burnt *via* a sequence of rapid proton captures (*rp*-process) and β^+-decays near the proton drip-line. Many of questions concerning the *rp*-process have not yet been answered. At the new GSI facility all relevant *rp*-nuclei will become accessible.

---

[1] See the report "Experimental study of nuclear spatial structure of neutron-rich He and Li isotopes", this issue, p. 176.

[2] The FAIR Conceptual Design Report, FAIR Technical Baseline Report and CBM, PANDA, R^3 ,MAILI ,EXL ,B MATS experiments LOI were widely used in the preparation of this report.

Fundamental interactions and symmetries.

Many high-energy physics experiments are aimed to search for possible extensions of the Standard Model. Besides these investigations in particle physics, low-energy precise experiments in nuclear and atomic physics also show a unique discovery potential for this field. The nuclear physics studies will focus on the weak interaction, in particular on precise experiments of the β-decay of specific exotic nuclei. Such studies comprise accurate tests of parity and time-reversal symmetry, sensitive tests of the conserved vector current (CVC) hypothesis and sensitive searches for other than vector-axial vector (V−A) contributions to the weak interaction, such as scalar or tensor or (V+A) terms that would be a hint at the existence of additional exchange bosons of the weak interaction.

The studies with exotic beams are realized in frame of the **NUSTAR** project that includes seven independent subprojects. Among these there are **R^{3}B**, **EXL**, **ILIMA** and **MATS** where PNPI is taking part.

2. 1. R^{3}B and EXL projects

PNPI participants: G.D. Alkhazov, A.V. Dobrovolsky, O.E. Fedorov, Yu.I. Gusev, A.G. Inglessi, A.V. Khanzadeev, O.A. Kisselev, G.A. Korolev, V.V. Sarantsev, D.M. Seliverstov, A.Yu. Zalite, Yu.K. Zalite

The **R^{3}B** (a universal setup for kinematical complete measurements of Reactions with Relativistic Radioactive Beams) will cover experimental reaction studies with exotic nuclei far from stability, with emphasis on nuclear structure and dynamics. Astrophysical aspects and technical applications are also considered. Reaction types and associated physics goals that can be achieved are given in Table. In case of light-ion scattering, the experiments at R^{3}B are complementary to ones proposed for the internal target in the NESR (EXL project). The R^{3}B program will focus on the most exotic short-lived nuclei which cannot be stored and cooled efficiently and on reactions with large-momentum transfer allowing the use of thick targets. The proposed experimental setup is adapted to the highest beam energies delivered by the Super-FRS, thus exploiting the highest possible transmission efficiency of secondary beams.

Table

Reaction type	Physics goals
Knockout	Shell structure, valence-nucleon wave function, many-particle decay channels, unbound states, nuclear resonances beyond the drip-lines
Quasi-free scattering	Single-particle spectral functions, shell-occupation probabilities, nucleon-nucleon correlations, cluster structures
Total absorption measurements	Nuclear matter radii, halo and skin structures
Elastic proton scattering	Nuclear matter densities, halo and skin structures
Heavy-ion induced electromagnetic excitation	Low-lying transition strength, single-particle structure, astrophysical *s*-factor, low-lying resonances in the continuum, giant dipole (quadrupole) strength
Charge exchange reactions	Gamow-Teller strength, soft excitation modes, spin-dipole resonance, neutron skin thickness
Projectile fragmentation and multifragmentation	Equation of state, thermal instabilities, structural phenomena in excited nuclei, γ-spectroscopy of exotic nuclei
Fission	Shell structure, dynamical properties
Spallation	Reaction mechanism, astrophysics, applications: nuclear-waste transmutation, neutron spallation sources

The proposed experimental scheme is based on that of the LAND apparatus which is used in experiments with secondary beams from the FRS facility at GSI. The most essential upgrades concern the target recoil detector and two magnetic spectrometers. A schematic view of the R^{3}B experiment setup is shown in Fig. 2.

The incoming secondary beams are tracked and identified on an event-by-event basis. Measurements of the magnetic rigidity $B\rho$ (position measurement at the dispersive focus in the Super-FRS), time of flight TOF, and energy losses ΔE provide the isotope identification and momentum determination. Although the secondary beam has a momentum spread of ±2.5%, the momentum will be determined to an accuracy of 10^{-4} (event-wise). After the target the forward focused projectile residues are again identified and the momentum is analyzed.

Two modes of operation are foreseen depending on the demands of the experiments:

1) A large-acceptance mode: heavy fragments and light charged particles (*i.e.* protons) are deflected by a large-acceptance dipole magnet and detected with a full solid-angle acceptance for the most reactions (left bend in Fig. 2). Resolutions for velocity and $B\rho$ measurements amount to about 10^{-3} allowing a unique identification in mass and nuclear charge of heavy fragments.

2) A high-resolution mode: here the dipole magnet is operated in reverse mode deflecting the fragments into magnetic spectrometer (right bend in Fig. 2). The envisaged resolution of 10^{-4} will allow a precise measurement of the fragment recoil momentum in single-nucleon knockout and quasi-free scattering experiments even for heavy nuclei.

The large gap of the dipole magnet provides a free cone of ±80 mrad for the neutrons which are detected in the forward direction by the large area neutron detector. At beam energies around 500 MeV/nucleon this corresponds to a 100% acceptance for neutrons with kinetic energies up to 5 MeV in the projectile rest frame. Depending of the requirements on resolution and acceptance, the detector with an active area of 2×2 m^2 is placed at a distance of 10 to 35 m from the target.

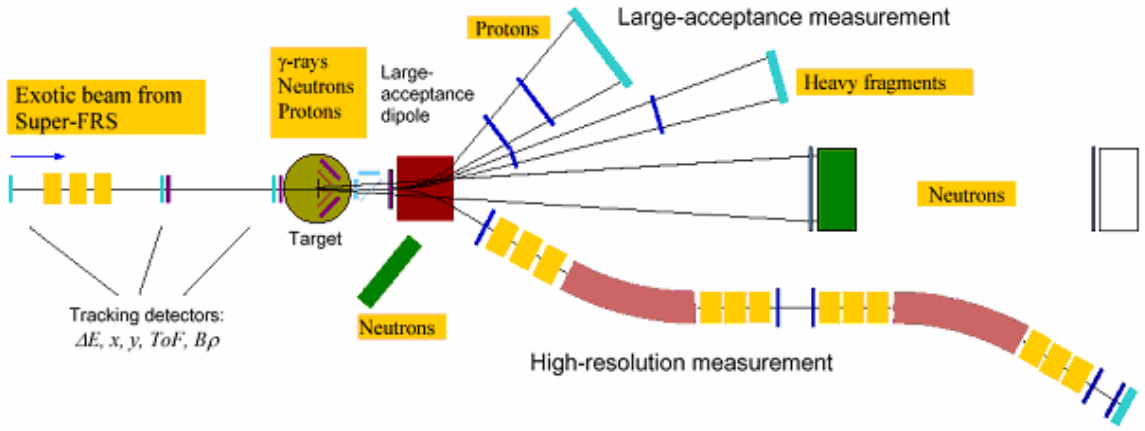

Fig. 2. Schematic drawing of the experimental setup comprising γ-rays and target recoil detection, a large-acceptance dipole magnet, a high-resolution magnetic spectrometer, neutron and light-charged particle detectors, and a variety of heavy-ion detectors

The target is surrounded by a γ-rays spectrometer. For most of the experiments a high efficiency total absorption spectrometer (cooled CsI) is the optimum solution which is also used to measure the energy of recoiling protons. For specific experiments requiring ultimate energy resolution for γ-detection, the germanium spectrometer will be used alternatively. For elastic, inelastic and quasi-free scattering experiments or charge exchange reactions, liquid or frozen hydrogen targets are considered. Recoiling protons and neutrons are detected by a Si-strip array and plastic scintillators, respectively. The Si-strip array is also used as a high-granularity multiplicity detector for measuring charged particles from the fireball created in semi-peripheral collisions. For measurements at low momentum transfer the use of an active target is foreseen. Fast neutrons stemming from (p, pn)-type knockout processes will be measured by placing part of the LAND detector at angles around 45°. Fast protons will be measured by two stations of large-area (100×80 cm^2) drift chambers measuring X- and Y-coordinates, each with required spatial precision of $\sigma \leq 200$ μm. For each coordinate two drift cell layers, each cell has a hexagonal geometry, are used to resolve the left-right ambiguity. The drift chambers with readout electronics CROS3 have been designed and assembled at PNPI. In March 2007 the chambers were commissioned with the 500 MeV beam of ^{12}C at GSI. Fig. 3 shows the detector setup in the test beam. First results of the test are presented in Figs. 4, 5.

Fig. 3. Detector setup behind the ALADIN magnet (Cave C) for the ^{12}C test beam

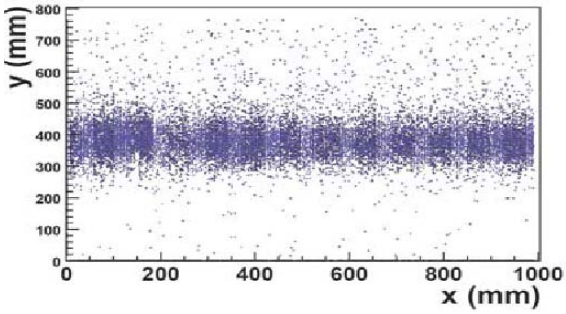

Fig. 4. Hit distribution obtained with sweeping the beam over the active area of the drift chamber

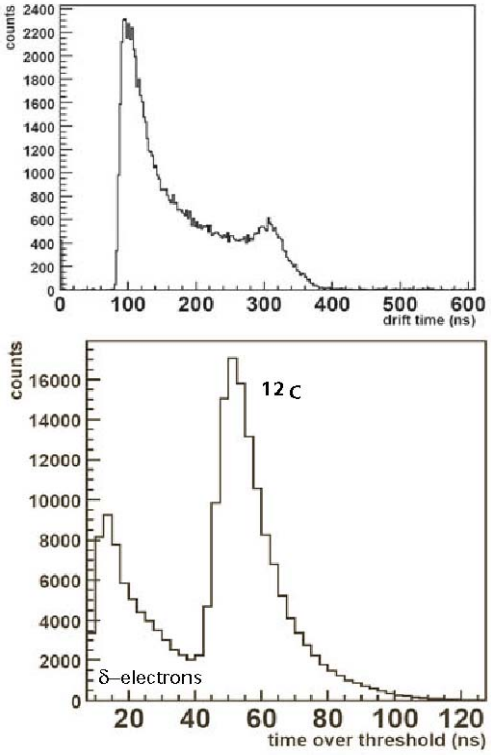

Fig. 5. Drift time (upper graph) and time-over-threshold (lower graph), *i.e.* charge distribution, measured with PNPI drift chambers

The **EXL** project (EXotic nuclei studies in Light-ion induced reactions) aims at studying the structure of exotic nuclei in light-ion scattering experiments in the inverse kinematics at intermediate energies (100–700 MeV/nucleon) using an internal target placed in the NESR storage-cooler ring of FAIR (see Fig. 1).

The EXL physics program has some overlap with that proposed in the R^{3}B project (see Table) as far as light-ion scattering is considered there. In the particular case of exploiting the active target concept within R^{3}B, for measurements at low momentum transfer, the two projects are actually complementary. For nuclear lifetimes around or below one second, where there is no enough time for beam preparation in the CR/NESR rings and for continuous accumulation and stacking, measurements with the external target (R^{3}B) are of preference. For longer lifetimes, cooling and beam accumulation in the storage ring should provide superior conditions. Keeping in mind that the rate capability of the active target technique will be limited, especially for very heavy projectiles, to about 10^5 s^{-1} or less, luminosities of the order 10^{28} cm^{-2}s^{-1}, as expected for EXL, will not be reachable with the external active target.

The experimental setup shown in Fig. 6 (right side) comprises (1) a silicon target-recoil detector for charged particles, completed by γ-rays and slow-neutron detectors, located around the internal target, (2) forward detectors for fast ejectiles (both charged particles and neutrons) and (3) an in-ring heavy-ion spectrometer.

Secondary beams are transferred from the fragment separator (Super-FRS) to the collector ring (CR) at a fixed energy of 740 MeV/nucleon for collection and stochastic pre-cooling to a relative momentum spread around 10^{-4} and an emittance of 1 mm × mrad within a cooling time below one second. The beam quality will be further improved by electron cooling in the NESR. The NESR will be equipped with a supersonic jet target having densities of 10^{14}–10^{15} atoms/cm^3 for the hydrogen and helium targets.

The design and construction of the universal detector is one of the most challenging tasks of the EXL project. The charged recoil particles will be detected by array of silicon detectors in an energy interval from about 100 keV up to several hundred MeV and in an angular region of $30° < \Theta_{lab} < 120°$. An overview of the detector geometry (horizontal cross section through the mid plane) is displayed in Fig. 6 (left side). Different

regions A-E of the lab-angular range correspond to a color code as defined in the Fig. 6. Except for the regions C and D, where particle tracking is foreseen, the angular resolution will be determined by the dimension of the gas-jet target and the distance of the detectors from the interaction point. Therefore a distance of 50 cm of the detectors in regions where highest angular resolution is required was chosen to obtain an angular resolution of $\Theta_{lab} \leq 2$ mrad for a target extension of 1 mm. For measurements at larger momentum transfer performed in regions C and D, a larger target extension in beam direction up to 5–10 mm may considerably increase the luminosity.

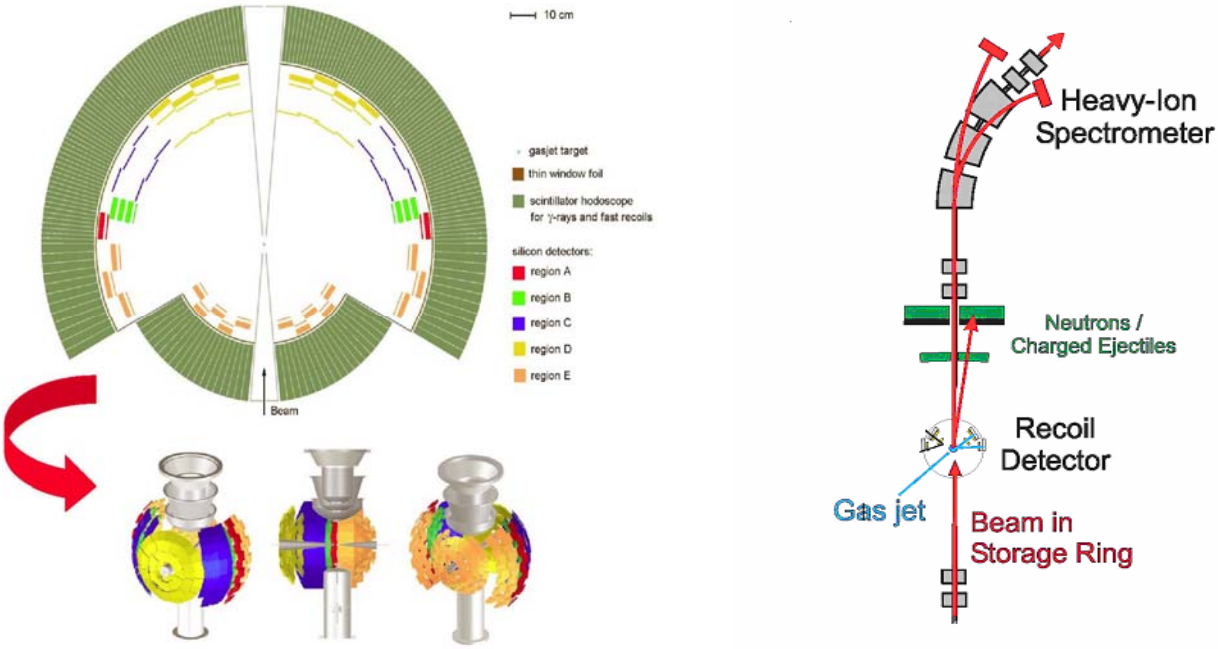

Fig. 6. Schematic view of the EXL detection systems. Right: setup built into the NESR storage ring. Left: the target-recoil silicon detectors and gas-jet target

The detectors for region A, for example, are ΔE-E telescopes consisting of a double-sided silicon strip detector (DSSD), 300 μm thick, and a 9 mm thick lithium drifted silicon detector (Si(Li)) behind. Low-energy recoils from elastic scattering near 90°, as well as from charge exchange reactions with positive Q-values, will be stopped in the DSSD, whereas higher energy recoils (up to 45 MeV protons and 170 MeV α-particles) will be stopped in the Si(Li). Therefore an energy threshold as low as 100 keV for the DSSD and a large dynamic range of 100 keV – 170 MeV for the combined telescope of DSSD and Si(Li) is required.

Total numbers of different types of DSSD and Si(Li) are: DSSD – 420, Si(Li) – 280.

At present, PNPI is carrying out the R&D on elaborating the 87×87 mm^2 and 9 mm thick Si(Li) detectors.

The scintillation hodoscope (see Fig. 6), behind the silicon array, is planned to detect γ-rays emitted from excited beam-like reaction products as well as the residual kinetic energy of fast target-like reaction products which punch through the silicon detectors. Almost 4π coverage, sufficient detector thickness for ~ 80 % γ-detection efficiency at E_γ = 2–4 MeV and for stopping of up to 300 MeV protons, an energy resolution of 2–3% for γ-rays and at least 1% for fast protons are supposed.

For a kinematically complete measurement, the momenta of the light particles (protons and neutrons or light clusters) emitted from the excited projectile will be determined from high-resolution time-of-flight and position measurements. In a first phase of the EXL detector implementation, the existing LAND detector will be used, for the second phase a new neutron and charged particle detector based on a RPC structure is foreseen.

The heavy projectile fragments will be detected by in-ring spectrometer. Two layers of position-sensitive ion detectors will be placed in front and behind the third dipole magnet (see Fig. 6) allowing to track the ions and to determine their rigidity.

2.2. Mass measurements and decay spectroscopy – ILIMA and MATS projects

PNPI participants: S.A. Eliseev, Yu.I. Gusev, Yu.N. Novikov, D.M. Seliverstov, G.K. Vorobjov

Nuclear masses and lifetimes of exotic nuclides in ground and isomeric states are the quantities essential for understanding the nuclear structure. The chart of nuclides with known and unknown masses is presented in Fig. 7, with the variation of neutron (proton) number along isotopic (isotonic) chains. From systematic precise mass measurements the important information such as location of drip-lines, the development of shell closures, the changes in shapes, pairing, and isospin symmetry can be derived. Beyond nuclear structure physics, precise mass values combined with decay spectroscopy are important for a variety of applications, ranging from nuclear-decay studies of the weak interaction and the Standard Model to astrophysical models for *X*-rays bursts and the creation of elements in stars.

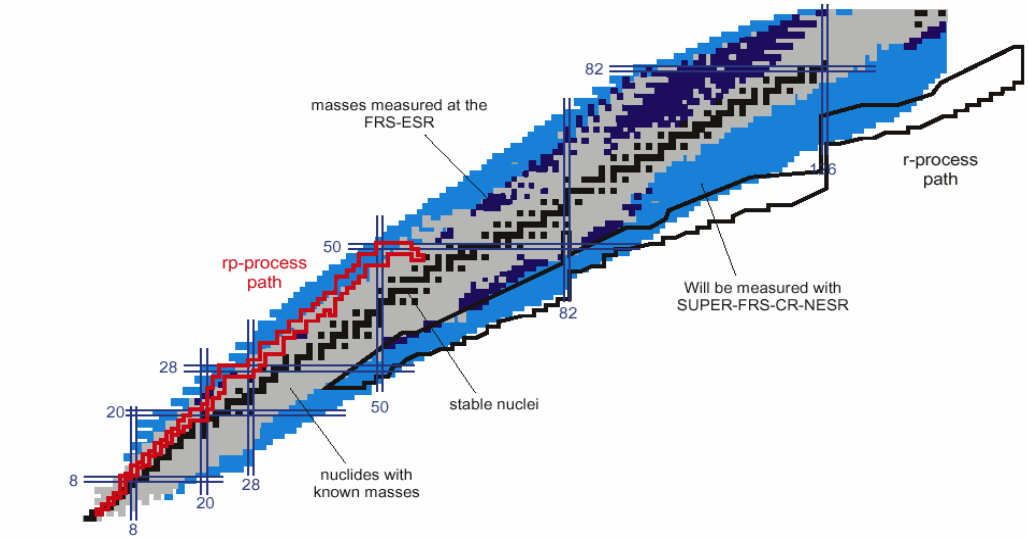

Fig. 7. The chart of nuclides with known and unknown masses. The range of the mass measurements performed presently in the storage ring ESR at GSI and nuclides with still unknown masses, which will become accessible with the new facilities, the Super-FRS, the double storage ring system of CR and NESR, are indicated. Astrophysical *r*- and *rp*-processes are shown as well

A real advantage is that at FAIR not only ground state properties can be studied, but also those of isomeric states which are populated in projectile fragmentation and fission reactions at relativistic energies. The experimental possibilities will expand the availability of pure isomeric beams that can be used for secondary nuclear reactions opening the novel way to explore the nuclear structure.
The investigations at FAIR proposed by two complementary projects ILIMA and MATS will focus on:
1. mapping the large areas of unknown mass surface:
   • near and at the drip-lines, *e.g.* to investigate pairing among loosely bound nucleons,
   • $N \approx Z$ nuclei, *e.g.* to investigate the role of the neutron-proton pairing,
   • in the region of shell closures, *e.g.* around doubly magic nuclides ^{48}Ni, ^{78}Ni, ^{100}Sn and ^{132}Sn,
   • along specific chains of isotopes and isotones, *e.g.* to explore predicted shell quenching far from stability,
   • at the pathways of nucleosynthesis in stars (*r*- and *rp*-processes), in particular waiting points,
2. lifetimes of highly-charged ions, their decay modes and branching ratios,
3. mass-resolved isomeric states and related nuclear properties,
4. the production of pure isomeric beams and investigations with them.

2.2.1. Study of Isomeric Beams, Lifetimes and Masses – ILIMA project

Mass measurements of exotic nuclei are a challenge because of the low production cross sections and the inherent large emittance and longitudinal momentum spread of radioactive beams. A further difficulty arises from the fact that the nuclides close to the drip-line are short-lived and thus limit the time of preparation and observation. Two methods, both with sensitivity down to single ions, have been developed at GSI for

accurate mass measurements of stored exotic nuclei at relativistic energies: Schottky Mass Spectrometry (SMS) for cooled beams of long-lived isotopes and Isochronous Mass Spectrometry (IMS) for hot beams of short-lived (down to microsecond range) fragments. Both methods, providing the mass resolving power of about 10^6 and accuracy of 30–50 microunits, are based on precise measurements of the revolution frequency which unambiguously characterizes the mass-to-charge ratio of the circulating in the ring ions. In SMS the velocity spread of the relativistic hot fragment beams is reduced by electron cooling. For IMS the ring optics is tuned to an isochronous mode such that the differences in velocities are compensated by different trajectories. These two methods are especially well-suited to measure effectively a large part of the mass surface in one run. In this way the systematic errors can be kept small if the reference masses for the calibration are reliable. The corresponding mass measurements in the Penning trap system (MATS project) of the Low-Energy Branch can provide very accurate reference masses.

The lifetimes of stored nuclei can be obtained with two independent methods. The first one is to measure non-destructively the intensity of both the mother and the daughter stored ion beams. These changes of the intensity are measured by applying Schottky spectrometry. The second one is based on the fact that the daughter and mother nuclides differ by their mass-to-charge ratio. Thus, the resulting daughter nuclei can be recorded with particle detectors placed near the orbit of the mother nuclides while the intensity of the mother nuclides is monitored by Schottky spectrometry. Both methods yield redundant information by a simultaneous measurement of the decay of the mother and the population of the daughter nuclides.

The experimental setup is schematically illustrated in Fig. 8. Experiments involving the nuclei with very short half-lives, down to μs range, will be performed in the CR operated in isochronous mode.

The experimental equipment in the CR will include time-of-flight detectors and sensitive Schottky probes, both enable precise revolution frequency measurements in very short time. Longer-lived nuclides (longer than 1 s) will be stochastically precooled in the CR and be transferred *via* RESR to the NESR for further electron cooling and measurements. An independent measurement of the lifetimes will be performed by measuring the daughter nucleus in particle-identification detectors placed near the closed orbit of the stored beam in both rings.

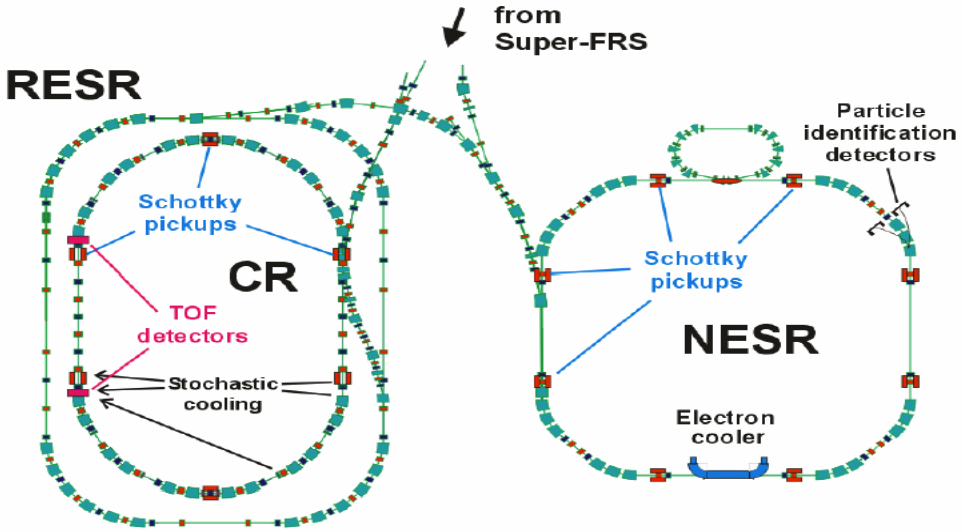

Fig. 8. The storage ring facilities for direct mass and half-life measurements and studies with isomeric beams

The combination of the Super-FRS with storage rings will provide access to pure isomeric beams. Already with the present FRS, the $B\rho$-ΔE-$B\rho$ method provides monoisotopic beams in the storage ring ESR as illustrated in Fig. 9. In the left panel of this Figure a Schottky spectrum is shown for the case when the FRS is operated as a pure magnetic-rigidity analyzer. Applying the energy-loss separation with shaped degraders leads to a pure monoisotopic beam of ^{52}Mn circulating in the ESR (right panel). Figure 9 demonstrates possibility to observe ground and isomeric states. In the ^{52}Mn case the excitation energy of the isomeric state is merely 378 keV.

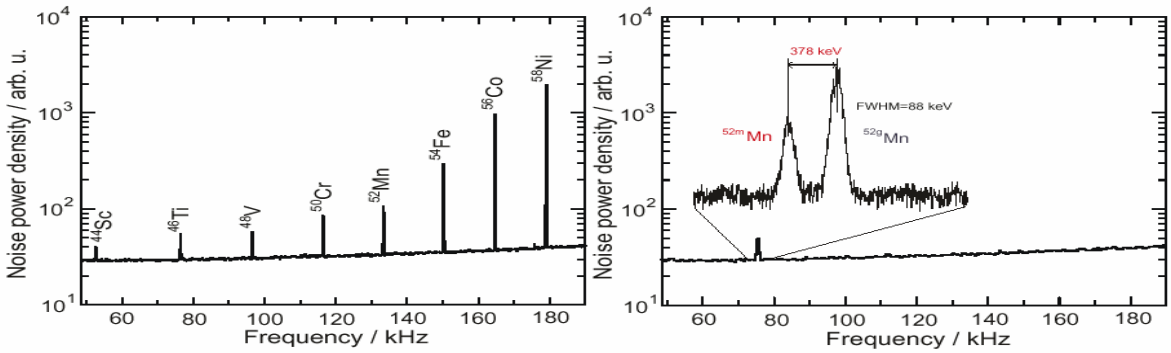

Fig. 9. Schottky spectra of stored fragments in the ESR. Left panel: the FRS is used as a magnetic-rigidity analyzer resulting in an isotope-coctail beam in the storage ring where the $B\rho$-ΔE-$B\rho$ separation method provides monoisotopic beams as demonstrated for ^{52}Mn ions (right panel). The stored ^{52}Mn ions consist of nuclei in the ground and isomeric states which are resolved by SMS, see zoomed part in the right panel

2.2.2. Precision Measurements of very short-lived nuclei using an Advanced Trapping System for highly-charged beams – MATS project

The MATS experiment will provide the mass measurements with relative uncertainty below 10^{-8}, accuracy better than 1 microunit, for radionuclides which most often have half-lives well below 1 s. Substantial progress in Penning trap mass spectrometry has made this method a prime choice for high precision mass measurements of rare isotopes. The technique has the potential to maintain high accuracy and sensitivity even for very short-lived nuclides. Furthermore, ion traps can be used and offer advantages for precision decay studies due to the well-defined storage conditions that are free of impurities.

The MATS setup, as schematically shown in Fig. 10, is a unique combination of an electron beam ion trap for charge breeding, Paul and Penning traps for beam preparation and a high-precision Penning trap system for mass measurements and in-trap spectroscopy of conversion-electron and alpha decays. A relative mass uncertainty of 10^{-9} can be reached by employing highly-charged ions and non-destructive Fourier-Transform-Ion-Cyclotron-Resonance (FT-ICR) detection technique on a single stored ion. The high charge state of the ions can also be advantageously used to reduce the required storage time, hence making measurements on even shorter-lived isotopes possible.

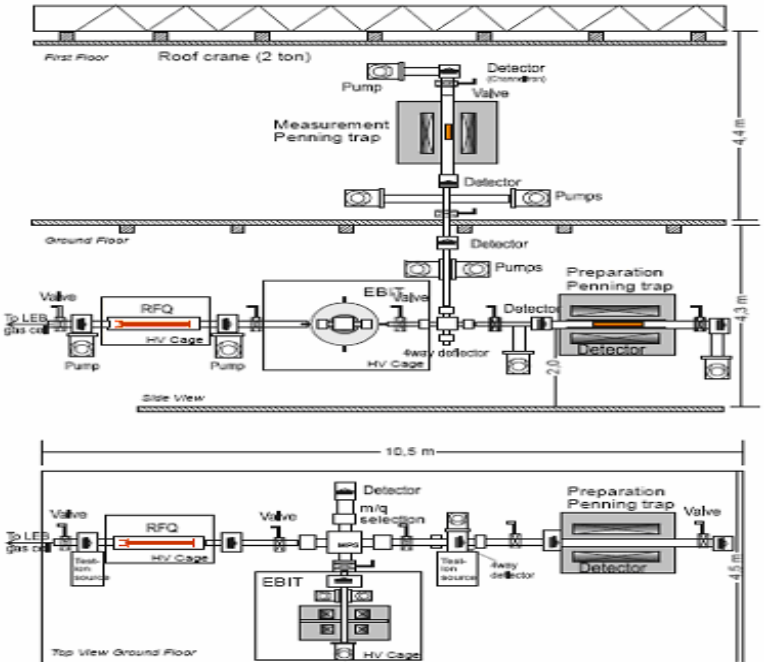

Fig. 10. High-precision Penning trap mass spectrometer and in-trap conversion electron spectroscopy setup

Decay studies in ion traps will become possible with MATS. Novel spectroscopic tools for in-trap high resolution conversion-electron and charged-particles spectroscopy from carrier-free sources will be developed aiming at the measurements of quadrupole moments and E_0 strengths. With the possibility both high precision mass measurements of shortest-lived isotopes and sensitive decay studies MATS is ideally suited to the investigation of very exotic nuclides that will only be produced at the FAIR facility.

PNPI contributes in the following activities:

• R&D and manufacturing the Si-detectors of different sizes (for particle detection in ILIMA and assisted spectroscopy at MATS).
• Simulation of the ion transport through the Penning trap system (for MATS and HITRAP/NESR – system).
• R&D of Penning trap with multi-segmented electrostatic field, partial manufacturing and assembling.

3. Compressed Baryonic Matter Experiment – CBM project

PNPI participants: V.V. Baublis, V.A. Evseev, A.N. Kiseleva, A.V. Khanzadeev, E.L. Kryshen, B.G. Komkov, L.G. Kudin, A.V. Nadtochi, V.N. Nikulin, E.V. Roshchin, G.V. Rubakov, V.M. Samsonov, D.M. Seliverstov, O.P. Tarasenkova, E.A. Vznuzdaev, M.B. Zhalov

The scientific goal of the CBM research program is to explore the phase diagram of strongly interacting matter in the region of highest baryon densities. This approach is complementary to the activities at RHIC (Brookhaven) and ALICE (CERN-LHC) which concentrate on the region of high temperatures and very low net baryon densities. The territory of dense baryonic matter accessible in heavy-ion collisions is located between the line of chemical freeze-out and the hadronic/partonic phase boundary, as indicated by the hatched area in Fig. 11. New states of matter beyond the deconfinement and chiral transition at high baryon densities and moderate temperatures may be within the reach of the experiment. The proposed CBM experimental program includes topics which are of fundamental interest for both astrophysics and QCD:

• the study of in-medium properties of hadrons,
• the search for the chiral and deconfinement phase transition at high baryon densities,
• the search for the critical point of strongly interacting matter,
• the study of the nuclear equation-of-state of baryonic matter at high densities (as it exists in the interior of neutron stars),
• the search for new states of matter at high baryon densities.

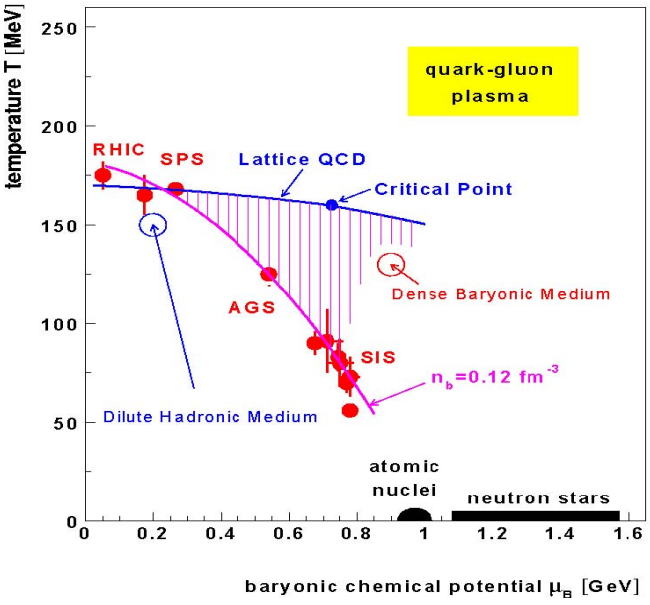

Fig. 11. The phase diagram of strongly interacting matter. The red symbols represent freeze-out points obtained with a statistical model analysis from particle ratios measured in heavy collisions. The pink curve refers to a calculation of the chemical freeze-out which occurs at a constant density (baryons + antibaryons) of $\rho_B = 0.75\ \rho_0$ (with $\rho_0 = 0.16$ fm^{-3}). The blue curve represents the phase boundary as obtained with a QCD lattice calculation with a "critical point" (blue dot) at T =160 ± 3.5 MeV and μ_B=725 ± 35 MeV ($\rho_B \approx 3\ \rho_0$). In the region of the blue circle the baryon density is $\rho_B = 0.038$ fm$^{-3} \approx 0.24\ \rho_0$ ("dilute hadronic medium"). The corresponding value for the red circles is $\rho_B = 1.0$ fm$^{-3} \approx 6.2\ \rho_0$ ("dense baryonic medium"). The hatched area marks the region of equilibrated matter at high baryon densities

The CBM experiment aims at comprehensive studying hadrons, muons, electrons and photons in heavy ion collisions. The key observables include:

• Low-mass vector mesons (ρ, ω, φ) decaying into e^+e^- ($\mu^+\mu^-$) pairs. *Via* the measurement of penetrating probes one can extract the in-medium spectral function of mesons and, hence, obtain information on the possible restoration of chiral symmetry in dense baryonic matter.

• Hidden and open charm (charmonium, *D* mesons). The measurement of charmed mesons at threshold beam energies will help in understanding the in-medium production processes and the properties of highly compressed strongly-interacting matter.

• (Multi-) Strange baryons (Λ, Ξ, Ω). The yields and phase-space distributions of baryons containing (newly created) strange quarks are expected to be sensitive to the early and dense stage of collision.

• Global features like the collective flow and critical event by event fluctuations. These observables contain information on the nuclear equation-of-state at high densities and on the existence of a critical point, and, hence, on the location and the order of the deconfinement phase transition.

• Direct photons from first collisions and thermal photons from the dense and hot fireball.

• Exotica like pentaquarks, bound kaonic systems, strange clusters, precursor effects of a color super-conducting phase, *etc.* The creation of compressed baryonic matter possibly will lead to unexpected phenomena.

The main experimental objective is the measurement of extremely rare signals in an environment typical for heavy-ion collisions. This requires the collection of a huge number of events which can only be obtained by very high reaction rates and long data taking periods. The CBM aims at reaction rates of up to 10 MHz (minimum bias) which corresponds to a beam intensity of 10^9 particles per second on a 1% interaction target. The rear signals are embedded in a large background of charged particles. For example, a central Au+Au collision at 25 A·GeV produces about 1000 charged particles which in addition create a similar amount of secondaries *via* reactions in the target and detector materials. Hence, the experimental challenge is to measure about 10^{10} charged particles per second, which are focused into a small cone, and to identify rare particles.

The layout of the CBM experimental setup is optimized for heavy-ion collisions in the beam energy range from about 8 to 45 A·GeV. Experiments on dilepton production at beam energies from 2 to about 8 A·GeV could be carried out with the HADES spectrometer if installed in front of the CBM target (at present time the HADES is acting in GSI).

A schematic view of the proposed CBM detector concept is shown in Fig. 12.

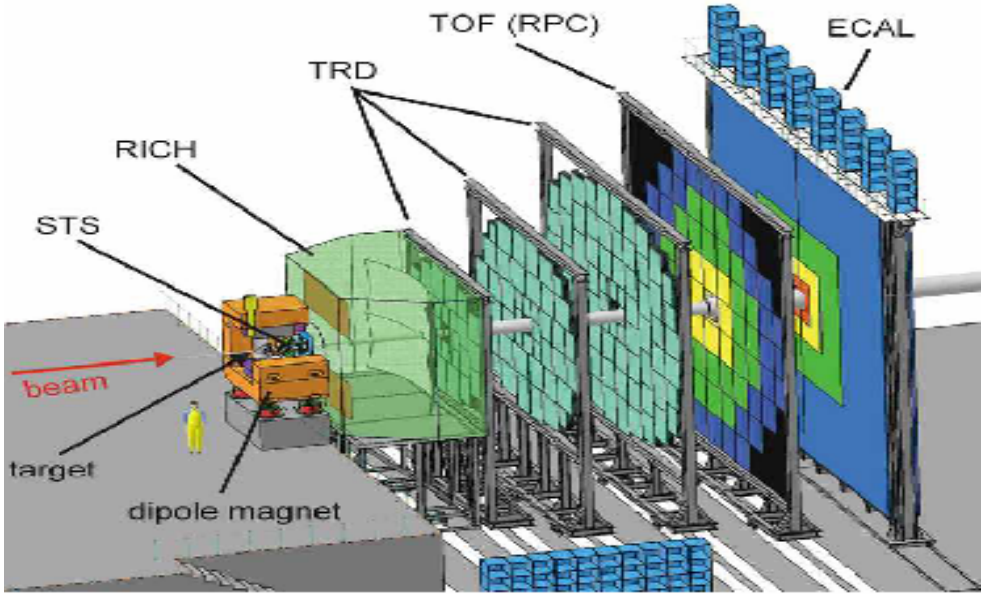

Fig. 12. Schematic view of the CBM experiment. The setup consists of a high resolution Silicon Tracking System (STS), a Ring Imaging Cherenkov detector (RICH), three stations of Transition Radiation Detectors (TRD), a time-of-flight (TOF) system made of Resistive Plate Chambers (RPC) and an Electromagnetic Calorimeter (ECAL)

The core of the setup is a Silicon Tracking System (STS) located inside the large gap of the superconducting dipole magnet. The STS consists of several planar layers of silicon-pixel and silicon micro-strip detectors which have to provide the capabilities for track reconstruction, determination of primary and secondary vertices with a resolution of better than 50 μm, and momentum determination with $\Delta p/p < 1\%$ in the range of $0.5 < p$ [GeV/c] < 4.0. Electrons from low-mass vector mesons decays will be identified with a Ring Imaging Cherenkov (RICH) detector. A Transition Radiation Detector (TRD) will provide charged particle tracking and the identification of high energy electrons and positrons. The hadron identification will be performed using a TOF wall of a Resistive Plate Chamber (RPC) array. The start signal for the TOF measurement will be taken from a diamond pixel (or micro-strip) detector. An Electromagnetic Calorimeter (ECAL) will be used for the identification of electrons and photons.

One of the major tasks of the CBM experiment is the measurement of open charm. *D* mesons will be detected *via* their weak decay into charged pions and kaons. This measurement poses a major challenge to the STS: the decay vertex of the *D* meson, which is displaced from the main vertex of the collision by several 10 μm, has to be determined with an accuracy of about 50 μm in order to suppress the combinatorial background caused by pions and kaons directly emitted from the fireball. The simulations show that an event suppression factor of about 1000 can be achieved when using a thin and highly granulated vertex pixel detector.

Another key observables are low-mass vector mesons which decay into lepton pairs with a branching ratio of 10^{-4}–10^{-5}. The major challenge, both for the measurement and for the data analysis, is to reject the physical background of electron-positron pairs from Dalitz decays and gamma conversion. As an alternative (or complementary) approach to the dielectron measurement is to study the possibility of detecting vector mesons (ρ, ω, φ, J/ψ) *via* their decay into $\mu^+\mu^-$ pairs. The idea is to replace the RICH detector by a "compact" muon absorber-detector system (Fig. 13) and to identify the muons just behind the STS. This configuration could work at the first stage of experiment as independent part of the CBM experiment. The simulations are based on track reconstruction algorithms taking into account a realistic response of the STS and of the muon chambers. Reconstructed charged particle tracks with hits in the muon chambers located behind the last absorber layer are associated with muons. The results of preliminary studies demonstrate the feasibility of dimuon measurements with the CBM detector setup using an active absorber, 5 Fe absorbers and 15 tracking detector layers, for Au+Au collisions at 25 A·GeV. This is particularly true for J/ψ mesons which can be identified within the full phase-space acceptance of the CBM setup with a signal-to-background ratio of 10–100.

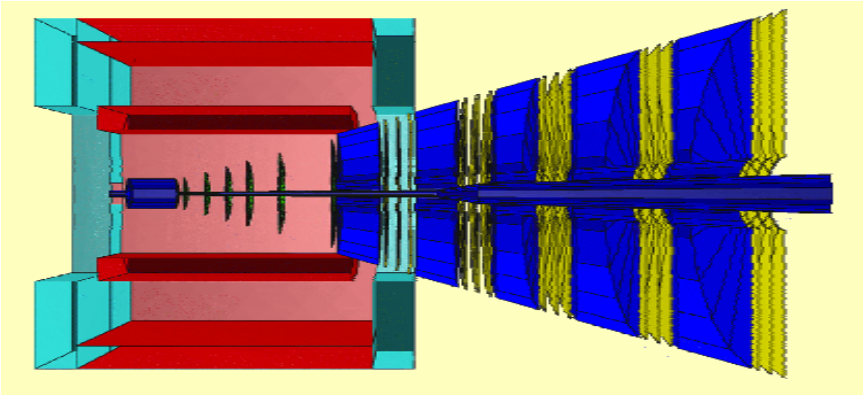

Fig. 13. Location of the "compact" muon detector

Preliminarily, PNPI contributes in the CBM project in several directions:

• Simulations to optimize the absorber and detector layout of the muon system aiming at receiving an acceptable signal-to-background ratio, especially in case of light vector mesons.

• Elaborating the muon tracking system, with special care for the central part where the highest rate and occupancy present. For today the muon tracking system might be a combination of micro-pattern gas detectors (such as GEM, Micromegas) for the central part and multiwire proportional chambers with cathode

readout to cover rest peripheral part of the aperture. R&D on the choice of the appropriate detectors is on the way.
• R&D of the tracking system for the TRT stations. At the present time, two variants are considered, one is based on the micro-drift chambers and the straw tubes are used in an alternative version. PNPI works on the straw tube approach.
• Mechanical design of the RICH detector.

4. Strong interaction studies with antiprotons – PANDA project (AntiProton Annihilations at Darmstadt)

PNPI participants: S.L. Belostotski, G.E. Gavrilov, A.A. Izotov, O.V. Miklukho, Y.G. Naryshkin, V.V. Vikhrov, A.A. Zhdanov

The PANDA project aims at studying the structure of hadrons and their interaction with medium using cooled antiproton beams of unprecedented quality and intensity in the momentum range of 1.5–15 GeV/c stored in the High Energy Storage Ring (HESR, see Fig. 1).

The physics program formulated for PANDA experiment will cover the following research directions:
• Charmonium ($c\bar{c}$) spectroscopy: precision measurements of mass, width, decay branches of all charmonium states, especially for extracting information on the quark confinement.
• Firm establishment of the QCD-predicted gluonic excitations (charmed hybrids, glueballs) in the charmonium mass range (3–5 GeV/c^2).
• Search for modifications of meson properties in the nuclear medium, and their possible relationship to the partial restoration of chiral symmetry for light quarks. Particular emphasis is placed on mesons with open and hidden charm in order to learn more about the origin of hadron masses.
• Precision γ-rays spectroscopy of single and double hypernuclei for extracting information on their structure and on the hyperon-nucleon and hyperon-hyperon interaction.

With increasing luminosity of the HESR facility further possibilities will emerge:
• *D*-meson decay spectroscopy (rare leptonic and hadronic decays).
• Search for *CP*-violation in the charm and strangeness sector (*D*-meson decays, $\Lambda\overline{\Lambda}$ system).
• Extraction of generalized parton distributions from $p\bar{p}$ annihilation.
• Fundamental physics with stopped antiprotons.

The experiments will be performed at an internal target station of the HESR (see Fig. 14).

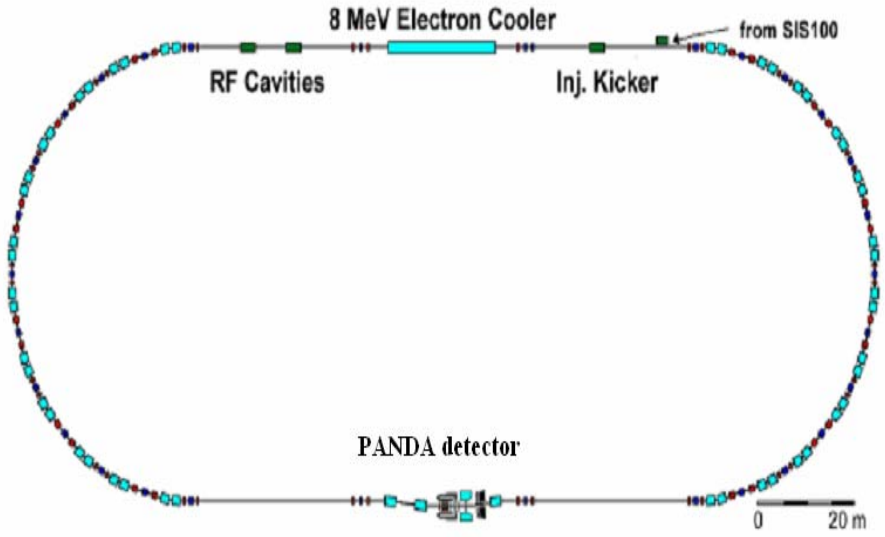

Fig. 14. Location of the PANDA detector at the HESR

Antiprotons traversing the target material without interaction are recirculated in the ring passing through the electron cooler which compensates the energy loss and straggling and thus maintains the high beam quality. The minimum momentum of the antiprotons is 1.5 GeV/c and the maximum is 15 GeV/c. The maximum energy in the center-of-mass system for antiproton-proton collisions is 5.5 GeV, sufficient for associated production of singly charmed baryons (up to Ω_c) and corresponding to the upper mass range predicted for charmonium hybrid states. Figure 15 shows the mass range of hadrons reachable at the HESP antiproton beam. Stochastic cooling of the beam over the whole energy range provides a momentum spread of $\Delta p/p \approx 10^{-4}$. In order to perform high precision charmonium spectroscopy, beam properties (at momentum below 8 GeV/c) will be improved by high energy electron cooling providing the momentum spread of 10^{-5} for the $\bar{p}$ beam.

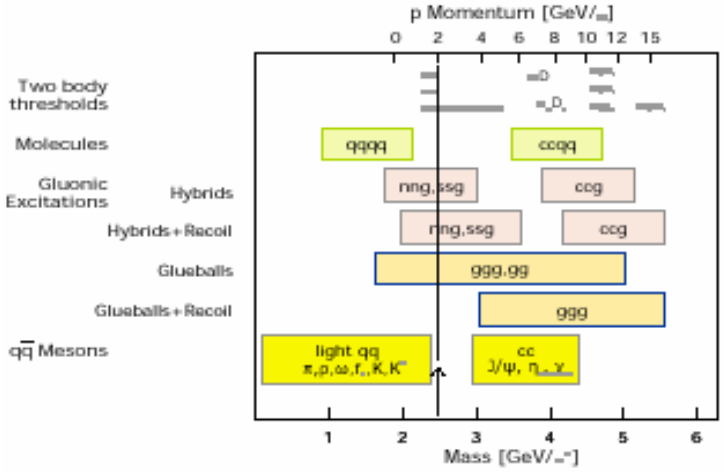

Fig. 15. Mass range of hadrons accessible at the HESR with antiproton beam. The figure indicates the antiproton momenta required for charmonium spectroscopy, the search for charmed hybrids and glueballs, the production of D meson pairs and the production of Σ pairs for hypernuclear studies. The energy range covered by the former Low Energy Ring (LEAR) at CERN is indicated by the arrow

The physics program puts stringent requirements on the detector. It has to accept the high rate of 2×10^7 annihilations per second at full luminosity originating from the total cross section of about 100 mb and simultaneously to allow for triggering events with nb cross section, involving (e^+e^-), $(\mu^+\mu^-)$, $(\gamma\gamma)$, $(\varphi\varphi)$ pairs.

For the major part of the experimental program (charmonium spectroscopy, the search for hybrids and glueballs, and the interaction of hidden and open charm particles with nucleons and nuclei) a general purpose detector will be used (see Fig. 16). The inner part of the detector can be modified for the experiments with strange hypernuclei or for the special needs of *CP*-violation studies. In order to retain the full information in particular for spectroscopy experiments, a nearly full coverage of the solid angle together with a good particle identification and high energy and angular resolutions for charged particles ($\pi^{\pm}$, $K^{\pm}$) and photons is necessary.

The PANDA detector is subdivided into the target spectrometer (TS) consisting of a solenoid around the interaction region and the forward spectrometer (FS) based on a dipole magnet for momentum analysis of the forward going particles.

It is planning the use of a pellet target for most experiments at the HESR facility. However, depending upon the amount of beam heating from the internal target, it may be necessary to use also a gas jet target. The remaining experiments that require a very precise primary vertex determination will use a thin fiber or wire target.

Particles emitted with laboratory polar angles larger than 5° are measured in the TS. Surrounding the interaction volume there will be 4 diamond or Si start detectors (each of 20×30 mm^2) followed by 5 layers of a silicon Micro-Vertex Detector (MVD). Starting from a radial distance of 12 cm from the beam-line up to 42 cm, there will be 15 double-layers of crossed straw tubes or a Time Projection Chamber (TPC), which extend from 40 cm upstream to 110 cm downstream of the target. At a radial distance of 45 cm there will be a layer of DIRC Cherenkov detectors. Surrounding the target region there is an electromagnetic calorimeter. This calorimeter consists of $PbWO_4$ crystals that are readout with avalanche photodiodes (APD). The use of $PbWO_4$ is required for higher granularity and shorter dead-time. The smaller Moliére radius of $PbWO_4$ furthermore reduces the dead space at the edge of the spectrometer. In the region between the calorimeter

and the endcap there will be 2 sets of mini-drift chambers (MDC) with 6 active planes each. In the forward direction there is an aerogel Cherenkov detector using proximity focusing onto gas based photon detectors. The TS is contained in a 2.5 m long and 80 cm radius solenoid. Behind the return yoke there will be scintillating strips for muon identification.

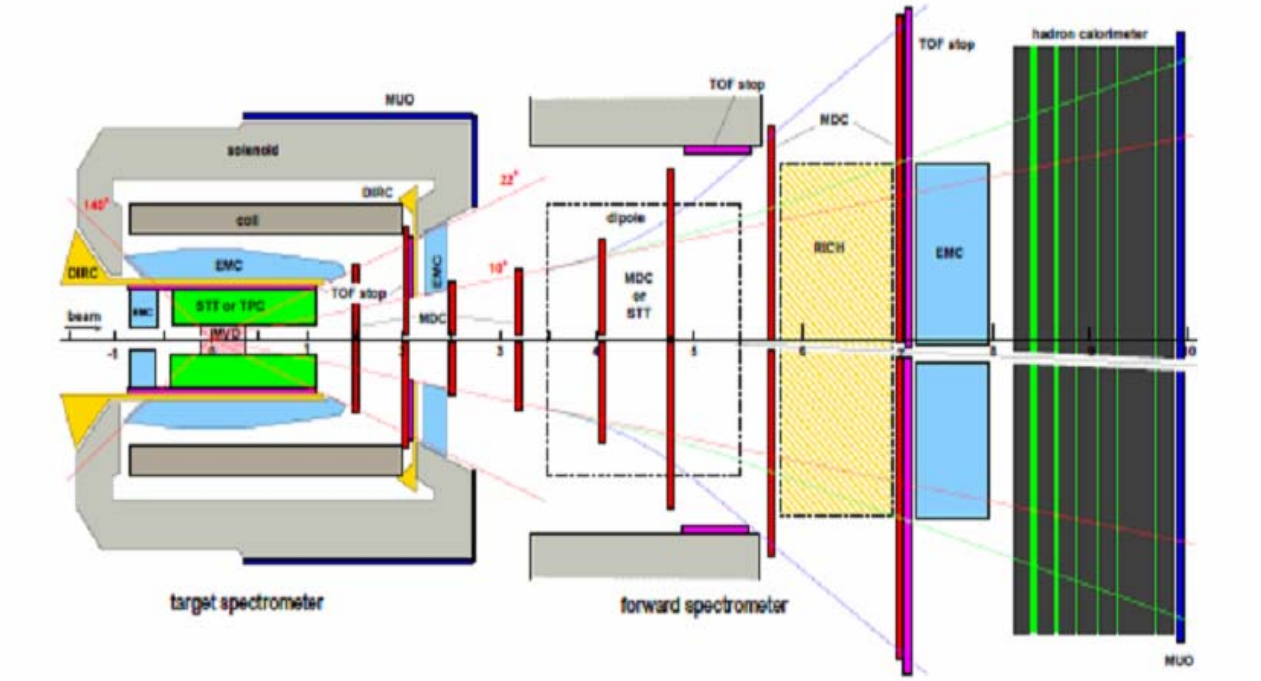

Fig. 16. Top view of the general purpose PANDA spectrometer for antiproton annihilation physics

Particles emitted with polar angles below 10° and 5° in the horizontal and vertical direction, respectively, are detected with the forward spectrometer (FS). The current design includes a 1 m gap dipole magnet (total bending strength of 2 T·m) and tracking detectors for a momentum analysis of charged particles, *i.e.* mini-drift chambers (MDC) and straw-tube trackers (STT). Photons will be detected by a shashlyk-type calorimeter consisting of lead-scintillator sandwiches (EMC). Other neutral and charged particles with momenta close to the beam momentum will be detected in the hadron calorimeter and muon counters. Additional RICH detector, like at the HERMES experiment, and time-of-flight measurements are required for particle identification. Particle identification for hadrons and leptons over a large range of solid angles and momenta is an essential requirement for the PANDA experiment. Several dedicated systems, complementary to the other detectors, will provide means to identify particles. A time-of-flight (TOF) system will include TOF start detectors in the MVD, a TOF barrel between STT/TPC and DIRC, a flat layer of TOF detectors in the endcap, TOF stop counters inserted into the dipole magnet of the FS, and a large TOF stop wall in the FS. Cherenkov detectors will enlarge the capabilities of this system to the high momenta where times of flight are too short for TOF measurements. In certain momentum ranges the particle identification will be done by using energy losses in the detectors (MVD for slow charged particles, EMC for γ-rays and leptons).

PNPI is responsible, and at the present time is conducting an intensive R&D, for elaborating the TOF stop detectors in the forward spectrometer. These detectors will consist of tiles made of plastic scintillator and read out on both ends by fast phototubes. Such counters will be placed as a wall about 7 m from the target and inside the dipole magnet opening. With the expected time resolution of σ = 50 ps, π-K and K-p separation on a 3σ level will be possible up to momenta 2.8 GeV/c and 4.7 GeV/c, respectively.

PROJECT OF NEW UNIVERSAL LASER COMPLEX OF IRIS FACILITY FOR ATOMIC AND NUCLEAR INVESTIGATIONS

V.N. Panteleev, A.E. Barzakh, D.V. Fedorov, V.S. Ivanov

1. Introduction

The Short-Lived Nuclei Laboratory based at the IRIS (Investigation of Radioactive Isotopes on Synchrocyclotron) facility has been carrying out successful systematic investigations of the far from stability nuclei with the aid of laser technique since the beginning of 1980-es. More than 120 nuclides were studied, new approaches and methods of production and investigation of short-lived isotopes were developed and applied during this period.

In the near future the following directions of the scientific activity seem to be the most promising and important:

1. Nuclear spectroscopy.

a. The nuclear characteristics of the nuclei very far from stability (lifetime, decay modes, their branching ratios, *etc.*) are of great importance for the models of astrophysical processes (*r*- and *rp*-processes *etc.*). Due to the extremely low production rate in proton-nucleon collisions, the investigation of these nuclides has to be done at the background of isobars with production rates of some orders of magnitude higher than the isotope under study. Hence, the availability of the isobaric pure sources of the investigated nuclei becomes the key point for the investigation of the basic nuclear characteristics of these exotic nuclei.

b. The problem of "the magic numbers conservation" for the far from stability nuclides has the fundamental importance and also is connected directly with astrophysics. Recently obtained data point to the change of the magic numbers for very far from stability nuclei (the vicinity of ^{78}Ni, ^{65}Mn). This may lead to a revision of the magic number concept itself. Detailed nuclear-spectroscopic investigations of this areas and the search for other similar areas require the pronounced isotope and isobar selectivity also.

c. There is a number of interesting problems when the source of pure isomer could give an excellent opportunity for new investigations (isomer-selective measurements of beta-strength functions *etc.*). To this end the isomer selectivity is very important point.

2. Laser spectroscopy.

The traditional area of the laser spectroscopy application for the nuclear physics research is the isotope shift and hyperfine splitting measurements. Differences in mean square charge radii, spins and electromagnetic moments can be evaluated from these experimental data.

One of the most interesting objects for this laser-nuclear spectroscopy is an investigation of the so called shell effect in the mean square charge radii, *i.e.* the marked kink in the isotopic mean square charge radius dependence on the magic number. A disappearance of this kink may point to the change of the magic number.

In this respect the most interesting nuclei are Sb, Sn, In, Cd, Ag with the neutron number N close to 82. It is worth noting that it is the systematic investigation of mean square charge radii for the long isotopic chains that has to be done to discover the general trends and basic properties of the nuclear matter.

There is no enough information about the shell effect in the region near $N = 50$. Here the most interesting isotope chains are the chains of Ge, Ga, Zn, Cu, and Ni isotopes. These isotopes attract additional interest as unique objects to test the mean square charge radius trend between the two neighbor closed sub-shells.

Very special case is a vicinity of $N = 126$. The three orders of magnitude drop of the half-life values takes place for the isotopes of Ac, Ra, Fr, Rn, and At at the $N = 126$ (see Fig. 1, for example: $T_{1/2}(^{212}\text{Rn}) = 24$ min, $T_{1/2}(^{213}\text{Rn}) = 20$ ms). This leads to a fast drop of the production rates of the very short-lived nuclei, and the usual laser-nuclear spectroscopy method cannot be applied because of lack of sensitivity. Making the production efficiency of such nuclides higher we can get a chance to investigate this very interesting area of anomalous short lifetimes.

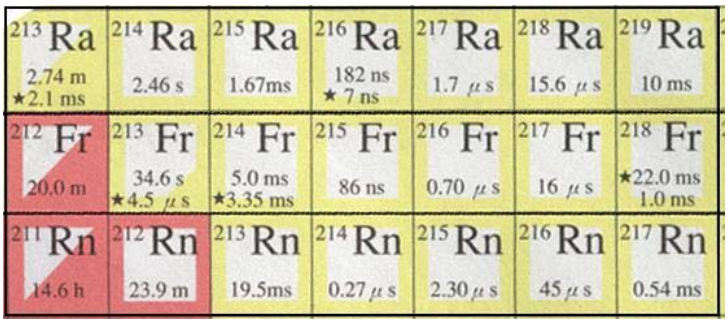

Fig. 1. Half-life drop in a vicinity of N =126

Obviously the anomalous half-life decrease in this region is connected with the enormous acceleration of alpha-decay. Besides the shell effect investigations, the systematic studies in this exotic region could clarify the influence of the alpha-particle binding energy on the shape and dimension of the nuclei.

The Hg isotope chain deserves a special attention. Investigations of these isotopes started the laser-nuclear direction in nuclear physics. Here the well known "jump" in the course of mean square charge radii and the "staggering effect" (unusually wide fluctuations of mean square charge radii at the transition from even to odd isotopes) were found. It would be very interesting to find whether the stabilization of this staggering effect takes place and, if yes, at which N it happens (see Fig. 2). For this purpose the investigations of the isotopes with $N < 181$ are necessary.

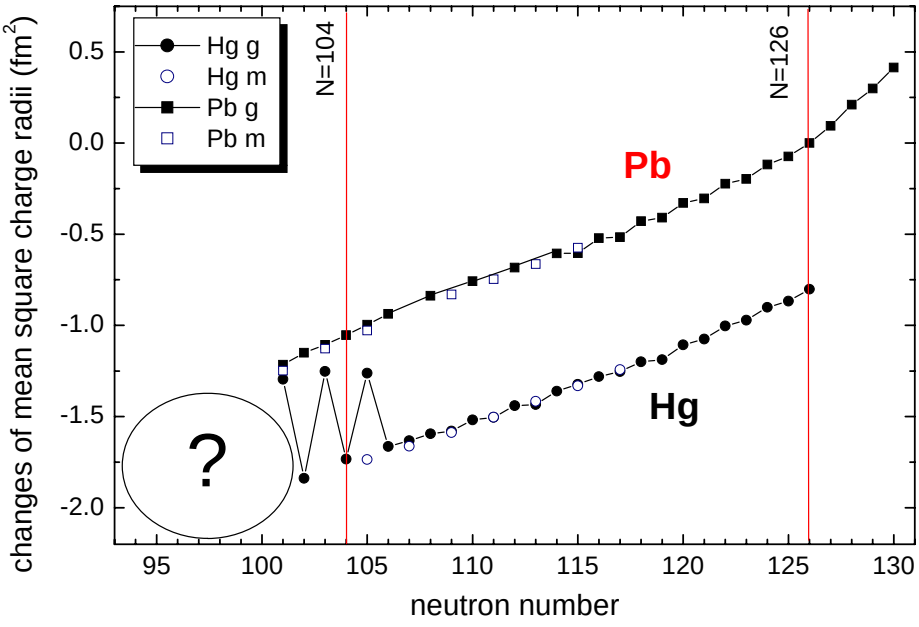

Fig. 2. Staggering effect in the course of mean square charge radii at N = 104 for Hg (Z = 80) and the smooth its behavior for Pb (Z = 82)

As we can see, the high production efficiency of the nuclei under investigation and the high isobar and isomer selectivity of the ionization method are the crucial conditions for the successful study.

2. Target-ion source system for efficient production of isotopes under investigation

In the course of the IRIS facility work at the proton beam of PNPI synchrocyclotron, the Short-Lived Nuclei Laboratory has accumulated a big experience in development and construction of target systems for on-line application. For more than thirty years uranium carbide targets [1,2] have been explored for production of a large variety of neutron-rich (fission reaction) and neutron-deficient (spallation reaction) nuclei. The main problem of uranium carbide target development was the creation of the target material with a high dispersivity and porosity in order to decrease the release time of the species produced by different reactions in the target material. On the other hand, for a more efficient use of a neutron beam after the primary beam converter in future ISOL facilities the uranium density of the target material should be as high as possible. Additionally, the target material with a higher density has a higher thermal conductivity that would allow dissipating a higher power introduced into the target by the primary beam, when the target is used for exotic nuclei production in the direct reaction. Hence, for more effective production of short-lived isotopes of the element chosen for investigation a special selection of a metal carbide target material is required, concerning not only the target material structure, but also its density. Recent developments at Short-Lived Nuclei Laboratory make it possible to produce a wide range of short-lived isotopes of different elements with good efficiency (*i.e.* production rates are enough to carry out physical experiments). In Fig. 3 the construction of a new high density thick uranium carbide target is presented [1].

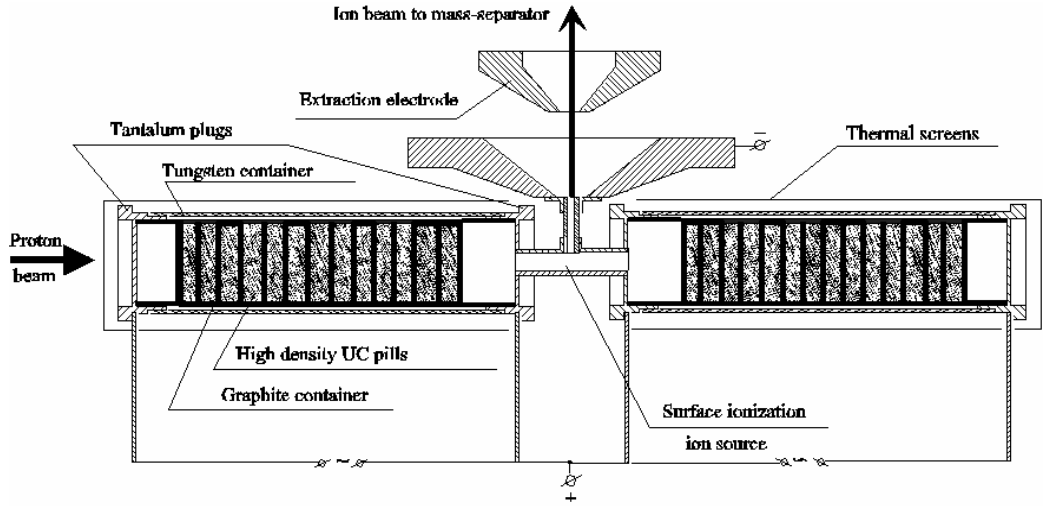

Fig. 3. High density thick uranium carbide target (91 g/cm^2)

Table 1 represents the normalized production rates of some isotopes of elements listed above as objects for investigations.

Table 1

Isotope	Half-life	Normalized production rate, 1/s (0.1 μA proton beam, target thickness 1 g/cm^2)
$^{219}Fr_{132}$	20 ms	$8.4(1.8)\times10^2$
$^{121}Ag_{74}$	0.78 s	$9.6(2.1)\times10^2$
$^{134}Sn_{84}$	1.12 s	$3.5(1.1)\times10^3$
$^{58}Mn_{33}$	65 s	$4.2(4)\times10^3$
$^{119}Cd_{71}$	2 min	$1.2(2)\times10^5$

[1] H.L. Ravn, Nucl. Instr. Meth. B **70**, 197 (1992).
[2] A.M. Evensen *et al.*, Nucl. Instr. Meth. B **126**, 107 (1997).

In Table 2 the production rates of the same isotopes extrapolated to the 91 g/cm^2 thickness of uranium carbide target and to the 0.2 μA proton beam intensity are shown.

Table 2

Isotope	Half-life	Production rate, 1/s
$^{219}Fr_{132}$	20 ms	$1.5(0.3)\times10^5$
$^{121}Ag_{74}$	0.78 s	$1.7(0.4)\times10^5$
$^{134}Sn_{84}$	1.12 s	$6.4(2)\times10^5$
$^{58}Mn_{33}$	65 s	$7.6(7)\times10^5$
$^{119}Cd_{71}$	2 min	$2.2(4)\times10^7$

3. LIS method of nuclear investigations

Method of the laser resonance ionization inside the cavity of the laser ion source (LIS), developed and firstly applied at the Short-Lived Nuclei Laboratory, meets the requirements of the efficient production of the isobaric and isomeric selective sources.

The idea of the laser photoionization is demonstrated in Fig. 4. The essential point of the method is step-by-step resonant laser excitation of atom from the ground state – through intermediate states – to the autoionization state or the continuum. Lasers tuned to the fixed wavelengths according to the specific atomic transitions provide the selective ionization of the investigated element [3] . The produced ions can be extracted from the ion source, mass-separated and delivered to the detector stations.

At the same time the method of resonance laser photoionization in the laser ion source proves to be one of the most efficient tools for isotope shift and hyperfine structure investigations [4].

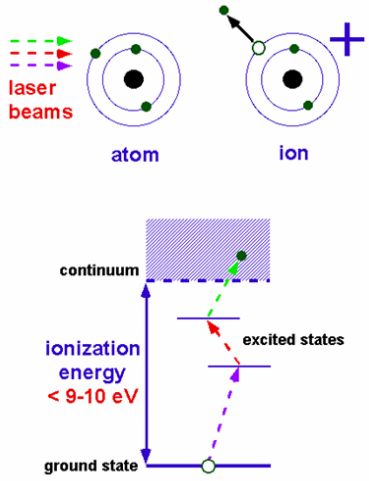

Fig. 4. Scheme of resonance ionization

The scheme of the experimental setup built at the IRIS facility of the Short-Lived Nuclei Laboratory at the beginning of 1980-es is presented in Fig. 5.

A description of the setup and experimental details can be found in Ref. [2]. The main points which should be mentioned here are as follows:

1. Now copper-vapor laser (CVL) pump system can provide three resonance wavelength channels with average laser power of 100–500 mW each.
2. Values of the available wavelength are in the region of 530–800 nm.

[3] V.S. Letokhov *et al.*, Optics Comm. **7**, 59 (1973).
[4] G.D. Alkhazov *et al.*, Nucl. Instr. Meth. B **69**, 517 (1992).

These restrictions mean that we are able to ionize the atoms with the ionization potentials lower than 6.5 eV. These are atoms of alkalis, alkali-earths, rare-earths and some other elements. Additionally, due to the lack of power, we can not saturate the third transitions of the ionization scheme (see Fig. 4). This considerably decreases the ionization efficiency.

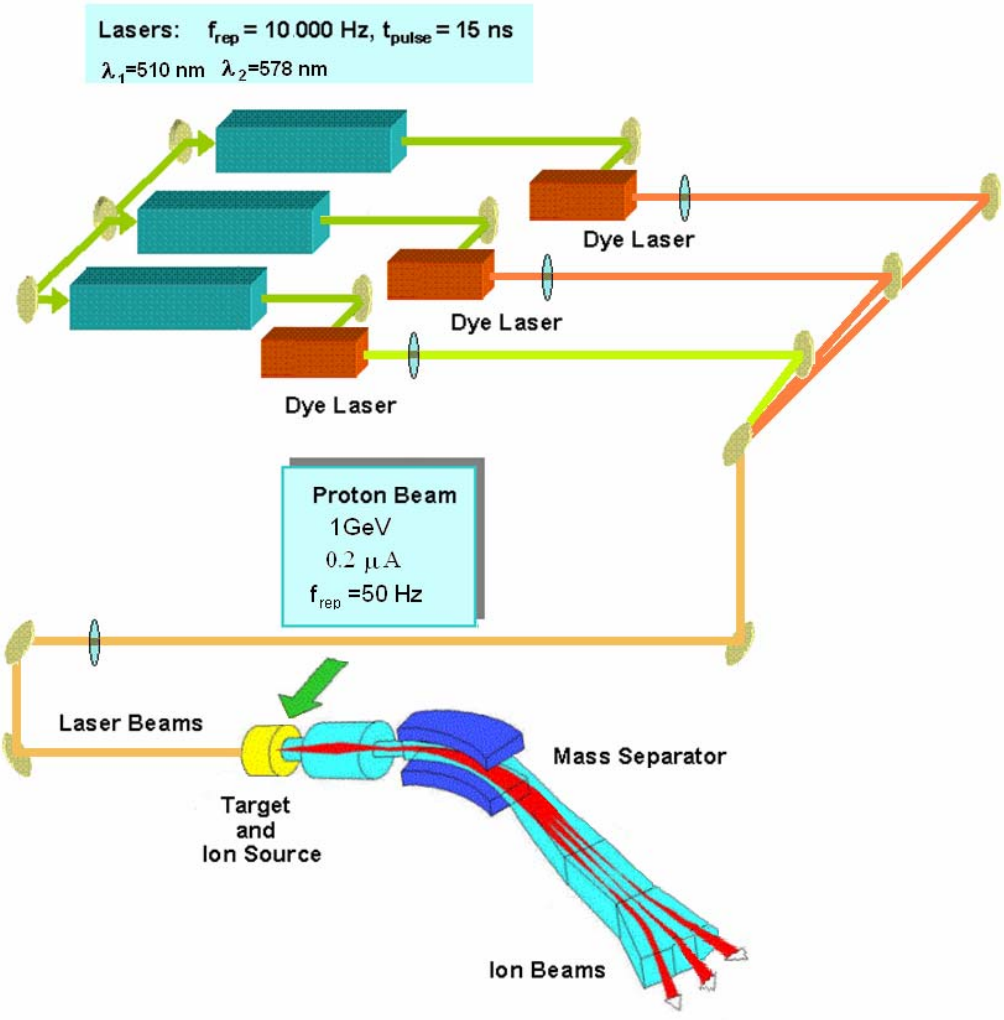

Fig. 5. Scheme of the laser-nuclear experimental setup used at the IRIS on-line facility for studies of Yb isotopes

To overcome these restrictions it is necessary to increase the pump power of the copper-vapor lasers and to produce the resonance wavelengths in higher energy ultraviolet diapason that allows to ionize the atoms with ionization potentials up to 10 eV (*i.e.* almost all elements of the Periodic Table). To meet these requirements a completely different, more sophisticated laser installation has to be built.

The scheme of a new laser-nuclear experimental setup to be constructed at the IRIS facility is presented in Fig. 6. A master oscillator – power amplifier system of copper vapor lasers (CVL) provides two output laser beams in the form of 15 ns pulses at a repetition rate of 9–11 kHz, each with an average power of typically 30–40 W. The lasers rely on stimulated emission from two copper spectral lines, resulting in laser light comprising of green (511 nm) and yellow (578 nm) components.

After separation of these components, four beams are available for the pumping of dye lasers and, where applicable, non-resonant ionization of atoms brought to a highly excited state by one or more resonant photon absorption steps. The LIS setup includes three dye lasers and, therefore, ionization schemes employing up to three resonant transitions can be used. The wavelength range of the dye lasers is 530–850 nm.

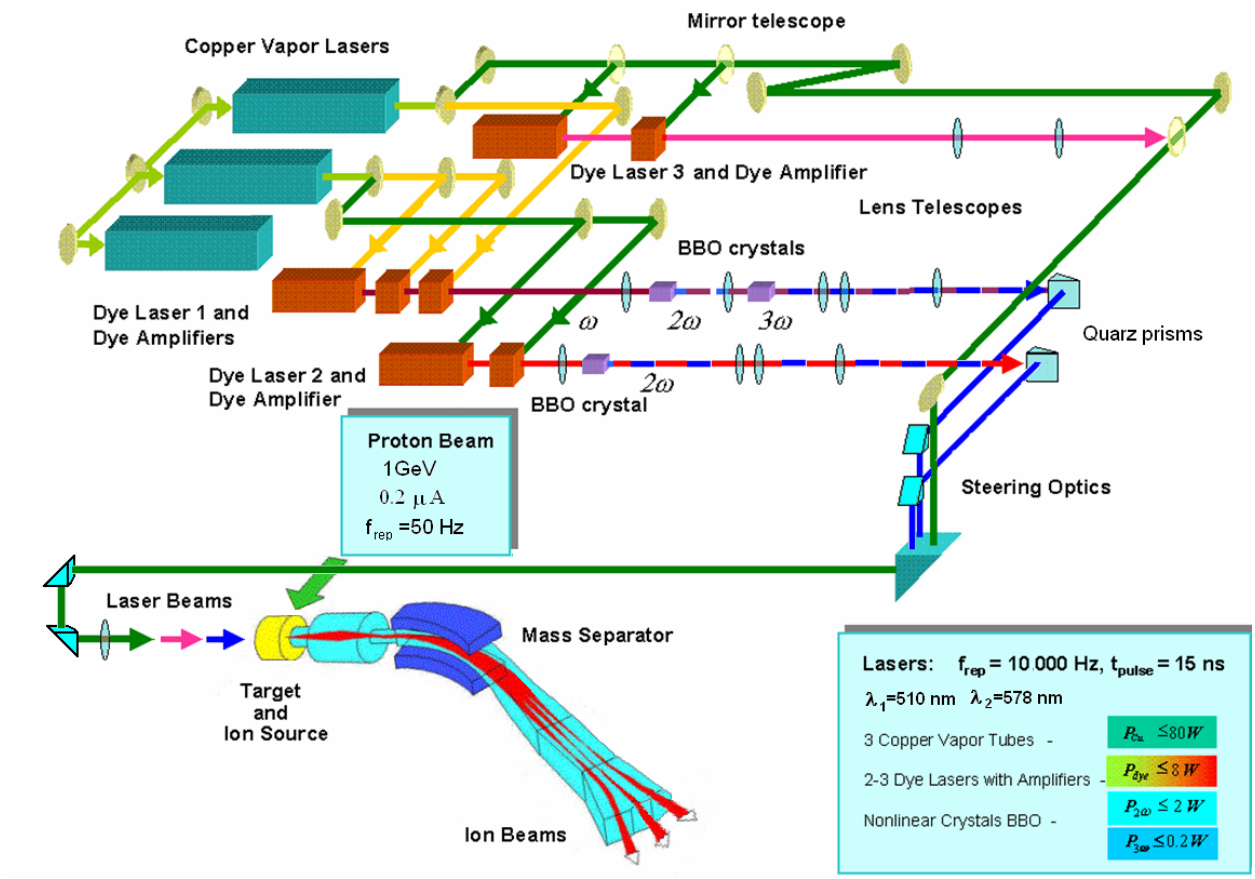

Fig. 6. Scheme of a new universal laser-nuclear experimental set-up which is under construction at IRIS facility

Tuning is achieved by rotation of the diffraction grating in the laser resonator cavity and, depending on the diffraction grating used, the spectral width of the laser line is between 9 and 30 GHz. Frequency doubling and summation (tripling) is carried out using non-linear BBO (beta-barium borate) crystals to generate second or third harmonics of the fundamental beam, extending the wavelength range to include 214–415 nm. This enables high lying first excited atomic states to be accessed and is crucial for elements with a high ionization potential. Schemes using one, two or three resonant transitions can be used. Most commonly, the last step is a transition to the continuum using an available CVL beam. Alternatively, the final step can be a resonant transition to an autoionizing state. A transition to the autoionizing state usually has a higher cross section than a non-resonant transition into continuum; this improves both the ionization efficiency and the stability of the ion current.

The ionization takes place in a hot cavity connected to the target. Reaction products enter this cavity as an atomic vapor at a high temperature (near 2300°C). The role of the cavity is to preserve the atoms for a certain time within a volume where they can be irradiated by the laser light and to confine the ions during their drift towards the extraction region. The ionization cavities are refractory metal (W, Ta or Nb) tubes. They are resistively heated to a temperature up to 3000°C (in the case of W ionizator) with a DC current of 200–350 A. After leaving the source, ions are accelerated to 30 kV, separated in a magnetic field and guided to the user by electrostatic ion-optical elements. Operating in narrow band mode where the laser bandwidth is reduced to 1 GHz, *i.e.* becomes close to that of the Doppler broadening of the atomic transitions (~ 1–3 GHz), the LIS can be used as a precise spectroscopic tool for the isotope shift and hyperfine structure study.

4. Conclusion

As one can see from the above consideration, the application of the laser ion source method opens wide possibilities for very different investigations with the chemically, isobar and isomer pure radioactive beams. The new universal laser complex at IRIS facility should provide these beams of exotic nuclides that is of great importance for many scientific areas. Presently, the first stage of the universal laser ionization spectroscopy system (new advanced pump copper-vapor lasers with their power supplies) has been built and delivered to the IRIS experimental hall. It will be put into operation in 2007. The following new developments in the region of the laser resonance ionization and the efficient target-ion source units will make it possible to enlarge considerably the areas of scientific applicability of the IRIS facility. Besides the studies of structure and properties of exotic nuclei, the new applications can be developed. As it has been demonstrated by the world leading ISOL facilities such as ISOLDE (CERN) and ISAC (TRIUMF, Canada), the high intensive and selective isotope and isomer beams can be used also in solid state physics to investigate the properties of new semiconductors and other materials. Another important application of ISOL facilities can be a radioisotope production for medical investigations. Short-lived isotopes can be used for non-invasive methods of internal organ and metabolism studies. It is of great importance for early and precise diagnostics.

References

1. V.N. Panteleev, in *Materials of the EURISOL town meeting*, CERN, Geneva, 26 – 29 November 2006.
2. A.E. Barzakh *et al*., Phys. Rev. C **61**, 034304 (2000).

PROJECT "EPECUR": SEARCH FOR EXOTIC BARYONS IN REACTIONS $\pi^- p \to \pi^- p$ AND $\pi^- p \to K\Lambda$ AT THE MESON CHANNEL OF THE ITEP ACCELERATOR

PNPI participants of the PNPI-ITEP Collaboration:
A.I. Kovalev, N.G. Kozlenko, V.S. Kozlov, A.G. Krivshich, D.V. Novinsky, V.V. Sumachev, V.Yu. Trautman, E.A. Filimonov

1. Introduction

Dramatic events in baryon spectroscopy took place during last years. The narrow exotic baryon θ^+ with strangeness +1 and mass 1540 MeV (Fig. 1) was discovered by LEPS [1] and by DIANA at ITEP [2], which was earlier predicted by the chiral soliton model [3]. Due to its quantum numbers θ^+ can contain four quarks and one antiquark as a minimum, and this is why this particle was called pentaquark. In the chiral soliton model θ^+ belongs to $SU(3)_F$ baryon antidecuplet with the spin and parity equal $½^+$. This antidecuplet should also contain the cryptoexotic baryons with the quantum numbers of the nucleon and Σ hyperon (Fig. 1).

The aim of this proposal is to perform the experimental search for the cryptoexotic non-strange neutral resonance $N_{\overline{10}}$ (isospin projection –1/2) in the reactions $\pi^- p \to \pi^- p$ and/or $\pi^- p \to K\Lambda$. According to the spin/parity of the antidecuplet ($½^+$) the resonant effect should be searched in the P_{11}-wave.

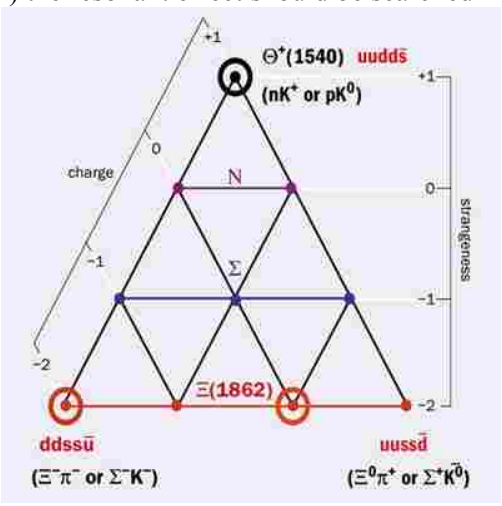

Fig. 1. "Pentaquark" antidecuplet

2. Experiment motivation and layout

The general idea of the proposal is to look for the $N_{\overline{10}}$ effects in the cross section in the "formation" type experiments using the $\pi^- p$ elastic scattering and the reaction $\pi^- p \to K\Lambda$. The scan of the mass interval under investigation will be done by changing the incident pion momentum. Secondary pion beams with appropriate intensity and energy are available at ITEP from its 10 GeV proton synchrotron. Two-focused beam-line optics provides the possibility to analyze the individual pion momentum with the accuracy up to 0.06–0.15%, having the total momentum range of $\Delta p/p = \pm 2\%$. The wide energy range of 0.8–2.5 GeV/c can be covered by changing the magnetic elements currents.

The results of measurements may be analyzed by the standard procedure of the partial-wave analysis (PWA), that is the important advantage of the "formation" type experiments. In particular, it means that all quantum numbers of the resonance, if found, can be unambiguously determined.

---

[1] T. Nakano *et al*. (LEPS Collaboration), Phys. Rev. Lett. **91**, 012002 (2003).
[2] V. V. Barmin *et al.* (DIANA Collaboration), Phys. Atom. Nucl. **66**, 1715 (2003).
[3] D. Diakonov, V. Petrov and M. Polyakov, Z. Phys. A **359**, 305 (1997).

2.1. Background information

The existing data on non-exotic P_{11} resonance in the region of 1700 MeV and estimates of the expected effect are presented in the following section.

2.1.1. "Common" resonance *N*(1710)

The following summary on the non-exotic P_{11} resonance $N(1710)$ is taken mainly from the "Review of Particle Properties" (RPP) [4]. This resonance has a rating of three stars (***). According to the results of the energy independent partial-wave analyses (IPWA) KH80 [5] and CMB80 [6], the mass and width of this resonance are M_R = 1723 ± 9 MeV, Γ = 120 ± 15 MeV and M_R = 1700 ± 50 MeV, Γ = 90 ± 30 MeV, respectively. The multichannel analysis of the $\pi N \to N\pi$ and $\pi N \to N\pi\pi$ partial waves by KSU [7] has two solutions, predicting either a wide resonance with Γ= 480 ± 230 MeV or a narrow one with Γ = 50 ± 40 MeV at the same mass of M_R = 1717 ± 28 MeV. In the recent energy dependent (DPWA) analysis FA02 [8] of GWU group the resonance $N(1710)$ is not observed. The estimates for the branching ratios for $N\pi$ and $K\Lambda$ channels are 10–20% and 5–25%, respectively. In spite of rather high RPP rating, the resonance parameters are poorly defined and even its existence is doubtful, suggesting further experimental studies in corresponding energy region.

2.1.2. Observable choice – some formulas

The formulas presented in this section are intended to illustrate the choice of the observables that should be measured in $\pi^- p$ interactions to get the optimal sensitivity for a resonant effect.

The decomposition of the scattering amplitude into partial waves:

$$f_{el}(\theta, E) = \frac{1}{2ik}\sum_{l=0}^{l_{\max}}(2l+1)(\eta_l \cdot e^{2i\delta_l} - 1)P_l(\cos\theta),$$

where δ_l is the phase, η_l is the elasticity of l-wave and the term

$$f_l = \frac{\eta_l \cdot e^{2i\delta_l} - 1}{2ik}$$

is called the partial amplitude. In the vicinity of a (narrow) resonance the partial amplitude can be written in the form:

$$f_l(E) = f_l^B + f_l^r(E),$$

where f_l^B is the "background" term weakly dependent on the energy, while $f_l^r(E)$ is the resonant term dominantly determining the local energy dependence. The corresponding partial cross section will be:

$$\sigma_l = 4\pi(2l+1)|f_l^B + f_l^r|^2 \ . \qquad (1)$$

The following considerations will be presented in parallel for the both reactions mentioned in this proposal in order to get direct comparison of the two cases.

---

[4] Particle Data Group, J. Phys. G **33** (2006).
[5] G. Hohler, *"Pion-nucleon scattering",* Landolt-Bornstein **I/9b2** (Springer-Verlag, 1983).
[6] R.E. Cutkosky *et al.*, Phys. Rev. D **20**, 2839 (1979).
[7] D.M. Manley and E. M. Saleski, Phys. Rev D **45**, 235 (1990).
[8] R.A. Arndt *et al.*, Phys. Rev. C **69**, 035213 (2004).

$\pi^- p \to \pi^- p$	$\pi^- p \to K\Lambda$

The Breit-Wigner resonant amplitude:

$f_l^r(E) = -\dfrac{e^{i\varphi}\Gamma_{el}}{2k\left[(E-E_r)+i\Gamma/2\right]}$	$f_l^r(E) = -\dfrac{e^{i\varphi}\sqrt{\Gamma_{el}\Gamma_{K\Lambda}}}{2\sqrt{kk_{K\Lambda}}\left[(E-E_r)+i\Gamma/2\right]}$

The BW amplitude value in the resonance

$f_l^r(E_r) = i\dfrac{e^{i\varphi}X}{k},$	$f_l^r(E_r) = i\dfrac{e^{i\varphi}\sqrt{X\cdot BR}}{\sqrt{kk_{K\Lambda}}},$
where $X = \Gamma_{el}/\Gamma$ is the branching ratio to the $\pi^- p$ channel	where $BR = \Gamma_{K\Lambda}/\Gamma$ is the branching ratio to the $K\Lambda$ channel

Neglecting the interference term in Eq. (1) for a rough estimate, the resonant effect in the total reaction cross section will be:

$\Delta\sigma_{el}^r = (2l+1)\cdot\dfrac{4\pi}{k^2}\cdot X^2$ (2a)	$\Delta\sigma_{K\Lambda}^r = (2l+1)\cdot\dfrac{4\pi}{kk_{K\Lambda}}\cdot X\cdot BR$ (2b)

For P_{11}-wave (l = 1), taking the resonance mass m_r = 1.7 GeV, k = 0.56 GeV/c, $k_{K\Lambda}$ = 0.2 GeV/c (both at $W_{cm} = m_r$) and assuming X = 0.01, BR = 0.1:

$\Delta\sigma^r{}_{el}$ = 0.005 mb	$\Delta\sigma^r{}_{K\Lambda}$ = 0.13 mb

Or in terms of the relative cross section change ($\sigma_{el} \approx 10$ mb, $\sigma_{K\Lambda} \approx 0.9$ mb)

$\Delta\sigma^r{}_{el}/\sigma_{el}$ = 0.05%	$\Delta\sigma^r{}_{K\Lambda}/\sigma_{K\Lambda}$ = 15%

The conclusion is obvious: the total cross section of the reaction $\pi^- p \to K\Lambda$ is highly sensitive to the resonant effect, even assuming very conservative values for the branching ratios. At the same time, the total cross section of the $\pi^- p$ elastic scattering has very low sensitivity to resonances with low X, because of the X^2 nature of the effect. Instead, as will be shown in the next section, the differential cross section of this process can be used for the search, because it reveals and, in certain angular regions, emphasizes the contribution of the interference terms containing the products of the resonant wave amplitude and the amplitudes of other (non-resonant) waves. It is worth mentioning that this contribution is proportional to X, but not to X^2.

2.1.3. Expected effects

In case of the $\pi^- p$ elastic scattering it is possible to evaluate accurately the sensitivity of the differential cross section to the resonant change of the phase δ_{P11} and of the elasticity η_{P11} of P_{11}-wave using the PWA results.

Figure 2 illustrates how $N_{\overline{10}}$ could be seen in the $\pi^- p$ elastic scattering assuming its mass and width equal to 1671 MeV and 6 MeV, respectively, and elasticity X = 5%. The insertion in the top right corner is the zoom of the area around the resonance. Error bars and the point density correspond to the proposed statistical accuracy and momentum resolution. It is worth mentioning that the effect of the resonance can be either a minimum (as in Figure), a maximum or a bipolar structure dependent on its unpredictable pole residue phase.

As shown above, the reaction $\pi^- p \to K\Lambda$ is even more promising for the search of the resonances with small elasticity. Compared to the elastic case the cross section of the process itself is low, making its resonant change relatively more pronounceable. The sensitivity of this process to the resonant effects is significantly enhanced by the fact that the energy region under study is close to the reaction threshold (mind the term $k_{K\Lambda}$ in the denominator of (2b)). Another argument in favor of this reaction is that the branching ratio of $N_{\overline{10}}$ to this channel is predicted larger than that to the $\pi^- p$ channel [9].

[9] R.A. Arndt *et al*., Phys. Rev. C **69**, 035208 (2004).

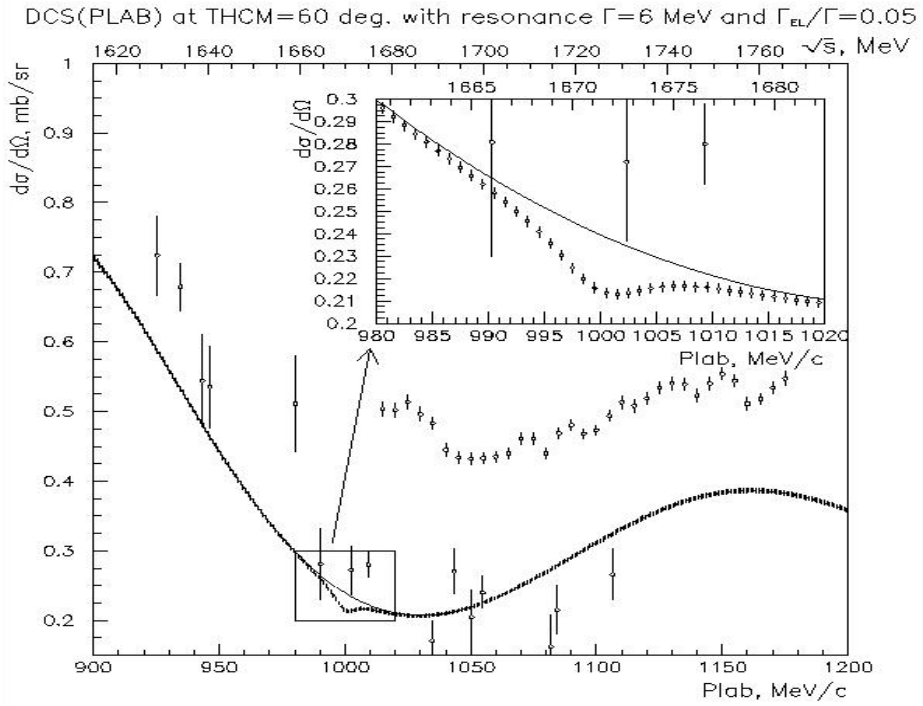

Fig. 2. $\pi^- p$ elastic differential cross section at 60° c.m.s. as a function of pion momentum in the presence of $N_{\overline{10}}$; the upper scale is the c.m.s. energy. The most accurate existing data are at a different angle

2.2. General requirements to the setup

Large uncertainties in expected parameters of the resonance under search lead to following requirements:

- Coverage of mass interval 1610–1770 MeV.
- Mass resolution ≤1 MeV.
- Statistics sufficient for registration of resonance with elasticity ≤5% and branching ratio to KΛ ≤10%.
- High detector efficiency.
- Long-term efficiency stability to get undistorted energy dependence in the mass interval ~160 MeV.
- Possibility of the internal cross-check of the results.
- Reliable background suppression.
- High accuracy of track detectors (better than 0.15 mm) for *K*- and Λ-decay vertex reconstruction.
- Minimal amount of substance on the path of initial particles and reaction products (momentum resolution and vertex reconstruction).

2.3. Setup for $N_{\overline{10}}$ resonance search in the $\pi^- p$ elastic scattering

2.3.1. Setup layout

The layout of the setup for the search for $N_{\overline{10}}$ in the $\pi^- p$ elastic scattering is shown in Fig. 3. The setup consists of the following main elements:

- Proportional chambers PC1–PC3 located at the first focus of the ITEP beam-line 322 for the incident pion momentum measurement.
- Proportional chambers PC4–PC6 for tracking of the incident pions.
- Liquid hydrogen target with 1 mm beryllium cover, 4 cm in diameter, 25 cm long.
- Sets of drift chambers DC1–DC4 for tracking of the reaction products.
- Beam scintillation counters S1, S2, trigger hodoscopes H2, H3 with time-of-flight measurements features, veto- and beam TOF counter A1.

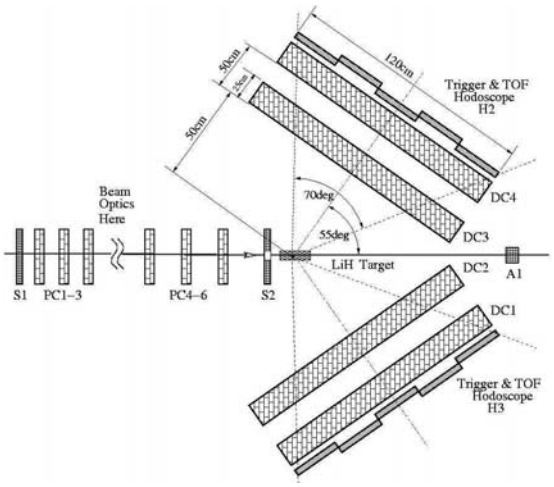

Fig. 3. Setup for $N_{\overline{10}}$ search in $\pi^- p$ elastic scattering

2.3.2. Setup geometry

The setup geometry was defined from the requirement of the coverage of c.m.s. angular interval 40°–120° including the interval 50°–100° highly sensitive to the P_{11}-wave and the interval of low sensitivity, that is essential for the result cross-check. The total azimuthal angle coverage is 2 rad. The angular error is determined by the multiple scattering in the target container, liquid hydrogen and the drift chamber materials. In the proposed experimental scheme the main criteria for the selection of elastic events are the angular correlations of the polar angles of scattered pions and protons and the coplanarity. The additional selection criterion is the requirement of the common interaction vertex for the pion and the proton. Therefore it is necessary to use the chambers with minimum amount of light substance (with large radiation length) on the path of scattered particles to achieve the cleanest experimental result.

2.3.3. Pion beam and momentum measurement

The ITEP 10-GeV proton synchrotron has secondary pion beams which are ideally suitable for the proposed experiment. The energy range, momentum resolution, beam intensity allow to measure the differential cross sections with a precision an order of magnitude better than in all previous measurements. Currently only ITEP has pion beams of such quality.

In this proposal wire drift chambers with honeycomb cells and modular structure are considered. The sensitive region of each module is 80×120 cm^2 in size, the thickness is 25 cm. Each module contains two X-planes, two Y-planes and two stereoplanes. The amount of substance for the module is determined mainly by the external walls of mylar and is equal to 0.2–0.3 mm per module. Drift length is 10 mm. One module contains 320 signal wires approximately. The expected coordinate accuracy is less than 0.15 mm. The set of two detectors in each arm provides the essential over-determination of the tracks (in average 5 coordinates in each projection). Such detector structure guarantees the high efficiency and stability of the tracking part.

The following is the summary of the ITEP 322 beam-line features:

- Momentum range 0.8–2.5 GeV/c.
- Intensity at the target $(2–3)\times10^5$ π^-/cycle.
- Beam impurities (other particles) <1% total.
- Repetition rate 15 cycles/min, up to 1000 ms flattop.
- 2-stage achromatic optics.
- Spot-size at the second focus of 10–12 mm (FWHM).
- Momentum dispersion at the first focus 50 mm/%.
- Momentum resolution of 0.08% in the interval ±2%.
- Transport length 40 m, 3 dipole magnets, 5 quadrupole lenses.

To measure the pion momentum one needs to define the crossing point of its track with the imaginary focal plane of the first focus. The focal plane is stretched along the beam-line for 2.5 m, while allowing the particles to travel such a distance in air would lead to unwanted increase of the momentum spread due to the ionization losses. This is why the set of three proportional chambers at the first focus is inserted into only 60 cm air gap in the beam-line vacuum pipe and the track is then continued to find the crossing with the focal plane. Such approach requires good coordinate accuracy of tracking detectors, together with small amount of substance on the path of the particles. Proportional chambers with 1 mm wire spacing will be used.

The momentum resolution is determined by the size of the internal target image at the first focus of the beam-line, which is defined by a number of factors including the shape of the internal target. Yet the momentum resolution ~0.1% can be readily obtained [10] leading to a conservative estimate of the mass resolution as low as $\Delta M_x \approx \Delta p \cdot M_p / M_x = 0.56$ MeV at the central pion momentum of 1 GeV/c.

The search for a resonance itself does not require the absolute momentum calibration. It is only necessary to maintain the stability of the internal target position and of the dipole magnetic fields. But the absolute mometum knowledge is required for the precise determination of the resonance mass, if found. Such calibration can be fulfilled using the process of elastic scattering of protons from an internal polyethylene target with an accuracy ≤0.3% defined by the knowledge of the proton energy in the accelerator ring.

The field stability of three dipole magnets must be checked by means of a magnetic field sensor with a precision better than 0.1%. A standard instrument based on the nuclear magnetic resonance (NMR) can be used for this purpose. Direct monitoring of the pion beam momentum is also possible by measuring the difference in the time of flight of the negative pions and antiprotons which are present in the beam at the level of 10^{-3}. But the absolute long-term stability of such TOF system may appear worse than the required precision[11].

2.4. Setup for baryon resonance study in the reaction $\pi^- p \to K\Lambda$

The reaction $\pi^- p \to K\Lambda$ has several properties attractive for the baryon spectroscopy studies in general and for the proposed experiment in particular.

- Pure isotopic state with isospin ½.
- Sizeable threshold of $K\Lambda$ production facilitating the study of resonances with small spin and large mass
- High analyzing power of $\Lambda \to \pi^- p$ weak decay with the asymmetry $\alpha = 0.642$.
- The threshold of $K\Lambda$ production is lower than that of a competitive process with $K^0\Sigma^0$ production.
- Significant fraction of the charged mode (22% of the total reaction cross section).
- Large total cross section (~0.9 mb[12]) in the considered energy interval.

These arguments along with the ones from Sec. 2.1.2 and 2.1.3 makes $\pi^- p \to K\Lambda$ reaction extremely attractive for the search of the cryptoexotic state $N_{\overline{10}}$.

2.4.1. Specific properties of $\pi^- p \to K\Lambda$ detection

The setup for $\pi^- p \to K\Lambda$ studying can be considered as an extension of the setup for the $N_{\overline{10}}$ search in the elastic scattering. The general requirements, listed in Sec. 2.2, are also applicable here. All elements considered in Sec. 2.3 can be reused, the detector placement changed according to the reaction kinematics. More drift chambers are necessary to cover larger acceptance, as well as significant improvements to the TOF system according to more strict requirements of the final proton identification.

The specific kinematical properties of the reaction $\pi^- p \to K\Lambda$ are enumerated below:

- It is necessary to detect 4 charged particles in the final state ($K^0 \to \pi^+\pi^-$, $\Lambda \to \pi^- p$).
- Most of the particles from the Λ decays go to the forward hemisphere but angles of the pion trajectories can be large relative to the incident pion direction.

---

[10] L.Z. Barabash *et al.*, Preprint ITEP-115-75, M., 1975.
[11] I.G. Alekseev *et al.*, Preprint ITEP-184-88, M., 1988.
[12] R.D. Baker *et al.*, Nucl. Phys. B **141**, 29 (1978).

- The pions from K^0 decays have a broad angular distribution with long tails covering 90° and backward regions.
- The identification of a single proton is highly important for the suppression of other inelastic reactions with four or more charged particles as well as for the Λ polarization measurement.
- Most of the events have either all four particles in the forward direction (~20%) or a proton and two pions going forward, the third pion sideward or upward (~80%).

Thus to reach the reasonable acceptance of the setup one needs nearly 4π hermetic detector system with a large coverage angle for the particles emitted in the forward hemisphere. Unlike the elastic case, the TOF hodoscope must be segmented taking into account the multi-particle feature of the reaction and its time resolution should be improved as it will be shown below.

2.4.2. Setup layout

The proposed setup is shown in Fig. 4.

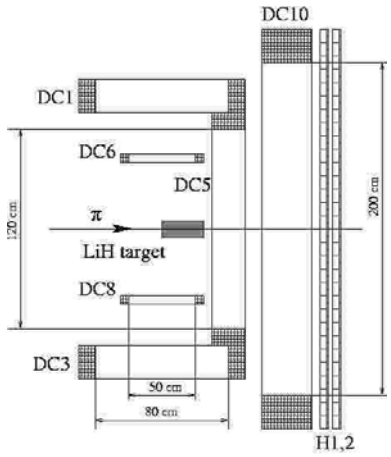

Fig. 4. Setup for $N_{\overline{10}}$ search in $\pi^- p \to K\Lambda$ reaction

- The outer chambers DC1–DC5 have the size of the sensitive area 80×120 cm^2, the same as described in Sec. 2.3. The number of chambers is increased from 4 to 5. The chambers cover both sides of the beam, top, bottom and forward directions, forming a parallelepiped open at one side.
- The smaller inner chambers DC6–DC9 cover the angular range in the up/down and left/right directions. These chambers have only X- and Y-pairs of signal layers, the size of the sensitive area is 50×70 cm^2, the thickness is 10 cm.
- The large chamber DC10 with the size of 140×200 cm^2 is used for the forward scattering registration.
- The two-coordinate segmented hodoscope H1,2 is placed at a distance of 2 m from the target and covers the whole sensitive area of DC10, providing the trigger logic and TOF measurement for proton identification. The cell size is 10×10 cm^2. Such granularity as well as the requirement of good TOF measurement are necessary only in the central part of the hodoscope with the size 100×100 cm^2, since the most of the protons from the Λ-decay go into this region.

2.5. Counting rates and run times

2.5.1. The $\pi^- p$ elastic scattering

It is proposed to divide the angular range sensitive to the P_{11}-wave into two subintervals and to reach 0.5% statistical error in each subinterval. In this case a separation of 5% resonant effect would be achieved at 10 standard deviation level. Assuming the bin width in the mass interval 1610–1770 MeV equal to the momentum resolution (0.56 MeV), the total number of momentum-angular intervals in the sensitive range is (160/0.56)×2 =570. The necessary total statistics of the elastic scattering events is thus $4\times10^4\times570 =$ **23×10^6**.

Using the following assumptions:

- the differential cross section is equal to 0.2 mb/sr,
- the solid angle acceptance of the setup is 1.7 sr,
- the target thickness is equal to 0.071 g/cm^3 × 25 cm = 1.78 g/cm^2
- the beam intensity is 50×10^3 s^{-1} (200×10^3 per 4 spill),
- the overall efficiency (accelerator + setup) is at a level of 0.7, the counting rate of the elastic events will be **18.7 s^{-1}** or 75 per an accelerator spill.

The duration of the experiment is: $23\times10^6/(18.7\times0.7) = 1.75\times10^6$ s or **20 days**, *i.e.* 2 runs 10 days each.

2.5.2. The reaction $\pi^- p \to K\Lambda$

For the counting rate calculation the total reaction cross section was taken equal to 0.9 mb at 1 GeV/c, and the acceptance for the charged mode of 20% was assumed. The assumptions about the beam and the target parameters are the same as in the elastic scattering case. The calculation results in the counting rate of 125×10^3 events per day. In order to provide the reliable separation of 10% resonant effect in the total reaction cross section at 10 standard deviation level, the statistics of $10^4 \times (160/0.56) =$ **2.9×10^6** is required, which can be obtained in **23 days** or in 2 runs of 12-day duration each.

3. Conclusion

As a conclusion, the authors would emphasize several statements concerning this proposal.

- The world scientific community reveals a big interest to the recently discovered exotic particles.
- As a result, numerous theoretical models got a powerful stimulus for their development, requiring an experimental confirmation or denial of their ideas.
- Pion beams at ITEP are ideally suitable for the experimental search for the non-strange cryptoexotic member of the pentaquark antidecuplet.
- At the moment there are no other pion beams in the world which may offer such possibility.
- The experimental conditions are extremely favorable for the suggested experiment.
- If the resonant state is discovered, not only its mass can be determined but also the width as well as all the quantum numbers. It is also possible to extract the branching ratio for the decays to $\pi^- p$ and $K\Lambda$ channels, providing the information about the amount of the strange component in $N_{\overline{10}}$.
- If no resonant effect is observed either in $\pi^- p \to \pi^- p$ or in $\pi^- p \to K\Lambda$ reaction, such negative result is also very important for the checks and development of theoretical models. In this case rather hard limit will be imposed on the $N_{\overline{10}}$ production cross section in the two reactions under consideration.
- Moreover, the data on the differential cross sections in both reactions and normal polarization in $\pi^- p \to K\Lambda$ are of great self-importance, it will be readily used by new partial-wave analyses.
- The discussion of this proposal with theorists showed their high interest to the expected results and the validity of the experimental idea as a whole. Several experimental groups from ITEP and PNPI expressed the readiness to participate in this project by manpower and existing equipment.
- There exist teams at ITEP and PNPI which have a long lasting experience in performing of such type experiments, including their setup, running and data analysis. Currently, both teams in collaboration are finishing a series of works on the study of the elastic pion-proton polarization parameters with the SPIN setup at ITEP (see, for example, Ref. [1]).
- The proposed experiment [2] is senseless if not completed on a reasonable time scale (3 years). This requires essential concentration of manpower and financial investments. Only united efforts of several physics institutions may allow to achieve this goal.

References

1. I.G. Alekseev *et al*. (PNPI-ITEP Collaboration), Eur. Phys. J. C **45**, 383 (2006).
2. I.G. Alekseev *et al*. (PNPI-ITEP Collaboration), Preprint ITEP-2-05, M., 2005. 20 p.

EXPERIMENT "FAMILON": SEARCH FOR MUON NEUTRINOLESS DECAY

V.A. Gordeev, V.S. Demidov[1)], V.N. Duginov[2)], Yu.V. Elkin

[1)] *Institute for Theoretical and Experimental Physics, Moscow*

[2)] *Joint Institute for Nuclear Research, Dubna*

The experimental test of possible expansion of the Higgs sector is under study. The standard model of particle interactions is based on the principle of gauge symmetry, offering the theoretically esthetical way to introduce the intermediate bosons of fundamental particle interactions and to explain the difference between weak and electromagnetic forces *via* the Higgs mechanism of symmetry breaking. After the discovery of $W^{\pm}$ and Z^0 bosons at LEP (CERN) there were only few doubts about the content of that part of the Glashow-Weinberg-Salam theory which concerns the interaction of vector bosons with quarks and leptons. It seems that the next and probably the decisive checkout of this theory would be the detection of Higgs bosons. Really, the major property of the Glashow-Weinberg-Salam theory is renormalizability. Nobody has managed to construct a renormalized theory containing massive vector bosons without introducing Higgs fields until now. In a simple version of the theory there is only one elementary Higgs doublet. It means that after the implication of Goldstone degrees of freedom to construct massive charged $W^{\pm}$ and neutral Z^0 bosons, only one observable neutral Higgs boson remains. However, there are no grounds to assume that the Higgs sector is so poor. Contrariwise, there are theoretical reasons to extend the symmetry beyond the Standard Model and to suppose that if scalar particles exist in general, their number can be significant.

Spontaneous breaking of the global family symmetry results in the prediction of Goldstone boson called familon. In the case of global $SU(3)_H$ family symmetry breaking, the octet of massless familons is predicted. In the model of singlet familon (Anselm and Uraltzev, 1983) the family symmetry breaking results in the prediction of a single familon state. The familon exchange leads to effective flavor changing neutral current processes, such as $\mu \to 3e$ or $K \to \mu e$. However, for small familon coupling constant f the probability of such processes is of the order of f^4, whereas decays with free familon emission are much less suppressed being of the order of f^2. Thus the familon model can find much more sensitive test in the searches for the free familon emission in decays of charged leptons, such as $\mu \to e\alpha$. In hardronic decays the search for familon decay modes is complicated by the necessity to account for the structure of hadrons and is restricted by the selection rules in the hadron transitions. It is important that familon decays of charged leptons take place both for scalar and pseudoscalar couplings and are much easier interpreted in the terms of bare familon interaction.

Anselm, Uraltsev and Khlopov has estimated the scale of family symmetry breaking from the unstable neutrino models of structure formation and predicted the rate of $\mu \to e\alpha$ decay close to the level of sensitivity reached in experiments. The increase of an experimental level of the sensitivity to the lepton family violation decays could play the role of "experimentum cruces" for dark matter cosmological scenarios and familon models underlying them. This aspect of searches for rare lepton decays was strongly evolved in the successive development of cosmoparticle physics, studying fundamental relationship between cosmology and particle physics.

The experimental method of the search for $\mu^+ \to e^+\alpha$ decay based on the dependence between the differential rate of the decay and electron energy, muon polarization and angle between electron and muon. The vector of positron momentum and muon polarization has to be measured.

The main components of the experimental setup such as the spectrometer magnet, tracking system and beam channel have been installed earlier. The "FAMILON" setup is mounted at the surface muon beam of the phasotron at LNP JINR (Dubna). It is the precision spectrometer for measuring momentum of positrons with energy near 50 MeV. The tracking system consists of 4 proportional chambers in front of and behind the magnet for measuring positron directions. For μSR-analysis two pairs of Helmholtz coils are used.

In the period 2002–2006 the results were taken in four fields of activity: **the computer support**, **simulation of the proposed experiment, development of the software and appropriate apparatus.**

The computer support of the experiment "FAMILON" represents the combination of INTERNET connected computers of the institutes – members of the experiment, while the information is concentrated at PNPI. Each individual computer should have the same set of special programs for processing of the experimental information.

The aim of **the simulation** [1, 2] is to evaluate the influence of the substance (air, wires, scintillators and so on) on the precision of the measured positron momentum and to optimize the position of detectors in the setup in order to reach maximum energy accuracy and positron registration efficiency. The magnet sizes, the map of the magnetic field, the construction of the proportional chambers sets, the relative position of the magnet and the target – those are the basic initial data having been introduced into the simulation program.

The uncertainty in the positron momentum p is defined mainly by the uncertainty in the reconstruction of its direction according to hit wires in the proportional chambers in front of the magnet and behind it. It depends on the wire spacing h in the coordinate planes and on the distance x between chamber planes. The value σ_p/p is used as the relative uncertainty, where σ_p is the r.m.s. deviation. The x-distance dependence of the direction uncertainty σ_θ for 52.83 MeV positron in vacuum and for h = 2 mm is shown in Fig. 1 by falling dotted line. In the real experiment, the positron multiple scattering in the substance of the setup is the main factor which increases errors. The average multiple scattering angle is shown in Fig. 1 as a function of the path length for positrons in air by asterisks connected by growing line. The summary error calculated as the mean geometrical value of these two components is shown by solid line with a wide minimum at 10–18 cm. The distance between sets of proportional chambers in air in front of the magnet and behind it should be obviously equal to ~20 cm to obtain the maximal precision of momentum measurements.

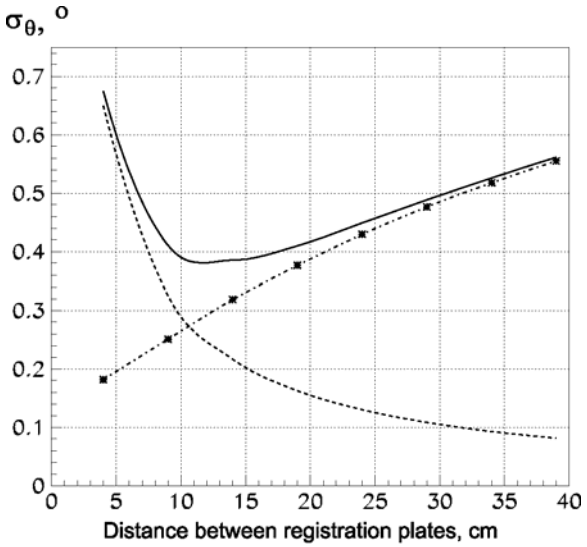

Fig. 1. The dependence of the uncertainty in the positron direction on the distance x (in cm) between registration planes for positron energy of E = 52.8 MeV. Dashed line – the measurement precision in vacuum; dashed-dotted line – the uncertainty due to the multiple scattering; solid line – the error in the real experiment

To evaluate the highest precision of the positron momentum measurement the simulation of the monochromatic positron registration in chambers was carried out without any substance on the positron path: for 52.8 MeV (maximum in the Mishel-spectrum) and 51.8 MeV (1 MeV less). The difference in Y-coordinates at the PC4-plane (see Fig. 2 in Ref. [1]) for the above two energies is 37 mm. From this the transition coefficient from the coordinate error to the energy error follows, it is equal to 0.027 MeV/mm.

To evaluate the influence of substance on the momentum uncertainty, the registration models were simulated for monochromatic positrons with the maximum energy in the Mishel-spectrum and various setup configurations. Fig. 2 shows the Y-coordinate distributions at the PC4-plane for three cases: a) only the construction materials of the proportional chambers are taken into account and the setup is in vacuum (solid line); b) vacuum is only inside the magnet (dots); c) the whole setup is in air (dashed line). One can see that air gives the main contribution to the coordinate dispersion.

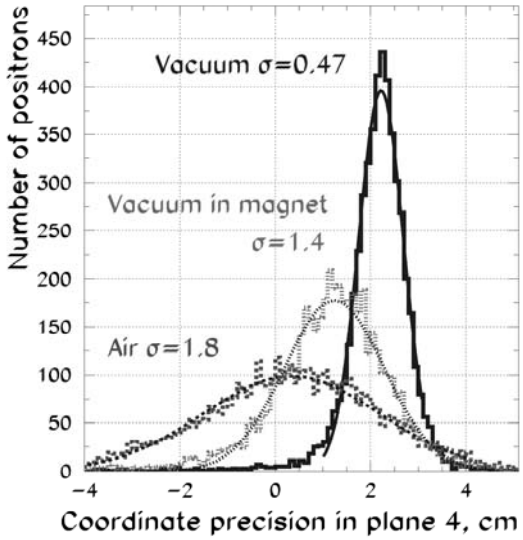

Fig. 2. Y-coordinate distributions at the PC4-plane for 3 cases: a) only construction materials of the proportional chambers are taken into account and the setup is in vacuum (solid line); b) vacuum is only inside the magnet (dots); c) the whole setup is in air (dashes)

Analogous calculations were carried out for another two cases: all space between chambers is filled with helium; vacuum is inside the magnet while the rest space of the setup is in helium.

Analyzing the simulation results one can get the evaluations of the accuracy of momentum measurements for various configurations of the setup. The scale of this accuracy is defined by the r.m.s. deviation in the Y-coordinate distribution at the PC4-plane (the horizontal coordinate of point where positron hits the chamber PC4). The most important results are presented below.

The highest precision of momentum measurements with h = 2 mm in the ideal case (positron in vacuum) is σ_p = 0.025 MeV or $\sigma_p/p \approx 5\times10^{-4}$ for the maximum of Mishel-spectrum.

The maximal attainable precision for the proportional chambers of given construction (a quantity of substance along the positron path) is $\sigma_p/p \approx 2.5\times10^{-3}$ if the whole setup is placed in vacuum.

If vacuum is only inside the magnet, then the momentum uncertainty rises up to $\sigma_p/p \approx 5\times10^{-3}$.

If the whole apparatus of the setup is placed in helium, the precision improves up to $\sigma_p/p \approx 3\times10^{-3}$.

In the case when the whole apparatus is in air $\sigma_p/p \approx 9\times10^{-3}$.

The configuration with vacuum inside the magnet while the rest space is filled with helium seems to be optimal. In this case $\sigma_p/p \approx 2.6\times10^{-3}$. Figure 3 demonstrates the trajectories of 50 positrons with energy of 52.8 MeV for this configuration.

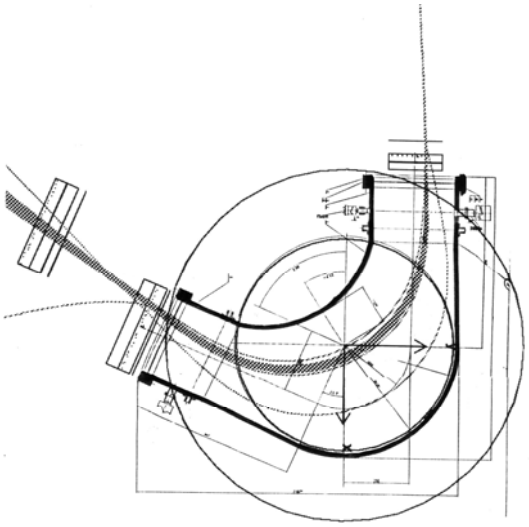

Fig. 3. The simulation results for 52.8 MeV positron trajectories in the setup "FAMILON"

Note that the real precision of momentum measurements will be slightly higher because coordinates of only one chamber have been used in the above evaluations, but for the momentum reconstruction at least two chambers are used.

The further improvement of the precision of momentum measurements may be obtained only if the constructive improvement of the coordinate detectors will decrease the quantity of substance on the positron path.

The important parameter of the experiment is the efficiency of the positron registration as a function of the positron energy and exit angle. This efficiency was also calculated by means of Monte Carlo method for the optimal setup configuration. It was assumed that positrons go isotropically out of the target at the exit angle up to 8° and the positron spectrum is described by the Mishel function. The spectrum in the interval 35–52.8 MeV was considered. The efficiency as a function of two parameters – the positron momentum and the exit angle – was determined as the ratio of two-dimensional histograms: one for registered positrons in chambers PC1–PC4 (see Fig. 2 in Ref. [1]), another – for positrons going out of the target. Figure 4 demonstrates the efficiency dependence on the positron momentum for various exit angles. It can be seen in Fig. 4 that the registration efficiency for positrons in the energy interval from 45 MeV up to maximal value does not fall less than 0.5 at exit angles up to 6°.

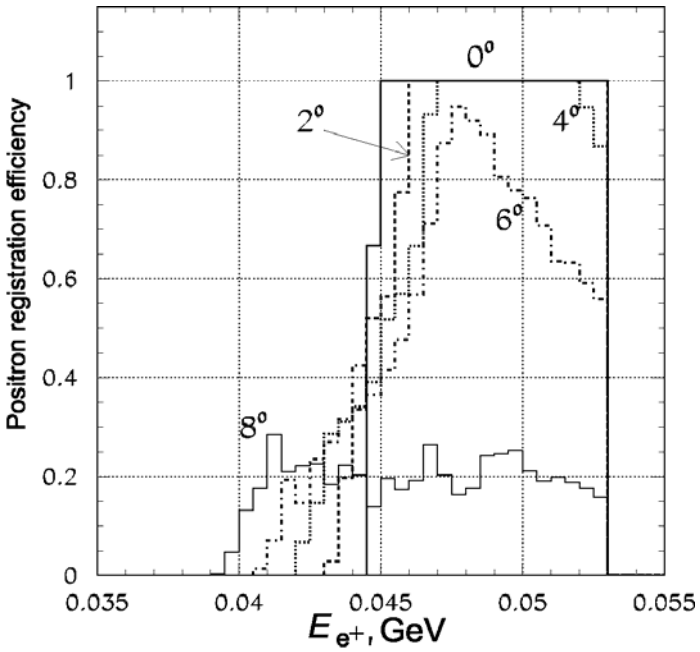

Fig. 4. The dependence of the positron registration efficiency on its energy for five exit angles

The software [3-5] was developed as two packages "alfa-ONL", "alfa-REC".

Software ON-LINE is realized in the system WINDOWS as the package **"alfa-ONL"**. All technologies of the object-oriented programming are maintained. Software ON-LINE functions are as follows [3, 4, 6]:

- test of subsystems of the setup and of the whole system;
- operation of information accumulation in experiments;
- management of on-line processing in experiments;
- parameter selection and the display of experimental information and on-line results;
- viewing of tracks and of the processing results in on-line and off-line regimes.

The resultant rate of apparatus and software is 300–1000 event/s and depends on the number of hit wires.

The main functions of the **"alfa-REC"** package are to reconstruct the positron trajectory in the magnetic field using the data from proportional chambers, to restore the positron energy and to create data array in the NTUPLE format [4]. For the elaboration of the reconstruction algorithm the methods used in another experiments have been analyzed [5]. As a result, the two-level (on-line and off-line) procedure was chosen.

In **on-line** processing two problems are being solved:

– the inspection of a quality of the setup operation, the control of background tracks and false chamber hits, the control of the field where particles going from the target are registered;

– the rough acquisition of the momentum distribution for positrons.

In **off-line** processing the maximum accuracy is required for track parameters. The convergence rate of the solutions of Lorentz equation while the momentum is calculated by the method of successive approximations depends on the choice of the initial approximation p_0.

– At the first stage the initial approximation of momentum is calculated (by the same method that is used in the on-line process).

– At the next stage the track parameter fitting is carried out using the error matrix which includes correlations of the coordinate measurement errors.

Because of non-uniform magnetic field ("end effects") and of the strong change of the field integral along the trajectory it is necessary to determine the initial approximation of the momentum p_0 much more exactly.

The algorithm was elaborated for the determination of parameter errors and for the momentum reconstruction with track hit coordinates in three chambers. This algorithm is used when events are processing in the **on-line** regime. The contribution of the multiple Coulomb scattering to parameter errors of the trajectories depends on the number of chambers in the setup, their position, particle path length in air and in vacuum. If the setup geometry is changed, it is necessary to modify the processing algorithm in the **off-line** regime. The correct evaluation of measurement errors and of the multiple scattering influence will allow to minimize errors of trajectory parameters under real conditions of the experiment.

Apparatus. The precision of measurement of positron energy is determined both by the energy resolution of the magnetic spectrometer and the uncertainty of the positron energy loss in the working target in which muons stop [6]. It is proposed to use in the experiment aluminum with thickness from 150 mg/cm^2 up to 250 mg/cm^2 (the average thickness is 200 mg/cm^2) as the working target. If the target is a single Al plate, then we cannot define the muon stopping point in the target and therefore cannot define the energy loss for positron from muon decay. The average energy loss in substance for relativistic positrons is 2 MeV/g/cm^2. Then the uncertainty in determination of the positron energy is 0.4 MeV and the relative precision for the high-energy region of Mishel-spectrum is not better than 8×10^{-3}. The obvious way to remove the above-mentioned uncertainty is to use an active target which consists of several thin metal foils working as plane-parallel avalanche counter.

The prototype of the active target for the "FAMILON" experiment has been worked out and produced at PNPI [7, 8]. Investigations at the surface muon beam of the LNP JINR phasotron show the high registration efficiency for muon passage through the gas gap of the avalanche detector (99% for 1 mm CO_2 gap at the atmosphere pressure). Also they show the high enough ability for the selection of muons and electrons by means of measuring the detector signal amplitude.

The electronics of the setup "FAMILON" is carried out in the CAMAC standard and has program manipulation through the personal computer. The used interface means – controllers of A2-type, branch drivers and the direct connection of the computer interface with K16 controller – permit to work with crates distant up to 100 m. At the same time the single operation takes 30 μs; this does not limit in our experiment the rate of the statistics accumulation because the maximum anticipated intensity of useful events is 100 s^{-1}.

At present the **new system (CROS3**) is being elaborated at PNPI for the readout of information from coordinate detectors in the experiment "FAMILON". The system CROS3 is the third generation of the data readout systems for coordinate detectors. The CROS3 takes into account all particularities of the previous systems and develops them on the basis of new technologies. The use of special micro-schemes (ASIC) and large micro-schemes with programmed logical connections (FPGA) lets to decrease essentially the system sizes and consumed power and to rise the rate of the information processing. New standards (LVDS, PCI, Optical Link) let to reach high integration not only for the readout system but for the whole experiment electronics. The main characteristics of the system CROS3 are as follows:

– program regulation of the threshold, of the delay time and of the duration of "window" in which signals are registered;

– small system sizes and low dissipated power;

– interfaces in standards LVDS, Optical Link, PCI, Ethernet;
– data readout rate up to 160 Mbite/s;
– reduction of the number of cables;
– small dead time;
– the measurement of the hit channel time distribution inside the registration “window”.

The methodical run was carried out with a purpose to check the working capacity of hard- and software, to evaluate the trigger system efficiency and to verify the validity of simulation [4, 9]. 94148 triggers were registered that have been worked out by the system of scintillation counters when muon decays were displayed in the setup. Events were treated with the program “alfa-REC”. As a result the reliability of proportional chambers and electronics readout system [4] was fixed .

The processing of information provided by the electronics readout system allows μSR-analysis of the registered events including those in which positrons were not registered. Fig. 5 presents the μ-meson lifetime distribution for 49480 events in the range from 0.1 to 4.5 μs. The distribution is the decay exponent modulated by sinusoid with the amplitude depending on the muon polarization value and with the period in accordance with the muon spin precession frequency in the magnetic field of the Helmholtz coils. The exponential fitting of the distribution gives muon mean lifetime of 2.185 ± 0.008 μs that coincides within errors with table value. The function correspondent to the experimental value is drawn by smooth line. Damped harmonic oscillations reflect the time dependence of muon polarization. It is possible to obtain from this fitting curve the precession frequency $f = 2.20 \pm 0.15$ MHz.

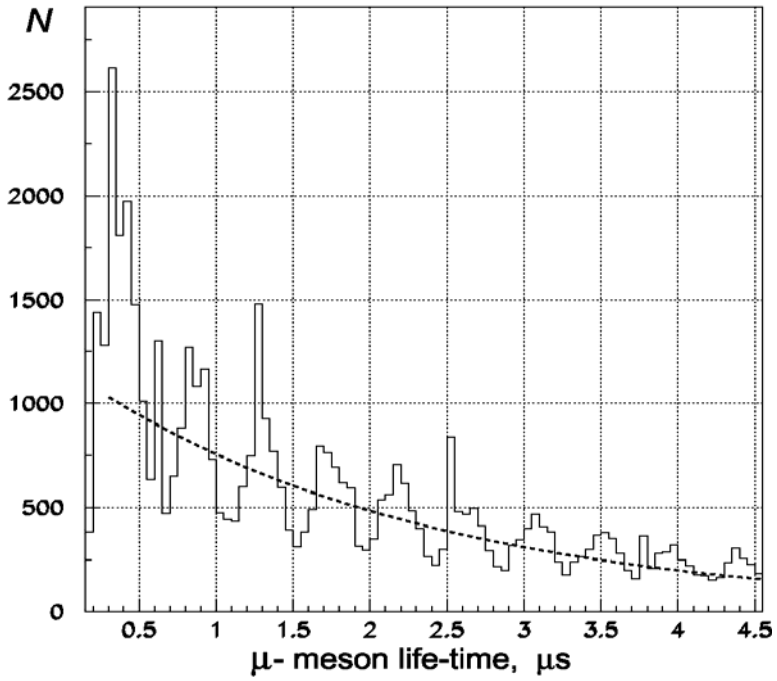

Fig. 5. μ-meson lifetime distribution for 49480 events. The dotted line – the result of the approximation by the exponential function with index 2.185 ± 0.008 μs

Figure 6 presents the positron energy distribution. Let us remind that it was the test run, therefore the spectrometer has not been tuned to register positrons with maximum energy. Nevertheless, the obtained energy spectrum is a good criterion for examination of the simulation program. The spectrum of positrons outgoing from the target was simulated in accordance with the Mishel distribution a part of which is shown by the dotted line. The simulated “measured” positron spectrum is shown by solid line. The coincidence of the calculated spectrum and the experimental one confirms once more that the simulation is correct.

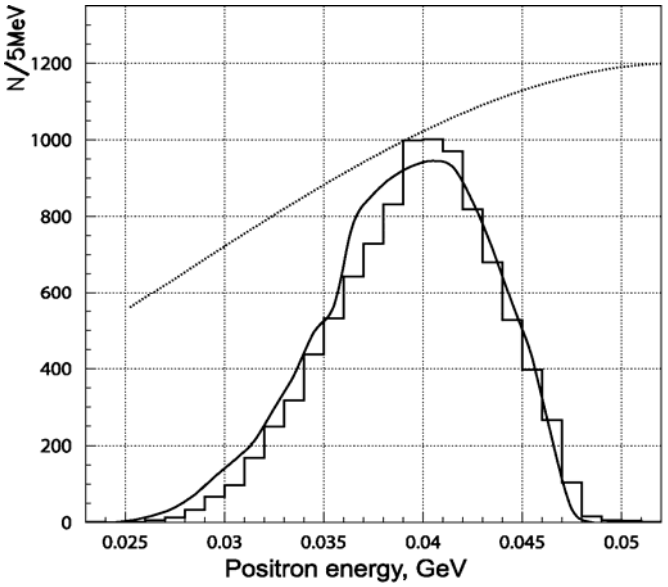

Fig. 6. The energy spectrum of positrons registered in the setup "FAMILON"

The list of participants of the experiment "FAMILON":
V.A. Andreev[1], N.F. Bondarev[1], V.S. Demidov[2], E.V. Demidova[2], V.N. Duginov[3], Yu.V. Elkin[1], V.L. Golovtsov[1], V.A. Gordeev[1], K.I .Gritsai[3], S.A. Gustov[3], V.G. Ivochkin[1], E.M. Karasev[1], M.Yu. Khlopov[4], E.N. Komarov[1], S.V. Kosianenko[1], A.G. Krivshich[1], M.P. Levchenko[1], T.N. Mamedov[3], I.V. Mirokhin[3], V.G. Olshevsky[3], Yu.A. Scheglov[1], G.V. Scherbakov[1], A.Yu. Sokolov[2], Yu.P. Schkurenko[2], A.V. Stoykov[3], L.N. Uvarov[1], S.I. Vorobyev[1], A.A. Zhdanov[1], V.A. Zhukov[3].

[1] – Petersburg Nuclear Physics Institute of RAS (Gatchina)
[2] – Institute for Theoretical and Experimental Physics (Moscow)
[3] – Joint Institute for Nuclear Research (Dubna)
[4] – Institute of Applied Mathematics of RAS, Center for Cosmoparticle Physics "COSMION" (Moscow)

The experiment "FAMILON" is carried out in the framework of special Scientific-Technical Russian Program "Research and elaboration in priority directions of scientific and technical development for civil purposes", subprogram "Fundamental nuclear physics" , project "Physics of rare processes" (State contract № 40.052.1.1.1111 on 31.01.2003); also in the frameworks of RAS Presidium Program "Neutrino physics", RFBR Project (project 99-02-17943-a) and Program of support the leading science schools in Russia (project SS-1867.2003,2).

References

1. V.A. Andreev *et al.*, Preprint ITEP 9-03, M., 2003. 18 p.
2. V.A. Gordeev *et al.,* in *Proceedings of the International Conference on the Spectral Theory of Differential Operation and Related Problems*, Sterlitamac-Ufa: Gilem, vol. **2**, p. 3 (2003)
3. Yu.N. Elkin, Preprint PNPI-2585, Gatchina, 2004. 34 p.
4. V.A. Gordeev *et al.,* Preprint ITEP 14-04, M., 2004. 31 p.
5. V.A. Gordeev *et al.,* Preprint ITEP 2-06, M., 2006. 25 p.
6. V.A. Gordeev *et al.,* in *Proceedings of the XXXIV Winter School of Petersburg Nuclear Physics Institute*, St.-Petersburg, 2004. p. 11.
7. V.G. Ivochkin *et al.*, Preprint PNPI-2507, Gatchina, 2003. 15 p.
8. S.I. Vorobyev *et al.*, Prib. Tekhn. Eksp., No. **5**, 29 (2005) [Instr. Exp. Techn. **48**, No. **5**, 585 (2005)].
9. V.A. Gordeev *et al.,* in *Proceedings of the Scientific Session of the Moscow Engineering and Physics Institute – 2002,* M.: MEPhI, 2002, 2 p.

METODICAL AND APPLIED RESEARCHES

STEREOTAXIC 1000 MeV PROTON THERAPY AT THE PNPI SYNCHROCYCLOTRON

N.K. Abrossimov, Yu.A. Gavrikov, V.Ya. Gersenstein[1)], E.M. Ivanov, N.N. Jalinitch[1)], D.L. Karlin[1)], V.I. Lasarev,V.V. Lysenko, Yu.A. Malov, T.V. Pushkareva[1)], G.A. Riabov, D.M. Seliverstov, R.A. Shalek[1)], V.M. Vinogradov[1)], A.A. Vorobyev, O.M. Zhidkova[1)], M.V. Zhidkov[1)]

[1)] Russian Scientific Center of Radiology and Surgical Technology – RSCRST

1. Introduction

At present the hadron (proton and light ions like ^{12}C) therapy is used successfully for the treatment different types of oncological tumors. Since the beginning of radiological bloodless surgery in 1961 till today more than 50000 patients were treated at 40 medical centers over the world. Figure 1 illustrates the progress in putting into operation medical centers with a number of treated patients more than 1000. On histogram the start year of center's operation is given. The PNPI-RSCRST medical complex as one of the first proton facilities has a long-term experience in the radiotherapy of brain diseases. All acting irradiation centers use in the irradiation treatment so called method of "Bragg peak" required proton energy of 200–250 MeV. PNPI uses in stereotaxic therapy protons with E_p = 1000 MeV, that is the unique method over the world. The advantage of the high energy proton beam is a low scattering of protons in the tissue.

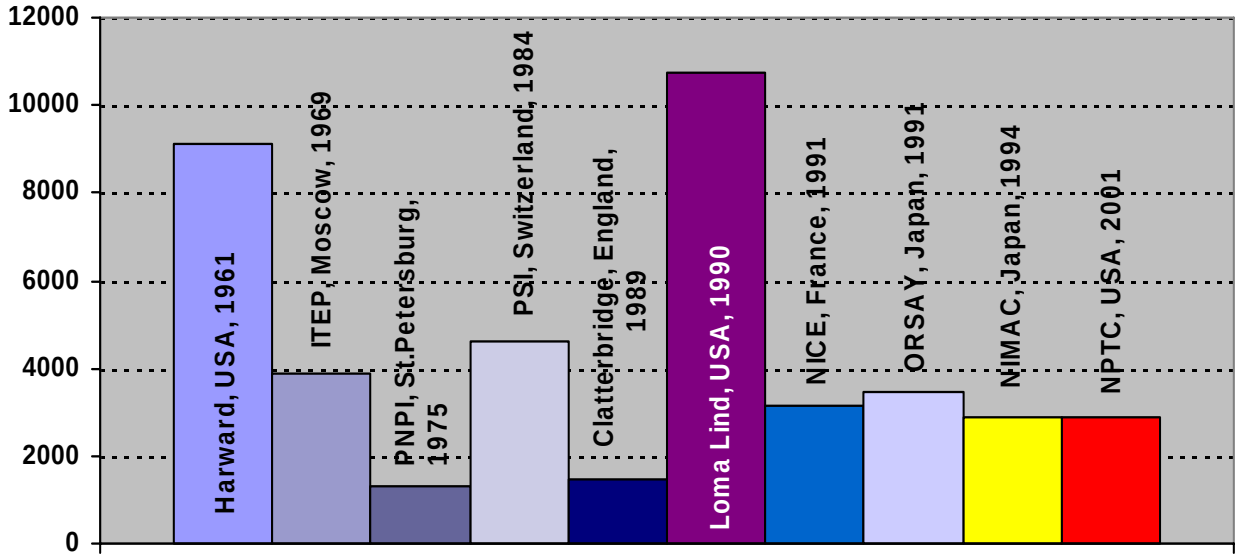

Fig. 1. Medical centers over the world with a number of patients more than 1000 treated by hadron therapy

Protons of this energy easily penetrate through an irradiated object producing a uniform ionization along their tracks. Due to low scattering of protons in the tissue, a narrow beam with sharp edges can be shaped at the entrance of the irradiated zone inside the object. Such irradiation method combined with two ways rotation technique allows to provide a very high ratio of the dose in the irradiated zone to the dose at the object's surface. Dose fields with high edge gradient obtained by such method are especially important in the cases when the irradiation is used for selective damage of the volumes placed in immediate proximity to the life-critical organs. Our method gives the most effective results at proton treatment of pituitary adenomas and arterio-venous malformations as well as the hormone-dependent forms of mammary gland and prostate cancer, *etc*. Detailed publication of PNPI method of proton therapy and obtained results during 1975–1996 are given in Refs. [1, 2]. In this paper we present the results of 1000 MeV proton steriotaxic therapy different head brain diseases performed during 2002–2006 and the description of a medical beam upgrade which has been done in 2003–2004.

2. Technical features of proton therapy facility

The PNPI proton therapy facility is based on the synchrocyclotron with fixed energy of proton beam (E_p = 1000 MeV), which was built for the purpose of research on the nuclear and particle physics at intermediate energies. Artistic view of synchrocyclotron is shown in Fig. 2. The current inside the vacuum chamber of the accelerator is 3 μA. The intensity of the extracted beam in the accelerator hall is 1 μA. The accelerator has three beam lines for the transportation of proton beams into the experimental hall with fixed energy of 1000 MeV with regulated intensities in the range 10^7–10^{11} proton/sec.

Extracted from the accelerator medical proton beam (Fig. 2) is produced by beam shaping collimator placed just at the entrance of the beam channel. It regulates the size of beam spot and consequently the intensity of the beam. Then the beam is deflected by bending magnet and focused by quadrupole lenses onto the irradiation hall (Fig. 3). The total length of the beam line is 70 m. The antihalo collimator is installed in the experimental hall. Such simple beam optics scheme allows to obtain in the irradiation zone a narrow beam of 6 mm in diameter with sharp edges. The beam is transported in a vacuum pipe to prevent the multiple scattering and inelastic interactions of protons in the air. The irradiation hall is separated from the experimental hall by two shielding walls made from iron and concrete provided the radiation background in the hall at quite low level. The beam position in the accelerator and experimental halls as well as in the irradiation hall and the beam intensity are under a permanent control from the accelerator and medical control

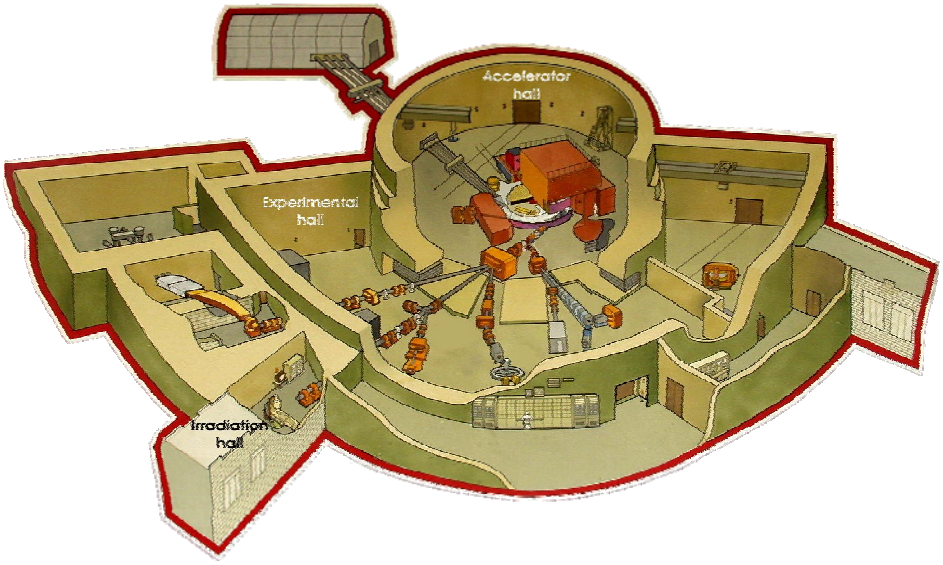

Fig. 2. Artistic view of synchrocyclotron and experimental halls

Fig. 3. Irradiation hall

rooms. Any deviation of the beam parameters beyond the reset limits stops immediately the acceleration process in the synchrocyclotron thus excluding completely any danger for irradiated patients. In 2002–2004 the upgrade of proton medical beam-line has been done including the construction of new collimators and special profile-meters of proton beam in accelerator and experimental halls.

In this paper we present the upgrade of proton beam-line only in the irradiation hall. Profiles in the irradiation hall are measured by two multiwire proportional chambers (X0Z plane) with a gold-tungsten anode wire of 20 μm diameter and stainless steel cathode wires of 50 μm diameter. The wire spacing is 1 mm, the surface of entrance window is 128 × 128 mm^2.

The final proton distribution at the position of patient head on the rotation table is measured by the silicon detector precisely moving along the X-axis by step of 153 μm and along the Z-axis by 9 μm. The range of such scanning is 25×25 mm^2. Profiles of proton intensity at the isodose center of irradiated target is shown in Fig. 4. The intensity of proton beam in the irradiation hall is measured by MWPC in current regime and then transformed into dose distributions, which are periodically calibrated by diamond detectors.

The constancy of a planning dose for each patient irradiation is controlled from accelerator and medical control rooms. The dose distribution during the patient irradiation is shown in Fig. 5. All elements of proton medical beam-line were upgraded by the installation of new mechanical systems and the change of electronics of all detectors to the contemporary base ones. The movable patient's table seen in Fig. 3 provides pendulum-like oscillations in the horizontal plane around the Z-axis within ±40°.

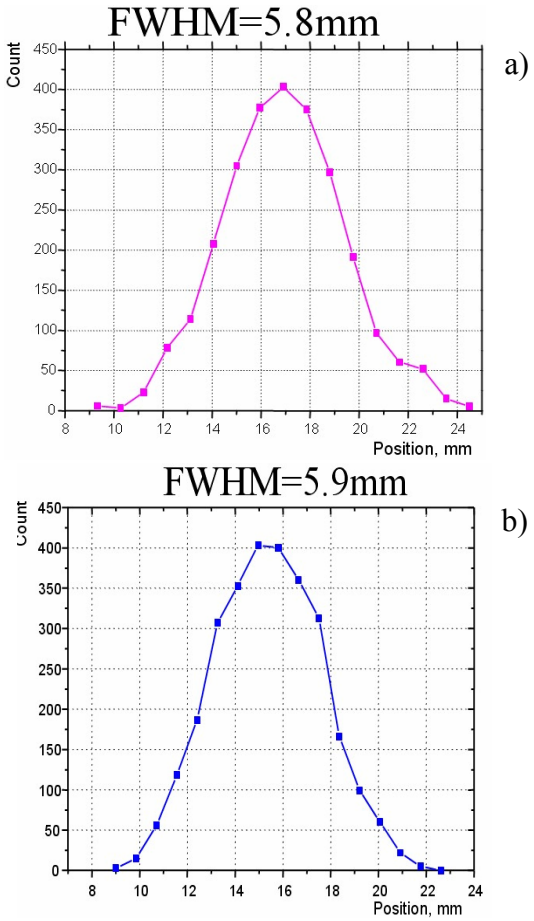

Fig. 4. Vertical (a) and horizontal (b) profiles of proton beam at the isodose center of irradiated target

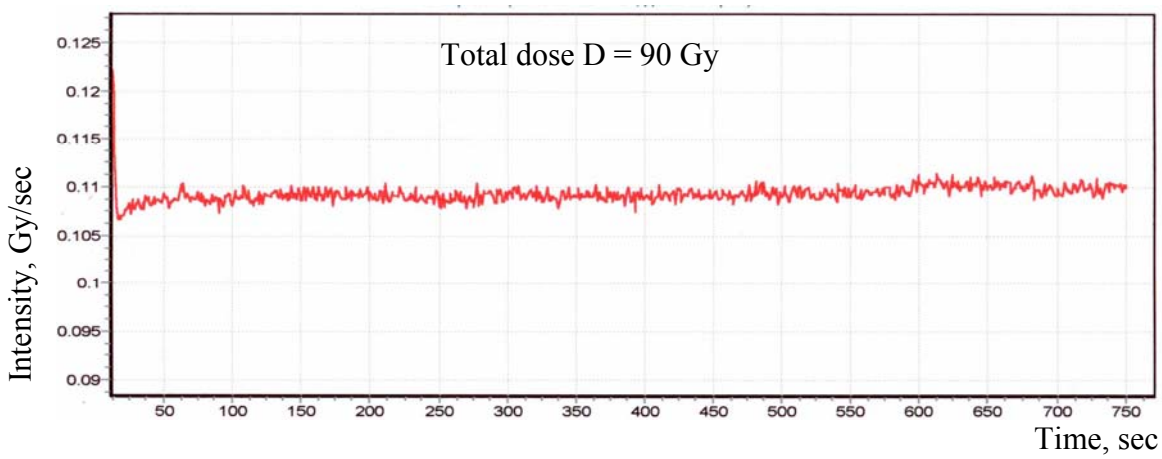

Fig. 5. Distribution of proton beam intensity during the patient irradiation

The anteriour part of the table represents a head fixation device performing an independent pendulum-like oscillation about the X-axis within ±36°. The crossover of the X- and Z-axes is the center of rotation (isocenter). The adjustment system allows to locate the isocenter precisely in the beam axis. Then the patient's position on the table is regulated in such a way that the zone selected for irradiation would be exactly in the center. This zone is determined in the hospital by computer tomography, and its coordinates are put in the protocol. The installation procedure in the irradiation hall is performed by means of a special head mask under the control of a high sensitive *X*-rays setup, which has fixed positions – along the Z-axis and along the beam Y-axis. The final precision in such installation is better than 1 mm. Figure 6a shows the scheme of simultaneous rotation of the patients table and head fixation device and also beam trajectories on the patient's head. Figures 6b-c show the dose distributions in X0Z and X0Y planes, which characterized very sharp decreasing in both directions.

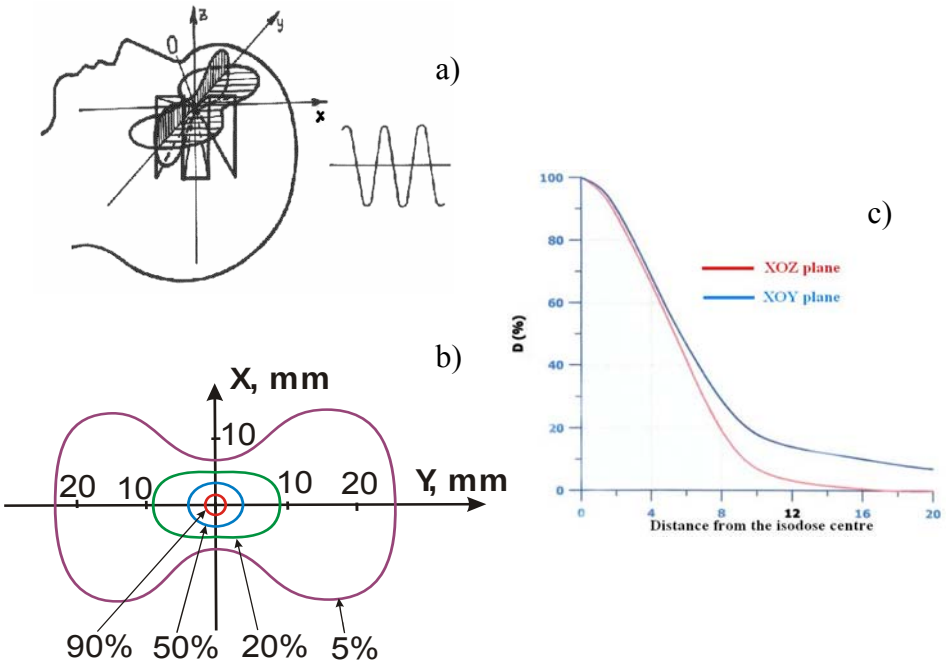

Fig. 6. Scheme of the patient's head rotation around Z- and X-axes. The proton beam is directed along Y-axis. a) The beam trajectories over the patient's head surface at simultaneous rotation of patient's table and head fixation device. b) Spatial distribution of the radiation dose for beam size X = Z = 6 mm. Isodoses: 1 – 90%, 2 – 50%, 3 – 20%, 4 – 5%. c) Profiles of dose distribution in planes X0Z and X0Y (distance in mm)

3. Patient's treatment procedure and results of the therapy

The procedure of patient's treatment is the some as it was described in Ref. [1]. This work included the localization of the zone for irradiation relative to the reference points on the head surface and the preparation of the special head mask used to fix firmly the patient's head on the table for irradiation. The time necessary for positioning of the patient on the table for the irradiation is 15–20 min, and the irradiation time ranges from 8 to 20 min. The oscillation movements of the patient's head proceed quite slowly, so the patients practically do not notice it. The proton therapy is painless, and it is carried out without anesthesia. During the irradiation process the doctors perform continuous control of the patient's state (pulse, breath rate, ECG). There is also a television control and audio communication with the patient from the control room. Statistics of proton therapy at the PNPI synchrocyclotron is presented in Fig. 7.

The dynamics of patient's treatment in 2002–2006 is shown in Fig. 8. Unfortunately, it has a negative tendency and the number of patients treated for this period is less than the corresponding number during 1985–1989 by a factor of two. In some cases such tendency can be explained by the increased competition between neurosurgical and radiological methods of patient's treatment. We observed in the case of pituitary adenomas increased number of patients undergoing a prior surgical operation but not always successful.

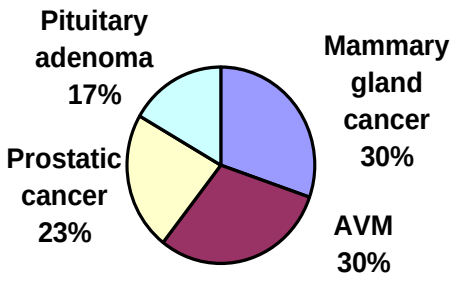

Fig. 7. Number of patients treated at the PNPI–RSCRST medical center during 2002–2006. Pituitary adenoma – 17%, AVM – 30%, mammary gland cancer – 30%, prostatic cancer – 23%. In total 132 patients

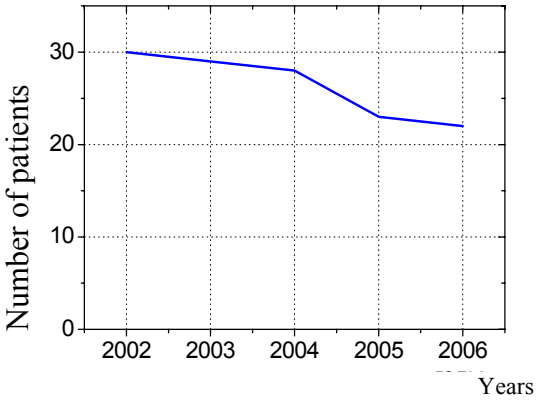

Fig. 8. Dynamics of treated patients

Other possible reason of partient's number reduction can be the total decreasing of inhabitants in Russia, especially in the North-West region of former USSR.

3.1. Proton therapy of pituitary adenomas

Pituitary adenomas comprise about 10–12% of all intracranial tumors [1]. They can be classified as benign histologically but can cause morbidity and occur through hormonal inbalances and functional deficits. Various radiation techniques such as gamma knife and linear accelerator-based stereotaxic radiosurgery [2] as well as charged-particle therapy [3,4] are used for the treatment of such diseases. The application of narrow 1000 MeV proton beam for the irradiation of intracranial tumors (Gatchina transmission method [1]) is very effective, especially in the treatment of different pituitary adenomas. In the case of the somatotropinomas in total 201 patients were treated during 1975–2006. The clinical remission observed during from 1 to 10 years was achieved for 83% patients with macroadenomas. The remission was manifested by the disappearance of tumor growth, the regress of the acromegaloid syndrome, the normalization of carbohydrate exchange and the restoration of working capability. In Fig. 9 the distribution of growth hormone (GH) concentration in blood of patients before and after proton therapy at the dose of D = 80 CGE observed during 5 years is shown. The number of patients analyzed during five years is 85.

It is seen in Fig. 9 that after 5 years the GH concentration is within the limits of physiological normal value 2.8 ± 0.3 ng/ml. The stabilization of symptoms is observed for 4% of patients, while there is no effect in 13% cases mainly when initial symptoms of the tumor arte spread out of borders of the turkish saddle. In the treatment of the prolactinomas (115 patients, 4 of them in 2002–2006) the clinical remission was stated in 80% cases of patients with microprolactinomas. It was accompanied by the disappearance of the galactorhea, the restoration of the ovarian menstrual cycle, the decrease of prolactin concentration and the stop of tumor's growth. In Fig. 10 the change of prolactin concentration in blood of treated patients after proton irradiation is shown. After 5 years such level is close to the normal one, corresponding in average more than 50% its reduction. Thirty women had a pregnancy ended in a live birth. The stabilization was observed in 17% cases, in which the decrease of prolactin concentration was less than 50%. The treatment of corticotropinoma adenomas (Icenko-Cushing's syndrome) is the most successful kind of pituitary adenoma proton therapy. From 205 (10 in 2002–2006) treated patients the clinical remission was observed in 96% cases, the stabilization – in 1%, and only in 3% cases there was the progress in the growth of a tumor.

---

[1] B.B. Ronson *et al*., Inter. J. Radiation Oncology, Biol. Phys. **64**, 425 (2006).
[2] M. Shin *et al.*, Biomed. Pharmacother **56**, 178 (2002).
[3] B. Konnov, L. Melnikov *et al*., in *Proceedings of the International Workshop on Proton and Narrow Photon Beam Therapy.* Ouly, Findland, 1989. p. 48
[4] Y.I. Minakova , L.Y. Eirpattovskaya *et al.*, Med. Radiology **28**, 7 (1983).

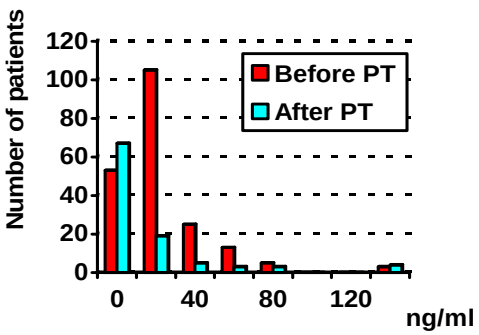

Fig. 9. Distribution of GH (growth hormone) concentration of patients before and after proton therapy (PT) for 5 years observation. Somatotropic pituitary adenoma.
Total number of patients before PT is 201

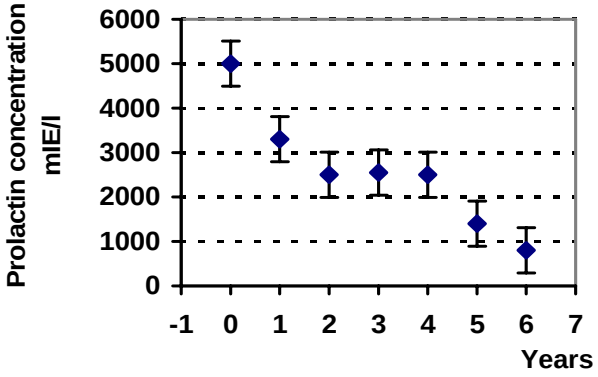

Fig. 10. Dependence of prolactin concentration as a function of time observation patients after proton therapy

In the case of the clinical remission the Icenko-Cushing syndrome was stopped already after 3 months of the irradiation. One can observe the decrease of ACTG and the cortisol secretion as well as the restoration of daily secretion rhythm. Women undergoing proton irradiation further had normal pregnancy and gave birth to child without the indication of endocrin pathology. Photo of patient K. (woman since 19 years suffered from Icenko-Cushing's syndrome) before (2003) and after (2005) proton irradiation at D = 80 CGE with normal child is shown in Fig. 11. One can note that usual neurosurgical operations do not give women the possibility to have pregnancy and to give birth to a child.

Fig. 11. Photos of patient K. with Icenko-Cushing syndrome before and after proton therapy

3.2. Proton therapy of cerebral arteriovenous malformations (AVM)

Surgical practice shows that only about 50% of AVM is medicable in clinics, especially in cases when AVM is placed in critical or inaccessible zones of head brain. Proton therapy of AVM with rather small volume – not more than 8 cm^3 – gives the positive result in 74% cases without any influence on neighboring life-important parts of the brain at doses of 40–80 CGE. The complete elimination of the AVM from the blood circulation is observed in 65% cases. This process continued for a year after the irradiation. For AVM's volume appreciably more than 8 cm^3 only in 27% cases one can have the positive result. After the proton therapy the majority of patients revealed a complete or partial regress of the neurologic symptoms, discontinuation or decrease of the rate and degree of epileptic attacks. The total number of patients treated in 1975–2006 is 491, in 2002–2006 – 40, from them 144 patients were treated secondly. To improve results of AVM's large volume treatment it is necessary to develop new methods of proton steriotaxic therapy or to use beams of more dimensions.

3.3. Proton therapy of mammary glands and prostatic cancer

In 2002–2006 the treatment of 40 patients with mammary gland cancer and 30 patients with prostatic cancer have been performed. The total number for 30 years is 184 and 117, correspondingly. In such treatment the irradiation of special zones of pituitary gland was used.

4. Proposal for 200 MeV proton therapy at PNPI-RSCRST medical center

As it was written above, the number of patients treated in last years at 1000 MeV proton beam is decreasing due to some reasons, main of which is the small number of patients with intracranial diseases of head brain in St.-Petersburg and even over the North-West region of Russia. According to estimates of different experts, the number of patients with pituitary adenomas, AVM and some others are approximately 2–3% of total patient's number with oncological tumors. For example, in St.-Petersburg there are about 100000 citizens suffered by cancer and every year this quantity is increasing by 20000 new patients. The PNPI method of stereotaxic 1000 MeV proton therapy is unique over the world; this method shows better results in pituitary adenoma treatment than widely used Bragg peak method and it needs to continue its performance with some upgrade of diagnostic tools. Taking into account very sharp necessity of St.-Petersburg in radiotherapy, which is satisfied only on 6–7%, the PNPI-RSCRST Medical Center suggests to use for the treatment of wide spectrum of cancer's diseases a new proton beam of 200–250 MeV providing the irradiation of patient's tumor by the Bragg peak method. Such proton beam is obtained by lowering the initial proton energy (1000 MeV) in a degrader, placed just at the exit of accelerator, up to required energy (see Fig. 2). Then 200 MeV proton beam is transported into the irradiation hall. The PNPI Accelerator Division has already the experience in obtaining 900–200 MeV proton beams for physical experiments [3]. Parameters of a new special medical beam line were calculated using GEANT 3, MESON and OPTIMUM codes. In Figs. 12–13 results of Monte Carlo simulations of horizontal and vertical proton beam profiles as well as the proton momentum distribution at the target position in the irradiation hall are shown. The intensity of the beam is equal to 8×10^8 p/sec, that corresponds to the accumulated dose of 12 Gy/min.

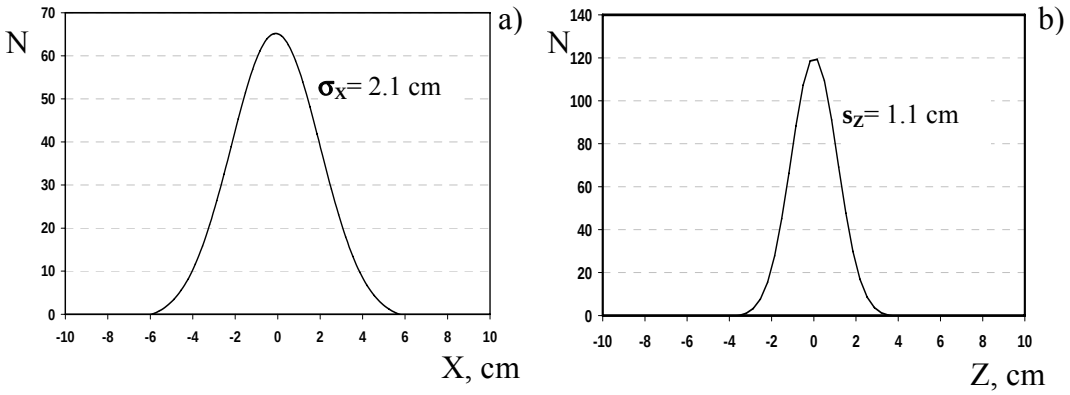

Fig. 12. Horizontal (a) and vertical (b) profiles of 200 MeV proton beam at the place of irradiated target in the irradiation hall. The distance from the exit of 1000 MeV proton beam in accelerator hall to irradiated target is 53 m

Such dose rate is enough for the multifractional irradiation of tumors by area of 15–20 cm^2 and even more using special device for conformal therapy. In the absence of special medical accelerators in Russia the upgrade of existing machines proposed for physics research (as, for example, Dubna synchrocyclotron [5]) to perform hadron radiotherapy is at present a real way in the improvement of total situation in cancer treatment.

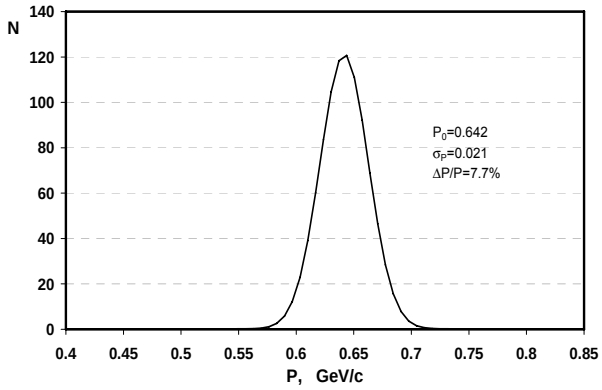

Fig. 13. Momentum distribution of 200 MeV proton beam in the place of the target in irradiation hall

5. Conclusion

The use of the 1000 MeV proton beam for stereotaxic therapy at the PNPI-RSCRST Medical Center has demonstrated the high efficiency of this method. The combination of the rotation irradiation technique and narrow proton beam with sharp edges allowed to deliver large radiation doses to small targets selected for the irradiation without damaging of neighbor volumes in the proximity to the life-critical zones of head brain. The treatment of 132 patients in 2002–2006 and of total 1320 patients for 30 years showed a high reliability and safety of the method, none of the patients had any complications related with the quality of irradiation process. As before 1000 MeV proton therapy can be applied for the treatment of wide spectrum of head brain diseases, in particular, pituitary adenomas. Upgrade of PNPI Medical Facility and the construction of a new 200 MeV beam-line will allow to satisfy in the most extent the need of the North-West region of Russia in bloodless radiosurgery.

References

1. N.K. Abrossimov *et al.*, in *PNPI XXV, High Energy Physics Division. Main Scientific Activities 1971–1996*, Gatchina, 1998, p. 295.
2. N.K. Abrossimov *et al.*, Journal of Physics: Conference Series **41**, 424 (2006).
3. N.K. Abrossimov *et al.*, Preprint PNPI-2525, Gatchina, 2003. 31 p.

[5] A.V. Agapov *et al.*, Particles and Nuclei Lett. **2, № 6 [129],** 80 (2005).

DEVELOPMENT AND ON-LINE TESTS OF DIFFERENT TARGET-ION SOURCE UNITS FOR PRODUCTION OF NUCLIDES FAR FROM STABILITY

V.N. Panteleev, A.E. Barzakh, D.V. Fedorov, A.M. Ionan, V.S. Ivanov, K.A. Mezilev, P.L. Molkanov, F.V. Moroz, S.Yu. Orlov, Yu.M. Volkov

1 . Introduction

The work carried out has as a general goal the development of a massive (up to 1 kg) uranium carbide target prototype for the third generation ISOL facilities, where two-step reactions will be used to produce intense neutron-rich nuclear beams.

For more than thirty years UC_x targets have been explored for the production of a large set of neutron-rich and neutron-deficient heavy nuclei. The main line of uranium carbide target development was the creation of the target material with a high dispersivity and porosity in order to decrease the release time of the species produced by different reactions in the target material, which is mainly determined by the diffusion and effusion processes. On the other hand, for a more efficient use of a neutron beam after the primary beam converter the density of the target material containing uranium should be as high as possible. Additionally, the target material with a higher density has a higher thermal conductivity that would allow dissipating a higher power introduced into the target by the primary beam, when the target is used for exotic nuclei production in the direct reaction. Hence, for more effective production of short-lived isotopes of the element chosen for the investigation, a special selection of a metal carbide target material is required – concerning not only the target material structure but also its density. At the IRIS (Investigation of Radioactive Isotopes at Synchrocyclotron) facility in Gatchina uranium carbide target materials of different structure and density have been tested.

The first general goal of the work is to find out whether the high density uranium carbide can be competitive with presently used low density UC_x targets in the production of short-lived nuclei far from stability. The yields and release characteristics are reported here to compare properties of tested target materials. The second goal is the development and tests of an effective, high-temperature target unit for the on-line production of short-lived rare nuclides. The peculiarity of the developed target unit is the absence of the ion source [1]. The ionization process happens in the target volume itself, so it can help to avoid an additional delay time due to the effusion inside the transfer tube and the ion source. The combined target-ion source (CTIS) unit could be especially useful for the production of isotopes of hard volatile elements with long sticking time, such as rare-earth elements Gd and Lu, and of many other nuclides with boiling points higher than 3000°C. The use of tungsten container [2] instead of a traditional tantalum one allowed to rise the target working temperature up to 2500°C, thereby decreasing the delay time for nuclides produced in the target and hence increasing the yield of short-lived isotopes. At the same time, a high work function of tungsten ensures a high efficiency of a surface ionization of the species with the ionization potentials lower than 6 eV produced in the target material.

2. Target materials tested on-line

A schematic view of the typical target unit used for different uranium carbide target material tests is shown in Fig. 1. As a first step in that comparison, the isotopes of alkali elements Rb, Cs and Fr have been selected for the yield and release efficiency measurements. The main reason of such a choice was their high ionization efficiency (theoretically up to 100%) on the hot inner surface of the target-ion source unit, that allows to obtain short-lived nuclei far from stability. This is very important for the target material comparison.

The second important point in the selection of alkalis is that the target construction can be very simple, including only the tungsten target cavity (ionizing target) [3], as the ionization process happens inside the target container itself. It allows to avoid some uncertainties concerning possible temperature difference of the tested units, as in that case only one parameter (the target container temperature) should be controlled in the course of the experiment.

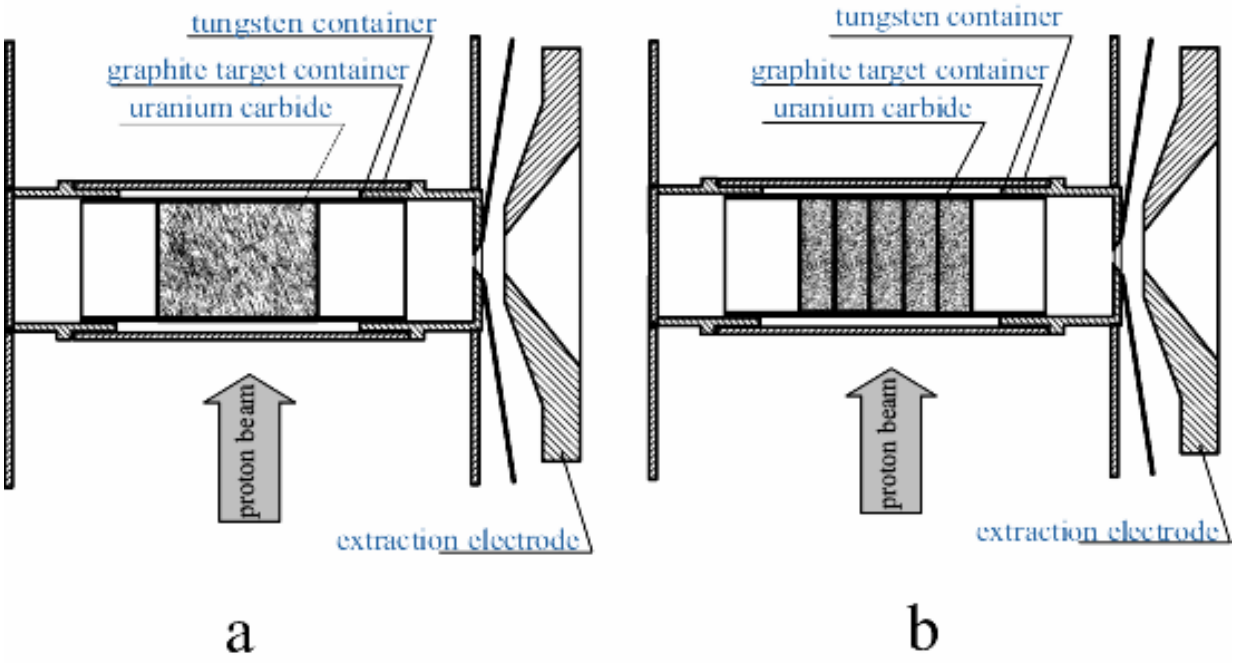

Fig. 1. Schematic drawings of a) high density rod (HDR) uranium carbide target; b) high and low density pellet uranium carbide target

Three kinds of the target materials were studied: a high density UC rod; a low density UC_x target prepared by the ISOLDE method at the IRIS facility (as few pellets placed transversely to the axis of the target); a high density UC powder target material prepared by the method of the powder metallurgy. The high density rod (HDR) target had the following characteristics: uranium rod density 11 g/cm^3, target thickness 6.7 g/cm^2, about 6 mm length and 11 mm in diameter. The grain size was about 200 μm. The low density target (LDT) had: uranium density 2.3 g/cm^3, target thickness 2.8 g/cm^2, about 12 mm length and 11 mm in diameter; 8 pellets, each of 1.2–1.6 mm thickness with the grain size about 20 μm. This target material has been prepared by the Orsay–PNPI collaboration at the IRIS facility, using the ISOLDE technology, a similar graphite powder brought by Orsay group and uranium dioxide from Russian producers. This target is also referred later as ISOLDE like or PARRNe-IRIS. The high density powder (HDP) target had: uranium density 12 g/cm^3, target thickness 6.3 g/cm^2, length 5.25 mm, diameter 11.2 mm; 3 pellets, each of 1.6–1.9 mm thickness, grain size about 20 μm. Targets were operated in the temperature range of 1900–2200°C. The investigated target materials were maintained in the target containers of the same dimensions and geometry. More detailed description of used target construction can be found in Refs. [4, 5]. The uranium fission reaction was produced by 1 GeV proton beam with the intensity of 50–70 nA. Mass-separated isotope beams were collected on a tape station and were either transported to γ-, β-, α-counting stations or directly counted by α-detector to be identified by the characteristic lines. Detailed description of γ-rays measurement and yield determination can be found in Ref. [4]. The yields of Cs isotopes were determined by means of β-counter as well as of γ-detector. Fr isotopes were produced in the same targets by the spallation reaction. The Fr isotope yields were measured using γ-rays and α-particles. To get consistent yield data obtained by α- and γ-measurements, the α-yield data were normalized to the yields obtained by γ-measurement (as the efficiency of the Ge detector is well known), taking as normalizing coefficient the yield ratio for isotopes measured by both methods.

2.1. Yield comparison

For the investigated target materials the Cs and Fr yields under similar temperature conditions (T = 2100°C) have been determined. All presented yield values were normalized to a target thickness of 1 g/cm^2 and 0.1 μA proton beam current. The error of the temperature measurement for different targets can reach 50°C. The experimental errors of the obtained yield values are within the limits of 30% for isotopes not far from stability and of 80% for short-lived neutron-rich isotopes. Cs yields from the investigated targets are plotted together with the ISOLDE yields obtained for standard target at the PS-Booster and for graphite cloth target at the synchrocyclotron. As one can see in Fig. 2, there is a good agreement of yields from similar target materials of ISOLDE and PARRNe-IRIS. The yields of short-lived Cs isotopes from a HDR target are 1.5–2 times lower. This fact demonstrates its lower release efficiency than the ISOLDE or PARRNe-IRIS target. It is an expected result, as the grain size of the HDR target is 10 times larger. Therefore the diffusion process should be much slower. The yields measured for Rb isotopes, which are not presented here, confirm the results obtained for Cs. The Cs yield trend from the lately developed HDP pellet target is similar to the fast PARRNe-IRIS target, but the efficiency is about 20 times less. It can be explained by a strong carbonization of the inner surface of the target container that leads to the ionization efficiency decrease, as the HDP target had been outgased much longer time than other targets. The calculated yields based on the experimental cross sections are also presented to show the in-target production rate of the investigated isotopes. The enhancement of the yield of ^{139}Cs from the HDR target respectively to the calculated one can be explained by the decay of the mother ^{139}Xe nucleus that has the production cross section comparable to the Cs daughter nucleus. It is worth stressing that the yield excess in respect to the calculated yield values was measured only for Cs isotopes produced from the HDR target. It can indicate that in the HDR target the Xe precursors may have longer release times, therefore allowing a large probability of decay in the target as an additional production mode. That assumption requires a special verification.

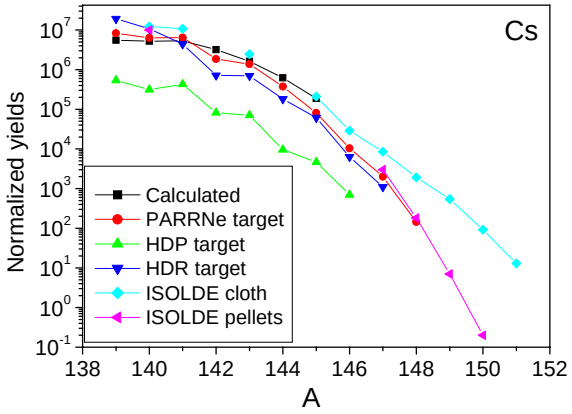

Fig. 2. The yields of Cs isotopes released from a high density rod, high density and low density pellet targets at 2100°C. The yields from ISOLDE UC_x pellet target are presented. The yields calculated on the basis of measured cross section are shown as well

It should be specially pointed out the extraordinary high yields of short-lived Rb and Cs obtained from the ISOLDE graphite cloth UC_x target at the SC. Unfortunately, these high yield data were not reproduced at the PS-Booster, where presently the ISOLDE standard powder-pellet UC_x target is used.

In Fig. 3 the yields of Fr isotopes from the HDR and HDP targets are presented. Fr isotopes have not been measured from PARRNE-IRIS target. The yields of short-lived ^{214}Fr ($T_{1/2}$ = 5 ms), ^{218}Fr ($T_{1/2}$ = 1 ms) and ^{219}Fr ($T_{1/2}$ = 21 ms) were measured by detection their characteristic α-decays. The yields of isotopes with longer half-

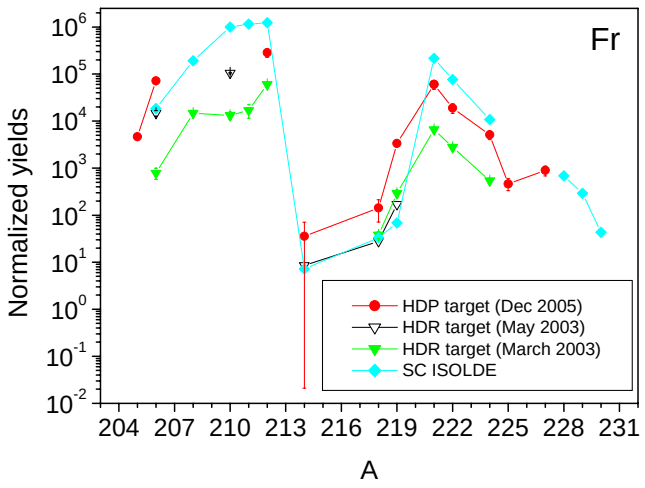

Fig. 3. The yields of Fr isotopes from the HDR, HDP and ISOLDE graphite-cloth targets

lives were determined using both α-particles and γ-rays. The Fr isotope yields obtained at the ISOLDE from the UC_x graphite-cloth target are also shown in the graph. The normalized yields of long-lived Fr isotopes from the ISOLDE graphite-cloth target are higher than from the HDR and HDP targets. The lower HDR and HDP target efficiency, which is the product of the ionization and release efficiencies, may be explained by lower value of the ionization efficiency of the ionizing targets used for experiments, where the ionization process takes place on the strongly carbonized inner surface of the target container. But, at the same time, the normalized yields of short-lived $^{214, 218, 219}$Fr are equal or even higher than the yields of these short-lived isotopes from the ISOLDE target. As there was only one measurement of the Fr yields from a newly developed HDP target, we give here the obtained yield values from that target as preliminary ones.

2.2. Comparison of the target release properties

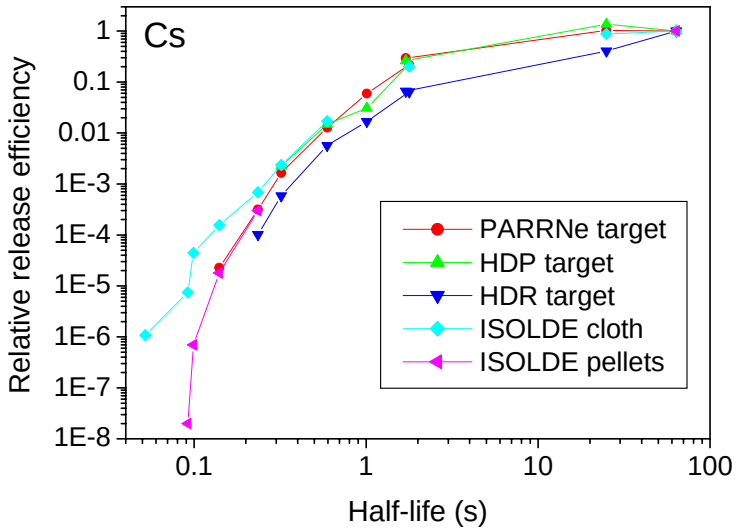

Fig. 4. Comparison of the Cs yield trends from HDR, HDP, LDP PARRNe IRIS and ISOLDE targets. The yields are normalized at the yield point of ^{140}Cs with the half-life $T_{1/2}$ = 63.7 s

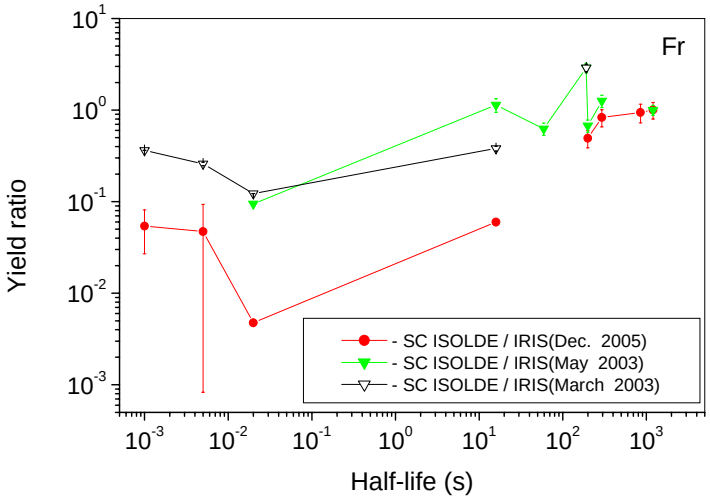

Fig. 5. Ratio of the yields of Fr isotopes from ISOLDE graphite-cloth target to the yields of the same isotopes from HDR (triangles) and HDP (circles) targets, plotted as a function of the half-lives. The obtained ratios are normalized at the point ^{212}Fr with the half-life $T_{1/2}$ = 20 min

The comparison of the relative release efficiencies of different targets for produced isotopes has been derived by normalizing the obtained yield values to the yield of a long-lived isotope ^{140}Cs ($T_{1/2}$ = 63.7 s) which is produced with the efficiency close to unity. In Fig. 4 the relative release efficiencies of Cs isotopes are presented as functions of their half-lives. The trend of the normalized yield values demonstrates that the ISOLDE and PARRNe-IRIS targets in general are slightly faster than the HDR target. A rather promising result is that the trend of the relative efficiency curve for the newly developed HDP target coincidences with one of the ISOLDE target.

For comparison of the Fr release efficiencies, the yields from the ISOLDE cloth target were divided by the measured yields of the same isotopes from the HDR and HDP targets and normalized to the yield ratio of ^{212}Fr. The obtained ratio values are shown in Fig. 5 as functions of the half-lives; as the Fr isotopes were not studied with the PARRNe target, only the ratios for the HDR and HDP targets are presented. The result for the HDP target is preliminary. As one can see, the HDR and HDP targets has considerably higher release efficiency for short lived-isotopes of ^{214}Fr ($T_{1/2}$ = 5 ms), ^{218}Fr ($T_{1/2}$ = 1 ms) and ^{219}Fr ($T_{1/2}$ = 21 ms). This can be explained by the fact that the sticking and flight time of species produced in the IRIS tested target prototypes is about six time less than in the ISOLDE target due to the ratio of the volumes of the target containers. To confirm or to reject the

assumption of a much shorter effusion time some additional on-line tests on the short-lived Fr isotope production from a HDP target will be carried out at the IRIS facility.

3. Ionizing targets for production of nuclides with high ionization potentials

For the production of nuclides with high ionization potentials three types of combined targets have been developed and on-line tested:

1. The ionizing foil target of the surface ionization for the Li and rare-earth isotope production.
2. The laser foil target for the production and resonance laser spectroscopy investigation of neutron-deficient rare-earth isotopes.
3. The combined target-ion source unit of the electron beam ionization with uranium carbide as a target material for the production of neutron-rich isotopes of the elements with the ionization potentials higher than 6 eV.

3.1. Off-line measurements of the ionization efficiencies for Li, Sm, Eu, Tm, and Yb

The schematic diagram shows the high-temperature ionizing target [6] used for on-line tests (Fig. 6). The only difference in the construction of the ionizing target (IT) used for off-line ionization efficiency measurements was the presence of a separately heated oven which was connected to the IT for a slow evaporation of the sample consisting of a known amount of atoms of the element being investigated.

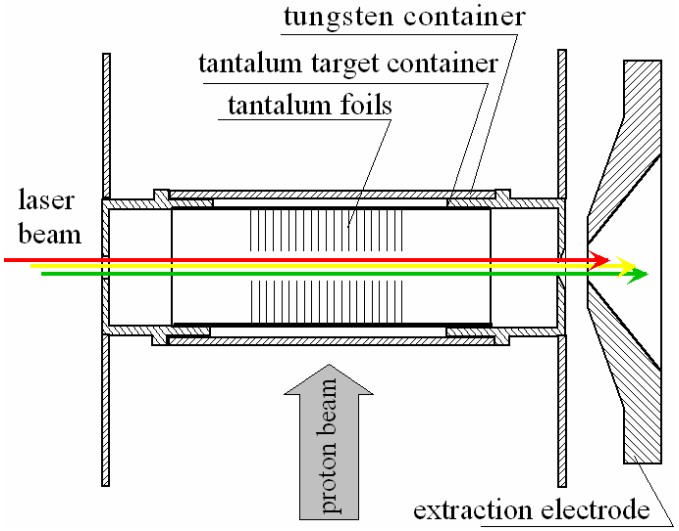

Fig. 6. Scheme of the combined target-ion source unit for Li, rare-earth isotope production and laser spectroscopy experiments

Off-line measurements of the surface ionization efficiencies for Li and rare-earth elements was carried out by using samples of LiF and oxides of pointed out rare-earth elements weighting from 10 to 20 μg placed into the oven connected with the IT volume. The current of each evaporated sample was measured by a Faraday cup placed in the focal plane of the mass-separator magnet and connected with the current integrator. The process of the laser ionization efficiency measurement of Eu and Gd atoms inside the target volume was carried out simultaneously with the surface ionization measurement. For that purpose three laser beams tuned in resonance with appropriate transitions in Eu and Gd were introduced into the CTIS. We indicate this method as the laser target (LT) [7], in order to emphasize that it differs from the method employing the resonance ionization in the laser ion source (LIS) [8].

Table 1

The efficiencies of ionization measured off-line with IT and LT

Element	Temperature, °C	Surface ionization efficiency, %	Laser ionization efficiency, %
Li	2000	6	
Rb	2000	40	
Cs	2000	55	
Sm	2200	7	
Eu	2200	10	7
Gd	2500	2	1
Tm	2200	3	
Yb	2200	5	

In Table 1 the efficiencies of surface and laser ionization measured off-line for some alkalis and rare-earth elements are presented. The error of the ionization efficiency measurements was 20% for Rb and Cs and up to 40% for other elements.

3.2. On-line measurements of the yield of neutron-deficient rare-earth isotopes

A 1 GeV proton beam induced spallation reactions in the target material (tantalum foils, target thickness 3 g/cm^2) producing nuclides of neutron-deficient isotopes of rare-earth elements. After surface or laser ionization and extraction from the target, the ions were separated by a mass-separator and implanted into a moving tape installed at one of the three beam-lines of the IRIS facility. An identification of the radioactive implanted specimens and yield determination were performed by means of appropriate γ-line measurements by a coaxial high-purity germanium detector. The proton beam intensity was 0.05 μA. In Table 2 the yields of the neutron-deficient rare-earth isotopes produced on-line, the yields calculated by the EPAX code and the values of the efficiency of the ionizing target are presented.

Table 2

On-line yields and production efficiencies of the IT at 2500°C

Nuclide	$T_{1/2}$	Yields measured, s^{-1}	Yields EPAX, s^{-1}	Production efficiency by surface ionization, %	Production efficiency by laser ionization, %
^{138}Eu	12.1 s	2.4×10^3	9.5×10^4		
^{139}Eu	17.9 s	1.6×10^4	4.9×10^5		
^{141}Eu	41.4 s	4.0×10^5	5.6×10^6		
^{142}Eu	1.22 min	4.1×10^5	1.2×10^7		
^{143}Eu	2.57 min	2.0×10^6	2.1×10^7	9	
^{139}Sm	2.57 min	2.8×10^5	8.4×10^6		
^{143}Sm	66 s	4.4×10^5	2.3×10^7		
^{139}Pm	4.15 min	3.1×10^5	2.6×10^7		
^{160}Tm	9.4 min	5.0×10^5	3.5×10^6		
^{164}Tm	5.1 min	9.6×10^4	1.6×10^7		
^{160}Yb	4.8 min	1.0×10^6	1.6×10^7	6	
^{160}Lu	40 s	2.2×10^4	1.5×10^7		
^{168}Lu	6.7 min	1.3×10^6	4.1×10^6		
^{143}Gd ^{143m}Gd	39 s 1.87 min	6.7×10^4	3.5×10^6		
^{145}Gd ^{145m}Gd	23.0 min 85.2 s	6.7×10^5	1.7×10^7	4	2

For ^{143}Gd and ^{145}Gd the total values of the yields summarizing the measured isomeric and ground states are given. The efficiency of the laser target for ^{145}Gd production is pointed out as well. The combined target-ion source unit efficiency, which is a product of the release and ionization efficiency, was obtained as the ratio of the measured yields to the yields calculated on the base of cross sections supplying by the EPAX code. That efficiency estimation was obtained only for isotopes with respectively long half-lives and which production cross sections are close to the maximum of the cross section curve (^{143}Eu, ^{145}Gd and ^{160}Yb). As one can see in Table 2, the on-line production efficiencies for pointed out long-lived isotopes are in a good agreement with the off-line measured values (Table 1).

3.3. The CTIS use for on-line laser spectroscopy experiment

The developed combined target-ion source unit has been used for a laser resonance spectroscopy investigation of neutron-deficient Gd isotopes [7]. The scheme of the CTIS used for the laser spectroscopy experiments is shown in Fig. 6.

For the comparison of two methods (LIS and LT), the ratio R of the photo-ion current to the thermal ionization background has been measured for two types of the target system: the first one was a traditional construction (target connected to the ion source) [8] and the second one was the laser target. In Table 3 the

beam intensities of ^{145m}Gd and ^{145g}Gd from both tested target systems at the equal temperature conditions are presented. During the tests the targets having an identical material thickness were used, which were irradiated in both experiments by the same proton beam intensity. Also we were trying to keep the same temperature conditions for the tested targets and the ion source. The temperature was (2500 ± 50)°C that ensured a rather fast escape of Gd radioactive atoms for which the effusion is considered to be the main delay dominating process. In spite of similar conditions of radioactive Gd production for both targets, we have obtained the ratio of ^{145m}Gd ($T_{1/2}$ =1.87 min) to ^{145g}Gd ($T_{1/2}$ = 23 min) almost 7 times higher from the laser target than from the usual target-ion source unit (see Table 3 "laser off"). The enhancement of ^{145m}Gd having a considerably shorter half-life than a long-lived ^{145g}Gd demonstrates that the integrated target-ion source is faster than the usual target-ion source unit.

Table 3

Beam intensities of ^{145m}Gd and ^{145g}Gd produced by different target-ion source units at a temperature of 2500°C

	^{145m}Gd beam intensity, s^{-1}		^{145g}Gd beam intensity, s^{-1}		Ratio ^{145m}Gd/^{145g}Gd	
Type of target-source unit used	Target with ion source	Laser target	Target with ion source	Laser target	Target with ion source	Laser target
Laser at resonance	$1.64(8)\times10^{5}$	$3.21(11)\times10^{5}$				
Laser off	$1.55(6)\times10^{5}$	$2.30(8)\times10^{5}$	$2.02(20)\times10^{6}$	$4.40(16)\times10^{5}$	$7.7(1.1)\times10^{-2}$	$5.20(37)\times10^{-1}$
R	0.06(6)	0.40(6)				

3.4. The uranium carbide CTIS for the production of neutron-rich isotopes

A schematic drawing of the CTIS for the production of nuclides with high ionization potentials is shown in Fig. 7. The electron beam was introduced into the target volume by a cathode shaped for that purpose and placed to the side of the extraction electrode. So the electron beam ionization took place inside the target container [3]. The yields of neutron-rich Ag and Sn isotopes are shown in Fig. 8. The production efficiency values obtained as a ratio of measured and calculated yields are, correspondingly, 4% and 2% for long-lived Ag and Sn. With a high value of probability it is equal to the ionization efficiency of that species, as the release times of these elements are shorter than their lifetimes.

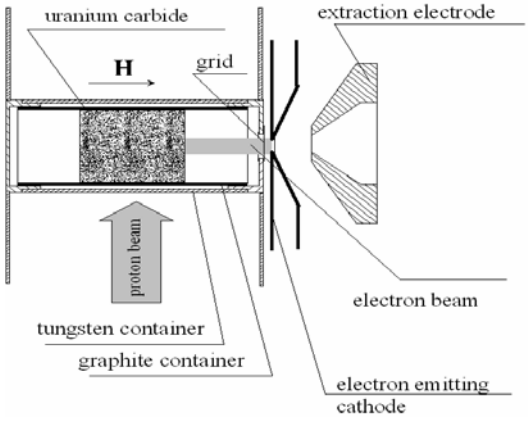

Fig. 7. Scheme of the electron beam ionizing UC target for production of neutron-rich isotopes

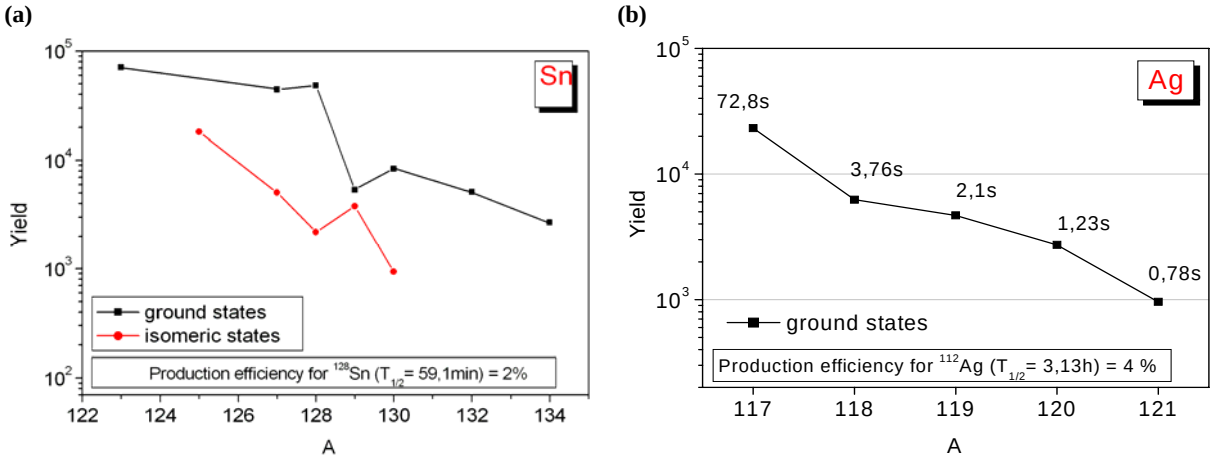

Fig. 8. Sn (a) and Ag (b) isotope yields from the electron beam IT

4. Conclusion

The yields of on-line mass-separated Cs, Rb and Fr isotopes have been studied at the IRIS. Properties of high density UC targets, in form of rod and powder, and a low density UC_x target prepared by the ISOLDE method similar to the PARRNe target are compared. According to the measured yield trends, the release efficiency of an ISOLDE like target for short-lived Cs isotopes is 1.5–2 times higher than that of a HDR (high density rod) uranium carbide target which was studied at the IRIS initially. It is rather encouraging result, as the grain size of the HDR UC target was ten times larger than the ISOLDE like target.

It should be pointed out that the on-line measured production efficiency and release properties of the ISOLDE like target specially prepared at the IRIS for that comparison tests coincide with the ISOLDE original target within the experimental errors (≤ 40%).

To compare target materials having different densities but a similar dispersivity, a new developed, high density pill (HDP) UC target with the grain size of 20 μm have been on-line investigated. According to the measured Cs yield trends, the release efficiency of the new HDP target coincides with the ISOLDE like target within the limits of the measurement errors.

The comparison of the yields of short-lived Fr isotopes from the HDR and HDP targets with the yields from the ISOLDE graphite-cloth target exhibits a rather unexpected result: the normalized yields of extremely short-lived Fr isotopes from high density targets are equal or even higher than those from the graphite-cloth target.

Off- and on-line tests of ionizing targets have demonstrated that they can be used for the on-line production of a large set of nuclides using surface and resonance laser ionization. The ionization efficiency measured off-line for surface and laser ionized different species is comparable with those published in the literature. A low ionization efficiency value for Li can be explained by a low temperature of the ionizing target. To ensure a higher Li ionization efficiency, a target temperature should be at least 2200°C or even higher. The ionization efficiency for the tested elements can be increased in our construction almost by a factor of two by decreasing the diameter of the hole for the beam from 2 to 1 mm, as the laser beam diameter is about 0.5 mm.

As it is seen in Table 2, the target can be successfully used for the production of neutron-deficient isotopes of all rare-earth elements. The ionization efficiency may be higher about 3 times, if the ionizing target is used only in a surface ionization mode when the hole for the laser beam introduction is eliminated.

References

1. V.N. Panteleev *et al*., Rev. Sci. Instr. **73**, 738 (2002).
2. V.N. Panteleev *et al*., Nucl. Phys. A **701**, 470c (2002).
3. V.N. Panteleev *et al*., Rev. Sci. Instr. **77**, 03A705(2006).
4. A. Andrighetto, A.E. Barzakh *et al*., Eur. Phys. J. A **19**, 341(2004).
5. A. Andrighetto, A.E. Barzakh *et al*., Eur. Phys. J. A **23**, 257 (2005).
6. V.N. Panteleev *et al*., Eur. Phys. J. A **26**, 147 (2005).
7. A.E. Barzakh *et al*., Phys. Rev. C **72**, 017301 (2005).
8. A.E. Barzakh *et al*., Phys. Rev. C **61,** 034304 (2000).

INVESTIGATION OF BORONIZATION IN GLOBUS-M TOKAMAK AND GAS-FILLED DETECTORS USING THE ELECTROSTATIC ACCELERATOR BEAMS

V.M. Lebedev, A.G. Krivshich, V.A. Smolin, B.B. Tokarev, E.I. Terukov[1)], V.K. Gusev[1)]

[1)] *Ioffe Physical-Technical Institute of RAS, St.-Petersburg*

At PNPI there is a Van de Graaf electrostatic accelerator with the energy of 1.5 MeV. The accelerator was used for a wide program of fundamental research (nuclear physics, physics of solids, films and surface semiconductors) as well as for technical and applied investigations (new materials, nuclear detectors, physical installations). At this accelerator the nuclear physics techniques of material research are used. They include a Rutherford backscattering spectrometry and a nuclear reaction analysis [1]. These techniques are nondestructive, high sensitive and precise.

The main results of investigations at this accelerator for past 5 years are presented in this article. They include:

- study of vacuum vessel boronization in Globus-M Tokamak,
- aging investigations (using nuclear microanalysis) of gas-filled particle detectors proposed for experiments at the Large Hadron Collider (LHC).

1. Study of vacuum vessel boronization in Globus-M Tokamak

1.1. Introduction

At Ioffe Physical-Technical Institute of RAS there is Globus-M Tokamak. Globus-M is a spherical small aspect ratio A tokamak (plasma major radius R = 0.36 m, minor radius a = 0.24 m, $A = R/a$ =1.5, toroidal magnetic field 0.1–0.6 T, plasma current up to 0.36 MA) presently operating in Ohmic heating regime [2, 3]. The first experiments were performed in the vacuum vessel with stainless steel limiters. Later on the vessel inner cylinder and partly the poloidal limiters were protected with graphite tiles.

The effective way to reduce the impurity contamination in tokamak plasma is the coating of the first wall with boron-carbon films. In the Globus-M experiment the boron-carbon film was deposited on the vacuum vessel inner surface in glow discharge (GD) in the mixture of helium and carboran $C_2B_{10}H_{12}$. The essential advantages of this method are the low cost and the simplicity of implementation. The carboran is the non-toxic and non-explosive substance. It is a powder at the room temperature, which is intensively evaporated at the temperature higher than 40°C.

The first boronization of the vacuum vessel was performed at a low percentage of carboran. The carboran vapor pressure was less than 10% of He pressure in glow discharge applied during 30 minutes. However, this procedure led to significant reduction of hydrogen recycling and to 20% increase of plasma current at the same loop voltage waveform. Then the Boron/Carbon films were deposited on the substrates from different materials in a high frequency glow discharge out of the Globus-M vacuum vessel and their properties were studied in details. The last boronization in the Globus-M was carried out at the essentially lower helium to carboran vapor pressure ratio in the range 3/1 – 5/1. After the boronization the analysis of the spatial distribution and the structure of the deposited film have been undertaken. For this purpose silicon probes (plates of approximately 1 cm^2 area) were placed in 16 points on the vessel inner surface and the graphite limiters.

1.2. Experiment

The Globus-M vacuum vessel is an all-welded stainless steel construction of ~1 m^3 inner volume. The vessel plan view is shown in Fig. 1, the contour of the vertical cross-section is depicted in Fig. 2. Figures 1–2 show also the position of silicon plates located in four sections along the torus.

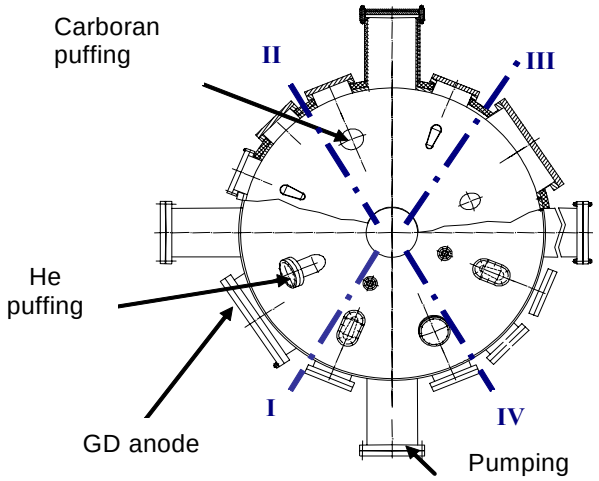

Fig. 1. Vacuum vessel plan view showing position of He and carboran puffing and CD electrode. I, II, III, IV – sections for silicon plates positioning

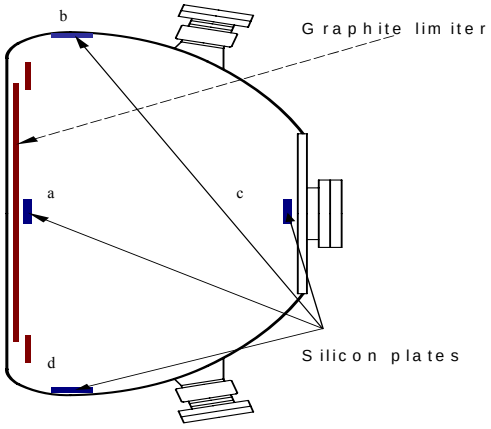

Fig. 2. Vacuum vessel cross-section showing the position of silicon plates and graphite limiter

The routine procedure of the vessel conditioning includes the bake-out at the temperature up to 200°C and the glow discharge cleaning in hydrogen and noble gases. The glow discharge voltage is applied between the single electrode (anode) and the earthed vessel. The electrode of 20 mm diameter is positioned in the tokamak middle plane (see Fig. 1). The parameters of the vessel and the glow discharge characteristics are shown in Table 1. The helium pressure was provided by the piezoelectric valve. The carboran was evaporated by heating the ampoule containing the carboran powder. The steady state temperature of 45°–48°C was sufficient to sustain the required pressure.

Table 1

The vessel parameters and glow discharge characteristics of the Globus-M Tokamak

Diameter of outer wall	1260 mm	Glow discharge voltage	300 V
Diameter of graphite limiter	252 mm	Current density	30 μA/cm^2
Vertical axis of torus	1.094 m	Gas pressure	0.2 Pa
Vessel volume	1.05 m^3	He to carboran pressure ratio	3/1 – 5/1
Inner surface area	5.7 m^2		

1.3. Results

First detailed study of carboran film properties was performed for the films deposited on the silicon, quartz and glass plates in 40 MHz He or Ar glow discharge in a small laboratory device (the distance between electrodes was 35 mm). The basic results can be summarized as follows.

The deposition rate decreased when the substrate temperature rose in the range of 20°–100°C. The films had the amorphous structure.

The Boron/Carbon ratio was determined from the nuclear reactions analysis (NRA) with deuterons. Figure 3 shows the energy spectra of protons and α-particles originated in the reactions of 1 MeV deuterons with nuclei of carbon and boron isotopes. The B/C ratio in the deposited films was determined by integrating the peaks of $^{10}B(d,\alpha)^8Be$ and $^{12}C(d,p)^{13}C$ reactions [2, 3] and appeared to be about 48/52 in percents.

The content of hydrogen (result of infra-red spectrum analysis) reached 40–50% at the room temperature and could be reduced by annealing at a higher temperature.

The characteristic values of the specific resistance is equal approximately to 10^6 Ohm·cm at the room temperature and ~10^5 Ohm·cm at the temperature of 100°C. The films are transparent in the visible range. After the vessel boronization with a small fraction of carboran vapor pressure (less than 10% of He pressure)

the subsequent analysis of silicon plates revealed a formation of thin films with a typical thickness of 100 Å. The film had an amorphous structure, but the content of boron did not exceed 4%. After 200 plasma shots with the plasma current of 150 kA accompanied by routine glow discharge cleaning in helium during 70 hours the amorphous structure transformed to the diamond-like one. It is remarkable that the hydrogen in the film was practically absent.

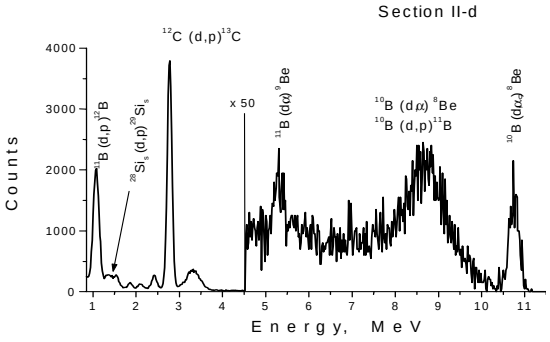

Fig. 3. Energy spectrum of protons and α-particles originated in the reactions of 1 MeV deuteron beam with carbon and boron isotopes in the deposited film. Angle of observation is 135° relatively to the beam

More detailed analysis was undertaken after the boronization with the ratio of helium to carboran pressure in the range 3/1 – 5/1 during 1.5 hour. The boronization was followed by a short experimental series from 80 plasma shots with plasma current of 200 kA and 12 hours of glow discharge cleaning in helium. The distribution of the film thickness deposited on silicon plates in different points of the vessel is shown in Table 2. The plates numbering is given according to Figs. 1–2.

The film composition in the cross-section II (Fig. 1) was studied by means of nuclear reaction analysis (NRA) and Rutherford backscattering spectrometry (RBS) at the PNPI electrostatic accelerator. The content of iron was obtained from the RBS spectrum of deuterons. These results are presented in Table 3.

Table 2

Film thickness on silicon plates in the Globus-M Tokamak

Film *thickness,* μm				
Position	a	b	c	d
I	-	1	0.5	0.4
II	0.03	0.65	0.1	0.3
III	-	0.3	0.3	0.3
IV	-	0.3	1.2	0.4

Table 3

Film composition in cross-section II of the Globus-M Tokamak

Substrate	Composition of film
II-a	$B_{0..32 \pm 0.02} C_{0.52} Fe_{0.16}$
II-b	$B_{0..01}$ $C_{0.52 \pm 0.02} Fe_{0.43}$
II-c	$B_{0..27 \pm 0.02} C_{0.55} Fe_{0.18}$
II-d	$B_{0..43 \pm 0.02} C_{0.47} Fe_{0.10}$

1.4. Conclusion

The described procedure of Globus-M vessel boronization leads to a formation of the amorphous boron-carbon film with a typical B/C ratio of 3/4–3/5. The film thickness varies within a factor of 4 along the vessel surface. No obvious correlation between the film thickness and the position of the glow discharge electrode and the gas puffing ports was observed. The physical properties of the B-C coating deposited in DC glow discharge on the vessel surface are similar to properties of the films obtained in 40 MHz discharge. The appearance of iron in the film structure can be explained by a sputtering of the vessel material during boronization and the tokamak routine operation. Thinner films have a lower content of boron. The tokamak operation (plasma shots and routine glow discharge cleaning) leads to a significant reduction of hydrogen content in the boron-carbon films.

2. Aging investigations of gas-filled particle detectors by means of Nuclear Reaction Analysis

2.1. Introduction

Some time ago it was demonstrated that the method of Nuclear Reaction Analysis (NRA) is very effective for investigation of the aging effects in the gas-filled detectors [4–6] operated under high accumulated dose. This technique is particularly efficient in quantitative evaluation of the light elements (oxygen, carbon, nitrogen, fluorine, *etc.*) presence in the gold coating of the anode wire. The NRA method is also adequate for determining light element distribution with a depth measurement over a range of more than 1 μm.

Such data are especially important in studies of gas discharge avalanche plasmas because they are a starting point for most of the aging processes in the gas filled detectors. Wire aging is an extremely complex chemical process. To obtain a general picture of wire aging, it is necessary to identify the dominant processes occurring in gas avalanches, which result in the production of active chemical species (radicals, ions, *etc*.). The avalanche environment is plasma of ions and neutral radicals, and thus the wire aging process should be studied in the framework of plasma chemistry. The most important plasma-chemical reactions for the gas mixtures ($Ar/CO_2/CF_4$ and $Xe/CO_2/CF_4$) produce many different active species including oxygen and fluorine [4–7].

Application of the NRA method in our aging investigations gave us a reliable confirmation of the oxygen key role in the wire-swelling mechanism and demonstrated the kinetics of oxygen transport into the depth of the gold coating of the anode tungsten wire [5–7]. Active elements, including radicals, penetrate through the already opened cracks in the gold layer and react directly with the wire tungsten. Finally, this causes a swelling of the tungsten in the wire and, as a consequence, forces break of the gold coating produced within the wire.

But initial imperfections in the gold crystallite structure, which can increase and develop under the influence of sustained irradiation and etching of the gold, can provide favorable conditions for active oxygen with broken bounds, and even for more complicated chemical radicals, to penetrate into the tungsten. Etching strongly attacks defects in the gold coating and results in its extension. It should be noted that etching is a dangerous process which can open a direct path for the active oxygen to the tungsten surface of the wire. Special interest for our gas mixture are two chemical agents which determine possible gold etching: fluorine and xenon-fluorine XeF_n (n = 2,4,6) compounds. These agents are strong oxidizers and may interact with the gold causing etching. So, in order to understand the aging (including the wire swelling) mechanism in more detail, it was principally important to develop the NRA method for investigation of fluorine distribution in the anode wires. In case of success we would get the method allowing to perform the detection and quantitative evaluation of all light elements (oxygen, carbon, fluorine, nitrogen) which are coming from gas mixtures used in gaseous detectors and concentrated in electrodes.

2.2. NRA technique

For the detection and quantitative evaluation of the fluorine content as a function of depth in the gold, the nuclear reaction $^{19}F(p,\alpha)^{16}O$ has been applied [5, 8]. The reaction is exothermic and thus the exiting α-particles have higher energies (E_α = 7 MeV) in compare with the incoming protons (E_p = 1.25 MeV) which are scattered on the target. This allows us to absorb completely the beam ions with a few microns of aluminum foil placed in front of the semiconductor detector, which is used for detection of the final state particles. Due to the Coulomb barrier the energy of the bombarding protons is not sufficient for nuclear interaction with higher atomic number elements (such as Al, Au, W). Hence, the α-particles produced in the interaction with fluorine atoms are detected practically without background.

The NRA was carried out at the PNPI electrostatic accelerator. The frame with investigated wire was fastened to the target apparatus of a vacuum chamber. A proton beam of 1.25 MeV was used. The diameter of the beam spot on the wire was about 4 mm. The beam current through the wire was about 3–5 nA. The heat consumption of the irradiated wire was 0.01–0.02 W/cm. The number of protons, which passed the wire, was evaluated with the current integrator. α-particles were detected by a surface-barrier Si(Au) detector positioned at an angle of θ = 135° relatively to the beam axis.

To measure the distribution of fluorine along the wire the target was scanned with the beam. The method is based on the analysis of the energy spectra of emitted particles and makes it possible to determine a light element concentration profile. Schematics and nomenclature for the (p,α) nuclear reaction process in a sample-target and the reconstruction of the resulting energy spectrum are presented in Fig. 4. The energy spectrum of the α-particles produced by the (p,α)-reactions at a constant energy of protons was measured using a semiconductor detector. Back-scattered protons are filtered out using a thin (6 mg/cm^2) aluminum foil.

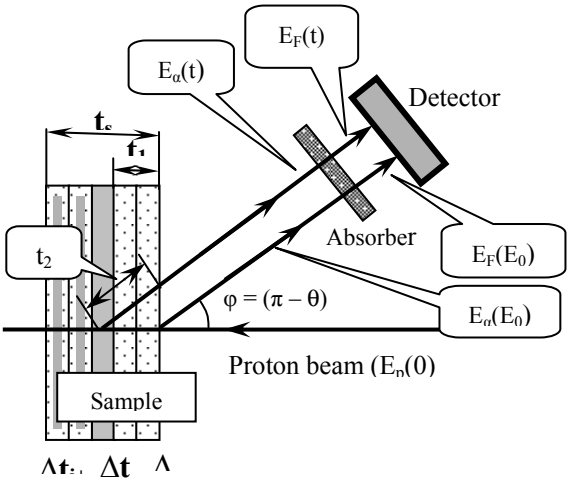

Fig. 4. Schematics and nomenclature for the (p,α) nuclear reaction process in sample

The energy of the detected α-particle resulting from the reactions at a depth t depends on the relation between the beam particle energy and the path traveled by the emitted particles. A reaction, which takes place near the surface of the specimen, will yield α-particles with higher energy than a reaction which occurs at a greater depth.

The *energy-depth* relation may be deduced from the fact that the measured energy of α-particle produced at the depth t depends on the energy loss of protons reaching the depth t and the energy loss of α-particle in the traversing the sample before it reaches the detector. To calculate this relation, a sample is sliced on thin layers with the thickness of Δt_i (Fig. 4). The energy of protons $E_p(t)$ with incident energy $E_p(0)$ at the depth t_1 is given by the equation:

$$E_p(t) = E_p(0) - \int_0^{t_1} \left| S_p(t) \right| dt,$$

where $S_p(t)$ is a stopping power of substance for protons, t_1 is a path length of protons in the target.

The energy $E_\alpha(E_p)$ of α-particle resulting from a reaction (p,α) is given by the well-known expression:

$$E_\alpha(E_p(t)) = M_\alpha M_p E_p \{2\cos^2\theta + B + 2\cos\theta[\cos^2\theta + B]^{1/2}\}/(M+M_\alpha)^2,$$

where θ is the angle between the beam direction and the detector direction; M_p, M_α, M – the masses of incident particle, outgoing particle and final nucleus; $B = M(M+M_\alpha)(Q_R/E_p - M_p/M + 1)/(M_\alpha M_p)$.

The energy of α-particle in the detector $E_F(t)$ is given by the equation below:

$$E_F(t) = E_\alpha(E_p(t)) - \int_0^{t_2} \left| S_\alpha(t) \right| dt - \int_0^{t_{Al}} \left| S_\alpha(t_{Al}) \right| dt,$$

where $S_\alpha(t)$ is the stopping power of substance for α-particles; $t_2 = t_1/\cos\theta$ is the path length of α-particles in the target; t_{Al} is the thickness of the aluminum foil-absorber.

Using tabulated stopping power data, the $E_F(t)$ dependence can be calculated from these equations. This approximation appears to be quite reasonable if we take into account that the energy loss of particles is relatively small compared with their initial energy and the stopping powers have a linear dependence on the energy and vary less then 15% over the relevant energy ranges: 1.0–1.25 MeV for protons, 4.0–7.0 MeV for α-particles [4, 8]. In this case the energy scale can be converted into a linear depth scale:

$$E_F(t) = E_F(E_0) - G_{NR}\, t,$$

where $G_{NR} = (\partial E_\alpha/\partial E_p)\, S_p + S_\alpha/\cos\theta$. G_{NR} is an effective energy loss related to single length. The G_{NR} depends on energy losses of α-particles and protons, reaction kinematics, geometry of experiment, and elemental composition of investigated sample. G_{NR} = 380 keV/mg/cm^2 for an investigated wire.

As shown in Fig. 4, we sliced the investigated sample per thin layers to provide the calculation. The thickness Δt_i connects with energy interval ΔE_i of experimental spectrum by equation $\Delta t_i = \Delta E_i / G_{NR}$.

The energy spectrum $Y(E_F)$ of the detected α-particles is given by the equation:

$$Y(E_F(t))\, dE_F = C(t) \cdot I \cdot \sigma(E_p(t)) \cdot \Delta\Omega \cdot dt \,,$$

where $C(t)$ is the concentration profile of fluorine, *i.e.* the number of element atoms per cm^3 at the depth t; I is the number of incident particles; $\sigma(E_p(t))$ is the differential cross section for the angle θ; $\Delta\Omega$ is the solid angle of a particle detection.

The sensitivity of NRA technique for the fluorine concentration measurements is about 1×10^{16} at/cm^2. An accuracy of the element concentration measurements is better than 5%. The thickness of the investigated layer depends on the range of particles in a sample (for protons and α-particles) and in the absorber (for α-particles). The available thickness of the gold or tungsten, which may be obtained from calculations, does not exceed 2–4 μm.

2.3. Results

The results obtained by the NRA analysis for different points along the wire are shown in Figs. 5-6. The fluorine concentration along the anode wire and their depth distributions have been measured for Ar(80%)+CO_2(10%)+CF_4(10%) gas mixture under the total accumulated charge up to 1.8 C/cm. Diameter of the gold plated wire is equal to 35 μm. The degradation test of the straw drift-tube (ATLAS TRT) was carried out using a 2 Ci ^{90}Sr β-source.

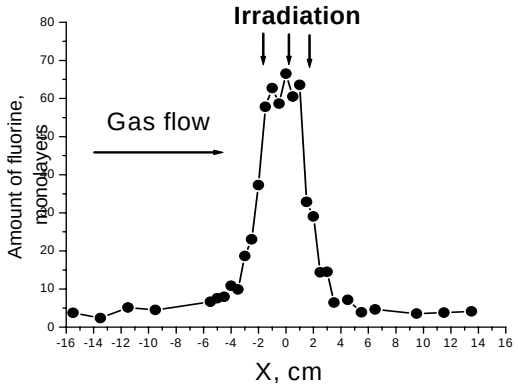

Fig. 5. The distribution of fluorine content along the irradiated wire. The element content of 1 monolayer is equal to 10^{15} at/cm^2

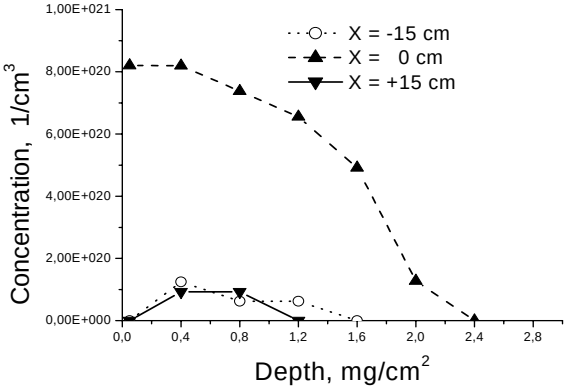

Fig. 6. The distribution of fluorine concentration as a function of depth into gold layer for different points along the irradiated wire

As one can see, after irradiation of the wires the amount of fluorine is noticeably increases. In the center of the irradiated zone the total amount of fluorine collected in gold has increased up to 15 times in comparison to the non-irradiated wire. Moreover, the maximum value of the fluorine peak concentration increased up to 10 times, reaching a value of 8×10^{20} at/cm^3. In irradiated places of the wire the depth of the fluorine penetration is up to 2.5 mg/cm^2. There is a direct correlation between the distribution of fluorine, oxygen and carbon concentrations along the wire and the beam irradiation profile (Fig. 7 and Table 4). It is shown that the fluorine concentration profile is correlated with changes of the wire diameter (increasing in the irradiation zone) and a gas gain (decreasing in the irradiation zone). For the detection and quantitative evaluation of the oxygen and carbon content as a function of depth in gold, the following nuclear reactions with deuterons in the energy range of 0.7–1.1 MeV have been applied: ^{12}C(d,p)^{13}C and ^{16}O(d,p)^{17}O [4].

Table 4

Dependence of element content, anode wire diameter and gas gain for different points along the wire. Center of irradiated area corresponds to X=0 cm. Total accumulated charge is about 1.8 C/cm

Distance along the straw	Content of elements in monolayers			Gas gain, relative units	Wire diameter, μm
	Fluorine	Oxygen	Carbon		
– 15 cm	4-5	50	25	1	35
0 cm	70	600	270	0.74	36.2
+15 cm	5-6	70	35	1	35

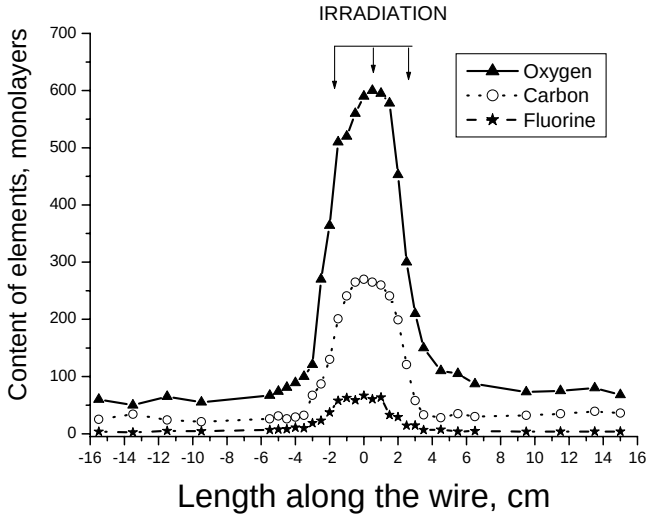

Fig. 7. The distribution of oxygen, carbon and fluorine content along the irradiated wire

2.4. Conclusion

The method of Nuclear Reaction Analysis (NRA) has been successfully developed at PNPI for investigation of the aging effects in the gas-filled detectors causing by fluorine and fluorine-containing compounds.

This method looks very promising and offers unique possibilities due to its high sensitivity, the fact that no etching is needed. The NRA method permits to investigate the lateral and depth distributions of the fluorine in samples.

Measurements of the oxygen, carbon and fluorine concentrations in the gold coating of the tungsten wire can provide an excellent method to compare the aging resistance of different wires which are intended to be used in the gas-filled detectors under high-accumulated dose.

References

1. V.M. Lebedev, V.A. Smolin and B.B. Tokarev, Preprint PNPI-2609, Gatchina, 2005. 24 p.
2. A.S. Ananiev, V.M. Lebedev, E.I. Terukov *et al*., Semiconductors, **36**, 941 (2002).
3. N.V. Sakharov, V.K. Gusev, V.M. Lebedev, E.I. Terukov *et al*., in *Proceedings of the 29th Conference on Plasma Physics and Controlled Fusion* (Montreux, Switzerland, 17 – 21 June 2002), p - 5.078 (2002).
4. G. Gavrilov, A. Krivshich and V. Lebedev, Nucl. Instr. Meth. A **515**, 108 (2003).
5. T. Ferguson, A. Krivshich, V. Lebedev *et al.,* Nucl. Instr. Meth., A **483**, 698 (2002).
6. T. Ferguson, A. Krivshich, V. Lebedev *et al.,* Nucl. Instr. Meth. A **515**, 266 (2003).
7. V.M. Lebedev, A.G. Krivshich and V.A. Smolin, Questions of Atomic Science and Technique, series: physics of nuclear reactors, **2**, 48 (2006).
8. V.M. Lebedev, A.G. Krivshich and A.N. Tatarinsev, Preprint PNPI-2616, Gatchina. 2005. 22 p.

COLLINEARITY LIMIT FOR THE MOVEMENT OF COMPLEMENTARY FRAGMENTS FROM THE SPONTANEOUS FISSION OF ^{252}Cf NUCLEI DETERMINED BY IMPLEMENTATION OF THE (2*E*, 2*V*)-MEASUREMENT METHOD

M.N. Andronenko, B.L. Gorshkov, A.V. Kravtsov, I.A. Petrov, V.R. Reznik, G.E. Solyakin

1. Introduction

The (2*E*, 2*V*)-measurement method was used for the study of mechanisms of nuclear disintegrations induced by relativistic projectiles. The account of this study is published in this issue [1]. The special attention was paid to collinear disintegrations induced in heavy and medium-heavy nuclei. The (2*E*, 2*V*)-measurement method was realized at the proton beam of the PNPI synchrocyclotron in the form of an angle-velocity-energy correlation spectrometer (SAVEC) described in Ref. [1]. The time and energy calibrations of the SAVEC were performed with the use of a weightless source of ^{252}Cf. At the same time it was supposed that because of the two-body kinematics of the spontaneous decay of ^{252}Cf-nuclei complementary fission fragments should move on the straight line with the folding angle between the two fragments equal to 180°. Any deviation from 180° would have physical reasons. Our experimental practice showed that there is a necessity to check this assumption. Since two distinct experiments were carried out with fission fragments of the same ^{252}Cf-source one can compare collinearity for two different experimental conditions.

2. Different variants of mosaic constructions

Two massive complementary fission fragments were detected by the SAVEC which comprises a vacuum chamber with two time-of-flight tubes. In the end of each tube at the distance L a mosaic of N semiconductor silicon surface-barrier detectors (SSBSD) was located. Two mosaics of SSBSD in combination with the independent start signal device (SSD) made it possible to measure kinetic energies E_i and times of flight T_i for both (i = 1, 2) complementary fragments. So each of the registered events may be characterized by the collection of six measured parameters (A_1, E_1, T_1; A_2,, E_2,, T_2) related to the two detected fragments. Ordinal numbers of SSBSD in mosaics were denoted by A_1 and A_2. When the kinetic energy E_i and time of flight T_i for each of the two complementary fragments are measured simultaneously, one can determine, unlike in (2*E*)- or in (2*V*)-measurement methods, fragment's absolute masses $M_i \sim E_i \cdot T_i^2$ and momenta $P_i \sim E_i \cdot T_i$. They may be used for the elimination of the distorted experimental events [1].

We want to describe two variants of the SAVEC construction which were implemented in experiments with fission fragments from the ^{252}Cf-source. They differ from each other by L = 1060 mm, N = 33 and L = 688 mm, N = 8. Both mosaic variants are shown in Figs. 1, 2. The first variant was used in experiments in which the maximum area of detecting elements was required. In this case among $33 \times 33 = 1089$ address combinations there were large variations for the folding angles between the two complementary fission fragments. For the second variant of the SAVEC construction, among $8 \times 8 = 64$ address combinations there were only 6 variations for the folding angles. This circumstance made angular measurements more effective. The binary code for the enumeration of detectors prevented the implementation of the variant with $9 \times 9 = 81$ address combinations which is shown in Fig. 3. For this case 6 variations for the folding angle detection are preserved. Figure 4 also shows a possible mosaic variant with $7 \times 7 = 49$ address combinations which have only 4 variations for the folding angle detection. Tables 1 and 2 contain all the information concerning values of difference $180 - \langle\theta\rangle$ in degrees for the $9 \times 9 = 81$ and $7 \times 7 = 49$ address combinations. In both cases $\langle\theta\rangle$ is an average folding angle for a certain address combination.

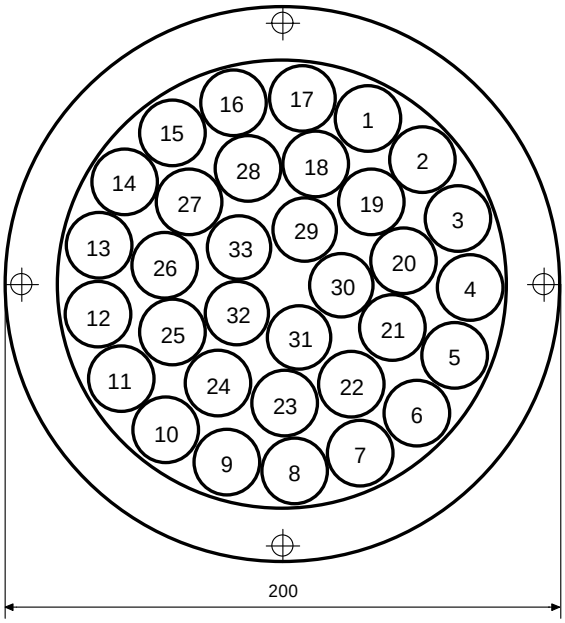

Fig. 1. Mosaic of the SAVEC construction with $N = 33$, $L = 1060$ mm

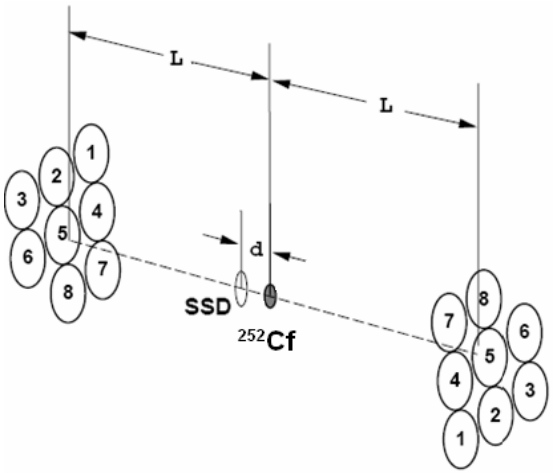

Fig. 2. Two mosaics of the SAVEC construction with $N = 8$, $L = 688$ mm. The distance between the ^{252}Cf-source and the start- signal device (SSD) $d = 37$ mm

Comparing mosaic constructions shown in Figs 2-4 one can conclude that they are almost equally effective for measurements of angular distributions. The chosen construction in Fig. 2 is nothing else but a truncated variant of $N = 9$ shown in Fig. 3.

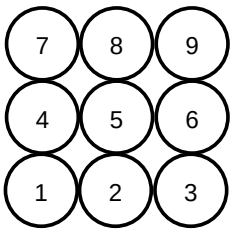

Fig. 3. Mosaic construction variant with $N = 9$

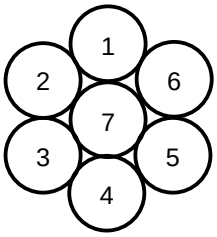

Fig. 4. Mosaic construction variant with $N = 7$

Table 1

	1	2	3	4	5	6	7	8	9
1	0	2.5	5.0	2.5	3.53	5.62	5.0	5.62	7.07
2	2.5	0	2.5	3.53	2.5	3.53	5.62	5.0	5.62
3	5.0	2.5	0	5.62	3.53	2.5	7.07	5.62	5.0
4	2.5	3.53	5.62	0	2.5	5.0	2.5	3.53	5.62
5	3.53	2.5	3.53	2.5	0	2.5	3.53	2.5	3.53
6	5.62	3.53	2.5	5.0	2.5	0	5.62	3.53	2.5
7	5.0	5.62	7.07	2.5	3.53	5.62	0	2.5	5.0
8	5.62	5.0	5.62	3.53	2.5	3.53	2.5	0	2.5
9	7.07	5.62	5.0	5.62	3.53	2.5	5.0	2.5	0

Table 2

	1	2	3	4	5	6	7
1	0	2.5	4.5	5.0	4.5	2.5	2.5
2	2.5	0	2.5	4.5	5.0	4.5	2.5
3	4.5	2.5	0	2.5	4.5	5.0	2.5
4	5.0	4.5	2.5	0	2.5	4.5	2.5
5	4.5	5.0	4.5	2.5	0	2.5	2.5
6	2.5	4.5	5.0	4.5	2.5	0	2.5
7	2.5	2.5	2.5	2.5	2.5	2.5	0

3. Experimental results

In the case of the SAVEC performance with L = 1060 mm, N = 33 and 33 × 33 = 1089 address combinations there were no detailed analysis on the angular distribution of the complementary fission fragments of ^{252}Cf nuclei. Since it was obtained at the level of 1.5% statistical accuracy, the value of the standard deviation of the total angular distribution from the collinearity σ_θ = 21 mrad. Advantages of the (2E, 2V)-measurement method were not utilized in this case for the further analysis. They were used in the second variant of the SAVEC performance with L = 688 mm, N = 8 and 8 × 8 = 64 address combinations. Owing to (2E, 2V)-measurement method it was possible to obtain a bi-dimensional plot (P_1, P_2) for complementary fragments of spontaneous fission of ^{252}Cf nuclei. The plot shown in Fig. 5 contains all the events in which at least one of the momenta P_1 or P_2 was smaller than 4000 MeV/c, as well as a small part of the total statistics where both P_1 and P_2 were greater than 4000 MeV/c.

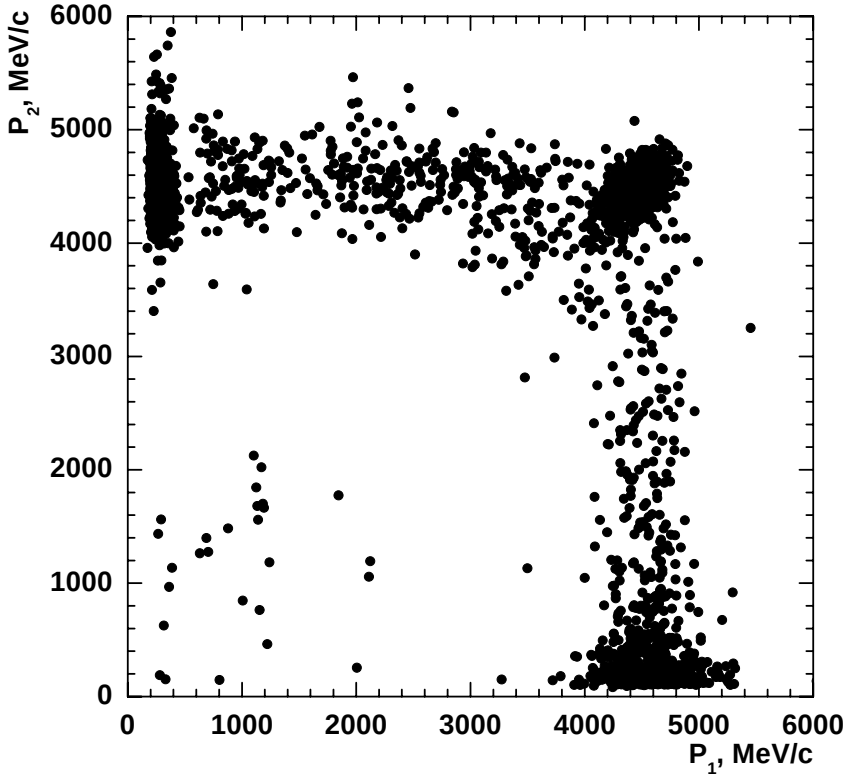

Fig. 5. Bi-dimensional plot P_2 versus P_1 for experimental events in which at least one of the momenta P_1 and P_2 is smaller than 4000 MeV/c as well as a small part (~0.5%) of the total statistics is used

Symmetric distribution of the events in Fig. 5 with respect to the diagonal $P_1 = P_2$ testifies the identity of both arms of the SAVEC. Events in which at least one of the momentum P_1 or P_2 was smaller than 4000 MeV/c comprised 1.3% of the total statistics. The events with clearly unbalanced momenta look like an evidence for the third body influence upon the two-body kinematics of the separating fragments. They can be considered as distorted events with respect to the normal fission events. One more advantage of the (2E, 2V)-technique compared with other experimental methods is an opportunity to measure a missing mass

$$\Delta M = M_0 - (M_1 + M_2), \tag{1}$$

where M_0 is the mass of the target nucleus and $M_{1,2}$ are the masses of the detected fragments. Using the information measured by the SAVEC one can determine the masses M_1 and M_2 for each distorted event. It turned out that one of the masses M_1 or M_2 was normal, *i.e.* belonged to the light or heavy group of the fragments, the other one being much smaller, imitating a large missing mass. The normal mass had the

normal fragment momentum (*i. e.* it was larger than 4000 MeV/c), the smaller mass having much smaller momentum (less than 4000 MeV/c). The detailed analysis showed that among the distorted events, composed 0.4% of the total statistics, only 0.12% belonged to the fragments of the light mass group and 0.28% to the heavy mass group. This observation testifies that a considerable part of the distorted events represents the Rutherford scattering. Since in the calibration experiment with the ^{252}Cf-source the amplitude thresholds were very low, it was rather difficult to separate the effect of the Rutherford scattering from random coincidences for small momenta in both arms of the SAVEC. In Ref. [2] the presence – among the detected fragments – of the masses in the range from 55 to 65 u, characteristic for the natural mixture of nickel isotopes, was demonstrated. The distorted events differ from normal ones also by address combinations (A_1, A_2) of the detectors hit by fragments. The number of non-collinear fragments is much larger for distorted events [3]. Thus the calibration experiment with registration of fragments of the spontaneous fission of ^{252}Cf nuclei by (*2E*, *2V*)-technique showed how to reject the distorted events. Figore 5 helps to eliminate all the distorted events. For this purpose elimination thresholds for P_1 > 4000 MeV/c and P_2> 4000 MeV/c were chosen. The corresponding bi-dimensional plot (P_1, P_2) is shown in Fig. 6. The angular distribution for experimental events from Fig. 6 is demonstrated in Fig. 7.

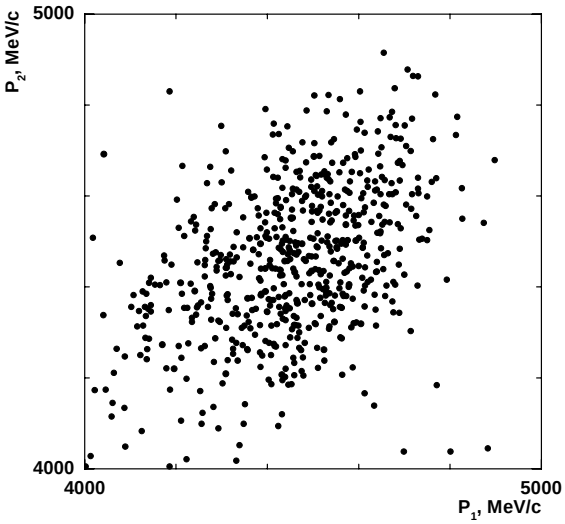

Fig. 6. Bi-dimensional plot (P_1, P_2) for events with momentum ranges 4000–5000 MeV/c

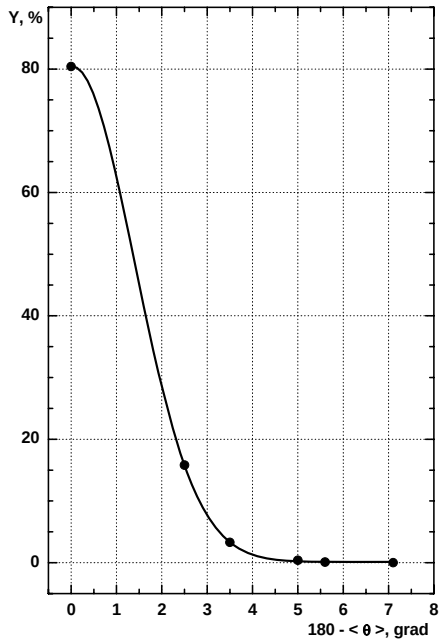

Fig. 7. Folding angle distribution for experimental events shown in Fig. 6

At the level of 4% statistical accuracy the spectrum shown in Fig. 7 satisfies to the standard deviation of the total angular distribution σ_θ = 19.2 mrad. Later on two attempts were undertaken. At first the momentum thresholds for P_1 and P_2 were decreased to 3800 MeV/c and after that they were increased to 4200 MeV/c. In both cases values of the standard deviation for these angular distributions became larger than 19.2 mrad. Thus the value of σ_θ = 19.2 mrad can be considered as a minimal possible standard deviation for angular distribution of complementary fragments from the ^{252}Cf-source measured with the help of the (*2E*, *2V*)-measurement method.

Returning to the experimental practice at the proton beam of the PNPI synchrocyclotron we can justify the division of experimental nuclear disintegration events in two groups according to the collinearity. The first group of events denoted by stars belongs to the folding angle interval of (180°–177.5°), the second group with events denoted by points belongs to the interval of (176.5°–172.9°). Fig. 8 shows two momentum distributions one of which is nothing else as a repetition of Fig. 6 for complementary fission fragments from the ^{252}Cf-source. The second distribution refers to the complementary fragments from disintegrations induced in tungsten nuclei by 1 GeV protons.

Experimental events for tungsten disintegrations were taken from Fig. 3 of Ref. [1]. All experimental events were denoted by stars and points in accordance with the value of the folding angle between complementary fragments.

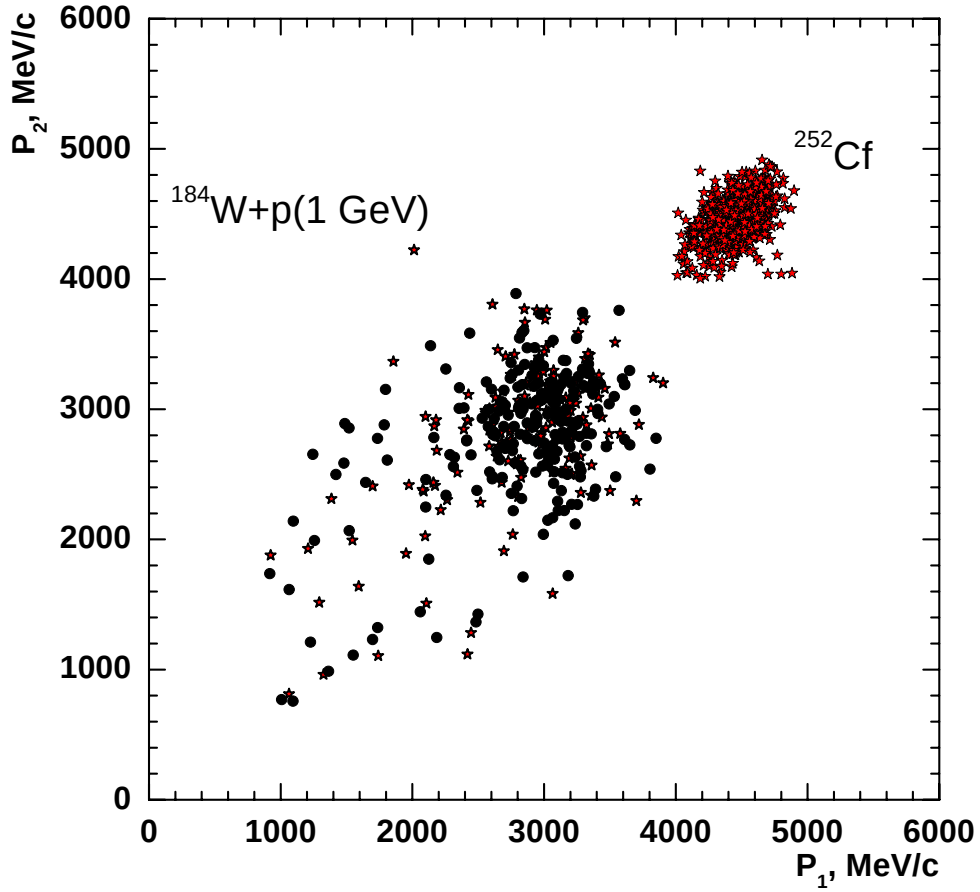

Fig. 8. Correlated momentum distributions (P_1, P_2) for complementary fragments from disintegrations induced in tungsten nuclei by 1 GeV protons and from the ^{252}Cf-source taken from Fig. 6. Stars and points are explained in the text

4. Conclusion

The value of $\sigma_\theta = 19.2$ mrad was obtained with detectors having angular acceptance $\delta\theta = 43.6$ mrad. It means that there is a possibility to get a better value for the measured standard deviation if one chooses detectors with a smaller angular acceptance. This limiting standard deviation can be evaluated according to the formula

$$\sigma_\theta^{\lim} = \left[(\sigma_\theta)^2 - \frac{(\delta\theta)^2}{12} \right]^{1/2} . \qquad (2)$$

Thus the final possible limiting standard deviation may be as low as $\sigma_\theta^{\lim}$ = 14.5 mrad.

References

1. B.L. Gorshkov, A.V. Kravtsov, V.R. Reznik and G.E. Solyakin, this issue, page 200.
2. A.V .Kravtsov and G.E. Solyakin, Phys. Rev. C **60**, 017601 (1999).
3. A.V. Kravtsov and G.E. Solyakin, in *Proceedings of the 1st International Workshop on Physics of Isomers* (St.-Petersburg, 18 – 21 June 2000), Sarov, VNIIFF, 2001. p. 74.

RADIATION HARD PHOTODETECTORS BASED ON FINE-MESH PHOTOTUBES FOR CALORIMETRY IN VERY FORWARD RAPIDITY REGION

Yu.I. Gusev, V.N. Lukianov[1)], G.A. Mamaeva[1)], D.M. Seliverstov, L.P. Shusterman[1)]

[1)] *Central Research Institute Electron, St.-Petersburg*

1. Introduction

In experiments using electromagnetic and hadron calorimeters, which are planned for the LHC in the very forward rapidity range (up to η =6), the radiation fields are very high. Ionizing radiation levels reach hundreds of kGy and neutron fluences go up to 10^{16} n/cm^2. In addition the photo-readout systems have to operate in the magnetic fields of LHC Detectors (ATLAS, CMS), which in the region of interest are at the level of 20–40 mT, and in the presence of helium gas which exceeds the normal helium concentration in the atmosphere by a factor of 100 to 1000.

Low gain fine-mesh photomultiplier tubes (VPT, or vacuum phototriodes) have been used in the end-cap electromagnetic calorimeter of CMS and have been shown to be able to withstand gamma radiation doses up to 50 kGy. The VPT anode response decreased by 10% in good agreement with what would be expected due to a change of UV faceplate light transmittance [1, 2]. High gain photodetectors proposed to be used in the experiment CASTOR at LHC for the detection of Cherenkov radiation must provide stable operation for higher gamma radiation doses − up to hundreds of kGy and simultaneously for neutron fluences up to 10^{16} n/cm^2. A suitable detector for such applications can be a multi-stage fine-mesh photomultiplier tube (PMT) FEU-187 with highly radiation hard faceplate made of UV glass.

2. Measurements of PMT radiation hardness

For studies of faceplate radiation hardness, the best type of glass produced in Russia (US-49A) was chosen. This type of glass has a light transmittance loss $\Delta T/T_0$ = 7% at a wavelength of 425 nm for a radiation dose D = 50 kGy. This value corresponds to the average wavelength of the HLMP-DB25 LED used for PMT illumination. The irradiation of the faceplates was performed at the PNPI nuclear reactor with neutrons of average energy E_n = 0.95 MeV up to a total fluence of 10^{16} n/cm^2 known to an accuracy of 10%. The accompanied gamma radiation dose was estimated to be 1600 ± 250 kGy. The glass transmittance spectra measurements were done one month after the irradiation. We did not take into account the gamma radiation dose caused by the activation radiation of the glass, so the value 1600 kGy is a lower limit on the gamma radiation dose. The results of the reactor irradiation test are shown in Fig. 1.

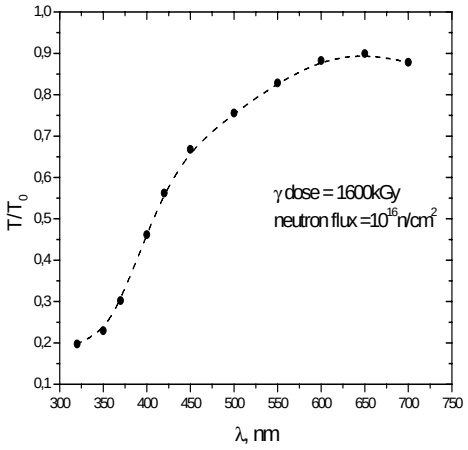

Fig. 1. US-49 relative glass transmittance after irradiation in nuclear reactor

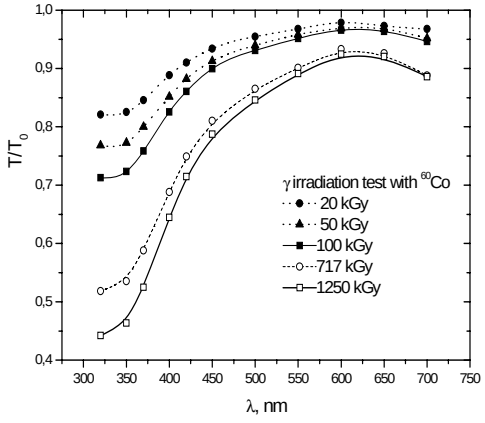

Fig. 2. US-49 relative glass transmittance for different of gamma radiation doses at ^{60}Co gamma facility

The total glass transmittance loss $\Delta T/T_0 = 1 - T/T_0$ can be estimated as a sum of terms due to gamma and neutron irradiation. For the wavelength of 450 nm $\Delta T/T_0 = 33\%$. In order to separate contributions of gamma and neutron irradiation to the value of T/T_0 we performed measurements of the light transmittance spectra for similar glass samples under the ^{60}Co γ-rays up 1250 kGy at the PNPI gamma facility. Results are shown in Fig. 2. On the basis of the glass transmittance measurements with gamma radiation doses of 471, 717 and 1250 kGy we made a linear extrapolation to a dose of 1600 kGy. This allowed us to define at λ = 450 nm separate losses of $\Delta T/T_0 = 39\%$ for gamma irradiation and $\Delta T/T_0 = 15\%$ for neutron irradiation. This procedure can be done for a set of wavelengths in the range 325–600 nm. An example of the extrapolation for λ = 450 nm is shown in Fig. 3.

Using the extrapolation method discussed above, one can obtain the transmittance loss caused by a neutron fluence of 10^{16} n/cm^2 at any gamma radiation dose. The US-49A faceplate transmission after 10^{16}n/cm^2 and 50 kGy gamma irradiation is shown in Fig. 4. For comparison, the glass transmittance after only gamma irradiation up to 50 kGy is also shown. The accuracy of this method to separate the neutron and gamma damages in the PMT faceplate is estimated not to be better than 3%. The dependence of the faceplate light transmission change at different neutron fluences (F) can be obtained by performing measurements for varying F and gamma radiation doses. Such studies were not a goal of our experiment. We present only studies of the behavior of PMT windows in extremely hard neutron and gamma irradiation conditions.

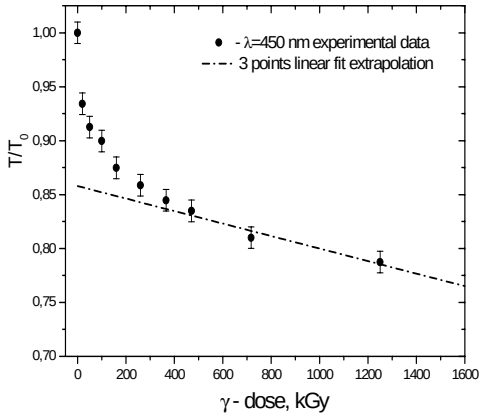

Fig. 3. The linear extrapolation of T/T_0 data at the different doses of ^{60}Co γ-irradiation

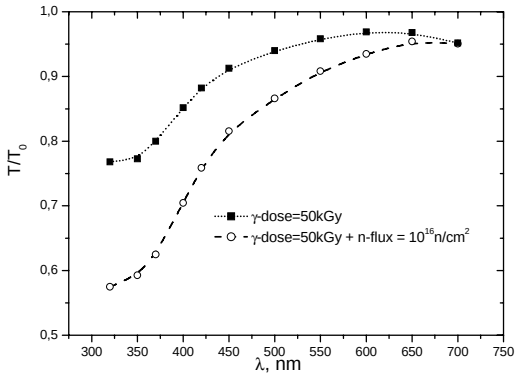

Fig. 4. Relative transmittance T/T_0 for a γ-dose of 50 kGy and neutron irradiation with fluence of 10^{16} n/cm^2

As it was mentioned above, the VPT anode response is following the rather small glass transmittance change under gamma irradiation up to 50 kGy. The same insensitivity of the VPT anode response to 14 MeV neutrons with fluences up to 2.8×10^{14}n/cm^2 was shown in Ref. [2]. With a knowledge of the US-49A transmittance change under gamma irradiation, we measured the anode response of FEU-187 photomultiplier tube before and after irradiation at 20 kGy and 50 kGy using a blue LED Lamp HLMP-DB25 with a wavelength peaking at λ = 426 nm with the method described in Ref. [3].

Examples of spectra obtained before and after gamma irradiation (50 kGy) of the PMT FEU-187 are shown in Fig. 5. The numeral "2" marks the PMT pulse spectrum. Similarly, "3" indicates the reference PMT pulse spectrum, and "1" – the ^{137}Cs γ-spectrum from the reference PMT with the same gain as for the measurements (a) and (b). Stability of the electronics and PMT gain was at the level of 1%. Overall statistical and systematic errors are estimated as not more than 3%. The results obtained during gamma irradiation at 50 kGy show good agreement of the anode signal change with the faceplate transmittance loss within experimental errors of ±2%. A burn-in test of the PMT was in a similar way to the irradiation test, with the PMT illuminated by a light emitting diode producing an anode current of 200 nA for 50 hours. Measurements of the anode signal before and after the illumination did not show any change of the amplitude with an accuracy of ±2%, which demonstrates the stability of this PMT under these conditions.

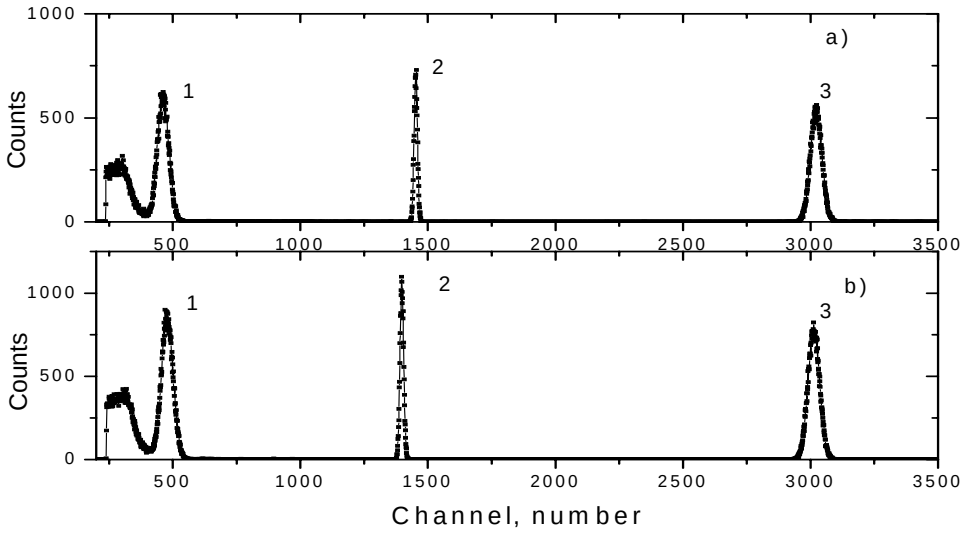

Fig. 5. Spectra from PMT FEU-187 before (a) and after (b) gamma irradiation up to 50 kGy

3. PMT immunity to the gaseous He

It is well known that helium gas can penetrate into PMT and degrade its performance increasing the dark count rate. Helium can also cause an ion pulse following a normal one. The presence of the gaseous He in the atmosphere of LHC Collision Hall and in the experimental pits is estimated to be between 100 and 1000 ppm. Immunity to the gaseous He is an important characteristic of photomultiplier tubes proposed for readouts in LHC environment. The helium immunity of the FEU-187 was measured using the experimental setup shown in Fig. 6. The PMT to be studied was placed into a vacuum-tight chamber. Dark current count rate and gain of PMT were measured in a constantly refreshed atmosphere of pure nitrogen during first 8 days. Later pure nitrogen was changed to a mixture of (N_2+He) where He admixture was 1600 ppm. The pressure in the chamber was equal to one atmosphere.

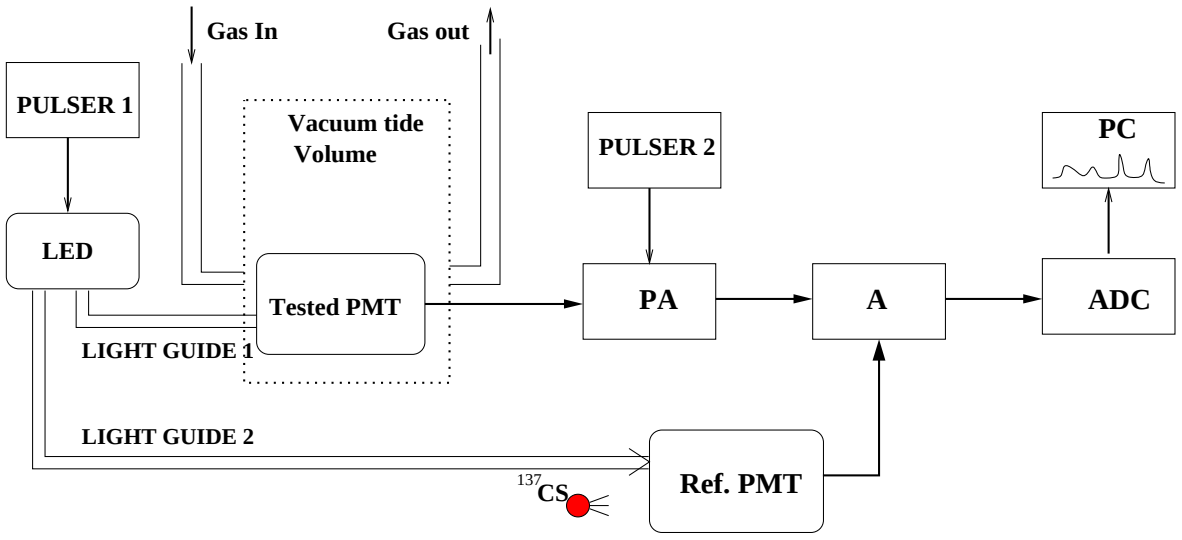

Fig. 6. Experimental setup for the He immunity test of PMT FEU-187

The PNT dark current without illumination was not more than 1 nA. The results of these measurements are shown in Fig. 7. The gain of the PMT was monitored during this test. Light pulses from the LED, driven by Pulser 1, were directed simultaneously by two fibers to the PMT under test and to a standard reference PMT placed outside of the He volume. The gain stability of the reference PMT coupled with NaI(Tl) crystal was tested by the detection of ^{137}Cs γ-rays during test measurements. The stability of electronics was tested by means of the precision amplitude signal generator (Pulser 2). All signals were digitized by an ADC and recorded with a PC. The dark noise count rate and the gain of PMT FEU-187 did not show any change during 4 weeks operation in an atmosphere of (N_2+1600 ppm He).

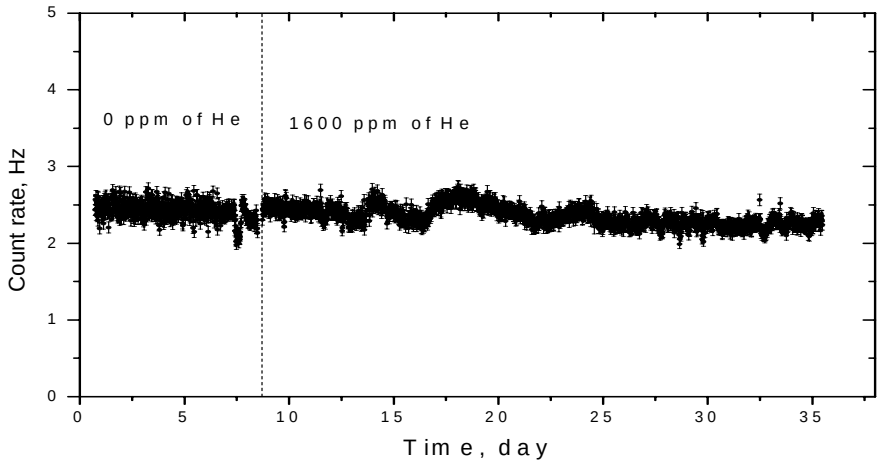

Fig. 7. Dark noise count rate in N_2 atmosphere with 1600 ppm of He admixture

4. Magnetic hardness and time resolution

Resistance to magnetic fields is an important issue for PMTs proposed to be used in the LHC environment. The gain dependence of the fine-mesh PMT FEU-187 on a magnetic field B was measured for two angles θ between the PMT axis and the magnetic field direction. The gain behavior over the large range of θ for B = 40.6 mT was also measured. Results of these measurements are shown in Fig. 8.

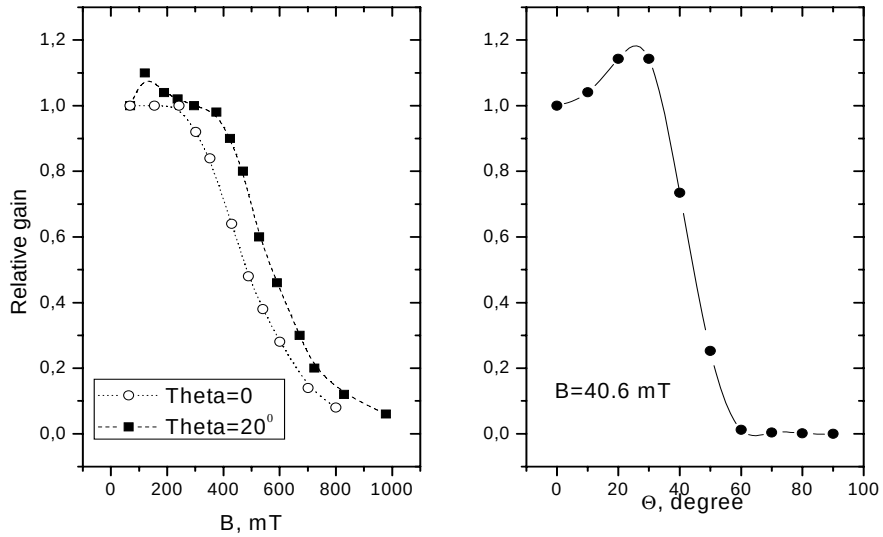

Fig. 8. Magnetic properties of fine-mesh FEU-187

Two different methods were used to evaluate time resolution of fine-mesh FEU-187.

1. Measurement of time of flight for different particles such as π, K and p with a momentum of p = 1.8 GeV/c, using two plastic scintillators (BS-420 with 2 cm thickness separated by 4 m). A time resolution of σ = 58 ps per photodetector was obtained.
2. Measurement with a pulsed light source with the pulse duration (FWHM) of 35 ps and the wavelength of 635 nm: with a threshold of about 0.2 photoelectrons, the measured time resolution was σ = 270 ps for a single photoelectron pulse (see Fig. 9).

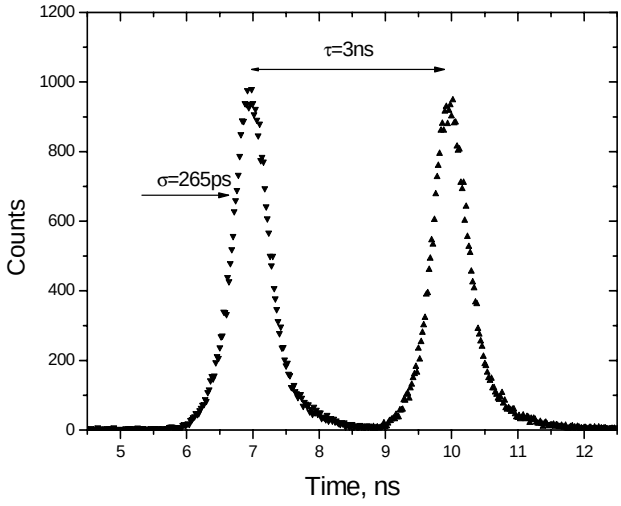

Fig. 9. Time resolution of FEU-187 measured in single photoelectron mode

5. Conclusion

In this paper we present the results of study of a very radiation hard photodetector – a high gain fine-mesh PMT (FEU-187) with a highly radiation hard faceplate from UV-transparent glass (type US-49A). Radiation resistance of PMT to γ-rays and neutrons was investigated at the PNPI gamma facility and nuclear reactor. A number of UV-transparent glasses were irradiated near active zone of reactor up to a fluence of 10^{16}n/cm^2 with an average neutron energy of E = 0.95 MeV and with gamma radiation doses of 1600 ± 250 kGy. In order to separate the light transmittance losses in the glass caused by neutron and gamma irradiation, the measurements of the glass transmittance spectra at different doses up to 1250 kGy were performed at the ^{60}Co gamma facility. In this way we were able to define the glass transmittance loss caused by the reactor radiation for the wavelength range λ = 350–650 nm separately for γ-rays and neutrons. For the wavelength λ = 400 nm, the light transmittance losses are equal to 43% and 11% due to gamma and neutron irradiation, respectively. In experiments with gamma irradiation to 100 kGy and neutron fluence of 10^{16} n/cm^2 the light transmittance at λ = 400 nm is reduced to 72% of its initial value. These results are an evidence of the high radiation hardness of the PMT faceplates that were studied. The irradiation of a PMT with US-49A faceplate by gamma radiation doses of 20–50 kGy has shown a change of the PMT anode response expected from the UV glass transmittance loss. Results of measurements of insensitivity to magnetic fields and immunity of the PMT against helium in the LHC environment are also presented.

At levels expected in the LHC environment, FEU-187 is radiation hard, resistant to magnetic fields and unaffected by the presence of helium. The PMT FEU-187 has an excellent time resolution of 58 ps measured by time-of-flight techniques with 1.8 GeV/c beams of pions, kaons and protons at CERN, and a time resolution of 270 ps measured with an ultrafast laser diode in a single photoelectron mode.

References

1. Yu. Blinnikov *et al.*, Nucl. Instr. Meth. A **504**, 228 (2003).
2. Yu. Gusev et *al.*, Nucl. Instr. Meth. A **535**, 511 (2004).
3. Yu. Gusev *et al.*, Preprint PNPI-2597, Gatchina, 2005. 16 p.

SYSTEM FOR DEEP PURIFICATION OF HYDROGEN IN MuCap EXPERIMENT

V.A. Ganzha, P.A. Kravtsov, V.A. Trofimov, G.N. Shapkin, A.A. Vasilyev, M.E. Vznuzdaev

1. Introduction

The MuCap experiment at PSI is a precision measurement of the rate Λ_S for the basic electroweak process of muon capture, $\mu^- + p \rightarrow n + \nu$. A measurement of 1% accuracy determines the last well-known of the nucleon charged current form factors, the induced pseudoscalar g_P, to 7%. The experiment is carried out at the πE3 muon beam of the 580 MeV proton accelerator at the Paul Scherrer Institute (PSI), Switzerland.

The capture rate is determined from a measurement of the disappearance rate $\lambda_- \approx \lambda_+ + \Lambda_S$ of negative muons in hydrogen and the world average of the free μ^+ decay rate λ_+. Muons are stopped in a time projection chamber (TPC) with sensitive volume $15 \times 12 \times 30$ cm^3 filled with ultrapure hydrogen at 10 bar. Electrons ionized by muons or other projectiles drift vertically in a homogeneous electrical field to the bottom of the TPC, where they are amplified with a multiwire proportional chamber (MWPC) and read out in two dimensions.

The experiment imposes strict and critical requirements on the hydrogen gas system supporting the active target – TPC detector. As the hydrogen gas density of the experiment of ten times higher than at standard temperature and pressure, the rates for muon transfer from μp to typical chemical impurities (N_2, H_2O, O_2) are 3 orders of magnitudes larger than the muon decay rate. Once a muon has been transferred to a μZ atom, nuclear muon capture proceeds more than 100 times faster than on a μp atom. Thus, gas impurities distort the observed lifetime spectrum, and transfer must be suppressed by keeping the gas contaminations below a level of typically 10 ppb. Isotopic purity is required as well, since muon transfers to deuterium lead to a difficult diffusion problem. A dedicated isotope separation device [1] was constructed to produce protium with a deuterium contamination of less than 70 ppb; this work will be published separately.

As the gas amplification in the MWPC of the TPC sensitively depends on the hydrogen pressure, the pressure inside the TPC must be stabilized on the level of 10 bar with 0.1% accuracy. This is required to keep the MWPC gas gain constant within 1%. There is also concern that large flow variation in the TPC might induce dust accumulation and breakdown of the chamber high voltage. Thus the flow has to be stabilized as well. Finally, the whole detection system operated with high voltage in a pure hydrogen environment, thus reliability and hydrogen safety were of utmost importance.

The "Circulating Hydrogen Ultrahigh Purification System" (CHUPS) was designed and built to provide continuous protium purification and achieved all design criteria over several experimental runs with typically 2 months of continuous operation per year.

2. Circulating system (CHUPS) design

2.1. CHUPS operation scheme

During the experiment the TPC can directly monitor the capture reactions on impurities, the yield roughly proportional to the impurity concentration. This technique was used in 2003 before CHUPS was installed, showing the yield increasing during several days after filling the TPC. The chamber was filled through the palladium filter and exposed to the muon beam. The experiment revealed accumulation rate of some tens ppb per day which is unacceptable for the experimental requirements. This is the main reason for development of CHUPS designed for continuous gas cleaning and circulation through the operating TPC.

Initially a circulation system consisting of a mechanical pump and a Pd filter was considered. Pumps with high vacuum rating operating at 10 bar pressure are not commercially available and Pd filters supporting the required flux of 3 slpm (standard litres per minute) are expensive. Instead the alternative CHUPS scheme was realized, which is based on an adsorption cryopump to maintain the hydrogen flow and a cryogenic adsorption filter for removing the impurities. The adsorption cryopump has essential advantages, such as intrinsic high purity and reliability due to the absence of moving parts. The circulating system was designed, mounted and tested at PNPI in Gatchina, Russia, and installed at PSI during the preparation period

of the MuCap experiment in 2004 [2]. It was upgraded in 2005 on the basis of the operating experience. A simplified diagram of the system is shown in Fig. 1. CHUPS consists of two main units which are mounted separately on a common frame: compressor and purifier.

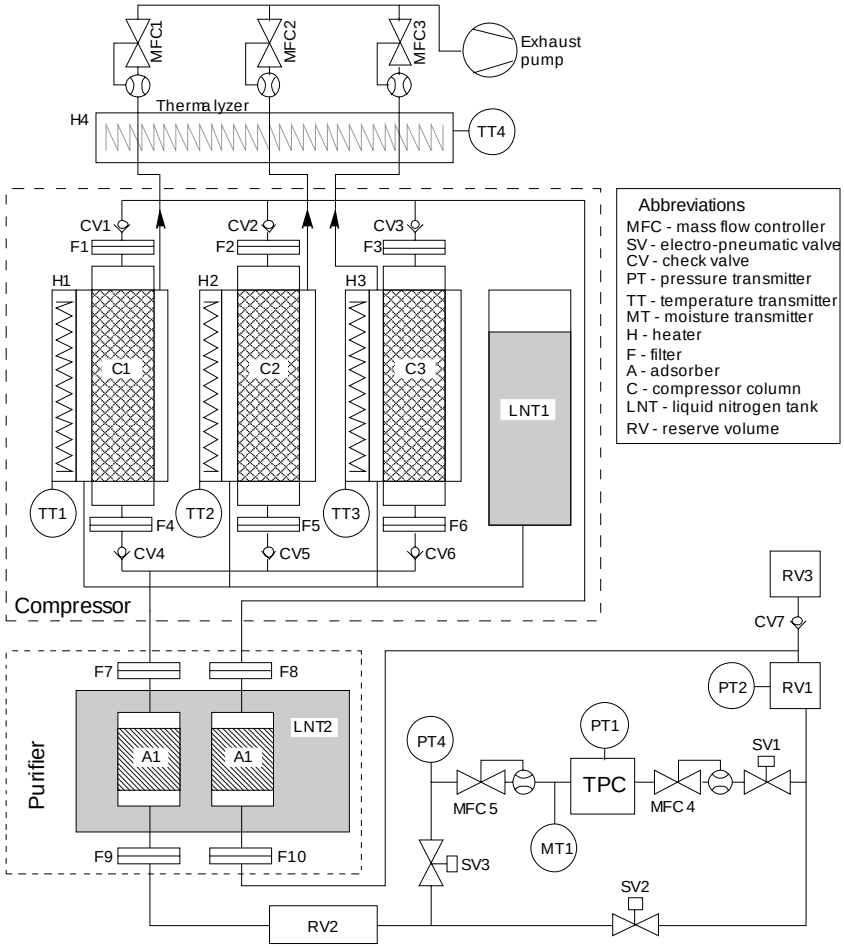

Fig. 1. Simplified CHUPS diagram

2.2. Compressor

The compressor is a triplex adsorption cryopump. It has three identical cartridges (columns) filled with activated carbon [1] and connected in parallel. The cartridges are made from thick-walled stainless steel tube and designed to keep high pressure. The volume of each column is about 1 liter and contains with respect to packed density of the carbon up to 0.6 kg of the adsorbent. Each column (C1, C2, C3 in Fig. 1) has a heat exchanger made of copper tube. It is coiled around the column and soldered to its outer surface by silver hard alloy. The heat exchanger is used to cool down the compressor column using liquid nitrogen flowing from the 40-litre supply vessel (LNT1). Liquid nitrogen flow is provided by an exhaust pump connected to the heat exchangers manifold. After cooling the columns nitrogen flows through the thermalizer (H4), which heats the gas up to the room temperature. Mass-flow controllers [2] MFC1, MFC2, MFC3 control the flow rate of the gaseous nitrogen and consequently regulate the liquid nitrogen flow rate and the cooling rate of the column. An electric heater is coiled around the column between the heat exchanger turns to provide the column heating. Each column has two check valves with the actuation pressure of 50 mbar that are installed in the inlet and outlet pipelines (CV1−CV6). Inlet and outlet lines of the columns are combined to the inlet and the outlet manifolds, respectively.

[1] Norit Nederland B.V. Nijverheidsweg Noord 72, 3800 AC AMERSFOORT, The Netherlands.
[2] Aalborg (http://www.aalborg.com/) stainless steel GFC series mass-flow controllers.

At the cooling stage the adsorbent inside the column adsorbs hydrogen, and the internal pressure drops below the pressure in the inlet line of the compressor. Consequently, the inlet check valve opens and passes hydrogen into the column. During the heating stage the adsorbent desorbs hydrogen, and the column internal pressure rises above the outlet line pressure. The outlet check valve opens and passes hydrogen into the outlet line. Thus, the combination of the check valves provides a pulsating flux of hydrogen in one direction. Cooling and heating rates are regulated by the balance of liquid nitrogen flow (controlled by MFC1, MFC2, MFC3) and heating power (managed by pulse-width modulation of the power supplies).

The temperature phases of the columns are shifted with respect to each other. Upper and lower temperatures and cycle frequency are regulated in accordance with the required average flow rate. A single compressor column pumps approximately 32 standard liters of hydrogen in one cycle employing a temperature range of 80–150 K. The maximum hydrogen flow of 3 slpm through the compressor is defined by the maximum cooling rate and the thermalization time of the activated carbon.

2.3. Purifier

The purifier contains two cartridges filled with NaX-type zeolite [3] (indicated as adsorbers A1 and A2 in Fig. 1). The adsorbers are immersed into liquid nitrogen vessel (LNT2) and permanently kept under temperature of 77 K during the whole experimental run. Low temperature is essential to increase the adsorption ability of zeolite for high-boiling contaminants (oxygen, nitrogen) against the main gas (hydrogen). Two adsorbers contain about 40 g of the sorbent in total, enough to accumulate up to 1 g of adsorbed water. The total amount of water supplied by the flow of 3 slpm during the two-month experimental run was about 2×10^{-2} g (allowing for 100 ppb constant humidity), which is 2% of the adsorber capacity. The adsorption capacity for other contaminants is comparable. Thus, the adsorbers guarantee full impurity removal in the hydrogen flow during the long term experiment. The adsorbent has to be exchanged or can be regenerated by heating up to 400°C and pumping before each experimental run.

The liquid nitrogen vessel is contained in the vacuum case and protected from external thermal radiation by a copper shield mounted on the secondary liquid nitrogen vessel which is also used to cool down the incoming hydrogen. This technique decreases liquid nitrogen consumption and prevents heating the zeolite adsorbers. The two adsorbers of the purifier (A1 and A2) are mounted on the hydrogen lines upstream and downstream of the TPC, respectively, providing two stage purification of the gas. The inlet zeolite adsorber takes out most of the impurities, which helps to avoid any decrease of the compressor capacity due to the accumulation of impurities in the activated carbon.

The system is equipped with mechanical 2 μm filters installed before and after the compressor and in the detector pipelines that prevent carbon or zeolite dust penetration to the clean part of the system. The final purification is provided by a special gas purifier [4] of limited capacity installed at the TPC inlet.

2.4. Control system

A special stand-alone microcontroller block provides all necessary regulation algorithms. The control block is connected to a PC *via* RS-232 or RS-485 serial interface. Due to implementation of all control algorithms in the independent control block, the system remains operational in the case of computer failure. Computer software is used for adjusting the parameters of the regulation algorithms, collecting and visualizing the process variables and keeping them in the database. All system events (including software messages and alarms) are also saved in the database. Special software was developed to access the parameters history and event log in the database.

The control block measures and controls all system devices like pressure sensors, valves, mass-flow controllers, *etc.* It provides the following regulation procedures:

- temperature stabilization of the three compressor columns and the thermalizer by regulating the heating and cooling provided by the heaters and the nitrogen mass-flow controllers, respectively;

[3] CECA company, http://www.adsorbents.com/sites/ceca/en/home.page.
[4] SAES Pure Gas - MicroTorr Ambient Temperature Gas Purifiers. http://www.puregastechnologies.com/microt.htm.

- cyclic operation of the compressor columns with phase shift;
- TPC internal pressure stabilization using mass-flow controllers;
- temperature stabilization of the humidity sensor.

Alarm and interlock functions are also implemented in the control block firmware (see Table). It protects the detector from underpressure and overpressure and controls differential pressure between the TPC and reserve volume RV1 to avoid hydrogen flux variations. Also, the software tracks liquid nitrogen level in the compressor tank (LNT1) and compressed air pressure that is used for the electro-pneumatic valves (SV1–SV3) actuation. All alarm events are attended with light and sound signal.

Table

Alarm events and interlock actions

Alarm description	**Condition**	**Action**
TPC pressure high	PT1>PT1max	Cut-off TPC and open bypass
TPC pressure low	PT1<PT1min	Cut-off TPC and open bypass
Differential pressure high	(PT2-PT1)>DPmax	Cut-off TPC and open bypass
Differential pressure low	(PT2-PT1)<DPmin	Cut-off TPC and open bypass
Compressed air pressure low	PT3<PT3min	Alarm signaling
Liquid nitrogen level low in LNT1	N2Level<N2Levelmin	Alarm signaling

2,5, TPC pressure and flow control

The three columns of the compressor induce the hydrogen flow to exchange the gas in the TPC. This flow is pulsating because of the periodical mode of the column operation. The pressure inside the TPC must be stabilized with 0.1% accuracy. In order to smooth the pressure variations caused by compressor, the CHUPS system is equipped with two reserve volumes of 15 liters content each (RV1 and RV2), pressure sensors (PT1, PT2, PT4) and mass-flow controllers (MFC4 and MFC5).

The reserve volumes are installed in the inlet and outlet lines of the TPC. They are used as buffering volumes. The RV1 also provides a hydrogen reserve to support the pressure stabilization algorithm. Each volume is equipped with a pressure sensor (PT2 and PT4, same model as PT1). Two mass-flow controllers with a maximal flow of 20 slpm are mounted at the inlet (MFC4) and outlet (MFC5) lines of the TPC.

The internal pressure of the detector (measured by PT1) is stabilized using PID (Proportional-Integral-Derivative) regulation. The mass-flow controller at the detector outlet (MFC5) is set to a constant flow rate. The TPC inlet mass-flow controller (MFC4) is operated by PID algorithm in the control software. The MFC5 set point defines the average flow rate through the TPC vessel. The pressure distribution histogram (Fig. 2) for the long term operation during 50 days shows excellent pressure stability on the level of 0.024% at a mean hydrogen flow of 3 slpm. The histogram bars correspond to the ADC discretization in the control system (1.2 mbar). Thus the pressure is kept within ±2 least significant bits of the ADC. The second reserve

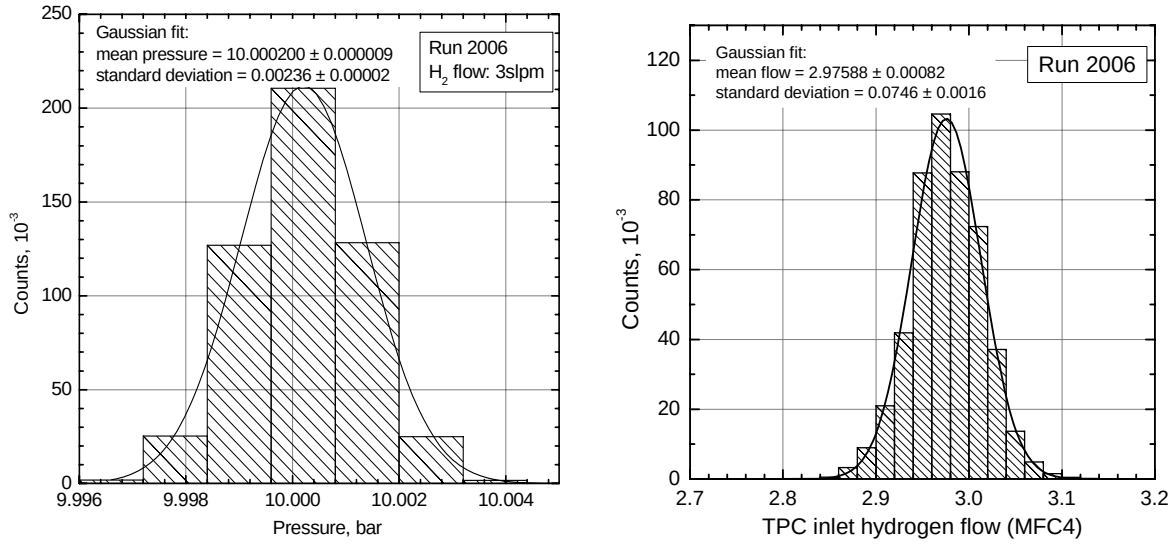

Fig. 2. TPC pressure and inlet flow distribution histograms. The gaussian fits gives a full width of 2.4 mbar and 0.075 slpm that correspond to 0.024% and 2.5% stability, respectively

volume (RV2) and the mass flow controller (MFC5) at the compressor inlet were installed to prevent pressure drops caused by the fast opening of the check valve. This results in a flow stability of 2.5% at the mean flow level of 3 slpm during 50 days of CHUPS operation (Fig. 2).

3. Monitoring impurities

The initial purity of the evacuated TPC system was provided by continuous pumping and baking of the TPC vessel. The residual gas contents were controlled by a quadrupole mass-spectrometer in the mass range from 2 to 100 atomic mass units (a.m.u.). During the protium runs atmospheric gases (oxygen and nitrogen) were analyzed by off-line gas sample chromatography, and the moisture of the gas was directly monitored with an on-line humidity sensor. The total amount of impurities was continuously monitored by direct measurements of the yield of muon capture on impurities as observed in the TPC.

3.1. Chromatographic analysis of nitrogen and oxygen

The oxygen and nitrogen content is measured by gas chromatography with a thermal conductivity sensor. After being filtered and purified in a cryogenic adsorption purifier, helium carrier gas is distributed in two directions with equally adjusted flow rates. The first flow passes through the reference chromatographic column. The second flow can be either routed to the working chromatographic column directly or through the accumulating column using the volume batcher which injects the fixed volume into specified direction. Both chromatographic columns are filled with a specially treated adsorbent (zeolite). The adsorbent in the working column separates the admixtures, while the one in the reference column provides a hydraulic resistance equal to the working column.

Preparatory enrichment is required for the very low concentrations of impurities in the hydrogen gas samples. Hydrogen from the sample bottle is directed to the accumulating column by the batcher. This column is filled with zeolite and immersed into a liquid nitrogen vessel at 77 K temperature. The amount of gas passed through the accumulating column is measured by a rotary drum gas meter. Impurities from the gas stream are adsorbed by the zeolite and remain in the accumulating column. After the desired amount of sample gas has passed through the adsorber, the accumulating column is removed from the cryogenic vessel and heated. Then the batcher directs the helium carrier gas flow through the accumulating column which washes the impurities out of the adsorbent.

In the next step, the carrier gas enriched by contaminants flows through the working column, where contaminants are separated on the adsorbent. Both reference and working flows pass through the detector in parallel, that measures their differential heat conductivity. The differential output signal is proportional to the admixture concentration. Signal peaks are registered by a PC and processed by special software. The enrichment coefficient (the sample volume passed through the accumulating column) and parameters of the measuring scheme are adjusted with respect to the admixture concentration. The final calculation of the concentration is based on a calibration measurement. A serial dilution method was used to obtain the set of calibrating samples with decreasing concentration of nitrogen and oxygen. With this method a sample of the air was serially attenuated by the hydrogen. The total calibration error, including non-linearity, is 10%. The traces of the main air components were monitored by gas samples of 8–10 normal liters from the TPC using the chromatographic method. A sensitivity of 5 ±1 ppb for oxygen and 7 ±1 ppb for nitrogen was obtained.

3.2. Humidity analysis

During the MuCap experiment 2004 we observed a capture yield corresponding to about 60 ppb impurities, significantly higher than the oxygen and nitrogen concentration derived from the gas chromatography

In 2005 an online humidity sensor [5] was installed to investigate whether the additional observed yield can

[5] Pura PUR-TX-120 Gas Dew-point Transmitter.MichellInstruments. http://www.michell.co.uk/cat/view/pura.html

be explained by residual water vapor in the hydrogen gas. The sensor has sensitivity of 0.02 ppb with error of +30–50% in the 2–100 ppb range. It was mounted in a temperature-stabilized box in order to reduce any influence of the ambient temperature to the sensor reading. Sensor and inlet pipeline were kept at 21°C with 0.2°C stability. As shown in Fig. 1, the humidity sensor (MT1) was installed in the gas circuit such that it could measure either the humidity in the outlet TPC flow or in the isolated CHUPS system (while hydrogen is circulating through the chamber bypass). Continuous bypass circulation gave 3 ppb humidity. During the production run the humidity sensor clearly demonstrated that humidity was the main additional impurity. To calibrate the effect of H_2O impurities on the experiment, a water permeation tube [6] was used for generation of the known water concentration in the hydrogen flow. The tube was placed in the temperature stabilized vessel. Stable hydrogen flow was passed through the volume with the tube.

3.3. Impurity capture rates

The specifics of the MuCap experiment allow unique in-situ measurements of impurity concentrations during the experimental runs. While the vast majority of negative muons remain in muonic hydrogen atomic (μp) and molecular ($p\mu p$) states during their lifetime, a small fraction can be captured on impurities in the following steps: $\mu p + N_Z \rightarrow \mu N_Z + p$; $\mu N_Z \rightarrow N_{Z-1} + \nu$. Here N_Z is a nucleus of an impurity atom, like N or O. The first transfer reaction proceeds with a rate proportional to the impurity concentration c_Z. The second capture reaction occurs with a probability $\Lambda_Z/(\Lambda_Z + \lambda_+)$, which is the result of the competing processes of capture with rate Λ_Z and free muon decay with rate λ_+. The charged recoil nuclei N_{Z-1} are detected in the TPC. The observed yield of capture recoils per muon is $Y_Z = c_Z k_Z$, where k_Z are coefficients which depend on Λ_Z and the detection efficiency for recoil N_{Z-1}. They are determined in dedicated calibration runs where hydrogen is doped with a single impurity N_Z of well measured concentration c_Z, typically 100–1000 times higher than in the clean run conditions. Typical values are $k_N = 70$ and $k_O = 400$ for both Y_Z and c_Z in ppm (the detection efficiencies slightly differ from run to run). In summary, the capture yield measurement allows a continuous and precise measurement of the overall observed capture yield from impurities, but it does not distinguish between their elemental composition.

4. Operating experience

4.1. Clean fills for production data

Before the 2004 experiment the TPC was baked for several weeks. The performance of the gas system over the whole run period is documented in Fig. 3. The chromatographic analysis allows monitoring the change of oxygen and nitrogen concentrations during the MuCap experimental run. Fig. 3 shows the behavior of nitrogen concentration for the MuCap experimental run after starting the CHUPS. The final chromatographic measurements resulted in nitrogen concentrations less than the method sensitivity (7 ppb). Oxygen traces dropped below the method sensitivity of 5 ppb within two days after starting the circulation.

The most reliable drying experience was obtained during the spring 2006 experimental run. Before the run, the TPC had been exposed to continuous (about 2 months) vacuum pumping with a simultaneous baking at ~120°C. This procedure led to an initial humidity level at the moment of CHUPS connection of 60 ppb (Fig. 4, left). During 400 hours of continuous cleaning with a mean hydrogen flux rate of 3 l/min the humidity exponentially decreased to ~18 ppb and remained at this level till the end of the main μ^- data run, providing a stable operation over more than 1000 hours. The minor fluctuations of the humidity are explained by temperature fluctuations in the experimental hall. The change of hall temperature affects the adsorption-desorption equilibrium in the chamber and, consequently, its outgassing rate. Then CHUPS was disconnected from the TPC and run through bypass line. The humidity decreased exponentially and reached the 10 ppb level in 20 hours (Fig. 4, right). The final CHUPS stand-alone humidity result is 3 ppb.

[6] Permeation tube providing 500 ppb ± 10% at 0.5 slpm flow. Valco Instruments Company Inc. P.O. Box 55603, Houston, TX 77255, USA.

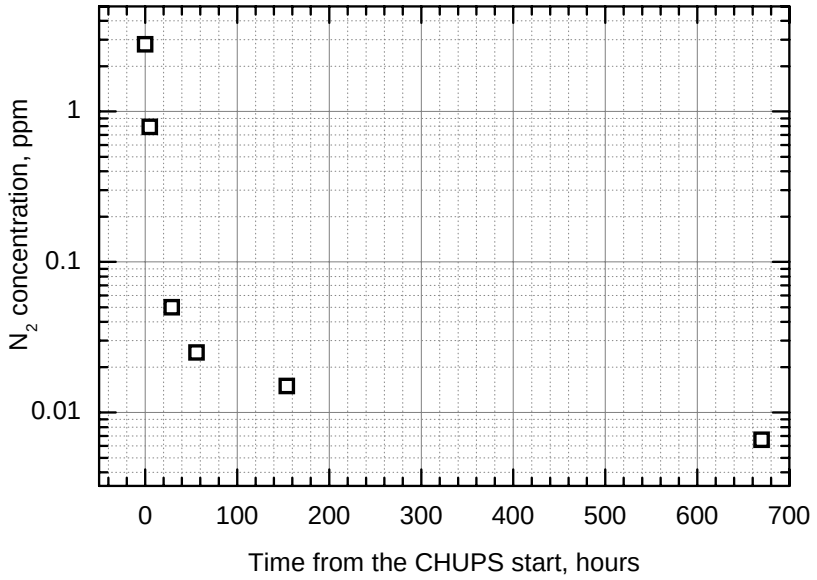

Fig. 3. Nitrogen concentration change during MuCap run 2004. Average hydrogen flow is 1.6 l/min

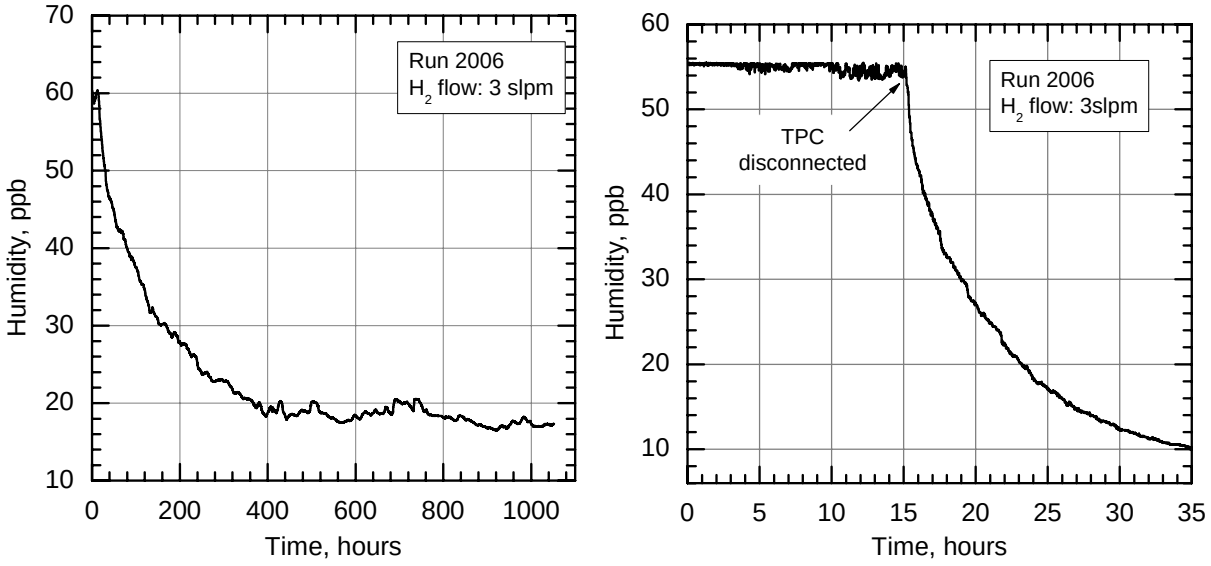

Fig. 4. Humidity decrease in the TPC after CHUPS connection (left) and after bypassing the TPC (right)

4.2. Impurity doped fills for calibration data

The cleaning power of CHUPS was greatly confirmed during systematic calibration studies of the TPC detector which were carried out during the last weeks of the MuCap experimental run in spring 2006. Several experiments were carried out for the TPC calibration and the determination of the major impurities. The high cleaning power of the CHUPS system makes it possible to return the detector to the normal clean operation in a short time.

The first experiment was a "water doped run". During this test the humidity inside the TPC was increased up to 2000 ppb approximately by a specially prepared humidity generator. Then CHUPS was connected and the gas was cleaned down to 400 ppb in one day (Fig. 5). The slower cleaning speed can be explained by wetting of the inner surfaces of the chamber.

The efficiency of CHUPS cleaning a large contamination of nitrogen in the detector hydrogen was tested by adding a "high" 22 ± 1 ppm nitrogen admixture from a known amount of nitrogen previously diluted

in a vessel with high purity protium. This "nitrogen doped" condition was intended as a detection efficiency calibration of nitrogen impurity capture events in the TPC. After measuring with the large nitrogen contamination (flat region) the CHUPS circulation through the TPC vessel was re-established and the nitrogen was removed. The cleaning progress observed on-line *via* capture events in the TPC is shown in Fig. 6. The cleaning started with a yield of more than 1000 ppb and proceeded until leveling off around ~30 ppb, a value established before the doping. The purification process took about 17 hours.

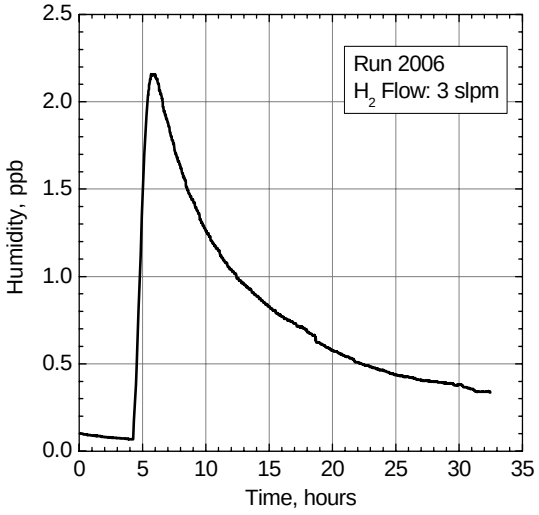

Fig. 5. Drying of TPC after the water doped run

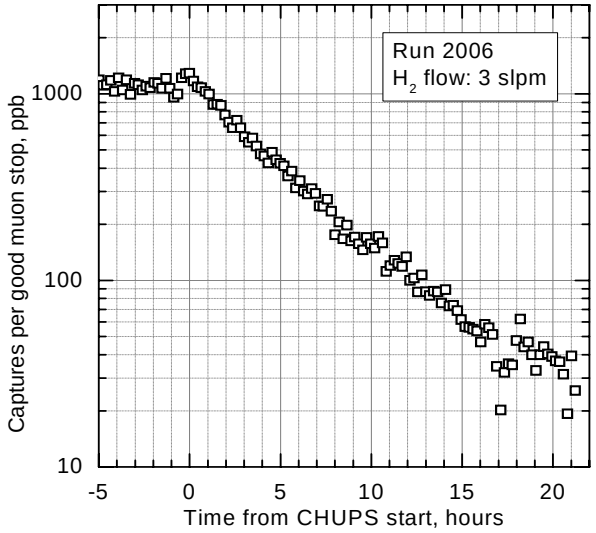

Fig. 6. Impurity captures per good muon stop during the nitrogen cleaning

4. Results

The CHUPS system was installed in the MuCap experiment at PSI and first connected to the TPC detector in 2004. The system proved to be very reliable and flexible during three experimental runs in 2004–2006.

The experience obtained during development and use of the CHUPS justifies the initial design decisions. The main result was a stable clean working gas of the TPC during the experimental runs. A smooth hydrogen flow of 3 l/min was kept during the whole TPC operation time (more than 1000 hours in one experimental run). The best purity reached was 18 ppb for moisture content and 8–10 ppb for nitrogen concentration. This result is sufficient to reach the main goal of the MuCap experiment and allows precise corrections of the proton capture rate for these impurities. In addition to regular cleaning, the CHUPS provided fast cleaning of the working gas after calibrations with contaminants doping. This feature was very useful for the nitrogen and water calibration experiments intended for systematic studies of the TPC detector. Also, variations of the CHUPS flow and correspondingly the equilibrium humidity in the chamber gave important additional calibration points for the systematic investigations.

With regards to the stable pressure requirement the CHUPS also yielded a good result. The pressure inside the TPC was kept at the appropriate level of 10 bar with 0.024% stability during all the operation modes. Pulsations of the hydrogen flow through the TPC chamber were also minimized to the level of 2.5% at the mean flow of 3 l/min.

References

1. I. Alekseev *et al.*, Preprint PNPI-2702, Gatchina, 2006. 26 p.
2. B. Bezymyannykh *et al*., Preprint PNPI-2611, Gatchina, 2004. 17 p.

HYDROGEN DISTILLATION AT THE DEUTERIUM REMOVAL UNIT OF MuCap EXPERIMENT

I.A. Alekseev, E.A. Arkhipov, S.D. Bondarenko, O.A. Fedorchenko, V.A. Ganzha, P.A. Kravtsov, V.A. Trofimov, A.A. Vasilyev, T.V. Vasyanina, M.E. Vznuzdaev

1. Introduction

The MuCap (Muon Capture on the Proton) experiment has been carried out during 1998–2006 at the Paul Sherrer Institute (PSI), Switzerland. The goal of this experiment is to measure the rate of the basic electroweak process of muon capture with hitherto unachievable high precision (1%). This measurement will provide an estimation of the nucleon charged form factor g_P with all-time high accuracy ~ 7%.

The method needs a very precise measurement of the muon lifetime in the $\mu^- p$ system in comparison with the lifetime of the free μ^+. To achieve this precision, ultra pure and deuterium depleted hydrogen gas (so-called protium) must be used. It is necessary to avoid transfers of μ^- to impurities or deuterium nuclei. These transfers lead to spoiled time spectra. A new experimental technique based on high pressure time projection chamber (TPC) filled with protium was used for the measurements. The experiment imposes strict and critical requirements on the hydrogen gas system supporting the detector. Desirable overall part of contaminants is about 10^{-8} for chemical impurities and 1×10^{-7} for deuterium. Circulating Hydrogen Ultrahigh Purification System (CHUPS) was built to provide the permanent purification of protium from the chemical contaminants during an entire statistics run (up to 2 months of continuous operation) [1]. This system was recently equipped with the Deuterium Removal Unit (DRU) – device for manufacturing of ultra pure protium from hydrogen [2]. A principle of hydrogen cryogenic distillation was used as a basis for the unit design.

The rectification method uses the difference in saturation vapor pressure of separating species above the surface of the mixture. This facility can be either a set of perforated plates or particular packing. The packing is more suitable for a column with a relatively small inner diameter. On the top of the column a condenser is placed which condenses vapor and returns it into the column in the form of liquid (reflux). The vapor from the top of the column can be partially taken away from the column as a product of the process. The reflux drains down along the column moistening the packing. An amount of the liquid suspended on the packing is a column holdup. Lower end of the column is equipped with reboiler. A separated mixture boils in the reboiler forming the vapor. The vapor rises upward along the column and interacts with the counterflow of draining reflux: the liquid is saturated by the high-boiling component, and the gas – by the low-boiling one.

In our case of hydrogen-deuterium separation a separating mixture is the mixture of regular hydrogen (H_2) and "deuterohydrogen" (HD). D_2 molecules are extremely rare and should not be considered. Besides, there is a division of the H_2 molecules into two groups, one of which has its protons aligned in the same direction (referred to as orthohydrogen) and the other in opposite directions (parahydrogen). Ordinarily, transition between ortho and para forms are relatively rare, so H_2 can be considered as a mixture of two distinct components. The ratio between the ortho and para forms is about 3:1 at standard temperature and pressure, but the para form dominates at low temperatures.

Separation factor α defines an elementary separation effect achieved at one contact of liquid and vapor hydrogen. Ideal separation factor is a ratio of saturation vapor pressures above pure components, it depends on temperature: the higher temperature the lower separation factor. But the separation factor for deuterium-protium is much larger than for ortho-para hydrogen at the same temperature. Throughout the contacting tower, liquid and vapor are brought into repeated contacts that multiply elementary separation effect. Thus the flowing down liquid hydrogen becomes steadily enriched in deuterium and orthohydrogen while the rising vapor becomes steadily depleted. According to the concept of Equilibrium Theoretical Plate, Height Equivalent to a Theoretical Plate (HETP) is the main performance characteristic of a separation column. HETP is the height of a part of a column left by liquid and gas flows which are in equilibrium to each other, (*i.e.*, for example, deuterium concentration in the liquid is α times higher than in the gas). The lower HETP value the higher column's separation power.

The column was designed to be operated so as to separate the initial mixture injected into the column through a feed port withdrawing pure H_2 (with deuterium content at least 30 times lower than in feeding gas) as distillate product and discarding the HD component in the reboiler stream. For the safety reasons and to select the most suitable operating mode, a number of studies and verifications were carried out. They include checks of the mechanical design and integrity and investigations of the pressure drop, the liquid holdup and column performance at different modes. Also, these investigations are very important to evaluate the accuracy of the measurements. The results of these studies are reported here.

Inefficiency of low deuterium content analysis in protium and the fact that possible residual deuterium content of the depleted product can be lower than the detection limit complicate the verification of separating power. It has made us find another approach. The use of gas chromatography method for ortho-para hydrogen analysis was found as a relatively fast and simple way of column performance evaluation. Also, low deuterium probes were measured on the small accelerator built specially for isotope analyses with special ion source giving extremely low backgrounds of hydrogen ions.

2. The mechanical design of the deuterium removal unit

The simplified layout of the DRU is presented in Fig. 1. Separation column of 2.2 cm inner diameter and 155 cm overall packing height is the main part of the unit. It consists of two sections connected with ISO CF40 flange coupling and is cased in a vacuum jacket. The 2.5 m vacuum jacket fixed on tripod is a basis for the setup. All working parts of the device are placed inside the jacket and its upper and lower attachments (so-called adaptors). The jacket and the adaptors comprise a common vacuum volume.

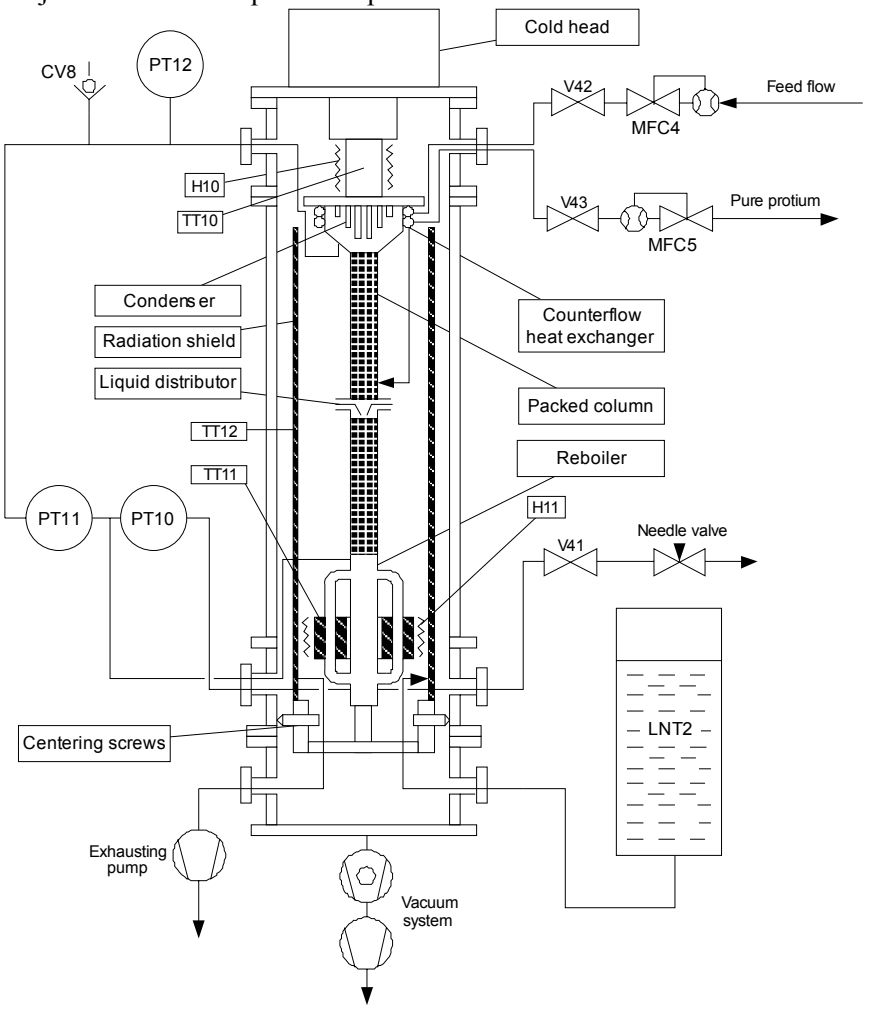

Fig. 1. DRU simplified diagram

The column has a condenser and a reboiler connected with its upper and lower parts. A COOLPOWER 140T (Leybold vacuum GmbH) cryogenerator was used for the cold operations, with the maximal cooling power of 20 W at 20 K.

A conical liquid distributor is fixed between the upper and lower sections of the column. Both sections of the column are filled with random packing. The liquid feed stream (see comments below) is introduced into the bottom of the upper section of the column. The distributor is intended to collect the liquid trickling down from the upper section and guide it to the center of the lower section. It is essential to prevent the effect of "adhesion" of the liquid to the column's wall.

The control system provides the algorithms necessary for column's operation in all modes. It operates two mass-flow controllers (MFC4 and MFC5) and two heaters (H10 and H11) and measures temperature and pressure sensors.

2.1. Condenser

The condenser is a closed conical bimetallic volume (Fig. 2, left). Its flat upper part is made of 10 mm copper plate. Inner part of this plate is processed in a form of a row of lamellas to develop the heat transfer surface area. Vertical orientation of the lamellas provides easy sliding of hydrogen condensed drops downward. The conical part has a flange for connecting to the column and welded to the copper plate by electron-beam. The condenser has two connections (tubes with 1 mm internal diameter) for conducting product hydrogen and its pressure to an upper point of the differential manometer PT11.

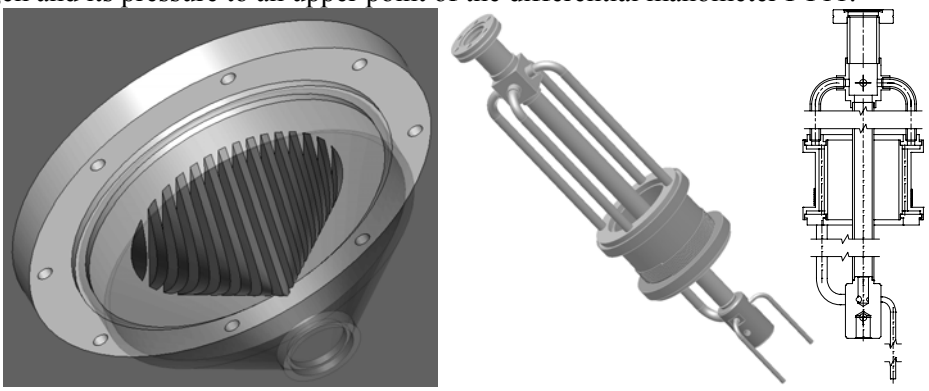

Fig. 2. The condenser (left) and the reboiler (right)

The cold head tightly contacts with outer surface of the copper plate through an indium foil. The cooled part of the condenser is mounted in the upper adaptor and that way in the common vacuum insulation of the column. A counterflow heat exchanger is mounted around the condenser and fixed on its upper flange. It cools down the feeding flux flow (inlet flow) by the deuterium depleted product flux (outlet flow).

2.2. Reboiler

The reboiler (Fig. 2, right) is essential to supply evaporation of the separating mixture. It has rather complicated arrangement to provide steady controllable boiling. This unit consists of central pipe, copper muff, upper and lower collectors and several connecting tubes. The central pipe keeps the most of liquid hydrogen collected in the bottom of the column. Both of collectors are welded to the pipe. The lower collector is also connected to the boiler by the short connecting tube. The massive copper muff has a large central hole. Several longitudinal apertures are drilled in the muff around the big hole. Their outlets are opened into common upper and lower grooves which are closed by stainless steel covers. The covers are welded to the boiler's body. Bimetallic structure allows the boiler to have very good heat conductivity owing to the copper body and therewith solid connection with other steel parts through the steel covers. The boiler is equipped with electric heater coiled around its body and PT100 thermometer to control its temperature. Liquid hydrogen boils in the longitude apertures and its vapor moves upward through four long connecting tubes. The short connecting tube provides a circulation between the lower collector and the boiler.

The advantage of the considered assembling is the separation of main amount of liquid hydrogen from the boiling section. Because of this separation, we obtain a steady level of liquid hydrogen inside the central pipe, which is measured by a differential manometer PT10. The low pressure point of this manometer is

connected to lower part of the column and the high pressure point – directly to the lower collector. ISO CF16 and CF40 connections are used for coupling of column parts. This type of connection is characterized by excellent vacuum tightness and good temperature cycling reliability.

2.3 Packing

The column is filled with specially designed spiral prismatic random packing made from 0.2 mm stainless steel wire. The packing is intended to provide a maximal surface of phases contact. At the size of the prismatic springs of 2 mm × 2 mm and total volume of packing in the column 560 ml it gives surface of 1.95 m^2. The choice of stainless steel as a material is caused by purity conditions of hydrogen. The packing surface was pickled by nitric acid to develop its roughness and improve wettability by liquid hydrogen.

It was the first test of the packing in a cryogenic distillation column. This type of packing (but bigger size – 3 mm × 3 mm) was earlier tested in PNPI's water distillation columns of 80 mm inner diameter and showed good separation characteristic (HETP = 2.5–3 cm) [3]. The similar packing made from stainless steel tested in cryogenic distillation column of small diameter gives HETP value about 5–6 cm. That is why the value of HETP equal to 5 cm was put in the design according to conservative approach.

3. Experiments and results

In April–May 2006 the DRU was tested during a few long (up to 7 days) periods of operation. The total amount of pure protium produced by the column in this run was 1300 litres. Almost all tests of columns performance were carried out at so-called "total reflux mode", with zero feed flow and correspondingly withdrawal flows from the column top and bottom.

3.1. Analysis

The analysis of low deuterium content in hydrogen is not prompt and besides the residual deuterium content of the depleted product can be lower than the detection limit. Nevertheless, a method for fast estimation of column performance was strongly needed. A chromatographic analysis of ortho- and para-isomers of hydrogen was proposed as a method of indirect estimation of the column separation power.

For the analysis the same chromatographic device was used as for analysis of nitrogen traces. However there are some changes introduced into the device for this specific method of analysis. The first distinction was the use of Al_2O_3-filled chromatographic column immersed into liquid nitrogen. The liquid nitrogen temperature is essential to provide the separation of the isomers that have temperate difference in adsorption affinity. The other essential difference is the direct injection of the sample into the carrier gas without the preliminary accumulation of impurities. The accumulation is unnecessary because of relatively high concentration of the separated components. The third serious property of this method was the use of neon as the carrier gas. It was used to provide more difference in thermal conductivity between the separated species and carrier gas in comparison with conventionally used helium.

Measurement of the concentration of ortho- and para- isomers in the top and bottom parts of the column allows to estimate its separation performance and recalculate the concentration profile for deuterium. A sample of chromatogram for samples taken from the top and bottom part of the column is shown in Fig. 3.

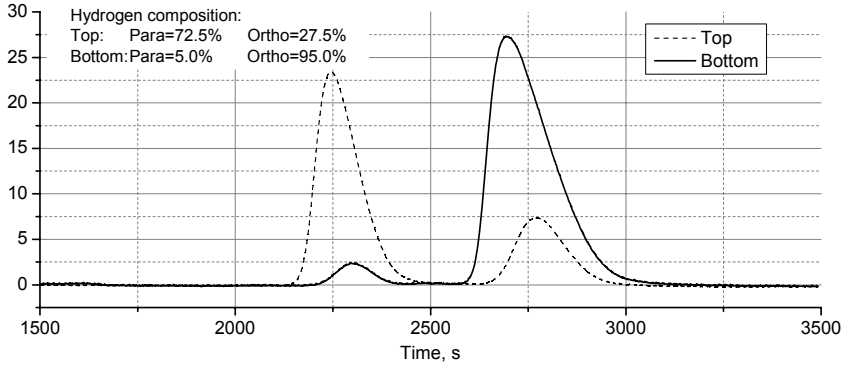

Fig. 3. Chromatogram of separated ortho- and parahydrogen (column pressure = 1.2 bar; reboiler power = 10 W; operation mode: total reflux)

Separation ratio is the ratio of relative concentration of a component of interest at the bottom to the top of the column: $SR = \frac{X_{Bottom}/(1-X_{Bottom})}{X_{Top}/(1-X_{Top})}$. If separation factors are known for the total reflux operating mode the recalculation of ortho-para hydrogen separation ratio (*SR*) into deuterium-protium separation ratio can be done easily with the help of Fenske equation: $SR = \alpha^N$, where N – the number of theoretical plates. A separation factor α is the value of elementary separation effect. It can be presented as a ratio between saturation vapor pressures for pure components. For ortho-para separation it can be shown as: $\alpha_{o-p} = \frac{P_{sat.Para}}{P_{sat.Ortho}}$, where α_{o-p} – ideal separation factor for ortho-para hydrogen system, $P_{sat.Para}$ and $P_{sat.Ortho}$ – saturation vapor pressures above pure para- and orthohydrogen, respectively. Thus, for the deuterium-protium case: $\alpha_{D-H} = \frac{P_{sat.H_2}}{P_{sat.HD}}$, where α_{D-H} – ideal separation factor for system of protium and deutherohydrogen, $P_{sat.H_2}$ and $P_{sat.HD}$ – saturation vapor pressures for pure normal H2 and pure HD, respectively.

Dependencies of separation factors for HD–H_2 and ortho-para hydrogen system on temperature are shown in Fig. 4. The significant difference between the separation factors according to Fenske equation results in much larger difference between the separation ratios for a large number of theoretical plates in the column (or height of the column: *N* = H/HETP). Height Equivalent to a Theoretical Plate (HETP) is the main characteristic of column's performance. The higher separation power corresponds to greater number of theoretical plates (*N*) and less HETP value.

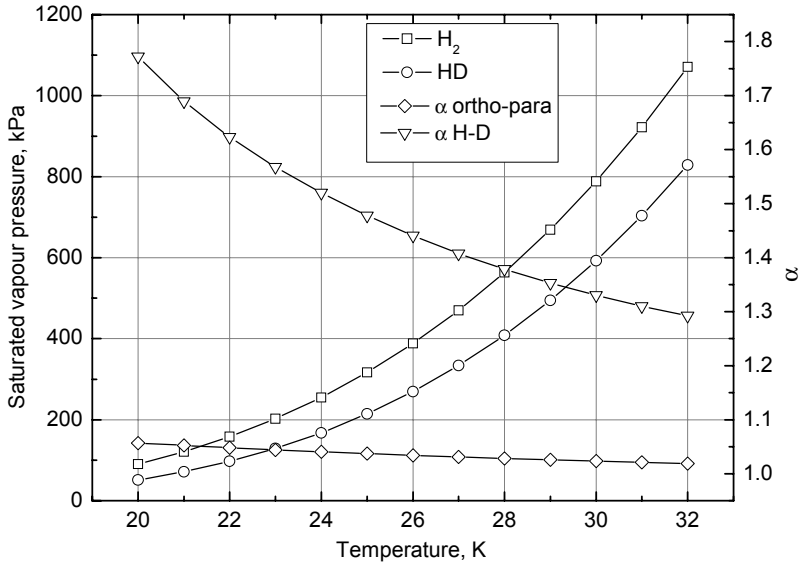

Fig. 4. Temperature dependencies of saturated vapor pressures and separation factors for H_2–HD and ortho- parahydrogen systems

3.2. Results of natural gas separation at total reflux mode

First DRU run was carried out with the natural hydrogen with 126.7 ppm of Deuterium. The column was filled by liquid hydrogen in large excess, and after 1 hour operation excess gas (84 litres) was withdrawn from the column bottom. This explains low final deuterium concentration in the bottom (Table 1). Withdrawn gas was sufficiently enriched to change largely the average concentration in the column. Initial gas volume was 181.6 litres. Negative deuterium concentration in the column top (~1.9 ppm) indicates the accuracy of the measurement. The method consists in extrapolation of sample measurement from deuterium concentration in natural hydrogen and gives low accuracy nearby zero concentration.

Table 1

Natural hydrogen run results

Probe location	**Deuterium, ppm**	**Ortho, %**
Original gas	126.7	75
Column top	–1.9	14.6
Middle	–	32.2
Column bottom	56.2	85
Average concentration calculated from the mass balance	7.7	53.5

The experimental data for the ortho-para separation was fitted by the Fenske equation. The average HETP calculated on the basis of tests with various vapor flow rates was 2.2 cm (Fig. 5), which is comparable with the best results in the world.

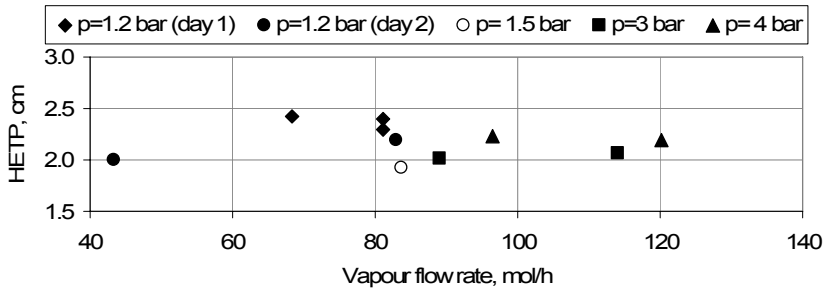

Fig. 5. HETP dependence on vapor flow rate

3.3. Studies on the pressure drop and the liquid holdup

Figure 6 (left) shows the relation between pressure drop across the column and vapor flow rate for the tested mass exchange packing. Unfortunately we did not reach flooding due to relatively large inner column diameter. Original design value was 16 mm, but according to the number of circumstances the inner diameter of 22 mm was chosen, this means that packing was working at relatively low load. We had some anxieties in this respect but fortunately they were relieved due to the excellent packing performance. Packing holdup presented in Fig. 6 (right) had an expected high value. In spite of this the time of reaching a steady state by the column is short – about 1 hour.

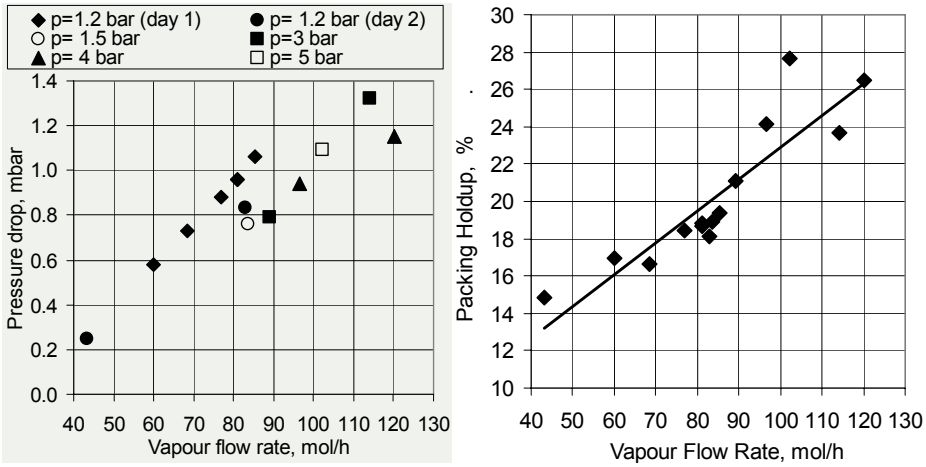

Fig. 6. Pressure drop across the column and packing holdup

3.4. Production of Deuterium Depleted Protium

There are several possible DRU operation modes for the deuterium depleted protium production. Four modes were tested during experiments: “feed through” with purging, “feed through” without purging, continuous circulation through CHUPS and so-called Rayleigh depletion. During the Rayleigh depletion the column was totally flooded by liquefied hydrogen. After the flooding, the hydrogen was discharged through the product line. Natural hydrogen was used only for preliminary tests. The accumulating of required product was carried out from pre-depleted protium. Mass-flow controllers of CHUPS system were used to operate the feed (MFC5) and for the product flow (MFC4). The rate of the purging flow was adjusted by manual needle valve with the help of bubble flow meter. The results of the cleaning runs are shown in the Table 2.

Table 2

Results of the cleaning

Mode		"Feed through" no purging	"Feed through" with purging	Rayleigh's depletion	CHUPS Circulation
Reboiler power, W		20.5	19.0	12.0	20.0
Pressure, bar		1.5	1.5	1.5	2.0
Feed flow, l/min		0.81	0.81	1.25	0.55
Ortho, %	Top	67.8	69.4	-	64.8
	Middle	69.2	74.6	94.2	69.3
	Bottom	96.4	98.5	-	98.2
HD initial, ppm		3	3	10	<3
HD expected, ppm	Top	< 0.01	< 0.01	0.09	< 0.01
	Bottom	123	~ 200	370	-
HD probe		№ 50	№ 57	№ 61	№ 67
Amount of gas, SL		572	630	390	420
Bottom probe HD measured, ppm		57.5 ± 1.2	76.9 ± 1.6	probe lost	16.2 ± 0.5

In addition, a number of deuterium depleted probes were collected (so-called zero protium samples). Expected HD concentrations were calculated using the special program “CD-2004” on the basis of the column’s model with known HETP and total height. The measurements of the probes were performed on the new 200 kV Tandem accelerator built for isotope analysis in Zurich. A special ion source was constructed giving extremely low backgrounds of hydrogen ions from walls, *etc.* The walls are continuously sputtered to keep the background low allowing measurements during 2 hours. The existence of the zero samples from the DRU system turned out to be crucial, since the accelerator gives a different background if the ion source is not fed with hydrogen gas. First zero sample measurement gave zero deuterium concentration at 0.14 ppm sensitivity. Thus, it contains less than 0.14 ppm of deuterium. The difference in expected HD concentration and measurement for probes 50 and 57 is most likely caused by wrong assumption about initial HD concentration, which was measured with extrapolation method and has large error. According to probe 50 measurement, the initial HD concentration should be 1.40 ± 0.03 ppm that corresponds to the initial hydrogen measurement on the accelerator (1.44 ± 0.13 ppm).

Deuterium concentration profile in the column, calculated on the base of the ortho- and para-hydrogen separation, gives very low concentration in the top of the column (Fig. 7). Such a low concentration could not be proved by direct measurement because of relatively low sensitivity of the mass spectroscopy.

The additional direct analysis of zero samples using accelerator mass spectrometry in Zurich gave a better result for depleted hydrogen from the top of the column: less than 60 ppb at 60 ppb sensitivity. This is ten times better than technical requirements of MuCap experiment.

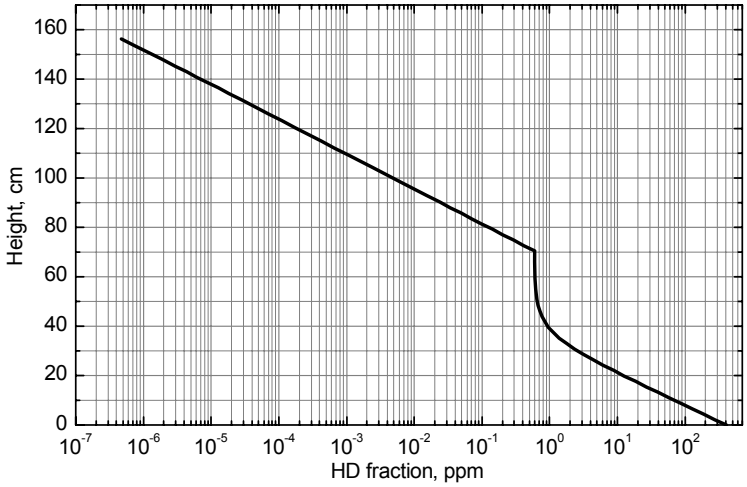

Fig. 7. Expected HD concentration profile. Feed flow = 1 L/min; pressure = 1.5 bar; purging flow = 0.015 L/min; HETP = 2.2 cm; initial deuterium atomic fraction = 3 ppm

4. Conclusion

The Deuterium Removal Unit was designed and manufactured in PNPI during the fall and winter of 2005–2006. The final installation, tests and protium manufacturing were carried out in spring 2006 at the PSI. The separation characteristics of the column were studied in details. Due to the absence of direct prompt method of deuterium measurements, the indirect method of chromatographic analysis for ortho- and para-isomers of hydrogen was used to estimate the column's separation efficiency. Some interesting data were obtained.

The height equivalent to a theoretical plate (HETP) for the column is 2.2 cm. It is one of the best ever obtained results for columns of low and medium cryogenic power. For the present column, HETP value is almost constant in a wide range of vapor flow rate.

The column has the separation power in excess for the goal to be sought. Output deuterium concentration lower than 0.1 ppm almost does not depend on the initial concentration (natural hydrogen can be used!).

The pure orthohydrogen useful for some experimental physics applications can be produced by the setup as well as protium.

After the selection of column's operating parameters and the development of its operating algorithm the protium production run was performed. Several modes of isotope purification were used. As a result about 1.3 m^3 of deuterium depleted hydrogen was obtained. The CHUPS system was put into the mode of continuous hydrogen circulation through the column to remove deuterium.

The productivity of the system in the "feed through" mode is 500 L/day. In the mode of circulation through the CHUPS system it comes to 150 L/day. The mode of Rayleigh depletion is considered to be inefficient because of small initial amount of hydrogen in the column.

The method of measurement of low deuterium content in hydrogen (1 ppm and less) is suggested. It is based on deuterium enrichment by a factor of 40 (and even more) in the reboiler.

This work is also of great importance for Detritiation Plant of PIK reactor as in accordance with a new developing design of the plant the cryogenic column with close parameters is needed. A good packing was developed and tested, successful experience was gained.

References

1. A. Vasilyev, B. Bezymyannykh, V. Ganzha, P. Kravtsov, G. Shapkin, V. Trofimov and M. Vznuzdaev, talk at *the National Hydrogen Association Annual Hydrogen Conference 2005*, Washington, USA.
2. I.A. Alekseev *et al.*, Preprint PNPI-2702, Gatchina, 2006. 26 p.
3. I.A. Alekseev, I.A. Baranov, S.D. Bondarenko, S.N. Chernoby, O.A. Fedorchenko, G.A. Sukhorukova, V.D. Trenin and V.V. Uborski, Fusion Technology **28**, 1579 (1995).

ARCHITECTURE Of SMALL COMPUTING CLUSTERS IN HIGH ENERGY PHYSICS

A.N. Lodkin, A.A. Oreshkin, A.Y. Shevel, T.S. Serebrova

1. Introduction

In last years we see that large **High Energy Physics (HEP)** collaborations use high performance computing clusters. Most of the clusters are integrated into World Grid infrastructure. At the same time, we observe that small clusters do continue to play their own role in the computing life. We mean ***small*** for the cluster up to about 50 machines or so. It is quite obvious that such small cluster is supposed to serve relatively small physics group, may be about 10 physicists. A good time is now to discuss a realistic scenario how physics data might be processed and analyzed and what computing architecture might be used by small physicist's teams.

Contemporary architecture of small computing clusters in **HEP** for physics analysis is based on the commodity hardware. In most of cases it is a Personal Computer (**PC)** based on Intel compliant microprocessors. Scientific Linux is the main operating system. It is better when the computing cluster is a member of a Grid Virtual Organization(s). Here we plan to discuss several aspects of computing cluster design and implementation and how small clusters are related to large computing installations.

2. Large clusters

Several important clusters of Tier 1 & Tier 2 are mentioned in Table 1 (N/A means that the information is *Not Available*). Each cluster of level Tier 1 has tens of **FTEs** in the staff. Most of such clusters have 10 Gbit or more external connectivity. Most of Tier 2 clusters have external channels in between 1 Gbit and 10 Gbit. There are expectations that in 2010 many Tier 1 clusters will have 1 Tbit channels.Each cluster uses a batch system – usually one or two from the range: **LSF**, **Condor**, **Torque**/**PBS**, **SGE**.

Table

Number of hosts and data volumes on several computing clusters in HEP (info from HEPiX October 2006)

Laboratory	**Facility type**	**Number of hosts in clusters**	**Data volume on disks**	**Data volume in Mass Storage**
BNL	Tier 1	~2.0 K	~400 TB	~4.0 PB
Canadian GridX	Tier 1	~1.2 K	~100 TB	~0.4 PB
FNAL Grid Computing Center	Tier 1	~3.0 K	~700 TB	~4.0 PB
GridPP/RAL	Tier 1	~2.9 K	~168 TB	N/A
NIKHEF	Tier 1	~0.3 K	~ 70 TB	N/A
SLAC	Tier 2	~1.7 K	~755 TB	N/A
GRIF(France)	Tier 2	~1.2 K	~700 TB	N/A
INFN	Tier 1	~1.3 K	~600 TB	N/A

Of course clusters are included into one or several Grid Virtual Organizations (**VO**). One of the consequences is that the bulk data moving over World Area Network (**WAN)** must be planned and performed with Grid tools. Each VO has its own rules on the data moving. There is special person (manager) responsible for data moving process. At the same time if the bulk data moving is started it is difficult to predict when the operation would be accomplished. Due to this fact in many large clusters the user jobs are planned to be cancelled if the data requested by jobs are not available in local disk space.

Apparently clusters Tier 1 (or even Tier 2) are main source of physics data and main repository for the software of almost any kind. Often it is required to create new data with special selection algorithm from other data before start an analysis. Because resulted data are peculiar or even private the small physicist's team needs to keep the data in own disk space which could be obtained on large cluster for relatively short period of time. In many cases a small computing cluster is best place to keep own data for long time.

When small physicist's team plans to use existing large cluster it important to know not only power of the cluster but the administrative conditions on the cluster [1,2]. For example if any non privileged user can keep just 40 jobs in the run stage (permitted to use 40 CPUs), it does not matter for him that the cluster consists of 10K machines. Of course in Grid architecture someone can easily send jobs to another cluster where the data are, i.e. it possible to use more than one computing cluster. However in most of real situations some data moving and other additional operations are required. Real advantage to use more than one cluster can be gained if specific conditions are taken place [3]. In this discussion it is assumed that clusters are really stable. The stability in general and difficulty to predict future status of the Grid clusters is a hot topic for now. Anyway, there is an expected advantage with using of two computing clusters instead of one.

3. Estimates for accelerating of computing with two clusters

Let us imagine two clusters where we can do some data analysis or data simulation. For example one cluster is in one research institute and another cluster is in another institute or university, the clusters have independent administration. For simplicity we will use terms *local cluster* and *remote cluster*. We consider the ***computation*** as bunch of simulation (data generation) jobs or data analysis jobs which could be performed on any of two clusters. Usually the bunch of jobs is performing many hours or many days. All jobs are considered as accomplished when the computing itself is ended and the data are moved to final (target) place, for instance to small computing cluster.

Let us introduce several variables:

$\boldsymbol{T}$ – the time for computing task with using one (local) cluster;

$\boldsymbol{\tau}$ – the time for computing with two clusters;

$\boldsymbol{t_l}$ – average time for processing of one portion of the data on one (local) cluster;

$\boldsymbol{t_r}$ – average time for processing of one portion of the data on one (remote) cluster;

$\boldsymbol{t_o}$ – the average overhead time which is required to process one portion of the data on remote cluster; we can include in this time anything we need to make computation possible in remote cluster, for example, time to transfer the data to (from) remote cluster;

$\boldsymbol{D}$ – total number of the data portions which have to be processed;

$\boldsymbol{S}$ – the number of data portions which are processed per time unit;

$\boldsymbol{\alpha}$ – acceleration of the computing due to use of additional cluster.

Now we can write for only (local) cluster $S = \frac{1}{t_l}$ and total time for data processing is

$$T = \frac{D}{S} = D \cdot t_l .$$

For two clusters (local and remote) we can write $S = \frac{1}{t_l} + \frac{1}{t_0 + t_r}$ and total time for the computing is

$$\tau = \frac{D}{\left(\frac{1}{t_l} + \frac{1}{t_0 + t_r} \right)} .$$

It is assumed that the jobs will be sent to remote cluster only when local cluster if fully loaded with our jobs. Now accelerating is

$$\alpha = \frac{T}{\tau} = t_l \cdot \left(\frac{1}{t_l} + \frac{1}{t_0 + t_r} \right) = 1 + \frac{t_l}{t_0 + t_r} .$$

Above might be rewritten as

$$\alpha = \frac{(t_0 / t_r + 1 + t_l / t_r)}{(t_0 / t_r + 1)} .$$

From above formula we see that the accelerating is quite sensitive to the overhead time t_o (please see in Fig. 1) Even in case when remote cluster has huge throughput, when value t_r can be considered close to 0, we have the acceleration is limited by t_o.

It is possible to conclude:

- the expected acceleration for the computing with two clusters can be relatively easy estimated;
- the use of two computing clusters instead one cluster does not mean guaranteed decreasing the computation time in all cases, concrete overheads are very important;
- in long term plan (many days or weeks) the probability that the remote cluster is up and running properly is important.

If we plan to keep the data on small cluster apparently it is more effective to analyze the data on the same cluster.

All above reasons do lead to understanding that in a range of cases the use of small computing cluster is very helpful. Let us consider the architecture of such clusters.

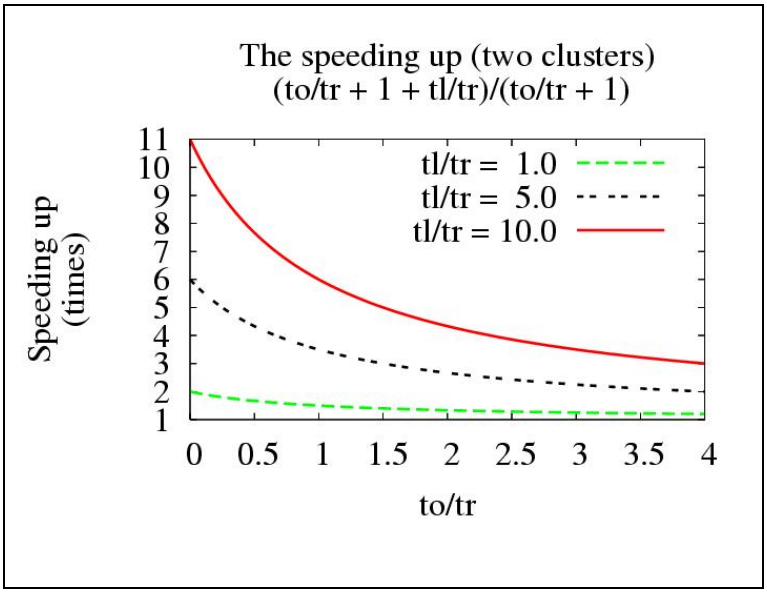

Fig. 1. Computing acceleration with two clusters with different conditions

4. Cluster architecture considerations

Last years **CPU** (microprocessor) performance is increasing at the rate around 60% per year. At the same time disk read/write speed is increasing about 10% per year. Also disk volume per spindle is increasing at the rate around 60% per year. It means that access to disk space (especially in **HEP**, due to extremely large volume of the data) is more and more often becomes a bottleneck. There are many reasons to think that such the relations in between mentioned values will be kept at least for several years in the future.

In the light of such facts and facing the need to analyze tremendous volume of the data the methods how to make read/write operations in parallel are most hot topic. One of the methods is to use advanced **RAID** controllers and advanced cluster file system, for example, **Lustre**, **PVFS**, **GFS**, **GPFS**, **Panasas**, **StorNext**, and the like.

Another very simple method was suggested in the presentation [4]. The approach assumes two opposite configurations and many in between. First is to use one central machine in the cluster where connected all **RAID**s. Opposite configuration is to use the disk space on each machine in the cluster as shown in Fig. 2. Here all file systems are mounted by **NFS** over separate network channel for each file system. More specialized systems like **xrootd** are addressing the same target: to make I/O operation in parallel. Another important point in small cluster is architectural features which permit to reduce the requirements of local maintenance to the minimum.

5. Remote maintenance for small computing cluster

When new cluster design is under consideration we need to take into account the trends with less available manpower in future years. In other words we have to plan as much as minimum local maintenance activity. To permit remote experts to do their job the cluster must be equipped with appropriate components.

Vital and stable solution may be implemented with using the special hardware. We mean type of devices so called **KVM** switch. **KVM** switch (or just **KVM**) is device which connects all control lines (keyboard, mouse, monitor) from each cluster node. **KVM** has connectors to connect real keyboard, monitor, and mouse. Also **KVM** has ability to connect (logically) real keyboard, mice, monitor to any desired server in the cluster.

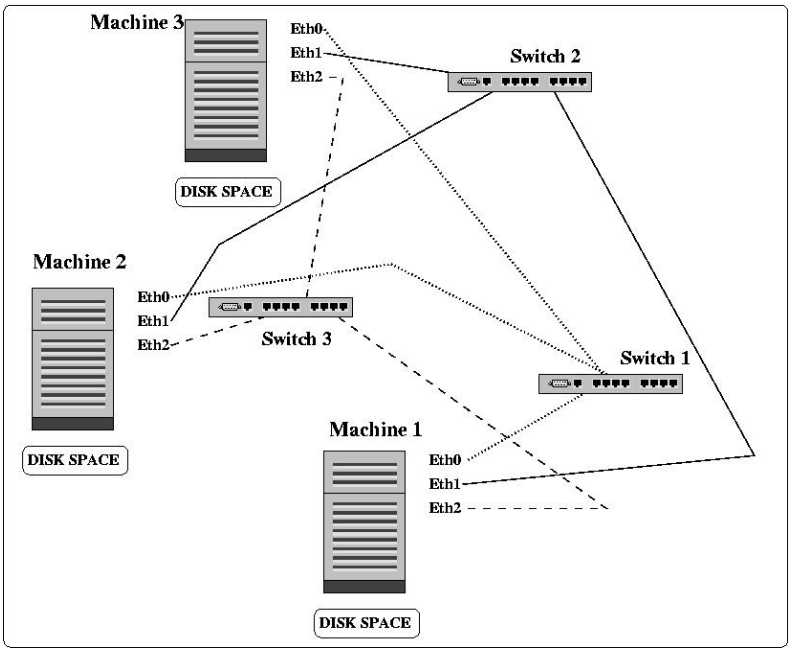

Fig. 2. Cluster scheme where each machine has own disk space

Another device entitled *remote IP console* (**RIPC)** is used as interface in between **KVM** and Internet. An expert on remote computer can use Web browser (with enabled Java functionality) to make connection to the device **RIPC** with protocol **https** and see the screen on **Java** applet. **Java** applet displays redirected console screen, keyboard, and mouse of the cluster where **RIPC** is attached. In other words the expert is able to use local for him keyboard, mouse as they would be attached to the cluster.

Among other mandatory components of the cluster we can mention **UPS** – to make electricity power more stable – and **PDU -** to have ability to switch electrical power **on** and **off** for specified machine in the cluster. An air conditioning is also in range of requirements.

The basic requirements were enumerated. Now other details concerning the software have to be discussed.

6. Technological cluster software and middleware

A range of technological services are seemed very important in contest of easier maintenance procedures. Usually it is very important to have reserve copy of critical data - backup service. Much better is to have reserve copy on the tape cartridges. The tape drive might be used for reserve copy for the physics data as well. Personal subsets of physics data copied on the tape cartridge are often great advantage for physicist.

All cluster users must be in cluster user mailing list. This list is to be used for the information about the changes on the cluster. Such the mailing list may be implemented in several places. One of the useful ways to keep mailing list for small physics team is site http://groups.google.com/.

Cluster administrative system is aimed to deploy, configure and support cluster (to keep all system parameters in consistent state) and is in active use on many clusters. Good examples of such the systems are **OSCAR**, **ROCKS**, and the like.

Batch processing on the cluster is usually performed with one of several batch systems: **Torque/PBS**, **Condor**, **Sun Grid Engine**, **LSF**. Fortunately batch systems in use on large clusters are pretty same as for small clusters. One of the specialized batch tools is **PROOF.** It is the system for users who does like to be all the time inside **ROOT** environment. Part of physicists do use **PROOF** for data analysis.

Monitoring systems are almost same as for large clusters, for instance **Ganglia** and **Nagios.**

Grid middleware is another large software component which is required if the cluster is included into one or more Grid Virtual Organizations. The part of middleware components are the same for all VOs (basic **Globus** toolkit and the like.). A good fraction of middleware is developed by concrete VO and it is not supposed to be used outside the VO.

7. Application software and related databases

Application software dedicated for concrete physics is large fraction of all software tools on the computing cluster. This software has as a rule many versions (may be several tens). Usually people keep all versions on the cluster. Such the software is kept on leading clusters (Tier 1) in **AFS** tree. In general it is possible to use it over **AFS,** however real experience shows that much better to keep local copy of the software. It is performed with one or another set of mirroring mechanisms for example once a week or so. It is quite safe for small physics team especially if some problems are appeared on leading clusters (**AFS** server is down, application software tree becomes unusable). Almost the same we can repeate about such databases as geometry/calibrations database, *etc*.

8. Small cluster support over years

The cluster is running, data analysis is in progress but time is going on and new versions of software (application, system, middleware) are appeared. Quite often you have to do upgrade the software to guarantee that you have same common software packages as your colleagues do. That means somebody has to be careful about consistency of the software.

Furthermore with the time (one, two, three years) you might (very probable) discover that some machines in the cluster are broken or out of date and do not meet newest requirements. Common rule is to remove from the cluster any machine which gives any kind of problems. In average if we like to keep the computing cluster abilities on top – we have to plan to change about 1/3 machines in the cluster every year. It means to remove old machine from cluster and add new machine instead. The machines retired from the cluster might be used as personal machines for students, physicists, *etc*. The reach source of useful information about computing clusters is available at the site http://hepd.pnpi.spb.ru/ClusterGate.RU.

9. Conclusion

Obviously it is not possible to use small computing clusters ***instead of*** large clusters of Tier 1 or 2. It is very useful as a complement to large computing installations; also they make use of large computing facility more optimal. Taking into account that prices for disks and CPUs are going down, it is clear that about 20–50 machines with 50–100 TB of disk space are foreseeable for small physicist's team for most of analysis needs.

References

1. B. Jacak, R. Lacey, S. Mioduszewski, D. Morrison, A. Shevel and I. Sourikova, talk presented at *the Conference on Computing in High Energy Physics CHEP2003* (La Jolla, USA, 24 – 28 March 2003), presentation TUCT009 in http://www.slac.stanford.edu/econf/C0303241/proceedings.html
2. A. Shevel, B. Jacak, R. Lacey *et al.*, in *the Proceedings of the Conference on Ccomputing in High Energy Physics CHEP2004* (Interlaken, Switzerland, 24 September – 1 October 2004), Geneva, 2005. p. 974.
3. A. Shevel and R. Lacey, talk presented at *the Clobus World Conference* (Boston, USA, 7 – 11 February 2005).
4. A. Shevel and R. Lacey, poster presentation at *the Conference on Computing in High Energy Physics CHEP2006* (Mumbai, India, 13 – 17 February 2006).

THIRD GENERATION COORDINATE READOUT SYSTEM – CROS-3

N.F. Bondar, V.L. Golovtsov, A.G. Golyash, E.A. Lobachev, L.N. Uvarov, S.L. Uvarov, V.I. Yatsura

The design and development of the fast and cost effective readout electronics for the tracking detectors is the scope of interest of the modern experiments such as LAND (performed at GSI, Darmstadt), FAMILON, *etc*. The setup of the experiments includes fine pitch MultiWire Proportional Chambers (MWPC) and wire Drift Chambers (DC) with hexagonal cell structure. Variety of modern integrated circuits together with advanced PCB technology allowed to develop the best quality CROS-3 devices and meet the requirements of the experiments.

Block diagram of the CROS-3 system in Fig. 1 includes:

- 96-channel MWPC Digitizers (CDR96);
- 16-channel DC Digitizers (AD16);
- 16-channel Concentrators (CCB16);
- System Buffer (CSB).

Analog part of the CDR96 is based on a CMP_G ASIC performing wire signal amplification and shaping as well as pulse discrimination with peaking time of 30 ns, minimum threshold of 7 fC, double pulse resolution of 80 ns, and power dissipation about 35 mW/channel.

Analog part of the 16-channel DC Digitizer is based on a ASD-Q ASIC [1] with similar functionality and the following characteristics: peaking time of 7 ns, operational threshold at 2–3 fC, double pulse resolution of 20 ns, and power dissipation about 35 mW/channel.

Digital part of either Digitizer is implemented in a Xilinx Spartan-3 FPGA that performs both digitization and readout tasks. Input signals are digitized and delayed to compensate for the trigger latency. Upon receiving a trigger signal, a temporary buffer stores programmable number of time bins. Then the encoder looks for the signal leading edge and encodes both its wire number and its relative time slice number. The delay range compensates trigger latency of up to 2.5 μs in 10 ns steps. The finest time bin resolution is 2.5 ns for the AD16 and 10 ns for the CDR96 cards. Maximim number of time slices is 255 for AD16 and 64 for CDR96. Readout is performed over a STP CAT5 cable at a 100 Mb/sec bit rate.

The CCB16 collects data from up to 16 Digitizers into temporary buffers, which are read out to the CSB via an optical fibre at a 2.0 Gb/sec bit rate.

The CSB is implemented as a universal PCI card.

Figure 2 shows system components mounted directly on the chamber.

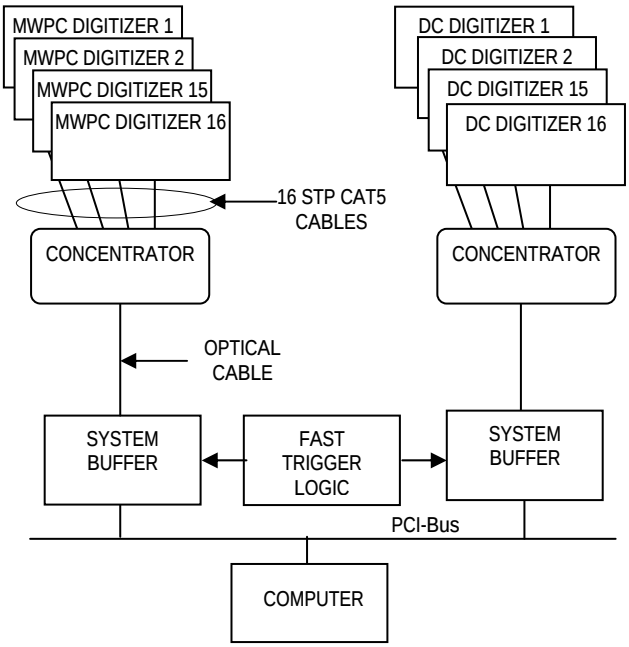

Fig. 1. CROS-3 block diagram

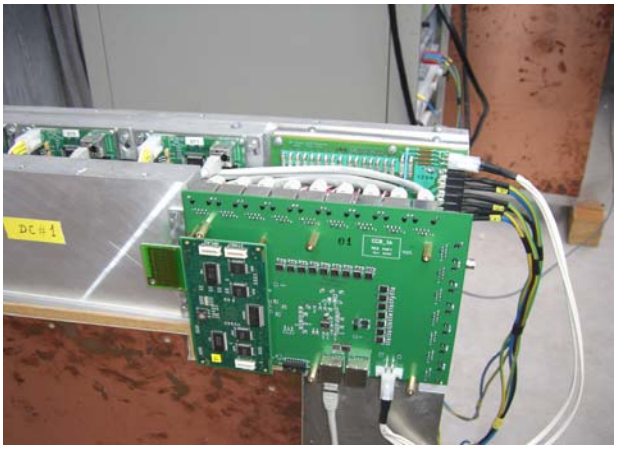

Fig. 2. CROS-3 Digitizers and Concentrator are on-chamber mounted system components

References

1. W. Bokhari *et al.*, CDF/DOC/TRACKING/CDFR/4515 December 1999.

MULTI-CHANNEL HIGH VOLTAGE DISTRIBUTION AND MONITORING SYSTEM FOR LHCb MUON CHAMBERS

S.V. Bondarev, N.B. Isaev, V.I. Lazarev, A.V. Mylnikova, L.O. Sergeev, S.S. Volkov

A multi-channel High Voltage Distribution and Monitoring System (HVDM) was designed and constructed for muon chambers produced at PNPI for the LHCb Muon detector. Two options of the system are developed to be used for the chambers. The first one (HVDM_16) allows linear regulation in each distributed channel in a range of 0-3000 V. The second (HVDM_LHCb) one, being radiation hard, allows linear regulation in each distributed channel only within 1000 V.

HVDM block diagram in Fig.1 includes:

1. 36-channel radiation hard Remote Distributors, performing high voltage fan-out from 1 input to 36 outputs, output voltage regulation within 1000 V in 1 V steps, output voltage measurement with 1 V resolution, and output current measurement with 10 nA resolution in $I < 1\ \mu$A, and 100 nA resolution in $I > 1\ \mu$A range (100 μA max current) for each output. The radiation hardness value is up to 4 krad at 2×10^{12} neutron/cm^2.

2. 8-channel Master Distributor, performing high voltage fan-out from 1 input to 8 outputs, voltage regulation from 0 to 3000 V in 1 V steps, output voltage measurement with 1 V resolution, and output current measurement with better then 100 nA resolution (1.5 mA max output current) for each output.

3. 16-channel Distributors, performing high voltage fan-out from 1 input to 16 outputs, output voltage regulation from 0 to 3000 V in 1 V steps, output voltage measurement with 1 V resolution, and output current measurement with 10 nA resolution in $I < 1\ \mu$A and 100 nA resolution in $I > 1\ \mu$A range (100 μA max current) for each output.

4. Primary High Voltage Power Supply, which can be any industrial rack mounted unit, like Matsusada High Voltage Power Supply, model AV-3*50, whose output regulates in a range from 0 to 3000 V.

5. System Interface/Buffer, providing control and monitoring of the Master and Distributors via the Control/Readout Line. It is implemented as a universal PCI card, compliant to PCI 2.2 specification. Card's buffer memory keeps both voltage setting and actual voltage and current values for each channel.

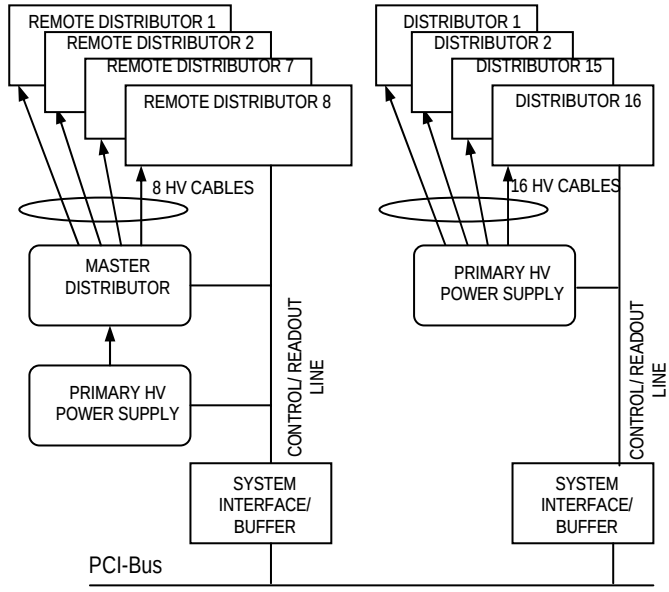

Fig. 1. Block diagram of the HVDM system

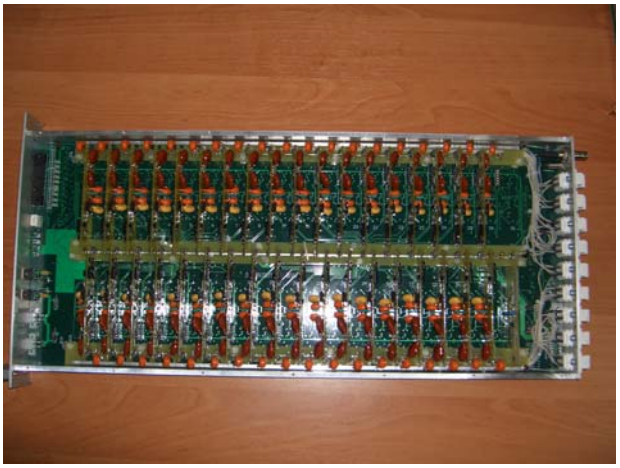

Fig. 2. 36-channel Remote Distributor

The HVDM module dimensions comply with the Eurocard (IEC 297 and IEEE 1101) form factor and are 240 mm × 6U for Master and Distributor, and 540 mm × 6U for Remote Distributor. The HVDM design follows that of the high voltage system developed for the CMS EMU CSC in cooperation with the University of Florida (USA).

Figure 2 illustrates design of 36-channel Remote Distributor with each channel served by a plug-in card.

TRACK FINDING PROCESSOR FOR THE CMS ENDCAP LEVEL 1 MUON TRIGGER

V.L. Golovtsov, L.N. Uvarov, D. Acosta[1)], D. Holmes[1)], K. Kotov[1)], A. Madorsky[1)], S.M. Wang[1)]

[1)] *University of Florida, USA*

A fast three-dimensional Track-Finding Processor was designed for the Level-1 trigger of the CMS endcap muon system. The Track-Finding Processor is implemented as 12 Sector Processors (SP), each of which identifies up to three best muons in a 60-degree azimuthal sector [1]. The purpose of the Track-Finding Processor is to link trigger primitives (track segments) from individual muon stations (four endcap stations ME1-4 and two barrel overlap regions MB1-2) into complete tracks, measure the transverse momentum P_t from the sagitta induced by the magnetic bending, and report the number and quality of tracks to the Level-1 Muon Trigger. The maximum number of track segments collected by one SP is 15 per 25 ns bunch crossing.

Block diagram of the SP logic in Fig. 1 includes:

1. Sector Receiver (SR), which receives local charge track information for 15 muons via optical links. This information is then synchronized and reformatted within the SR (*via* look-up tables) into angular variables for the muons: azimuthal angle φ, local bent angle in φ (φb) and pseudo-rapidity η.

2. Five Extrapolation Units (EU), where all possible pairwise combinations of track segments are tested for consistency with a single track. Each EU takes spatial information from two track segments in different stations and tests if those two segments are compatible with a muon originating from the nominal collision vertex with a curvature consistent with magnetic bending in that region.

3. Three Track Assembly Units (TAU) to examine all outputs of the EUs and determine if any two track segment pairs belong to the same muon. If so, those segment pairs are combined and rank is assigned based on the muon stations involved. For this SP design, stations ME2 and ME3 are the key stations. A valid trigger in the end-cup region must have a hit in one of these two stations. The output of the EUs can be separated into three streams: two for patterns keying off ME2 and ME3 in the end-cup region, and one for pattern keying off ME2 in the end-cup or/and barrel overlap region. Up to three tracks may be found per data stream, nine tracks in total for all three streams.

4. Final Selection Unit, which selects the best three muon candidates. It also features cancellation logic for redundant tracks.

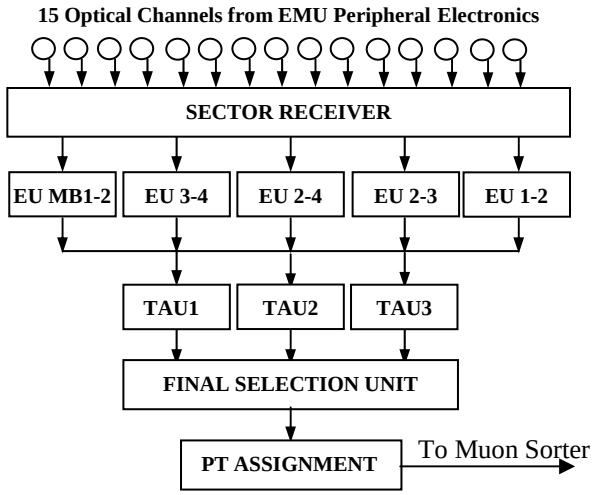

Fig. 1. Sector Processor block diagram

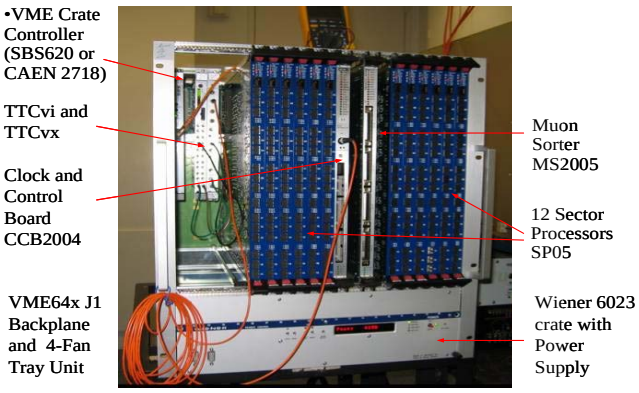

Fig. 2. Track-Finding Crate

5. Assignment Unit, which measures the track parameters of the best three selected muon candidates.

Finally, the best three muon candidates are sent to the Muon Sorter that in turn selects the best four candidates within all tracks of the 12 Sector Processors and sends them to the Global L1 Muon Trigger.

Figure 2 shows a fully assembled Track-Finding Crate with 12 Sector Processors and Muon Sorter.

References

1. D. Acosta *et al.*, Nucl. Instr. Meth. A **496**, 64 (2003).

CONTENTS

NUCLEAR AND ATOMIC PHYSICS

NEW PROJECTS

METODICAL AND APPLIED RESEARCHES